Phase Multipath Estimation for Global Positioning System (GPS) Using Signal-to-Noise-Ratio (SNR) Data

by
Francesca Sciré Scappuzzo

B.S. and M.Eng., *Summa Cum Laude* , Electrical Engineering
University of Catania, 1989

Submitted to the Department of
Earth, Atmospheric, and Planetary Sciences
in Partial Fulfillment of the Requirements for the Degree of

Master of Science in Earth and Planetary Sciences

at the

MASSACHUSETTS INSTITUTE OF TECHNOLOGY

May 1997

Signature of Author _____
Department of Earth, Atmospheric and Planetary Sciences
May, 1997

Certified by _____
Thomas A. Herring
Associate Professor of Geophysics
Thesis Supervisor

Accepted by _____
Thomas H. Jordan
Department Head

This thesis is dedicated to

Prof. Sebastiano Barbarino
Associate Professor of Electromagnetics
University of Catania, Italy

... perche' il Suo amore per lo studio e per la scienza,
la Sua encomiabile dedizione all'insegnamento e
la Sua grande umanita'
siano da esempio ai Suoi studenti e colleghi
ed ispirino le generazioni a venire ...

Phase Multipath Estimation for Global Positioning System (GPS) Using Signal-to-Noise-Ratio (SNR) Data

by

Francesca Sciré Scappuzzo

Submitted to the Department of Earth, Atmospheric, and Planetary Sciences
in Partial Fulfillment of the Requirements for the Degree of
Master of Science in Earth and Planetary Sciences

Abstract

A method for the estimation of GPS multipath phase error is proposed. Because the Signal-to-Noise-Ratio (SNR) of the GPS measurements is strictly related to the multipath phase error, the algorithm implemented manipulates the SNR of the received GPS signal itself to perform the estimation. No additional information about the geometry of the surroundings of the receiving station or the weather conditions at the time of acquisition are needed. The scattering phenomenon is generally due to the composition of several single multipath contributions, each one characterized by a specific frequency. The algorithm takes advantage of this property to decompose the variations of the SNR into individual components in an iterative procedure. The contributions due to each frequency are then superimposed to obtain the total multipath phase error.

The algorithm was applied to several data sets affected by strong multipath to test the performance of the method. Spectral and statistical analyses were performed to compare the observed phase residual obtained from the GPS measurements and the estimated multipath phase error retrieved by the algorithm.

In most of the cases analyzed, a broad-band coherence function between the observed phase error and the estimated multipath phase error was found in presence of strong multipath. This suggests that the effects of multiple reflectors are correctly retrieved by the proposed algorithm.

The set of data which show the highest coherence have multipath frequencies between 0.001 and 0.01 Hz. Therefore, the estimation algorithm presents good performances when the reflectors are located at a distance between 5.50 m and 55.0 m from the receiving antenna, for an elevation angle of about 10° and a rate of change of the elevation angle of 0.1 mrad/sec. The high coherence is confirmed by the statistical analysis, which shows a significant decrease of the RMS of the phase residual after the multipath correction.

At lower frequencies it was found that the performance of the algorithm depends on the receiver type, the antenna gain and the weather conditions.

Thesis supervisor: Thomas A. Herring

Title: Associate Professor of Geophysics

Contents

Chapter 1

Introduction

Over the last decade the Global Positioning System (GPS) has become a very useful tool for several scientific and civilian applications, playing a leading role in geodynamic studies, from a local to a global scale. High accuracy GPS is being extensively used in large scale dynamics of the Earth, such as plate tectonics, Earth's rotation studies, sea-level change, post-glacial rebound, tidal effect and sea-surface topography.

The extensive utilization of GPS in geosciences is mainly due to the recent significant improvements of the techniques involved in high-accuracy GPS positioning. The relatively low costs of post processing software and new GPS receivers and their availability and portability during field work, make the GPS a very convenient and useful instrument. The international collaboration in the GPS scientific community is also sensibly contributing to such a wide diffusion of the system.

However, even though research and technology on high accuracy GPS positioning have rapidly developed, there is still a broad range of critical issues that scientists and engineers need to exploit. Most of the new questions arise from the fact that the fields of application and the accuracy required today for positioning instruments,

have greatly overcome the purposes for which GPS was originally designed, producing a series of new challenging riddles.

One of the main problems to be faced when performing high-precision GPS measurements is the error in positioning due to the occurrence of multipath. This phenomenon is caused by the interference of multiple reflections with the direct EM signal transmitted by the satellite, and represents a considerable source of error in the GPS carrier phase observations (fig. 1.1).

The level and characteristics of the noise deriving from multipath depends upon the geometry of the surrounding of the receiving antenna (presence of buildings, trees, towers, and the mount itself), the reflectivity of nearby reflectors, the elevation angle of the satellite at the time of acquisition, and other parameters which might sensibly change with weather conditions and time.

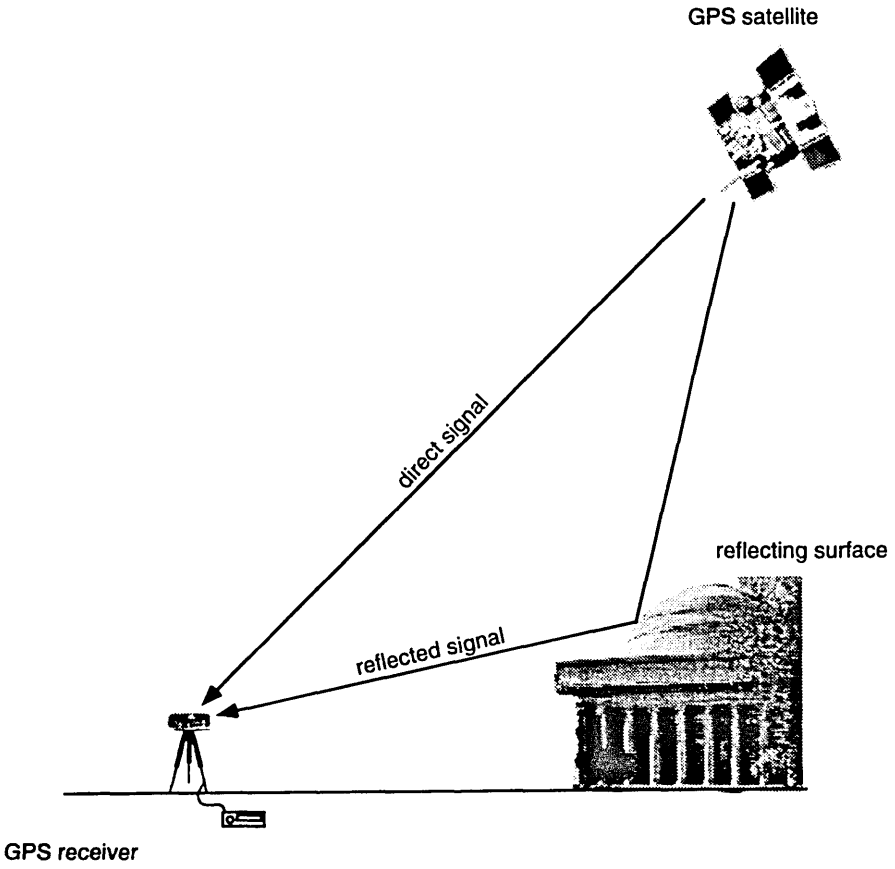

Fig. 1.1: GPS multipath phenomenon

Due to the variability of the parameters involved, it is very difficult or even impossible to predict multipath with sufficient accuracy using a deterministic approach such as electromagnetic modeling or analog techniques.

1.1 Objectives

The objective of the study presented in this thesis is to estimate the multipath phase error from the SNR (Signal-to-Noise-Ratio) data, without using any a priori information about the location of the receiving station, the weather conditions and the geometry of the surroundings. This method manipulates the SNR of the received signal, which in GPS data processing is usually only used as an indicator of the data reliability and is not used for the positioning itself.

In order to test the performance of the estimation algorithm for different sites and different GPS receiver types (Ashtech Z-12, Trimble SSE and SSI, and Turbo-Rogue SNR8000), the method was applied to a large number of data sets, chosen for the strong multipath in the phase error measurements.

1.2 Outline

In chapter 2 a mathematical representation of the multipath phenomenon is derived. The dependency of the multipath phase error on the SNR, the antenna gain, the multipath frequency and the reflection coefficient of the reflecting surface is discussed.

After a brief introduction on the basic operation of GPS receivers, chapter 3 focuses on how a GPS signal corrupted by multipath is processed by different receivers.

The algorithm for the estimation of the multipath phase error from the SNR data is described and discussed in chapter 4.

In order to test how well the estimated multipath phase error matches the phase error observed in the GPS measurements, statistical and spectral analyses were performed. The theory of these analyses is presented in chapter 5.

The estimation algorithm was applied to several data sets affected by significant multipath effects. Its performance was studied comparing the results obtained in the different cases. The results of this analysis are discussed in chapter 6 and the conclusions are drawn in chapter 7.

The plots relevant to the estimation and spectral analysis of the 42 data sets studied are collected in appendix A. In appendix B, the tables containing the results of the statistical analysis are shown. The matlab programs implemented for the analysis can be found in appendix C.

Chapter 2

Multipath Modeling in phasor space. Relationship between Multipath Phase Error and SNR

2.1 Introduction

The correction of GPS multipath phase errors is one method of improving the accuracy of GPS measurements. In literature several approaches for GPS multipath correction can be found. Hajj (1990) developed an algorithm to produce maps of the multipath for a given environment around the receiving antenna. Unfortunately, multipath errors are very sensitive to parameters such as the geometry or the reflection coefficient of nearby reflectors which strongly depend on the particular weather condition and season. This limits the efficiency of this method in predicting the multipath effects with time.

An easy solution to the multipath problem consists in selecting a proper site, far from possible reflectors. However in many applications it is not possible to choose the site for the GPS positioning. Other ways to minimize multipath consist in the design of antennas which reduce back-plane gain. Receivers manufacturers are trying to correct multipath using particular selections of the cross-correlation function. A branch of research on GPS multipath, is now oriented toward the analysis of the data itself for the error estimation in post-processing mode (Georgeadu and Kleusberg, 1988). One new promising method is to compute the multipath error by using the SNR, as in Axelrad et al., (1994).

The circumstances in which the measurements are acquired are usually recorded on the log sheets of the GPS measurements, which report the geometry of the site, the weather conditions during the data acquisition, etc. But to gather the correct information about the GPS receiver surroundings and relevant measurements can be extremely difficult and inefficient. The possibility to correct for multipath contribution to the phase error without a priori information is particularly important for applications that require networks of GPS stations distributed over large areas on the globe, such as geosciences.

The multipath phase error estimation algorithm proposed in this thesis makes use of the SNR of the data itself, without the need for additional information about the geometry and conditions of the surrounding of the receiving antenna. The method for the estimation of $\delta\Phi$, is based on the spectral analysis of the SNR information provided by the GPS receiver. We assume that the multipath effects are due to multiple reflectors, which will each have a particular frequency. Through spectral decomposition of the SNR we can isolate the contributions of each reflector. Inverting for the phase error of all the single contributions and superimposing the results together, we obtain the total multipath correction (total multipath phase error).

This chapter is devoted to the definition of the theoretical model of the multipath phenomenon used in the multipath phase error estimation algorithm. The important relationship between the multipath phase error to be estimated , $\delta\Phi$, and the SNR data, used as input of the estimation algorithm, is discussed in section 2.2.2. The dependency of the signal strength (A_C) and the multipath phase error ($\delta\Phi$) on the phase of the multipath signal, on the multipath frequency and on the reflection

coefficient of the reflecting surface is derived in sections 2.2.4 and 2.2.5. The influence of the antenna gain on the signal strength is shown in sections 2.2.6.

2.2 Multipath representation

2.2.1 Multipath Modeling in the Phasor Space

In this section the mathematical model of the multipath phase error used for the estimation algorithm is derived.

The multipath phase error, $\delta\Phi$, is defined as the angle between the direct signal, $S_d(t)$, and the total received signal, $S_c(t)$, which is the composition of the direct signal and the multipath signal, $S_m(t)$. The signals can be written as:

$$\vec{S}_d(t) = A_d(t) \cdot e^{i\left(\omega \cdot t + \phi_d\right)} \qquad [2.1]$$

$$\vec{S}_m(t) = \sum_i A_{m_i}(t) \cdot e^{i\left(\omega \cdot t + \phi_{m_i}\right)} \qquad [2.2]$$

$$\vec{S}_c(t) = A_c(t) \cdot e^{i\left(\omega \cdot t + \phi_c\right)} = A_d(t) \cdot e^{i\left(\omega \cdot t + \phi_d\right)} + \sum_i A_{m_i}(t) \cdot e^{i\left(\omega \cdot t + \phi_{m_i}\right)} \qquad [2.3]$$

where:

A_d = Amplitude of the direct signal

A_{mi} = Amplitude of the i-th multipath contribution

A_c= Amplitude of the total measured signal

ϕ_d = Phase of the direct GPS signal.

ϕ_{mi} = Phase of the multipath signal due to the i-th reflector.

ϕ_c = Phase of the total measured GPS signal.
$\omega = 2\pi f$ and f is the carrier frequency (L_1 or L_2)

In figure 2.1 the total signal measured by the receiver, the direct signal and the signal due to the composition of several multipath reflections are shown in the phasor space.

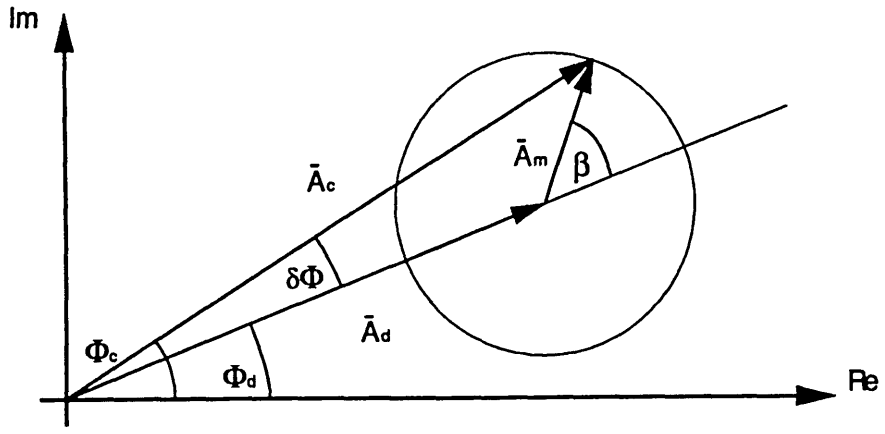

Figure 2.1: Phasor diagram of the GPS signal. $\delta\Phi$ is the multipath phase error in presence of a single reflector. It depends on the amplitude ($A_m=R_f A_d$) and phase ($\phi_m=\phi_d+f_m t$) of the multipath phasor.

In the phasor space the signals of fig. 2.1 can be written as:

$$\bar{A}_d = |A_d| \cdot e^{i\phi_d} \qquad [2.4]$$

$$\bar{A}_m = \sum_i |A_{m_i}| \cdot e^{i\phi_{m_i}} \qquad \phi_{m_i} = \phi_d + \beta_i = \phi_d + (f_{m_i} \cdot t) \qquad [2.5]$$

$$\bar{A}_C = |A_C| \cdot e^{i\phi_C} \qquad \phi_c = \phi_d + \delta\Phi \qquad [2.6]$$

where:

β_i = Phase of the i-th multipath signal with respect to the direct GPS signal.

f_{mi} = Multipath frequency relevant to the i-th contribution, such that $\beta_i = f_{mi}\, t + \beta_{oi}$

β_{oi} = Phase of the i-th multipath signal with respect to the direct GPS signal at the initial time t=0.

$\delta\Phi$= Total multipath Phase Error

R_{fi}= Reflection coefficient for the i-th reflector. $|A_{mi}| = R_{fi}\ |A_d|$.

The composite signal is given by:

$$\vec{A}_c = \vec{A}_d + \vec{A}_{mi} = A_d \cdot e^{j\phi_d} + \sum_i R_{fi} \cdot A_d \cdot e^{j(\phi_d + \beta_i)} \qquad [2.7]$$

The multipath phase error depends on the amplitude of the multipath signal and its phase. Because β changes with time as a function of the multipath frequency f_m, the multipath phasor spins around the tip of the direct signal, producing positive and negative values of the phase error $\delta\Phi$.

If we rotate the diagram of figure 2.1 as in figure 2.2, so that $\phi_d = 0$ and A_d is along the Real axis, the total strength of the received signal and the phase error can be written as:

$$|A_c| = A_d \sqrt{(1 + \sum_i R_{f_i} \cdot \cos\beta_i)^2 + (\sum_i R_{f_i} \cdot \sin\beta_i)^2} \qquad [2.8]$$

$$\delta\Phi = \tan^{-1}\left[\frac{\sum_i R_{f_i} \cdot \sin\beta_i}{1 + \sum_i R_{f_i} \cdot \cos\beta_i}\right] \qquad [2.9]$$

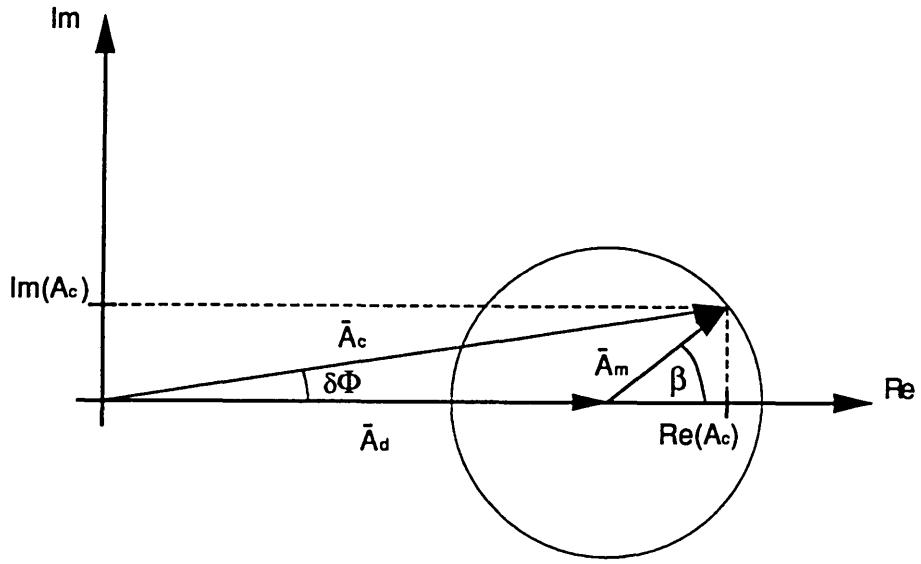

Figure 2.2: Phasor diagram 2.1 for $\phi_d = 0$ and A_d real.

2.2.2 Relationship between the signal strength and the multipath phase error.

The amplitude of the composite signal A_c is related to the total phase error, $\delta\Phi$ through the angle β, phase of the multipath vector A_m with respect the direct signal A_d (fig. 2.1, formulas [2.8] and [2.9]).

To describe the phenomenon, we consider the simple case of a single reflector (i=1). (The same theory is applicable to multiple reflections, considering the superposition of the multipath contribution).

Because the multipath signal rotates around the tip of the direct signal , with frequency f_m , the amplitude of A_c oscillates between a maximum value A_d+A_m and a minimum value, A_d-A_m. The change in amplitude of A_c due to the rotation of A_m can be easily deduced from 2.3. A_c is plotted as function of time for different values of β. Every time A_c presents a maximum (for $\beta=0°$) or a minimum (for $\beta=180°$), the multipath phase error is zero. The maximum phase error occurs for $\beta=90°$ and $\beta=270°$. (see fig. 2.1 and formula [2.9]).

In table 2.1 the values of A_c and $\delta\Phi$ as functions of β are summarized . It is important to notice that A_c can assume the same amplitude for different values of β (for example for $\beta=90°$ and $\beta=270°$). This produces an uncertainty in the determination of the sign of $\delta\Phi$, which represent a very critical problem in the multipath phase error estimation algorithm.

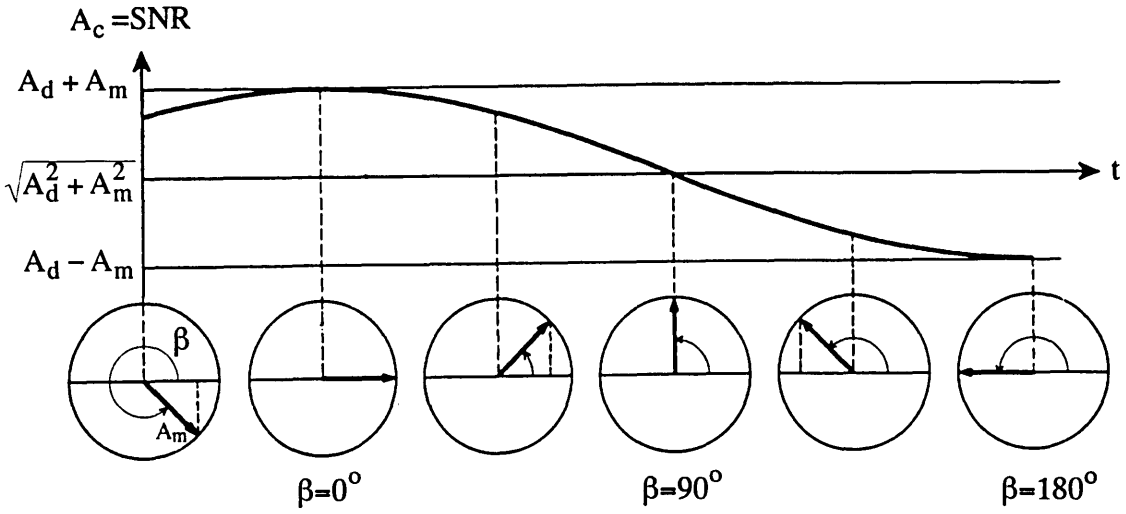

Figure 2.3: Variation of A_c with the time, as function of the angle β.

$\beta = f_m t = 0°$	$\Rightarrow$ Phase error	$\delta\Phi = 0°$	
	SNR	$A_c = A_d + A_m$	(Max SNR)
$\beta = f_m t = 90°$	$\Rightarrow$ Phase error	$+\delta\Phi = \tan^{-1}\left[\frac{A_m}{A_d}\right]$	(Max $\delta\Phi$)
	SNR	$A_c = \sqrt{A_d^2 + A_m^2}$	
$\beta = f_m t = 180°$	$\Rightarrow$ Phase error	$\delta\Phi = 0°$	
	SNR	$A_c = A_d - A_m$	(Min SNR)
$\beta = f_m t = 270°$	$\Rightarrow$ Phase error	$-\delta\Phi = -\tan^{-1}\left[\frac{A_m}{A_d}\right]$	(Min $\delta\Phi$)
	SNR	$A_c = \sqrt{A_d^2 + A_m^2}$	

Table 2.1 : Signal strength, A_c and multipath phase error, $\delta\Phi$, as functions of β. In section 2.2.3 it is shown that A_c and the Signal-to Noise-Ratio (SNR) actually represent the same quantity in the GPS receiver processing. The relationship between the SNR and $\delta\Phi$, is crucial for the phase error estimation algorithm presented in chapter 4.

2.2.3 The SNR and the measured signal strength, A_c

In table 2.1 the amplitude of the received signal is assumed to be equal to the value of the SNR computed in the receiver. This section shows why A_c and SNR in the receiver represent the same quantity.

From formula [2.3], considering the PRN code function, the signal received by the GPS ground antenna can be expressed as:

$$\vec{S}_c(t) = A_d(t) \cdot P(t) \cdot e^{i\left(\omega \cdot t + \phi_d\right)} + \sum_i A_{m_i}(t) \cdot P(t+\delta) \cdot e^{i\left(\omega \cdot t + \phi_{m_i}\right)} \qquad [2.10]$$

where:

P(t) is the PRN code (±1)

δ= multipath time delay

The signal internally generated in the receiver is given by:

$$\vec{S}_{LO}(t) = P(t+\tau) \cdot e^{i(\omega_{LO} \cdot t + \theta)} \qquad [2.11]$$

where:

ω_{LO} = Local Oscillator frequency

τ = Tracking error of the Delay Lock Loop (DLL)

θ = Tracking error of the Phase Lock Loop (PLL)

In the receiver the GPS signal [2.10] is down-converted, cross-correlated with the signal internally generated, and filtered. The result of this sequence of operations gives the equations [2.4], [2.5] , and [2.6] introduced at the beginning of this chapter.

In particular, A_c represents the normalized average correlation coefficient, which is the ratio signal/noise. In formulas:

$$A_C = \left(S_C(t) \cdot S_{LO}(t)\right) = \textit{normalized corr. coeff.} \equiv \text{SNR} \qquad [2.12]$$

where:

$$SNR = \frac{Signal\ Strength}{Noise} \qquad [2.13]$$

However, the precise normalization used in the receiver is not always the same, but depends on the particular manufacturer. We can assume that the values of the correlation coefficient are normalized by the expected correlation coefficient when only noise is present.

It follows that the SNR is equivalent to the signal strength of the total composite signal, A_c. Therefore, all the properties we found for A_c are valid also for the SNR. In table 2.1 the values of the SNR and $\delta\Phi$ as function of β were summarized.

2.2.4 Multipath frequency

The multipath phase error depends on the multipath frequency. The implications of this dependency are very important in the spectral analysis performed for the multipath phase error estimation algorithm described in the following sections.

As already shown in section 2.2.1, the phase of the i-th multipath signal A_{mi} is given by [2.5] :

$$\phi_{m_i} = \phi_d + \beta_i \qquad [2.14]$$

where

$$\beta_i = f_{m_i} \cdot t \qquad [2.15]$$

Substituting 2.15 in 2.9 we obtain an expression of $\delta\Phi$ as a function of f_m :

$$\delta\Phi(f_{m_i}) = \tan^{-1}\left[\frac{R_{f_i} \cdot \sin(f_{m_i})}{1 + R_{f_i} \cdot \cos(f_{m_i} t)}\right] \qquad [2.16]$$

The frequency of the i-th multipath error depends on the carrier frequency, the distance of the i-th reflector and the receiving antenna, the rapidity of the change in elevation angle of the satellite and the elevation angle.

For an horizontal reflector at distance h_i below the antenna, the multipath frequency is (Leich, 1995):

$$f_{m_i} = \frac{2 \cdot h_i}{\lambda} \cdot \sin \psi \cdot \left| \frac{\partial \psi}{\partial t} \right| \qquad [2.17]$$

where:

h = Distance between the antenna phase center and the reflector

λ = Wavelength

ψ = Zenith angle = (90° - Elevation angle)

One of the consequences of equations [2.16] and [2.17] is that $\delta\Phi$ varies with time due to changes of the elevation angle, as the satellites rises or sets.

Moreover, the multipath phase error, $\delta\Phi$, presents a particular frequency component f_{mi} for each reflector located at a certain height below h_i from the receiving antennas. From [2.8] and [2.9] we can deduce that A_c (=SNR) and $\delta\Phi$ present the same spectral content, being both functions of $\beta=f_m t$.

Therefore, the multipath phase error $\delta\Phi_i$ due to a particular reflector can be identified by the spectral analysis of the total signal strength A_c (SNR).

The method for the estimation of the total composite $\delta\Phi$, is based on the spectral analysis of the SNR information provided by the GPS receiver. We assume that the multipath effects are due to multiple reflectors, which will each have their own frequency. Through spectral decomposition of the SNR we can isolate the contributions of each reflector. Inverting for the phase error of all the single contribution and adding them together, we obtain the total multipath correction, as it will be shown in more detail in chapter 4.

2.2.5 Influence of the Reflection coefficient on the multipath phase error

The multipath phase error $\delta\Phi_i$ is a function of the Reflection Coefficient R_{fi}, as shown in formula [2.9]. The reflection coefficient depends on the electromagnetic characteristics of the reflecting surface, such as permittivity (ε), permeability (μ), and conductivity (σ). It depends also on the frequency of the electromagnetic signal and the elevation angle of the satellite θ.

In this section we derive the expression of the reflection coefficient R_f for one single reflector as a function of ε, μ, and σ, and discuss how these electromagnetic properties of the reflector influence the multipath phase error.

The geometry of our problem is shown in figure 2.4, where $\mathbf{E}_{inc}$ is the incident electromagnetic wave transmitted by the GPS satellite, $\mathbf{E}_t$ is the EM wave refracted into the material and $\mathbf{E}_r$ is the EM wave reflected by the surface.

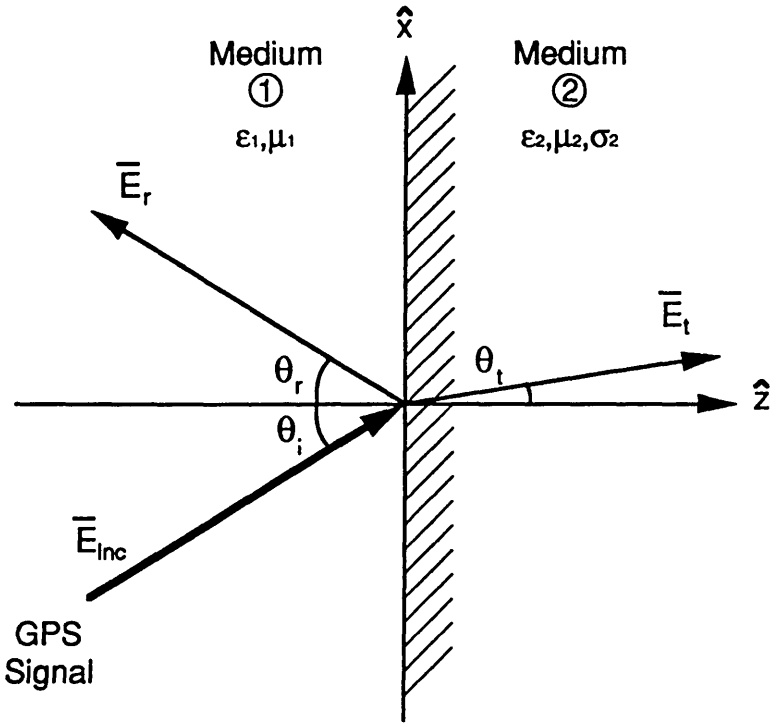

Figure 2.4: Electromagnetic plane waves propagating in medium 1 (air) and medium 2 (reflector).

The incident electromagnetic plane wave emitted by the satellite, propagating in medium 1 toward medium 2, can be written as:

$$\overline{E}_{inc} = Eo \cdot e^{-i(\omega \cdot t - \bar{k}_1 \cdot \bar{r}_{inc})} \qquad [2.18]$$

The plane wave reflected by the surface, propagating in medium 1 away from medium 2, can be written as:

$$\overline{E}_r = E_{ro} \cdot e^{-i(\omega \cdot t - \bar{k}_1 \cdot \bar{r}_r)} \qquad [2.19]$$

where :

$\bar{k}$ = Wave number

$$\bar{k} = \beta + i\alpha \qquad [2.20]$$

$$k^2 = i\omega\varepsilon\mu(\sigma - i\varepsilon\omega) = \omega^2\varepsilon\mu + i\mu\sigma\omega$$

Substituting k([2.20]) in [2.18] and [2.19] we obtain:

$$\overline{E}_{inc} = Eo \cdot \left(e^{-\alpha \cdot r_{inc}}\right) \cdot e^{-i(\omega \cdot t - \beta \cdot r_{inc})}$$
$$\overline{E}_r = E_{ro} \cdot \left(e^{-\alpha \cdot r_r}\right) \cdot e^{-i(\omega \cdot t - \beta \cdot r_r)} \qquad [2.21]$$

where:

α = Attenuation Coefficient (Np/m)
β = Propagation Coefficient (rad/m)
$e^{-(\alpha r)}$ = Attenuation factor
$e^{-(\beta r)}$ = Propagation factor

Solving [2.20] for α and β, the Attenuation Coefficient and the Propagation Coefficient can be written as (Balanis, 1989):

$$\alpha = \omega \sqrt{\frac{\varepsilon\mu}{2}\left[\sqrt{1+\frac{\sigma^2}{\varepsilon^2\omega^2}}-1\right]} \qquad [2.22]$$

$$\beta = \omega \sqrt{\frac{\varepsilon\mu}{2}\left[\sqrt{1+\frac{\sigma^2}{\varepsilon^2\omega^2}}+1\right]} \qquad [2.23]$$

The term $e^{-(\alpha r)}$ represents the attenuation of the electromagnetic wave in the material, and the exponential $e^{-j(\beta r)}$ represents the propagation term. Note that for air (medium 1 where the GPS signal propagates), $\alpha_1 \approx 0$, and therefore $e^{-(\alpha r)} \approx 1$.

The electric fields of the incident and reflected wave can be decomposed in a component perpendicular to the plane of incidence (horizontal polarization) and a component parallel to the plane of incidence (vertical polarization). In formulas:

Horizontal Polarization:

$$\begin{aligned} \overline{E}_{inc}^{h} &= \left[E_o^h \cdot e^{-i\beta_1(x\sin\theta_i + z\cos\theta_i)}\right]\cdot \hat{y} \\ \overline{E}_{r}^{h} &= \left[E_{ro}^h \cdot e^{-i\beta_1(x\sin\theta_r - z\cos\theta_r)}\right]\cdot \hat{y} \end{aligned} \qquad [2.24]$$

Vertical Polarization:

$$\begin{aligned} \overline{E}_{inc}^{v} &= \left[E_o^v \cdot e^{-i\beta_1(x\sin\theta_i + z\cos\theta_i)}\right]\cdot (\hat{y}\cos\theta_i - \hat{z}\sin\theta_i) \\ \overline{E}_{r}^{v} &= \left[E_{ro}^v \cdot e^{-i\beta_1(x\sin\theta_r - z\cos\theta_r)}\right]\cdot (\hat{y}\cos\theta_r + \hat{z}\sin\theta_r) \end{aligned} \qquad [2.25]$$

where:

θ_i = Incidence angle

θ_r = Reflection angle

The Fresnel Reflection Coefficient for the horizontal (perpendicular) polarization is given by:

$$R_h = \frac{E_r^h}{E_{inc}^h} = \frac{\eta_2 \cos\theta_i - \eta_1 \cos\theta_t}{\eta_2 \cos\theta_i + \eta_1 \cos\theta_t} \approx \frac{\cos\theta_i - \dfrac{\eta_1}{\eta_2}}{\cos\theta_i + \dfrac{\eta_1}{\eta_2}} \qquad [2.26]$$

The Fresnel Reflection Coefficient for the vertical (parallel) polarization is given by:

$$R_v = \frac{E_r^v}{E_{inc}^v} = \frac{-\eta_1 \cos\theta_i + \eta_2 \cos\theta_t}{\eta_1 \cos\theta_i + \eta_2 \cos\theta_t} \approx \frac{-\cos\theta_i + \dfrac{\eta_2}{\eta_1}}{\cos\theta_i + \dfrac{\eta_2}{\eta_1}} \qquad [2.27]$$

where:

θ_t = Refraction angle

η = Intrinsic impedance of the medium.

The angles of Incidence, Reflection and Refraction, of fig. 2.4 are related by the Snell's laws:

$$\theta_r = \theta_i \qquad \text{Snell's law of reflection} \qquad [2.28]$$

$$k_1 \sin\theta_i = k_2 \sin\theta_t \qquad \text{Snell's law of refraction} \qquad [2.29]$$

The Intrinsic Impedance of a medium is given by:

$$\eta = \frac{E}{H} = \begin{cases} \sqrt{\dfrac{\mu}{\varepsilon}} & \text{for dielectric materials} \\ \sqrt{\dfrac{i\omega\mu}{\sigma + i\omega\varepsilon}} & \text{for conductive materials} \end{cases} \qquad [2.30]$$

In our case, the medium 1, where the incident and reflected signal propagate, is air. For air the intrinsic impedance can be considered as the one for dielectric materials.

Depending on the electromagnetic characteristics of the reflector, we can distinguish 3 cases, which represent 3 different categories of materials.

Case I: Good Dielectrics

If the reflector (medium 2) is a good dielectric at the frequency of the GPS signals (Microwaves) we obtain:

$$\frac{\sigma_2^2}{\varepsilon_2^2\omega^2} << 1 \qquad \frac{\eta_1}{\eta_2} = \frac{\sqrt{\frac{\mu_1}{\varepsilon_1}}}{\sqrt{\frac{\mu_2}{\varepsilon_2}}} \qquad \text{and} \qquad R_f = \left\{ \begin{array}{l} R_h = \dfrac{\sqrt{\frac{\mu_2}{\varepsilon_2}}\cos\theta_i - \sqrt{\frac{\mu_1}{\varepsilon_1}}\cos\theta_t}{\sqrt{\frac{\mu_2}{\varepsilon_2}}\cos\theta_i + \sqrt{\frac{\mu_1}{\varepsilon_1}}\cos\theta_t} \\ R_v = \dfrac{-\sqrt{\frac{\mu_1}{\varepsilon_1}}\cos\theta_i + \sqrt{\frac{\mu_2}{\varepsilon_2}}\cos\theta_t}{\sqrt{\frac{\mu_1}{\varepsilon_1}}\cos\theta_i + \sqrt{\frac{\mu_1}{\varepsilon_2}}\cos\theta_t} \end{array} \right\}$$

Case II: Quasi-conductors

If he reflector is a quasi-conductor at the frequency of the GPS signals, it follows that:

$$\frac{\sigma_2^2}{\varepsilon_2^2\omega^2} \approx 1 \qquad \frac{\eta_1}{\eta_2} = \frac{\sqrt{\frac{\mu_1}{\varepsilon_1}}}{\sqrt{\frac{i\omega\mu_2}{\sigma_2 + i\omega\varepsilon_2}}} \qquad \text{and} \qquad R_f = \left\{ \begin{array}{l} R_h = \dfrac{\sqrt{\frac{i\omega\mu_2}{\sigma_2 + i\omega\varepsilon_2}}\cos\theta_i - \sqrt{\frac{\mu_1}{\varepsilon_1}}\cos\theta_t}{\sqrt{\frac{i\omega\mu_2}{\sigma_2 + i\omega\varepsilon_2}}\cos\theta_i + \sqrt{\frac{\mu_1}{\varepsilon_1}}\cos\theta_t} \\ R_v = \dfrac{-\sqrt{\frac{\mu_1}{\varepsilon_1}}\cos\theta_i + \sqrt{\frac{i\omega\mu_2}{\sigma_2 + i\omega\varepsilon_2}}\cos\theta_t}{\sqrt{\frac{\mu_1}{\varepsilon_1}}\cos\theta_i + \sqrt{\frac{i\omega\mu_2}{\sigma_2 + i\omega\varepsilon_2}}\cos\theta_t} \end{array} \right\}$$

In this case the reflector is not a good dielectric, nor a good conductor, having inter medium characteristics. The reflection coefficients (horizontal and vertical) can be determined using the general formulas [2.26] and [2.27] , respectively.

Case III: Good Conductors

If the reflector is a good conductor at the frequency of the GPS signals, considering the approximation of formulas [2.26] and [2.27] we obtain:

$$\frac{\sigma_2^2}{\varepsilon_2^2\omega^2} >> 1 \qquad \frac{\eta_1}{\eta_2} = \frac{\sqrt{\frac{\mu_1}{\varepsilon_1}}}{\sqrt{\frac{i\omega\mu_2}{\sigma_2 + i\omega\varepsilon_2}}} >> 1 \geq \cos\theta_i \qquad \text{and} \qquad R_f = \begin{Bmatrix} R_h \approx -1 \\ \\ R_v \approx +1 \end{Bmatrix}$$

Thus, for a very good conductor the magnitude of the reflection coefficients for horizontal (perpendicular) and vertical (parallel) polarization approaches unity. This implies that $A_m \approx A_d$ and, therefore, the multipath phase error, $\delta\Phi$, is very high.

It can be noticed that for a very good conductor the reflection coefficients become essentially independent of the angle of incidence.

In fig. 2.5 a summary of the electromagnetic properties of some materials at different frequencies is shown. (Kraus, 1992).

At microwave frequencies (at which GPS operates) sea water and wet rural ground are quasi-conductive, while dry ground and urban ground are in the dielectric region.

It is interesting to notice that because wet ground is more conductive than dry ground, it reflects the GPS signal better, producing a stronger multipath, even if the geometry of the antenna surroundings is maintained constant.

In general fresh water has a $\sigma = 10^{-3}$ mho/m while salt water has a much higher conductivity $\sigma = 4.0$ mho/m. Depending on the soil conditions (i.e. how much salt is in the soil) the ground presents different conductivity after rain.

Quartz (which is a good approximation to sandy soil) has a dielectric constant of 4 and, therefore, the reflection coefficients persent values between 0.3 and 0.6, depending on the incidence angle. At low elevations an increase of moisture

content might increase the reflection coefficient of 60%, so that the reflection coefficient is almost unity. (R_f=1).

This example suggests that the weather conditions might influence the performance of GPS measurements, because of the different multipath environment they can produce.

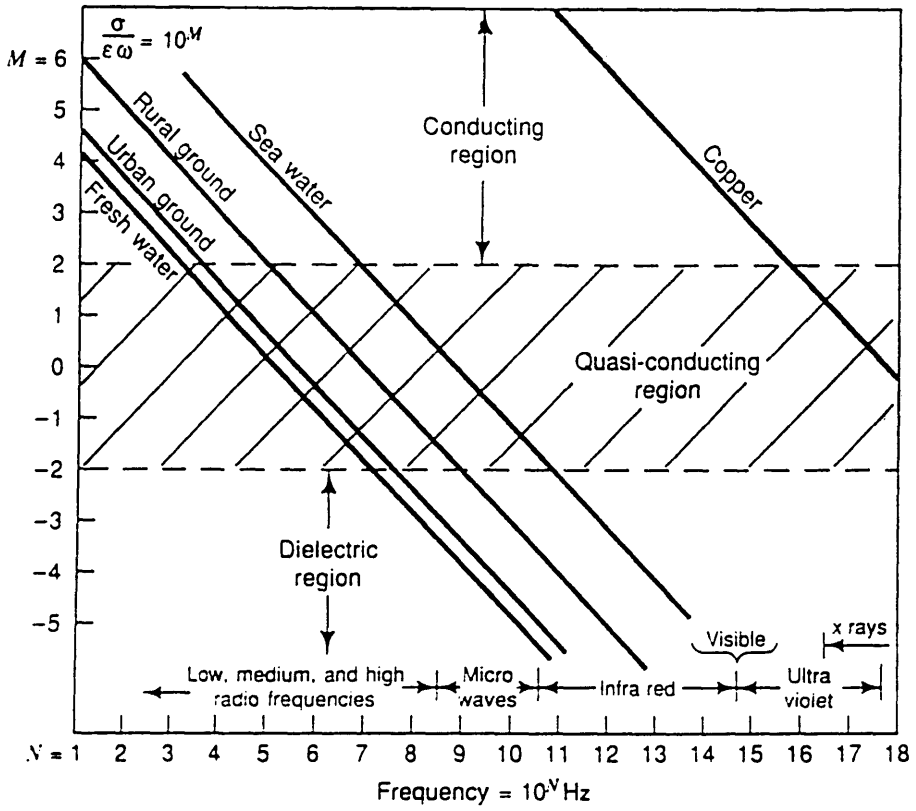

Fig. 2.5 Ratio $\sigma/\omega\varepsilon$ as a function of frequency for some common media.
At Microwave frequencies the most of the media shown are in the quasi-conductive region (urban ground, rural ground, sea water), with the exception of copper, which, being a metal, is a very good conductor even at higher frequencies, up to the Visible spectra. (Kraus, 1992)

2.2.6 Antenna Gain contribution to the Signal strength

In formula [2.8], A_c is described as a function of A_d, R_f and β. We already discussed its dependency on R_f and β. To complete this theoretical analysis of $\delta\Phi$ and A_c we need to study how the amplitude of the direct signal, A_d is influenced by A_c. The direct signal sent by the transmitting antenna, A_d, is a function of the GPS satellite antenna pattern, as will be discussed in section [2.2.6.1]. The total signal measured by the receiver, A_c, depends on the receiving antenna pattern (section [2.2.6.2]).

2.2.6.1 GPS Transmitting antenna gain and its influence on A_d

The purpose of a GPS transmitting antenna is to illuminate the Earth surface in the field of view of the satellite with a uniform strength.

The GPS transmitting antennas present patterns properly shaped to compensate for the path loss occurring at low elevation angles. The path loss of the signal is a function of the distance between the antenna phase center and the point on the surface of the Earth where the GPS receiver is located. The path loss is minimum when the satellite is at 90° elevation angle (at zenith) and is maximum when the satellite is at 0° elevation angle (at the horizon). A comparison between the pattern of an ideal antenna pattern and a typical GPS antenna is shown in fig. 2.6.

The edge of the Earth in view subtends an angle of approximately 27.74 ° from the GPS satellite altitude. The satellite antenna pattern extends behind the edge of the Earth, as shown in fig. 2.7. The transmission power from the satellite is not uniform with the angle of bore-sight of the satellite. The beam transmits more power toward the Earth's limbs, so that low elevation angle measurements on the ground will see more power.

The direct signal A_d is a function of the signal strength transmitted by the satellite, A_{trans} , and also of the transmitting antenna pattern $G_t(\theta,\phi)$, where θ and ϕ are elevation angle and azimuth of the satellite, respectively:

$$A_d = A_d(\theta,\phi) = A_{trans} \cdot G_t(\theta,\phi) \qquad [2.31]$$

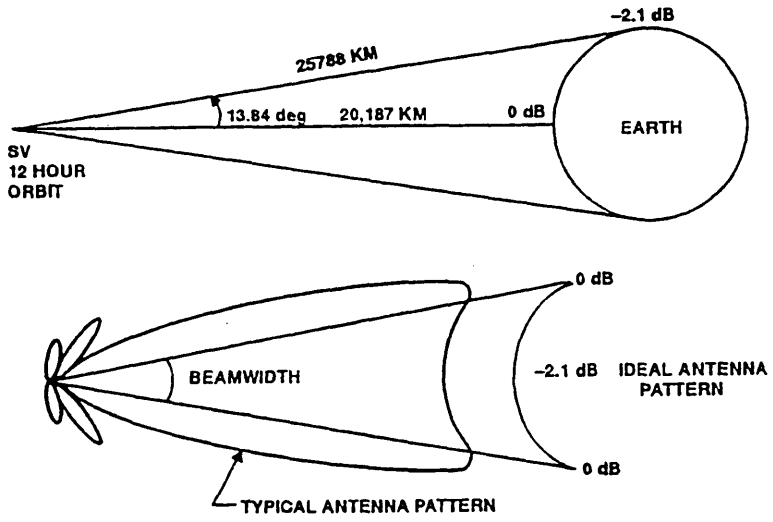

Figure 2.6: Comparison between the antenna patterns of an ideal GPS transmitting antenna and a typical one (Parkinson, 1996).

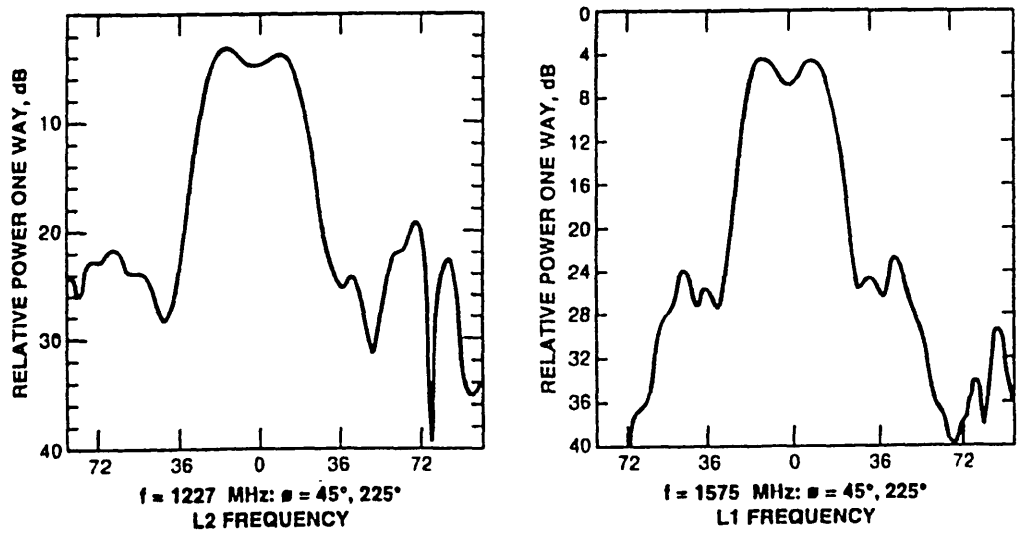

Figure 2.7: Antenna patterns of a GPS transmitting antenna at L_1 and L_2. Block II satellites (Parkinson, 1996).

2.2.6.2 GPS Receiving antenna gain and its influence on A_c

The signal strength received by the ground antenna (A_c) is also a function of the receiving antenna gain $G_{rec}(\theta,\phi)$.

GPS receiving antennas present a low directive gain, to acquire data simultaneously from as many visible satellites as possible. This implies that multipath signals scattered from any positive elevation cannot be rejected during the data acquisition.

The fact that GPS antennas have a non zero gain below the horizon, represents a trade-off between the need of rejection of reflected signals and the attempt to receive direct signals at low positive elevation angles with a reasonable gain.

But why are data incoming from low elevation angles so important? Data from low elevation angles are useful to reduce the correlation between estimates of the vertical component of the site position and estimates of the corresponding zenith propagation delay.

Because of this dependency of A_c on the receiving antenna, the pattern of the signal strength follows the antenna gain pattern, showing lower values for low elevation angles and higher values for high elevation angles.

The performance of each particular GPS user antenna has a great effect on the accuracy and precision of the GPS measurements. The antenna patterns of some of the most commonly used receiving antennas are shown in fig. 2.8 and 2.9 (Shupler and Clark, 1994) . These measurements were performed in an anechoic chamber and represent the results for the azimuthally averaged L1 amplitude patterns of the antennas, measured as the antenna zenith angle was varied.

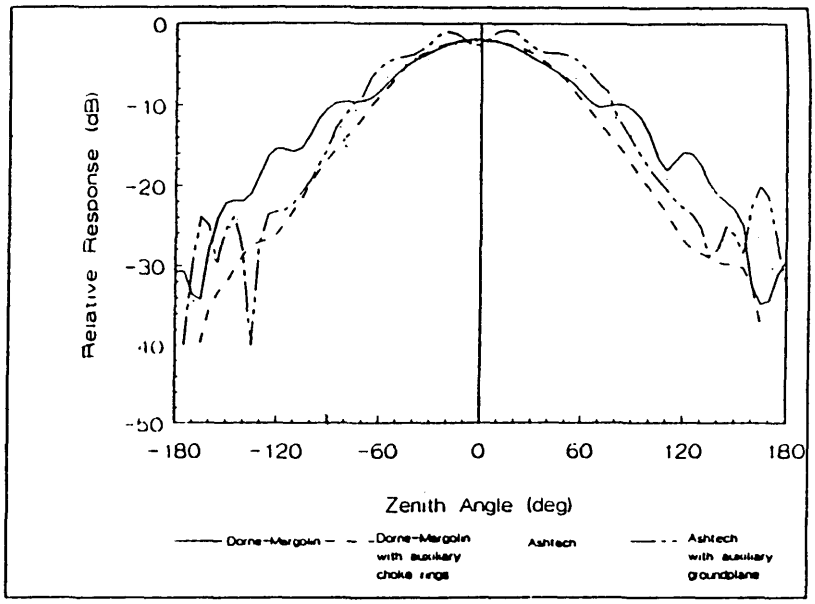

Figure 2.8: L1 relative amplitude patterns of GPS user antennas: Dorne-Margolin and Ashtech. (Shupler and Clark, 1994).

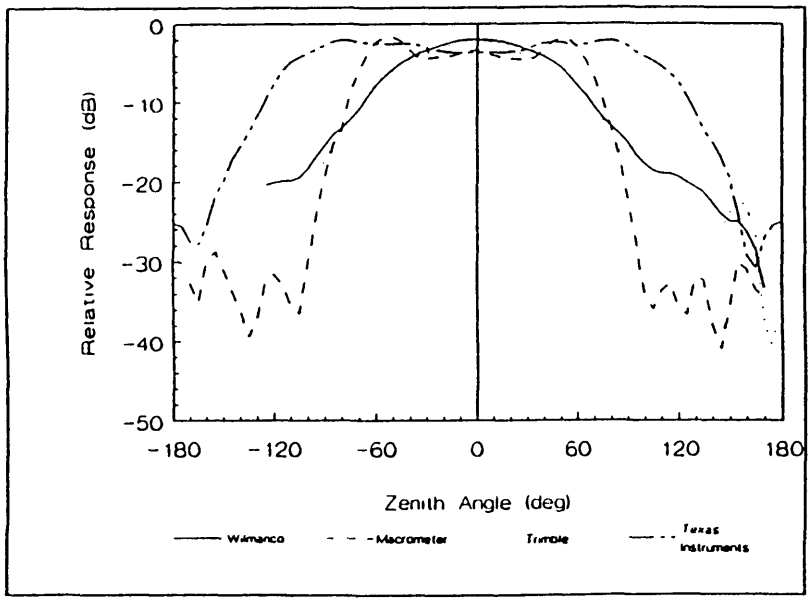

Figure 2.9: L2 relative amplitude patterns of GPS user antennas: Trimble, Texas Instruments, Macrometer and Wilmanco. (Shupler and Clark, 1994).

2.3 GPS receivers in presence of multipath

2.3.1 GPS receivers

Multipath reflections affect both, the signal amplitude (SNR) (section 2.2) and the carrier phase measured by the Phase Lock Loop (PLL). In this section a brief discussion on GPS receivers is presented, with particular attention to how multipath noise is processed in the DLL (Delay Lock Loop) and the PLL.

A GPS receiver is constituted of several components (hardware and software) that process the incoming signal from a GPS satellite.

The GPS carrier signal is biphase modulated with C/A and P-codes. When it is received by the antenna, it is first filtered by the receiver (in preprocessing mode) in order to eliminate unwanted RF (Radio Frequency) environment from the desired GPS signal band.

Because GPS signals are spread spectrum signals, it is necessary to up or down convert them in order to reallocate their spectrum. The Down-Converter in the receiver mixes the LOs (signals from the Local Oscillator), generated by the frequency synthesizer, with the amplified RF input to obtain a shift of the frequency spectrum of the signal to IF frequencies.

The IF signal obtained after down conversion, is then converted to a baseband signal composed of in-phase (I) and quadraphase (Q) signals.

State of the art GPS receivers, after sampling and quantization, split the signal processing into multiple channels for simultaneous tracking of multiple satellites, by using the CDMA (Code Division Multiple Access) method.

Each satellite is tracked by the Delay Lock Loop (DLL) and the Phase Lock Loop (PLL). These devices assure that the incoming codes and carrier phases are matched (or locked) to the receiver-generated codes and phases, and remain locked throughout the tracking of continuously received signals. Code matching directly generates the pseudorange and the phase matching generates the ambiguous carrier phase observable.

GPS satellites transmit highly coherent radio signals with right-hand circular polarization over two L-band channels, L1 (1575.42 MHz) and L2 (1227.60 MHz). The L1 carrier signal is modulated by two pseudo-random (PRN) sequences: the P-code (precision code, 10.23 MHz) and the C/A code (coarse code, 1.023 MHz). L2 carrier signal is modulated by the P-code, only.

When Anti-spoofing is activated, the GPS signal is intentionally corrupted. AS is implemented through a modification of the P-codes: authorized users are equipped with a decryption devise, in order to lock on the P-codes.

If the P-code is available, both carriers can be reconstructed by the code correlation technique.

If only the Y-code is available (i.e. the encrypted P-code), the L1 carrier can still be reconstructed by code correlation using the C/A-code, but a codeless technique needs to be applied to reconstruct the L2 carrier.

Some of the codeless techniques commonly used are the L2 squaring (Macrometer), the Cross-correlation of L2 with L1 (Trimble and Rogue), and the z-tracking mode (Ashtech).

2.3.2 The DLL and PLL in the presence of multipath

The main operations performed by a receiver are the tracking and the locking . A receiver is code-locked when the code internally generated by the receiver has been aligned with the received code from the satellite. The tracking consists in shifting continuously the receiver code to match the incoming signal. This shifting of the locally generated receiver code is controlled by the Delay Lock Loop. The discriminator function (which is defined to identify the maximum of the correlation between the internally generated signal and the GPS signal) is zero when the time tracking error is zero. In the presence of multipath the zero crossing of the discriminator function value is shifted in time by δ , the time delay of the reflected signal with respect the direct signal. Moreover the discriminator function is

modulated by the reflection coefficient of the scattering surface and by $\cos(\beta-\delta\Phi)$, where β and $\delta\Phi$ were defined in [2.4] and [2.5].

After removing the PRN code in the DLL, the unmodulated carrier wave is passed to the PLL, where the phase measurement is performed. The result is the phase offset between the received signal and the reference signal generated in the receiver. In the presence of multipath the carrier tracking error is the multipath phase error $\delta\Phi$.

2.3.3 L2 signal processing in the presence of AS (Anti-spoofing)

AS can severely limit the use of GPS for high accuracy positioning for unauthorized users. However there are several solutions proposed for dealing with AS, which are implemented by the GPS receivers.

Because L2 is biphase-modulated (by either the P-code or the C/A code), it is possible to recover the L2 carrier without knowledge of the P-code, by simply squaring the signal or cross-correlating L2 with L1. There is noise degradation added in this codeless carrier recovery, because of the non-linear squaring operation or the cross-correlation with a noisy signal (L1). Other new techniques, such as z-tracking, are used in new receivers, which presents better characteristics of the SNR.

2.3.3.1 L2 signal squaring

Signal squaring is one of several methods used to recover the pure carrier from the biphase-modulated signal. Autocorrelating the received signal (squaring) all modulations are removed, because a 180° phase shift during modulation is equivalent to a change in the sing of the signal. As a result of this processing , the signal frequency increases by a factor of two and the effective wavelength is half-wavelength

carrier phase observation L2. A serious drawback of this method (not any longer in use in the new receivers) is also that the SNR is reduced by 30 dB with respect to the code correlation technique. .

2.3.3.2 Cross correlation of L2 with L1

This technique is based of the fact that both, L1 and L2 carriers are modulated with the same P(Y)-code, although the Y-code is not known. Due to the dispersive nature of the ionosphere, the propagation of the electromagnetic signal is different: the Y-code on L2 is slightly slower than the one on L1. The time delay necessary to match the L1 and L2 signals is a measure of the travel time difference between the two signals.

The result of the correlation process between L1 and L2 are the range difference between the two signals and the phase difference between the beat frequency carriers. With this method the SNR decreases of 27 dB with respect the code correlation technique, reporting a 3 dB improvement with respect L2 squaring.

2.3.3.3 Z - tracking

This quasi-codeless technique is the most recent and provides the best SNR performance in the presence of AS. This technique is based on the fact that the Y-code is the module-2 sum of the P-code and is a substantially lower rate encryption code. The L1 and L2 signals are separately correlated with locally generated P-codes. Since there is a separate correlation on L1 and L2, the W-code on each frequency can be obtained. The encryption code is estimated for each frequency and removed from the received signal to allow locally generated code replicas to be locked with the P-code signals of L1 and L2.

With this method the full-wavelength carrier phases of L1 and L2 is obtained. The output pseudoranges and phases of the Z-tracking technique, are directly those which would be obtained by a code correlation without antispoofing, but with a SNR degradation of 14 dB.

Chapter 3

Description of the algorithm for the Multipath Phase Error Estimation from the SNR data

3.1 Introduction

Among other sources of noise, multipath phase errors represent a significant limiting factor in high precision GPS positioning [Parkinson and Spilker, 1996]. By using differential techniques in dual frequency mode it is possible to eliminate the most of the GPS errors (clock errors, ionospheric effects, etc. ...). However, the multipath phenomenon is characteristic of the surroundings of the receiving antenna and needs to be corrected with other more local techniques.

Multipath reflections affect the SNR (section 2.2) and the carrier phase observable measured by the Phase Lock Loop (PLL) (section 2.3).

In this chapter we describe the algorithm implemented for the estimation of the multipath phase error from the frequency and amplitude of the oscillations of the SNR data.

3.2 Errors in the GPS Phase Measurements

The dominant source of error in phase measurements is the clock error between the transmitter (satellite) and the receiver (ground station).

To eliminate the effects of bias or instabilities in the satellite clock, differential GPS methods can be applied. One method consists in computing the single-differences, by differencing the phases of signals received simultaneously by two ground stations. If the receivers are closely spaced (short baseline) the computation of the single difference phase residual also reduces the effects of tropospheric and ionospheric refraction on the propagation of the radio signal.

The effects of variations in the station clock can be corrected by computing the double-differences phase residual. This observable is obtained by subtracting the single-difference phase residuals relevant to the two satellites from one other (double-differences).

Apart from clock errors, other significant sources of errors in GPS positioning are due to orbital errors, phase center models, ionospheric and tropospheric effects, multipath, and noise in the receiver. It is usually difficult to distinguish among different errors, especially between ionospheric and multipath effects, because they can produce similar oscillations in the carrier phase.

The spectrum of the ionospheric variations is a function of the elevation angle of the satellite, the time of the day, the season and solar activity. The dispersive nature of the ionosphere produces a different effect on the signal at different frequencies. By combining the two carrier beat phase observations, L_1 and L_2, it is possible to remove the ionospheric contribution. This is the reason why GPS satellites transmit in two different frequencies, f_1 (1575.4 MHz) and f_2 (1227.6 MHz).

One way to filter the ionospheric effects is to apply the so called dual-band processing. It consists in computing a linear combination of L_1 and L_2 (LC):

$$LC = \delta\Phi_{obs} = 2.546 \cdot \phi_{L1} - 1.984 \cdot \phi_{L2} \qquad [3.1]$$

In the following chapters we will denote LC with $\delta\Phi_{obs}$ and we will refer to it as the observed phase residual.

By computing $\delta\Phi_{OBS}$ the effects due to other sources of error (different than the ionosphere) are magnified. This is the reason why, for short baselines, where the ionospheric errors cancel out with single differencing, it is preferable to treat L1 and L2 as two independent observables. For long baselines (more than a few kilometers apart) the ionospheric errors are uncorrelated and it is necessary to use the dual-band processing (computing LC) to eliminate all the effects of the ionosphere.

In general we would like to eliminate both, multipath and ionospheric effect. For short baselines L1 and L2 can be treated as two independent observables, thus eliminating the need for calculating LC, which in return would amplify the multipath error.

For long baselines, the ionospheric effects are not strongly correlated and it is necessary to use LC in order to eliminate them. The ionosphere does not decorrelate after a few kilometers. It is in fact correlated for many hundred's of kilometers. But how large is the decorrelated part? An approximate rule (discussed in many of the early papers on GPS) is that the differential ionospheric delay is between 1-10 parts-per-million of the separation between the sites, where the exact amount depends on latitude, time of day, time of year and solar activity. Using this approximation, for baselines of 1 km, the ionospheric contribution is likely to be between 1 and 10 mm. 1 mm is small compared to the phase noise, but 10 mm (0.05 cycles) is large. Therefore, when the ionosphere is active, dual frequency may be needed on baselines as short as 1 km.

When only distant receivers are available, it is usually necessary to compromise between the amplification of other types of noise and the need to eliminate the effects of the ionosphere by dual band processing.

Either case (short or long baselines) the multipath error cannot be filtered with differential GPS techniques, because it is a distinct characteristic of the environment around one particular receiver.

One technique for the estimation and correction of the multipath error is proposed in the following sections.

3.3 Multipath Phase Error Estimation Algorithm

The algorithm proposed in this thesis manipulates the variations of the SNR for the estimation of the total multipath phase error $\delta\Phi_{EST}$, computed as the superposition of several single reflections.

With reference to fig 2.1, the amplitude of the direct and multipath signals are assumed constant for the time T, in which A_m rotates around the tip of A_d. During this time the angle β varies of at least 360° and the composite signal A_c shows an oscillation of period T. This implies that the amplitude of the direct signal arriving to the antenna and the multipath frequency f_m are constant over T.

3.3.1 Antenna Gain removal

The first step of the estimation algorithm consists in removing the variations of the SNR due to change of position of the satellite. This changes are due to the fact that the direct GPS signal reaches the receiving antenna under different angles (θ, ϕ) which are associated to different values of the antenna pattern.

In order to remove the antenna pattern contributions and the differences in the transmission power from the satellites, we fit a 4-th order polynomial in sin(elev) to all of the SNR data at each station. In this fit we include a zero-order term (i.e. a constant offset) for reasons to be discussed below. Separate fits are made for L1 and L2 data. With L2 data a distinction is made between data processed in cross-correlation mode and those data that are directly tracked. The latter occurs for the 1 or 2 GPS satellites that do not have Anti-spoofing turned on. This fitting processes also normalizes the gain-corrected SNR data so that they are near unity. The polynomials estimated with the procedure previously described look similar to the

anechoic chamber gain curves but tend to be larger in the mid-elevation angle range. This discrepancy is probably be due to the effects of the transmission power from the satellites.

For all receivers, except the Ashtech z12, the measured SNR and the gain curves tend to approach zero as the satellite elevations tend to zero. (See fig. 3.2). For Ashtech z12 the SNR near zero degrees elevation angle is still about 90% of its value at zenith. This behavior is not consistent with the gain pattern of the Dorne-Margolin antennas used with these receivers. Therefore, it can only be explained by increased integration time at lower elevation angles (thus increasing the SNR) or by the SNR values being biased. After comparing Ashtech and Trimble SSE data collected on the same site (and showing similar multipath signals), we concluded that latter was more likely explanation. This is the reason why we include an offset term in gain fitting process and simply remove this offset from all the SNR values.

In the algorithm a problem with the gain removal is represented by the dependency of the SNR on the elevation and azimuth angle, as well. The main dependency is the elevation angle, but not taking in to account the azimuthal dependency an error is introduced in the estimation, which influences the performance of the algorithm. The main dependency is with elevation angle, but for Trimble SST and SSE antenna there is a sizable azimuthal dependence that we have not accounted for. The impact of this neglect has not been evaluated and is likely to influence the lower frequency multipath signal estimation.

The impact of the antenna gain on the SNR depends on the particular signal processing procedure performed by each receiver. For receivers which use the L2 squaring techniques, the SNR_L2 is a function of the elevation angle and decreases as the square of the L2 gain pattern of the antenna. In receivers which use the cross-correlation between L1 and L2, the SNR_L2 decreases as the product of L1 and L2 gain patterns. In receivers which perform the standard tracking the SNR_L2 decreases simply as the gain pattern.

In the algorithm, the SNR_L2 derived from the receivers which performs L2 squaring and standard tracking, can be processed directly. But the SNR_L2 deriving from an operation of cross correlation needs to be either divided by SNR_L1 (so that SNR_L2 / SNR_L1 is the input for the algorithm for the estimation of the L2 phase error) or considered without modifications. In the first case the estimated phase

error is directly $\delta\Phi_2$ and, in the second the estimated phase error is given by the difference between the phase error estimated from SNR_L2 ($\delta\Phi'_2$) and the one estimated from SNR_L1 ($\delta\Phi_1$). In other words: $\delta\Phi_2 = (\delta\Phi'_2) - (\delta\Phi_1)$. For the estimation algorithm proposed the first technique was adopted.

In figure 3.2 the SNR for L1 for the station MANA (Turborogue) and the satellite PRN 26, is show, as a function of time. As it can be noticed comparing fig. 3.1 with fig. 3.2, the SNR as obtained from the receiver is strongly dependent on the elevation angle of the satellite. After the gain removal and normalization, the estimation algorithm is ready to manipulate the new SNR for L1 shown in fig. 4.3.

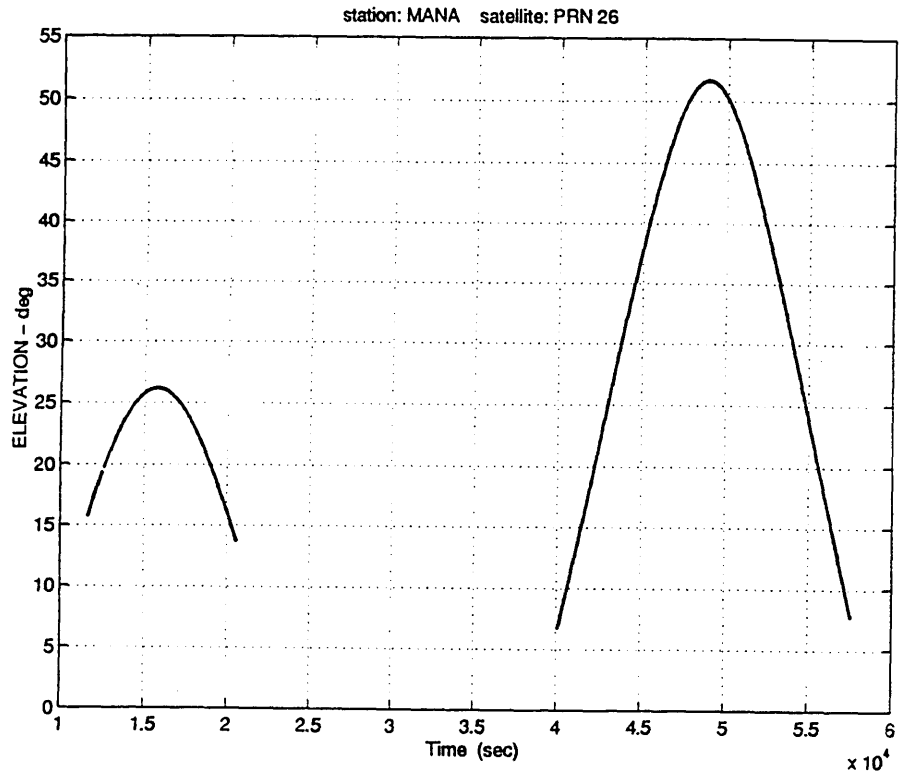

Figure 3.1: Elevation angle for the satellite PRN 26

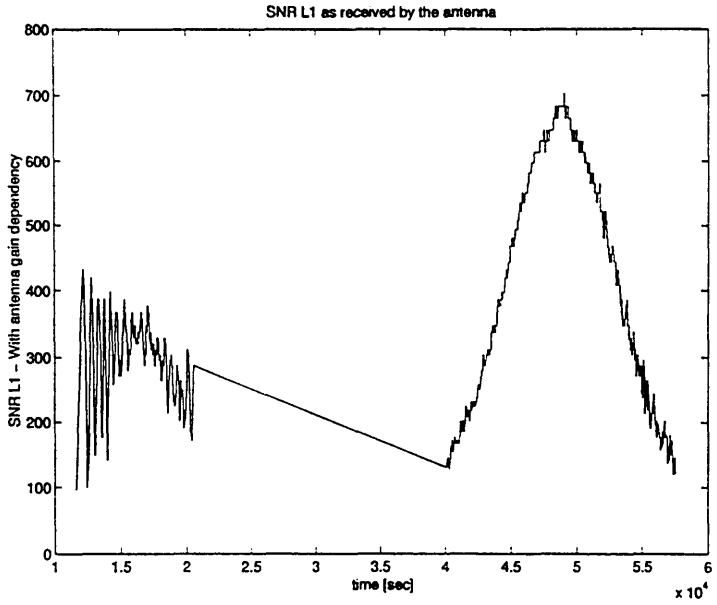

Figure 3.2 : SNR_L1 for the station MANA (Turborogue) and the satellite PRN 26.

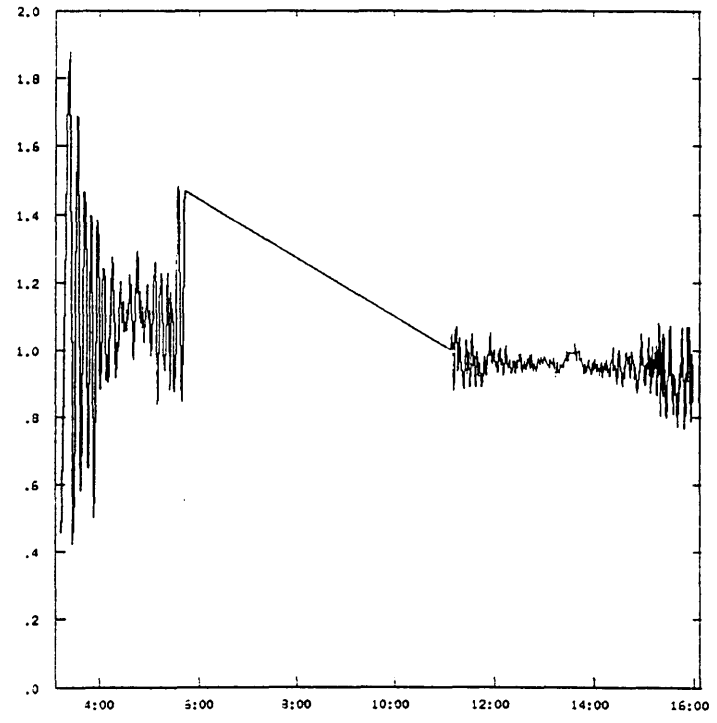

Figure 3.3 : SNR_L1 for the station MANA after gain correction and normalization.

3.3.2 Data Segment Selection

After the gain correction, the SNR is divided into segments. The length of these segments is based on gaps that the data might have, or on the rate of change of the elevation angle, so that portions of data relevant to a rising or setting satellite are treated separately.

The SNR might have missing data in the sequence due to problems with the reception of the signal or to obstruction of the satellite. The algorithm presents a gap tolerance of about 10 epochs. If the missing data are less than 10 points, the program linearly interpolates before the computation of the spectra. However, the algorithm does not interpolate when fitting the sine and cosine components, because the interpolation introduce false data which might produce a wrong estimation of the phase error. On the other hand, not having enough data for the estimation of the sine and cosine components, can cause anyway an inaccurate estimation of the phase error. If the gap is too large, separate analyses are done for the two segments of data. Because the length of the segment of data determines the frequency resolution, also a too short time series can lead to a wrong phase error estimation.

3.3.3 Spectral Decomposition of the SNR

As already discussed in section 2.2.4, the scattering phenomenon is generally due to the superposition of several single multipath contributions, each characterized by a specific frequency f_m. Multipath is not a stationary phenomenon because its frequency varies with the rate of change of the satellite elevation angle (formula [2.5]). Therefore, spectral estimation must be performed on a span of data long enough to provide the required frequency accuracy, but short enough to allow the hypothesis of constant frequency.

The purpose of the spectral estimation performed by the algorithm is to decompose the total multipath phase error in several components and isolate them to compute the GPS phase error due to each component. The multipath

contributions are determined sequentially and the correspondent phase error are computed. The total phase error $\delta\Phi_{EST}$ is created from the sum of the complex components of all of the contributions.

We decompose the SNR variations into individual components in an iterative procedure. At each iteration, we compute the power spectra of the current SNR residuals, which in the first iteration are simply the values of the SNR after we remove the gain corrections. We select the frequency with the largest amplitude: if this amplitude (sqrt of the power spectral density) is larger that 1/500 of the mean SNR strength (obtained from the zero frequency component in the PDS) then the iteration is continued. The 1/500 limit is set so that the phase contribution from the remaining components will be less than 0.4 mm (190 mm/ 500).

For each period of the maximum frequency through the data segment, we estimate a mean value and sine and cosine components at this frequency. Since the frequencies are obtained from a FFT, we are assured that there will be an integer number of these periods in the data segment. As can be seen in fig. 3.4, for example, the frequency of the multipath is reasonably constant but the amplitude changes with time. Our algorithm estimates separate sine and cosine components for each full wavelength through the data segmant. The sine and cosine components are saved and the contribution to the SNR computed and removed from the SNR values. These residual SNR values are then used in the next iteration. In addition to the 1/500 amplitude limit, the iteration is continued for no more than 50 iterations although this limit is rarely reached. At the end of the spectral decomposition, we have a series of sine and cosine components, each applicable to different times in the data depending on the frequency they represent. For each data epoch, there are N applicable component pairs, where N is the number of iterations. The compex sum of the N pairs (with their time arguments dependent on the frequency they each represent) is formed and the phase error and amplitude computed from the sum. The N multipath contributions estimated with the algorithm are superimposed in figure 3.6, to provide the total multipath phase error $\delta\Phi_{EST}$.

There are limits on the spectral components estimated. When the maximum spectral components are found, we search frequencies for 2/T to n/(2T), where T is the total duration of the segment, and n is the number of measurements in the span.

Because the high frequency end is half of the maximum frequency in the spectrum, the algorithm will tend to smooth the SNR as well. This smooting can be observed in fig. 3.4.

As explained in section 2.2.2, the determination of the sign of the multipath phase error estimate remains ambiguous. In the algorithm the sign attributed to the multipath phase error is based on the sign of the rate of variation of the elevation angle ($d\theta/dt$). The sign actually depends on the rate of change of distance to the reflector. Because we never try to compute the location of the reflectors, we use the rate of change of the elevation angle instead. If $d\theta/dt$ is positive, $\delta\Phi_{EST}$=-atan2(Imag,Real); if If $d\theta/dt$ is negative, $\delta\Phi_{EST}$=+atan2(Imag,Real). The assumption made is that, as the satellite rises, the distance to the reflector decreases (at least for reflections from a flat Earth). This is verified in most of the cases, but it is not true in general. This ambiguity in the sign of the multipath phase error strongly influences the performances of the estimation algorithm in those case when an abrupt change of sign of the estimated phase error is observed.

The total multipath phase error estimate $\delta\Phi_{EST}$ is shown in figure 4.7 and is indicated with LC_EST. The observed phase residual measured from the GPS measurements $\delta\Phi_{OBS}$ is shown in the same figure (LC_OBS) and compared with the estimated phase error due to multipath. In this example, the visual correlation of the two curves is striking: the frequency content and the amplitude of the two curves seems to agree very well. In the following chapters, quantitative analyses (spectral and statistical) are performed to compare estimated and observed phase residuals.

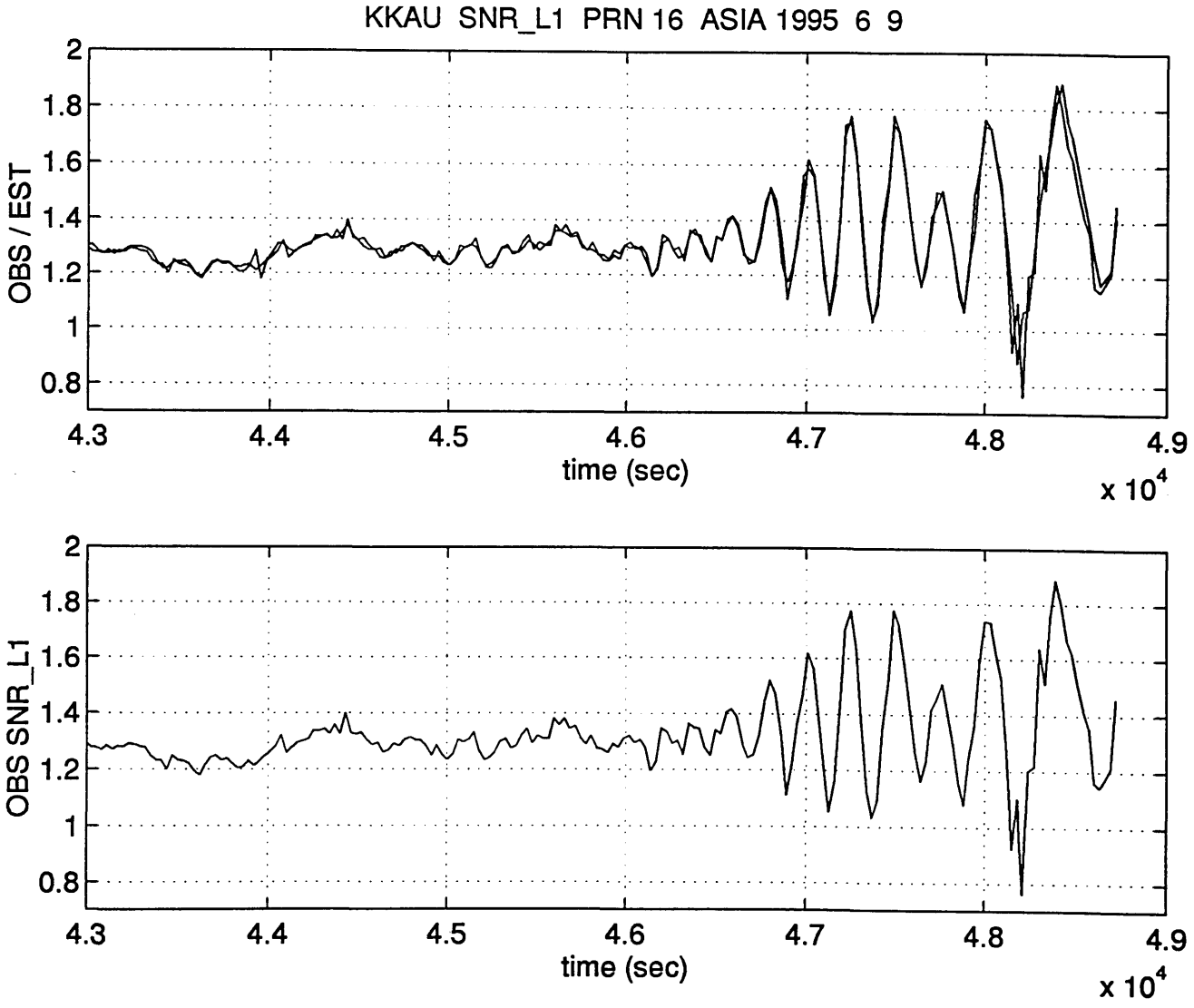

Figure 3.4: Curve fit for SNR_L1 satellite PRN 16 . Station KKAU.

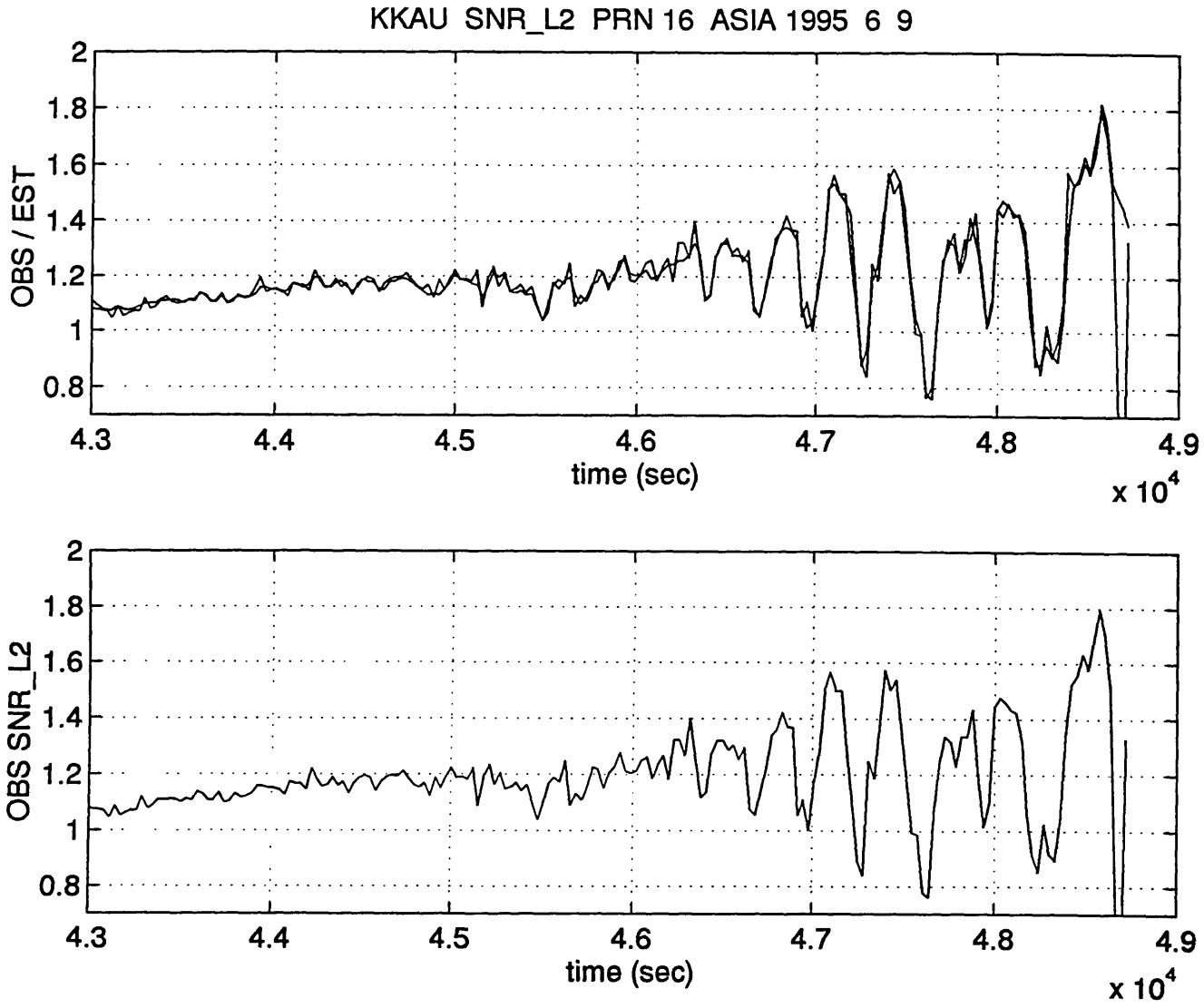

Figure 3.5: Curve fit for SNR_L2 satellite PRN 16 . Station KKAU.

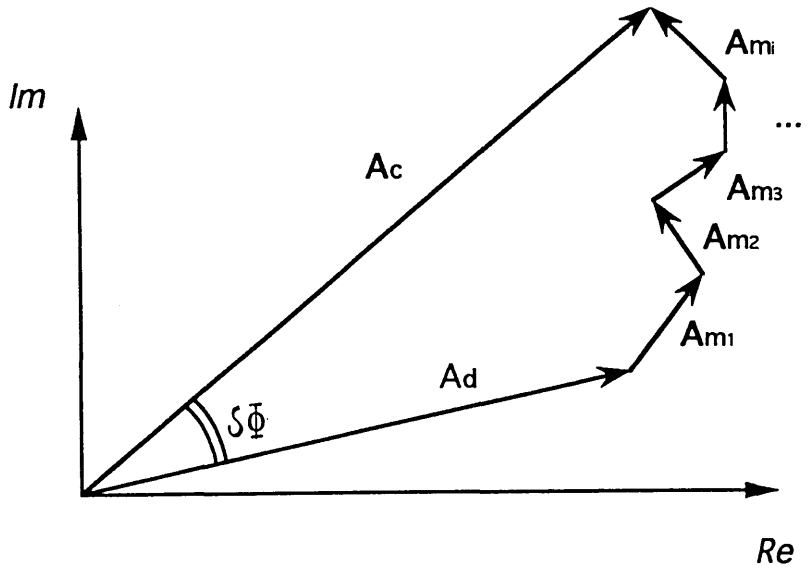

Figure 3.6: Composition of multipath single components.

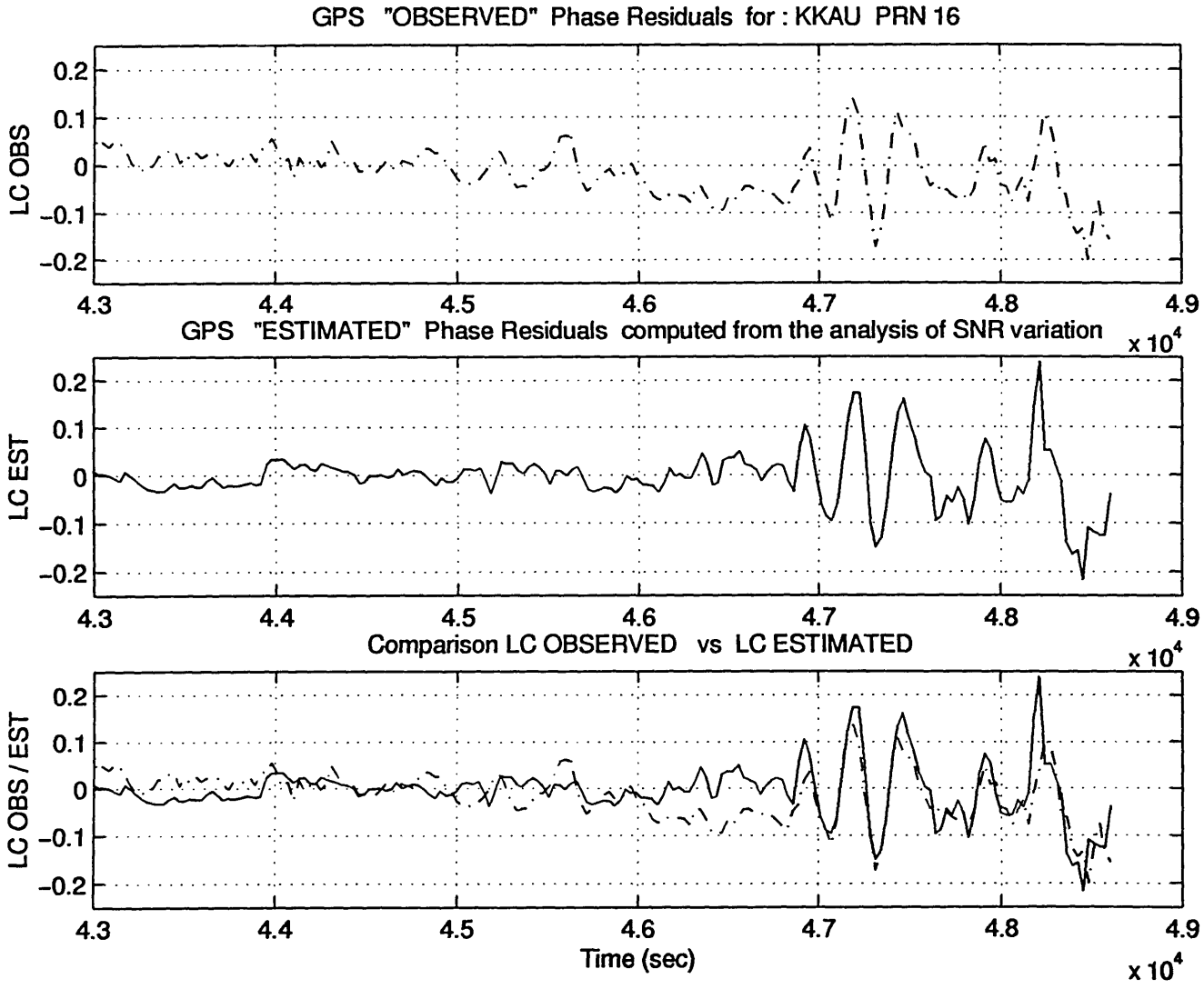

Figure 3 .7: The multipath phase error ($\delta\Phi_{EST}$ = LC_EST) estimated by the algorithm is compared with the observed phase residual ($\delta\Phi_{OBS}$=LC_OBS) computed from the measurements.

Chapter 4

Statistical and Spectral Analysis of estimated and observed GPS phase errors

4.1 Introduction

The aim of the spectral and statistical analysis described in this chapter is to test how well the retrieved multipath phase error from the Signal-to-Noise-Ratio (SNR) agrees with the phase error observed in the GPS measurements. To this purpose two time series, the observed phase residual ($\phi_{OBS} = \delta\Phi_{OBS}$) and the estimated multipath phase error ($\phi_{EST} = \delta\Phi_{EST}$), were studied and compared. This analysis provided important information about the applicability, limits and performance of the

GPS multipath estimation method described in chapter 3. The results of this study applied to actual GPS measurements are discussed in detail in chapter 5.

4.2 Data Preprocessing

With data preprocessing we indicate the procedure for the selection and formatting of the GPS data before applying the analysis. The first goal of this operation was to choose data sets containing a strong multipath error in the phase observable.

As mentioned in chapter 2, the occurrence of multipath produces large regular oscillations in the SNR. However, the simple analysis of the SNR might not provide enough information for evaluating the characteristics of the data, as ionospheric effects can also cause wave-like patterns in the signal received by the antenna. A discussion on the errors in the GPS phase measurements can be found in section 3.2.

Because the observed phase residual, ϕ_{OBS}, does not contain ionospheric effects, the combined analysis of SNR and ϕ_{OBS} gives enough information for the selection of the data. Whenever large structured oscillations were found in both SNR and ϕ_{OBS}, because in the observed phase residual the ionospheric effects are filtered out, we could be confident in having GPS measurements affected by multipath, and the data were considered appropriate for the analysis.

ϕ_{OBS} was computed by using the GAMIT GPS analysis software package implemented at MIT (King and Bock, 1993). The data chosen for this analysis were selected by using the CVIEW option of the program.

The data sets chosen were then divided into subsections having well defined statistical properties and multipath interference. This operation permitted us to isolate the phenomena without averaging out the effects of multipath over a large number of samples.

4.3 Spectral Analysis

4.3.1 Multipath frequency

The multipath phenomenon is caused by the interference of electromagnetic reflections with the direct electromagnetic signal transmitted by the satellite. The level and frequency of the GPS noise deriving from multipath depends upon the distance, geometry and reflectivity of nearby objects, the elevation angle of the satellite and the rapidity of change of the elevation angle with respect the receiver, and the value of the carrier frequency (section 2.2).

Because of the dependency of multipath on these parameters, each multipath component due to a particular reflector have a distinct frequency. Therefore, the multipath noise caused by the surrounding of a receiving GPS antenna can be studied and identified by spectral analysis (section 3.3.3).

Spectral analysis is used here to compare the estimated multipath phase error (ϕ_{EST}) and the observed phase residual (ϕ_{OBS}).

4.3.2 Power Spectral Density

In spectral analysis we try to represent a stationary process in terms of a sum of sinusoids, in order to define its spectrum. We applied this analysis to the observed and estimated phase errors, to determine their spectral content and how this was related to the multipath phenomenon.

The two time series $\{\phi_{OBS\,n}\}$ and $\{\phi_{EST\,n}\}$, are assumed Stationary Ergodic Random Processes. In other words, we infer that their statistical properties do not vary with time (Stationary) and that the average values computed over the ensemble at a time t_o, $\phi_{x\,i}(t_o)$ [for x = OBS, EST], will equal the corresponding average values computed over time for a single time history record, $\phi_x(t_i)$[for x = OBS, EST] (Ergodic).

This important assumption allows us to perform our statistical and spectral analysis within one time series, without the need of independent realizations of the process.

Let us consider a stationary ergodic random process:

$$\{\phi_n\} = \{\phi(n \cdot \Delta t)\} \qquad \text{for } n = 1,2,3,\ldots,N. \qquad [4.1]$$

where the time resolution interval between the sample values is Δt , the total number of samples is N and the total length of data analyzed is $T=N\,\Delta t$.

The Discrete Fourier Transform (DFT) of $\{\phi_n\}$ is defined as:

$$\{\Phi_K\} = \{\Phi(k \cdot \Delta f)\} = \Delta t \sum_{n=1}^{N} \phi_n e^{\left(-j2\pi \frac{kn}{N}\right)} \qquad \text{for } k = 1,2,3,\ldots,N. \qquad [4.2]$$

The Nyquist cutoff frequency of the sequence is $f_c = 1/(2\,\Delta t)$, and the minimum frequency-resolution bandwidth is $\Delta f = 1/T = 1/N\,\Delta t$.

Therefore, the Power Spectral Density of $\{\phi_n\}$ is given by :

$$S_\phi(k) = \frac{2}{N \cdot \Delta t} |\Phi_k|^2 \qquad [4.3]$$

For each couple of time series, $\{\phi_{OBSn}\}$ and $\{\phi_{ESTn}\}$, we computed the Power Spectral Densities S_{OBS} , S_{EST}, and S_{DIFF}, power spectral density of their difference $\{\phi_{DIFF}\}$.

Each time series was previous normalized by subtracting its mean. The DFT was computed via FFT (Fast Fourier Transform).

The Power Spectral Density was computed by using a Matlab algorithm (FFT_obs_est_diff.m) which can be found in Appendix C.

4.3.3 Auto Correlation and Cross Correlation

An other way to compare $\{\phi_{OBSn}\}$ and $\{\phi_{ESTn}\}$ is to compute the Auto-Correlation of each of the two time series (R_{OO} and R_{EE}) and the Cross-Correlation between them (R_{OE}) .

To define R_{OO}, R_{EE} and R_{OE} between two time series $\{\phi_{OBSn}\}$ and $\{\phi_{ESTn}\}$, we first introduce the Cross-Covariance Function, C_{OE}.

The Cross-Covariance Function between two processes $\{\phi_{OBSn}\}$ and $\{\phi_{ESTn}\}$ for any time delay τ, is given by :

$$C_{OE}(\tau) = \frac{1}{N}\left[\sum_{n=1}^{N}\left(\phi_{OBSn} - \mu_{OBS}\right)\left(\phi_{ESTn}(t+\tau) - \mu_{EST}(t+\tau)\right)\right] \qquad [4.4]$$

If we assume again that the two time series are stationary ergodic processes, their means μ_{OBS} and μ_{EST} are constants and independent of t. Therefore, C_{OE} can be written as:

$$C_{OE}(\tau) = \frac{1}{N}\left[\sum_{n=1}^{N}\left(\phi_{OBSn}\right)\left(\phi_{ESTn}(t+\tau)\right)\right] - \mu_{OBS}\mu_{EST} \qquad [4.5]$$

We define the Cross-Correlation function between $\{\phi_{OBSn}\}$ and $\{\phi_{ESTn}\}$ as:

$$R_{OE}(\tau) = \frac{1}{N}\left[\sum_{n=1}^{N}\left(\phi_{OBSn}\right)\left(\phi_{ESTn}(t+\tau)\right)\right] \qquad [4.6]$$

and it follows that:

$$C_{OE}(\tau) = R_{OE}(\tau) - \mu_{OBS}\mu_{EST} \qquad [4.7]$$

The equivalent Auto-Covariance Functions for the time series are:

$$\begin{aligned} C_{OO}(\tau) &= \frac{1}{N}\left[\sum_{n=1}^{N}\left(\phi_{OBSn} - \mu_{OBS}\right)\left(\phi_{OBSn}(t+\tau) - \mu_{OBS}(t+\tau)\right)\right] \\ C_{EE}(\tau) &= \frac{1}{N}\left[\sum_{n=1}^{N}\left(\phi_{ESTn} - \mu_{EST}\right)\left(\phi_{ESTn}(t+\tau) - \mu_{EST}(t+\tau)\right)\right] \end{aligned} \qquad [4.8]$$

and the Auto-Correlations for $\{\phi_{OBSn}\}$ and $\{\phi_{ESTn}\}$ are:

$$R_{OO}(\tau) = \frac{1}{N}\left[\sum_{n=1}^{N}(\phi_{OBSn})(\phi_{OBSn}(t+\tau))\right]$$
$$R_{EE}(\tau) = \frac{1}{N}\left[\sum_{n=1}^{N}(\phi_{ESTn})(\phi_{ESTn}(t+\tau))\right] \qquad [4.9]$$

Therefore:

$$C_{OO}(\tau) = R_{OO}(\tau) - \mu_{OBS}^2$$
$$C_{EE}(\tau) = R_{EE}(\tau) - \mu_{EST}^2 \qquad [4.10]$$

If the mean of either measurement is zero (μ_x=0, μ_y=0 or μ_x=μ_y=0) it follows that :

$$C_{OO}(\tau) = R_{OO}(\tau)$$
$$C_{EE}(\tau) = R_{EE}(\tau) \qquad [4.11]$$
$$C_{OE}(\tau) = R_{OE}(\tau)$$

The Matlab program implemented for computing the Auto and Cross-Correlation of $\{\phi_{OBSn}\}$ and $\{\phi_{ESTn}\}$ is called Auto_Cross_CORR.m, and is presented in Appendix C.

4.3.4 Auto and Cross Spectral Density Function

The spectral density function between two stationary ergodic random processes can be defined as the Discrete Fourier Transform of the Correlation function between those records:

$$S_{OE}(k) = \Delta t \sum_{n=1}^{N} R_{OE} e^{\left(-j2\pi\frac{kn}{N}\right)} \qquad \text{for } k = 1,2,3,\ldots,N. \qquad [4.12]$$

The two correspondent Auto-Spectral density functions for $\{\phi_{OBS}\}$ and $\{\phi_{EST}\}$ are, therefore:

$$S_{OO}(k) = \Delta t \sum_{n=1}^{N} R_{OO} e^{\left(-j2\pi\frac{kn}{N}\right)} \qquad \text{for } k = 1,2,3,\ldots,N.$$
$$S_{EE}(k) = \Delta t \sum_{n=1}^{N} R_{EE} e^{\left(-j2\pi\frac{kn}{N}\right)} \qquad \text{for } k = 1,2,3,\ldots,N. \qquad [4.13]$$

The Matlab algorithm for the computation of the spectral density via correlation function is shown in Appendix C and is called SP_CORR_obs_est.m.

4.3.5 Coherence Function

The frequency relationship between $\{\phi_{OBSn}\}$ and $\{\phi_{ESTn}\}$ can be also studied by computing their coherence function, γ^2_{OE}. The computation of γ^2_{OE} provides information on what fraction of the power in ϕ_{EST} can be explained by ϕ_{OBS} i.e. which fraction of the total Phase Residual is due to multipath.

The results of this analysis allow us to recognize the range of frequencies for which the two sets of data under analysis present an high correlation. In general this test is used to verify and study the results obtained from previous Spectral Analysis.

The Coherence function computed was defined as:

$$\gamma^2_{OE} = \frac{|S^2_{OE}|}{S_{OO} \cdot S_{EE}} \qquad [4.14]$$

The algorithm implemented for the computation of the coherence function (Coherence_obs_est.m, Appendix C) divides the total time interval of the two processes in subsections. The number of these subsections depends on the particular data set considered. Several numbers of subsections are examined (2 to 12) and after several trials the more appropriate number is chosen. Because of the sampling, the maximum value does not necessarily indicates the maximum of the

coherence function. The only information we can extract from the coherence function computed in this analysis is the range of frequencies where the two time series correlate better.

4.4 Statistical Analysis of GPS Phase Residuals

In this section we compute the statistical properties of the variance estimates of GPS phase residuals. The procedure followed in the statistical analysis presented in this section is analogous to the one derived in vanDam and Herring, 1994.

For each set of data, the observed phase residual from the GPS measurements, the estimate of the phase error due to the multipath effect, and the phase residual after correction, can be written as functions of the noises affecting the GPS positioning. In order to assess the statistical properties of the phase error before and after the correction for multipath, we can define:

$$\begin{aligned} \phi_{OBS} &= \phi_{MPN} + v_{MN} \\ \phi_{EST} &= \phi_{MPN} + v_{EN} \\ \phi_{DIFF} &= \phi_{OBS} - \phi_{EST} = v_{MN} - v_{EN} \end{aligned} \qquad [4.15]$$

where:

ϕ_{OBS} = Phase residual observed directly from the GPS measurements
ϕ_{MPN} = Multipath phase error ("true" multipath phase contribution)
v_{MN} = Noise in the measurements due to other sources different from multipath
ϕ_{EST} = Multipath phase error estimated from the SNR data
v_{EN} = Noise in the retrieval of the multipath phase error
ϕ_{DIFF} = Phase residual after the correction for multipath

In this analysis it will be assumed that the time series under study are stationary ergodic, with zero mean and standard deviation σ.

Of all the quantities previously defined, only ϕ_{OBS}, ϕ_{EST} and ϕ_{DIFF} are known, and the unknown phase errors v_{MN}, v_{EN} and ϕ_{MPN} are assumed to be independent.

A very useful method of statistical analysis is the Chi-square test, where the Chi-square distribution (with N-1 degrees of freedom) is given by the estimates of the variance normalized by the expected variances. However, because ϕ_{OBS}, ϕ_{EST} and ϕ_{DIFF} and the estimates of their variances are correlated, a simple Chi-square test cannot be used to determine the statistical significance of the changes in the variance estimates, due to the correction for the multipath phenomenon.

In order to perform an appropriate statistical analysis, we computed the expectation and variance of the difference between the variance estimates of the phase error, before and after applying the corrections for the multipath contribution.

If N is the number of samples and σ the standard deviation of the time series, the estimates of the variances of $\{\phi_{OBS\,n}\}$, $\{\phi_{ESTn}\}$, and $\{\phi_{DIFFn}\}$ are given by :

$$\hat{\sigma}^2_{OBS} = \sum_{n=1}^{N} \frac{(\phi_{OBSn})^2}{N-1} = \sum_{n=1}^{N} \frac{(v_{MNn} + \phi_{MPNn})^2}{N-1}$$

$$\hat{\sigma}^2_{EST} = \sum_{n=1}^{N} \frac{(\phi_{ESTn})^2}{N-1} = \sum_{n=1}^{N} \frac{(\phi_{MPNn} + v_{ENn})^2}{N-1} \qquad [4.16]$$

$$\hat{\sigma}^2_{DIFF} = \sum_{n=1}^{N} \frac{(\phi_{DIFFn})^2}{N-1} = \sum_{n=1}^{N} \frac{(v_{MNn} + v_{ENn})^2}{N-1}$$

It should be noticed that in these formulas the processes have been normalized by subtracting their mean before computing the variances.

The expectation of the estimates of the variance can be written as:

$$\begin{aligned}\left\langle \hat{\sigma}^2_{OBS} \right\rangle &= \sigma^2_{MN} + \sigma^2_{MPN} \\ \left\langle \hat{\sigma}^2_{EST} \right\rangle &= \sigma^2_{MPN} + \sigma^2_{EN} \\ \left\langle \hat{\sigma}^2_{DIFF} \right\rangle &= \sigma^2_{MN} + \sigma^2_{EN}\end{aligned} \qquad [4.17]$$

The expectation of the difference of the variance estimates of ϕ_{OBS} and ϕ_{DIFF} is given by :

$$\left\langle \hat{\sigma}^2_{OBS} - \hat{\sigma}^2_{DIFF} \right\rangle = \sigma^2_{MPN} - \sigma^2_{EN} \qquad [4.18]$$

The variance of the difference in the variance estimates is :

$$\mathrm{var}\left(\hat{\sigma}^2_{OBS} - \hat{\sigma}^2_{DIFF}\right) \equiv \left\langle \left(\hat{\sigma}^2_{OBS} - \hat{\sigma}^2_{DIFF} - \left\langle \hat{\sigma}^2_{OBS} - \hat{\sigma}^2_{DIFF} \right\rangle \right)^2 \right\rangle \qquad [4.19]$$

If we assume that :

$$\left\langle v_{MNi} \phi_{MPNi} \right\rangle = 0 \quad \text{and} \quad \left\langle v_{MNi} v_{ENi} \right\rangle = 0 \quad \text{for each i}$$
$$\left\langle \phi_{MPNi} \phi_{MPNj} \right\rangle = \left\langle v_{MNi} v_{MNj} \right\rangle = \left\langle v_{ENi} v_{ENj} \right\rangle = 0 \quad \text{for each } i \neq j$$

then the variance of the difference in the variance estimates can be written as:

$$\mathrm{var}\left(\hat{\sigma}^2_{OBS} - \hat{\sigma}^2_{DIFF}\right) = \frac{4 \cdot \sigma^2_{MN} \cdot \left(\hat{\sigma}^2_{MPN} + \hat{\sigma}^2_{EN}\right)}{N-1} \qquad [4.20]$$

where σ_{MN}, σ_{EN} and σ_{MPN} are unknown, and can be retrieved by inverting the system:

$$\begin{aligned}\left\langle \hat{\sigma}^2_{OBS} \right\rangle &= \sigma^2_{MN} + \sigma^2_{MPN} \\ \left\langle \hat{\sigma}^2_{EST} \right\rangle &= \sigma^2_{MPN} + \sigma^2_{EN} \\ \left\langle \hat{\sigma}^2_{DIFF} \right\rangle &= \sigma^2_{MN} + \sigma^2_{EN}\end{aligned} \qquad [4.21]$$

Chapter 5

Applying the method of multipath estimation to GPS data

5.1 Introduction

In this chapter we discuss the results obtained from the phase error estimation algorithm applied to GPS measurements. In particular, three GPS data sets were chosen for this study and will be discussed in the next paragraph: the Tien-Shan data, the LIGO data and the IAP data. Among these three collections, 42 data sets, acquired between June 1995 and January 1997, were selected for multipath estimation and analysis.

Although these measurements were not originally intended for studying multipath effects on GPS measurements, they are suitable for testing the

performance of the method for their strong multipath contribution to the phase error observable.

A brief description of the data sets selected, their characteristics and their significance in this study are provided in section 5.2.

5.2 Description of the GPS stations and the data sets analyzed

5.2.1 The Tien-Shan data

This data set was acquired during the 1995 -1996 Tien-Shan field project. The original purpose of this campaign was to define a north-south deformation across Tien-Shan and to study the interaction of the strike-slip faulting and thrust faulting along the Talaso-Ferghana fault.

The two stations selected for the multipath analysis, KKAU and MANA, are part of a network of approximately 95 sites. The network stretches across three of the former Soviet Republics, a region extending from Uzbekistan east to the Chinese border, and from Taldy-Kurgan (Kazakhstan) south to Tajikistan.

The station KKAU is located in Kazakhstan, at 41.695248° lat., 72.893497° long., and 1423.2 m elevation and uses a Trimble antenna as a receiving antenna.

The station MANA was located at a seismic observatory in the town of Manas, 30 km east of Talas, in Kyrgyzstan (lat. 42.493067°, long. 72.497956°, elev. 1423.2 m). The receiving antenna is a Dorne Margolin antenna.

MANA was one of three permanent sites, besides POL2 and TALG. In the fall of 1995, the receiver was moved to a new site near the town of Talas. This was a better location for the receiver, because it was far enough from strong reflectors and could be more easily mantained as a continuously operating site.

These two stations were chosen for the strong multipath effect present in the phase measurements. Every time a GPS satellite was in a particular region of the sky,

a similar clear strong multipath was observed. This fact leads to the conclusion that large reflecting surfaces were located near the receiving antennas.

However, the different frequencies of the multipath relevant to the two stations, suggests that the reflectors were located at different distances from the receivers. Therefore, from the comparison of the results of the statistical and spectral analysis it was possible to gain useful information about the performance of the estimation algorithm at different multipath frequencies and for different geometries.

KKAU and MANA use different types of antennas, Trimble and Dorne-Margolin, respectively. The performance of the algorithm for data sets acquired with different antennas was studied.

5.2.2 The LIGO data

This data set was chosen for the particular geometry of the surroundings of the receiver 0036 (fig. 5.1)

A strong multipath was observed when a satellite was at about 15° elevation and 45° azimuth. Among the LIGO measurements two data sets, relevant to the stations 0028 and 0036, had the same high sampling rate (Δt = 5 sec). These two stations are located at close distance from each other. As mentioned in chapter 3, the ionospheric errors can be filtered using single differencing when dealing with short baselines. Therefore, in this case, it is possible to treat L_1 and L_2 separately as two independent observables, rather than their linear combination LC.

Both estimations were performed for the dual-frequency phase residual, LC, and for the frequencies L_1 and L_2 individually.

5.2.3 The IAP data

This data set was acquired in January 1997, in California, during a two week field work carried out as part of a course on High Accuracy GPS held at MIT. The same

measurements were repeated at the same site in two successive days, but using two different receiving antennas: Trimble (station COSE) on January 23, 1997 and Ashtech (station GS29) on January 24, 1997. The measurements are relevant to the same satellites at the same time of the day, shifted by 3.5 minutes to account for the daily change in geometry.

Moreover, the two antennas present a different gain at low elevation angles. Because of the antennas characteristics, the multipath error is perceived differently by the two receivers, even though the actual multipath environment is maintained the same during the two sets of measurements.

However, it should be mentioned that the weather conditions during the second day of measurements (performed by the Ashtech antenna) were different. On the second day of measurements (January 24) the ground was wet, due to persistant rain. Rain usually increases the reflection coefficient of reflecting surfaces, which can produces an higher multipath error in the phase observable.

To study how the multipath effects can change due to weather conditions, the estimation algorithm was tested using data acquired on two different days, one sunny and dry, and the other gray and rainy. Comparing the measurements performed with the same receiver in the same location under these weather conditions, yielded very interesting results.

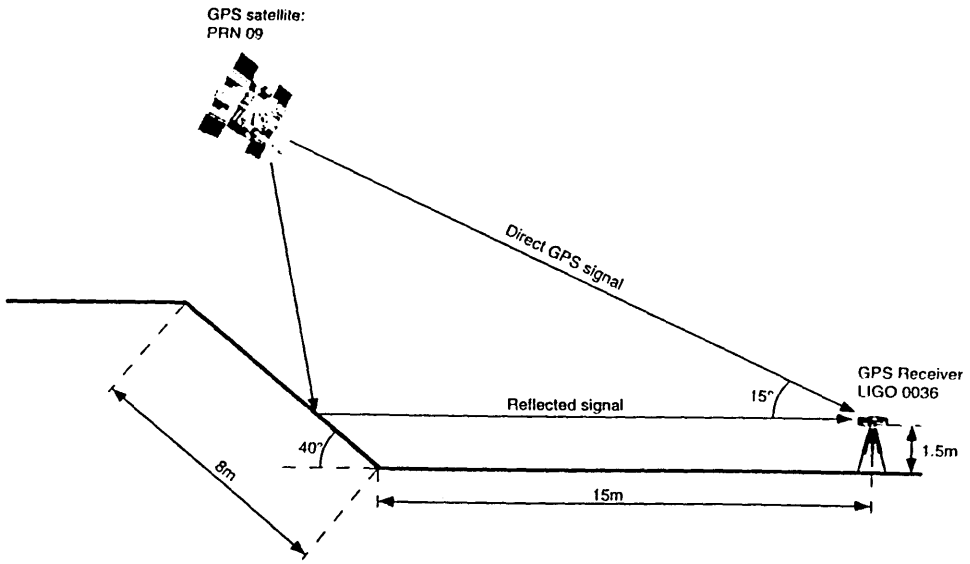

Fig. 5.1: Geometry of the surroundings of the receiver 0036 (LIGO data).

5.3 Multipath Estimation and Results of Spectral Analysis.

5.3.1 KKAU and MANA

5.3.1.a) KKAU (TRIMBLE 4000SSE)

The data relevant to the GPS measurements acquired by KKAU on June 10, 1995 were analyzed. Large oscillations were observed in the SNR every time a satellite passed through a specific region in the sky (low elevation angle and 50° azimuth).

An example of this phenomenon is shown in fig. A.1.1 and A.1.2. The SNR presents large fluctuations when the satellite PRN 16 is at an elevation θ = 10° - 20° and azimuth ϕ = 50° - 60°, at the time t=4.5 - 5.0 10^4 sec.

The observed phase error determined from the measurement, ϕ_{OBS}, and the multipath phase error estimated from the SNR, ϕ_{EST}, are plotted and compared in figures A.1.4 and A.1.7. In the plots, ϕ_{OBS} and ϕ_{EST} are referred to as LC OBS and LC EST, respectively. The residual phase error given by the difference of these two phase errors, ϕ_{DIFF}, is plotted in fig. A.1.8.a) and is called LC DIFF. The observed phase error shows very large values in correspondence of the structured oscillations. The amplitude of ϕ_{DIFF} decreases significantly after applying the correction for multipath.

To study the characteristics and frequency content of the three time series, (observed, estimated and residual phase error) the Power Density Spectra (PSD) was computed and plotted in fig. A.1.8.b). The PSD of ϕ_{OBS} and ϕ_{EST} are very consistent for amplitude and frequency content. They exhibit three narrow distinct peaks at frequencies between 0.001 Hz and 0.01 Hz, and one large peak at a lower frequency. The frequency content of ϕ_{DIFF} is not as rich as it is for ϕ_{OBS} and ϕ_{EST}.

This result suggests that the contribution due to the multipath effect is filtered out and the remaining phase error, which does not present a clear spectral content, is due to other sources of GPS random noise in the carrier phase observable. In this particular case, where the multipath effect has a predominant role in the observed phase error, the estimation algorithm and multipath filtering is efficient in reducing

the phase residual, as well as the error in the final GPS positioning. However, a low frequency residual component is evident in the PSD of ϕ_{DIFF}. This low frequency component might be caused by reflectors located around 1 - 2 m distance from the antenna phase center of the receiving antenna. An other explanation for this low frequency component could be the atmospheric refraction errors, that produce a very similar pattern. Therefore, with only one example, it is difficult to judge if this low frequency residual error after correction should be considered a limitation of the performances of the estimation algorithm or just an error due to atmospheric effects.

The auto correlation functions of ϕ_{OBS} and ϕ_{EST} shown in fig. A.1.8.c) are very similar and recall the auto correlation of wide-band random noise (the envelope decreases very rapidly, with a first zero crossing at τ=1/(2B), were B is the bandwidth). The cross correlation function between ϕ_{OBS} and ϕ_{EST} is nearly symmetrical and is well centered at zero, again confirming the strong affinity of the two time series being compared. Additionally, the cross-spectral density and the coherence function of fig. A.1.8.d) corroborate this conclusion. The two time series show a very high coherence function (about 0.8) for frequencies between 0.001 Hz and 0.01 Hz.

Another good example of how well the estimation algorithm works in presence of strong multipath is shown in fig. in fig. A.2.1 and A.2.2. The SNR shows distinguished oscillations whenever the satellite PRN 20 is observed by the receiver at an elevation θ = 10° - 24° and azimuth ϕ = 40° - 80°, at the time t= 7.0 - 7.5 10^4 sec. The observed phase error determined from the measurement, $\phi_{OBS,}$ and the multipath phase error estimated from the SNR, $\phi_{EST,}$ are plotted and compared in figures A.2.3, A.2.4 and A.2.7 (segment 2.b). The residual phase error given by the difference of the two phase errors, $\phi_{DIFF,}$ is depicted in fig. A.2.8.a).

In the PSD of ϕ_{OBS} and ϕ_{EST} (fig. A.2.8.b) two main peaks at the same frequencies are predominant , but a significant difference in amplitude can be noticed.

The auto and cross correlations of fig. A.2.8.c) deserve special attention. The auto correlation function of a random process can be directly interpreted as a measure of how well future values can be predicted from past observations. The key information is how large in time is the envelope of the auto correlation function. An envelope which decays rapidly to zero as in fig. A.1.8.c) resembles the auto correlation of wide-band random noise. If the auto correlation decays very rapidly, the knowledge of the exact time history from zero to time t will not significantly help us to predict future

values beyond the very near future, i.e. beyond 1/(2B) past the end of the observed record.

A very large envelope which does not decay rapidly, but which remains almost constant over the near future (central peak 1/(2B)), as in fig. A.2.8.c), resembles the auto correlation of a sin/cos wave + random noise. This suggests that it is possible to predict future values of the data, based on past observations, assuming that the data remain stationary. This comparison of the auto correlations of the two time series with the auto correlations of functions equal to the sum of a sinusoid and random noise, confirms the influence on ϕ_{OBS} and ϕ_{EST} of the multipath (sinusoidal in shape) and of the contributions due to other GPS noises (random noise).

Auto and cross spectral power density and high values of the coherence function (fig. A.2.8 d)), confirm the strong affinity of estimated multipath phase error and observed phase error. As will be discussed in section 6.4, the multipath estimation algorithm is very effective when multipath is the main source of phase error in the GPS measurements, as for the receiver-satellite pair KKAU-PRN 20, segment 2.b.

This is confirmed by another interesting example relevant to KKAU -PRN 22, segment #1. The SNR (fig. A.3.2) presents an evident sinusoidal pattern when the satellite PRN 22 is at an elevation θ = 10° - 30° and azimuth ϕ = 50°, at t=0.0 - 5.0 10^3 sec. The observed phase error determined from the measurement and the multipath phase error estimated from the SNR are presented in figures A.3.3 and A.3.4. The residual phase error ϕ_{DIFF} is plotted in fig. A.3.5.a). For the Power Spectral Density (fig. A.3.5.b)), the auto and cross correlation (fig. A.3.5.c)), the auto and cross spectral density and the coherence function (fig. A.3.5.d)) were computed. Analogous observations than those for KKAU-PRN 20 can be applied.

The examples reported so far are relevant to cases in which a strong, clear multipath phenomenon at frequencies between 0.001 Hz and 0.01 Hz is observed in the phase residual. In these cases the estimation algorithm showed good performances, as determined by spectral analysis. But how does the estimation algorithm work in the presence of other sources of noise or in the presence of a lower frequency multipath? To answer this question segment #2 of the data set relevant to KKAU-PRN 22 was studied. In fig. A.3.6 the observed phase error shows a low frequency component which is not present in the phase error estimated from the SNR. As discussed above, this low frequency undulation might be caused

by multipath due to close reflectors or by atmospheric refraction. In fig. A.3.7 a) ϕ_{DIFF} presents a large amplitude, and a low frequency component.

The PSD of fig. A.3.7b) shows the very different frequency content of the observed and estimated phase error. In fig. A.3.7.c) the two auto correlation functions show very different properties, and the correlation between the two series presents low amplitude and evident asymmetry with respect to the zero. A very low coherence function is found in fig. A.3.7.d) for all the frequency spectra.

5.3.1.b) MANA (ROGUE SNR-8000)

When the SNR data relevant to the measurements acquired by MANA on June 10, 1995 were analyzed, large oscillations were observed every time a satellite was found at low elevation angle and about 300° azimuth.

It appears evident in fig. A.4.1 and A.4.2 that the SNR exhibits large fluctuations when the satellite PRN 26 is at θ = 18° - 22° and ϕ = 250° - 320°, at t=1.0 - 2.0 10^4 sec. ϕ_{OBS} and ϕ_{EST} are shown in figures A.4.3 and A.4.4. ϕ_{DIFF}, is plotted in fig. A.4.5.a). Even though the large oscillations of ϕ_{OBS} are well matched by ϕ_{EST}, the frequency content of the two time series is quite different. ϕ_{OBS} presents a broader spectra (Δf=0.0003 - 0.003 Hz), while ϕ_{EST} has a sharp peak at about 0.0015 Hz, therefore a frequency component at 0.00085 Hz is still present in ϕ_{DIFF}, as shown in fig A.4.5.b).

The auto and cross correlations are shown in fig. A.4.5.c). The coherence function (fig. A.4.5.d) is about 0.6 in the interval of frequency between 0.001 and 0.01 Hz.

Large oscillations of the SNR were also observed for PRN 28 (fig. A.5.2) when the satellite was at an elevation θ = 15° - 35° and azimuth ϕ = 250° - 310°, at t=4.5 - 5.3 10^4 sec (fig. A.5.1). ϕ_{OBS} and ϕ_{EST} are presented in figures A.5.3 and A.5.8. ϕ_{DIFF} is depicted in fig. A.5.9.a). Even though the statistical analysis shows a very strong decrease of the phase error after the correction for multipath, the frequency content of ϕ_{OBS} and ϕ_{EST} is quite different, and a large lower frequency component is found in ϕ_{DIFF}, as observed in fig. A.5.9.b).

The auto and cross correlations of fig. A.5.9.c) suggest a predominance of random noise on the multipath effect in the phase error. The coherence function (fig. A.5.9.d) is close to 0.7 in the interval of frequency between 0.001 and 0.01 Hz.

5.3.1.c) Discussion and Comparison

The previous analysis shows that the multipath frequency for KKAU is usually higher than the one observed for MANA.

In figures A.1.8.b) , A.2.8.b) and A.3.5.b) it is evident that the multipath frequency for KKAU is usually in the range 0.002-0.004 Hz.

For MANA, the multipath frequency is lower than for KKAU and it is in the range 0.0009 - 0.0010 Hz. This indicates that the reflecting surface producing the multipath in this case (MANA) is closer to the receiving antenna and its effect is also more intense. The relationship between the distance of the reflector and the multipath frequency is given in [2.17].

5.3.2 Stations 0036 and 0028 (TRIMBLE 4000SSE)

5.3.2.a) 0036: Dual-band processing

Some a priori information relevant to this site were available and were used to better interpret the results of the spectral and statistical analyses. The geometry of the surroundings of the receiver 0036 is depicted in figure 5.1, where the incoming signal from the satellite PRN 09, located at about 15° elevation and 45° azimuth, reaches the receiver after multiple reflections. The SNR relevant to this satellite-receiver pair is plotted in fig. A.6.4. The SNR is affected by very distinct large oscillations when the satellite is at an elevation θ = 14° - 22° and azimuth ϕ = 40° - 50°, at t=7.3 - 7.5 10^4 sec (fig. A.6.3).

ϕ_{OBS} and ϕ_{EST} are compared in figures A.6.5 and A.6.6. The difference between the two phase errors is plotted in fig. A.6.7.a).

The PSD of ϕ_{OBS} and ϕ_{EST} (fig. A.6.7.b) exhibit one narrow distinct peak at about 0.001 Hz. This information suggests that in this case the multipath is not produced by a complex scattering from several reflectors, but from one distinct reflector producing one distinct frequency component.

Because of the coherence of the two time series, the frequency content of ϕ_{DIFF} does not present any strong predominant frequencies. This implies that the main contribution to the phase error is due to multipath and is filtered out by the correction. The remaining phase error is due to the other sources of GPS random noise, which cannot be corrected with this method.

The auto correlation functions of ϕ_{OBS} and ϕ_{EST} shown in fig. A.6.7.c) present very interesting patterns. The envelope amplitude diminishes slowly and recalls the auto correlation of a narrow-band random noise, where the first zero crossing is at t=1/B (B is assumed small). The bandwidth is smaller in $\phi_{EST,}$ causing its auto correlation function to decay slower than the auto correlation of ϕ_{OBS}. It can be concluded that ϕ_{OBS} contains more random noise and a larger bandwidth scattering.

The cross-spectral density and the coherence function of fig. A.6.7.d) reinforce the conclusion that a distinct frequency is dominant in the signal, with very narrow bandwidth. The two time series show a high coherence function (about 0.7) for frequencies between 0.001 Hz and 0.01 Hz.

Another example of strong multipath is shown in fig. A.8.5 and A.8.6. The SNR relevant to the satellite PRN 25 shows large oscillations when the satellite was at an elevation θ = 15° - 20° and azimuth ϕ = 164° - 168°, at t= 7.5 - 7.7 10^4 sec. The observed phase error determined from the measurement and the multipath phase error estimated from the SNR are plotted and compared in figure A.8.7 (segment #1). ϕ_{DIFF} is shown in fig. A.8.8.a). In this case the oscillations are not as distinct as for PRN 09.

The PSD of ϕ_{OBS} (fig. A.8.8.b) show two narrow peaks, respectively, at frequencies of 0.001 Hz and 0.002 Hz. ϕ_{EST} presents a narrow main peak at 0.002 Hz and a broad band low frequency peak between 0.0001 Hz and 0.0005 Hz. As a result of this spectral difference, the PSD of ϕ_{DIFF} has a predominant low frequency spectral content.

The auto and cross correlations of fig. A.8.8.c) present an envelope rapidly decreasing to zero, as for wide band random noise. This suggests that the multiple phase error does not come from a single reflector, as in the previous case for PRN 09, but might be due to a more complex scattering phenomenon from close and distant surfaces. The cross-spectral density and the coherence function of fig. A.8.8.d) reinforce this conclusion. The two time series show a coherence function of about 0.6 for frequencies between 0.001 Hz and 0.01 Hz.

An interesting example where there is a noticeble difference of amplitude between ϕ_{OBS} and ϕ_{EST}, rather than of frequency content, is given by LIGO 0036, PRN 15. (segment #4). ϕ_{DIFF} is computed in fig. A.7.10.a). The observed phase residual presents small oscillations similar to the ones found in the estimated phase error, but with a different amplitude: ϕ_{OBS} is always negative while ϕ_{EST} is shifted upward and presents some positive and negative values.

The Power Spectra Density (PSD) of this segment of data is shown in fig. A.7.10.b). The PSD of ϕ_{OBS} and ϕ_{EST} are consistent at high frequencies. They both exhibit one peak close to 0.001 Hz.

The auto correlation functions in fig. A.7.10.c) are very different and the cross correlation is asymmetric and small in amplitude.

5.3.2.b) 0036 and 0028: Single Differences for short-baseline L_1 and L_2

As discussed above, for short baselines the ionospheric effects can be filtered using single differencing. In this case it is possible to study the effect of multipath at each of the two GPS frequencies and the performance of the estimation algorithm for L_1 and L_2.

In this section we show the results of the analysis of L_1 and L_2 separately, as two independent observables. ϕ^1_{OBS}, ϕ^1_{EST}, and ϕ^1_{DIFF} indicate respectively, the observed phase residual, the multipath phase error and their difference, respectively, for L_1.

ϕ^1_{OBS} and ϕ^1_{EST} are compared in fig. A.9.1 and A.9 2. ϕ^1_{DIFF} is shown in fig. A.9.3.a). PSD of ϕ^1_{OBS} and ϕ^1_{EST} are presented in fig. A.9.3.b).

The spectral content of ϕ^1_{OBS} and ϕ^1_{EST} is very similar at higher frequencies, showing a predominant peak at 0.002 Hz, but does not agree at lower frequencies. Therefore, the PSD of ϕ^1_{DIFF} shows a spectral content only at lower frequencies (below 0.001 Hz).

The auto correlation of ϕ^1_{EST} (fig. A.9.3.c) recalls the one of a narrow-band random noise. The cross correlation R_{oe} is well centered but slightly asymmetric. A good coherence is found at f=0.001 Hz.-0.01 Hz (fig. A.9.3.d). In this case the frequency content matches very well, but the shift in amplitude causes ϕ^1_{DIFF} to stay large also after the correction. A very different result is obtained for L2 (fig. A.9.4 and A.9 5), where the amplitude of ϕ^2_{DIFF} is well reduced (fig. A.9.6.b)), even though a low coherence is observed (fig. A.9.6.d)).

5.3.3 COSE and GS29

5.3.3.a) COSE (TRIMBLE 4000SSE)

The data considered for this analysis were acquired on January 23, 1997 using a Trimble antenna . Any time a satellite was at a low elevation angle (θ = 10° - 20°) and azimuth ϕ = 50° - 70°, the SNR showed large oscillations at L1 and L2. An example of the multipath phenomenon occurring in proximity of COSE is provided in fig. A.11.1 and A.11.2.

The satellite PRN 25 passed through the critical region in the field of view of COSE at t=5.6 - 6.2 10^4 sec. ϕ_{OBS} and ϕ_{EST} are plotted and compared in figure A.11.3 (segment #3). ϕ_{DIFF} is computed in fig. A.11.6.a).

The observed phase error presents only one very large oscillation at the end of the segment, probably due to reflections from the ground because the antenna was located on a large slope. The satellite was setting and this strong reflection can therefore take place at a very low elevation angle (θ = 10°).

The Power Spectral Density of this segment of data is shown in fig. A.11.6.b). The PSD of ϕ_{OBS} and ϕ_{EST} are very consistent for amplitude and frequency content.

They both exhibit large peaks at the same frequency, about 0.001 Hz, but with very different amplitudes. This is the reason why ϕ_{DIFF} still carries a considerable frequency content. In this particular case, it is not the frequency content, but the amplitude of the multipath phase error estimated by the algorithm that produced the critical result. An overestimation of the amplitude of the oscillation increases the total phase error after the multipath correction.

The auto correlation functions of ϕ_{OBS} and ϕ_{EST} shown in fig. A.11.6.c) recall the auto correlation of a wide-band random noise. The cross-spectral density of fig. A.11.8.d) confirm the previous results of the spectral analysis. The two time series show a very high coherence function (about 0.8) for frequencies between 0.0005 Hz and 0.01 Hz.

An interesting case to study is COSE PRN 01, segment 1b., In chapter 3 the technique for the multipath estimation was described. When the fit of the multipath model and the SNR curve is performed, some problems can rise, due to the method used for the fit (section 3.3.3). ϕ_{DIFF} presents sudden changes of sign deriving from ϕ_{EST} (fig. A.9.6.a)). Correlation and spectral analysis show a poor agreement between ϕ_{OBS} and ϕ_{EST}.

5.3.3.b) GS29 (ASHTECH Z-XII3)

The same set of GPS measurements discussed in section 5.3.3.a) were repeated by using an Ashtech antenna, placed at the same location of COSE, the day after (on January 24, 1997). As for COSE, the satellite PRN 25 was considered, and the analysis on the station GS29 was performed (fig. A.14.1 and A.14.2)

ϕ_{OBS} and ϕ_{EST} are shown in figure A.14.3 and A.14.4 (segment #3). ϕ_{DIFF} is computed in fig. A.14.7.a). The observed phase error presents only one very large oscillation at the end of the segment, as was observed for COSE.

The PSD of this segment of data is shown in fig. A.14.7.b). The PSD of ϕ_{OBS} and ϕ_{EST} are very consistent for amplitude and frequency content. They both exhibit one large peak of similar amplitude at about 0.001 Hz. ϕ_{DIFF} does not present a considerable frequency content, because in this case the frequency content and the

amplitude of the multipath phase error estimated by the algorithm match very well the observed phase error. Therefore, as will be discussed in the statistical analysis, the application of the algorithm produces a strong decrease of the phase error after the multipath correction.

The auto correlation functions of ϕ_{OBS} and ϕ_{EST} presented in fig. A.14.7.c) is similar to those found for wide-band random noise. The cross-spectral density of fig. A.14.7.d) confirms the previous results of the spectral analysis. The two time series show a very high coherence function (about 0.8) for frequencies close to 0.002 Hz.

In the conclusion of section 5.3.3.a) and 5.3.3.b), it was found that the estimation algorithm applied to data acquired at the same location and the same time of the day with two different antennas presented different performances. The algorithm seems to work better for Ashtech antennas. However, because the weather conditions during the two successive days were not the same, it is difficult to assess if the results are actually due to the antenna type, or to the higher multipath effect observed on rainy days. We already noticed that the multipath estimation algorithm is very efficient when strong multipath is observed, especially if it is predominant with respect to other kinds of noise. It is therefore possible that a different wetness of the ground, producing a higher reflectivity of the reflecting surfaces, might have caused a better performance of the algorithm. One way to answer this question is to consider two sets of measurements acquired with the same antenna, during these two days of observations and compare the results. This is done in the next section, for COSO(Ashtech).

5.3.3.c) COSO (ASHTECH Z-XII3)

For this analysis we selected the measurements relevant to the satellite PRN 30 , because of the large oscillations observed in SNR and ϕ_{OBS} (fig. A.15.1 and A.15.2). The phase residual ϕ_{DIFF} is shown in fig. A.15.3.a). The PSD of ϕ_{OBS} and ϕ_{EST} (fig. A.15.3.b)) present the same peaks at 0.0005 Hz, but ϕ_{OBS} also has peaks at lower and higher frequencies (0.0001 and 0.001), which are found again in the PSD of ϕ_{DIFF}.

The correlation of the two series (fig. A.15.3.c)) as well as the coherence (fig. A.15.3.d)) is very poor.

The same measurement was repeated the next day, in weather conditions favorable for strong multipath (rainy day). The phase residuals relevant to these measurements are plotted in fig. A.16.1 and A.16.2. The PSD of ϕ_{OBS} and ϕ_{EST} (fig. A.16.3.b)) present a very similar spectral content, showing a predominant peak at 0.0004 Hz. The correlation (fig. A.16.3.c)) and coherence (fig. A.16.3.d)) are higher than in figures A.16.3.c)) and (fig. A.16.3.d)). This result confirms that the wetness of the ground increases the multipath effects, and therefore the performance of the estimation algorithm improves.

5.4 Multipath Estimation and Results of the Statistical Analysis

The following is a summary of the results obtained from the statistical analysis of the GPS phase residuals, described in Chapter 4. The study focused on 6 GPS stations, MANA, KKAU, 0028, 0036, COSE and GS29, because of their strong multipath environment. The analysis includes 42 sets of data, collected and sorted in tables B.1.a) and b) through B.5.a) and b).

The variance of the observed phase residual is referred to as σ_{OBS}^2 , and denotes the total phase error due to the combined effects of different sources of noise for the GPS carrier phase observable. σ_{EST}^2 is the variance of the estimate of the multipath phase error retrieved by using the SNR information. The difference between σ_{OBS}^2 and σ_{EST}^2 is the corrected phase error, and its variance is denoted with σ_{DIFF}^2. The difference of variance of the phase error before and after the correction for multipath was computed along with the statistical uncertainty of the estimate of the change. This computation allows us to determine how well the correction improves the GPS positioning by quantitative means.

Whenever a negative value is obtained for (σ_{OBS}^2 - σ_{DIFF}^2), the correction for the multipath phase error does not reduce the variance of the total phase error. A positive value, on the other hand, would imply a decrease of the variance of the GPS

phase error, and, thus, an improvement in the final GPS positioning. When such a positive value is obtained, the percentage decrease of variance was computed, to make it easier to quantify the improvement of the variance after correction.

There is a noticeable decrease of the variance after the multipath correction any time the variance of the "true" multipath noise σ_{MPN}^2 is higher or at least comparable to the variance of the GPS measurement noise, σ_{MN}^2, due to other sources of noise different from multipath. In other words, the algorithm for multipath phase error estimation shows very good performance whenever the multipath effect is the main source of phase error. Good examples of this observation are given in MANA 26 1b and MANA 28 2a (Table B.1.a and b), KKAU 16 2c (Table B.2.a and b), LIGO 0028-0038 09 1 (Table B.3.a and b) and GS29 25 3 (Table B.5.a and b). In these cases the decrease of variance of the phase error after correction is more than 35%.

The value σ_{EN}^2 is a measure of the error due to the estimation process and gives information about the accuracy of the procedure for the phase error estimation.

The examples previously discussed present a small σ_{EN}^2 value with respect to the multipath noise variance σ_{MPN}^2. This result confirms that the estimation algorithm is most accurate when a strong multipath is present.

However, an exception to the previous cases is COSE 01 1c (Table B.4.a and b), a measurement performed with a Trimble antenna. Even though the multipath noise variance is more than 3 times larger than σ_{MN}^2, the multipath estimation noise is of the same order of magnitude as σ_{MPN}^2 and the decrease of variance after correction is only 4%. This measurement was repeated the following day , in rainy weather, exactly at the same location, using an Ashtech antenna (GS29 01). It turns out that σ_{MN}^2 drops to 1/10 the value of σ_{MPN}^2 and the decrease of variance after correction improves to 16 % (Table B.5.a and b).

Good examples of poor multipath in an otherwise very noisy measurement ($\sigma_{MPN}^2 << \sigma_{MN}^2$) are MANA 26 2c (Table B.1.a and b) , KKAU 22 2 (Table B.2.a and b) and GS29 25 1 (Table B.5.a and b). In these cases there is no decrease of variance after correction and the estimation noise variance σ_{EN}^2 is larger than the multipath noise variance σ_{MPN}^2 itself.

Chapter 6

Conclusions

The algorithm for the estimation of the GPS multipath phase error presented in this thesis was applied and analyzed, to test its performance and limits. The estimated multipath phase error and the observed phase residual were compared by spectral and statistical analysis.

In most of the cases analyzed, a broad-band coherence function between the observed phase error and the estimated multipath phase error was found in presence of strong multipath. This suggests that the effects of multiple reflectors are correctly estimated by the proposed algorithm. In other words the technique of estimating each multipath phase error iteratively from the spectral analysis of the SNR and of adding each contribution to obtain the composite value, produces a correct estimation of the total multipath phase error.

In particular, the set of data which show the highest coherence (MANA and KKAU and LIGO 0036) have multipath frequencies between 0.001 and 0.01 Hz. Because the multipath frequency depends on the distance of the receiving antenna from the reflecting surface, knowing the elevation angle of the satellite and its variation with time, we can derive the distance of the reflecting object. The spectral analysis suggests that the estimation algorithm presents good performances for reflectors located at distances between 5.50 m and 55.0 m from the receiving

antenna, for an elevation angle of 10° and a rate of change of the elevation angle of 0.1 mrad/sec. The high coherence is confirmed by the statistical analysis, which shows a significant decrease of the RMS of the phase residual after the multipath correction.

When the multipath effect is due to reflections from the ground (about 1.5 - 2.0 m) the multipath frequencies are lower (COSE and GS29). At lower frequencies it was found that the algorithm performed better for data sets acquired in the same location by an Ashtech receiver (GS29, January 24,1997), rather than a Trimble (COSE, January 23,1997). This result can be due to the different receiver types, the different antenna gains or/and the weather conditions.

As explained in section 2.3, Trimble and Ashtech receivers use different techniques for the signal processing of L_2 in presence of antispoofing. Trimble receivers cross correlate L_2 with L_1 and the available SNR limits the bandwidth of the L_2 carrier. A narrower bandwidth corresponds to a longer integration time, which makes it more difficult to track large oscillations of the SNR, especially at low frequencies. Ashtech receivers use the Z-tracking technique, which provides a better SNR compared to other techniques. Because the estimation algorithm proposed in this thesis manipulates the SNR information to retrieve the multipath phase error, the errors introduced by each receiver in the determination of the SNR strongly influence the performance of the algorithm.

GPS measurements acquired by the station COSO in the same days, one sunny and dry (January, 23 1997), the other rainy and gray (January, 24 1997), suggests that also the weather conditions considerably change the performance of the algorithm. A higher water content in the ground increases its reflection coefficient, causing the multipath effects to be stronger in rainy more than in dry weather. On the other hand, the performance of the algorithm is good when strong multipath is observed, because the main contribution to the observed phase residual is due to the multipath phase error. In other words, when multipath is the main error contribution, the estimated multipath phase error is highly correlated to the total observed phase residual.

Low frequency oscillations of the SNR might also be produced by the ionosphere (scintillation) but these effects are likely to be small. Low frequency SNR variations are most likely to be due to the gain pattern of the antenna, especially for the

Trimble antennas. These antennas are known to have azimuthally dependent gain patterns, which are not accounted for in the estimation algorithm. The algorithm might interpret these oscillations as multipath, and, therefore, estimate a false phase error.

We already pointed out that different antennas might influence the performances of the algorithm. The Dorne-Margolin antennas have a higher gain pattern at very low elevation angles with respect Trimble antennas: this suggests that more multipath contributions from lower elevation angles are received with a higher amplitude.

The study of short baselines (LIGO 0036-0028, PRN 09) allows as to consider the single differences for L1 and L2 separately: the results of the spectral analysis show a high broad-band coherence for the multipath phase error at L1 but a very low coherence at L2. However, in both cases the multipath estimation produces a decrease of the RMS of the total phase error after correction, as it is shown by the results of the statistical analysis. The best performance in terms of both, spectral and statistical analysis was obtained using the estimation algorithm for the dual-frequency mode (LC_EST). Because the square root of the PSD (power spectral density) of the observed phase error is almost equal to the sum of the square root of the estimated phase error and the difference between observed and estimated for the most of the cases, we can deduce that the two curves we are comparing (LC_OBS and LC_EST) are in phase, and there is only a difference in amplitude between them. This is consistent with having a very high correlation function and with L2 having the correct phase but the wrong amplitude.

One problem of the estimation algorithm which is important to mention is related to the sign of the phase error. As it was pointed out in chapter 2, the same SNR can be due to opposite values of the phase error, (positive and negative). Therefore, the sign of the phase error cannot be uniquely determined. In some cases this indetermination might cause an abrupt change of the sign of the estimated phase error (COSE PRN 01, segment 1b), producing a considerable degradation of the performances of the estimation procedure.

In summary, the proposed algorithm shows good results when multipath is the main contribution to the total phase error and it frequency is in the range 0.001-0.01 Hz. At lower frequencies, the performance depends on the receiver-antenna type

and the weather conditions. The sign of the phase error and the nature of the low frequency oscillations are critical for the results of the estimation.

References

Axelrad, P., C. J. Comp and P. F. MacDoran, "Use of Signal-to-noise Ratio for Multipath Error: Correction in GPS Differential Phase Measurements: Metodology and Experimental Results", Proceedings of ION GPS-94, September 1994.

Balanis, C.A., 1982, Antenna theory: analysis and design. New York : Harper and Row series in electrical engineering.

Balanis, C.A., 1989, Advanced Engineering Electromagnetics, John Wiley & Sons

Becker, D., P. Hartl and K.-H. Thiel, A special method of managing multipath effects,

Bendat, J.S. and A.G. Piersal, Engineering Applications of Correlation and Spectral Analysis, John Wiley&Sons, Inc., 1993.

Bletzacker, F. " Reduction of Multipath Contamination in a Geodetic GPS Receiver," Proceedings of the First International Symposium on Precise Positioning with the Global Positioning System, U.S., Department of Commerce, National Oceanic and Atmispheric Administration, Rockville, MD, pp. 413-422, April 1985.

Blewitt, G., "Advances in Global Positioning System Technology for Geodynamic Investigations: 1978-1992" in Contributions of Space Geodesy to Geodynamics: Technology, Geodyn. Ser., Vol.25, edited by D.E. Smith and D.L. Turdotte, pp.195-213, AGU, Washington, DC, 1993.

Blewitt, G., "Carrier Phase Ambiguity Resolution for the Global Positioning System Applied to Geodetic Baselines up to 2000 km", Journal of Geophysical Research, Vol. 94, No. B8, pp 10187-10203, August 10, 1989.

Bock, Y., Gourevitch, S.A., Counselman III C.C., King R. W., and Abbot R.I., " Interferometric analysis of GPS phase observations, Manus. Geod., 11, 282-288, 1986.

Braasch, M., " On the Characterization of Multipath in Satellite-Based Precision Approach and Landing Systems", Ph.D. Dissertation, Deparment of Eleectrical Engineering and Computer Engineering, Ohio University, Athens, OH, June 1992.

Braasch, M., "Isolation of GPS Multipath and Receiver Tracking Errors," Proceedings of the ION National Technical Meeting, San Diego, CA, Institute of Navigation, Washington, DC, pp. 511-521, Jan. 1994.

Breeuwer, E., "Modeling and Measuring GPS Multipath Effects," Master's Thesis, Department od Electrical Engineering, Delft University of Technology, Delft, The Netherlands, January 1992.

Clark, T., "GPS antennas: De-mystivying Multipath", NASA Goddard International Memorandum, March 5, 1992.

Collin, R.E., Zucker F.J., Antenna Theory, McGraw-Hill, 1969.

Counselman, C., and Gourevitch, S., "Miniature Interferometer Terminals for Earth Surveying: Anbiguity and Multipath with Global Positioning System," IEEE

Transaction on Geoscience and Remote Sensing, Vol. GE-19, No.4, pp. 244-252, 1981.

Counselman, C., "Miniature Interferometer Terminals for Earth Surveying (MITES): Geodetic Results and Multipath Effects," Digest of the International Geoscience and Remote Sensing Symposium, Washington, DC, Institute of Electrical and Electronics Engineers, New York, pp 219-224, June 1981.

Dong, D., Bock Y., " Global Positioning System Network Analysis With Phase Ambiguity Resolution Applied to Crustal Deformation Studies in California.

Elosegui, P., J. L. Davis, R. T. K. Jaldehag, J. M. Johansson, A. E. Niell and I. I. Shapiro, "Geodesy using Global Positioning Systems: The effects of signal scattering on estimates of site position", Journal of Geophysical Research, Vol. 100, No. B7, pp. 9921-9934, 1995.

Evans, A., "Comparison of GPS pseudorange and Biased Doppler Range Measurements to Demonstrate Signal Multipath Effects," Proceedings of the International Telemetering Conference, Las Vegas, NV, Instrument Society of America, Research triangle Park, NC, pp.795-801, Oct. 1986

Georgiadou, Y. and Kleusberg, A., "On Carrier Signal Multipath Effects in Relative GPS Positioning" Manuscritpa Geodetica, Vol.13, pp. 172-179, 1988.

Hajj, G. A., The Multipath Simulator: A Tool Toward Controlling Multipath, in Proceedings of the 2nd Symposium on GPS Applications in Space, Hanscom AFB, MA, 1990.

Herring, T.A., "Precision of Vertical Position Estimates from Very Long Baseline Interferometry", Journal of Geophysical Research, Vol. 91, 9177-9182, 1986.

Herring, T.A., "Precision and Accuracy in Intercontinental Distance Determinations Using Radio Interferometry", Ph.D. Dissertation, Department of

Earth and Planeraty Sciences, at the Massachussets Institute of Technology, July, 1983.

King, R.W., and Y. Block, Documentation for the MIT GPS analysis software: GAMIT, Mass. Inst. of Technology, Cambridge, 1993.

Kong, J.A., Electromagnetic Wave Theory, John Wiley & Sons, 1990.

Kee, C. and B. W. parkinson, Calibration of Multipath Errors on GPS Pseudorange Measurments,

Kraus, J.D., "Electromagnetics", McGraw-Hill Inc., 1992.

Meehan, T., and Young, L., "On-Receiver Signal Processing for GPS Multipath Reduction," Proceedings of the 6th International Geodetic Symposium on Satellite Positioning, Columbus, OH, Defense Mapping Agency and the Ohio State University, Columbus, OH, pp. 200-208, March 1992.

Oppenheim, A.V., R.W. Schafer, Discrete-Time Signal Processing, Prentice-Hall Inc., Englewood Cliffs, New Jersey 07632, 1989.

Parkinson, B., Spilker Jr, J., "Global Positioning System: Theory and Applications," Vol.I and Vol. II, Volume 163 and Volume 164, Progress in Astronautics and Aeronautics, Published by the American Institute of Astronautics and Aeronautics, Inc. 370 L"Enfant Promenade, SW, Washington, DC 20024-2518.

Schupler, B. R. and R. L. Allshouse, "Signal Characteristics of GPS User Antennas", Navigation: Journal of the Institute of Navigation, Vol. 41, No.3, pp 277-295, 1994.

Schupler, B. R., R. L. Allshouse and T. A. Clark, Signal Characteristics of GPS User Antennas, Navigation, Vol. 41, 277-295, 1994.

Sennott, J., and Pietraszewski, d., "Experimental Measurements and Characterization of Ionospheric and Multipath Errors in Differential GPS,"Navigation, Vol. 34, No.2, pp.160-173, 1987.

Spilker, J.J., "GPS Signal Structure and Performance Characteristics", J. of Inst. Navig., Vol. 25(2), pp. 121-146, 1978.

Tranquilla, J., and Carr, J., "GPS Multipath Field Observations at Land and Water Sites", Navigation, Vol. 37, No.4, pp.393-414, 1991.

Tranquilla, J.M., Carr, J.P., Al Rizzo, H.M., "Analysis of a Choke ring groundplane for multipath control in Global Positioning System (GPS) applications" , IEEE Trans. Antennas Propag., Vol. 42, pp 905-911, 1994.

Van Dam, T.M., T.A. Herring, "Detection of atmospheric pressure loading using very long baseline interferometry measurments", Journal of Geophysical Research, Vol. 99, No. B3, pp. 4505-4517, March 10, 1994.

Van Nee, R., "Multipath Effects on GPS Code Phase Measurements," Proceedings of ION GPS-91, Albuquerque, NM, Institute of Navigation, Eashington, DC, Sept. 1991, pp. 915-924.

Van Nee, R., "Spread Spectrum Code and Carrier Synchronization Errors Caused by Multipath and Interference," IEEE Transactions on Aerospace and Electronic Systems, Vol. 29, No. 4, pp. 1359-1365, 1993.

White, P.H., "Cross-Correlation In Structural Systems: Dispersive ans Non-Dispersive Waves", Journal of the Acoustic Society of America, Vol. 45, No. 5, pp. 1118, May 1969.

Young, L.E., Neilan R.E., and F.R. Bletzacher, "GPS Satellite Multipath: An Experimental Investigation" Proceedings of the First Symposium on Precise Positioning With the Global Positioning System, National Oceanic and Atmospheric Administration, Rockville, Maryland, pp.423-432, 1985.

Appendix A

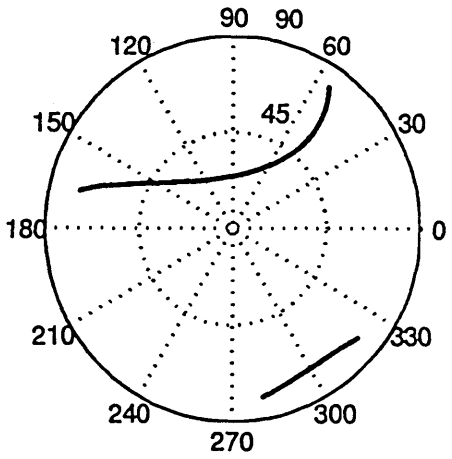

GPS DATA: receiver location: CENTRAL ASIA acquisition date: 10 6 1995

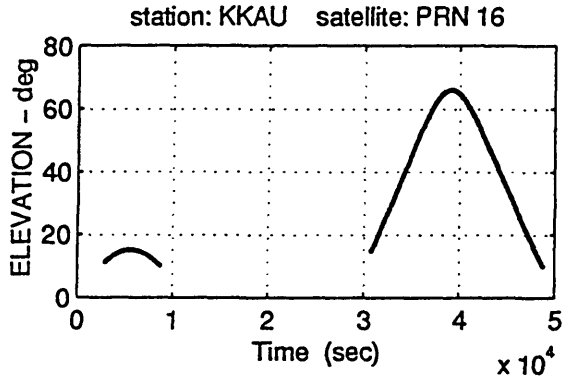

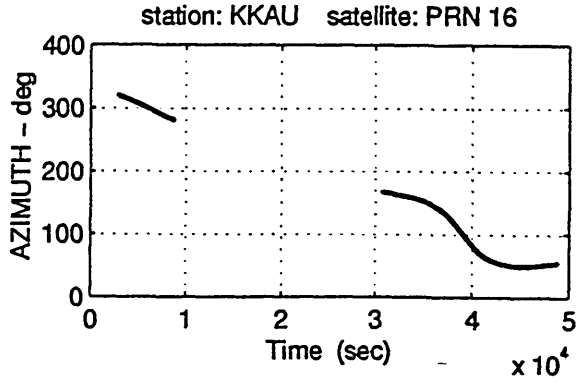

Fig. A.1.1 : Satellite visibility chart for PRN 16 (skymap). Elevation and azimuth of PRN 16 with respect to the station KKAU.

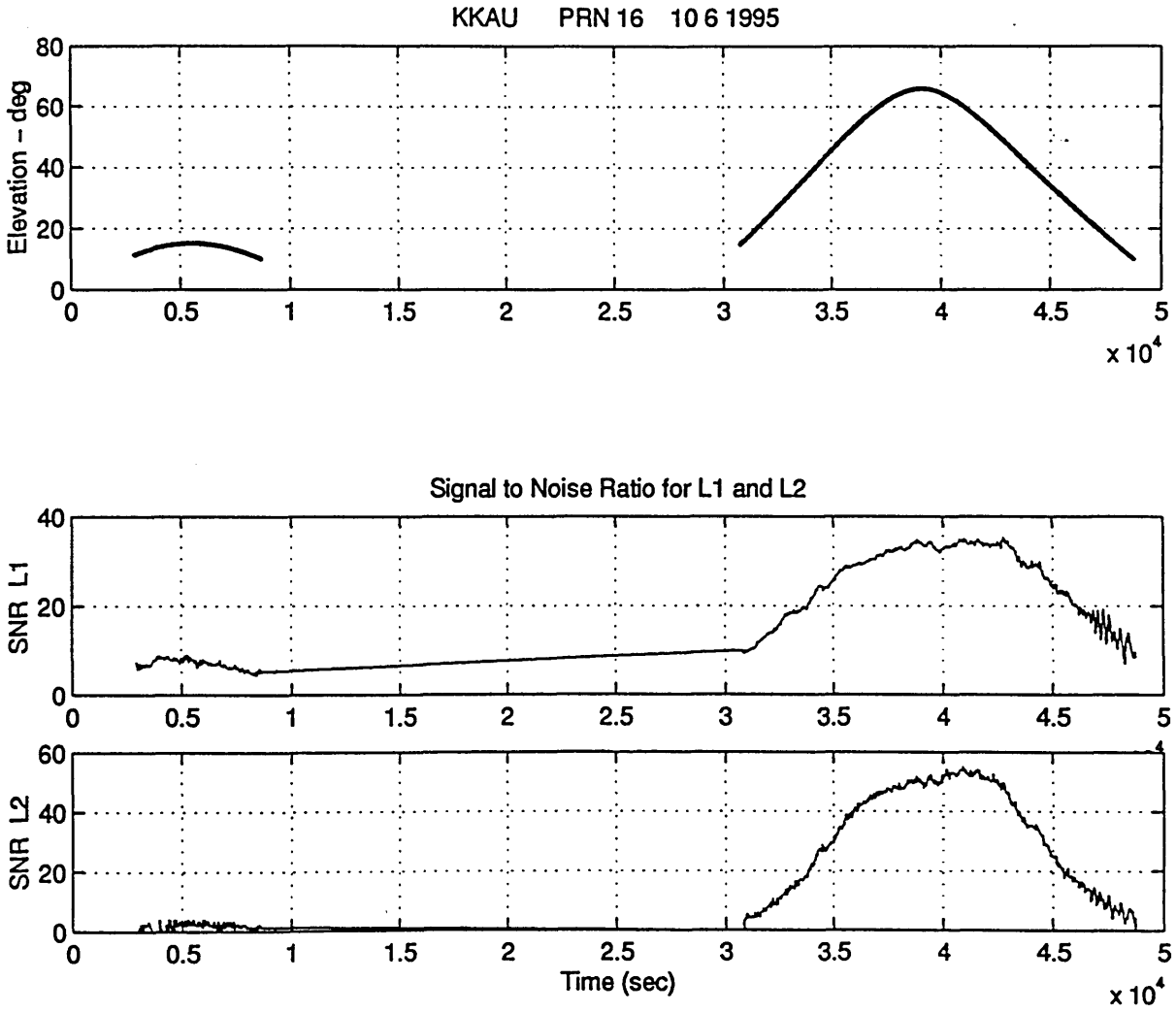

Fig. A.1.2 : Station: KKAU - Satellite: PRN 16 -
Data acquisition date 10 6 1995.
Signal-to-Noise-Ratio (SNR) for L1 and L2.

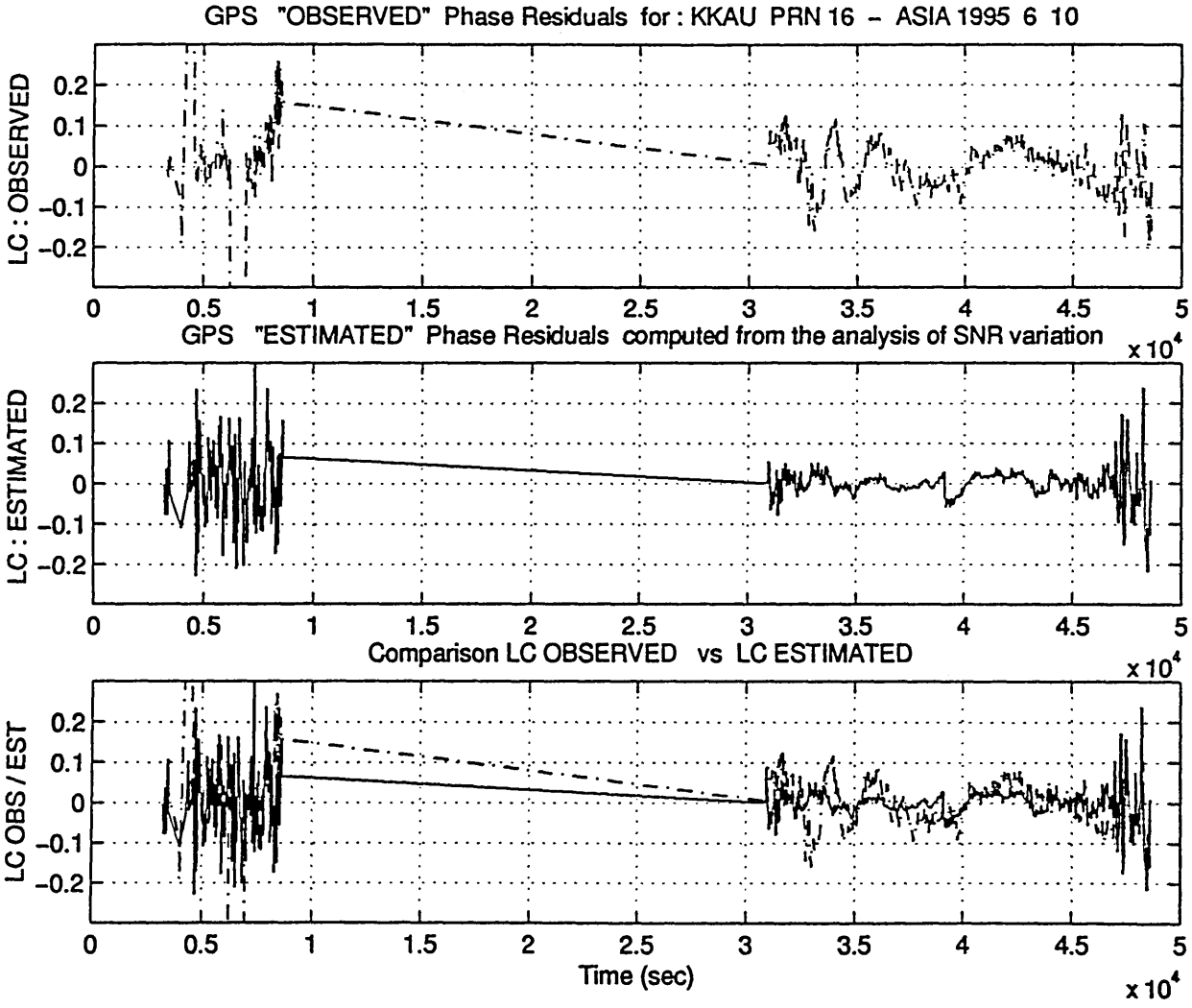

Fig. A.1.3 : Station: KKAU - Satellite: PRN 16
Data acquisition date 10 6 1995
The observed phase residual (LC_OBS) is compared with the multipath phase error estimated from the SNR (LC_EST).
Unit: [cycles].

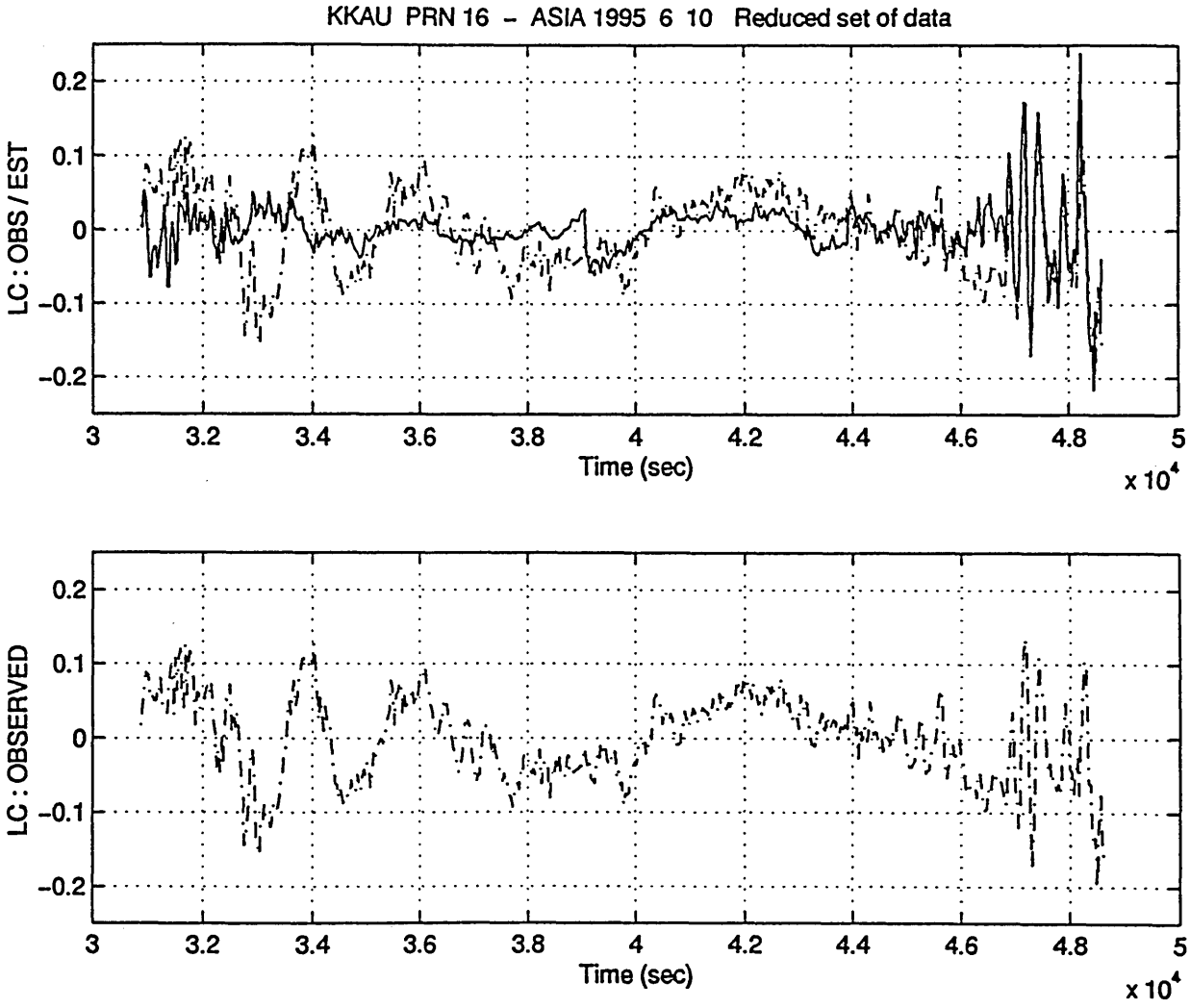

Fig. A.1.4 : Station: KKAU - Satellite: PRN 16 -
Data acquisition date 10 6 1995
LC_OBS and LC_EST compared for t=3.0 - 5.0 10^4 sec
Unit: [cycles].

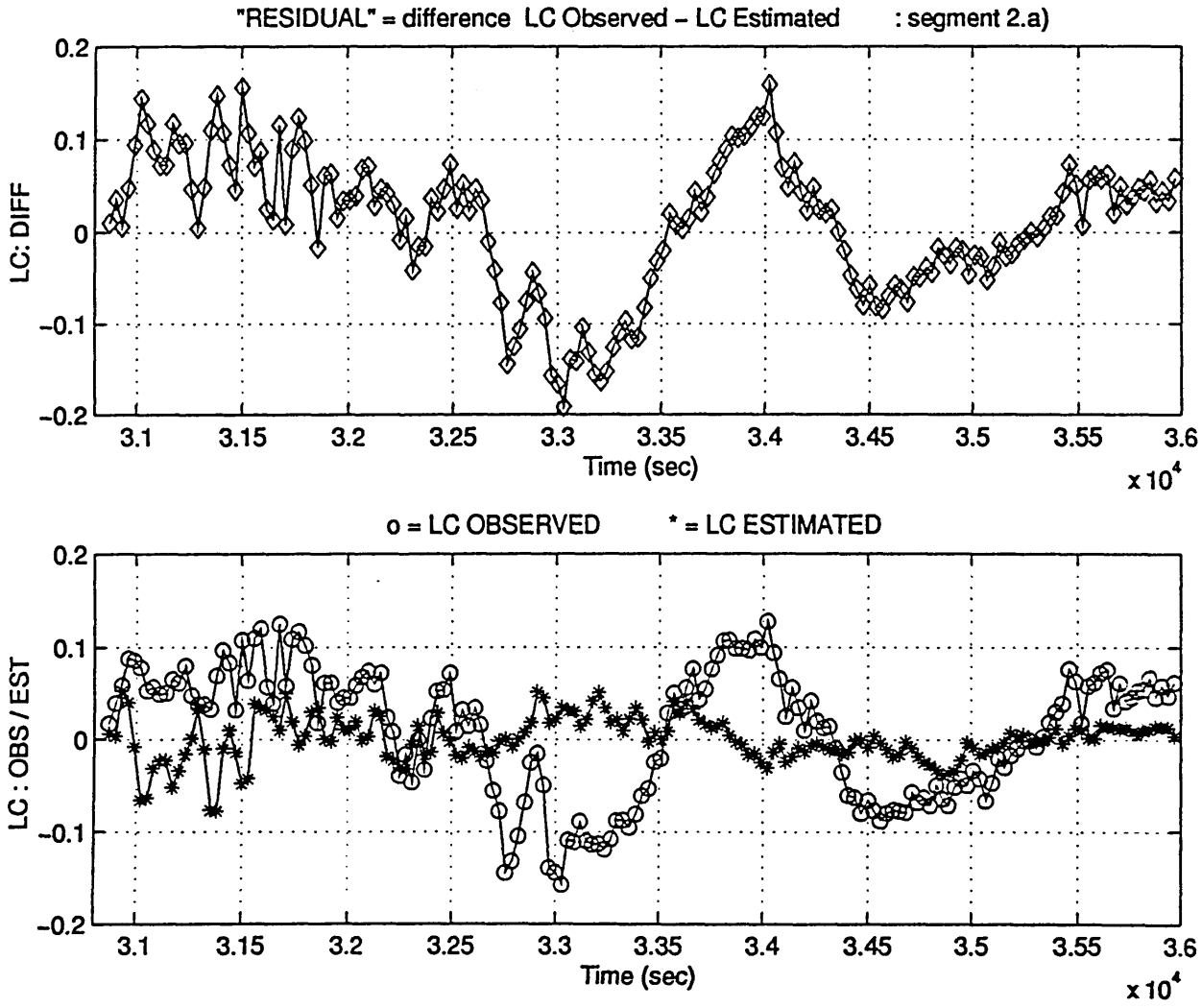

Fig. A.1.5.a) : KKAU - PRN 16 (10 6 1995) - [segment 2a]
Phase residual LC_DIFF, determined as the difference between LC_OBS and LC_EST.
Unit: [cycles]

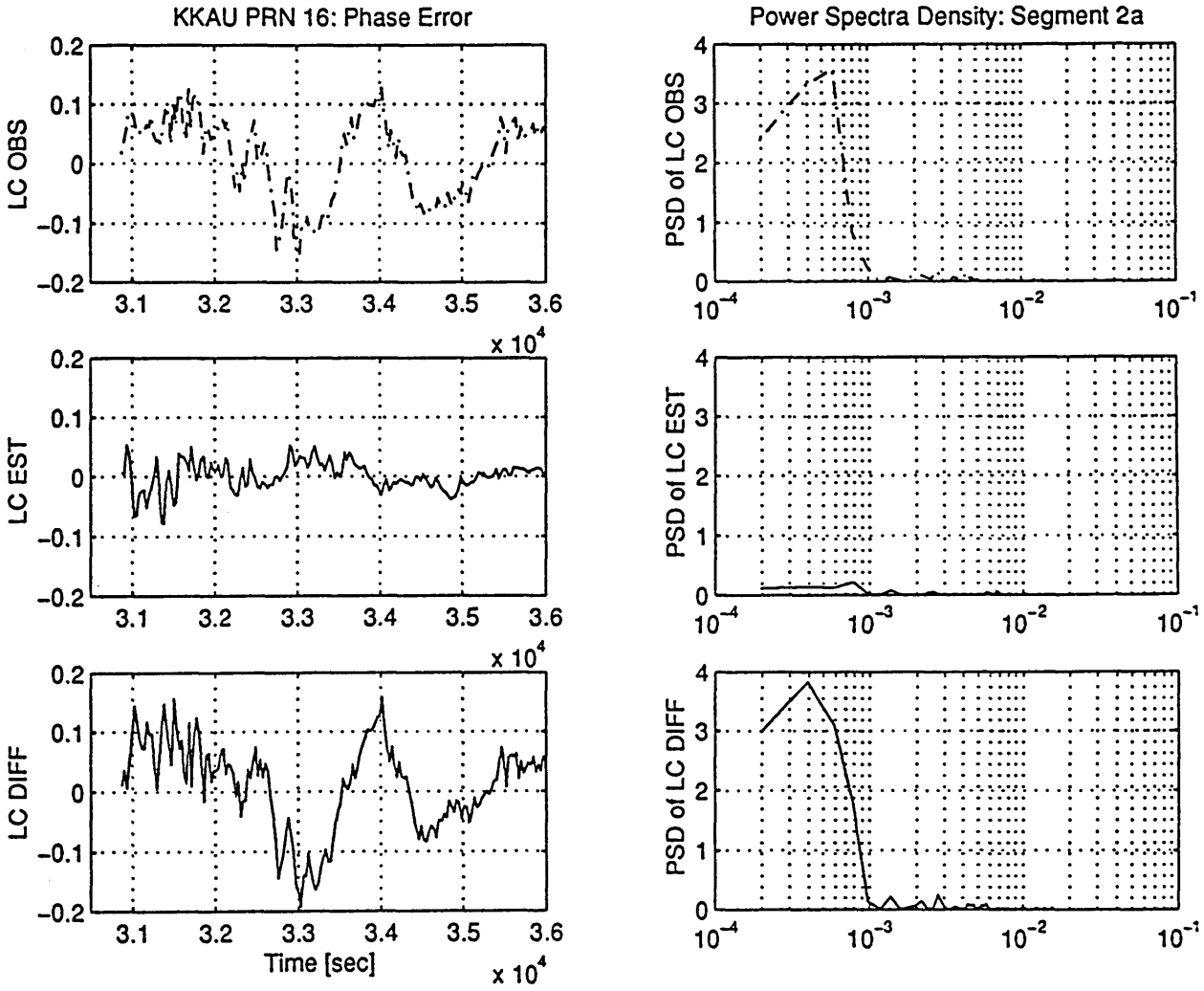

Fig. A.1.5.b) : KKAU - PRN 16 (10 6 1995) - [segment 2a]
PSD of LC_OBS, LC_EST and LC_DIFF.
Unit: [cycles]^2

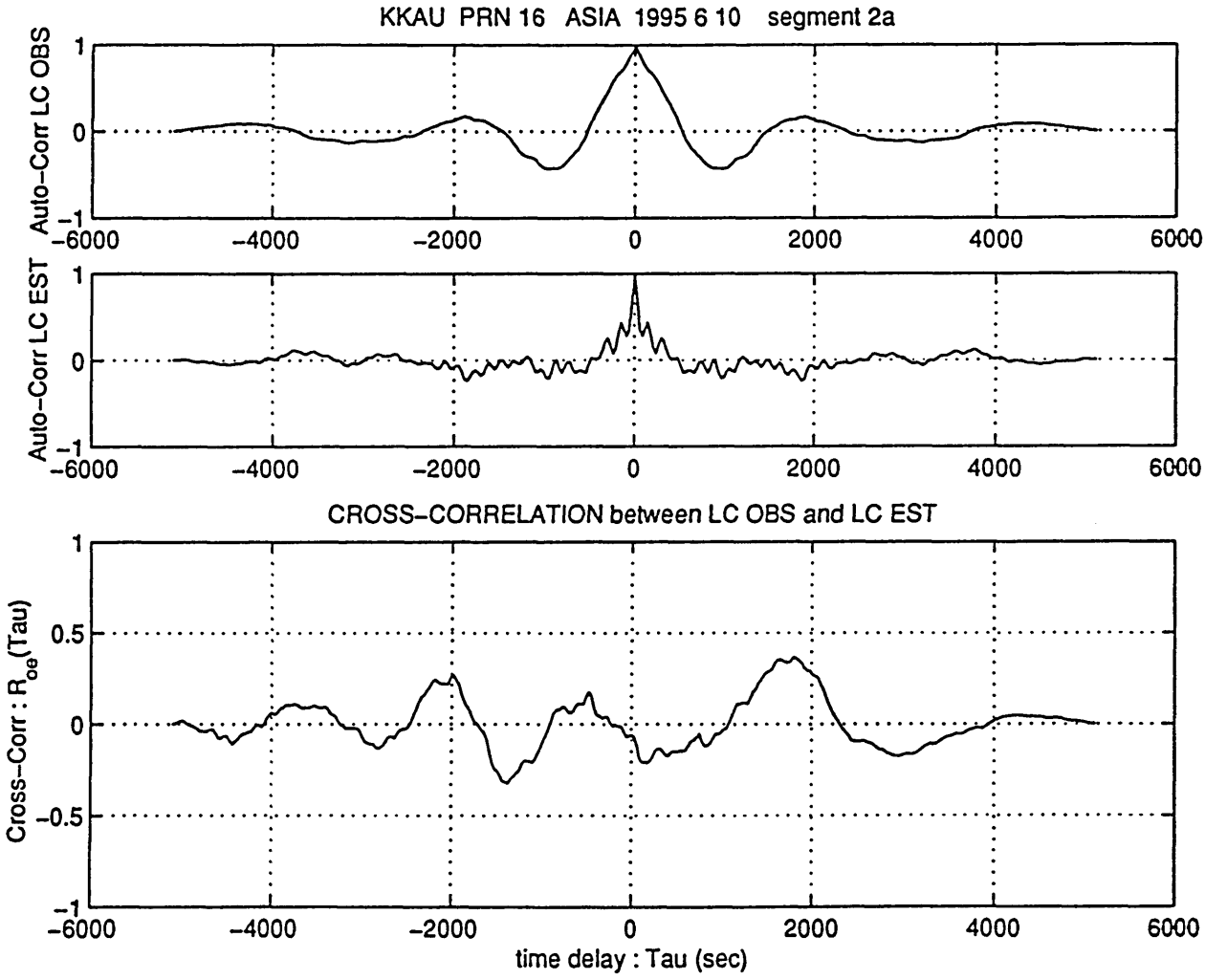

Fig. A.1.5.c) : KKAU - PRN 16 (10 6 1995) - [segment 2a]
Auto Correlation of LC_OBS (R_{oo}) and LC_EST (R_{ee})
Cross Correlation between them (R_{oe})
Unit: [cycles]^2

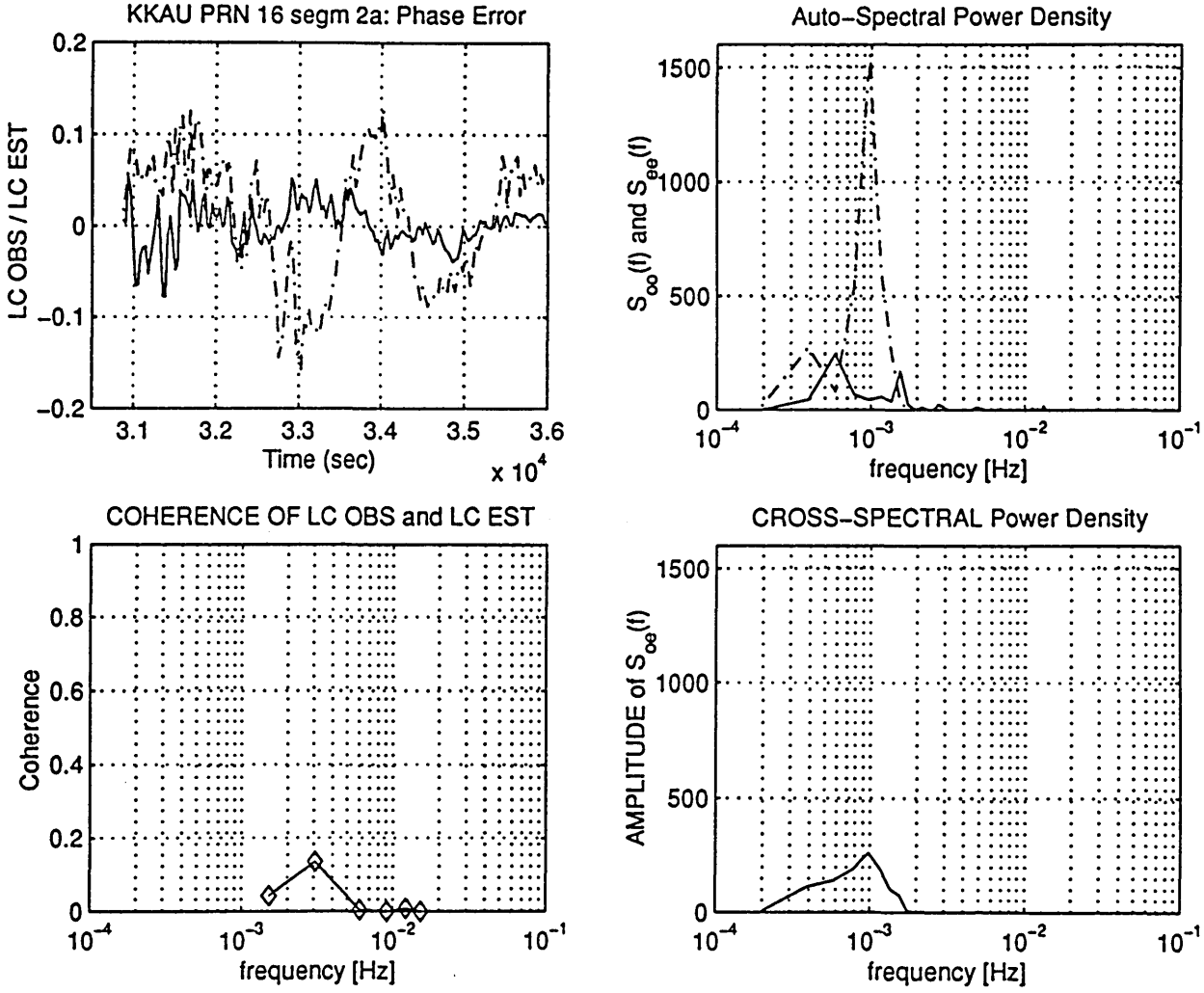

Fig. A.1.5.d) : KKAU - PRN 16 (10 6 1995) - [segment 2a]
Auto Power Spectral Density of LC_OBS (S_{oo}) and of LC_EST (S_{ee}). Cross PSD between them (S_{oe})
Unit: [cycles]^2
Coherence function of LC_OBS and LC_EST

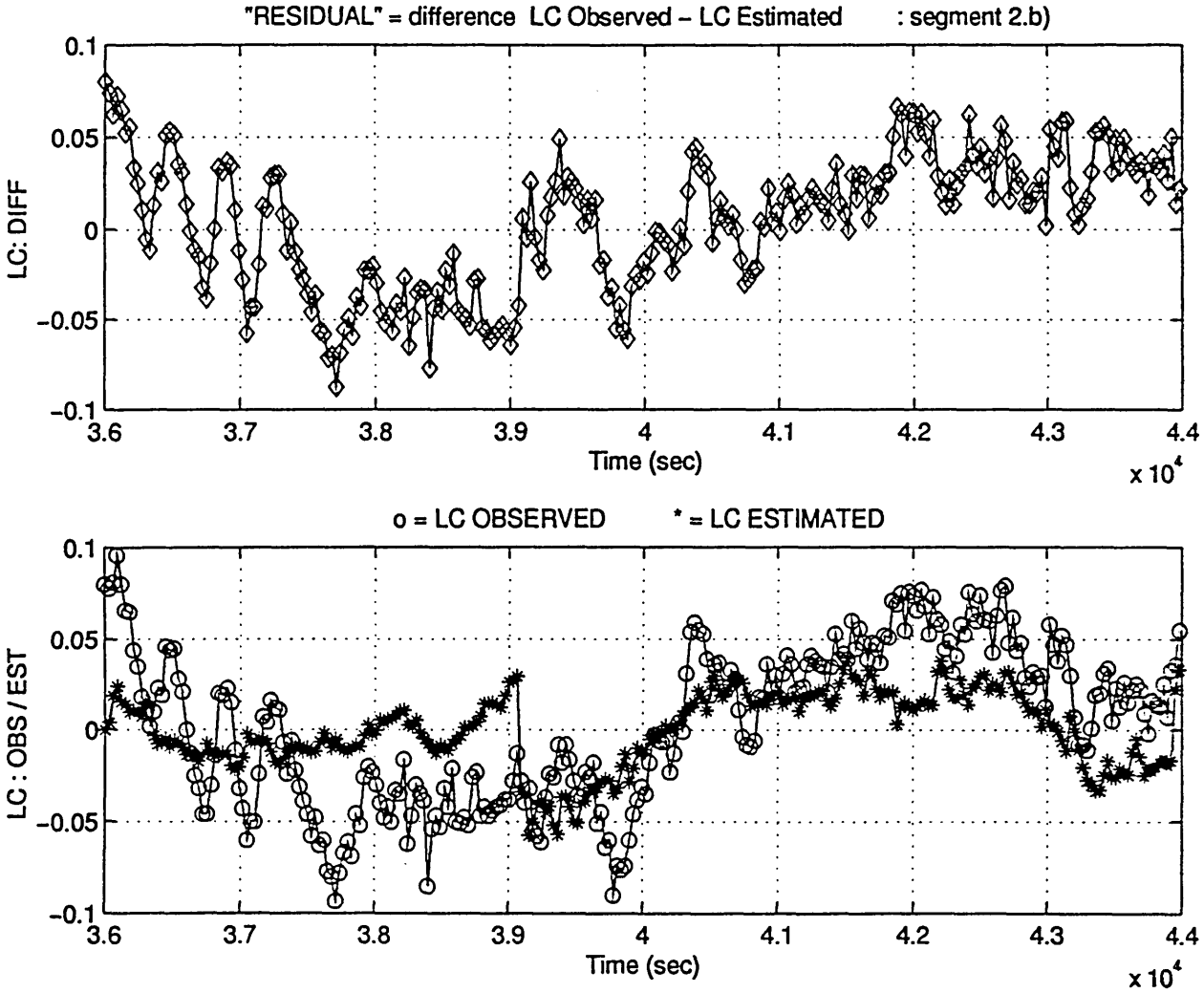

Fig. A.1.6.a) : KKAU - PRN 16 (10 6 1995) - [segment 2b]
Phase residual LC_DIFF, determined as the difference between LC_OBS and LC_EST.
Unit: [cycles]

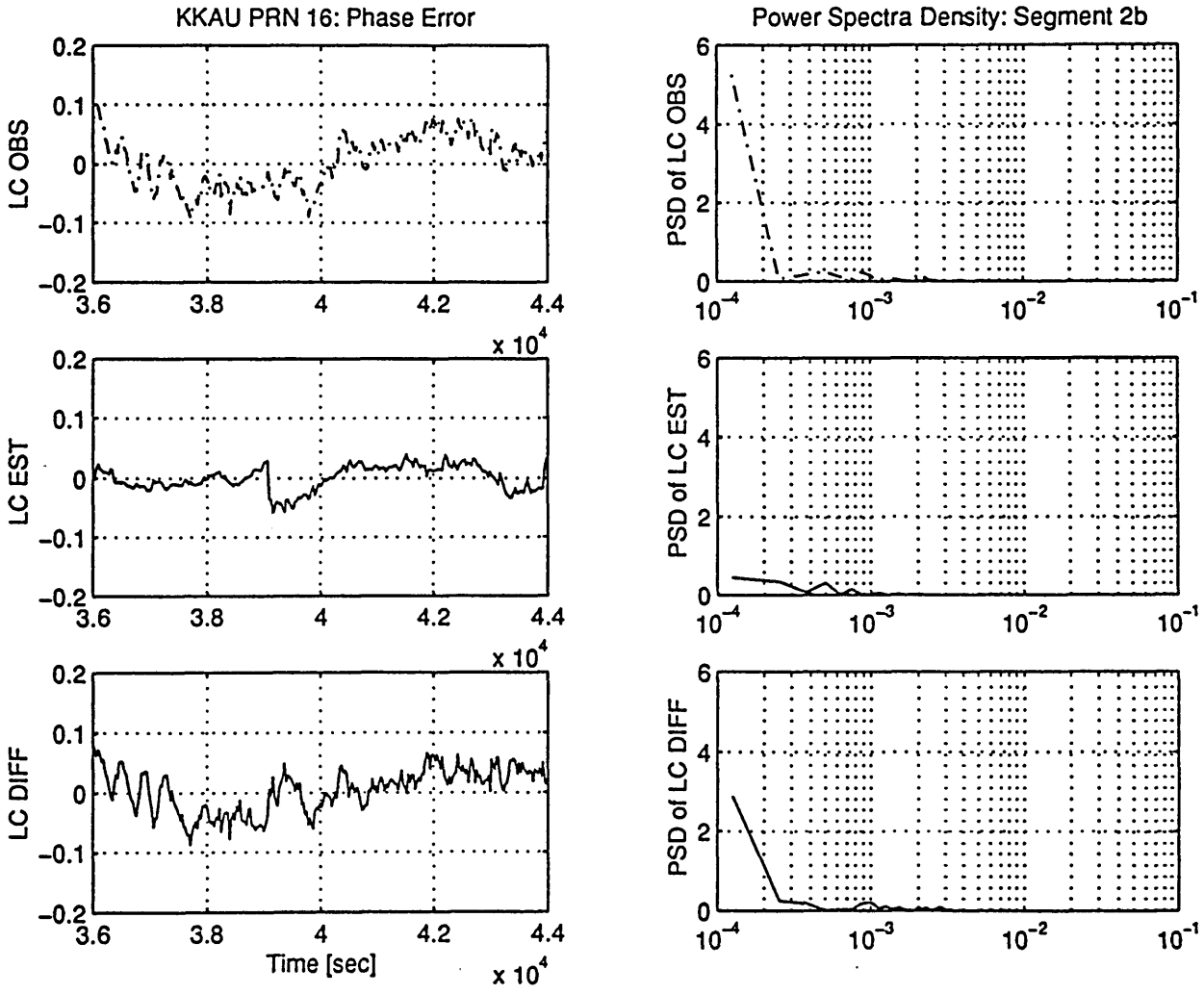

Fig. A.1.6.b) : KKAU - PRN 16 (10 6 1995) - [segment 2b]
PSD of LC_OBS, LC_EST and LC_DIFF
Unit: [cycles]^2

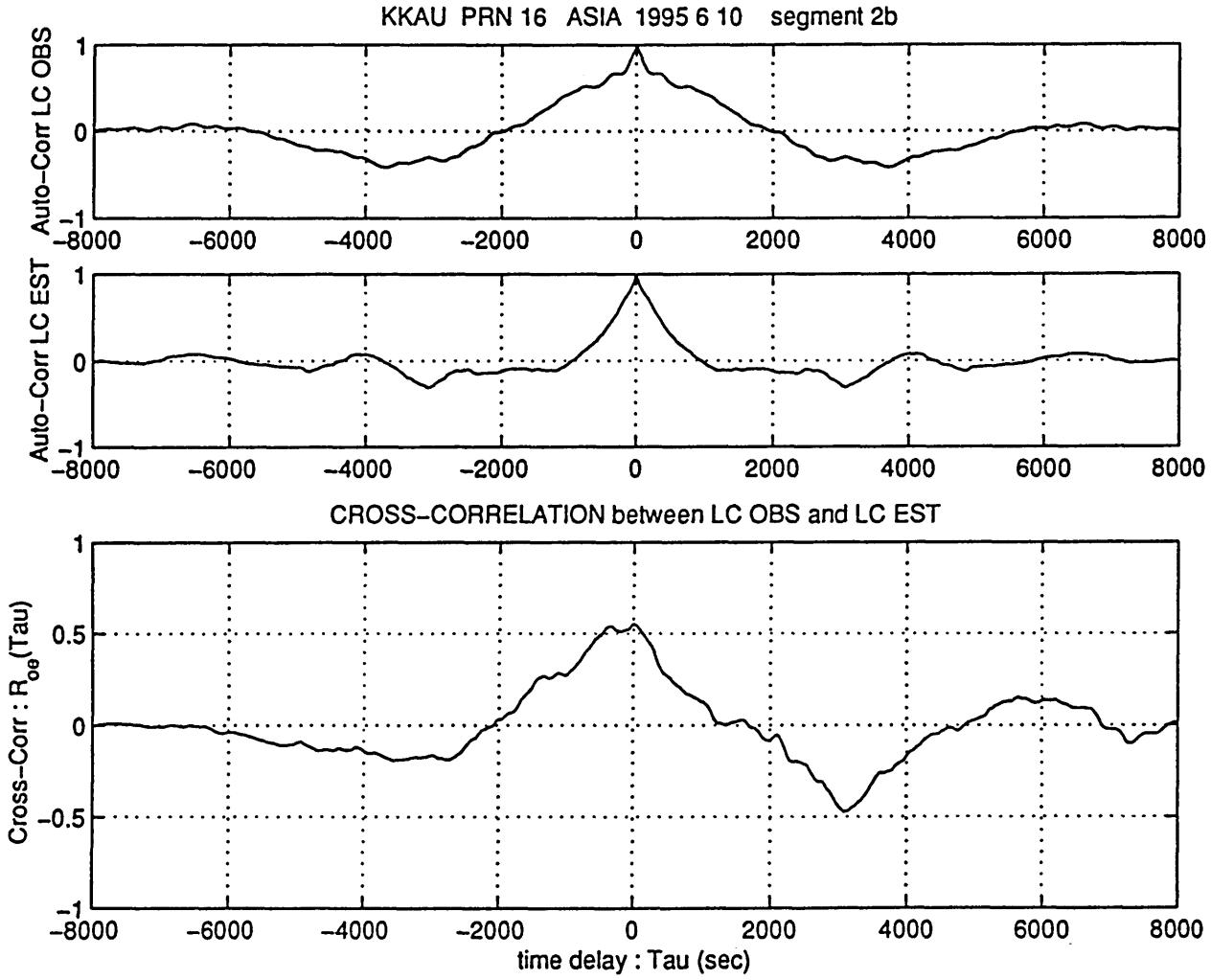

Fig. A.1.6.c) : KKAU - PRN 16 (10 6 1995) - [segment 2b]
Auto Correlation of LC_OBS (R_{oo}) and LC_EST (R_{ee})
Cross Correlation between them (R_{oe})
Unit: [cycles]^2

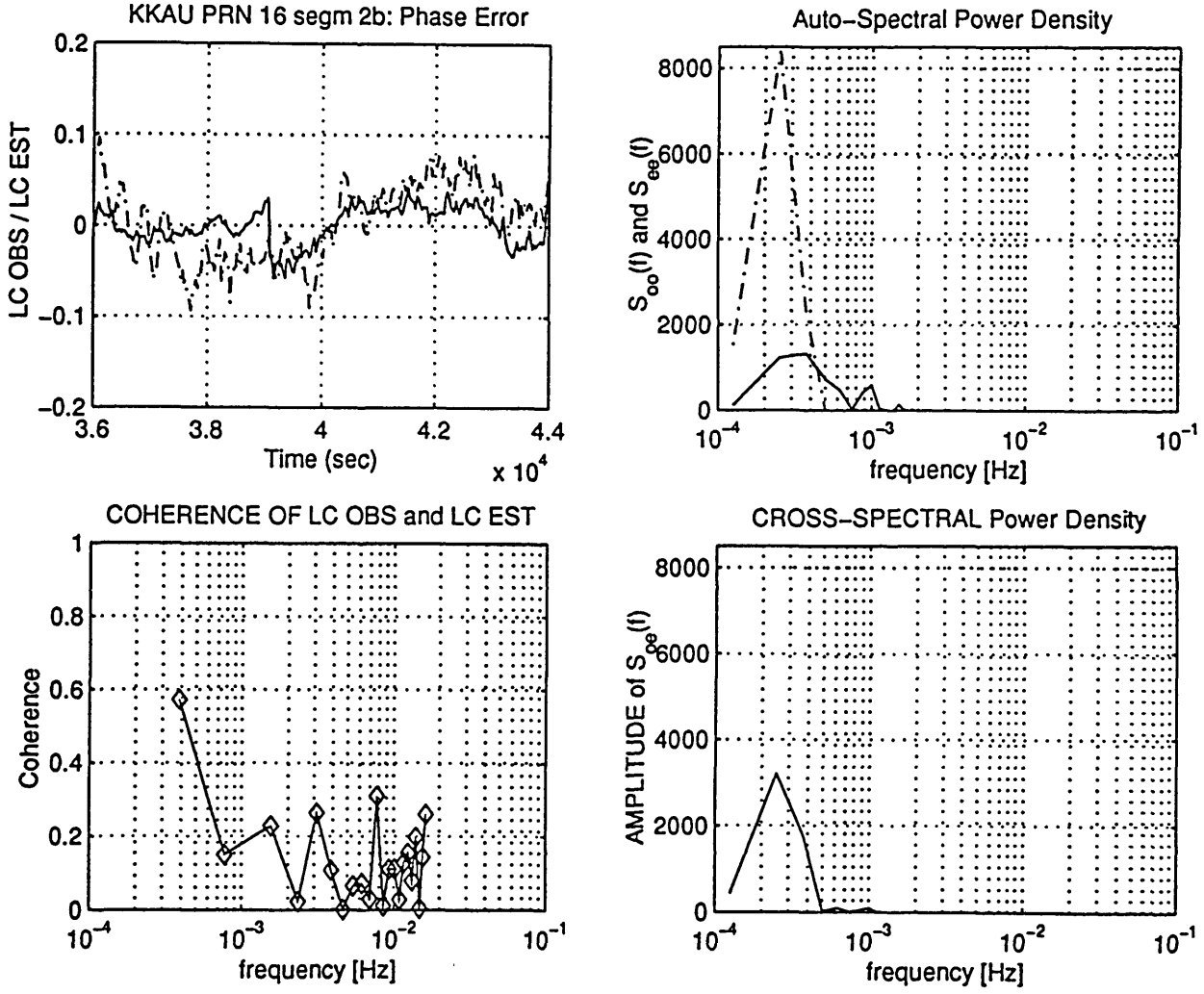

Fig. A.1.6.d) : KKAU - PRN 16 (10 6 1995) - [segment 2b]
Auto Spectral Power Density of LC_OBS (S_{oo}) and of LC_EST (S_{ee}). Cross PSD between them (S_{oe})
Unit: [cycles]^2
Coherence function of LC_OBS and LC_EST.

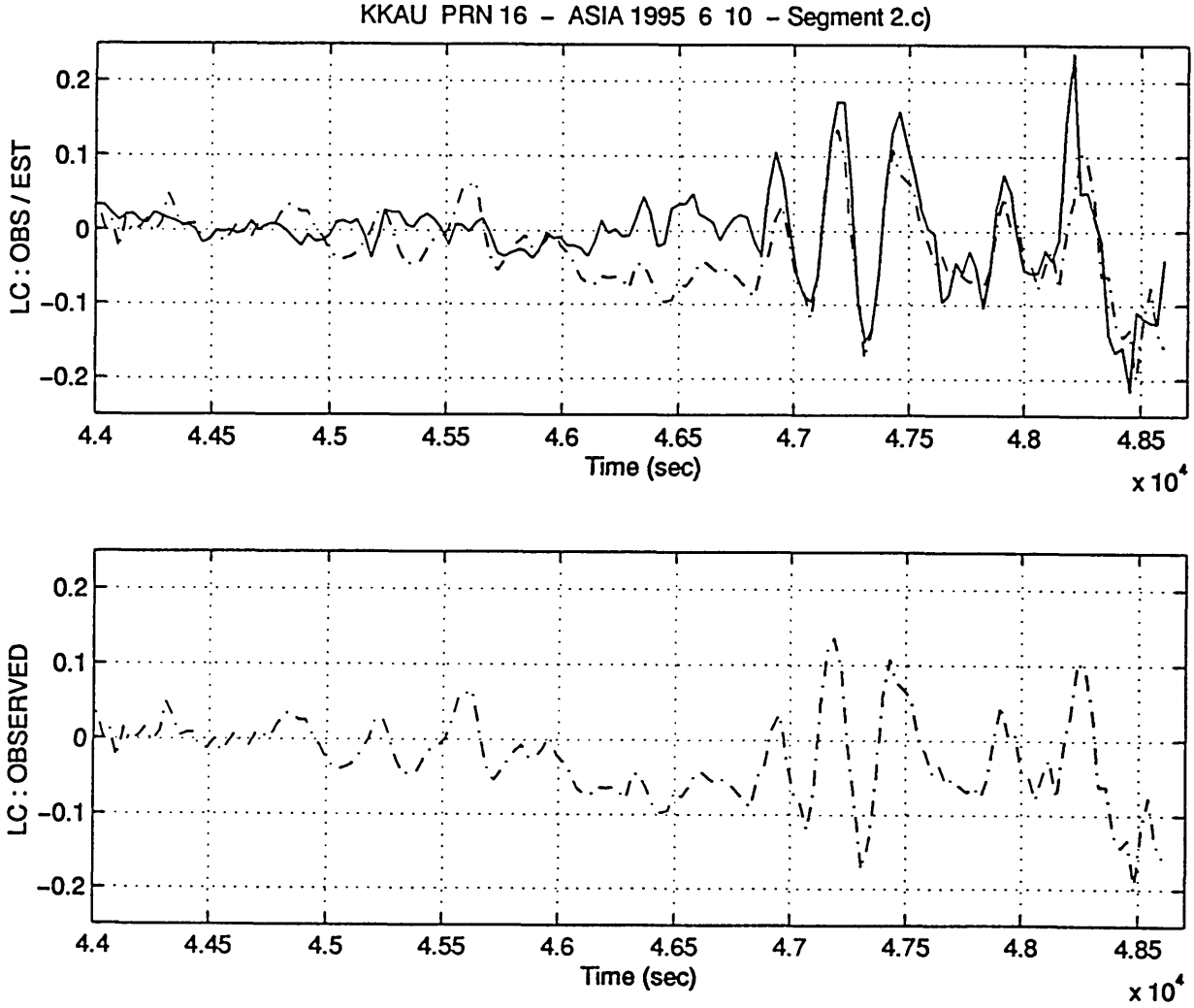

Fig. A.1.7 : Station: KKAU - Satellite: PRN 16 -
Data acquisition date 10 6 1995
LC_OBS and LC_EST compared for t=4.40 - 4.85 10^4 sec
Unit: [cycles]

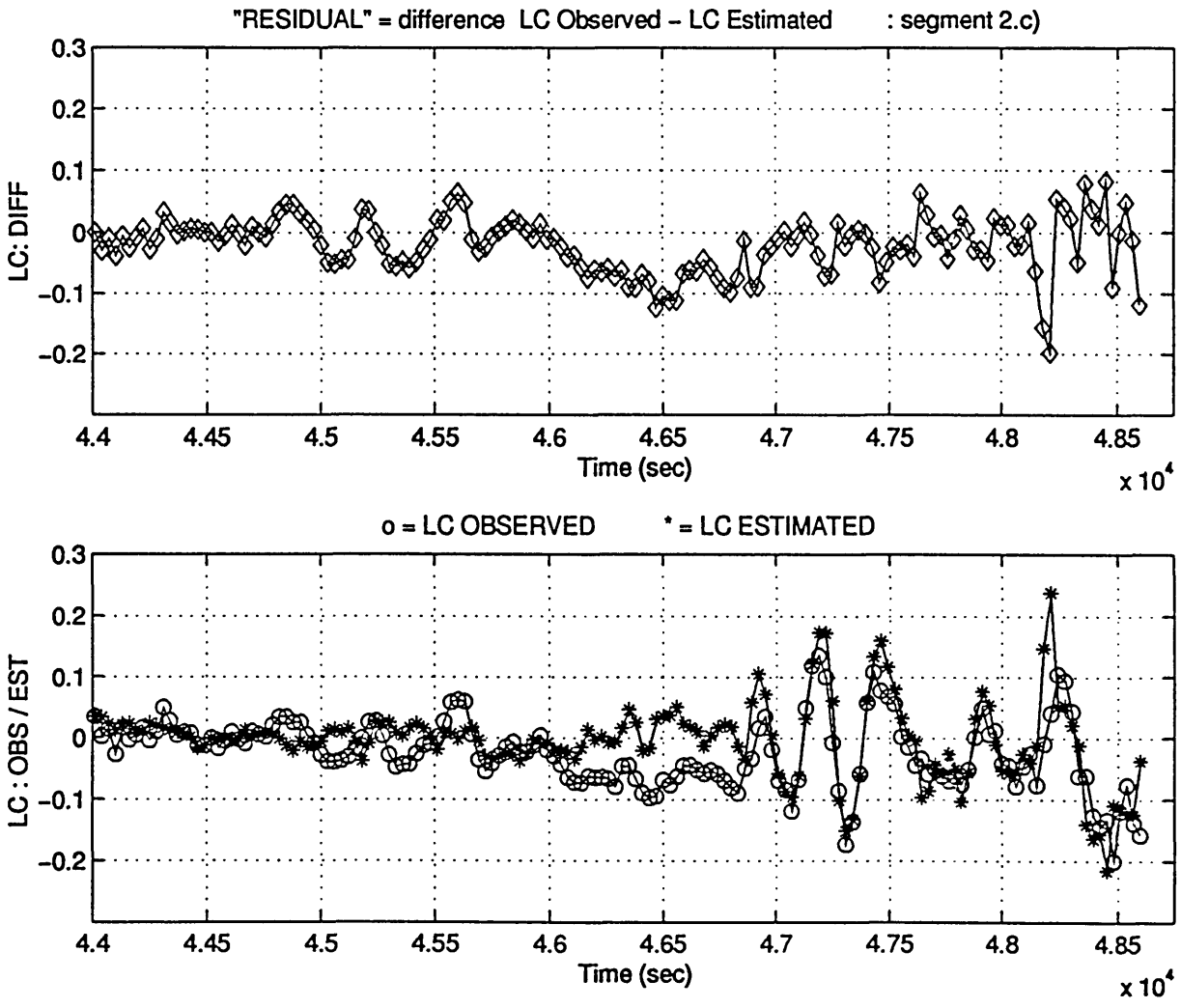

Fig. A.1.8.a) : KKAU - PRN 16 (10 6 1995) - [segment 2c]
Phase residual LC_DIFF, determined as the difference between LC_OBS and LC_EST.
Unit: [cycles]

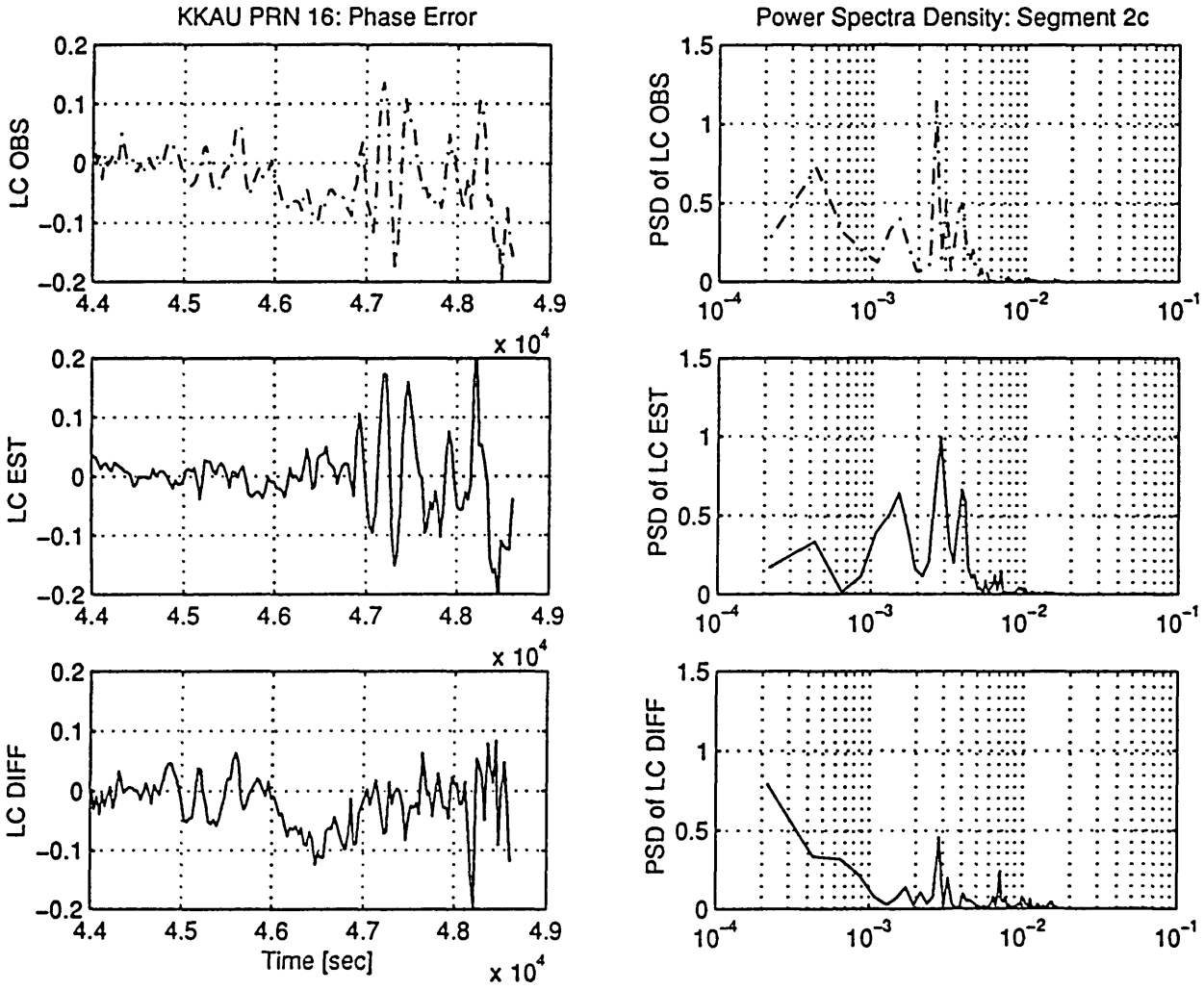

Fig. A.1.8.b) : KKAU - PRN 16 (10 6 1995) - [segment 2c]
PSD of LC_OBS, LC_EST and LC_DIFF
Unit: [cycles]^2

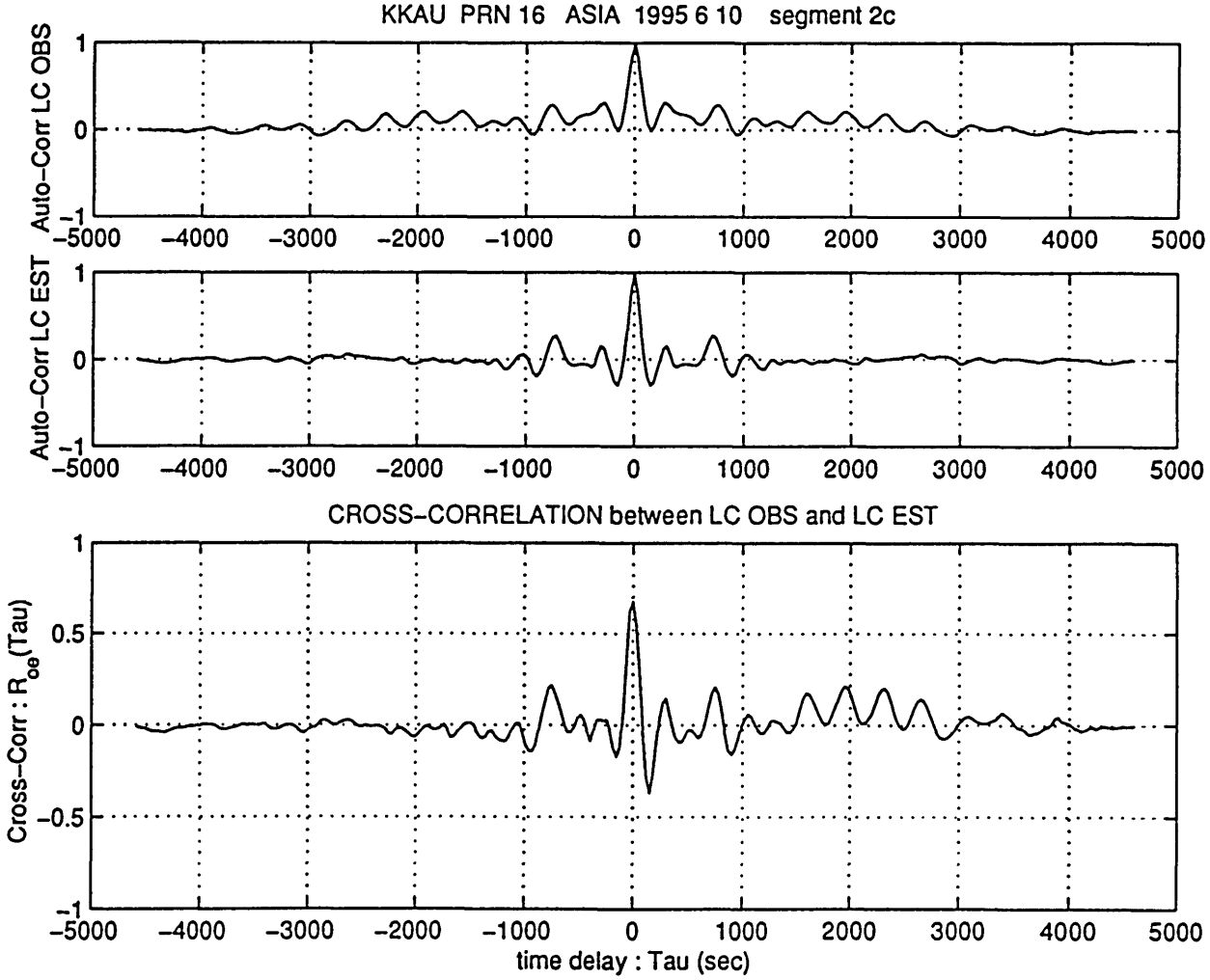

Fig. A.1.8.c) : KKAU - PRN 16 (10 6 1995) - [segment 2c]
Auto Correlation of LC_OBS (R_{oo}) and LC_EST (R_{ee})
Cross Correlation between them (R_{oe})
Unit: $[cycles]^2$

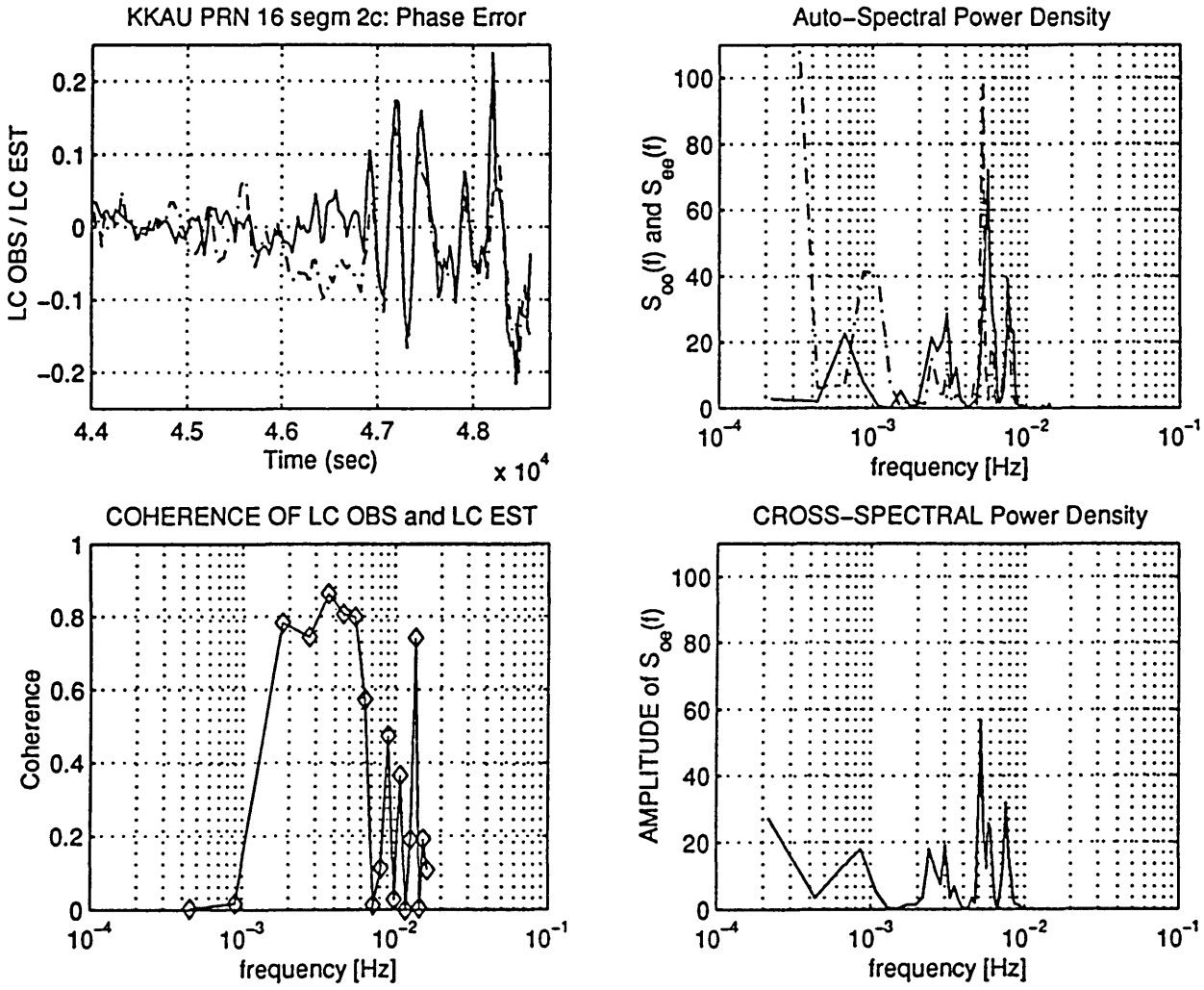

Fig. A.1.8.d) : KKAU - PRN 16 (10 6 1995) - [segment 2c]
Auto Spectral Power Density of LC_OBS (S_{oo}) and of LC_EST (S_{ee}). Cross PSD between them (S_{oe})
Unit: [cycles]^2.
Coherence function of LC_OBS and LC_EST.

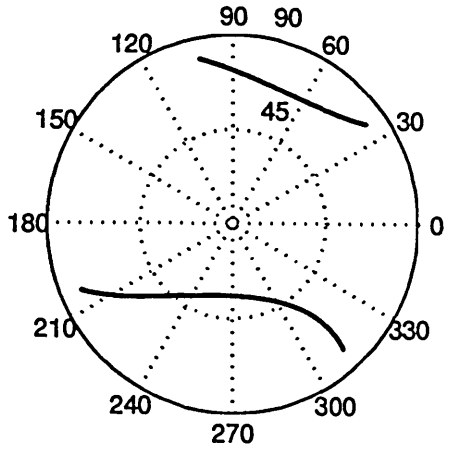

GPS DATA: receiver location: CENTRAL ASIA acquisition date: 10 6 1995

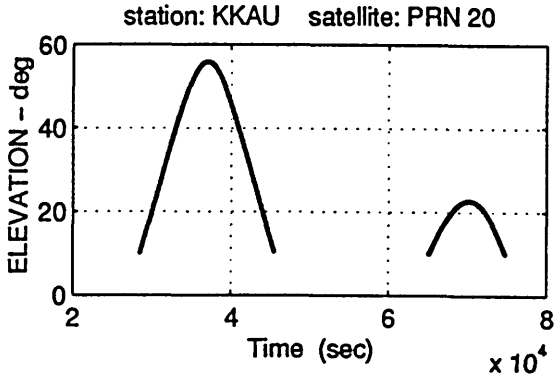

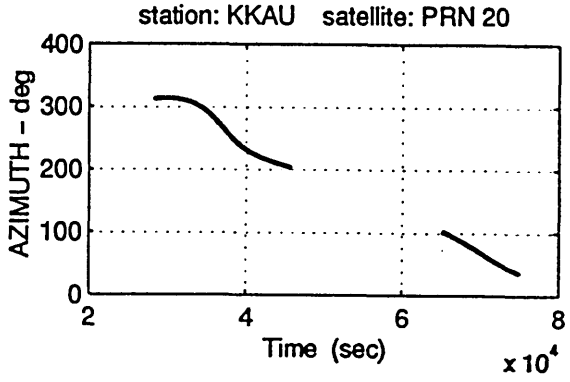

Fig. A.2.1 : Satellite visibility chart for PRN 20 (skymap). Elevation and azimuth of PRN 20 with respect to the station KKAU

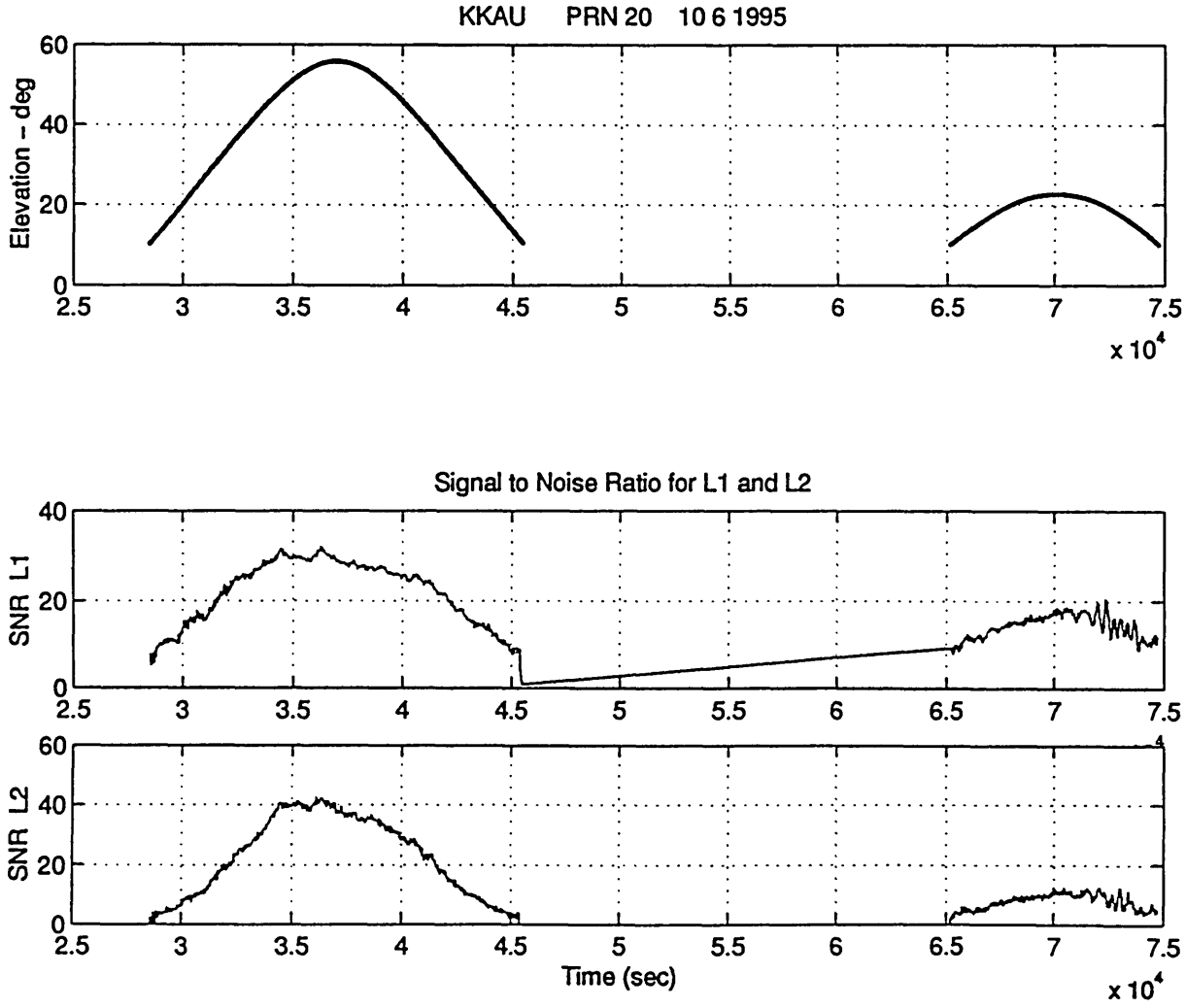

Fig. A.2.2 : Station: KKAU - Satellite: PRN 20
Data acquisition date 10 6 1995
Signal-to-Noise-Ratio (SNR) for L_1 and L_2.

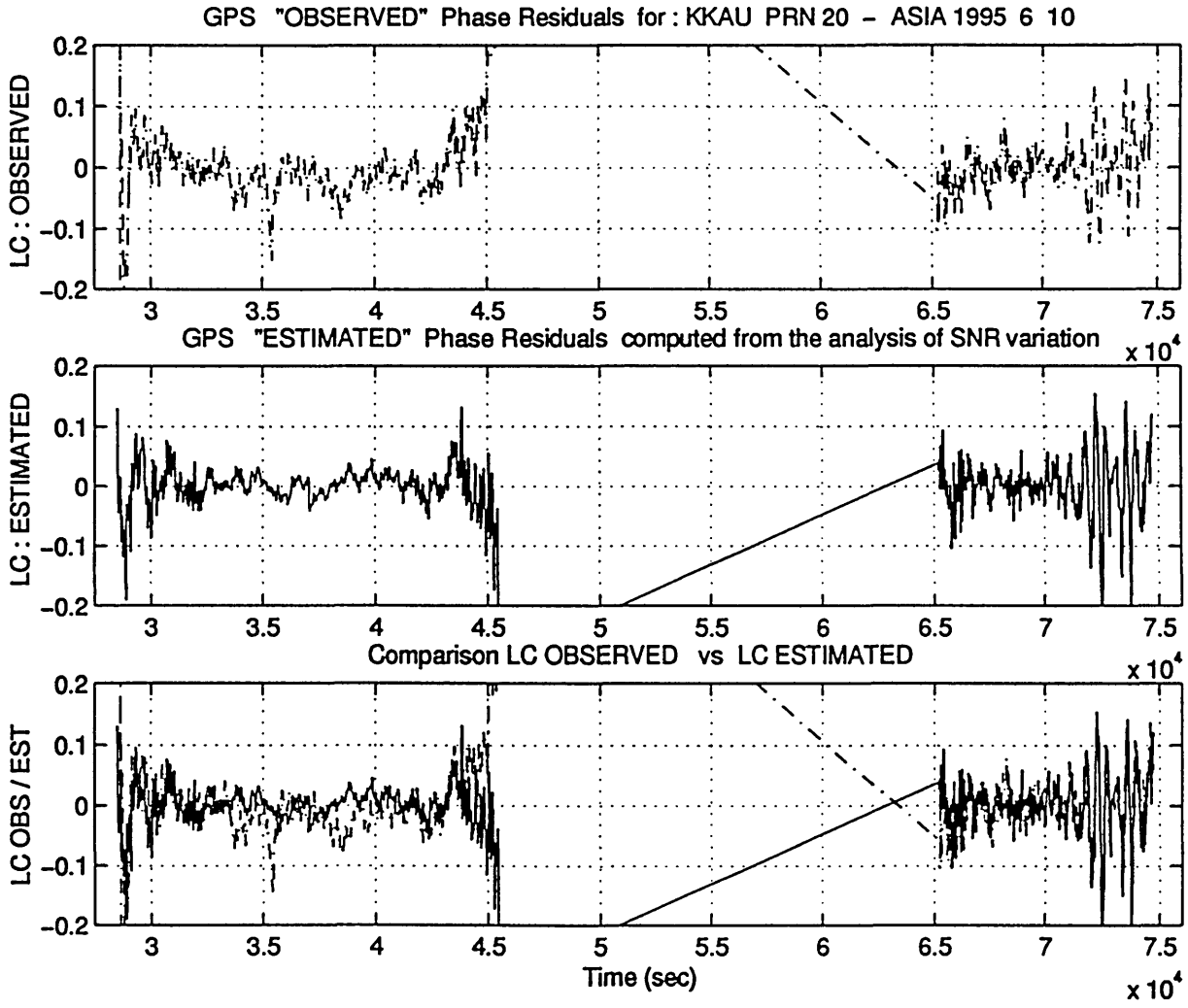

Fig. A.2.3 : Station: KKAU - Satellite: PRN 20
Data acquisition date 10 6 1995
The observed phase residual (LC_OBS) is compared with the multipath phase error estimated from the SNR (LC_EST).
Unit: [cycles]

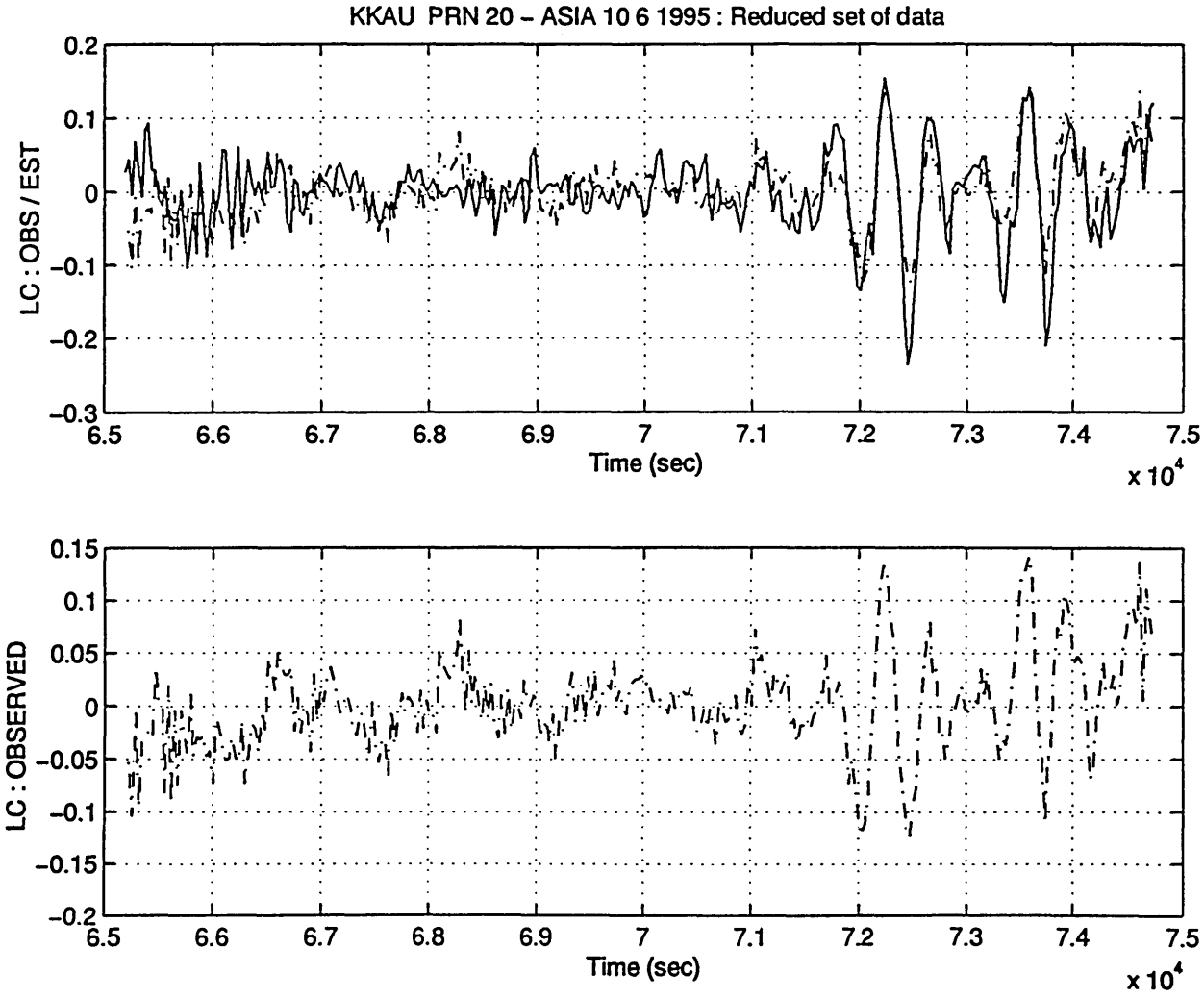

Fig. A.2.4 : Station: KKAU - Satellite: PRN 20
Data acquisition date 10 6 1995
LC_OBS and LC_EST compared for t=6.5 - 7.5 10^4 sec
Unit: [cycles]

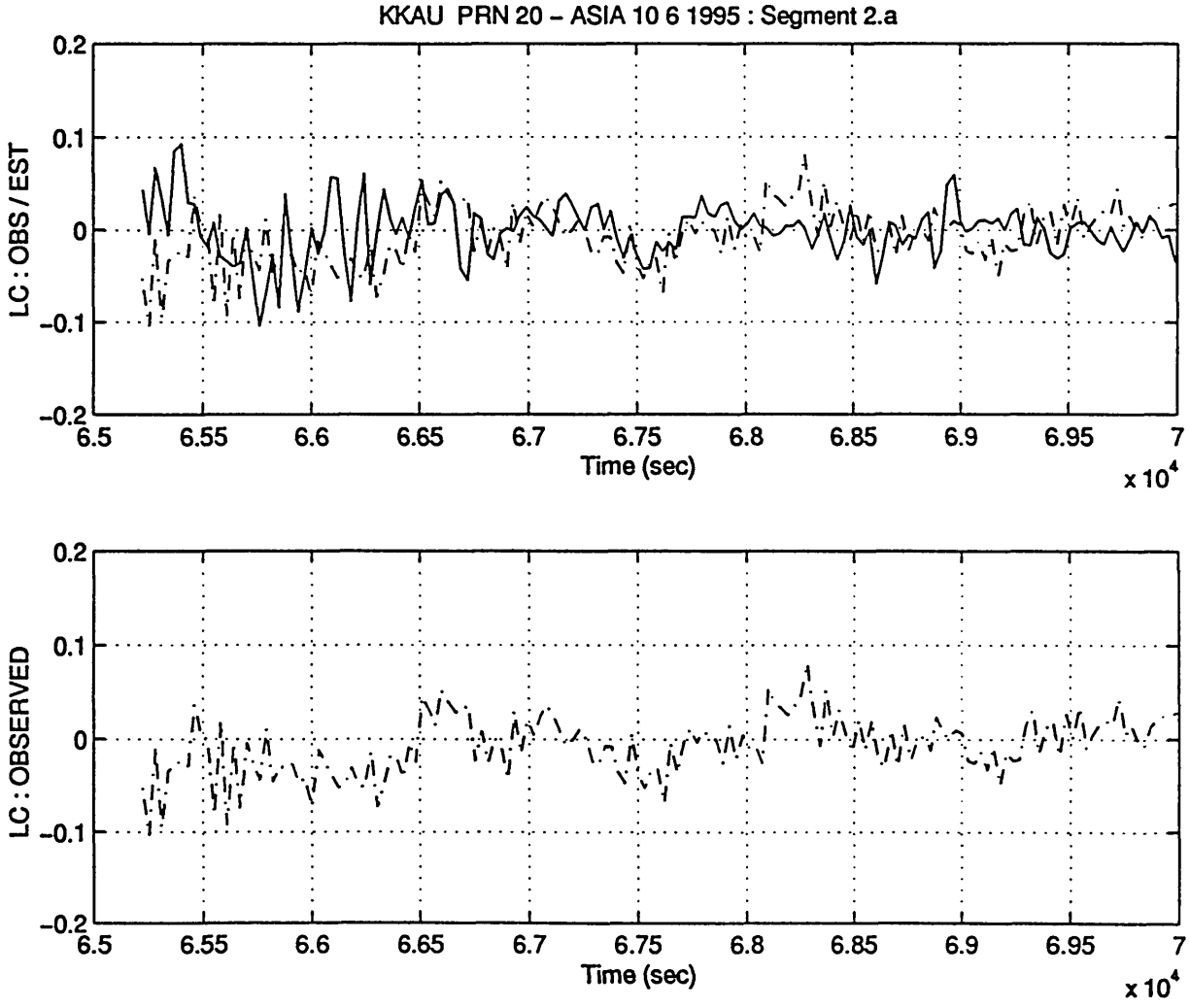

Fig. A.2.5 : Station: KKAU - Satellite: PRN 20 - [segment 2a]
Data acquisition date 10 6 1995
LC_OBS and LC_EST compared for t=6.5 - 7.0 10^4 sec
Unit: [cycles]

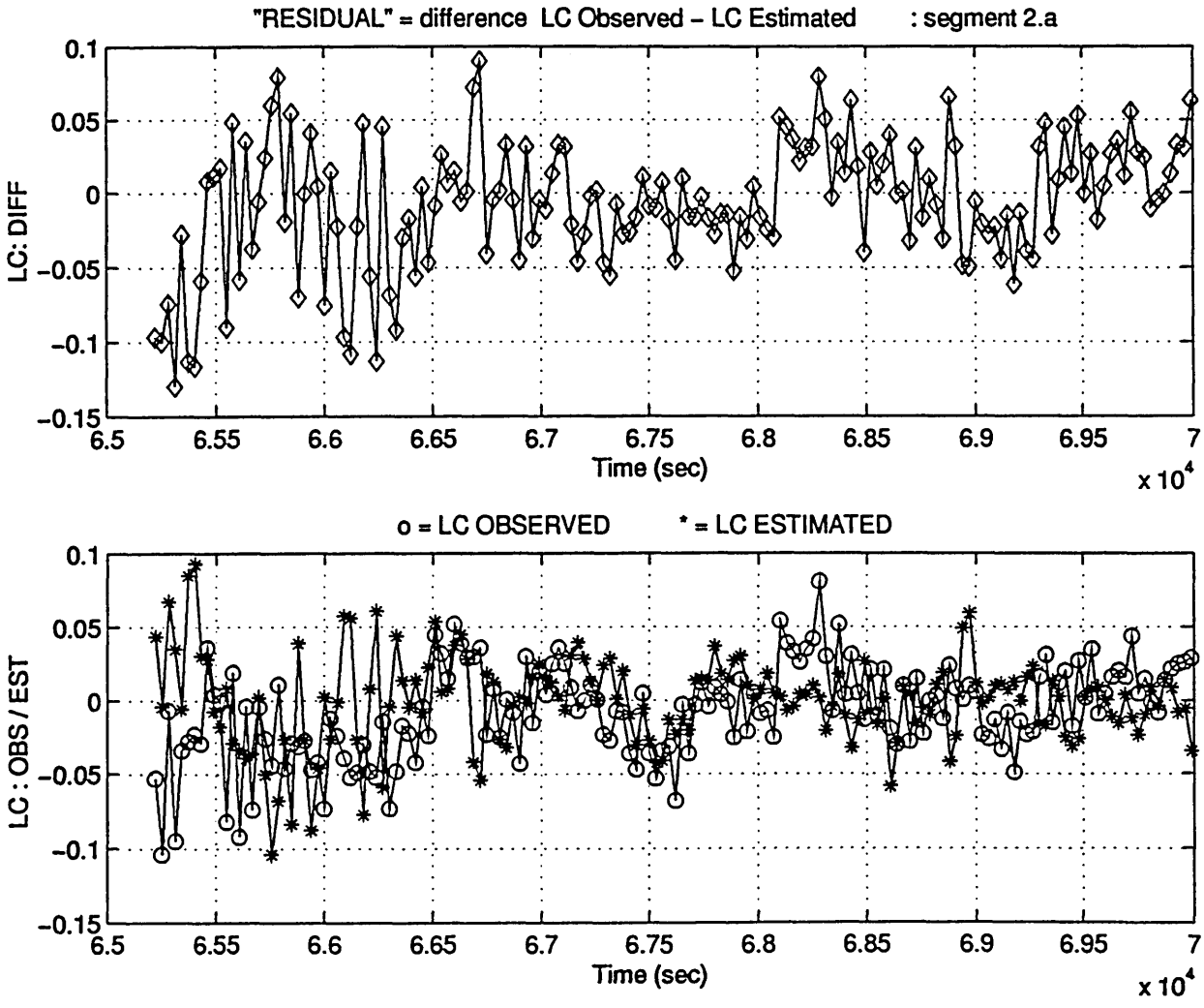

Fig. A.2.6.a) : KKAU - PRN 20 (10 6 1995) - [segment 2a]
Phase residual LC_DIFF, determined as the difference between LC_OBS and LC_EST.
Unit: [cycles]

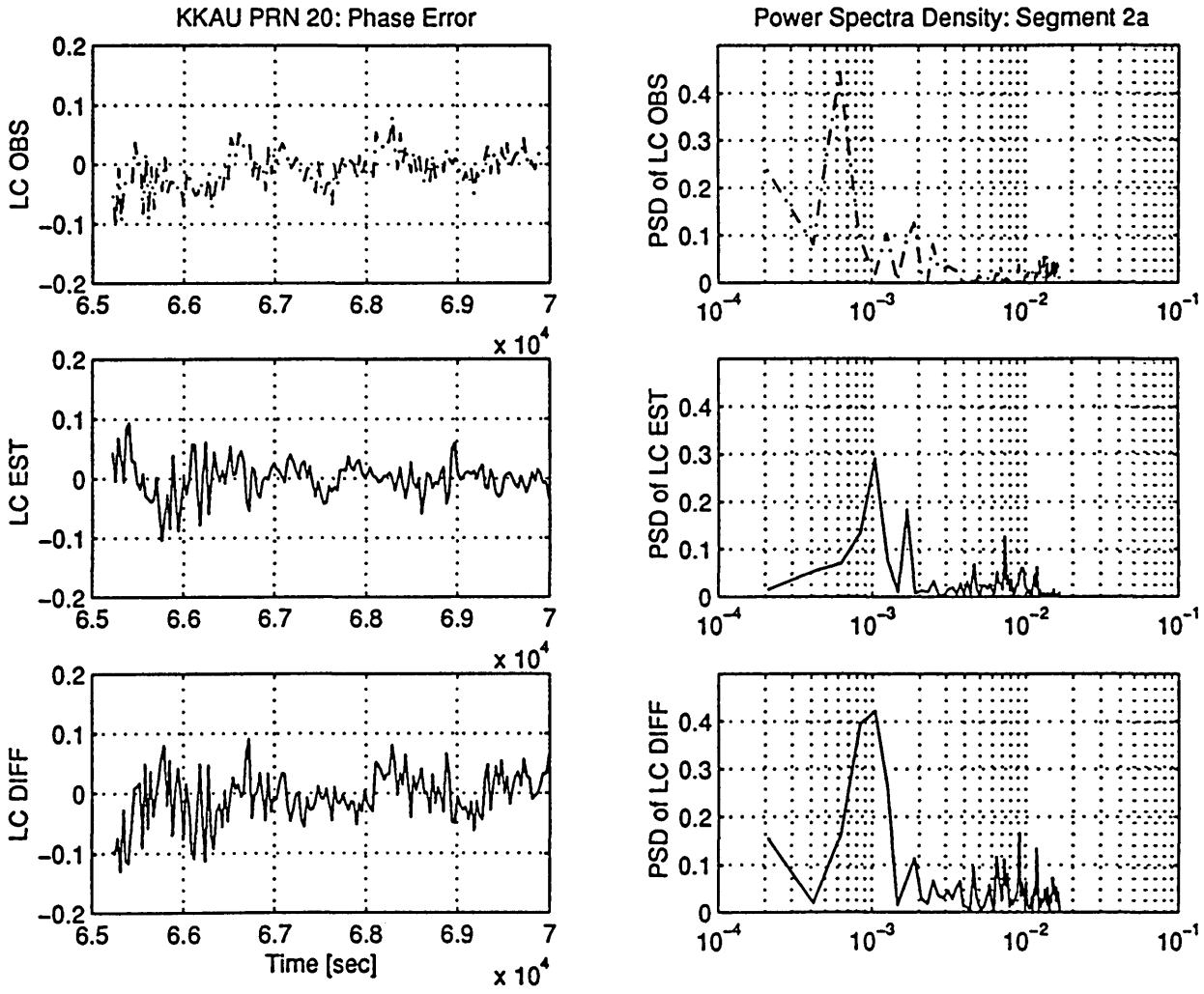

Fig. A.2.6.b) : KKAU - PRN 20 (10 6 1995) - [segment 2a]
PSD of LC_OBS, LC_EST and LC_DIFF.
Unit: [cycles]^2

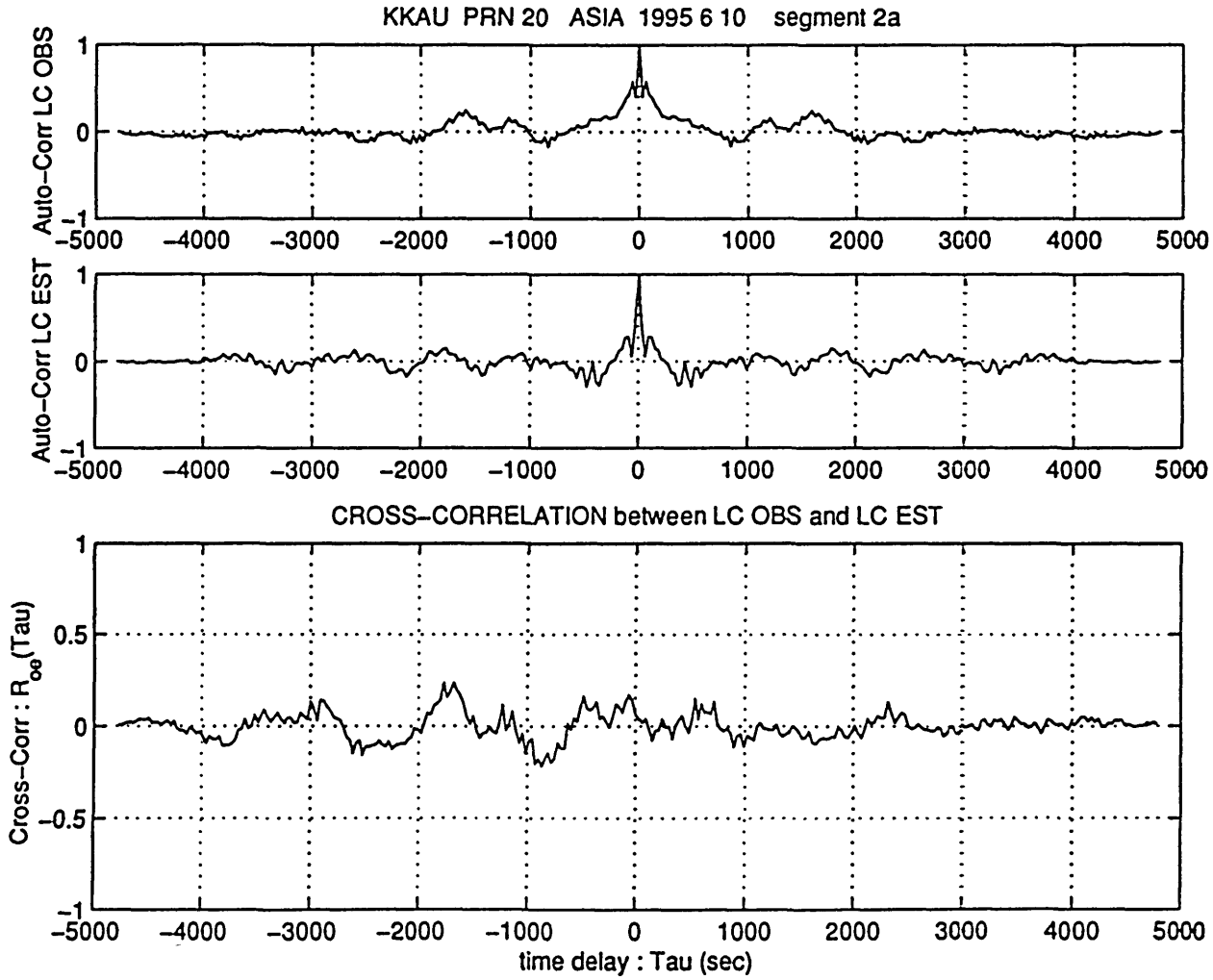

Fig. A.2.6.c) : KKAU - PRN 20 (10 6 1995) - [segment 2a]
Auto Correlation of LC_OBS (R_{oo}) and LC_EST (R_{ee})
Cross Correlation between them (R_{oe})
Unit: [cycles]^2

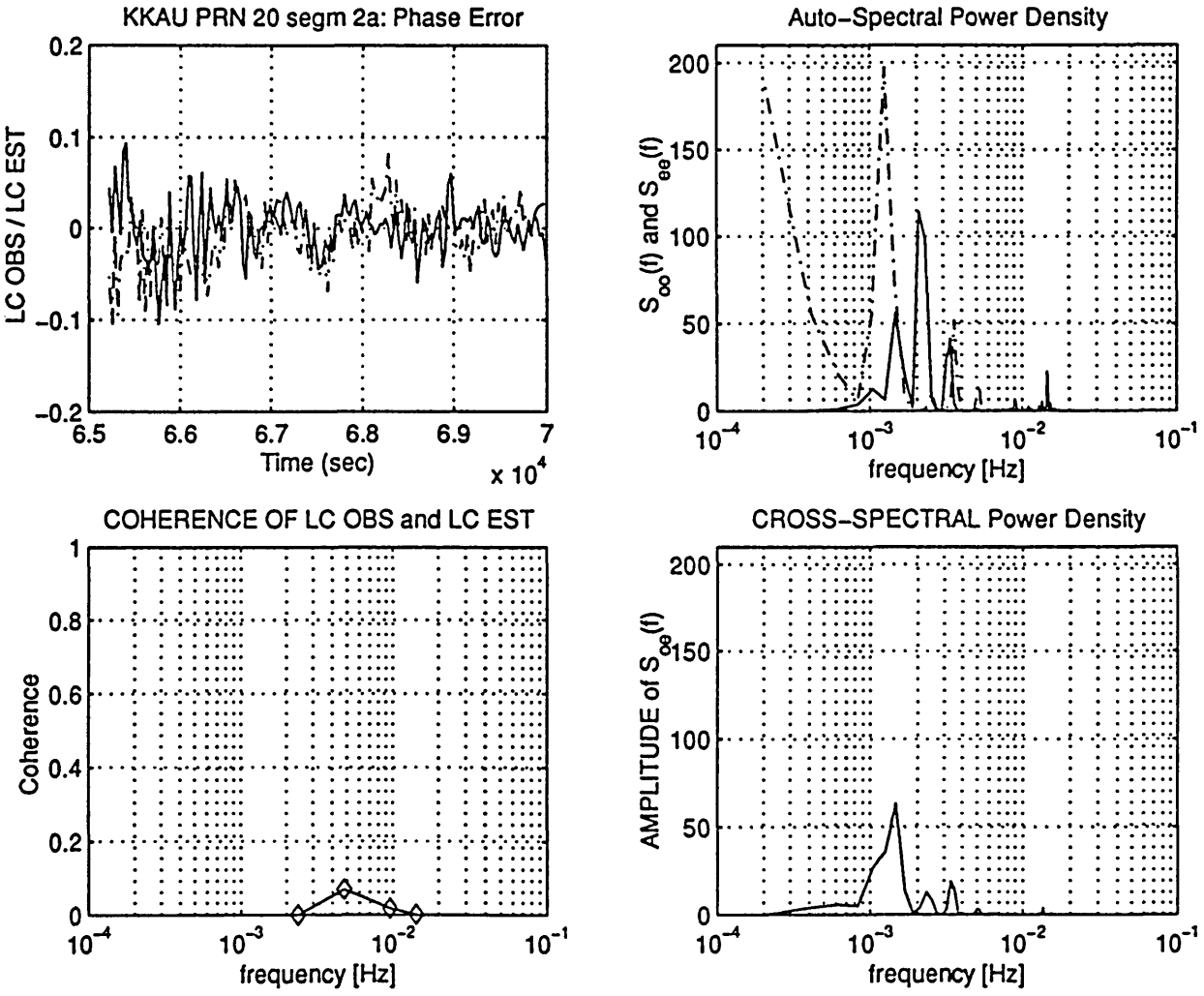

Fig. A.2.6.d) : KKAU - PRN 20 (10 6 1995) - [segment 2a]
Auto Spectral Power Density of LC_OBS (S_{oo}) and of LC_EST (S_{ee}). CrossPSD between them (S_{oe})
Unit: [cycles]^2
Coherence function of LC_OBS and LC_EST.

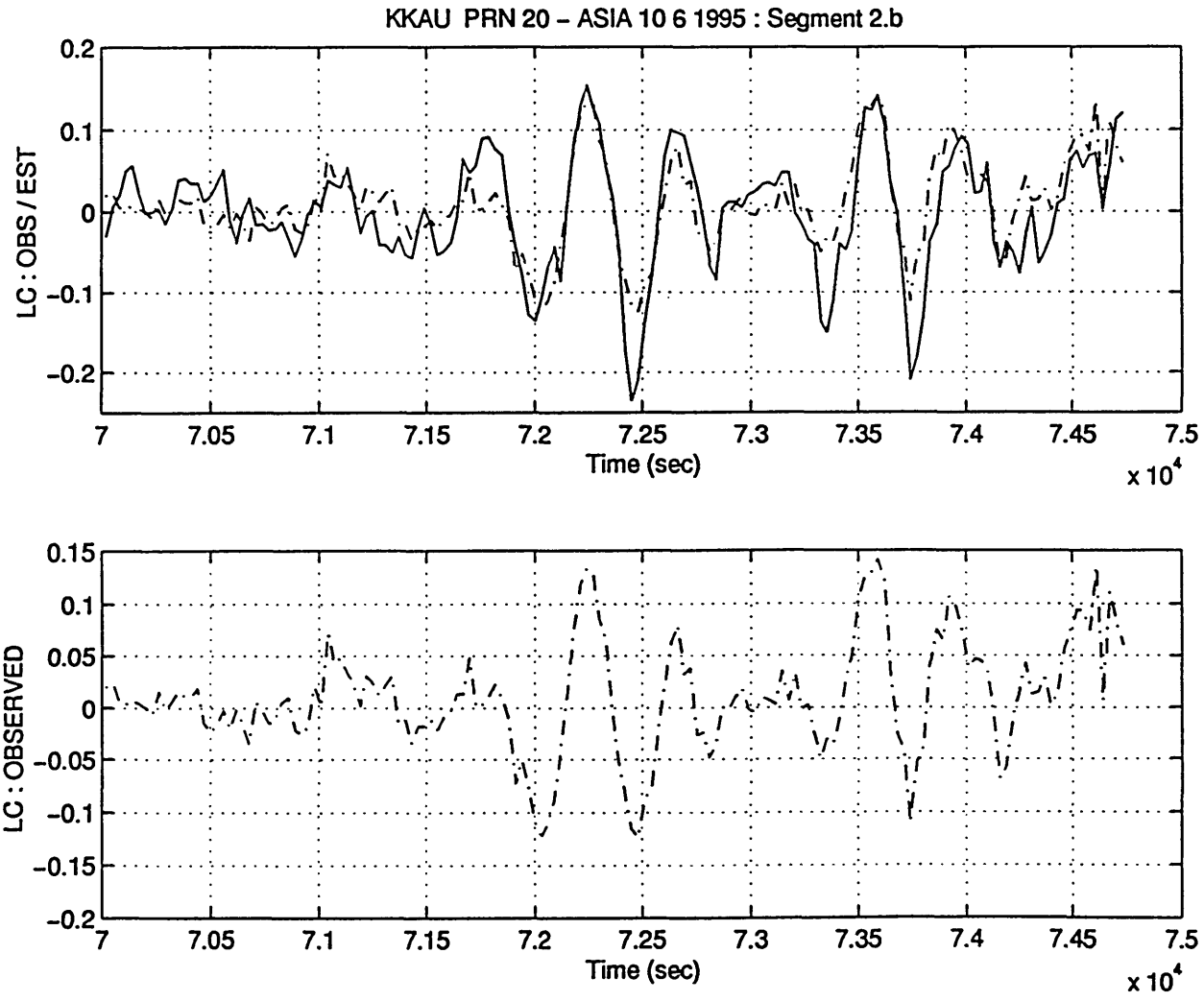

Fig. A.2.7 : Station: KKAU - Satellite: PRN 20
Data acquisition date 10 6 1995
LC_OBS and LC_EST compared for t=7.0 - 7.5 10^4 sec
Unit: [cycles]

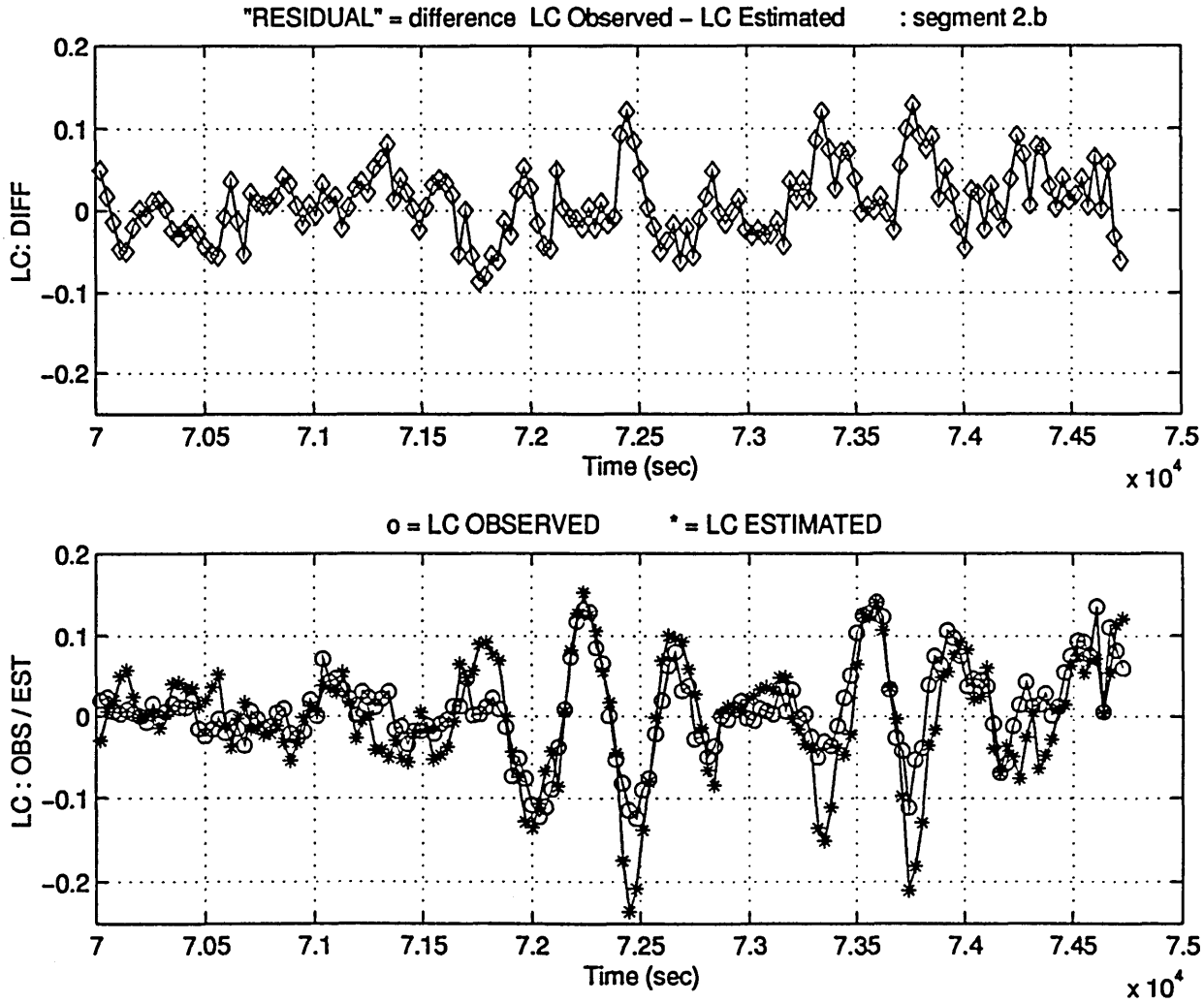

Fig. A.2.8.a) : KKAU - PRN 20 (10 6 1995) - [segment 2b]
Phase residual LC_DIFF, determined as the difference between LC_OBS and LC_EST.
Unit: [cycles]

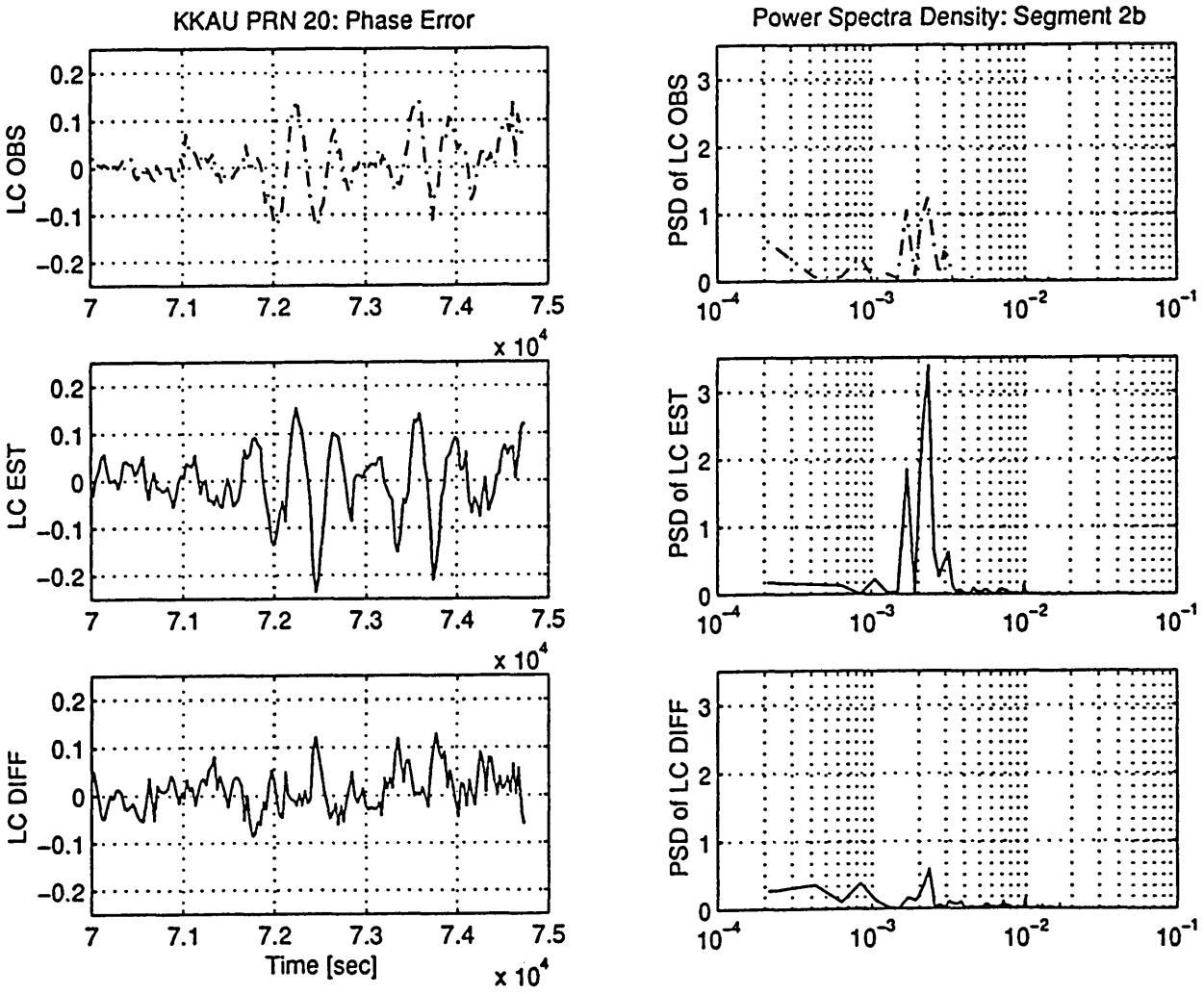

Fig. A.2.8.b) : KKAU - PRN 20 (10 6 1995) - [segment 2b]
PSD of LC_OBS, LC_EST and LC_DIFF.
Unit: [cycles]^2

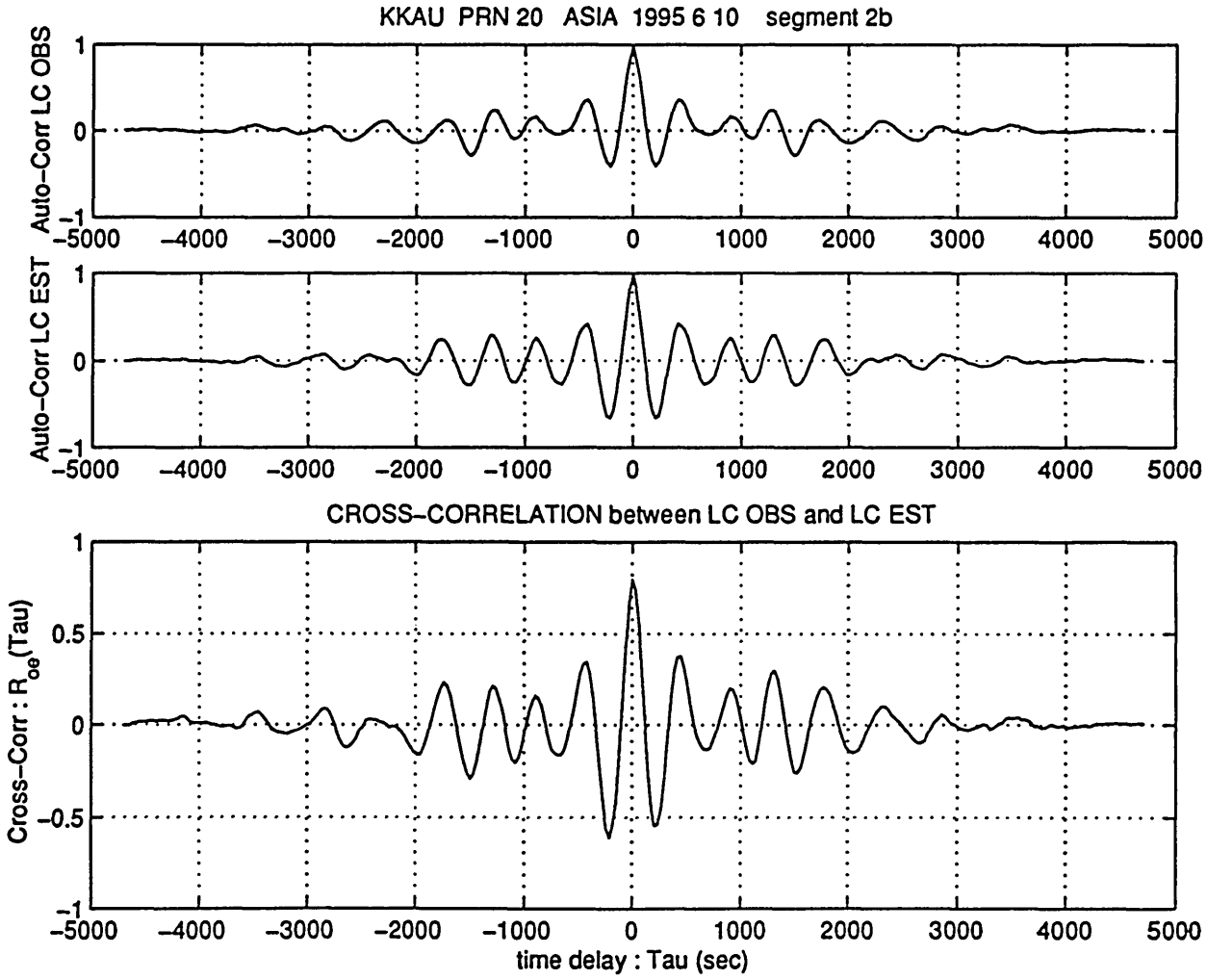

Fig. A.2.8.c) : KKAU - PRN 20 (10 6 1995) - [segment 2b]
Auto Correlation of LC_OBS (R_{oo}) and LC_EST (R_{ee}).
Cross Correlation between them (R_{oe})
Unit: [cycles]^2

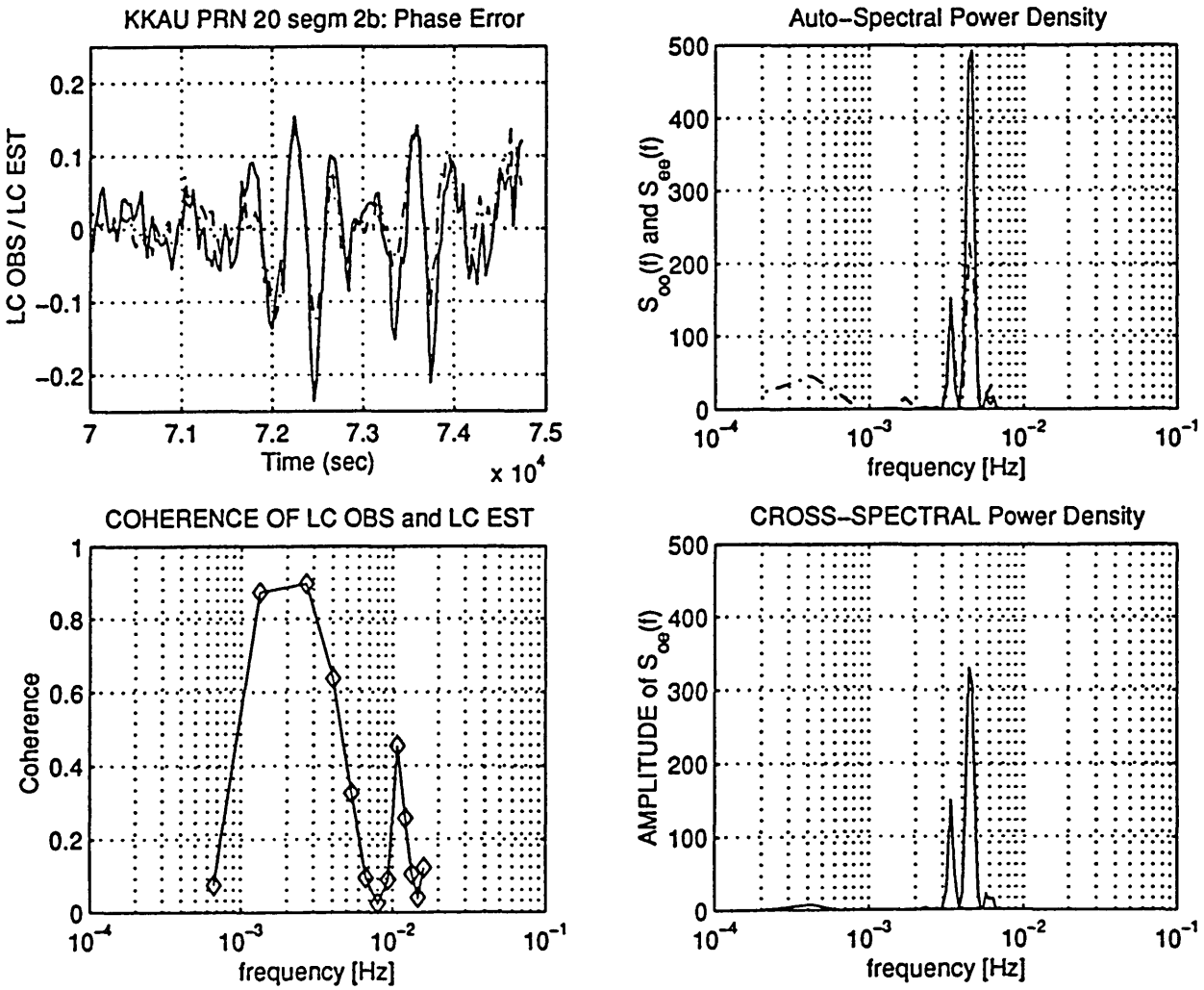

Fig. A.2.8.d) : KKAU - PRN 20 (10 6 1995) - [segment 2b]
Auto Spectral Power Density of LC_OBS (S_{oo}) and of LC_EST (S_{ee}). Cross PSD between them (S_{oe})
Unit: [cycles]^2
Coherence function of LC_OBS and LC_EST

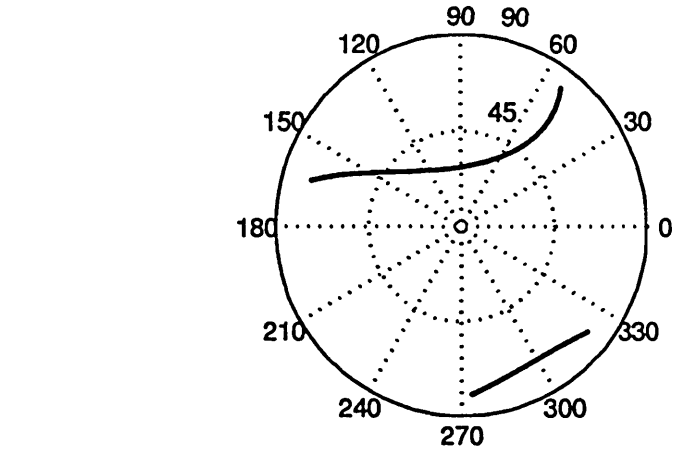

GPS DATA: receiver location: CENTRAL ASIA acquisition date: 10 6 1995

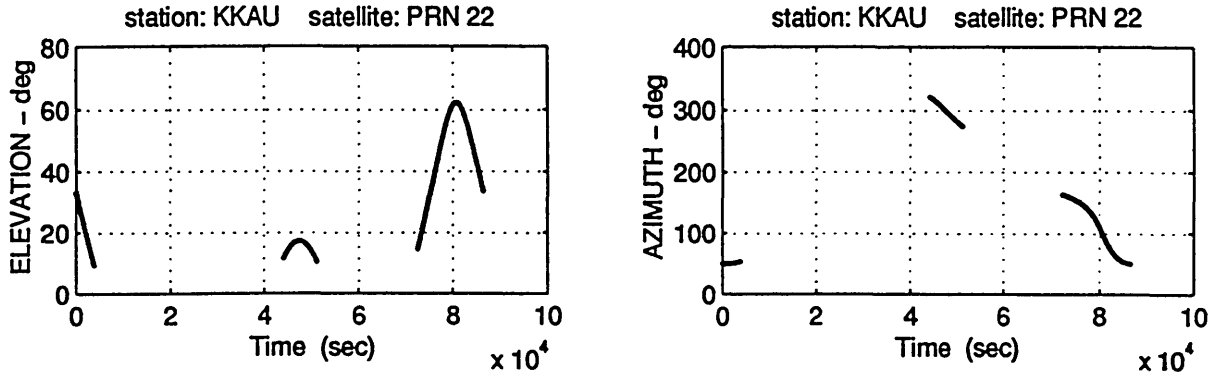

Fig. A.3.1 : Satellite visibility chart for PRN 22 (skymap). Elevation and azimuth of PRN 22 with respect to the station KKAU

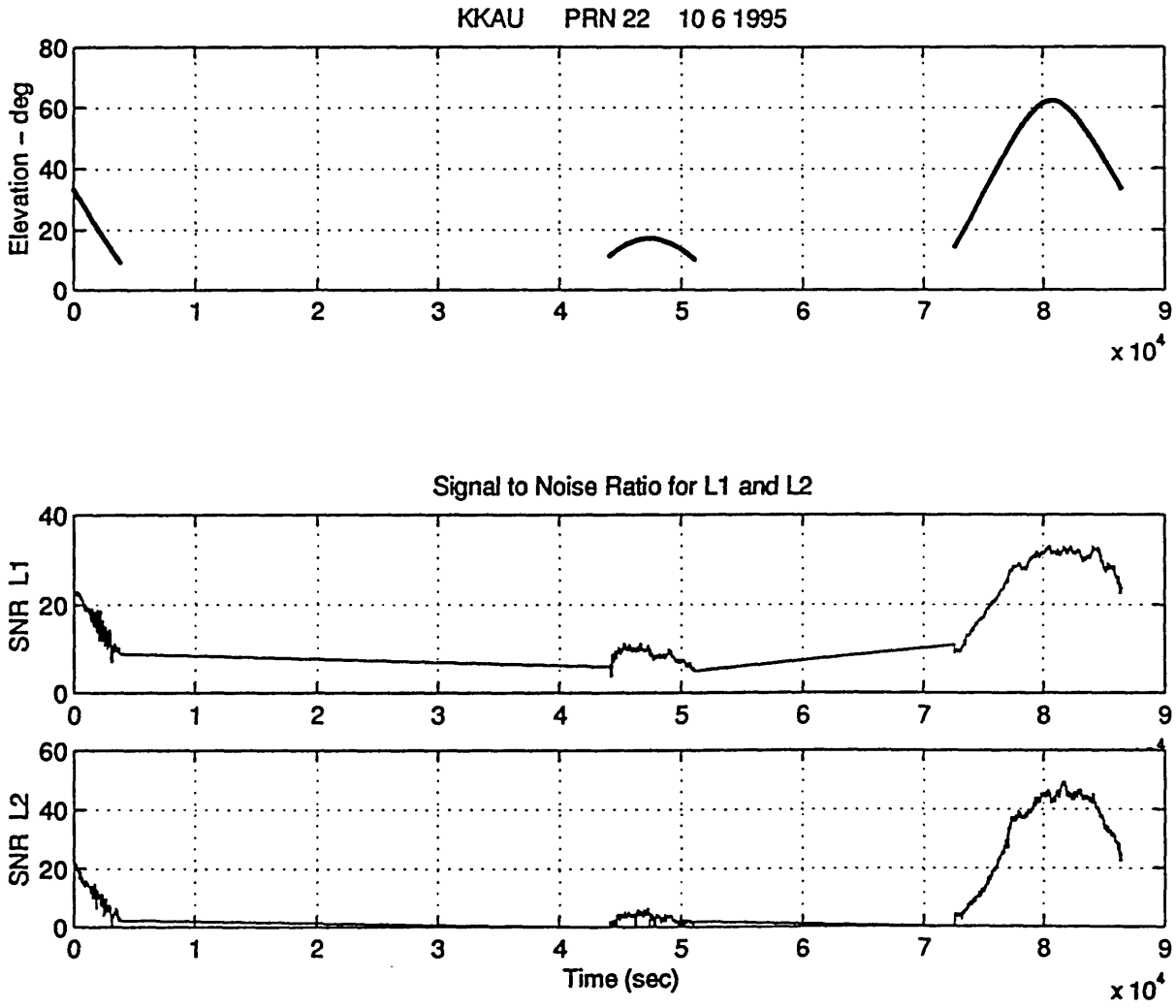

Fig. A.3.2 : Station: KKAU - Satellite: PRN 22
Data acquisition date 10 6 1995
Signal-to-Noise-Ratio (SNR) for L_1 and L_2.

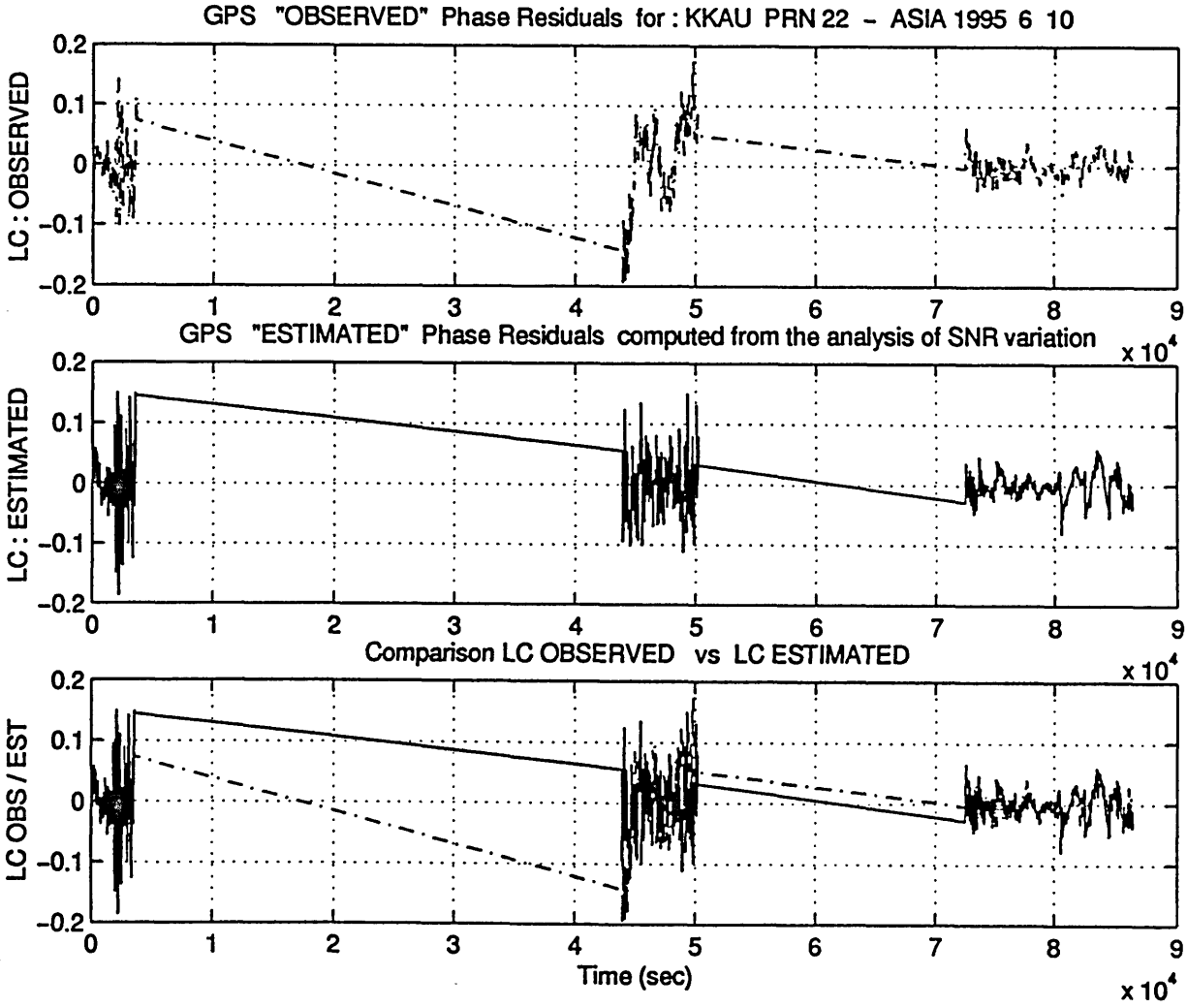

Fig. A.3.3 : Station: KKAU - Satellite: PRN 22
Data acquisition date 10 6 1995
The observed phase residual (LC_OBS) is compared with the multipath phase error estimated from the SNR (LC_EST).
Unit: [cycles]

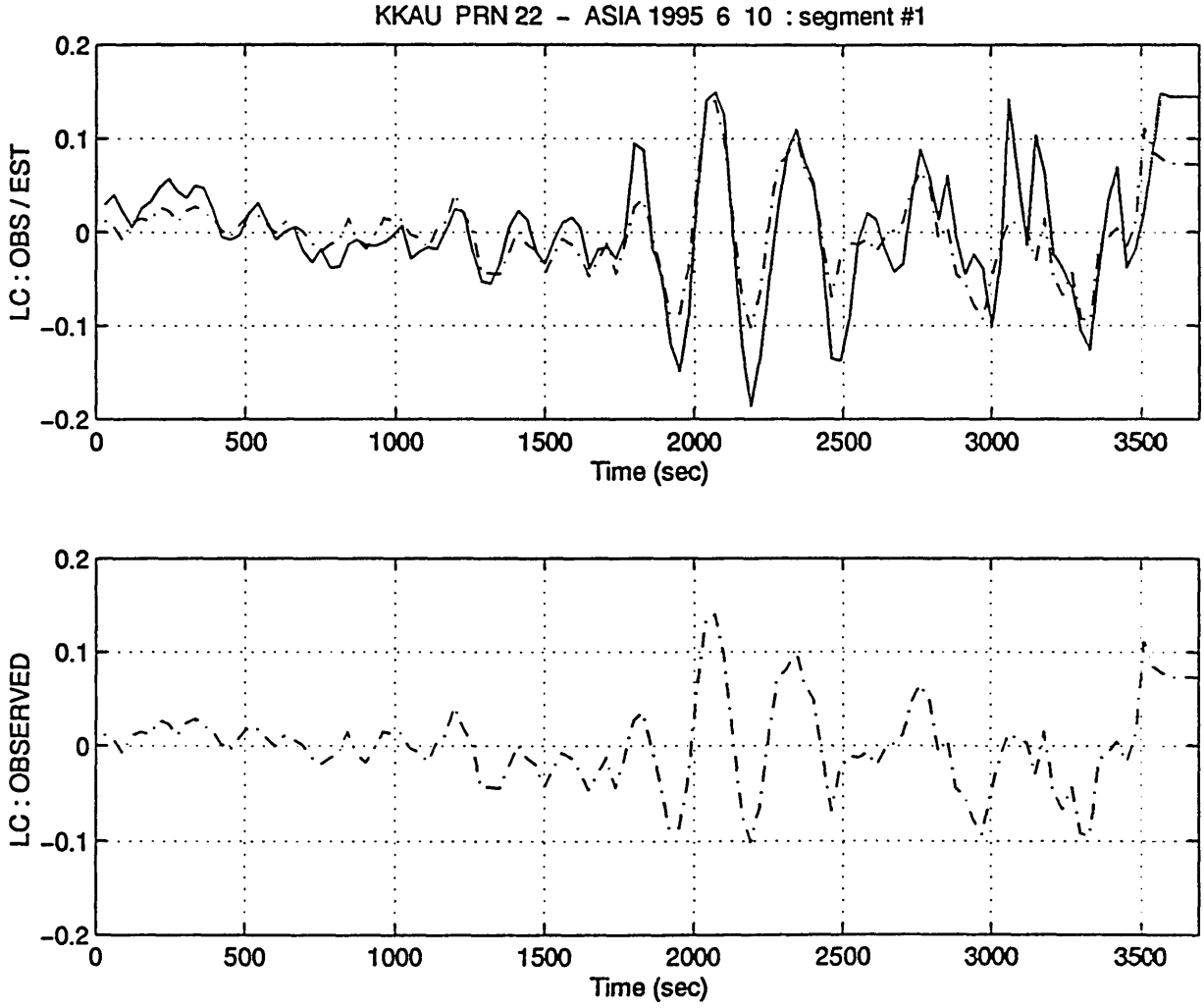

Fig. A.3.4 : Station: KKAU - Satellite: PRN 22
Data acquisition date 10 6 1995
LC_OBS and LC_EST compared for t=0.0 - 3.5 10^3 sec
Unit: [cycles]

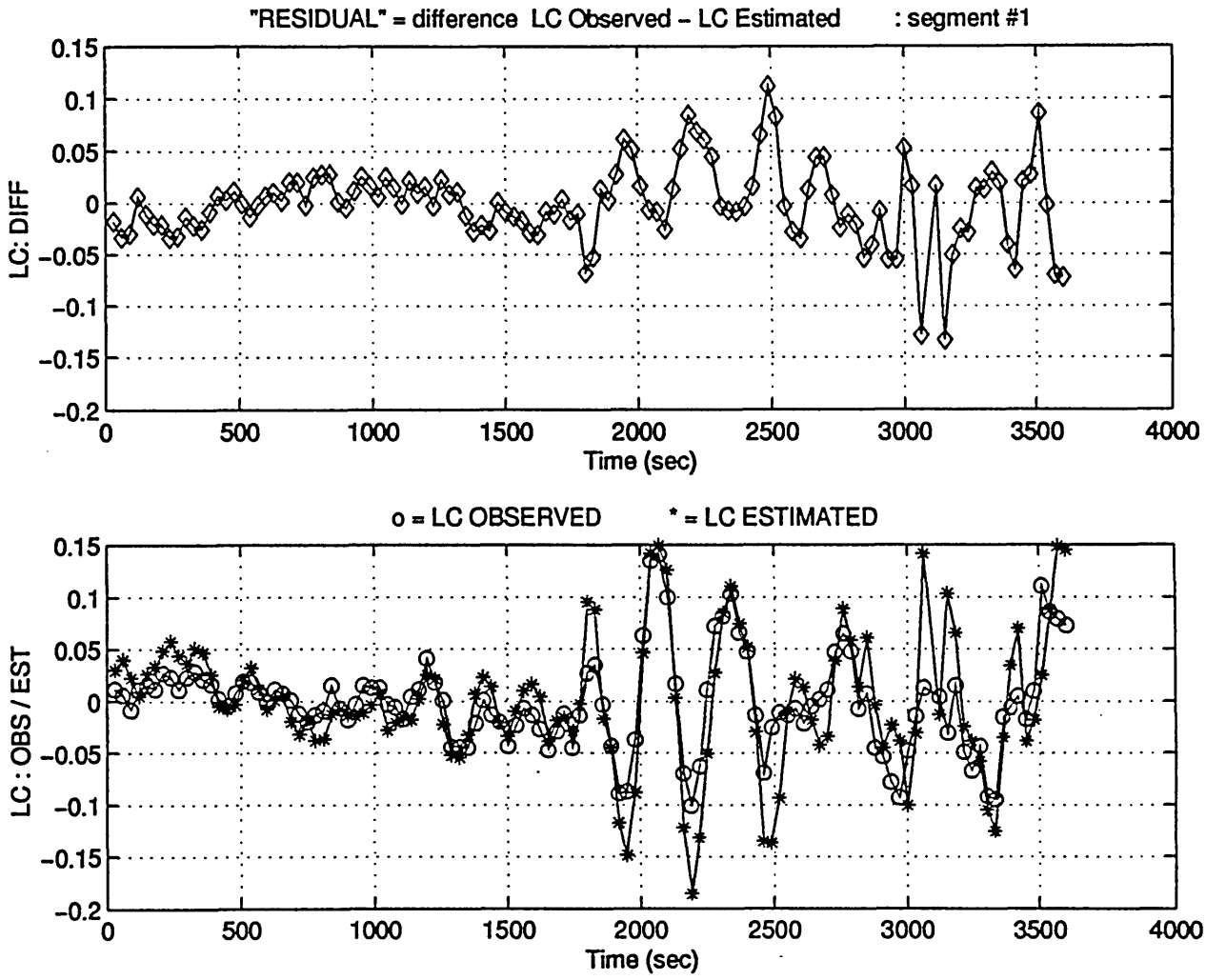

Fig. A.3.5.a) : KKAU - PRN 22 (10 6 1995) - [segment #1]
Phase residual LC_DIFF, determined as the difference between LC_OBS and LC_EST.
Unit: [cycles]

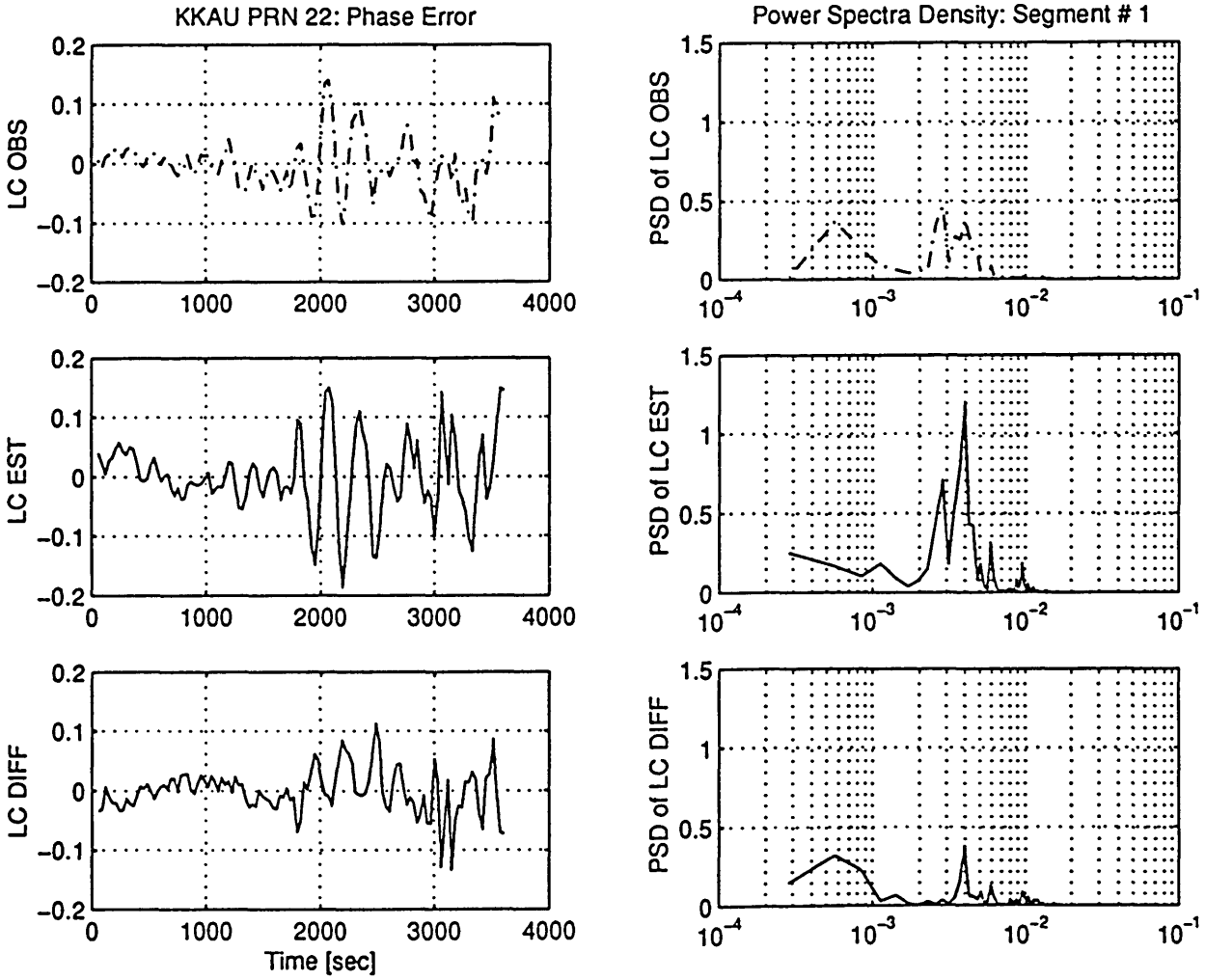

Fig. A.3.5.b) : KKAU - PRN 22 (10 6 1995) - [segment #1]
PSD of LC_OBS, LC_EST and LC_DIFF.
Unit: [cycles]^2

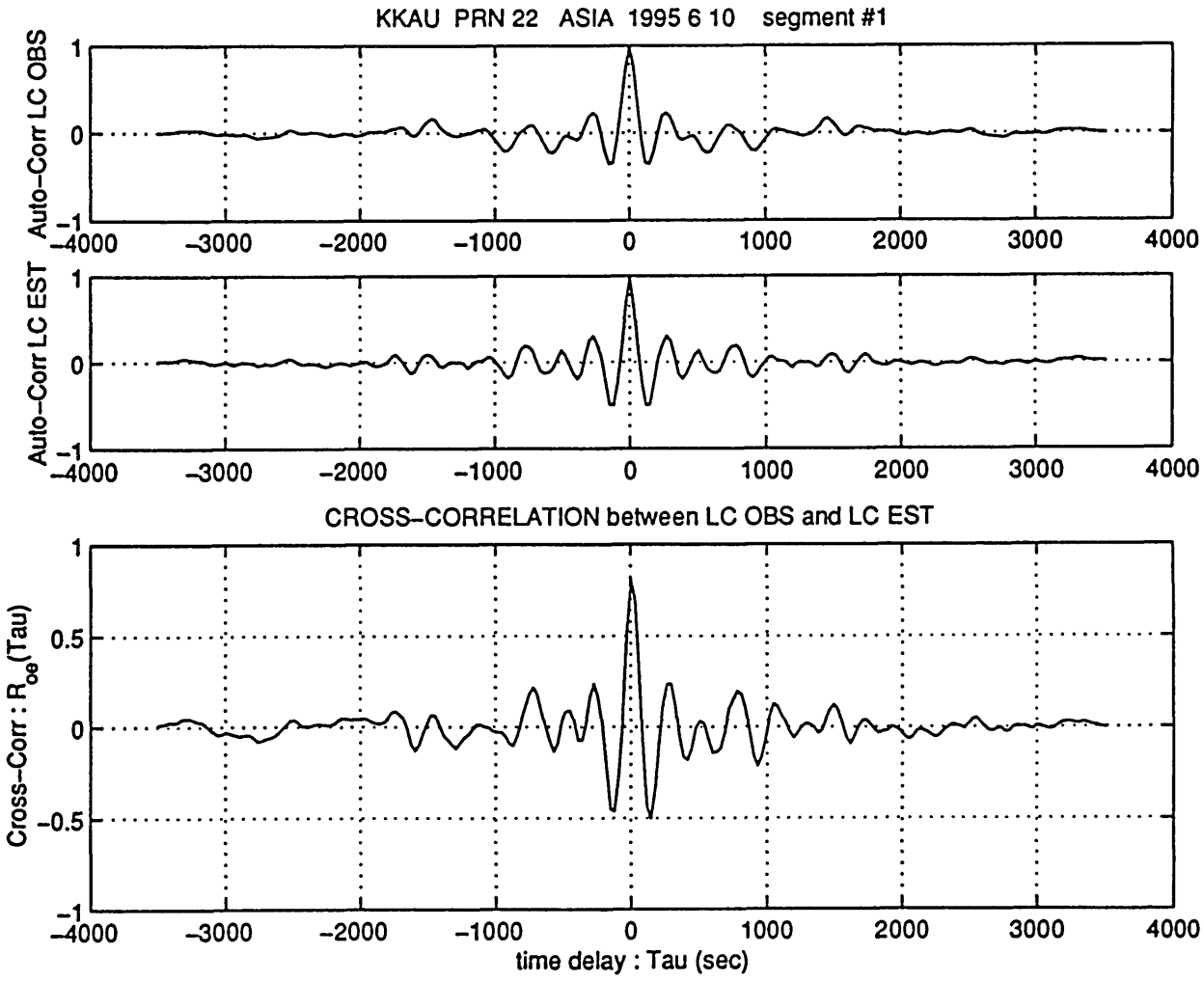

Fig. A.3.5.c) : KKAU - PRN 22 (10 6 1995) - [segment #1]
Auto Correlation of LC_OBS (R_{oo}) and LC_EST (R_{ee}).
Cross Correlation between them (R_{oe})
Unit: [cycles]^2

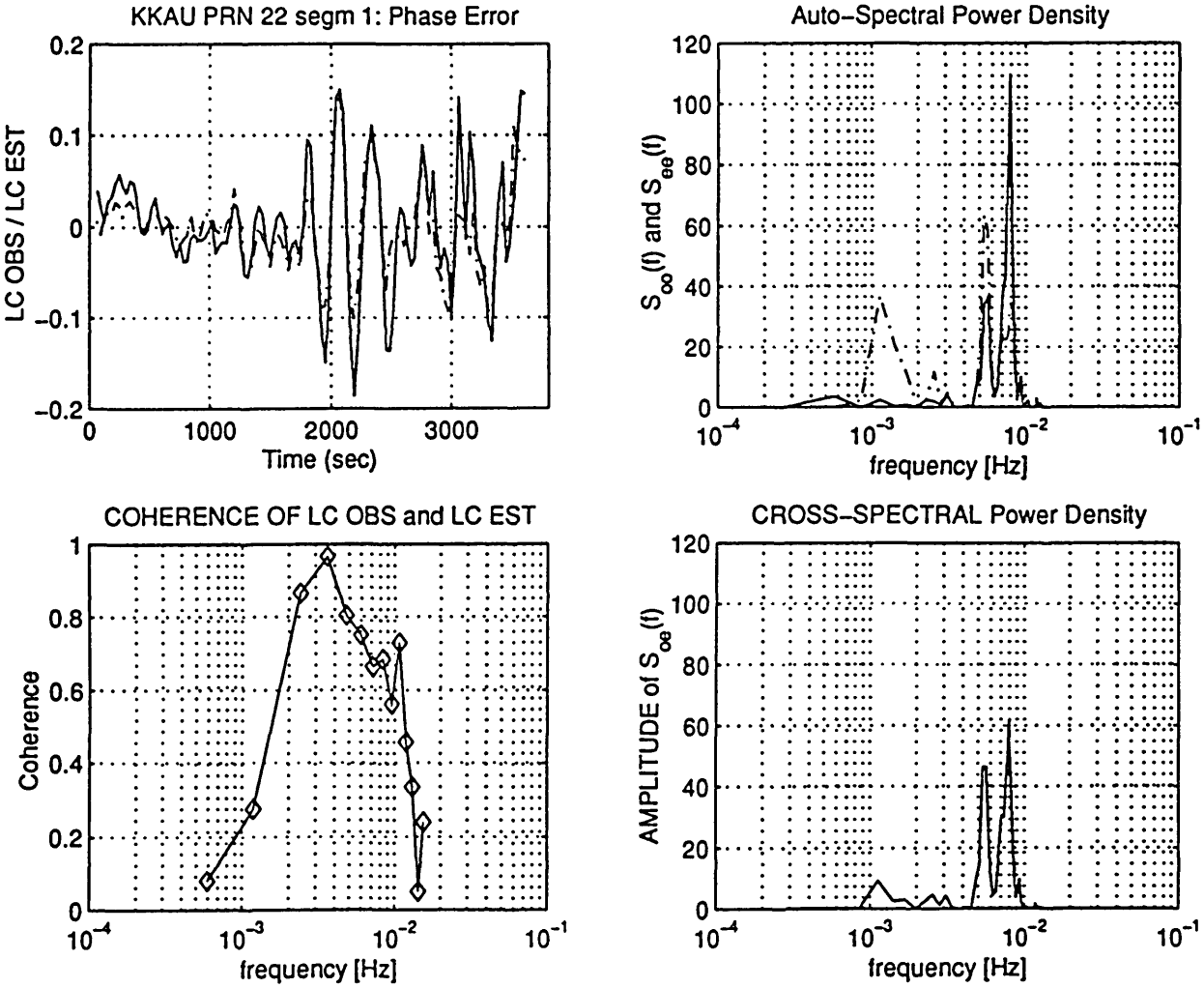

Fig. A.3.5.d) : KKAU - PRN 22 (10 6 1995) - [segment #1]
Auto Spectral Power Density of LC_OBS (S_{oo}) and of LC_EST (S_{ee}). Cross PSD between them (S_{oe})
Unit: [cycles]^2
Coherence function of LC_OBS and LC_EST.

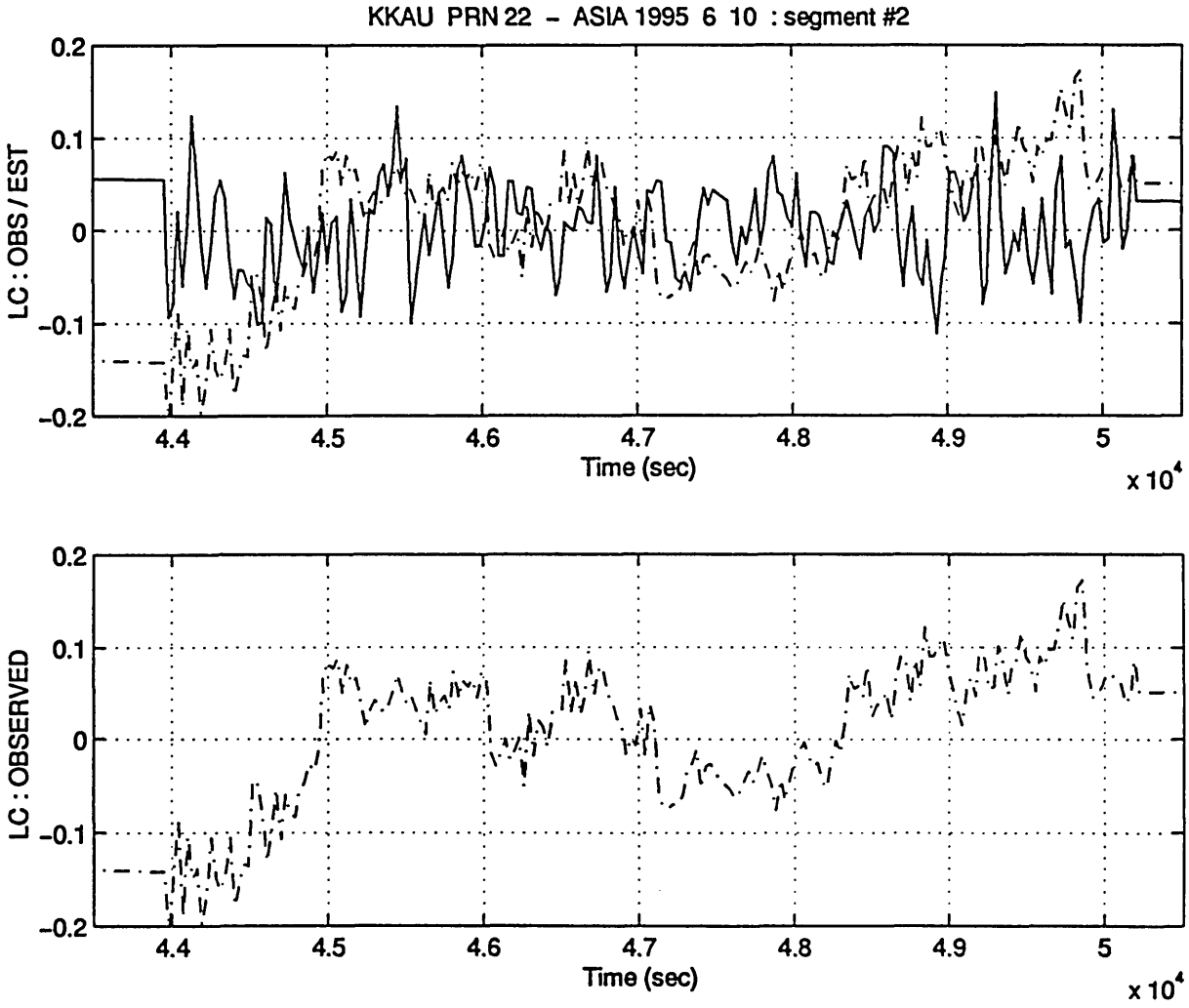

Fig. A.3.6 : Station: KKAU - Satellite: PRN 22
Data acquisition date 10 6 1995
LC_OBS and LC_EST compared for t=4.3 - 5.1 10^4 sec
Unit: [cycles]

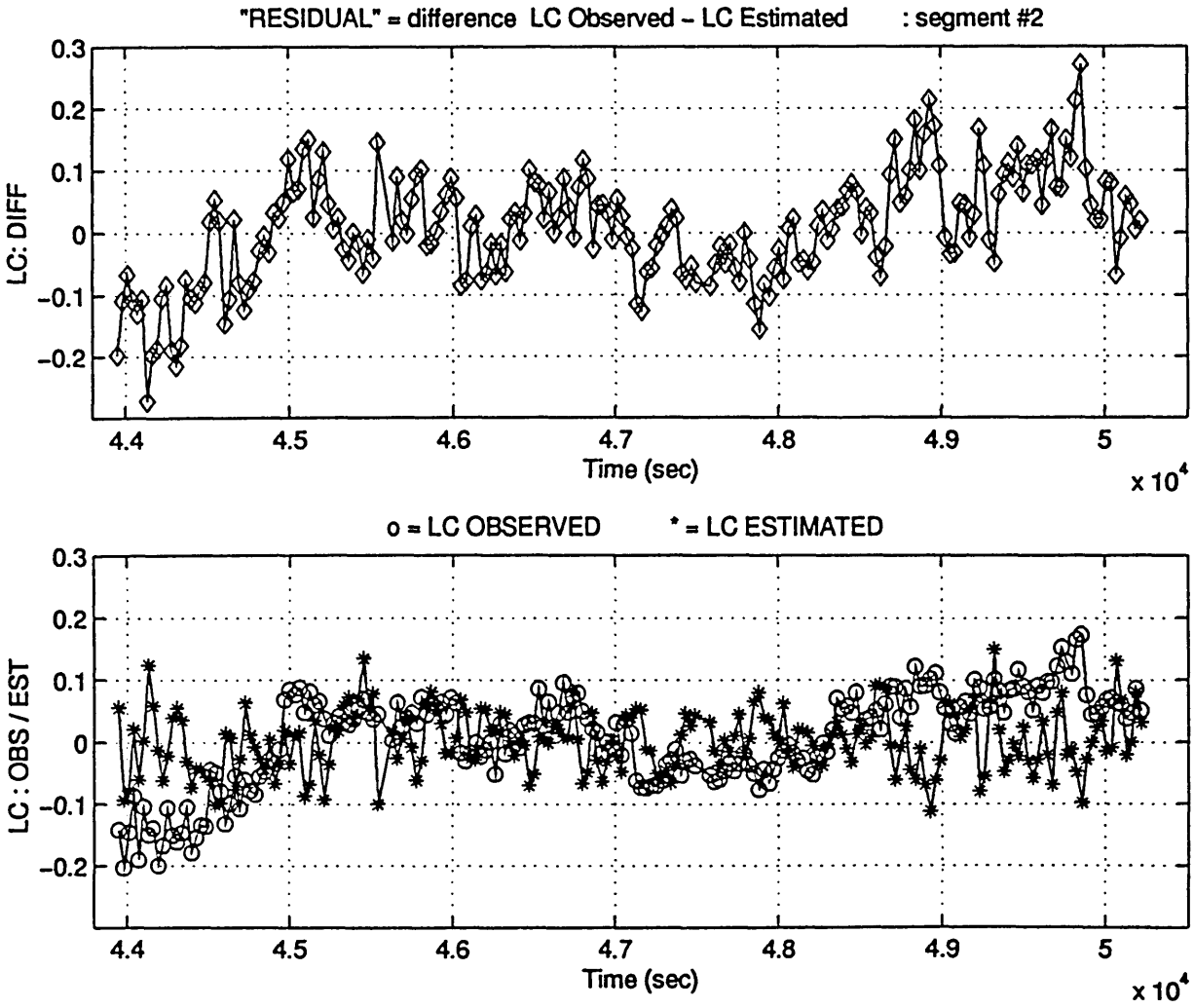

Fig. A.3.7.a) : KKAU - PRN 22 (10 6 1995) - [segment #2]
Phase residual LC_DIFF, determined as the difference between LC_OBS and LC_EST.
Unit: [cycles]

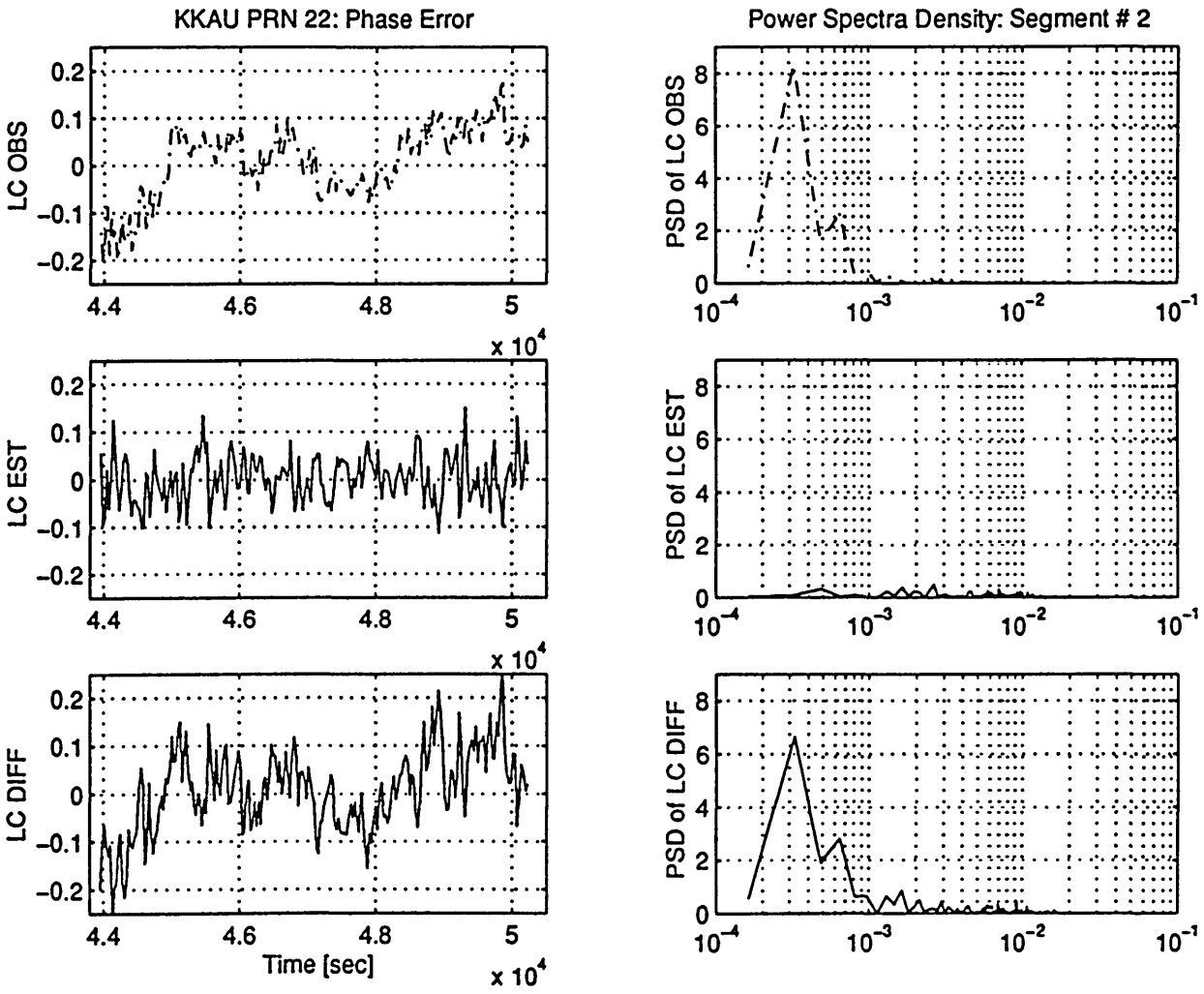

Fig. A.3.7.b) : KKAU - PRN 22 (10 6 1995) - [segment #2]
PSD of LC_OBS, LC_EST and LC_DIFF.
Unit: [cycles]^2

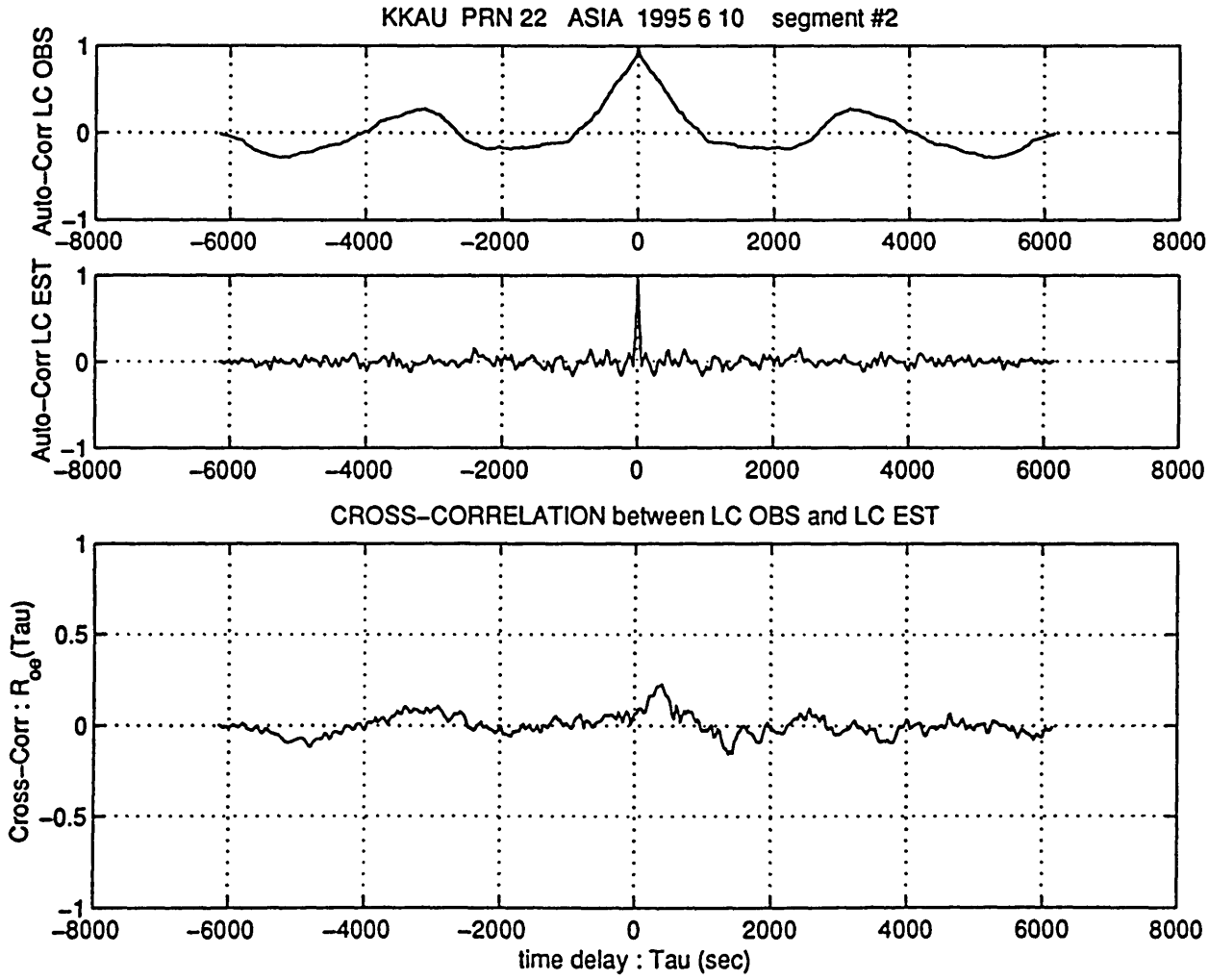

Fig. A.3.7.c) : KKAU - PRN 22 (10 6 1995) - [segment #2]
Auto Correlation of LC_OBS (R_{oo}) and LC_EST (R_{ee}).
Cross Correlation between them (R_{oe})
Unit: [cycles]^2

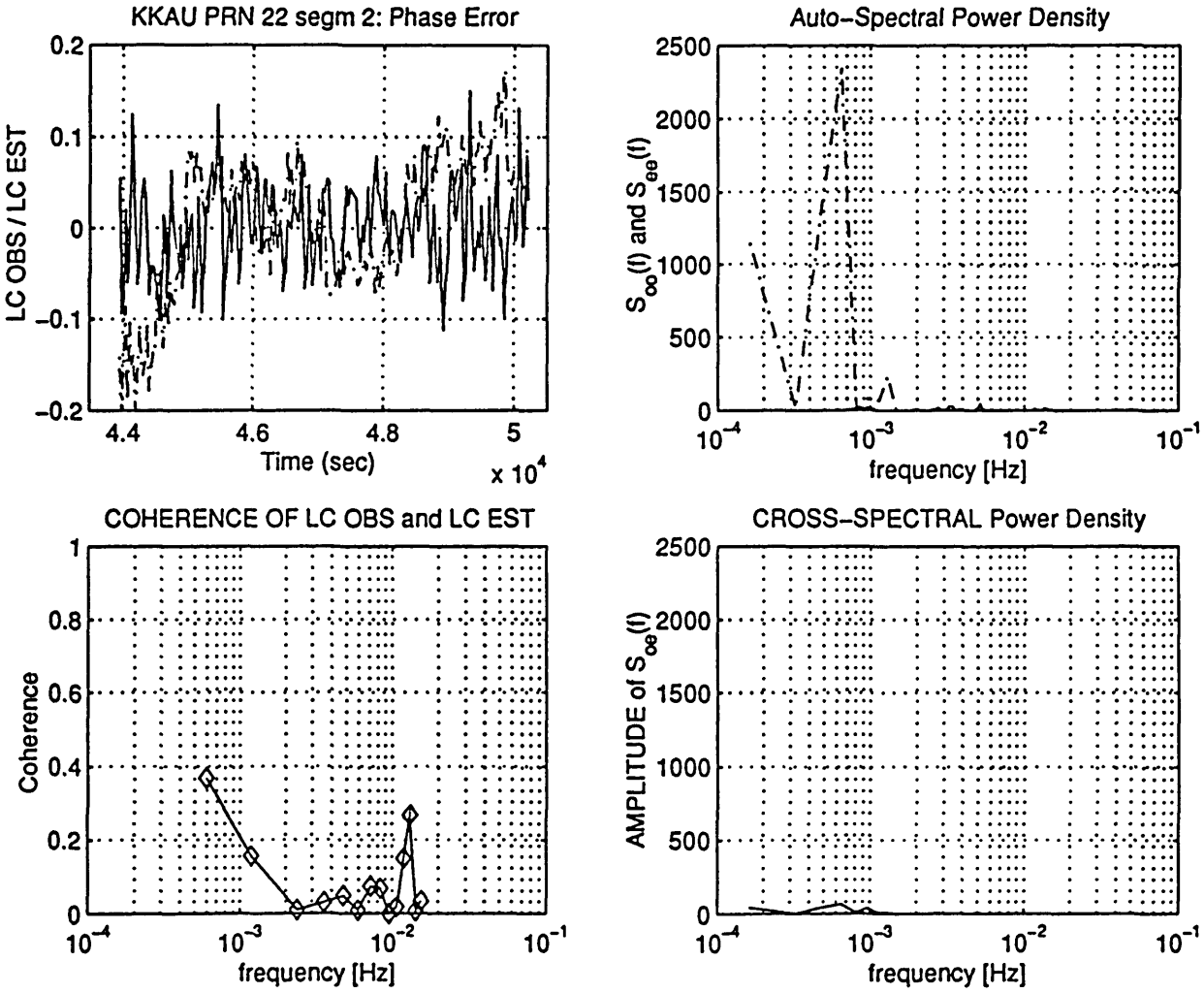

Fig. A.3.7.d) : KKAU - PRN 22 (10 6 1995) - [segment #2]
Auto Spectral Power Density of LC_OBS (S_{oo}) and of LC_EST (S_{ee}). Cross PSD between them (S_{oe})
Unit: [cycles]^2
Coherence function of LC_OBS and LC_EST.

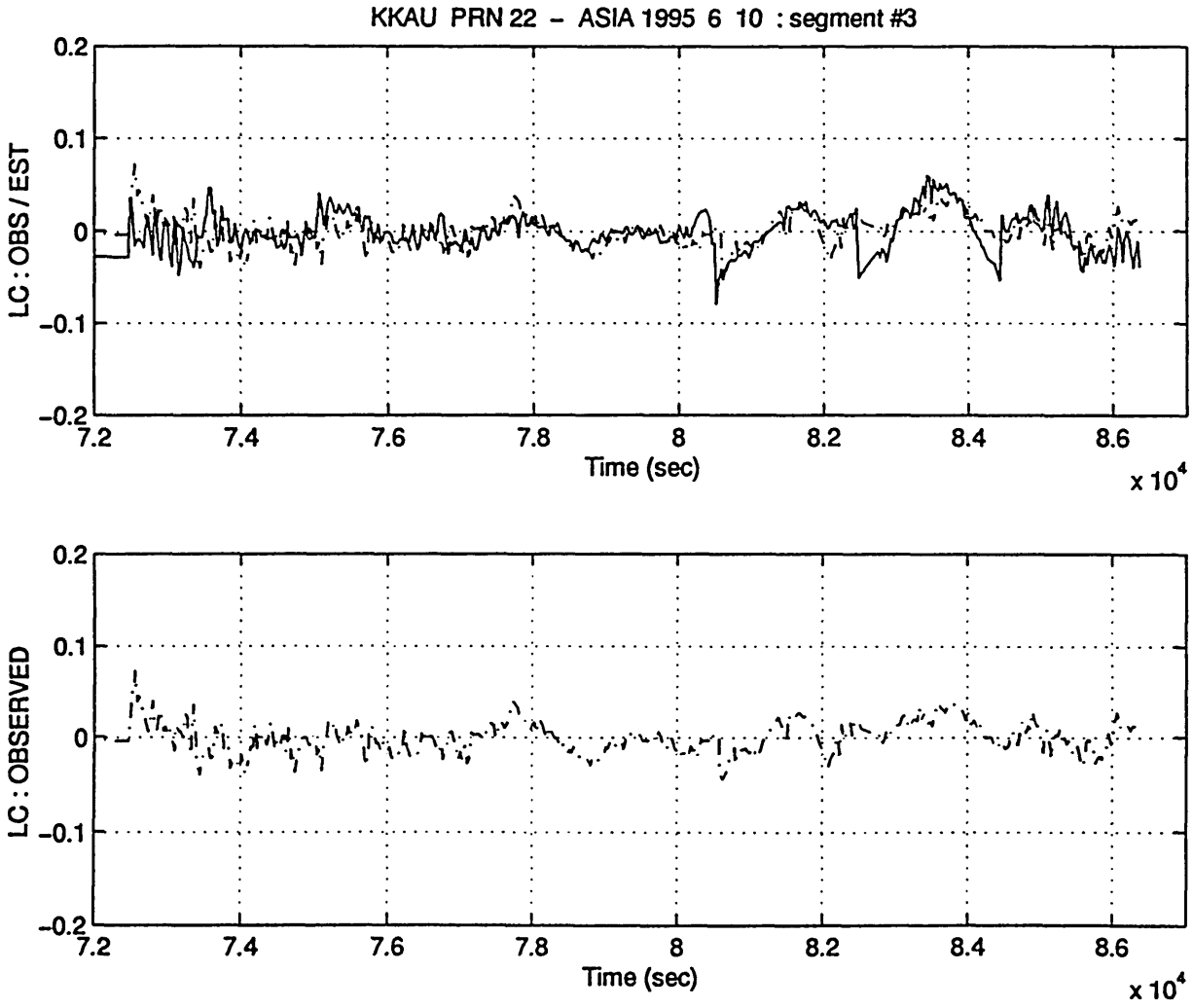

Fig. A.3.8 : Station: KKAU - Satellite: PRN 22
Data acquisition date 10 6 1995
LC_OBS and LC_EST compared for t=7.2 - 8.7 10^4 sec
Unit: [cycles]

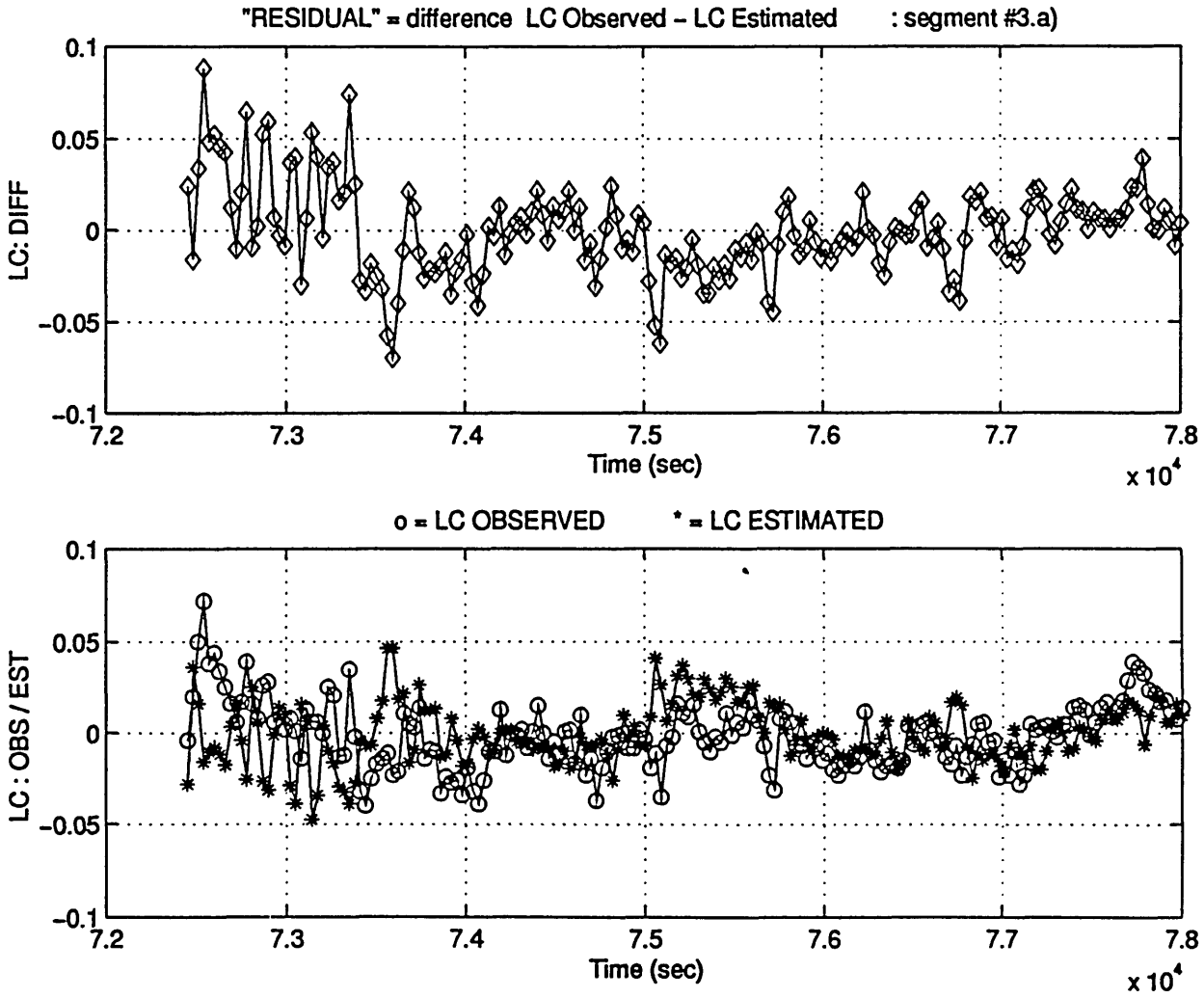

Fig. A.3.9.a) : KKAU - PRN 22 (10 6 1995) - [segment #3.a]
Phase residual LC_DIFF, determined as the difference between LC_OBS and LC_EST.
Unit: [cycles]

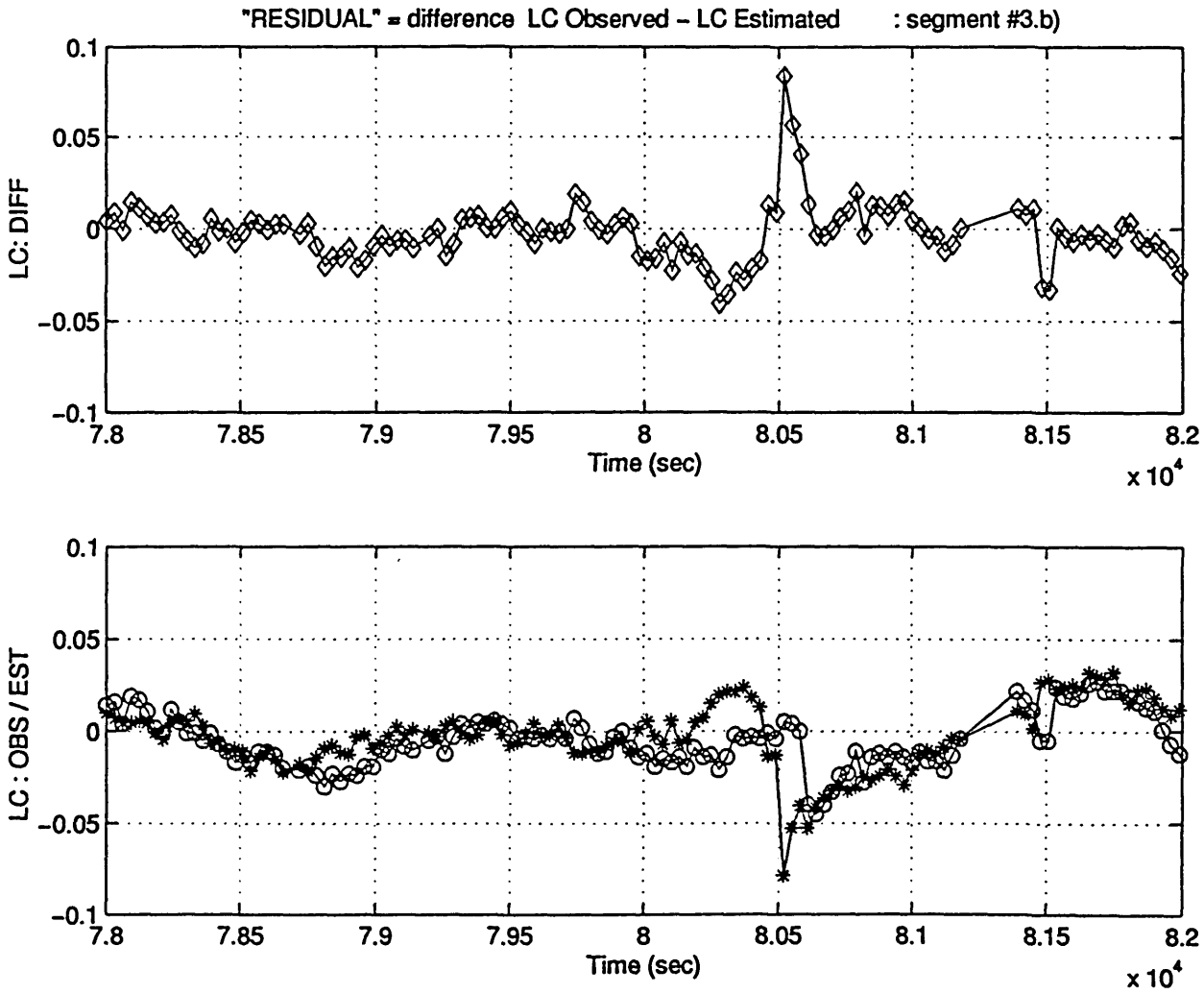

Fig. A.3.10.a) : KKAU - PRN 22 (10 6 1995) - [segment #3.b]
Phase residual LC_DIFF, determined as the difference between LC_OBS and LC_EST.
Unit: [cycles]

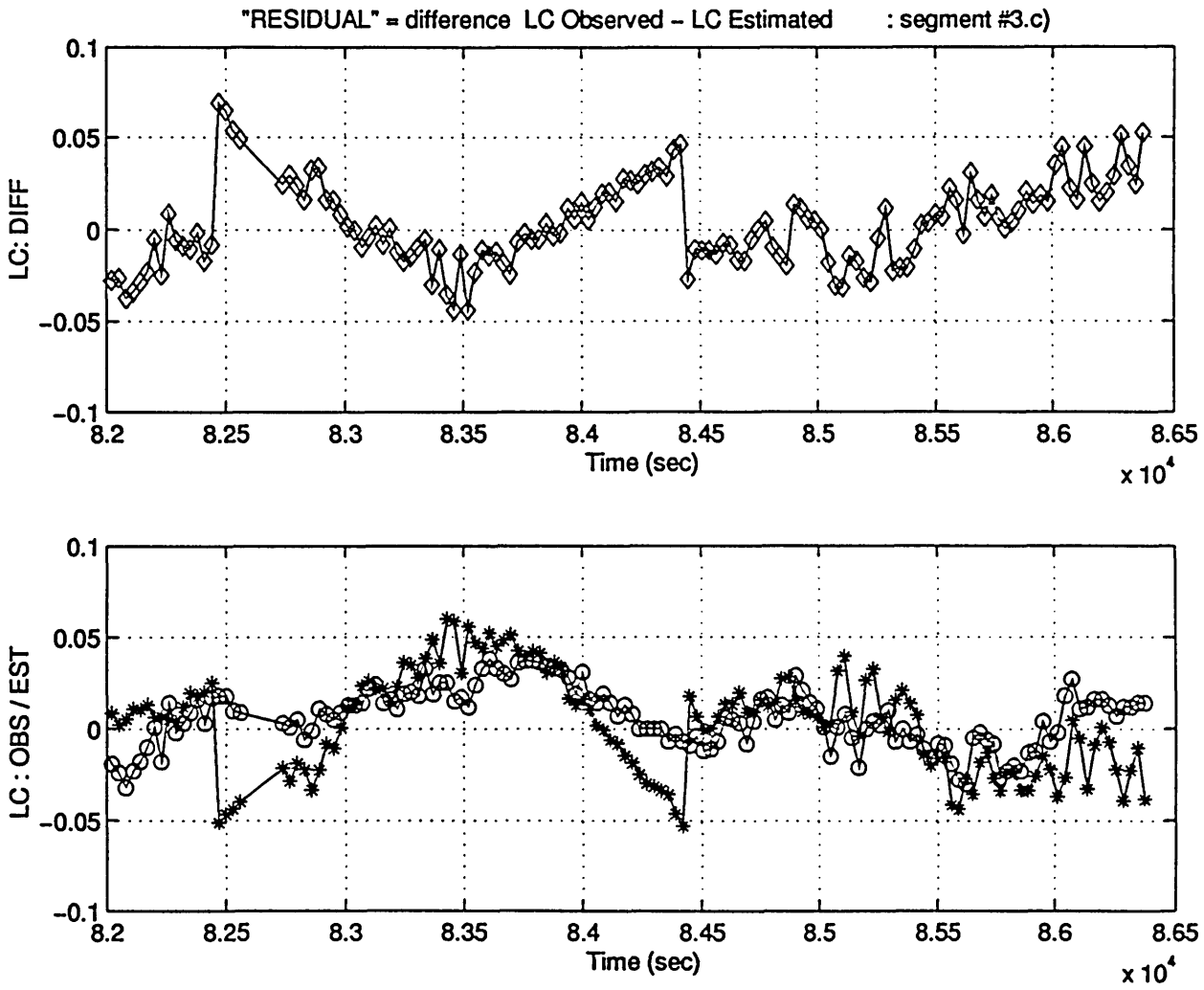

Fig. A.3.11.a) : KKAU - PRN 22 (10 6 1995) - [segment #3.c]
Phase residual LC_DIFF, determined as the difference between LC_OBS and LC_EST.
Unit: [cycles]

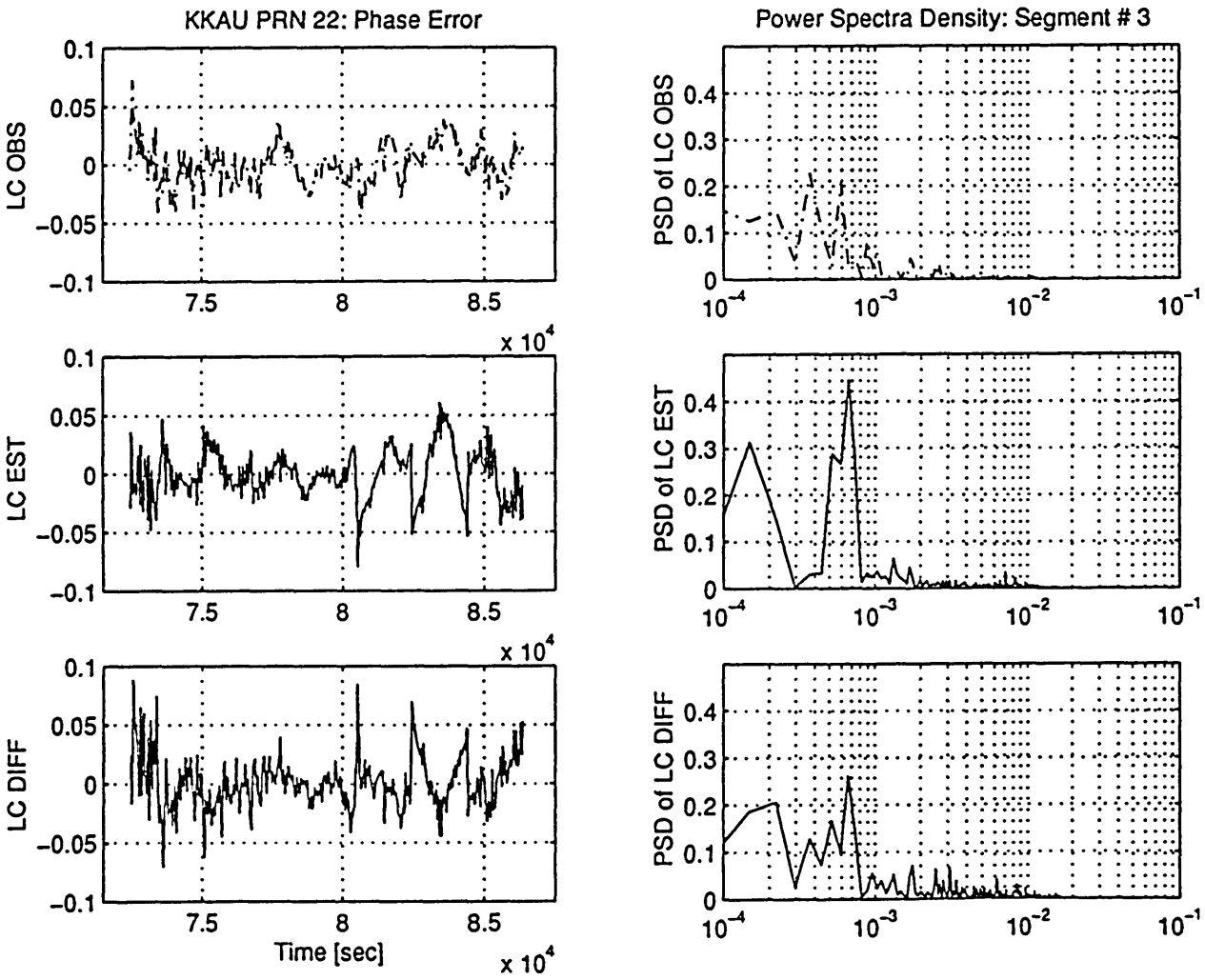

Fig. A.3.8.b) : KKAU - PRN 22 (10 6 1995) - [segment #3]
PSD of LC_OBS, LC_EST and LC_DIFF.
Unit: [cycles]^2

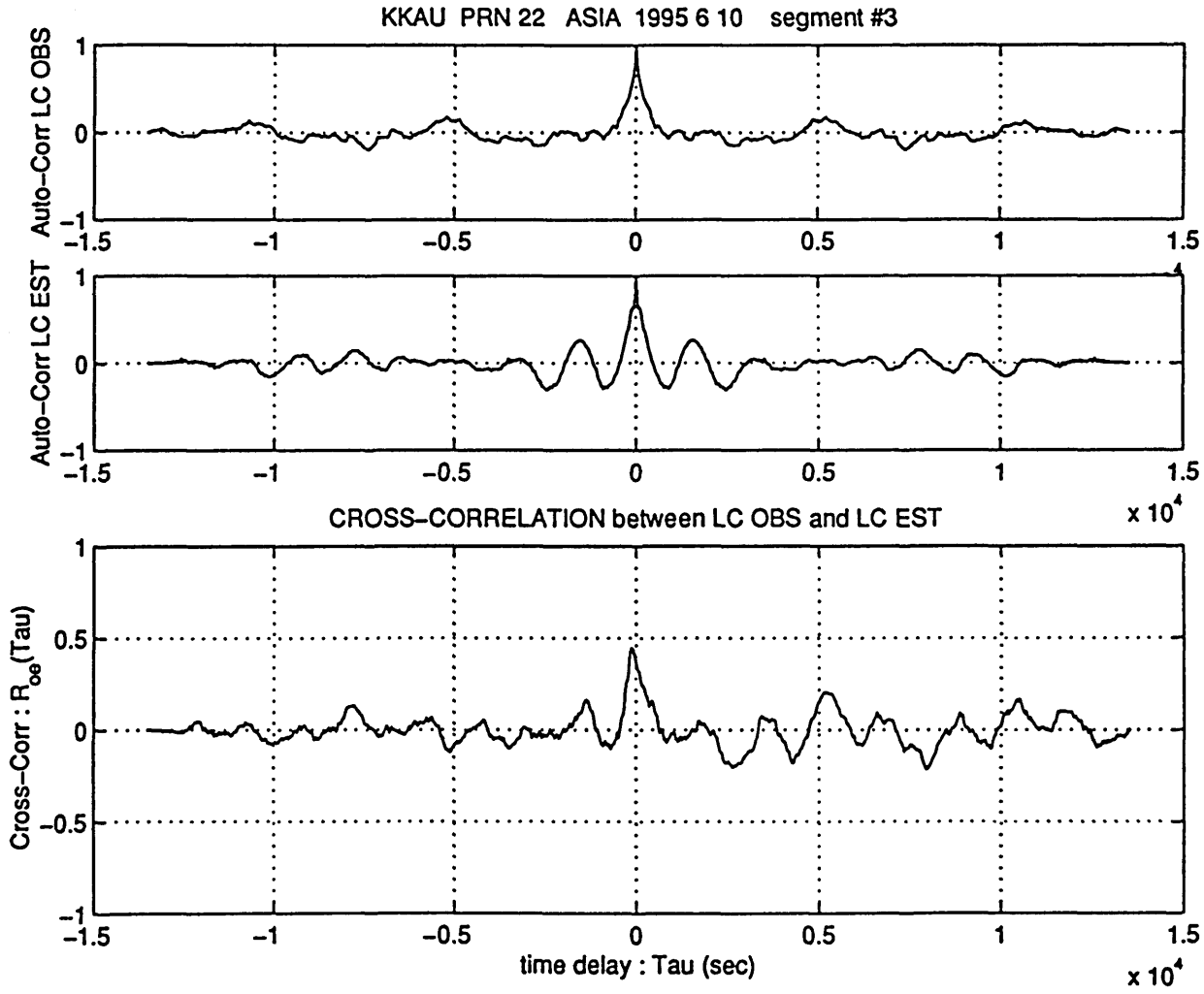

Fig. A.3.8.c) : KKAU - PRN 22 (10 6 1995) - [segment #3]
Auto Correlation of LC_OBS (R_{oo}) and LC_EST (R_{ee}).
Cross Correlation between them (R_{oe})
Unit: [cycles]^2

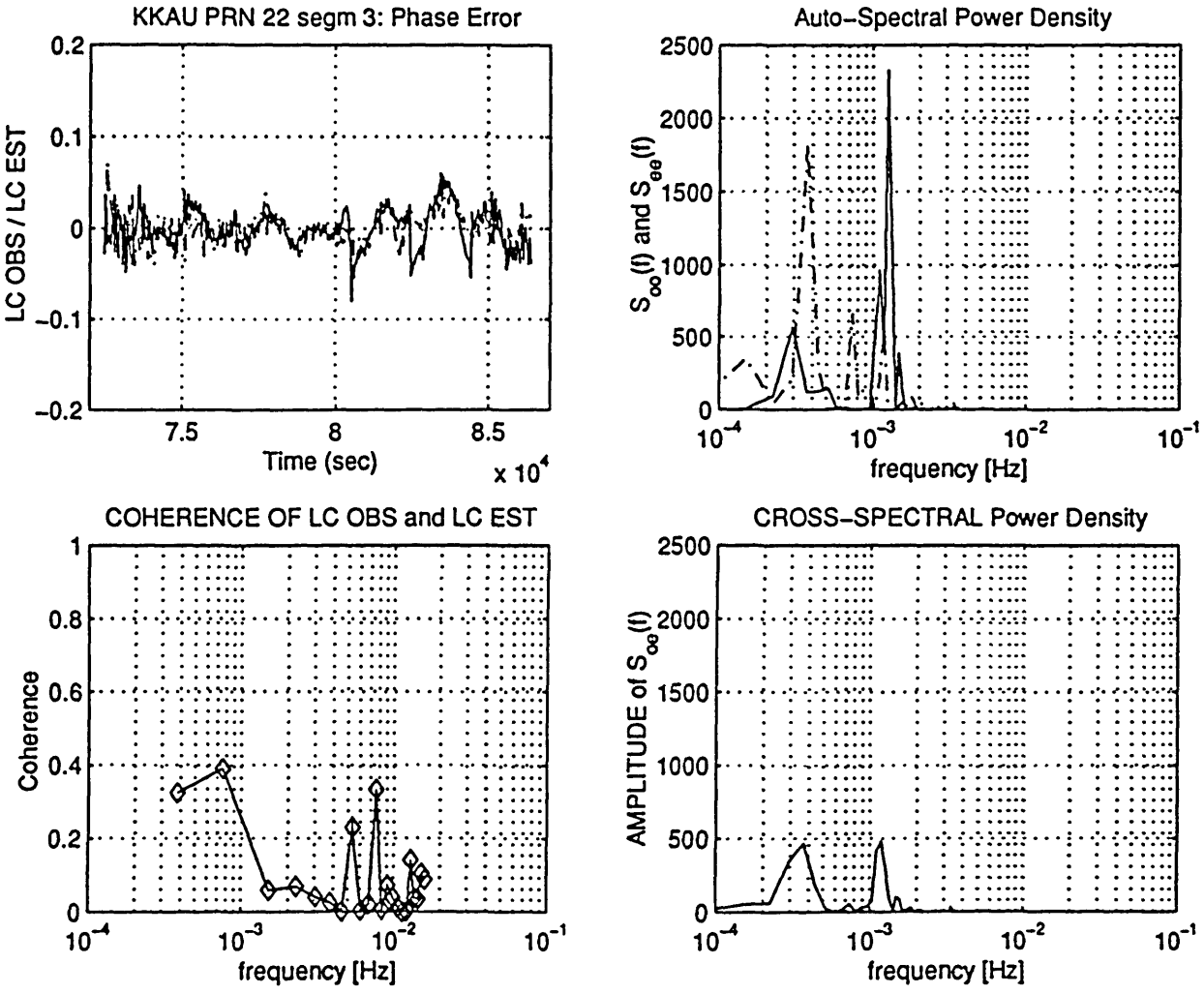

Fig. A.3.8.d) : KKAU - PRN 22 (10 6 1995) - [segment #3]
Auto Spectral Power Density of LC_OBS (S_{oo}) and of LC_EST (S_{ee}). Cross PSD between them (S_{oe})
Unit: [cycles]^2
Coherence function of LC_OBS and LC_EST.

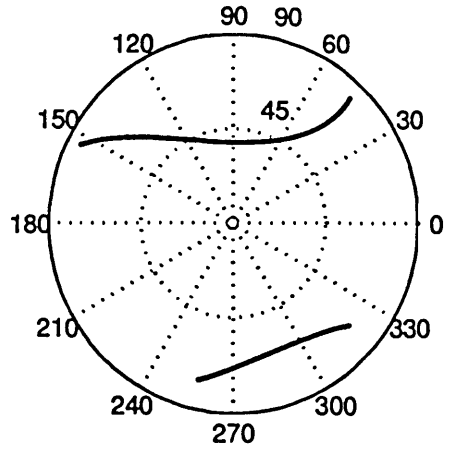

GPS DATA: receiver location: CENTRAL ASIA acquisition date: 10 6 1995

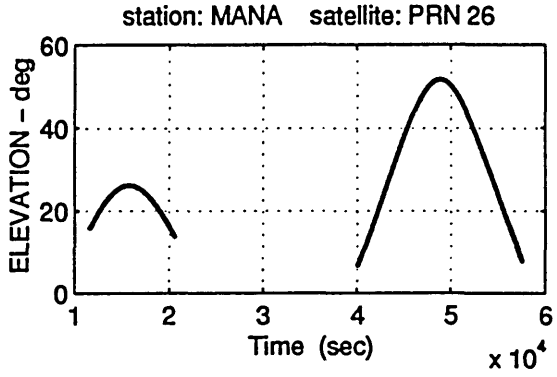

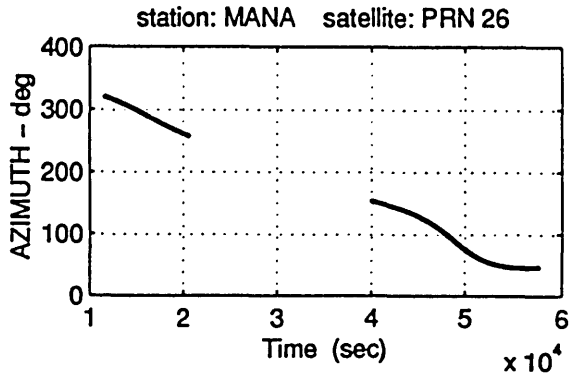

Fig. A.4.1 : Satellite visibility chart for PRN 26 (skymap). Elevation and azimuth of PRN 26 with respect to the station MANA

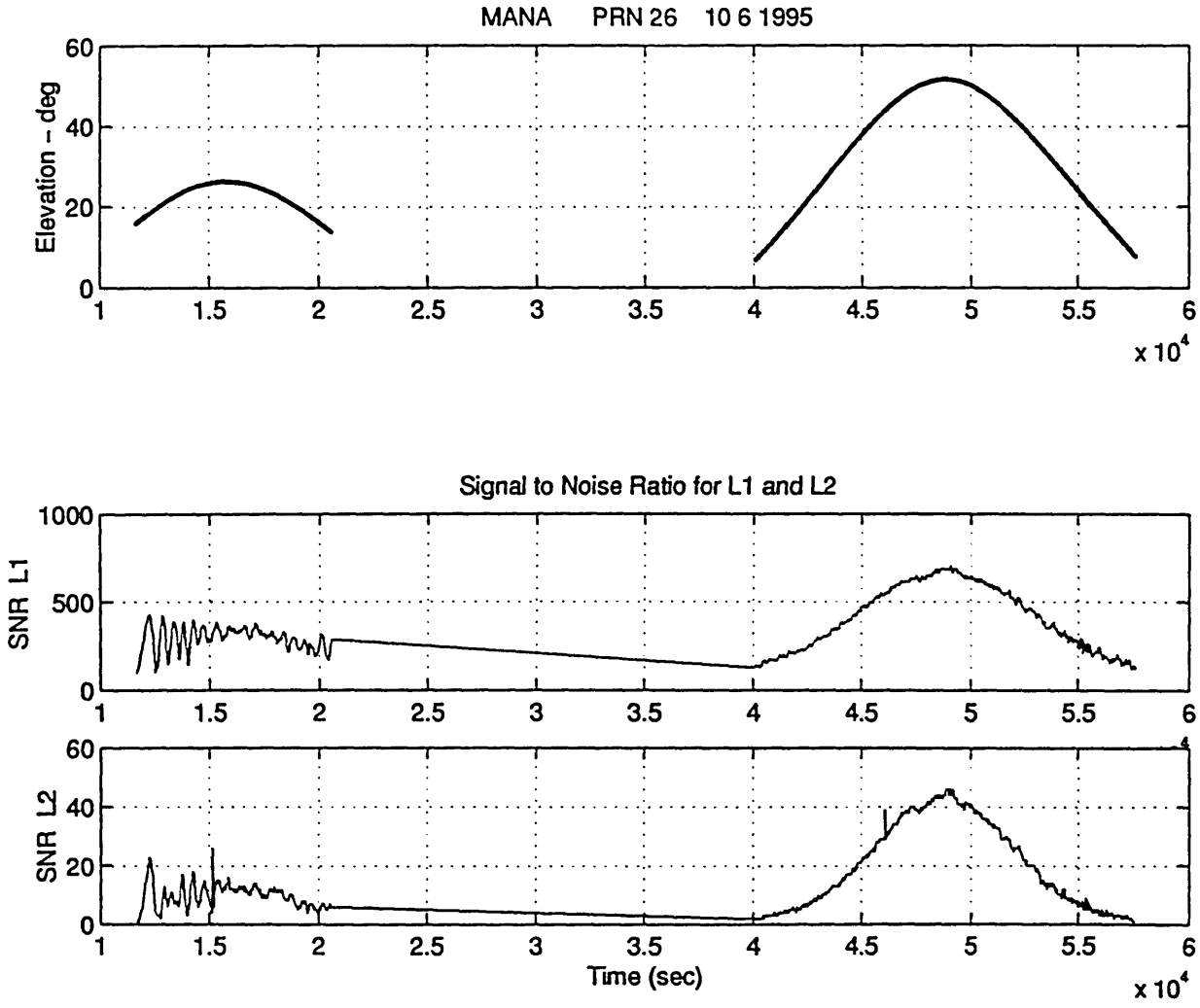

Fig. A.4.2 : Station: MANA - Satellite: PRN 26
Data acquisition date 10 6 1995
Signal-to-Noise-Ratio (SNR) for L_1 and L_2.

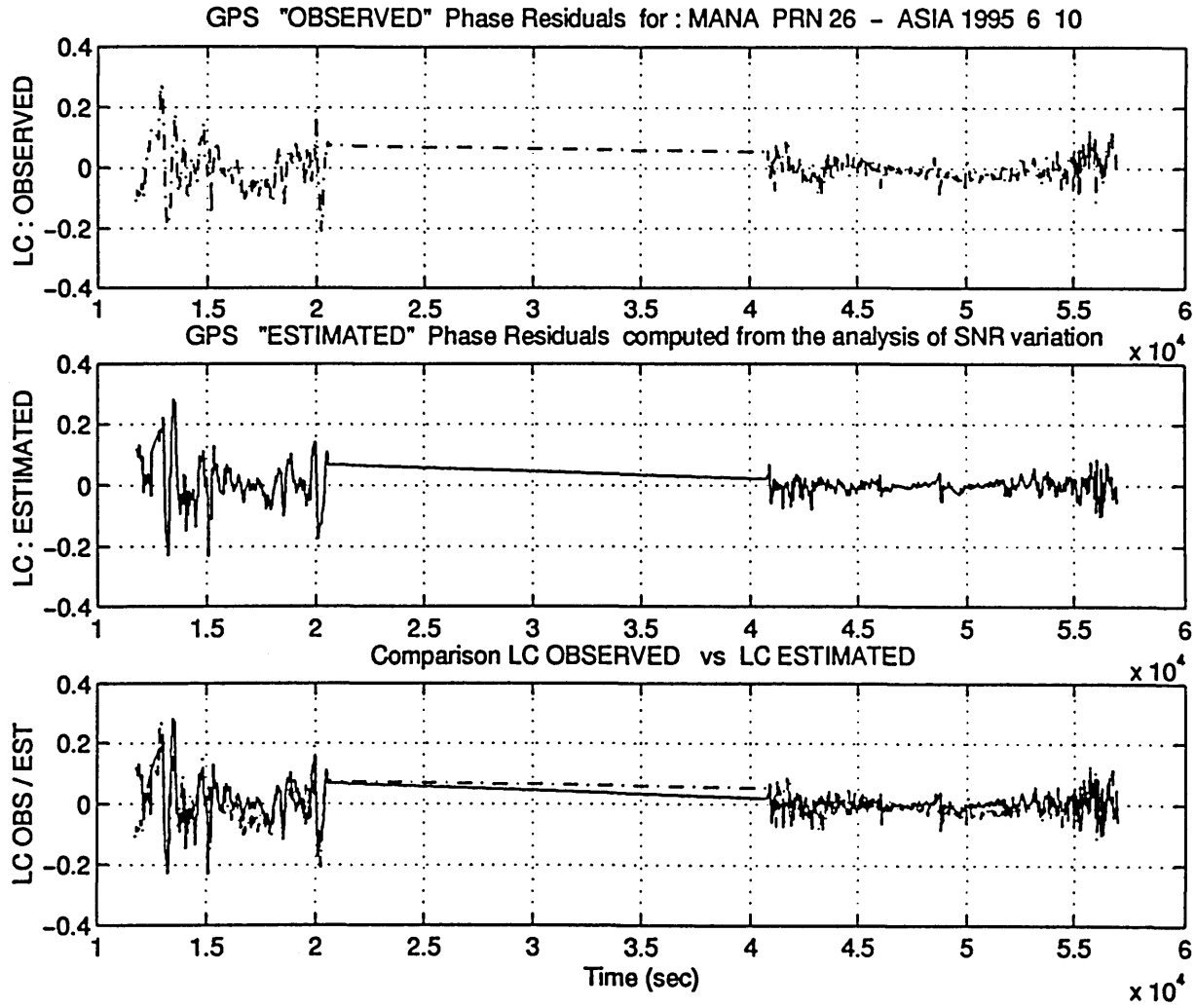

Fig. A.4.3 : Station: MANA - Satellite: PRN 26
Data acquisition date 10 6 1995
The observed phase residual (LC_OBS) is compared with the multipath phase error estimated from the SNR (LC_EST).
Unit: [cycles]

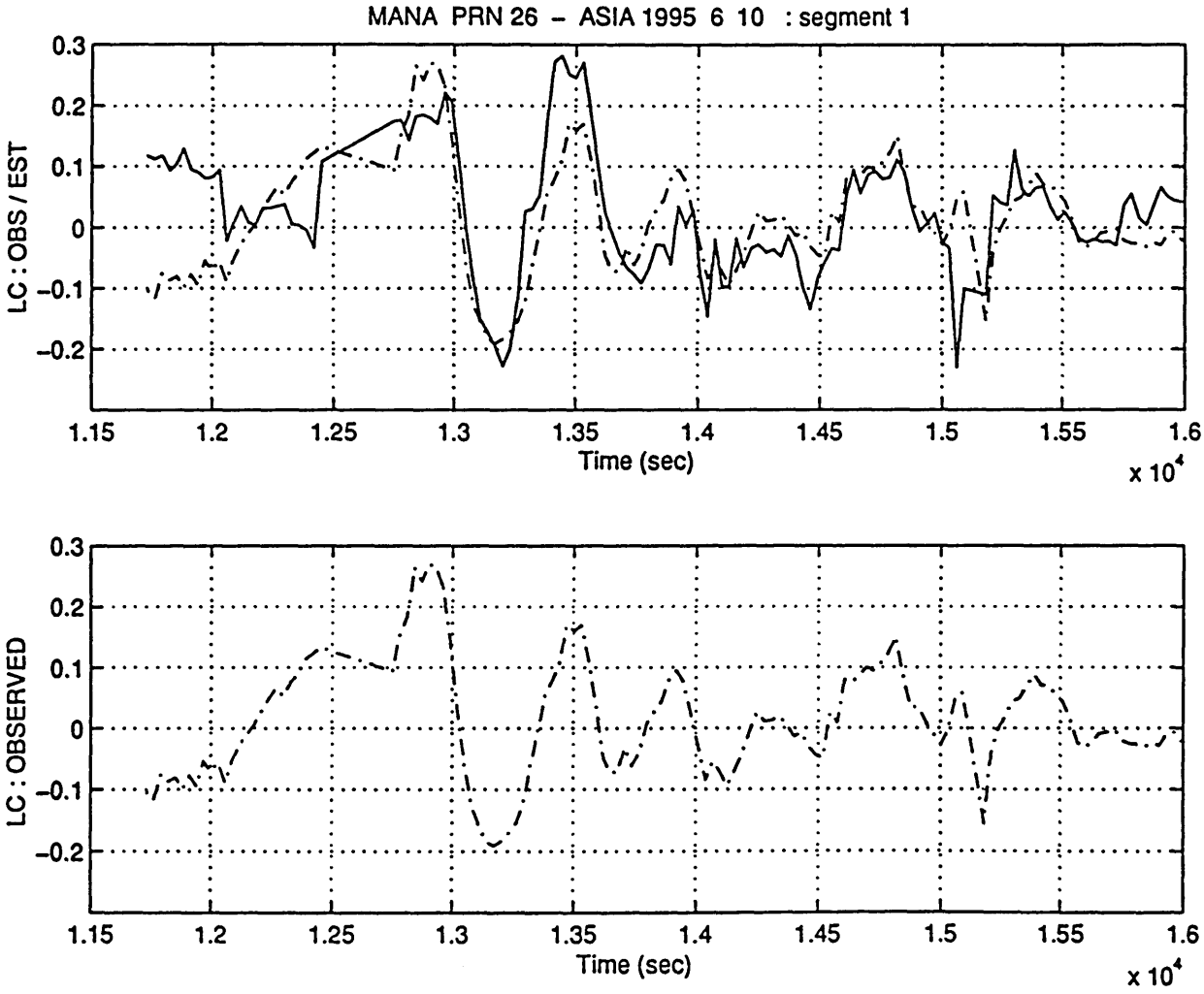

Fig. A.4.4 : Station: MANA - Satellite: PRN 26
Data acquisition date 10 6 1995
LC_OBS and LC_EST compared for t=1.1 - 1.6 10^3 sec
Unit: [cycles]

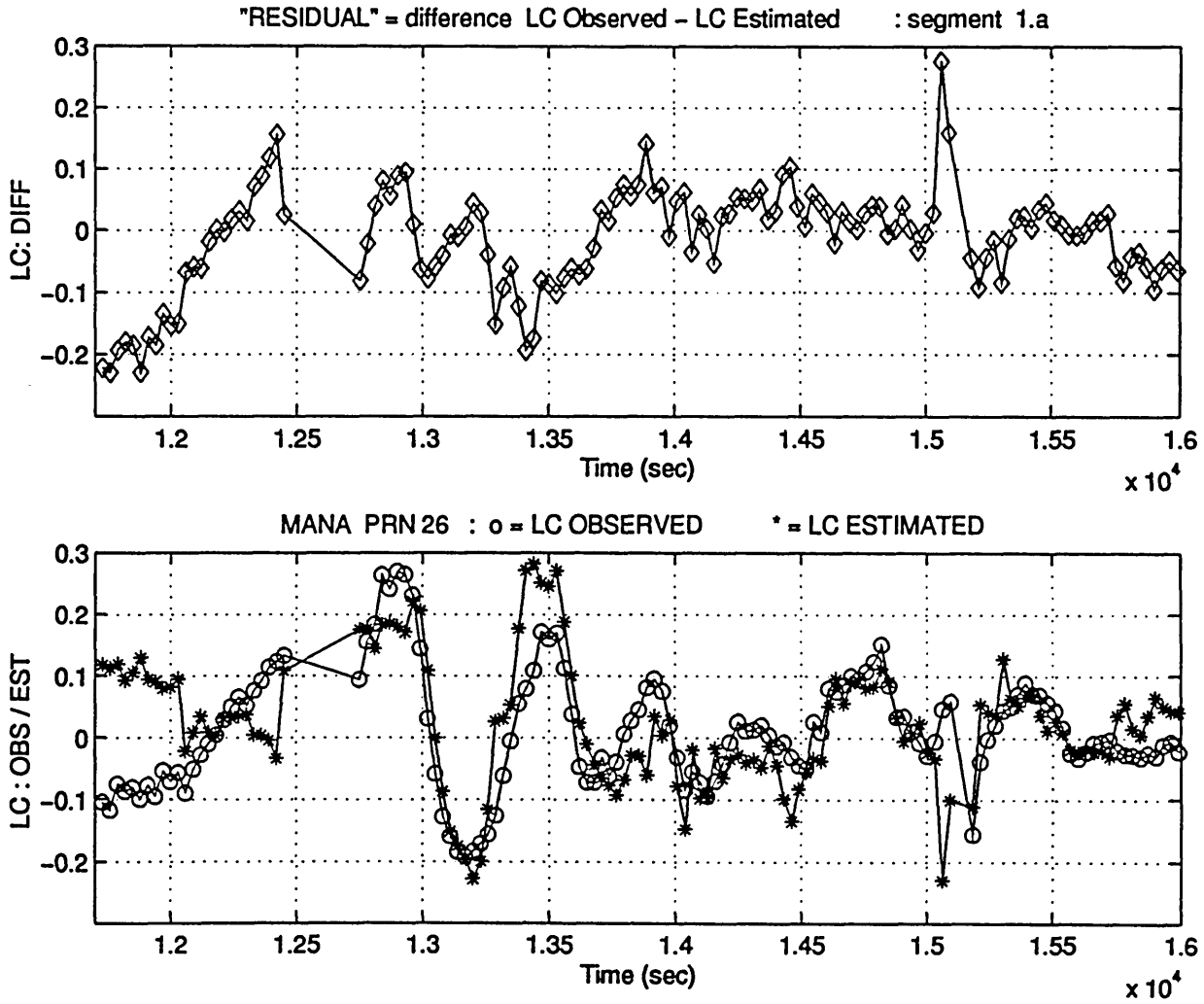

Fig. A.4.5.a) : MANA - PRN 26 (10 6 1995) - [segment 1.a]
Phase residual LC_DIFF, determined as the difference between LC_OBS and LC_EST.
Unit: [cycles]

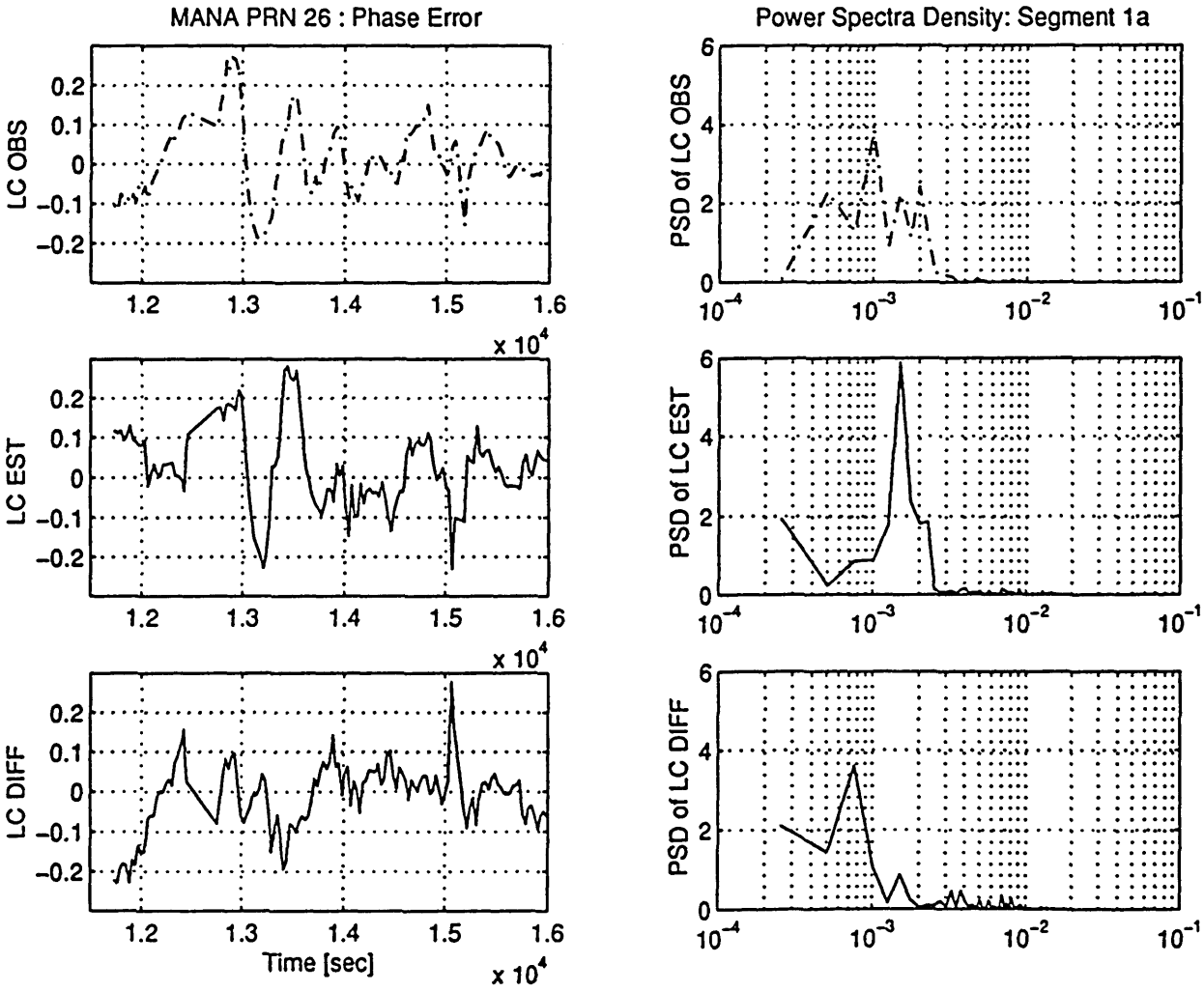

Fig. A.4.5.b) : MANA - PRN 26 (10 6 1995) - [segment 1.a]
PSD of LC_OBS, LC_EST and LC_DIFF.
Unit: [cycles]^2

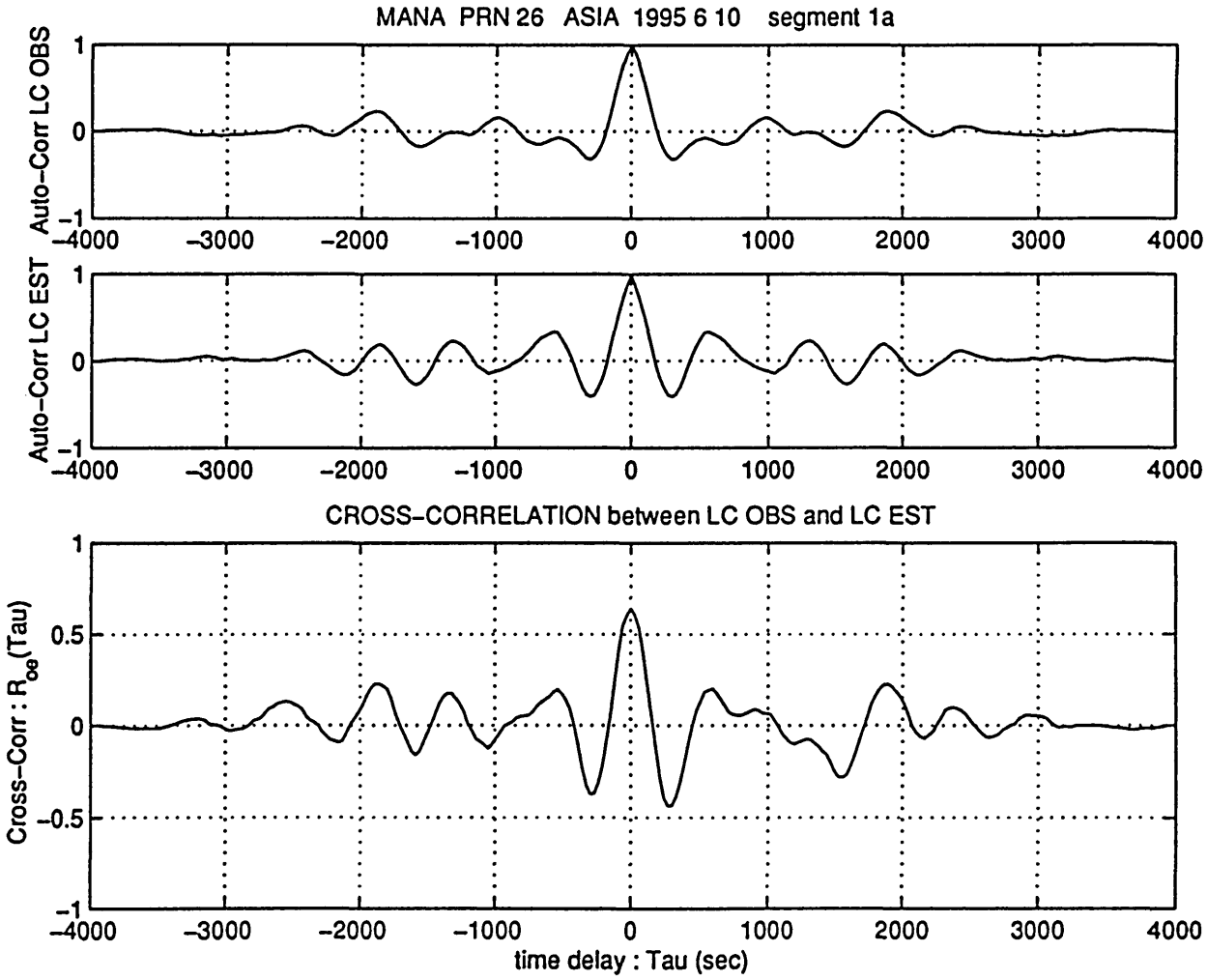

Fig. A.4.5.c) : MANA - PRN 26 (10 6 1995) - [segment 1.a]
Auto Correlation of LC_OBS (R_{oo}) and LC_EST (R_{ee}).
Cross Correlation between them (R_{oe})
Unit: [cycles]^2

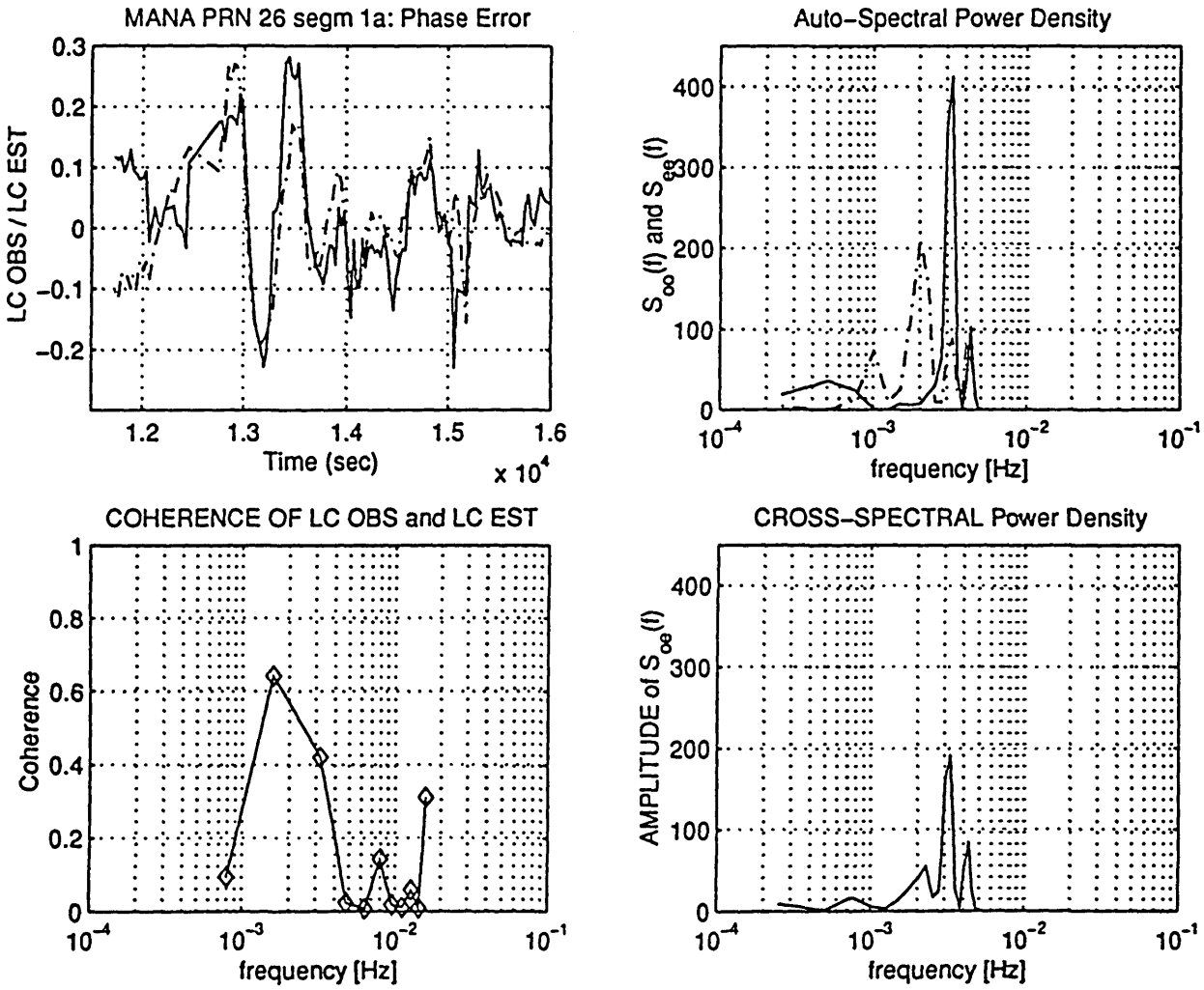

Fig. A.4.5.d) : MANA - PRN 26 (10 6 1995) - [segment 1.a]
Auto Spectral Power Density of LC_OBS (S_{oo}) and of LC_EST (S_{ee}). Cross PSD between them (S_{oe})
Unit: [cycles]^2
Coherence function of LC_OBS and LC_EST.

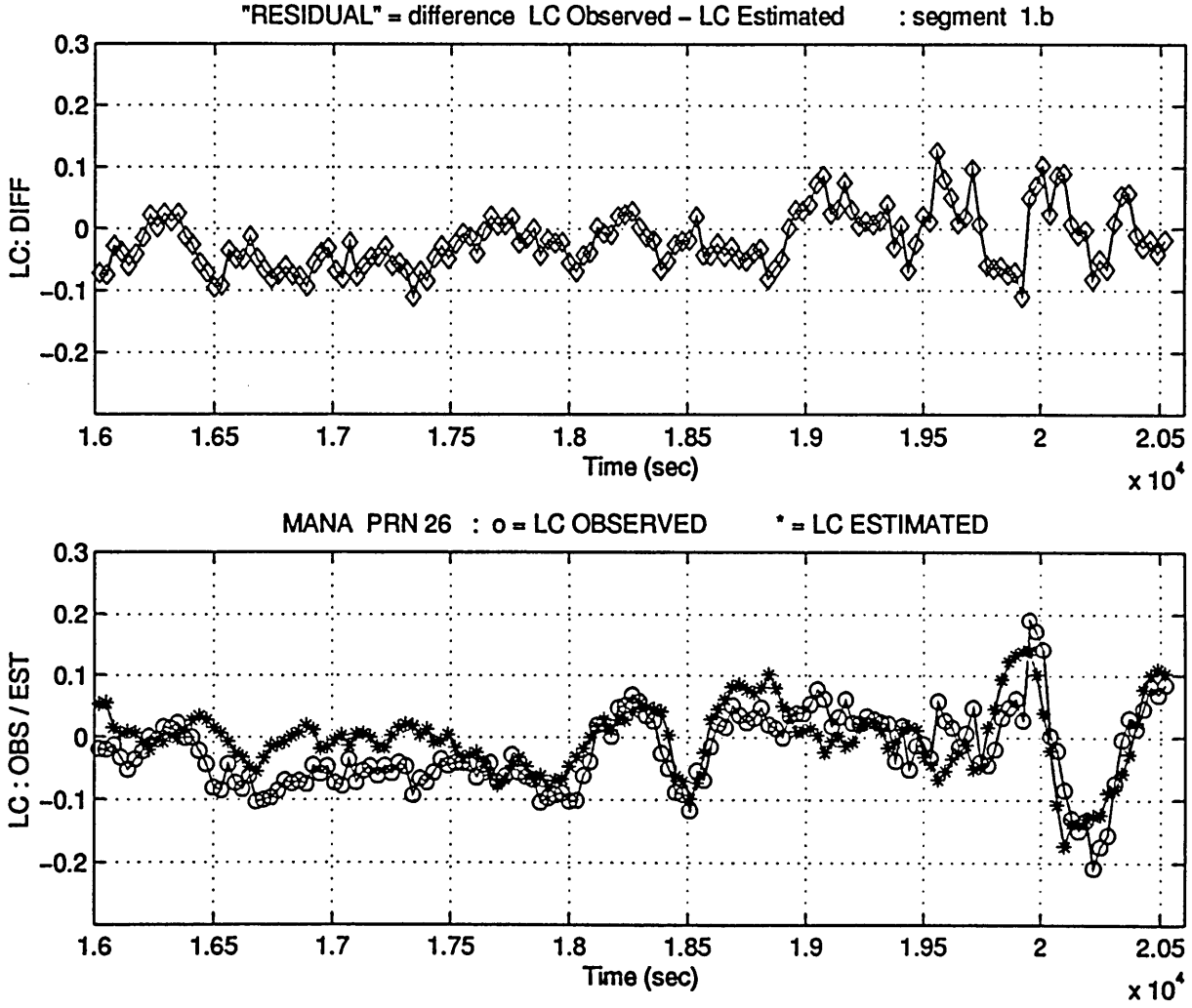

Fig. A.4.6.a) : MANA - PRN 26 (10 6 1995) - [segment 1.b]
Phase residual LC_DIFF, determined as the difference between LC_OBS and LC_EST.
Unit: [cycles]

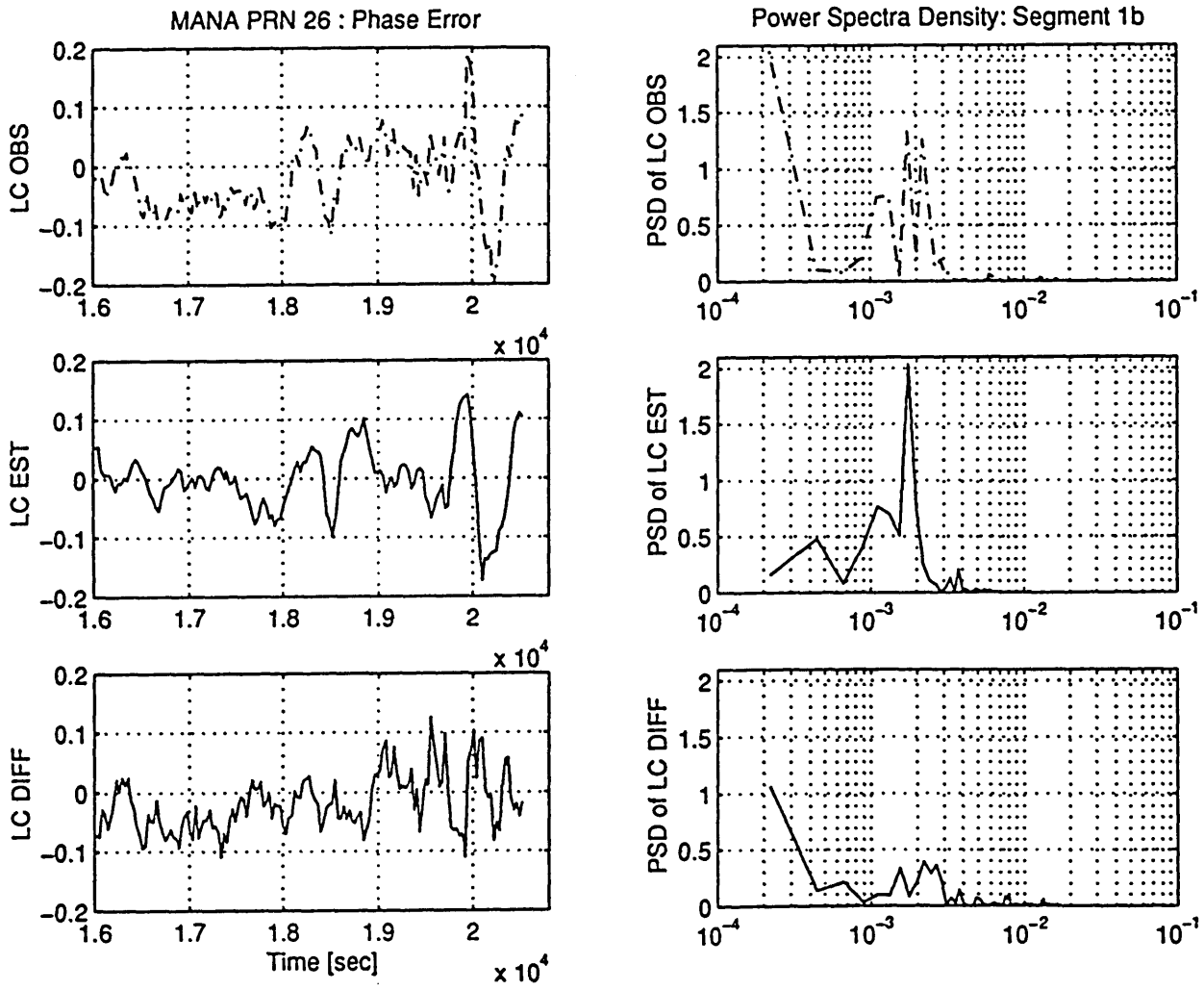

Fig. A.4.6.b) : MANA - PRN 26 (10 6 1995) - [segment 1.b]
PSD of LC_OBS, LC_EST and LC_DIFF.
Unit: [cycles]^2

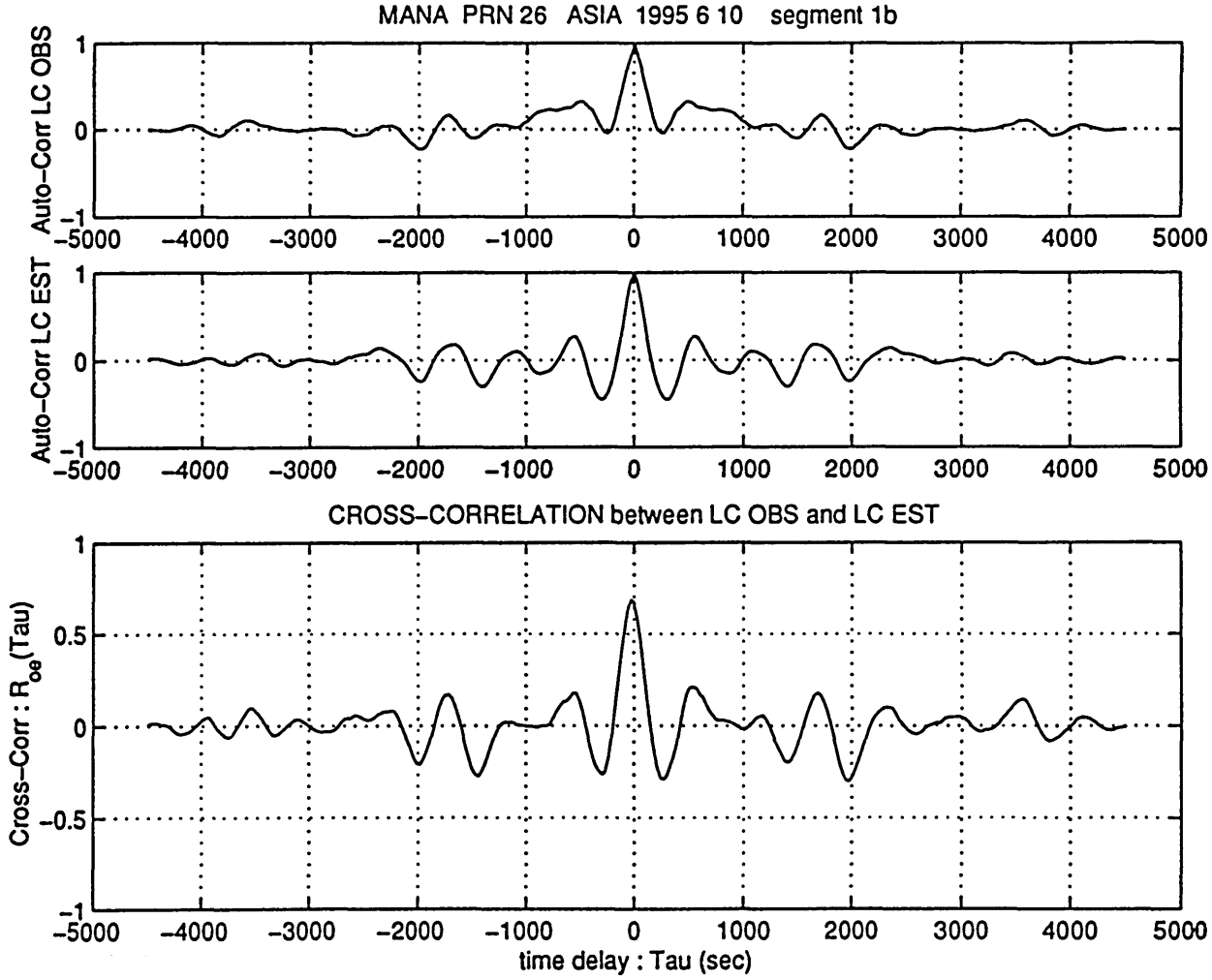

Fig. A.4.6.c) : MANA - PRN 26 (10 6 1995) - [segment 1.b]
Auto Correlation of LC_OBS (R_{oo}) and LC_EST (R_{ee}).
Cross Correlation between them (R_{oe})
Unit: [cycles]^2

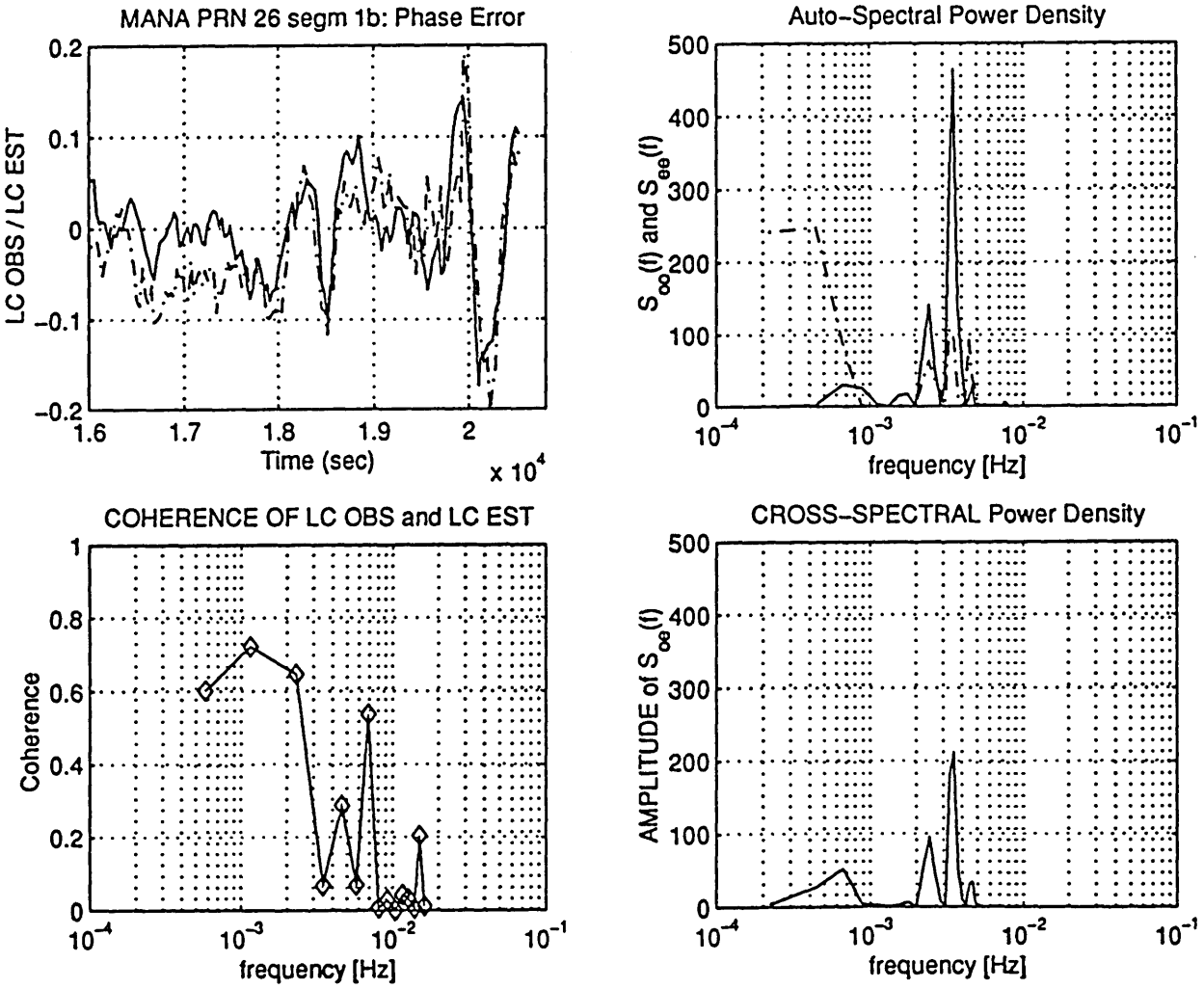

Fig. A.4.6.d) : MANA - PRN 26 (10 6 1995) - [segment 1.b]
Auto Spectral Power Density of LC_OBS (S_{oo}) and of LC_EST (S_{ee}). Cross PSD between them (S_{oe})
Unit: [cycles]^2
Coherence function of LC_OBS and LC_EST.

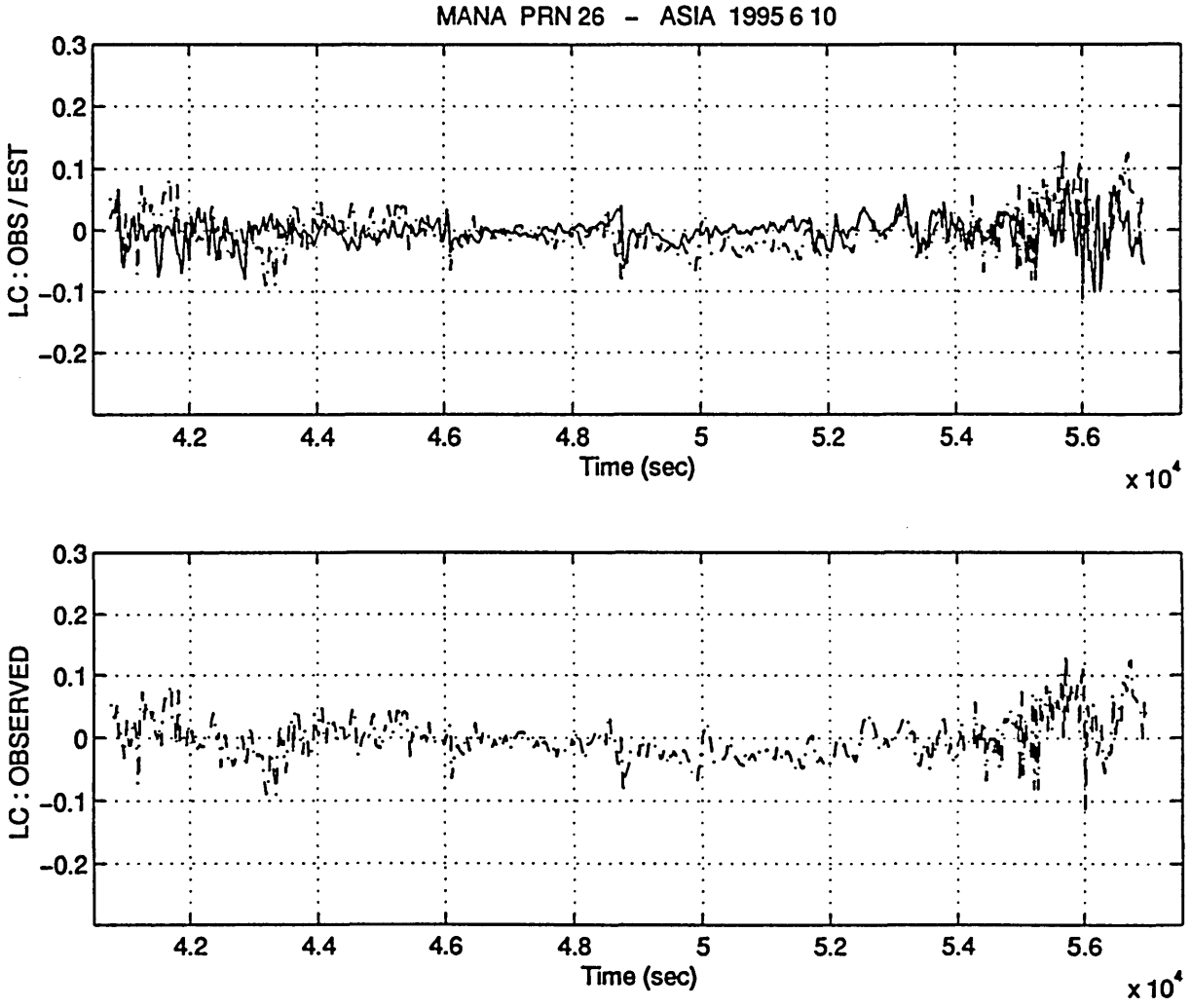

Fig. A.4.7 : Station: MANA - Satellite: PRN 26
Data acquisition date 10 6 1995
LC_OBS and LC_EST compared for t=4.1 - 5.8 10^3 sec
Unit: [cycles]

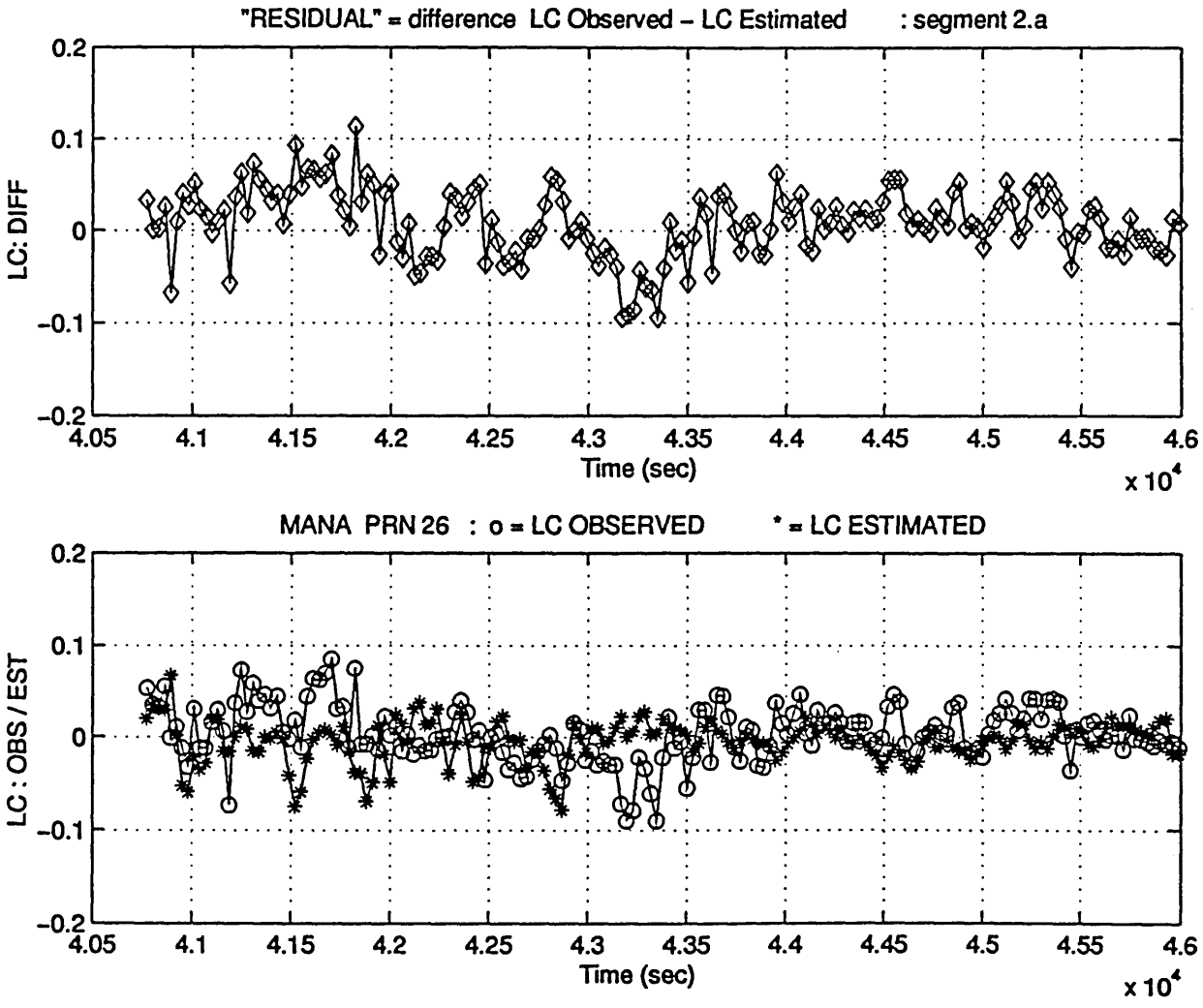

Fig. A.4.8.a) : MANA - PRN 26 (10 6 1995) - [segment 2.a]
Phase residual LC_DIFF, determined as the difference between LC_OBS and LC_EST.
Unit: [cycles]

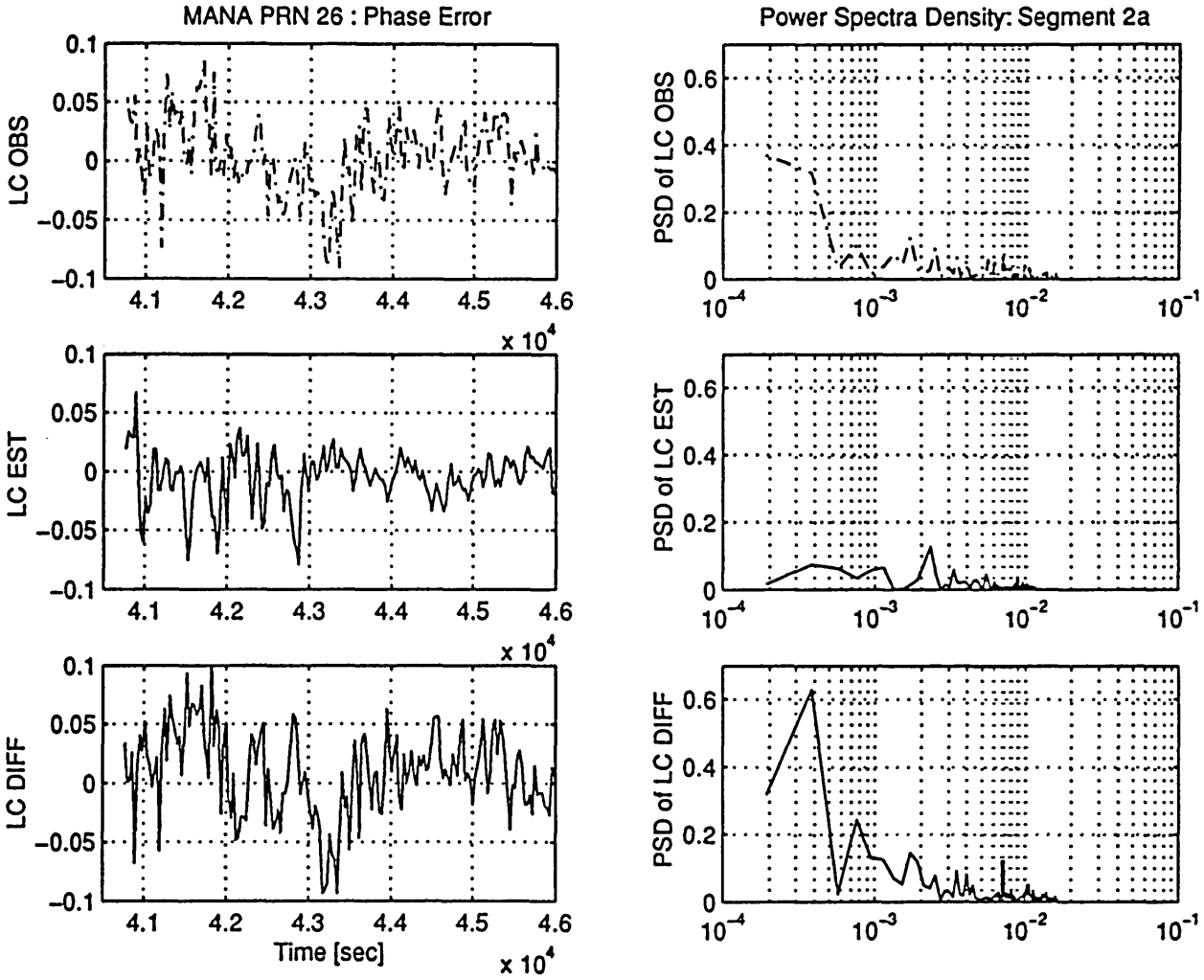

Fig. A.4.8.b) : MANA - PRN 26 (10 6 1995) - [segment 2.a]
PSD of LC_OBS, LC_EST and LC_DIFF.
Unit: [cycles]^2

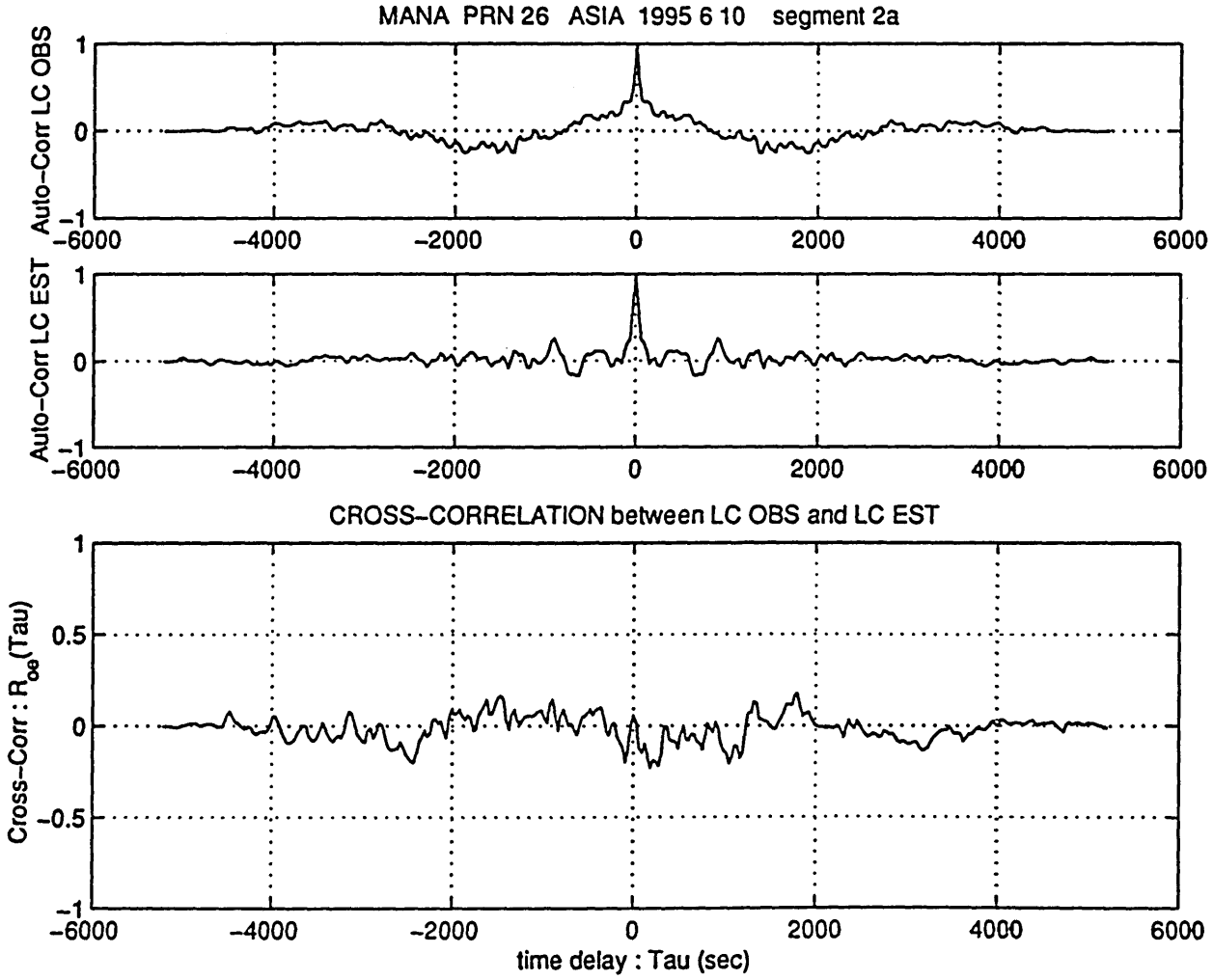

Fig. A.4.8.c) : MANA - PRN 26 (10 6 1995) - [segment 2.a]
Auto Correlation of LC_OBS (R_{oo}) and LC_EST (R_{ee}).
Cross Correlation between them (R_{oe})
Unit: [cycles]^2

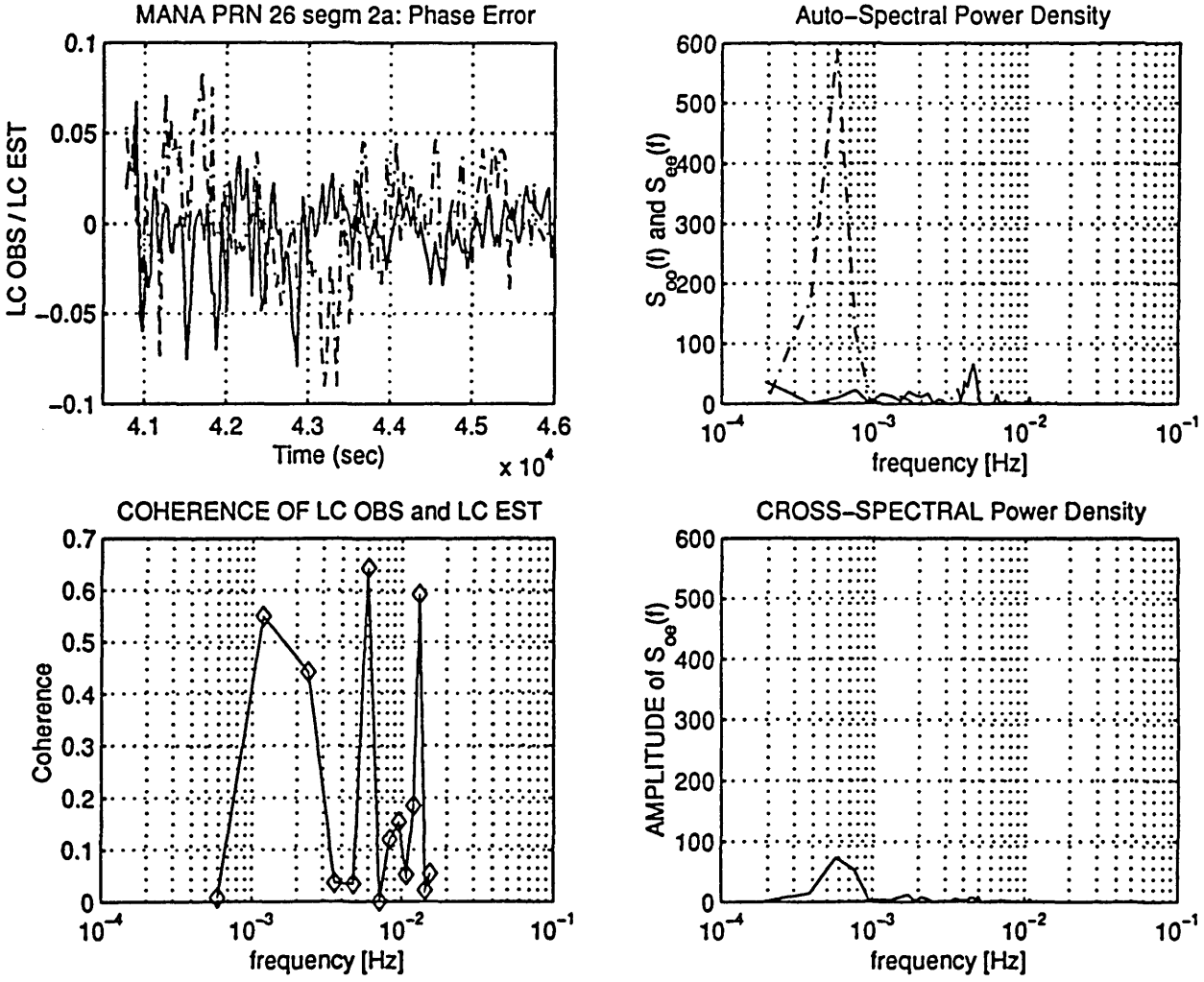

Fig. A.4.8.d) : MANA - PRN 26 (10 6 1995) - [segment 2.a]
Auto Spectral Power Density of LC_OBS (S_{oo}) and of LC_EST (S_{ee}). CrossPSD between them (S_{oe})
Unit: [cycles]^2
Coherence function of LC_OBS and LC_EST.

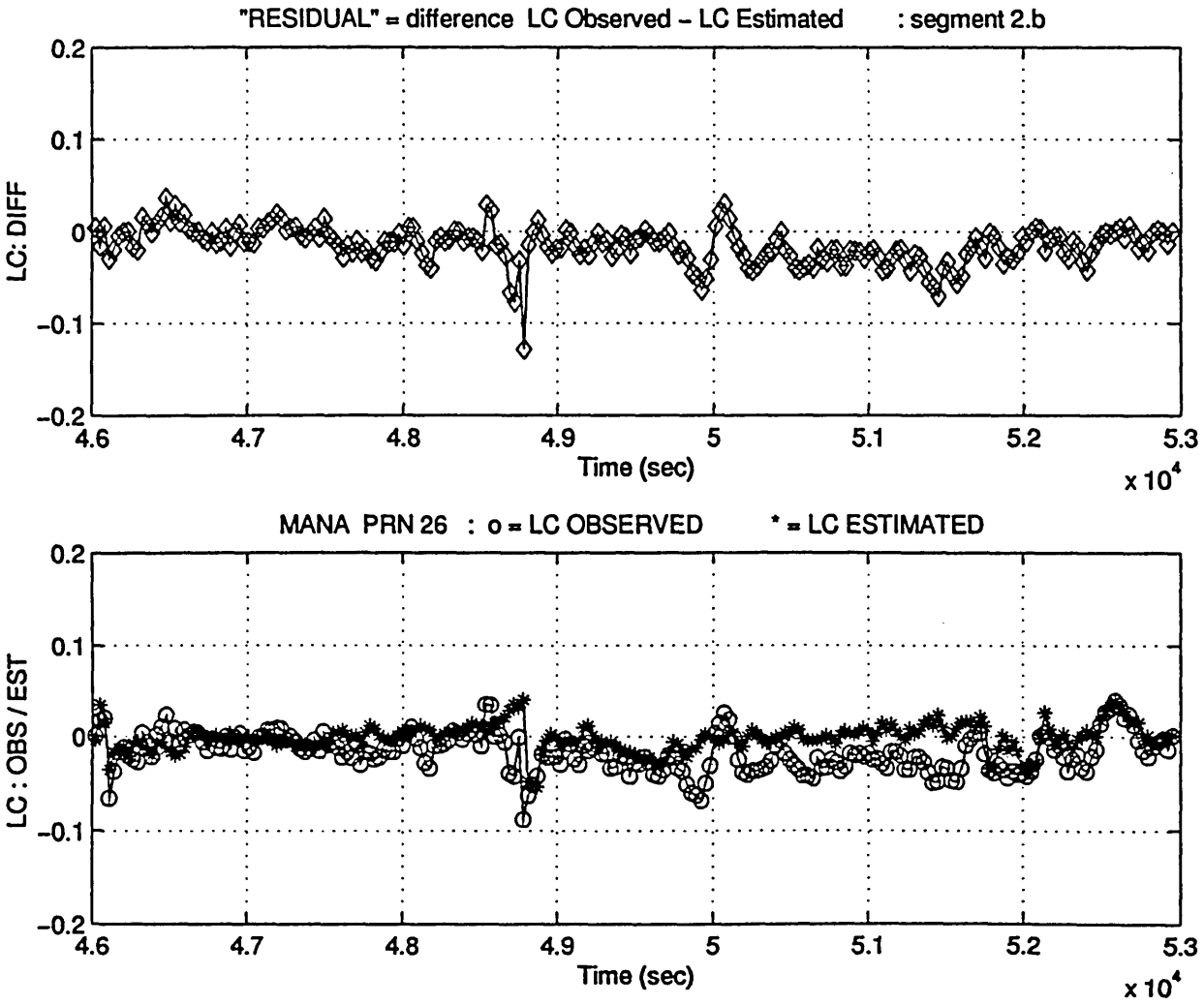

Fig. A.4.9.a) : MANA - PRN 26 (10 6 1995) - [segment 2.b]
Phase residual LC_DIFF, determined as the difference between LC_OBS and LC_EST.
Unit: [cycles]

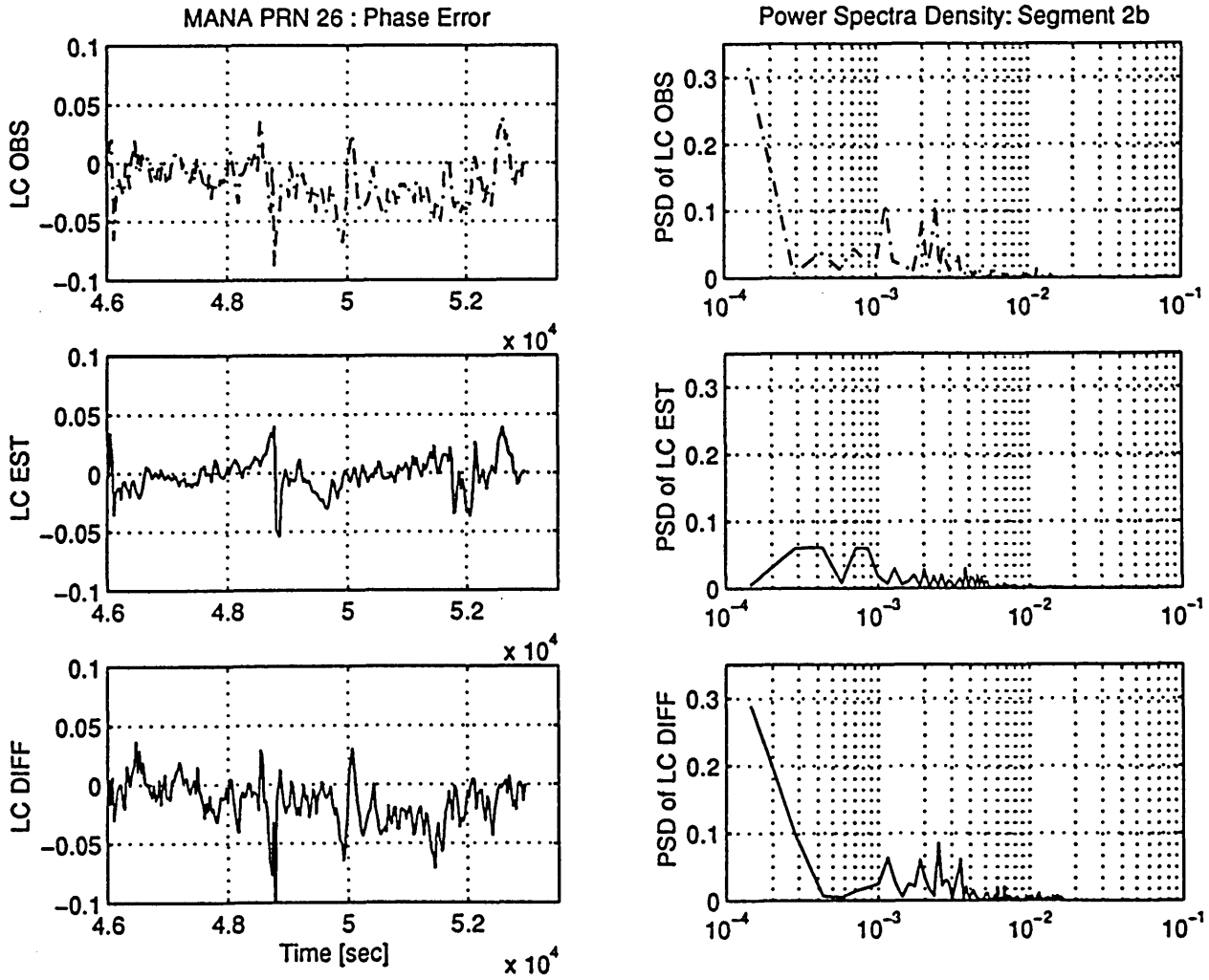

Fig. A.4.9.b) : MANA - PRN 26 (10 6 1995) - [segment 2.b]
PSD of LC_OBS, LC_EST and LC_DIFF.
Unit: [cycles]^2

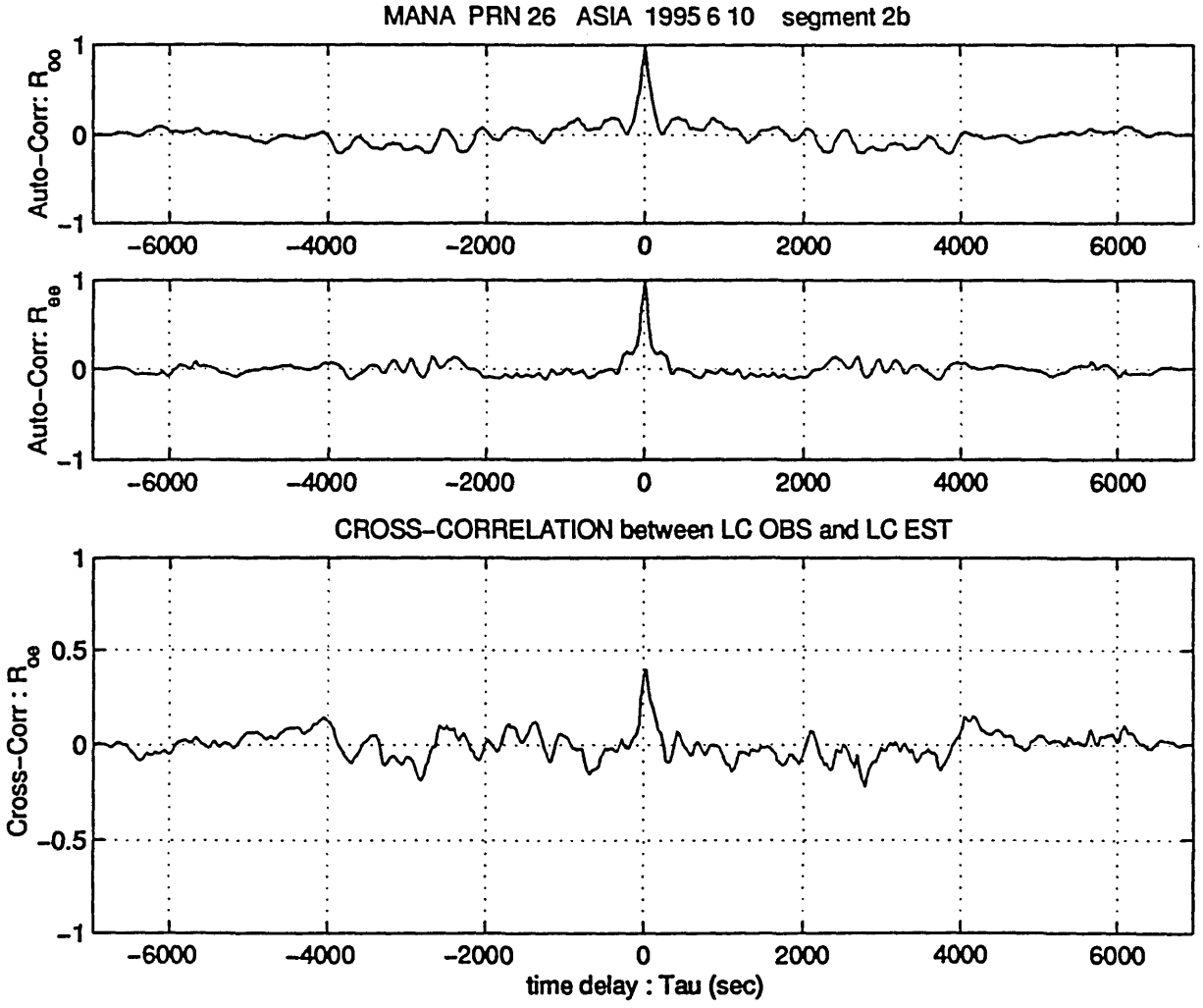

Fig. A.4.9.c) : MANA - PRN 26 (10 6 1995) - [segment 2.b]
Auto Correlation of LC_OBS (R_{oo}) and LC_EST (R_{ee}).
Cross Correlation between them (R_{oe})
Unit: [cycles]^2

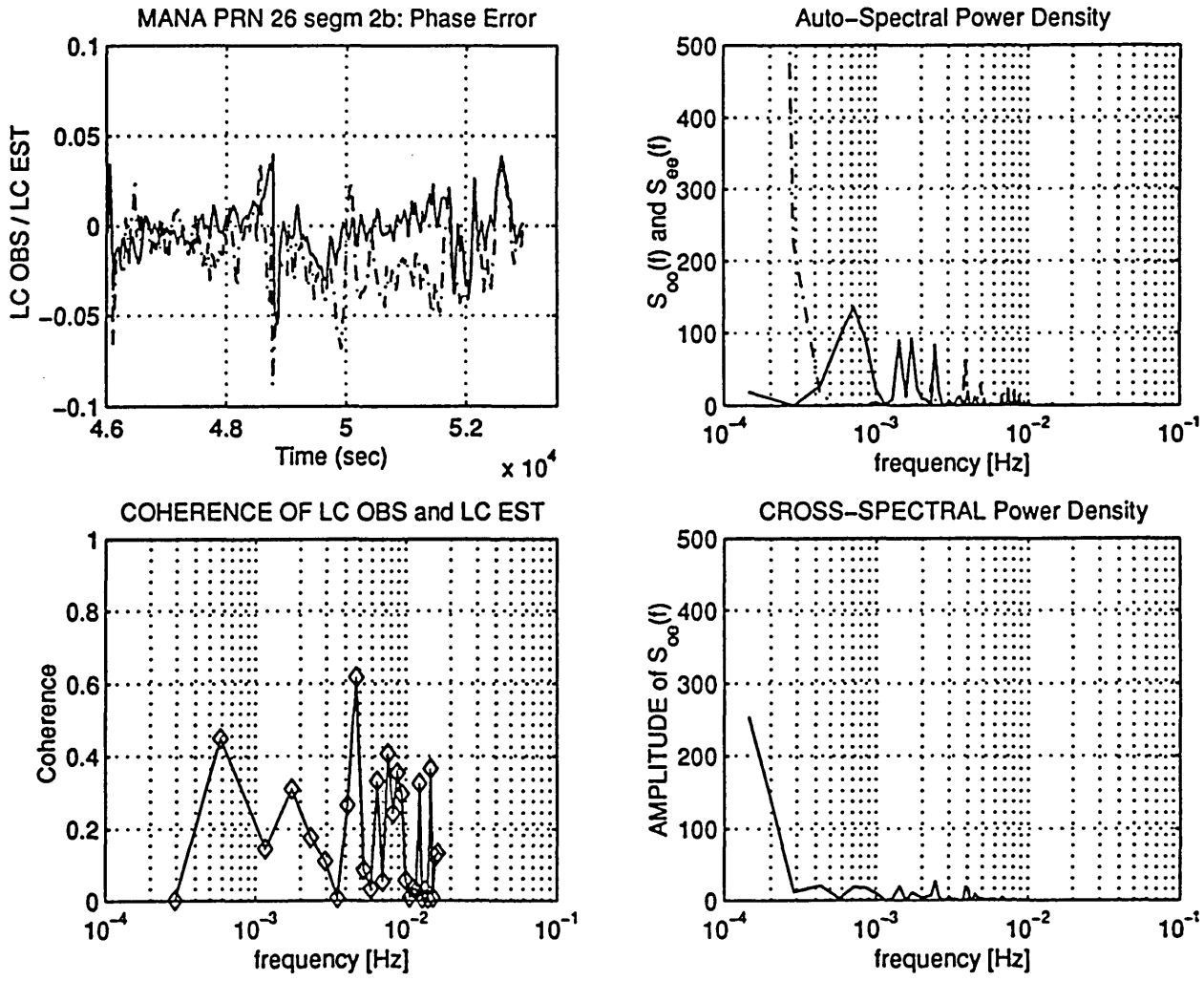

Fig. A.4.9.d) : MANA - PRN 26 (10 6 1995) - [segment 2.b]
Auto Spectral Power Density of LC_OBS (S_{oo}) and of LC_EST (S_{ee}). Cross PSD between them (S_{oe})
Unit: [cycles]^2
Coherence function of LC_OBS and LC_EST.

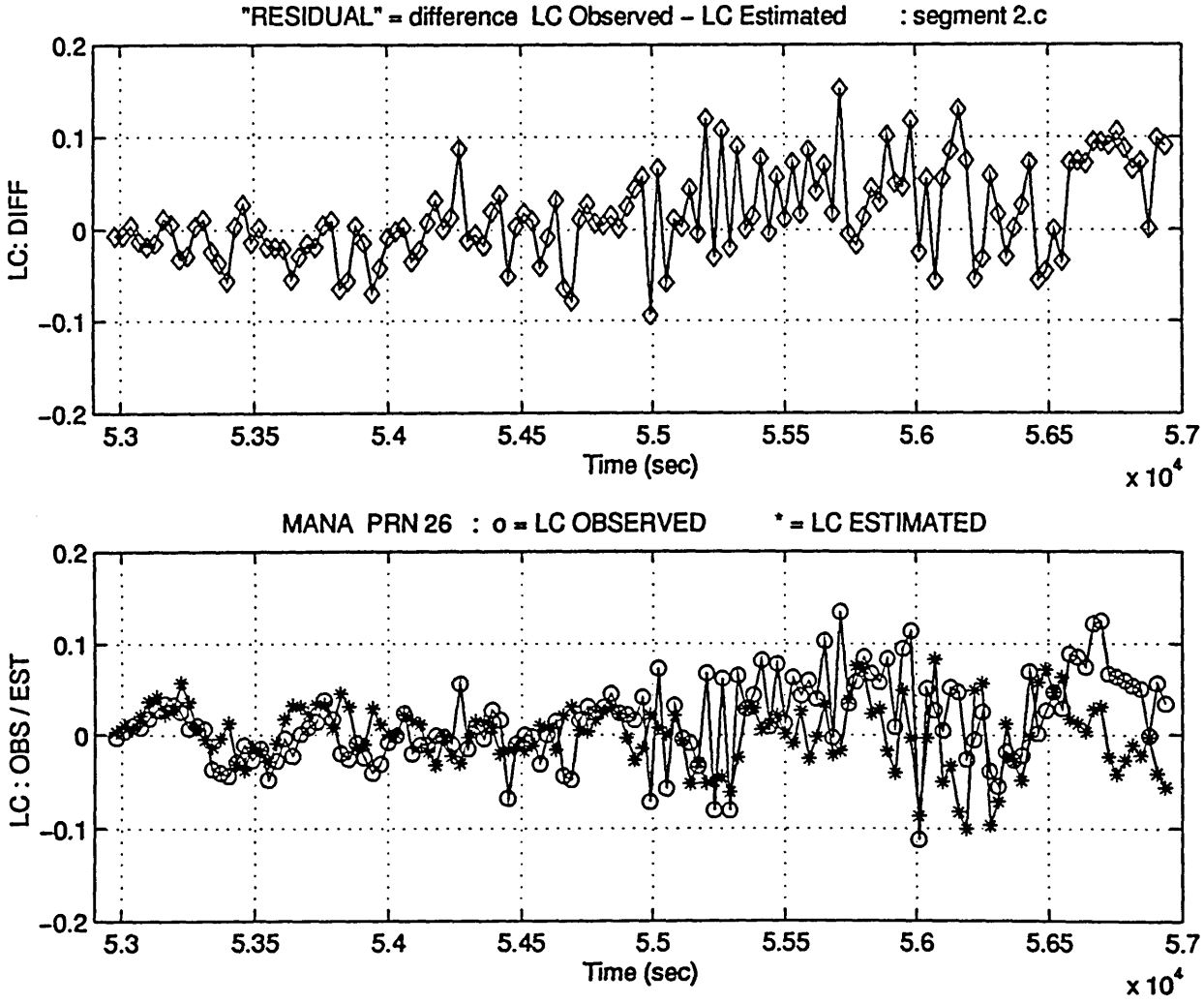

Fig. A.4.10.a) : MANA - PRN 26 (10 6 1995) - [segment 2.c]
Phase residual LC_DIFF, determined as the difference between LC_OBS and LC_EST.
Unit: [cycles]

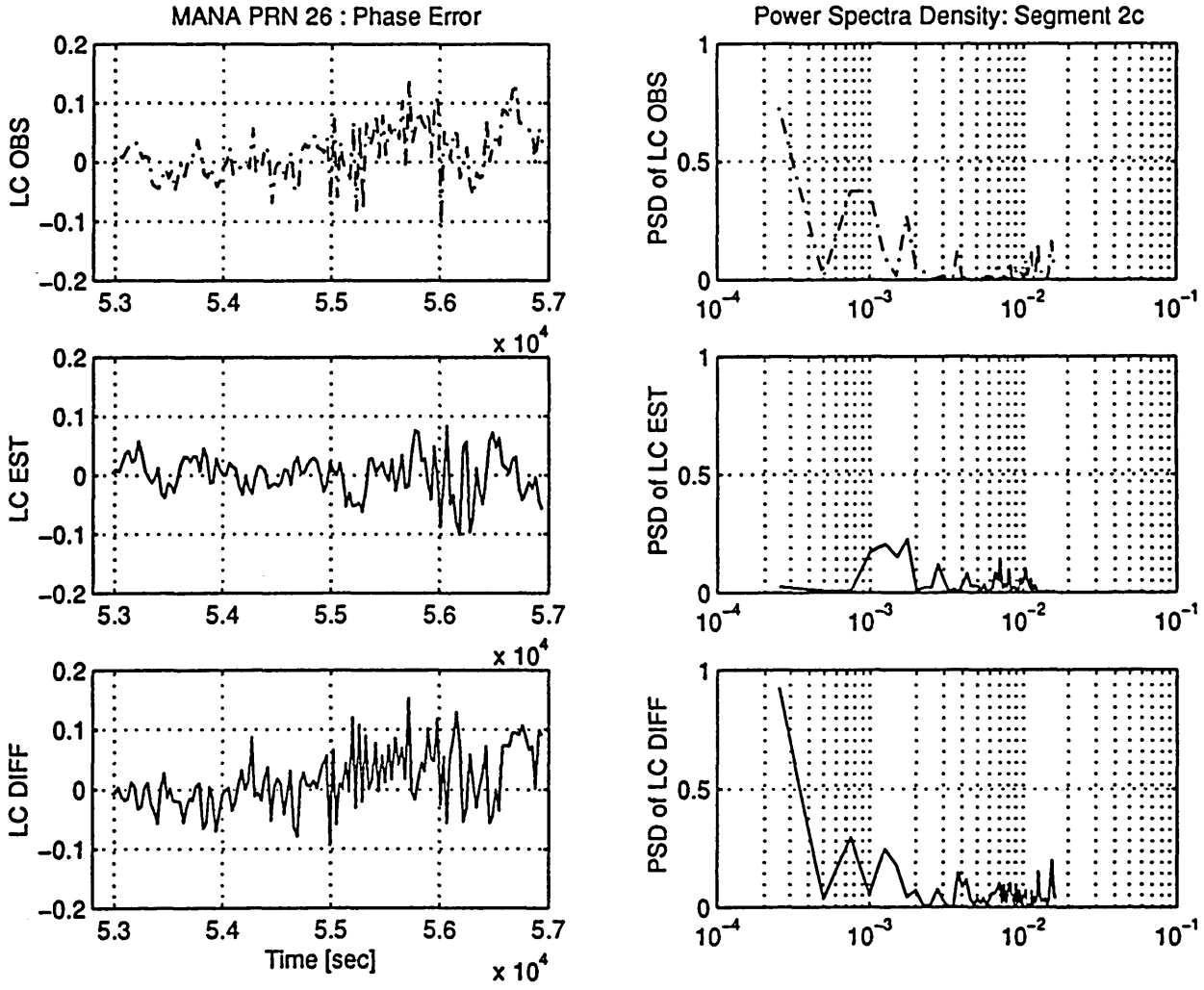

Fig. A.4.10.b) : MANA - PRN 26 (10 6 1995) - [segment 2.c]
PSD of LC_OBS, LC_EST and LC_DIFF.
Unit: [cycles]^2

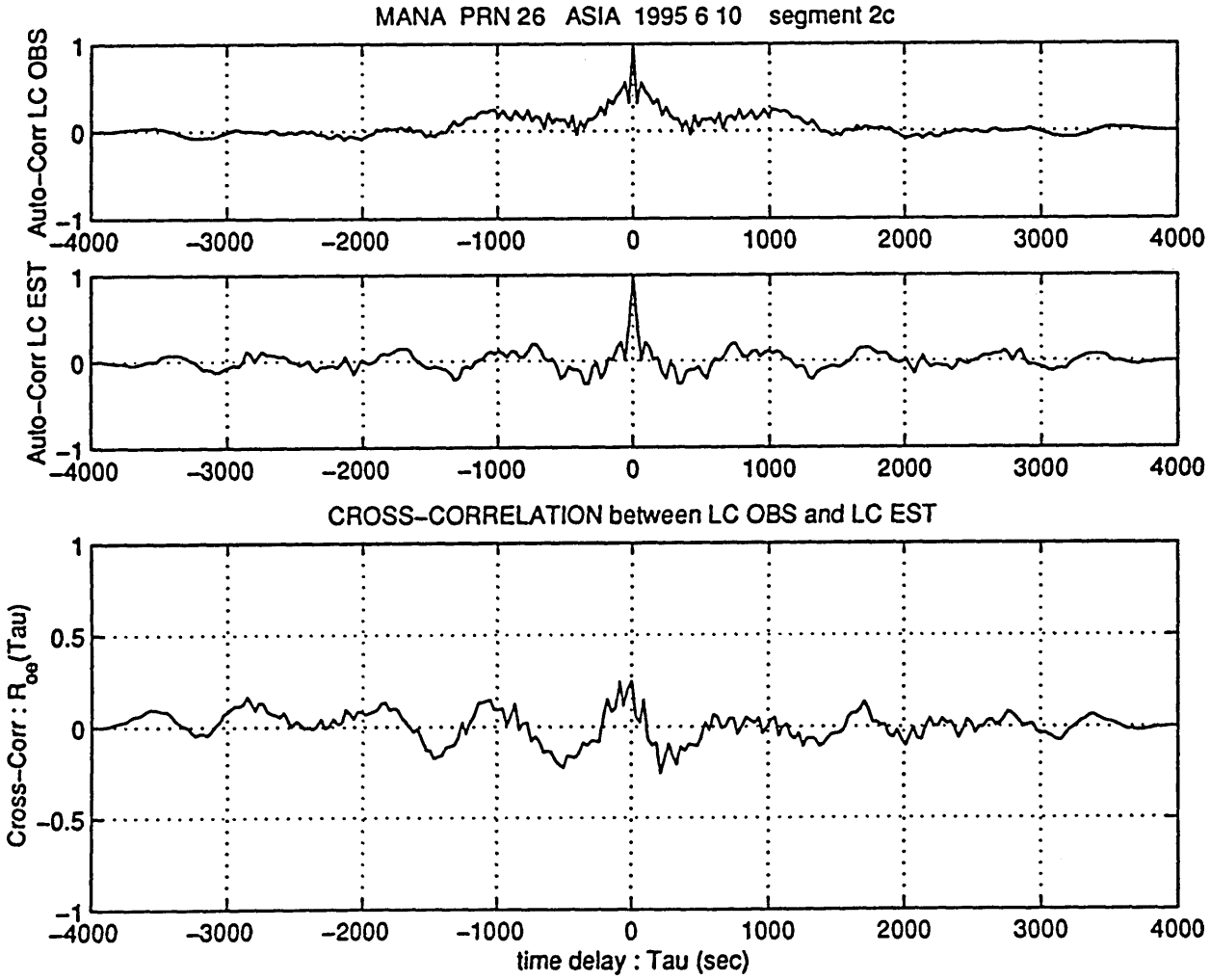

Fig. A.4.10.c) : MANA - PRN 26 (10 6 1995) - [segment 2.c]
Auto Correlation of LC_OBS (R_{oo}) and LC_EST (R_{ee}).
Cross Correlation between them (R_{oe})
Unit: [cycles]^2

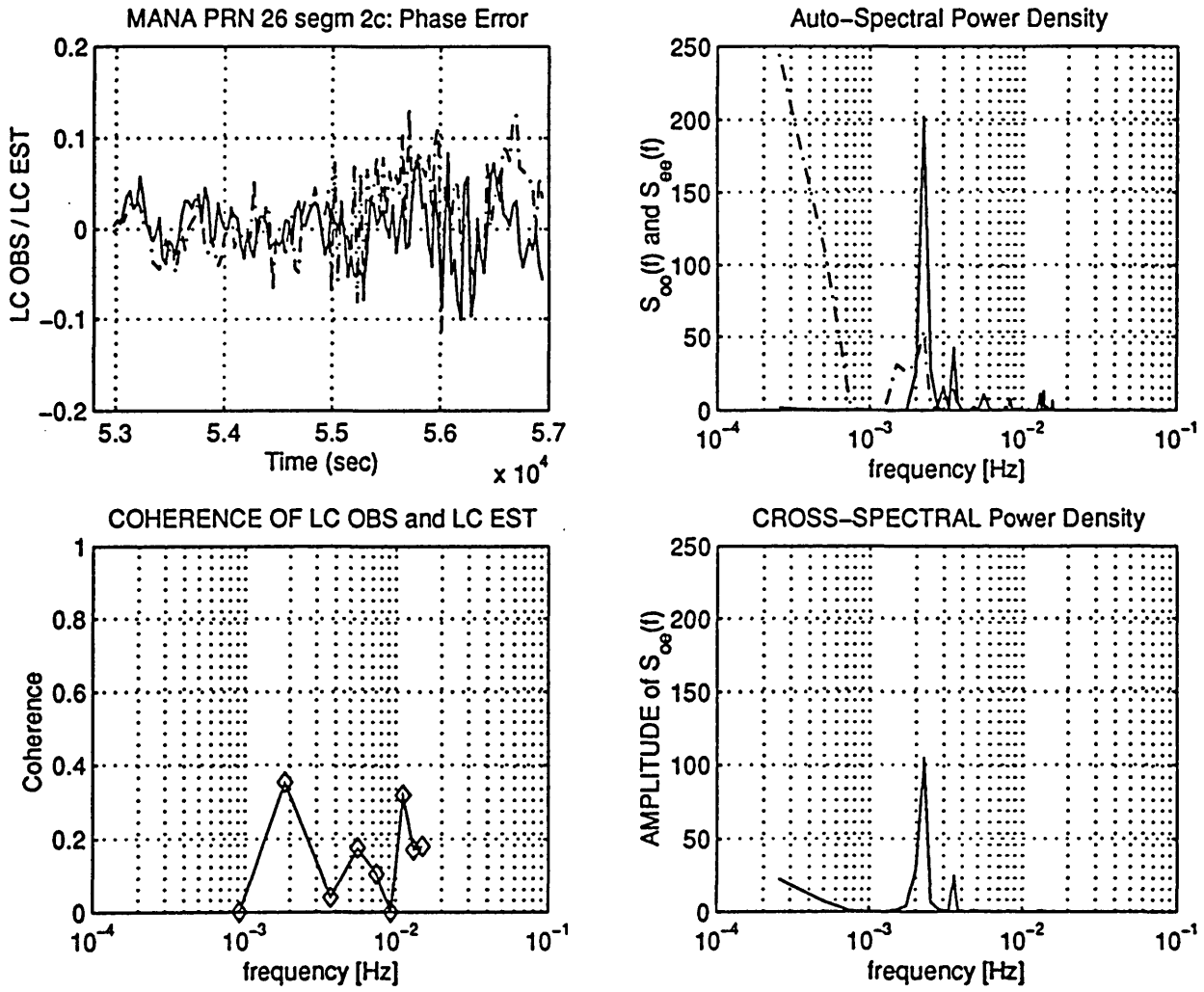

Fig. A.4.10.d) : MANA - PRN 26 (10 6 1995) - [segment 2.c]
Auto Spectral Power Density of LC_OBS (S_{oo}) and of LC_EST (S_{ee}). Cross PSD between them (S_{oe})
Unit: [cycles]^2
Coherence function of LC_OBS and LC_EST.

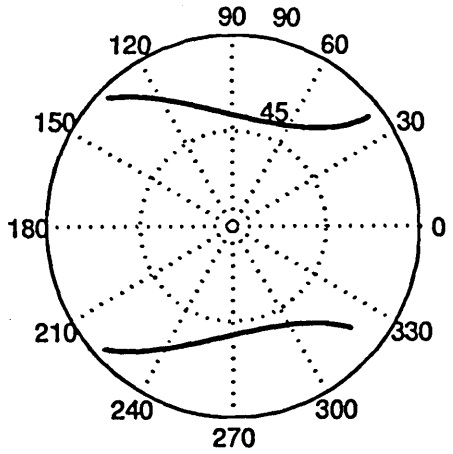

GPS DATA: receiver location: CENTRAL ASIA acquisition date: 10 6 1995

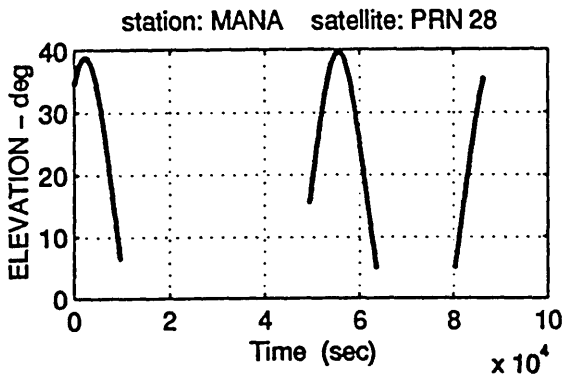

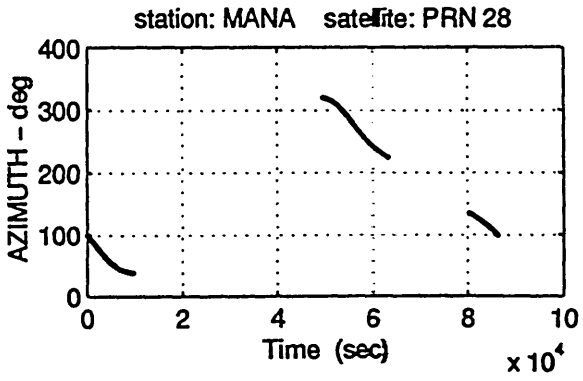

Fig. A.5.1 : Satellite visibility chart for PRN 28 (skymap). Elevation and azimuth of PRN 28 with respect to the station MANA

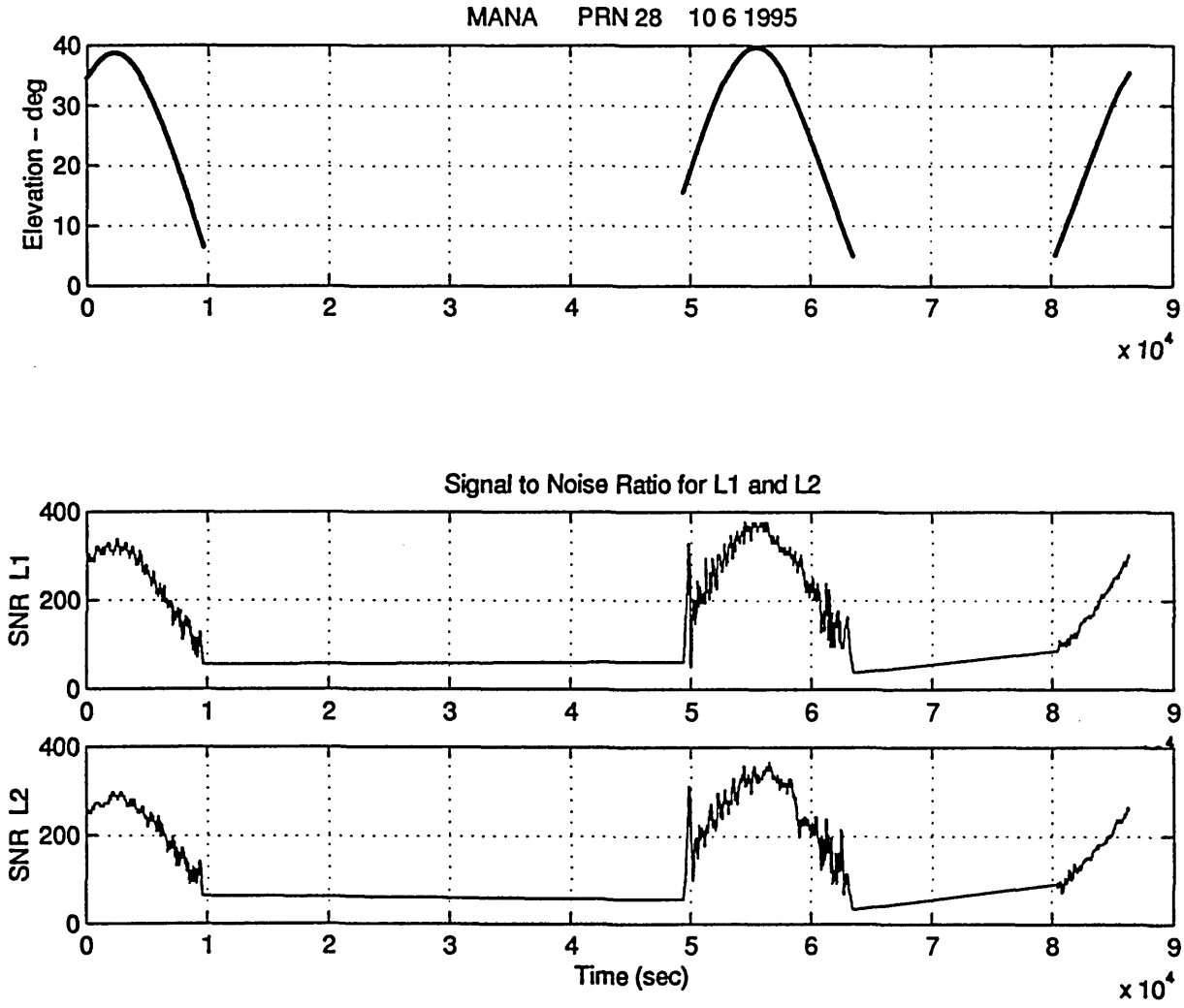

Fig. A.5.2 : Station: MANA - Satellite: PRN 28
Data acquisition date 10 6 1995
Signal-to-Noise-Ratio (SNR) for L_1 and L_2.

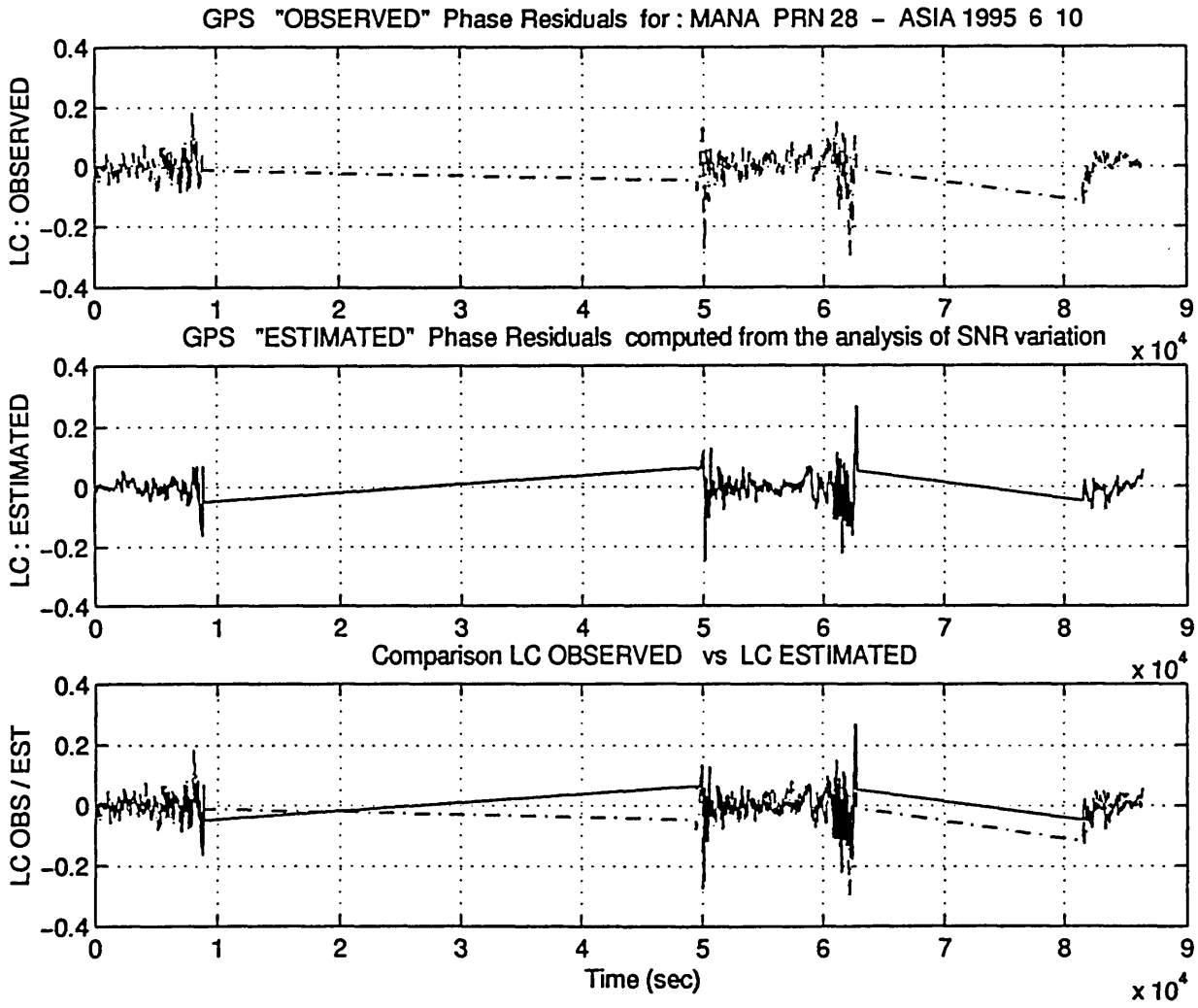

Fig. A.5.3 : Station: MANA - Satellite: PRN 28
Data acquisition date 10 6 1995
The observed phase residual (LC_OBS) is compared with the multipath phase error estimated from the SNR (LC_EST).
Unit: [cycles]

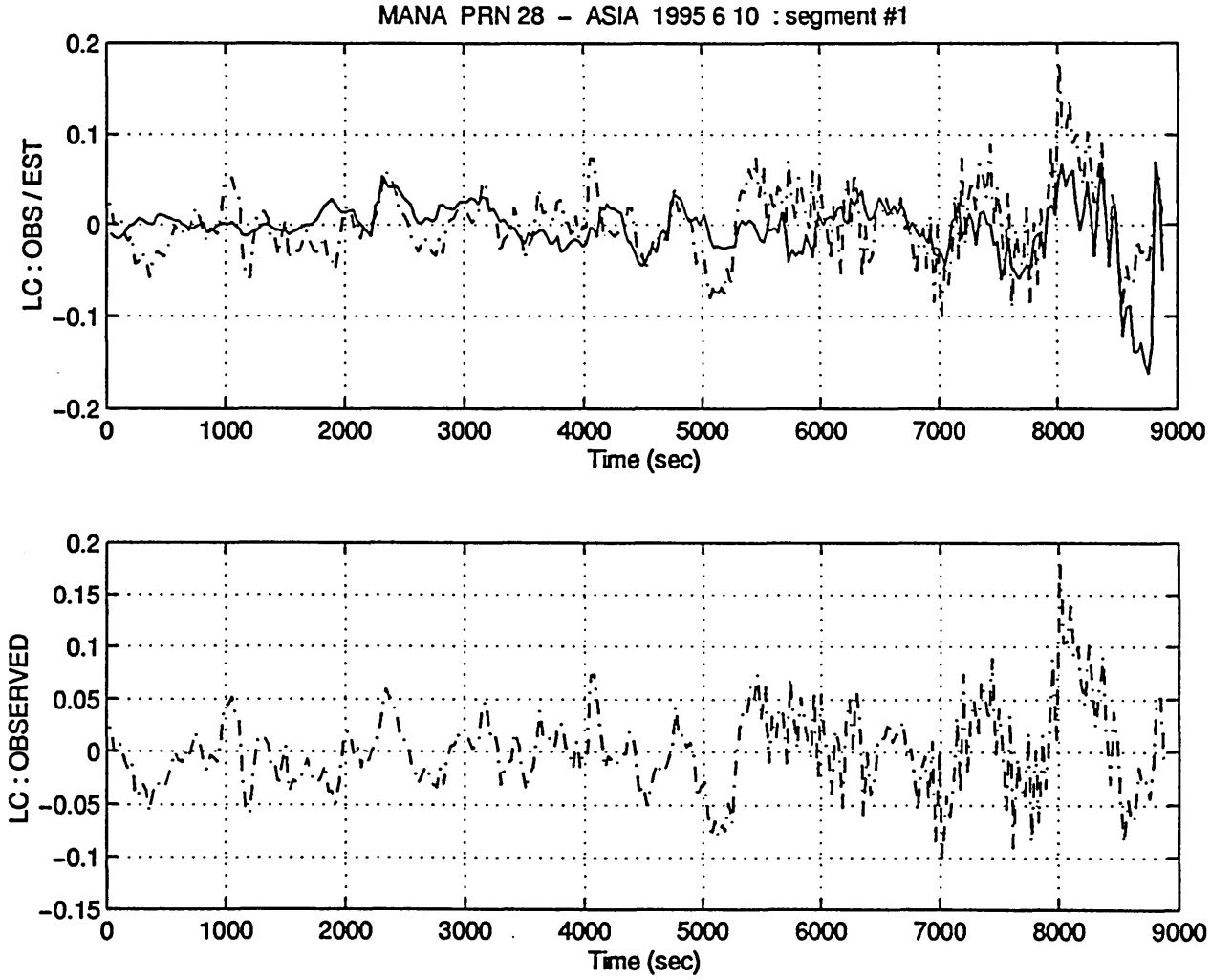

Fig. A.5.4 : Station: MANA - Satellite: PRN 28
Data acquisition date 10 6 1995
LC_OBS and LC_EST compared for t=0.0 - 0.9 10^4 sec
Unit: [cycles]

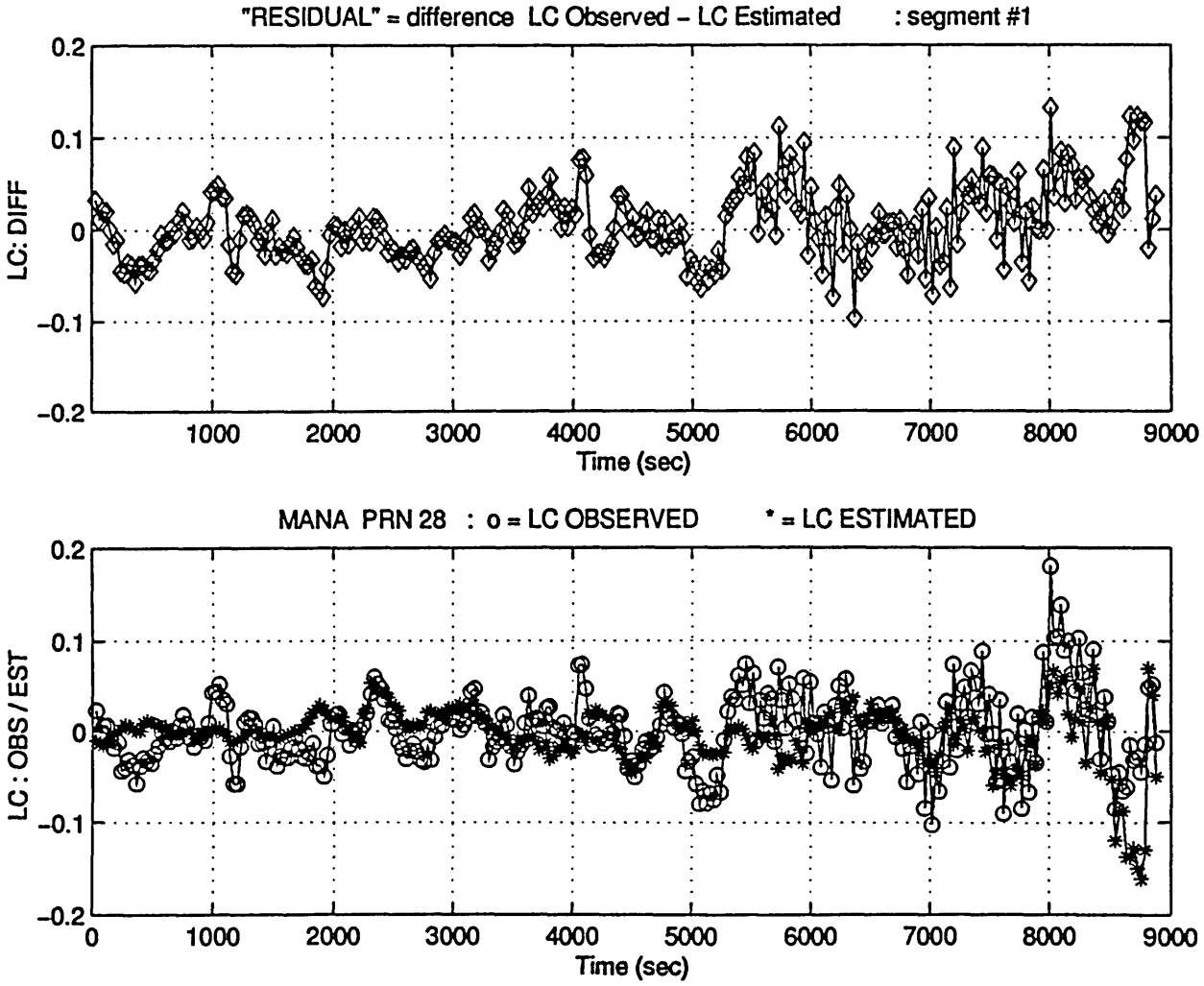

Fig. A.5.5 : MANA - PRN 28 (10 6 1995) - [segment #1]
Phase residual LC_DIFF, determined as the difference between LC_OBS and LC_EST.
Unit: [cycles]

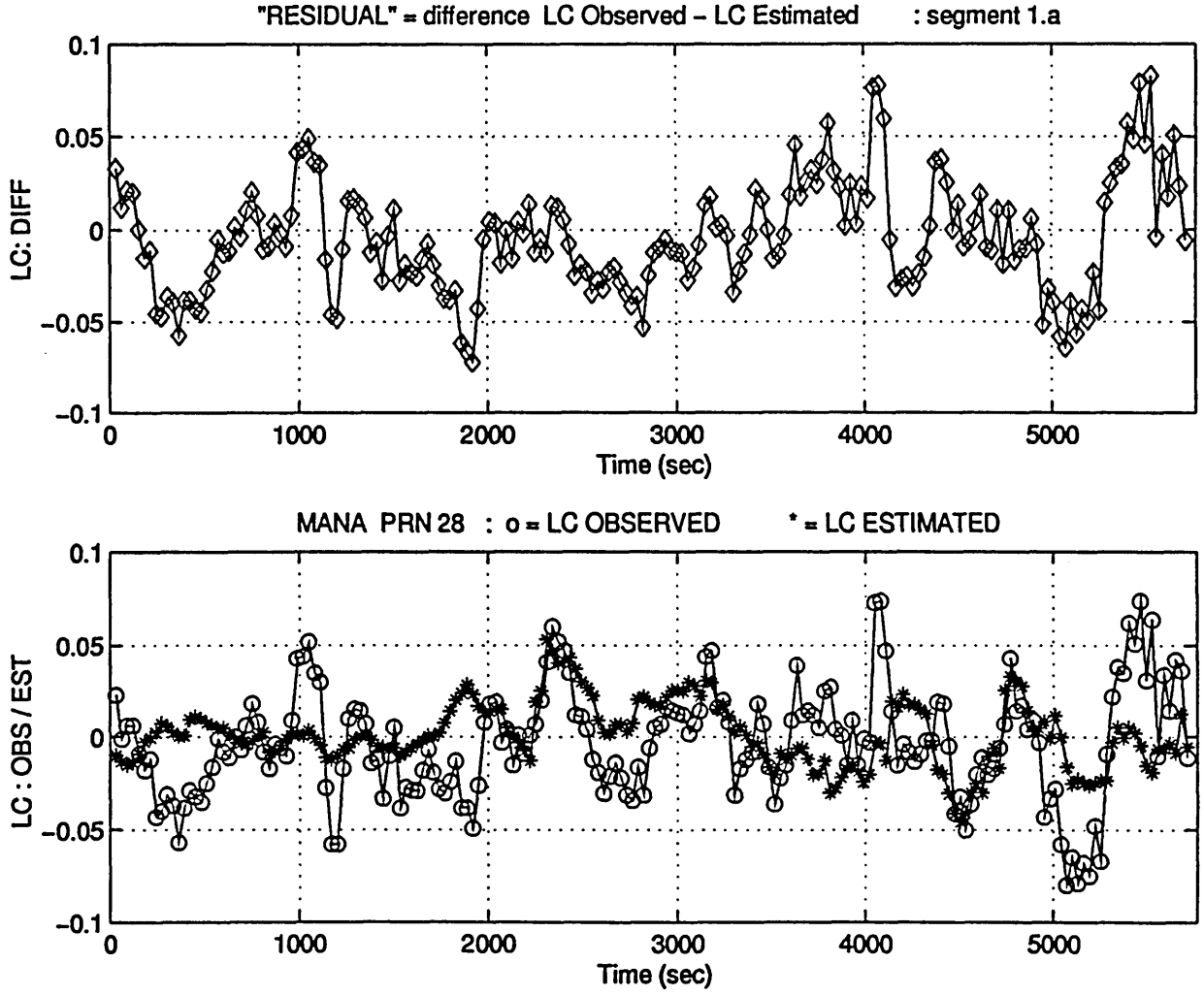

Fig. A.5.6.a) : MANA - PRN 28 (10 6 1995) - [segment 1.a]
Phase residual LC_DIFF, determined as the difference between LC_OBS and LC_EST.
Unit: [cycles]

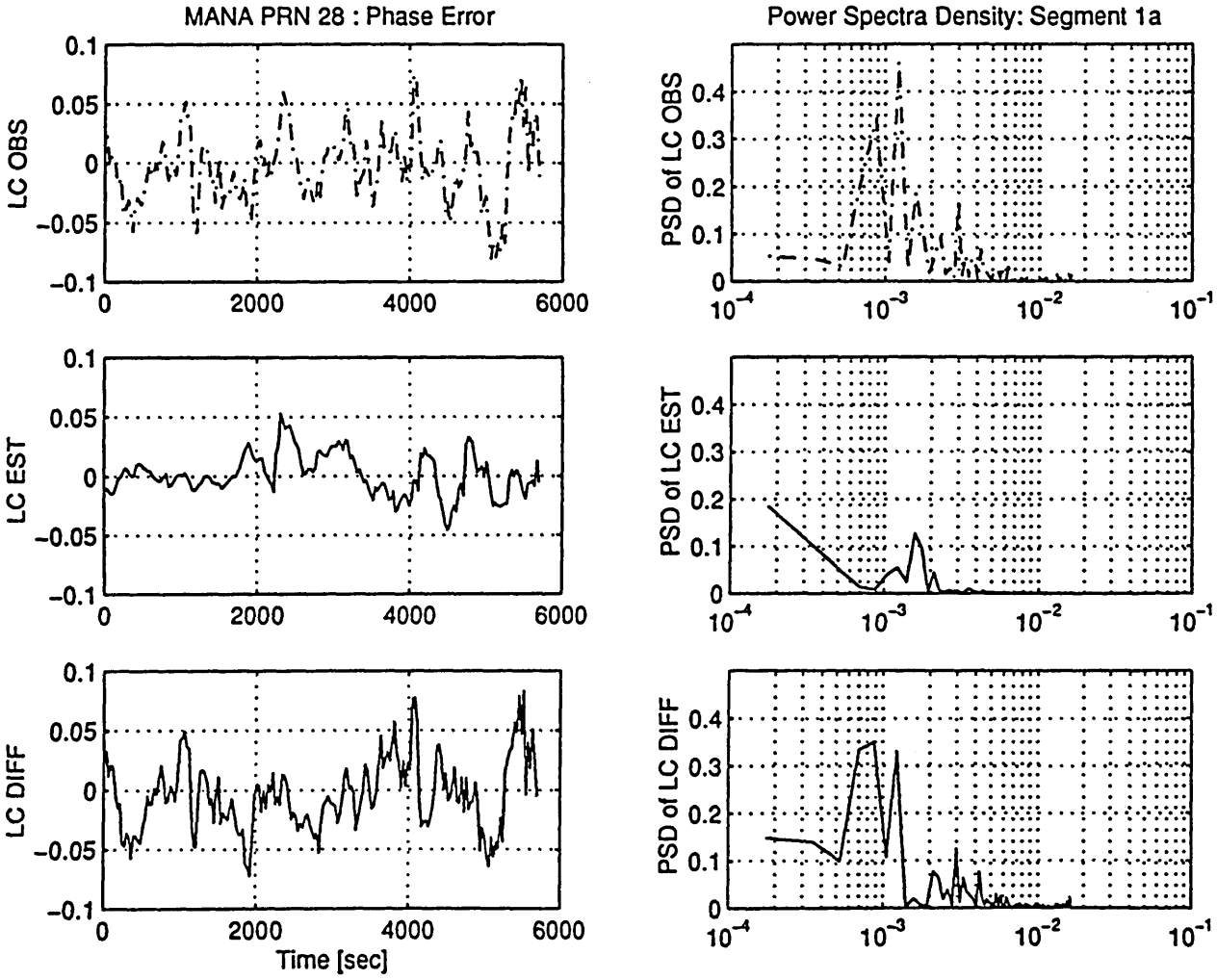

Fig. A.5.6.b) : MANA - PRN 28 (10 6 1995) - [segment 1.a]
PSD of LC_OBS, LC_EST and LC_DIFF.
Unit: [cycles]^2

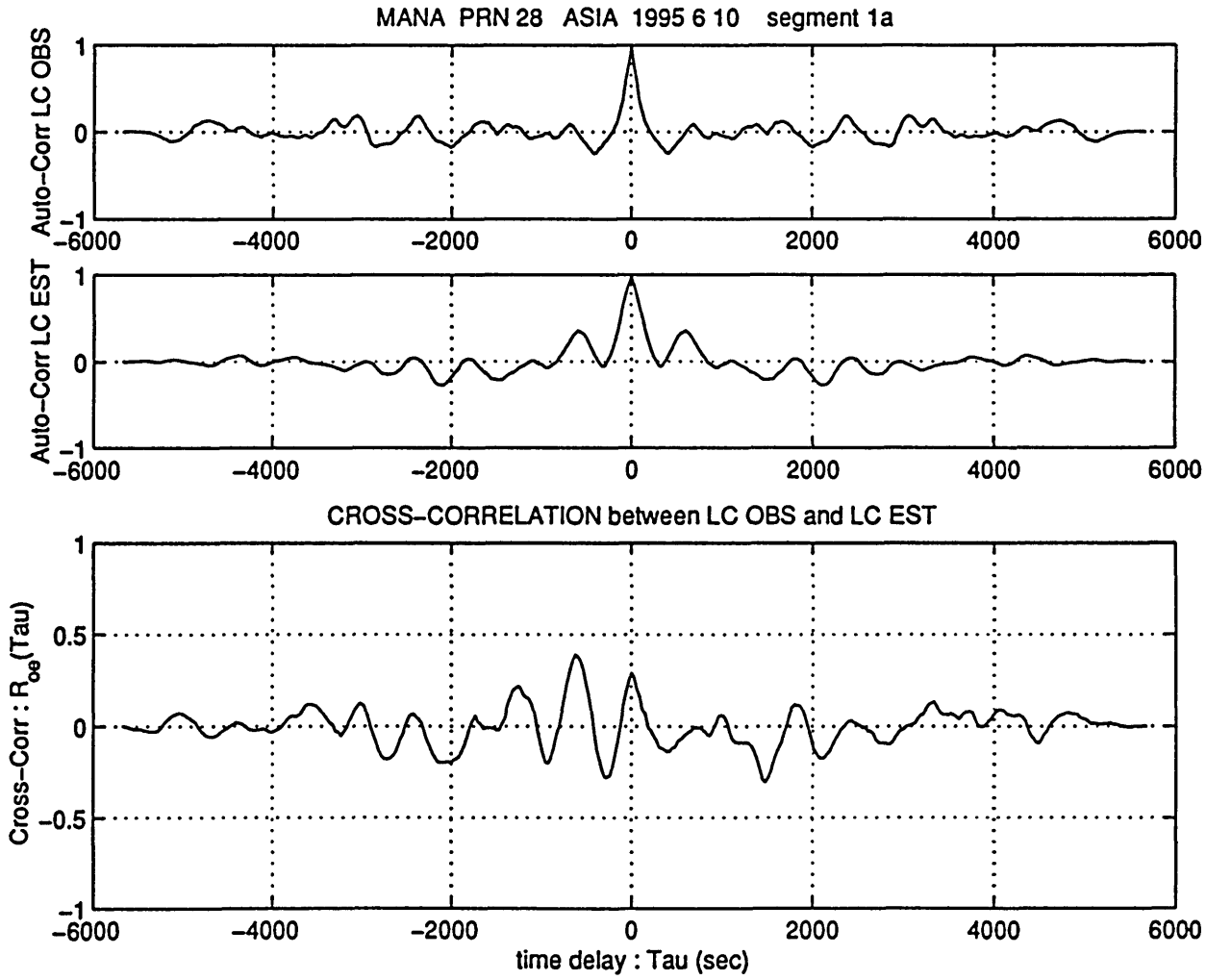

Fig. A.5.6.c) : MANA - PRN 28 (10 6 1995) - [segment 1.a]
Auto Correlation of LC_OBS (R_{oo}) and LC_EST (R_{ee}).
Cross Correlation between them (R_{oe})
Unit: [cycles]^2

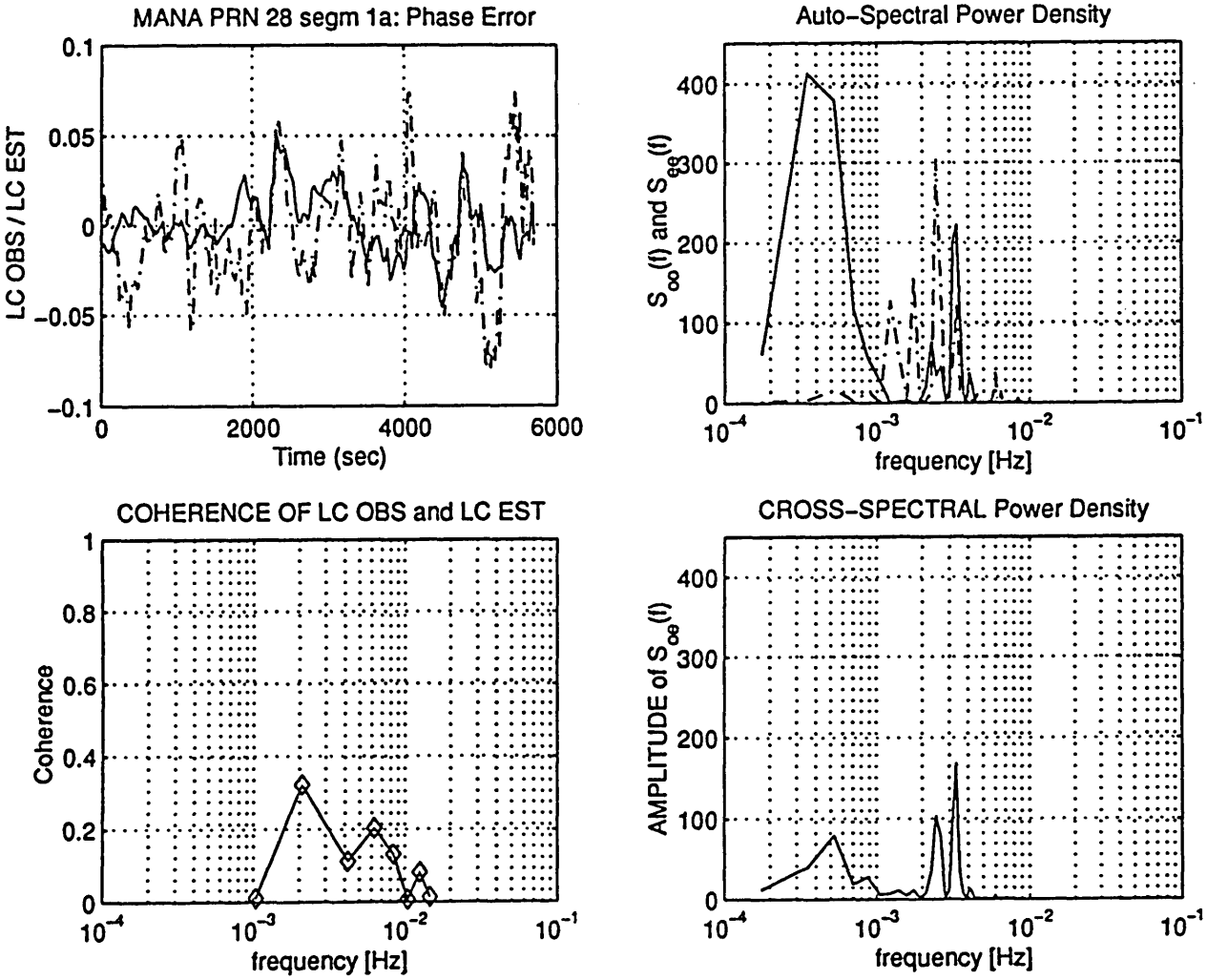

Fig. A.5.6.d) : MANA - PRN 28 (10 6 1995) - [segment 1.a]
Auto Spectral Power Density of LC_OBS (S_{oo}) and of LC_EST (S_{ee}). Cross PSD between them (S_{oe})
Unit: [cycles]^2
Coherence function of LC_OBS and LC_EST.

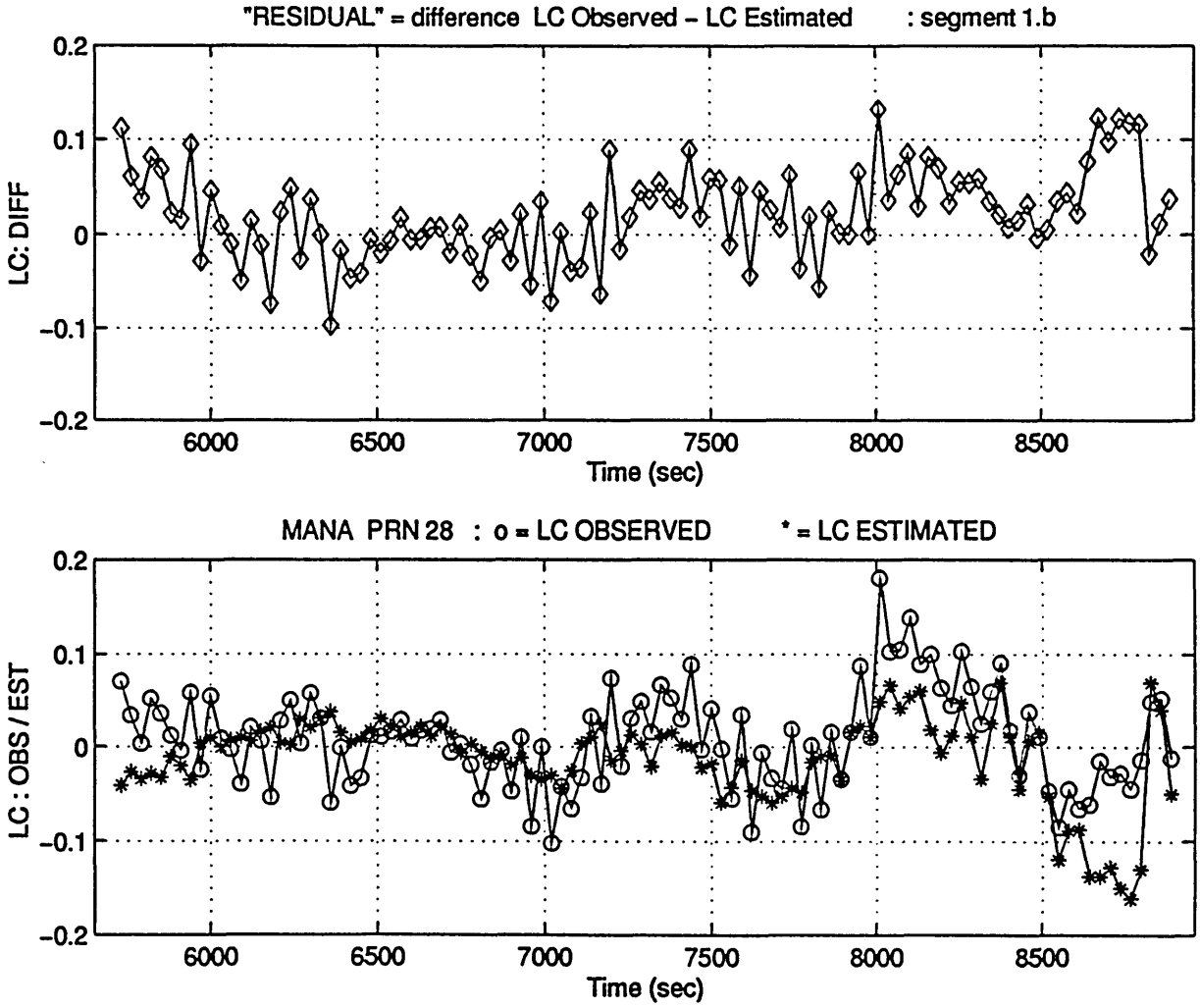

Fig. A.5.7.a) : MANA - PRN 28 (10 6 1995) - [segment 1.b]
Phase residual LC_DIFF, determined as the difference between LC_OBS and LC_EST.
Unit: [cycles]

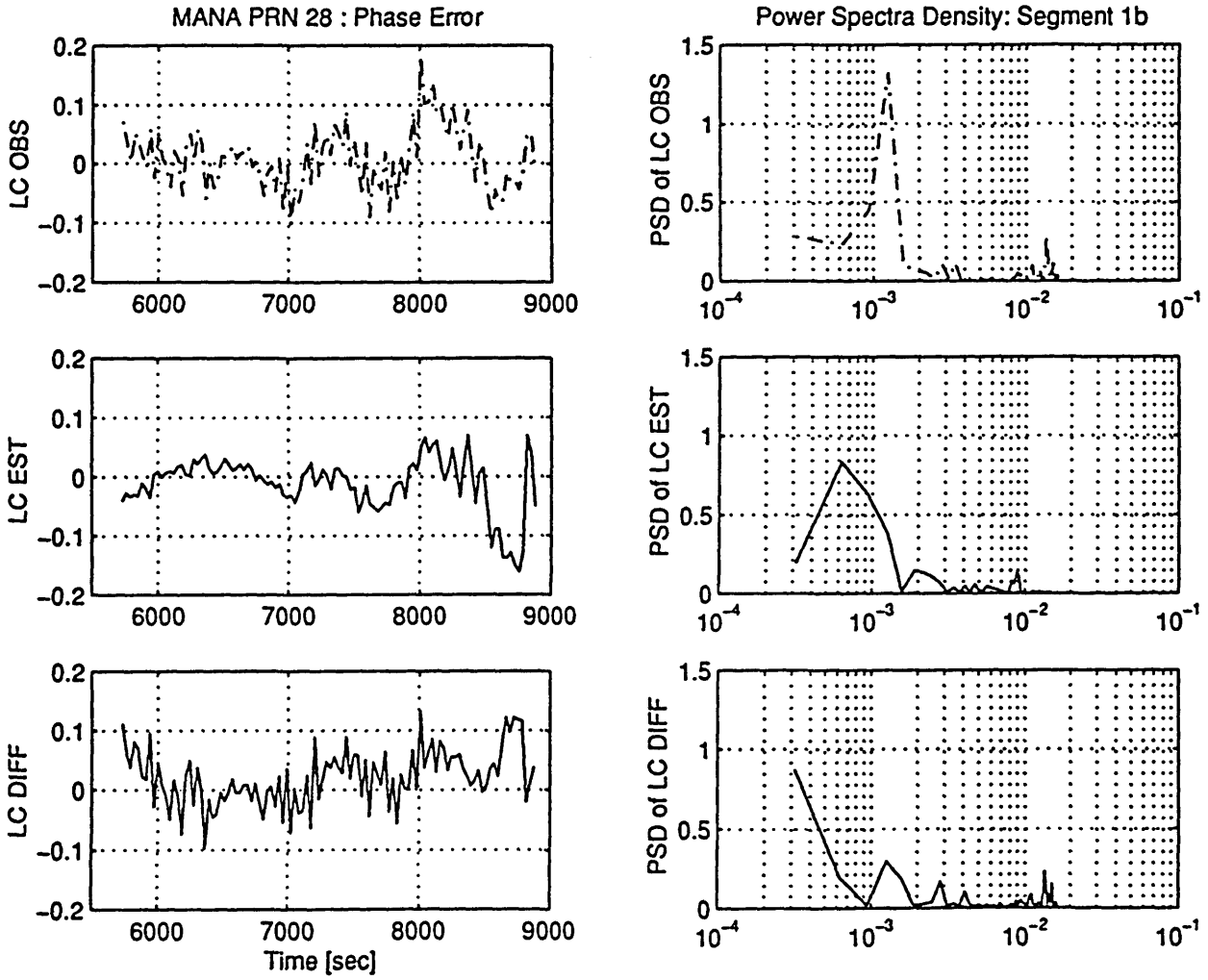

Fig. A.5.7.b) : MANA - PRN 28 (10 6 1995) - [segment 1.b]
PSD of LC_OBS, LC_EST and LC_DIFF
Unit: [cycles]^2

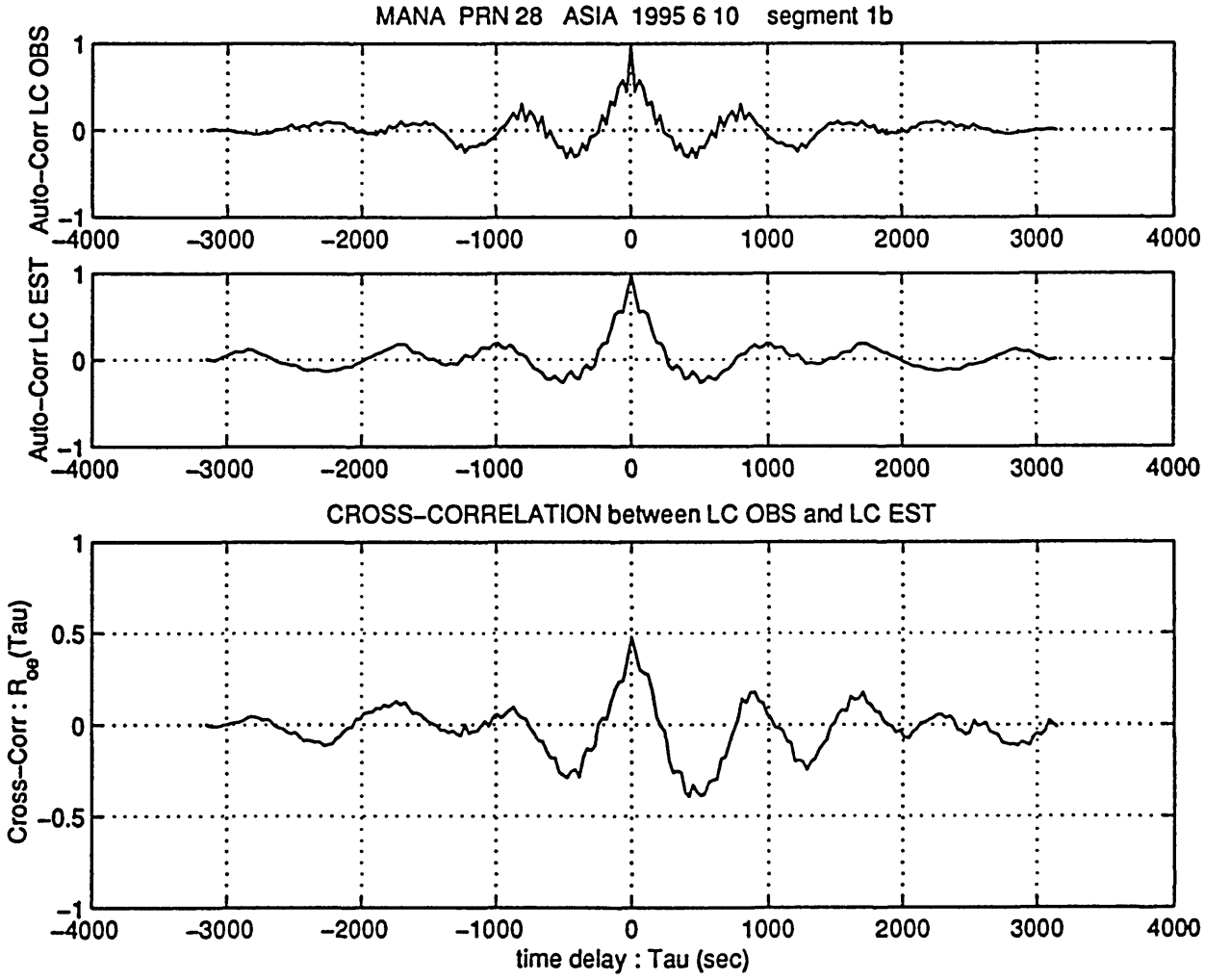

Fig. A.5.7.c) : MANA - PRN 28 (10 6 1995) - [segment 1.b]
Auto Correlation of LC_OBS (R_{oo}) and LC_EST (R_{ee}).
Cross Correlation between them (R_{oe})
Unit: [cycles]^2

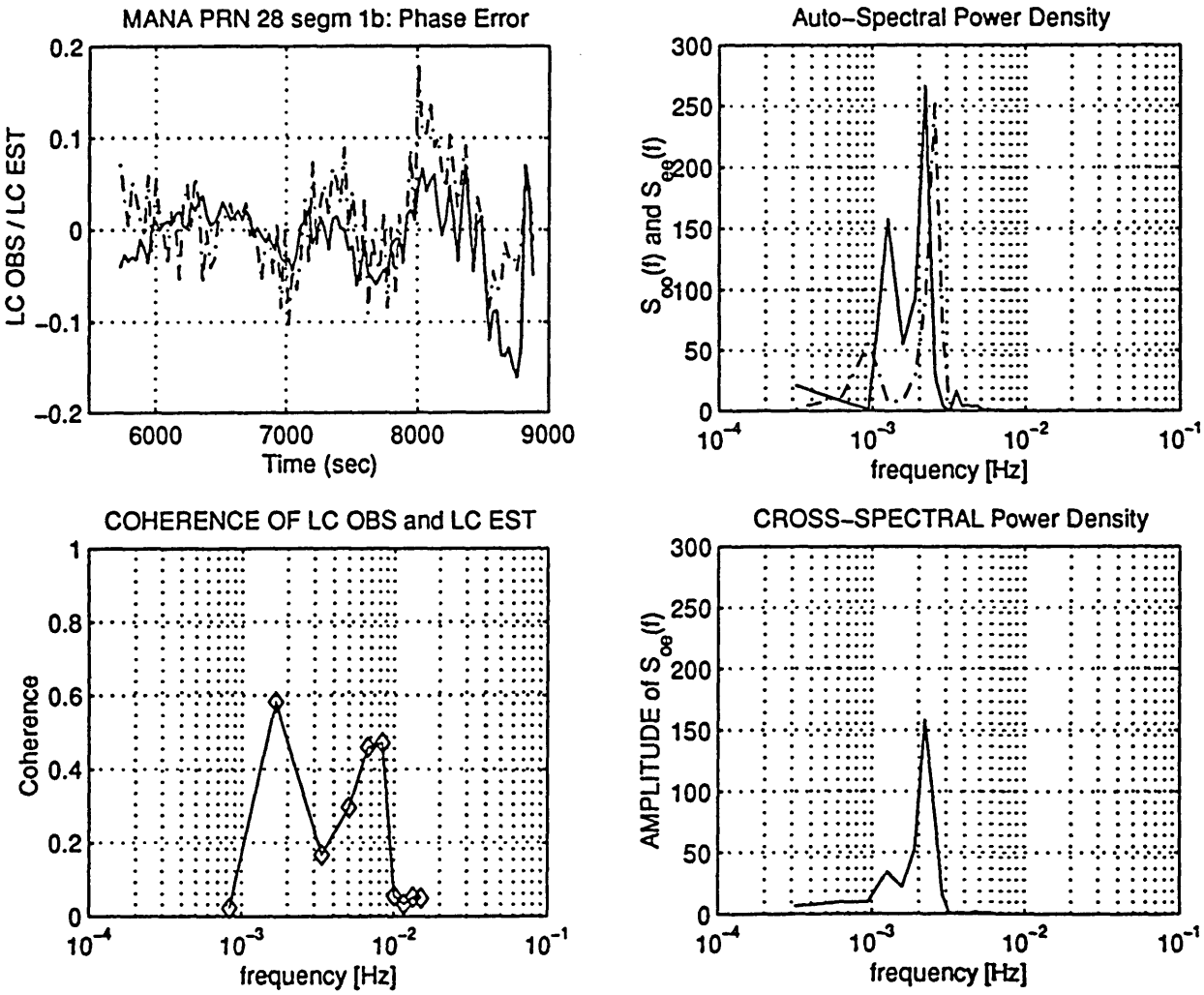

Fig. A.5.7.d) : MANA - PRN 28 (10 6 1995) - [segment 1.b]
Auto Spectral Power Density of LC_OBS (S_{oo}) and of LC_EST (S_{ee}). Cross PSD between them (S_{oe})
Unit: [cycles]^2
Coherence function of LC_OBS and LC_EST.

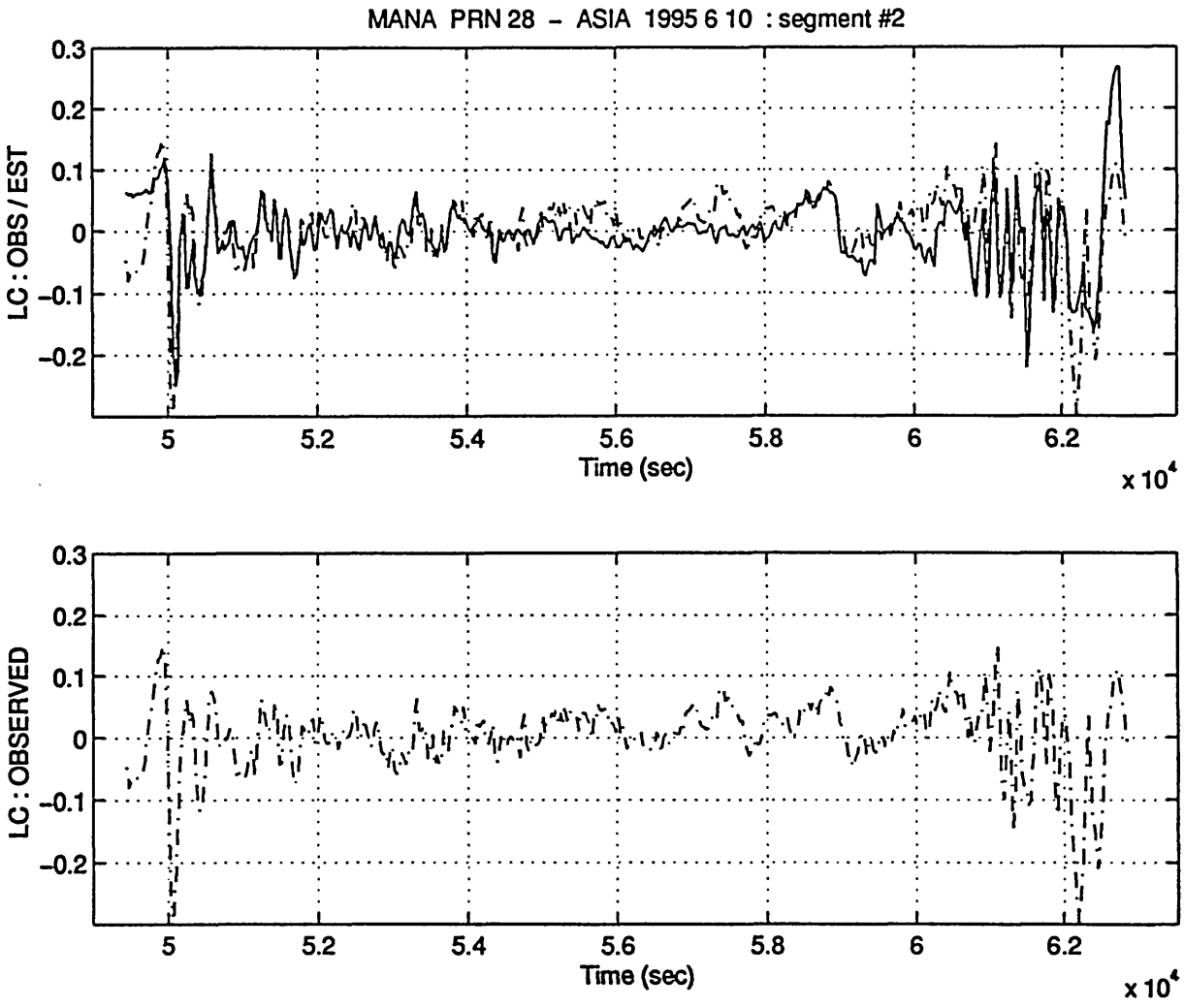

Fig. A.5.8 : Station: MANA - Satellite: PRN 28 - [segment #2]
Data acquisition date 10 6 1995
LC_OBS and LC_EST compared for t=4.8 - 6.3 10^4 sec
Unit: [cycles]

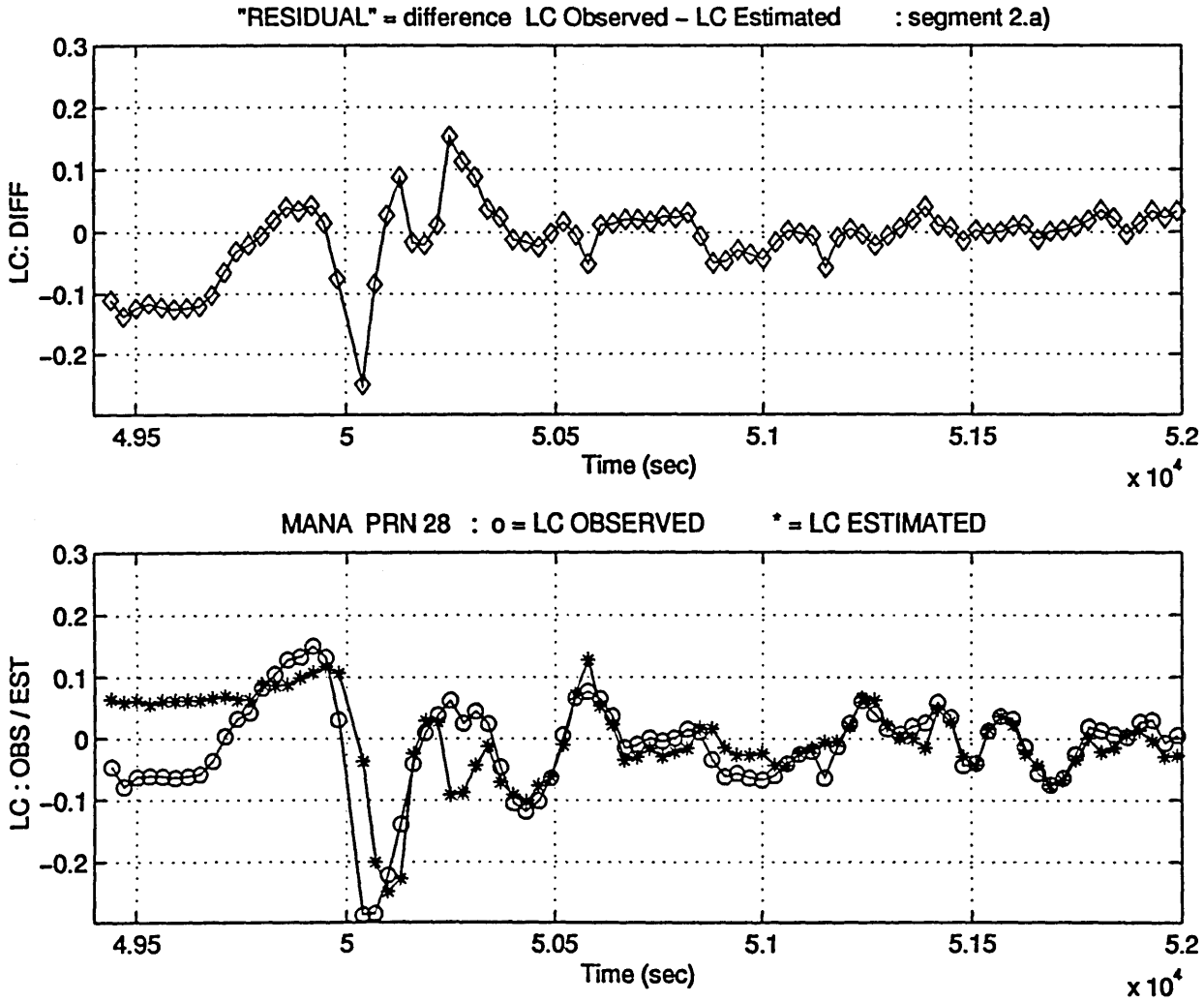

Fig. A.5.9.a) : MANA - PRN 28 (10 6 1995) - [segment 2.a]
Phase residual LC_DIFF, determined as the difference between LC_OBS and LC_EST.
Unit: [cycles]

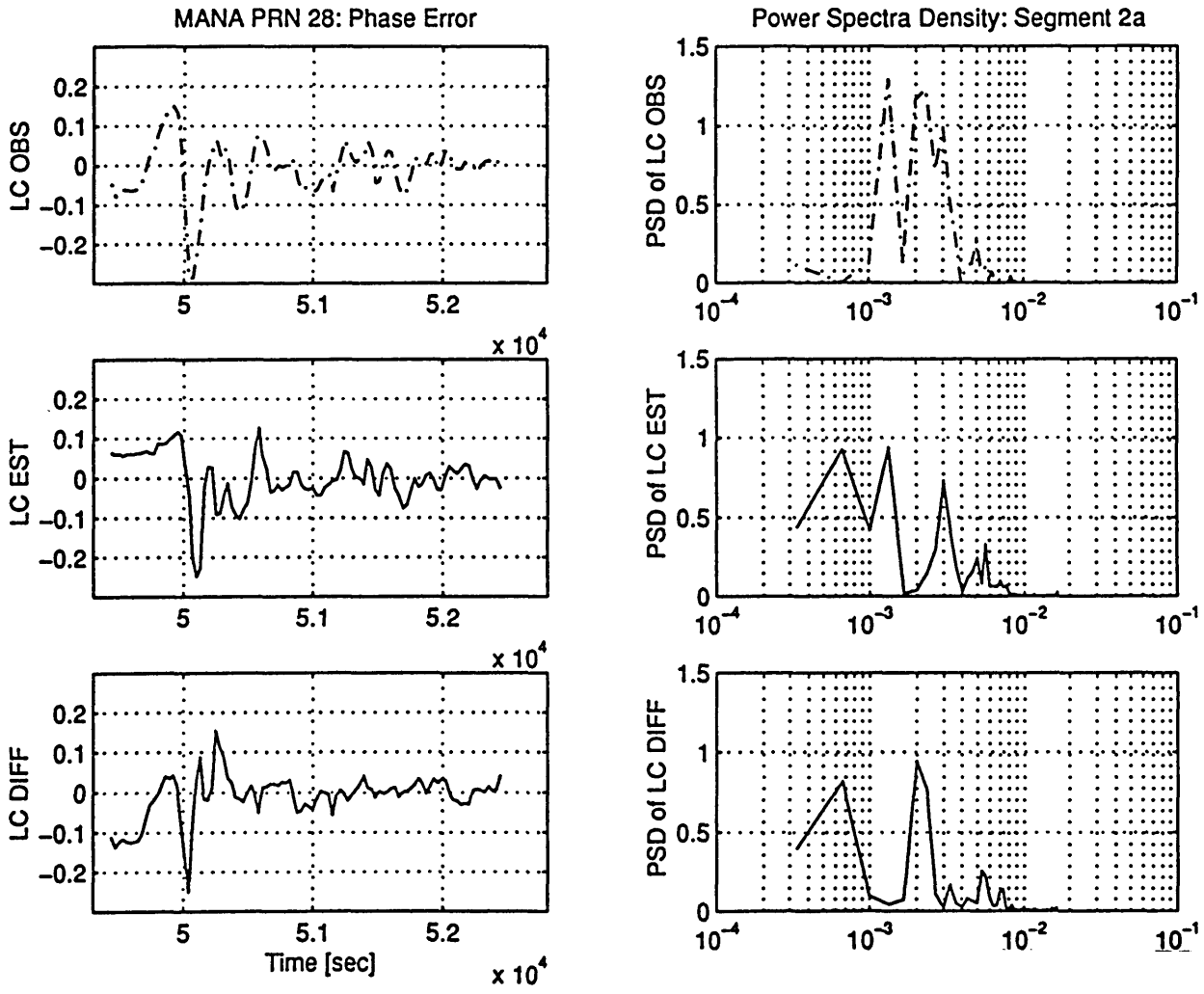

Fig. A.5.9.b) : MANA - PRN 28 (10 6 1995) - [segment 2.a]
PSD of LC_OBS, LC_EST and LC_DIFF.
Unit: [cycles]^2

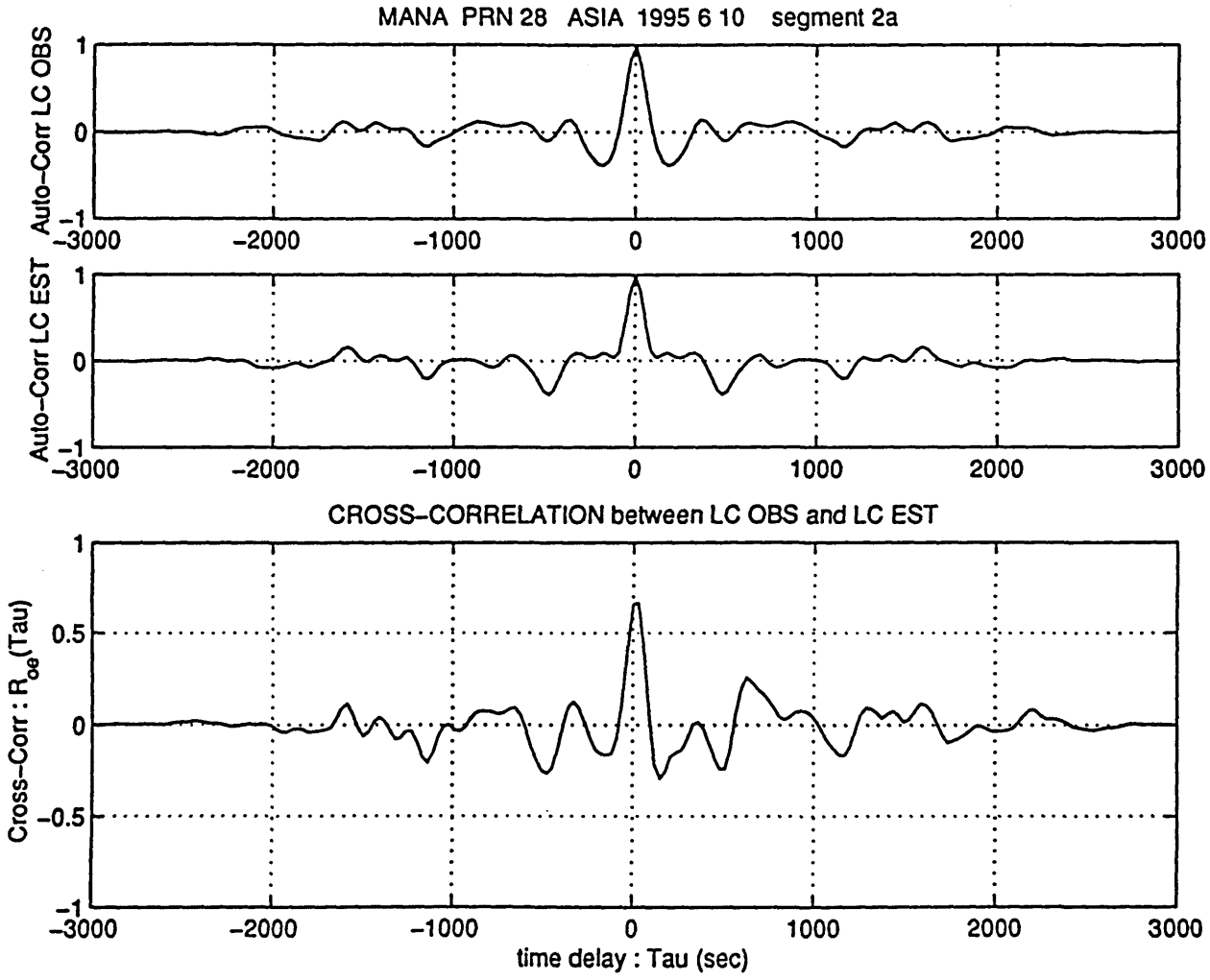

Fig. A.5.9.c) : MANA - PRN 28 (10 6 1995) - [segment 2.a]
Auto Correlation of LC_OBS (R_{oo}) and LC_EST (R_{ee}).
Cross Correlation between them (R_{oe})
Unit: [cycles]^2

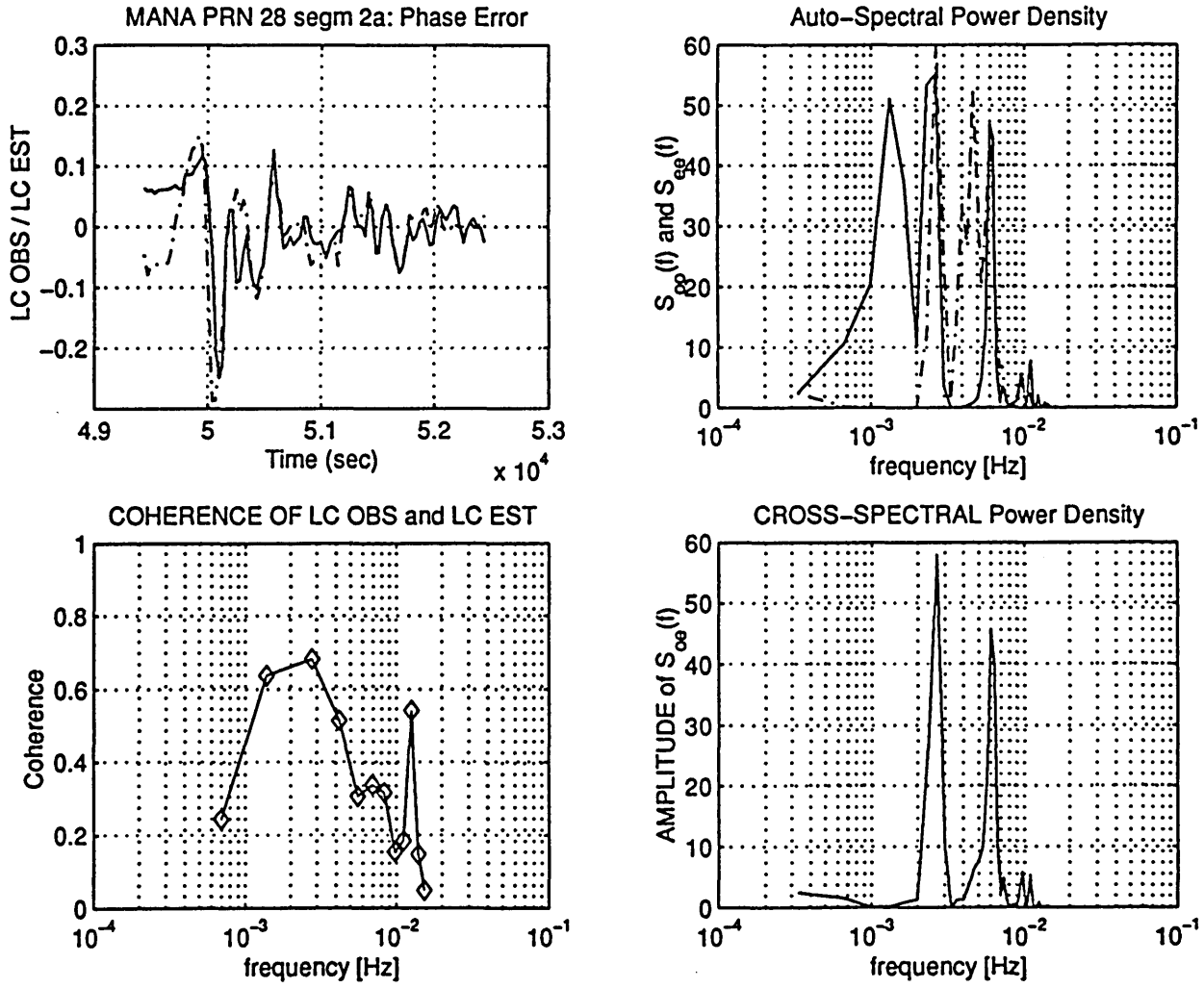

Fig. A.5.9.d) : MANA - PRN 28 (10 6 1995) - [segment 2.a]
Auto Spectral Power Density of LC_OBS (S_{oo}) and of LC_EST (S_{ee}). CrossPSD between them (S_{oe})
Unit: [cycles]^2
Coherence function of LC_OBS and LC_EST.

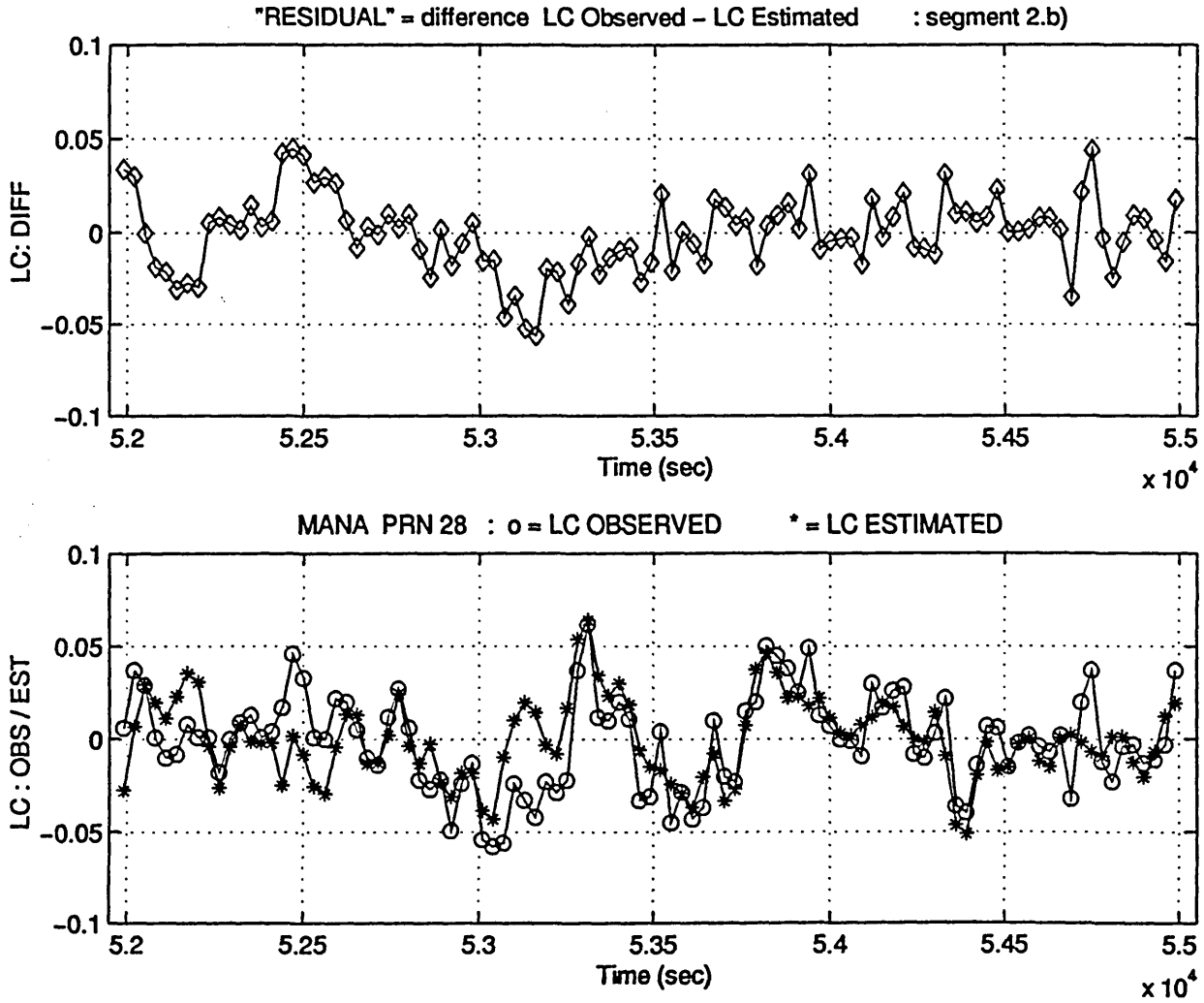

Fig. A.5.10.a) : MANA - PRN 28 (10 6 1995) - [segment 2.b]
Phase residual LC_DIFF, determined as the difference between LC_OBS and LC_EST.
Unit: [cycles]

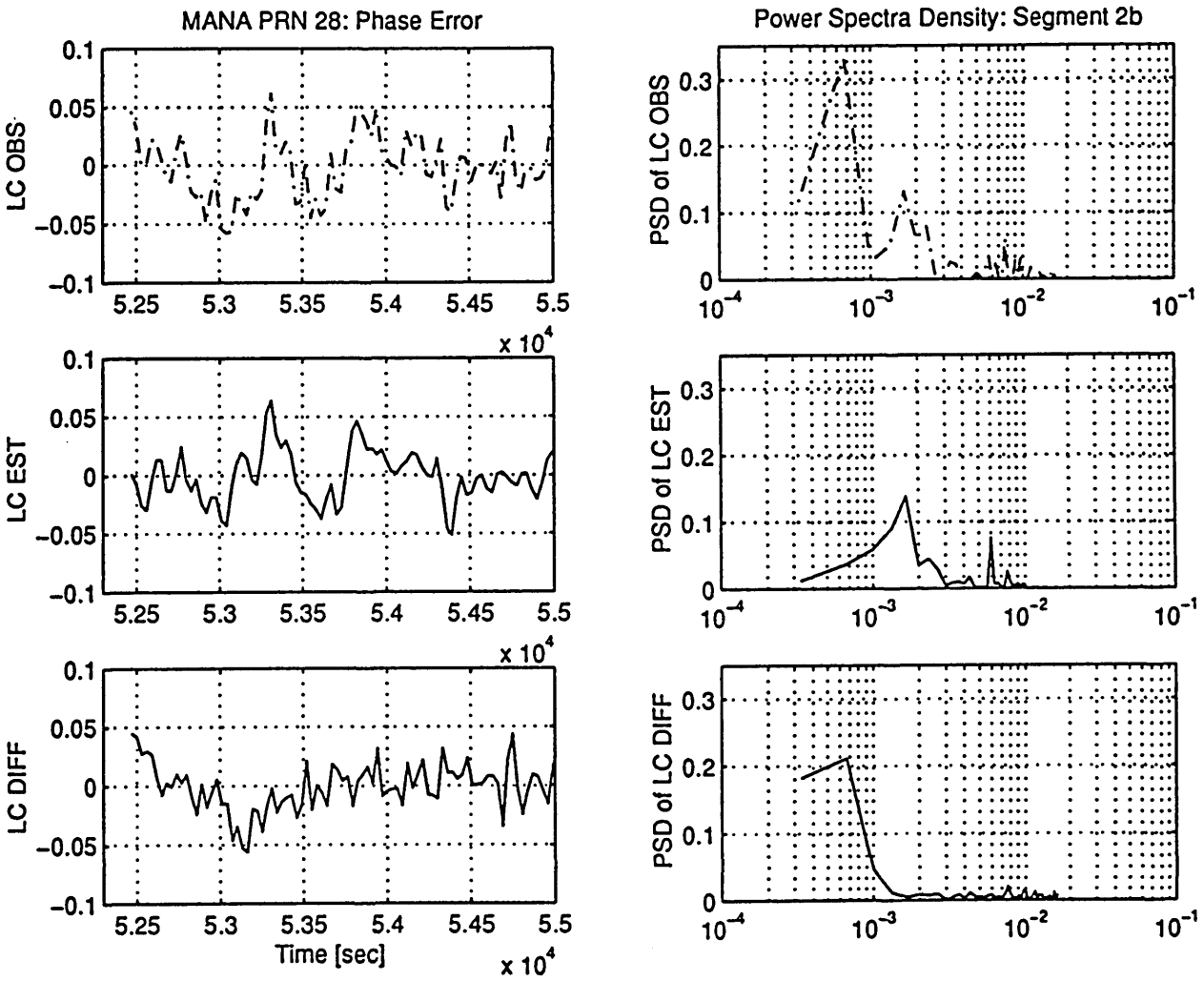

Fig. A.5.10.b) : MANA - PRN 28 (10 6 1995) - [segment 2.b]
PSD of LC_OBS, LC_EST and LC_DIFF.
Unit: [cycles]^2

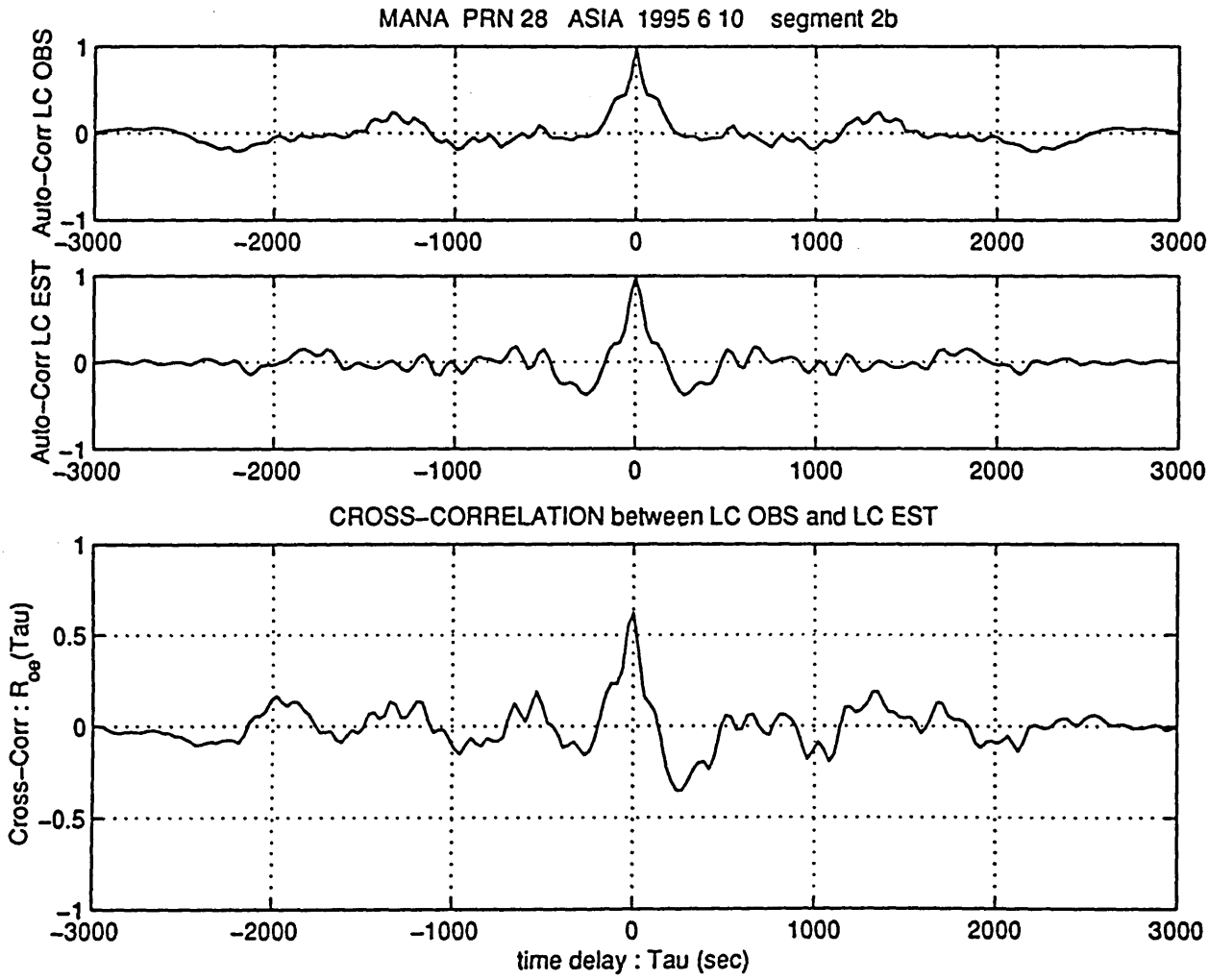

Fig. A.5.10.c) : MANA - PRN 28 (10 6 1995) - [segment 2.b]
Auto Correlation of LC_OBS (R_{oo}) and LC_EST (R_{ee}).
Cross Correlation between them (R_{oe})
Unit: [cycles]^2

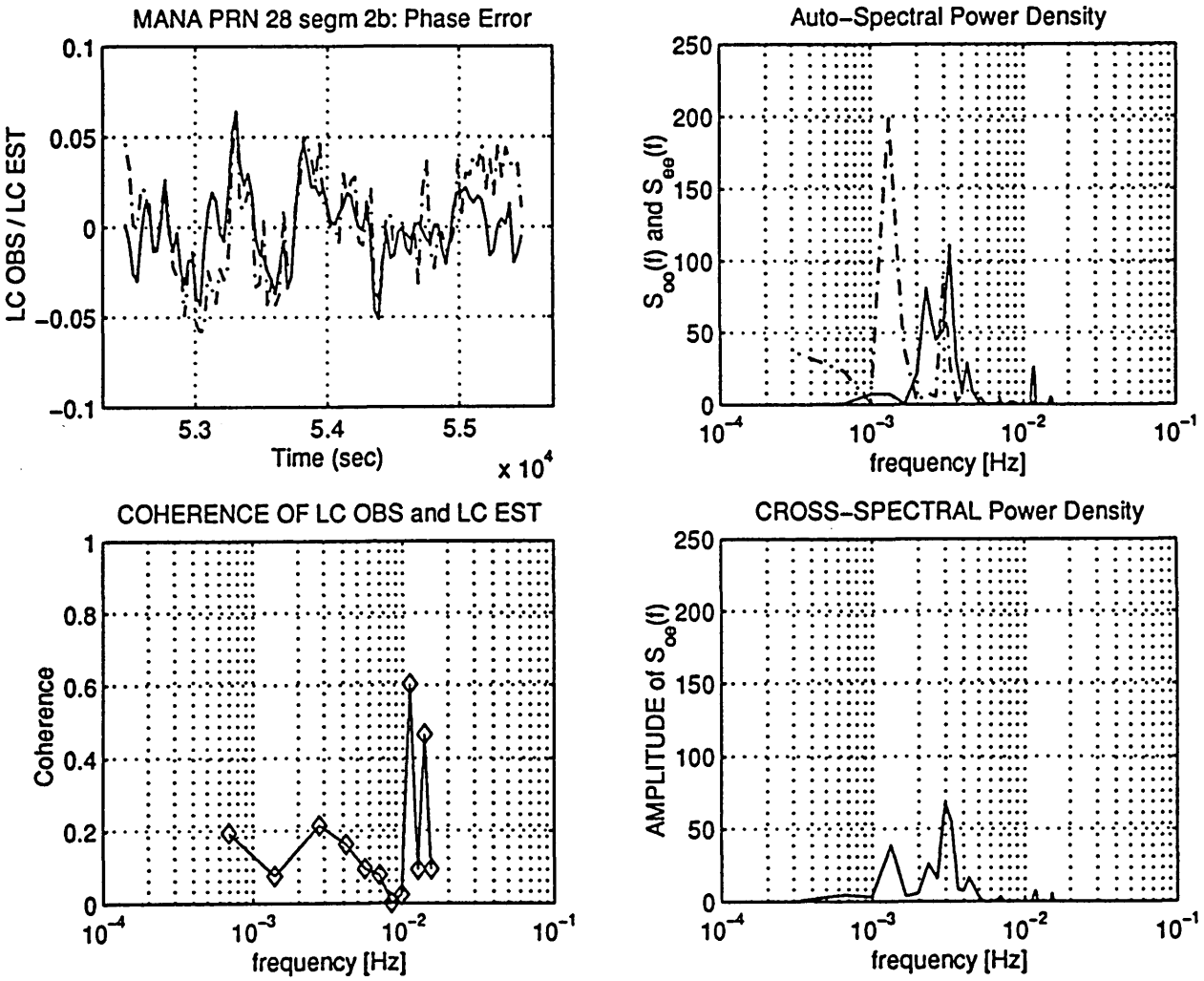

Fig. A.5.10.d) : MANA - PRN 28 (10 6 1995) - [segment 2.b]
Auto Spectral Power Density of LC_OBS (S_{oo}) and of LC_EST (S_{ee}). Cross PSD between them (S_{oe})
Unit: [cycles]^2
Coherence function of LC_OBS and LC_EST.

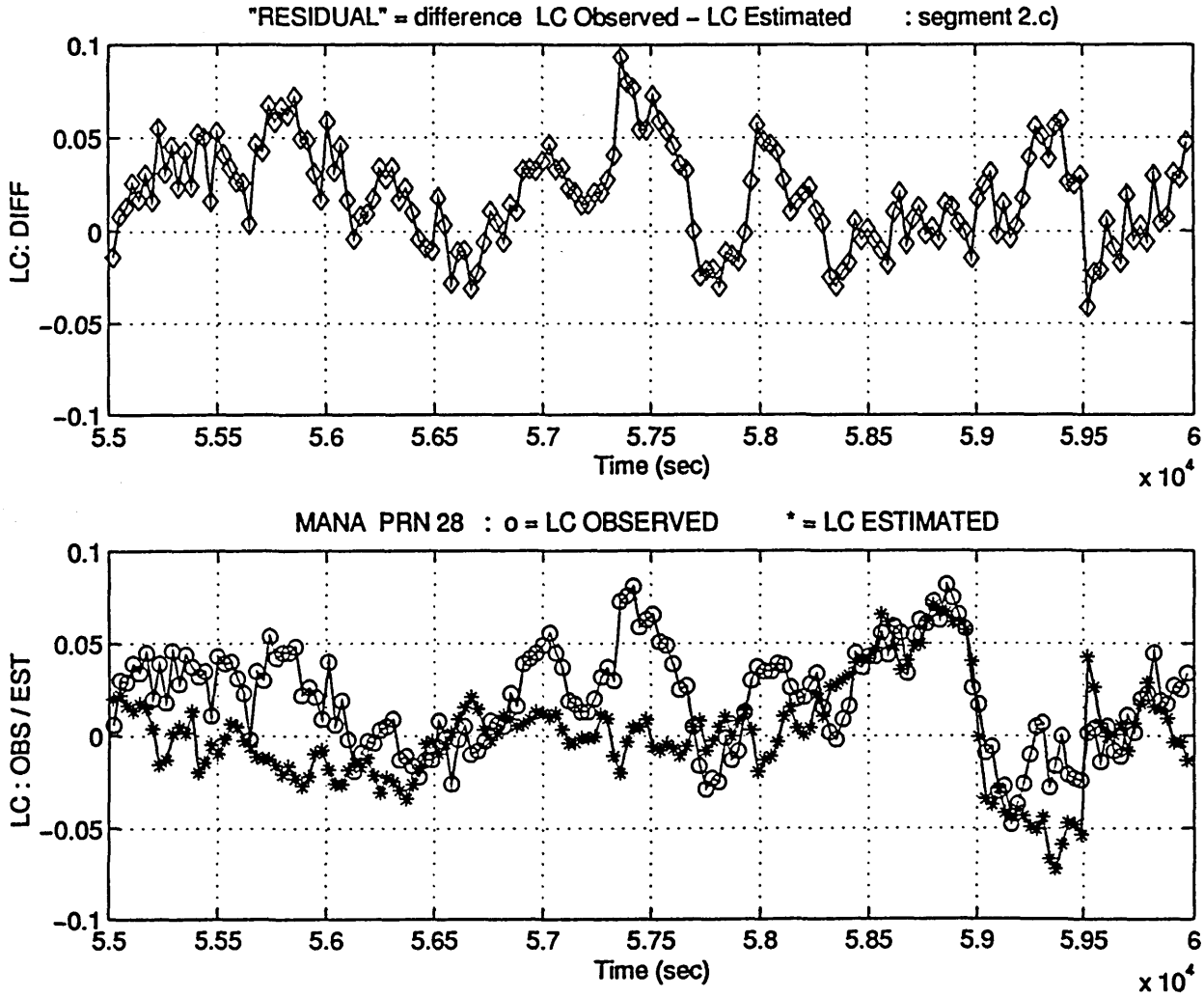

Fig. A.5.11.a) : MANA - PRN 28 (10 6 1995) - [segment 2.c]
Phase residual LC_DIFF, determined as the difference between LC_OBS and LC_EST.
Unit: [cycles]

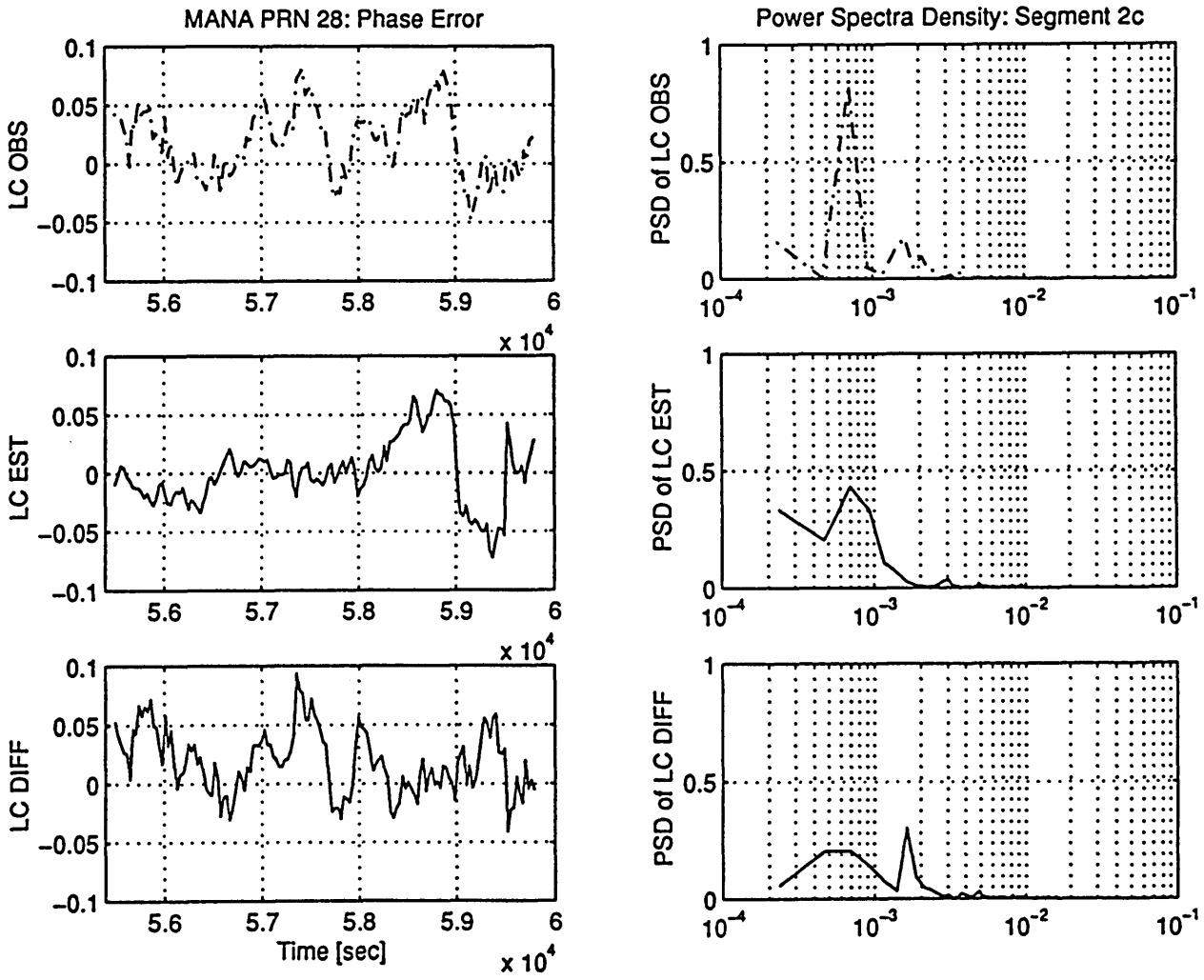

Fig. A.5.11.b) : MANA - PRN 28 (10 6 1995) - [segment 2.c]
PSD of LC_OBS, LC_EST and LC_DIFF.
Unit: [cycles]^2

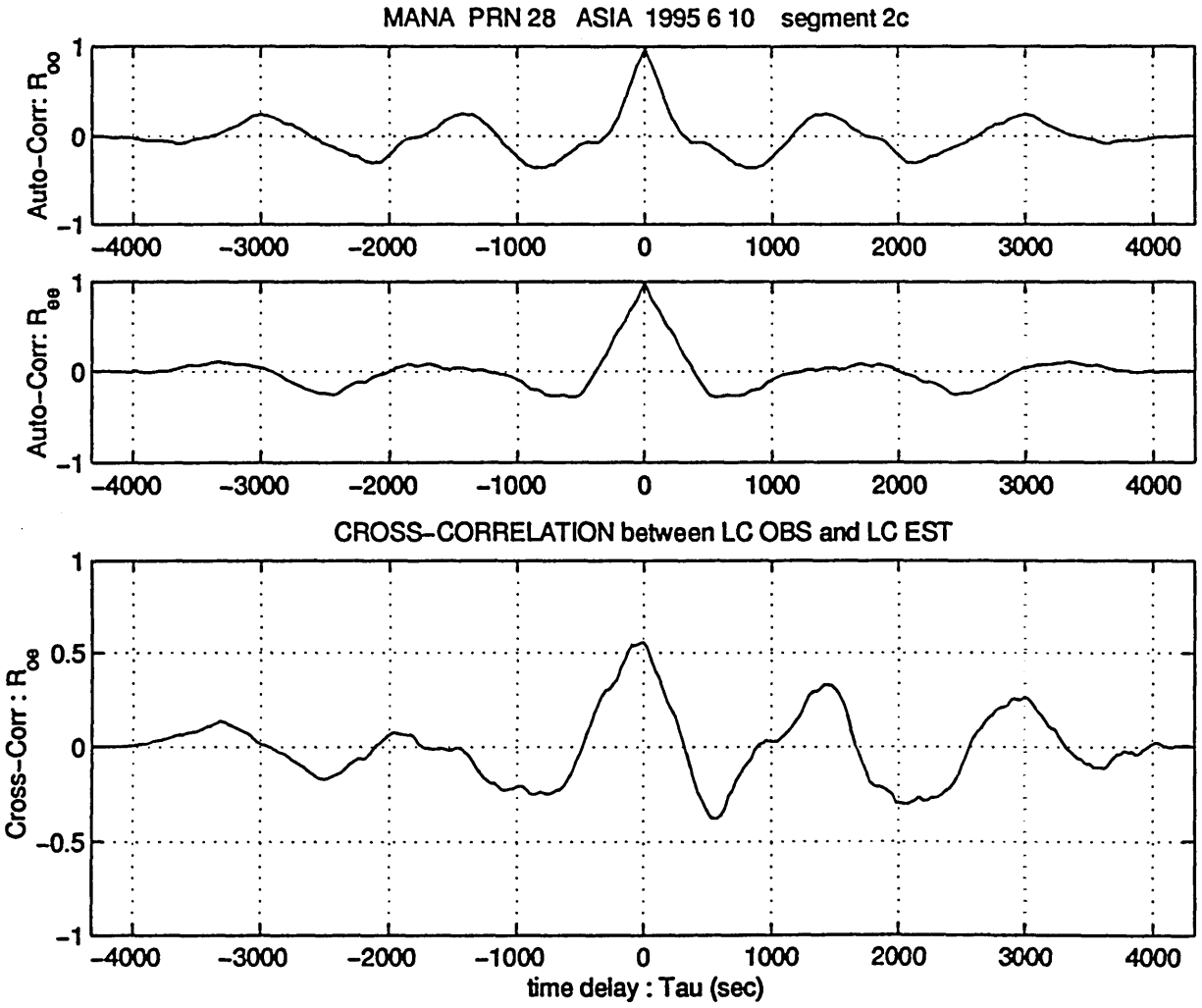

Fig. A.5.11.c) : MANA - PRN 28 (10 6 1995) - [segment 2.c]
Auto Correlation of LC_OBS (R_{oo}) and LC_EST (R_{ee}).
Cross Correlation between them (R_{oe})
Unit: [cycles]^2

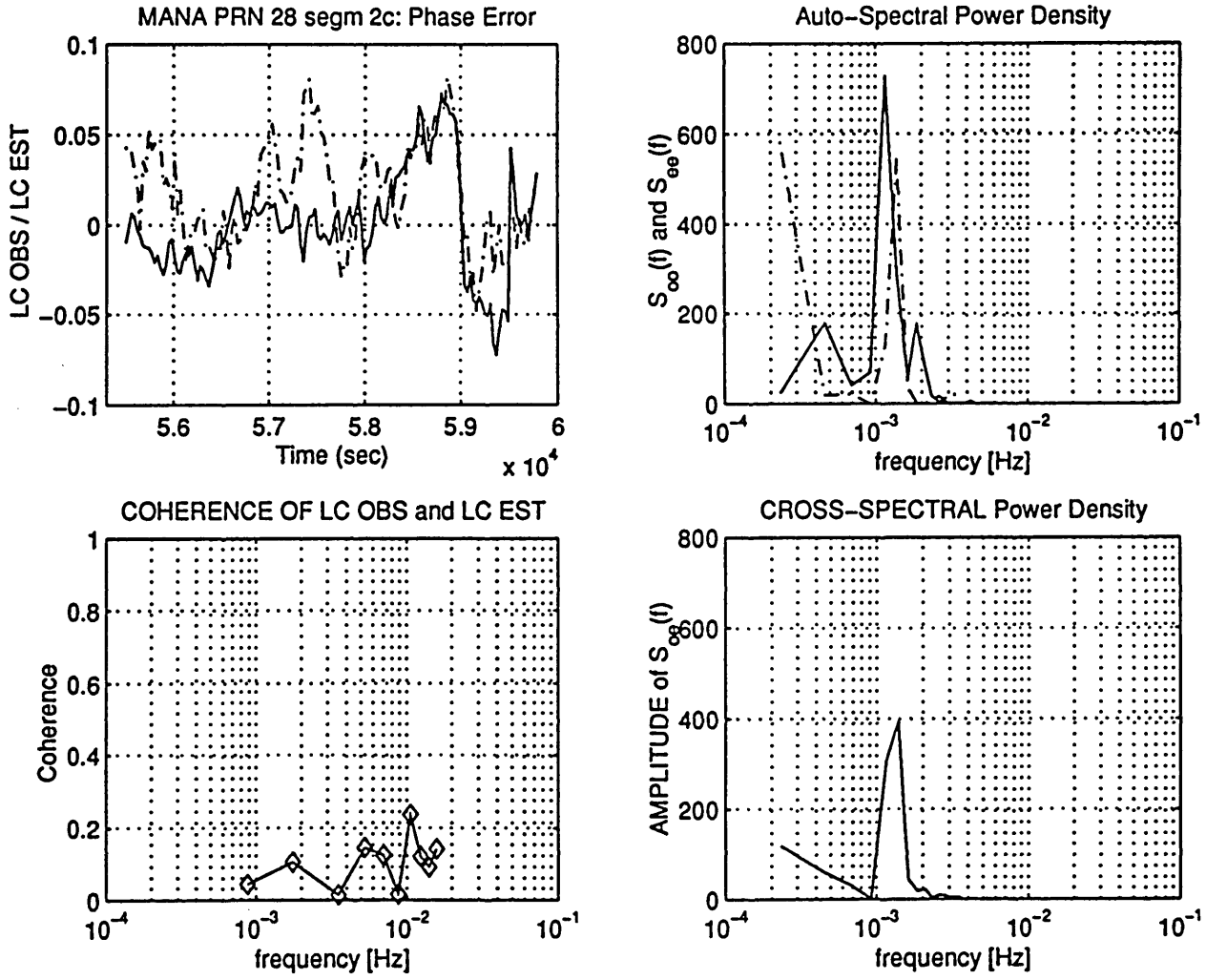

Fig. A.5.11.d) : MANA - PRN 28 (10 6 1995) - [segment 2.c]
Auto Spectral Power Density of LC_OBS (S_{oo}) and of LC_EST (S_{ee}). Cross PSD between them (S_{oe})
Unit: [cycles]^2
Coherence function of LC_OBS and LC_EST.

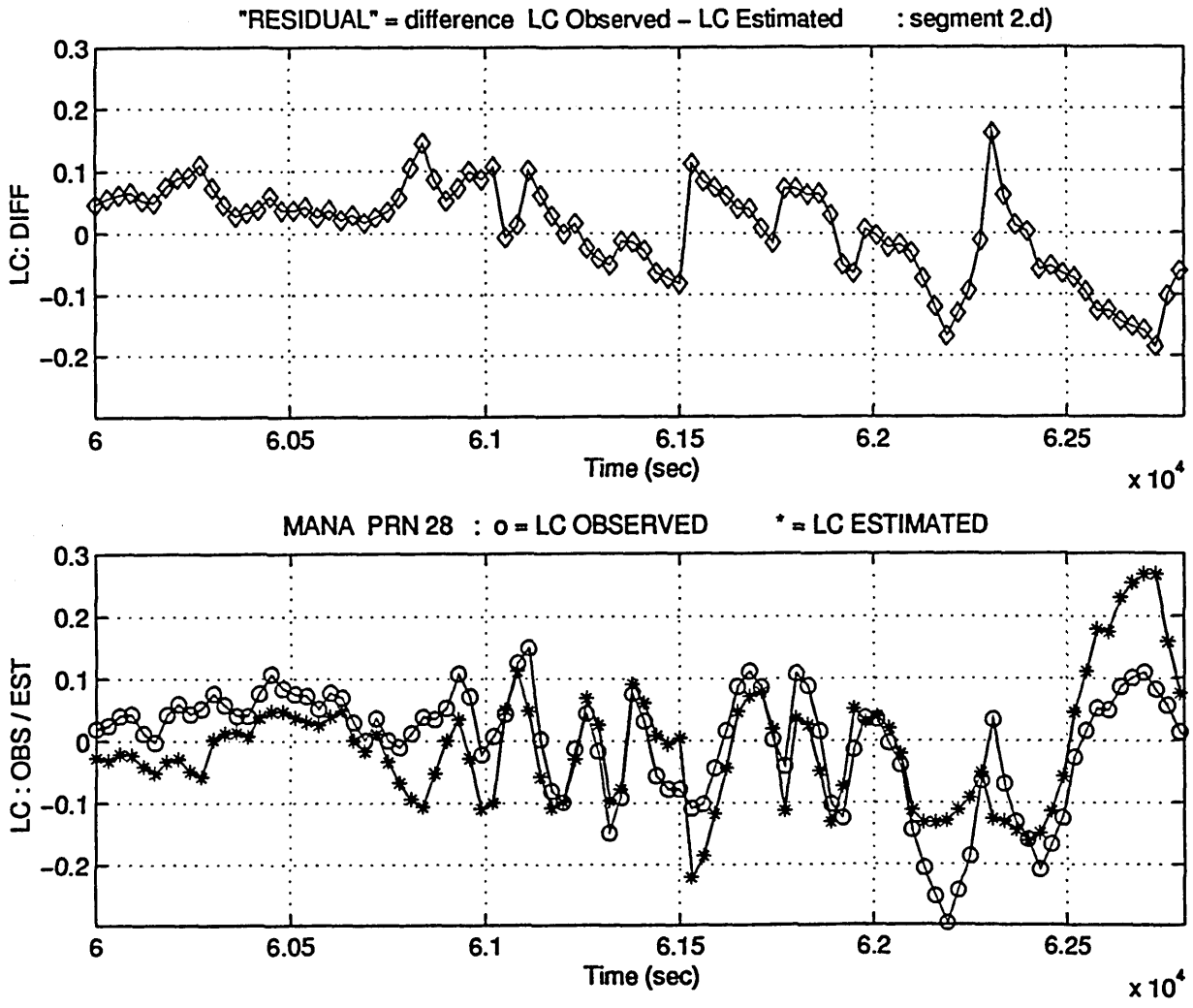

Fig. A.5.12.a) : MANA - PRN 28 (10 6 1995) - [segment 2.d]
Phase residual LC_DIFF, determined as the difference between LC_OBS and LC_EST.
Unit: [cycles]

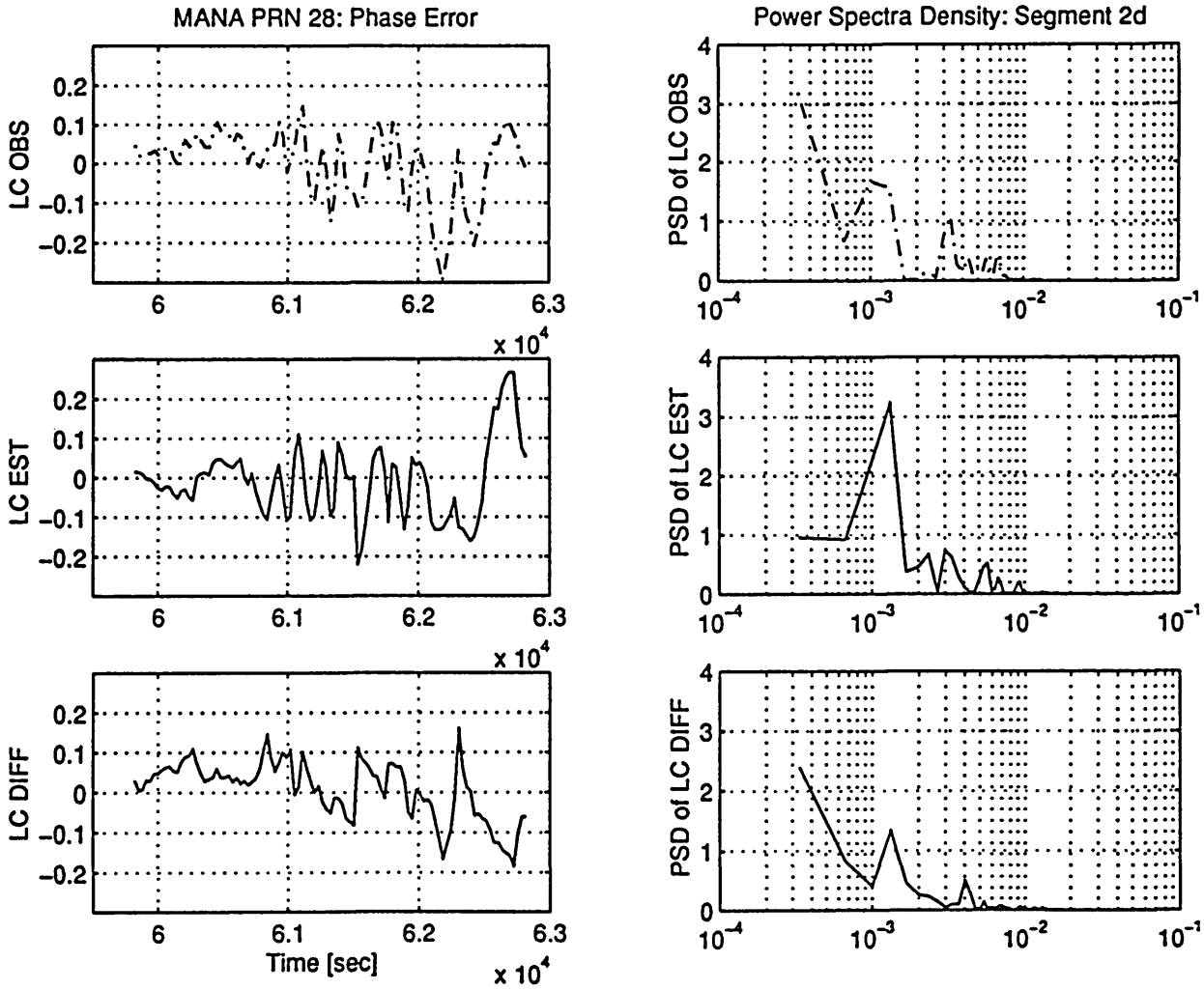

Fig. A.5.12.b) : MANA - PRN 28 (10 6 1995) - [segment 2.d]
PSD of LC_OBS, LC_EST and LC_DIFF.
Unit: [cycles]^2

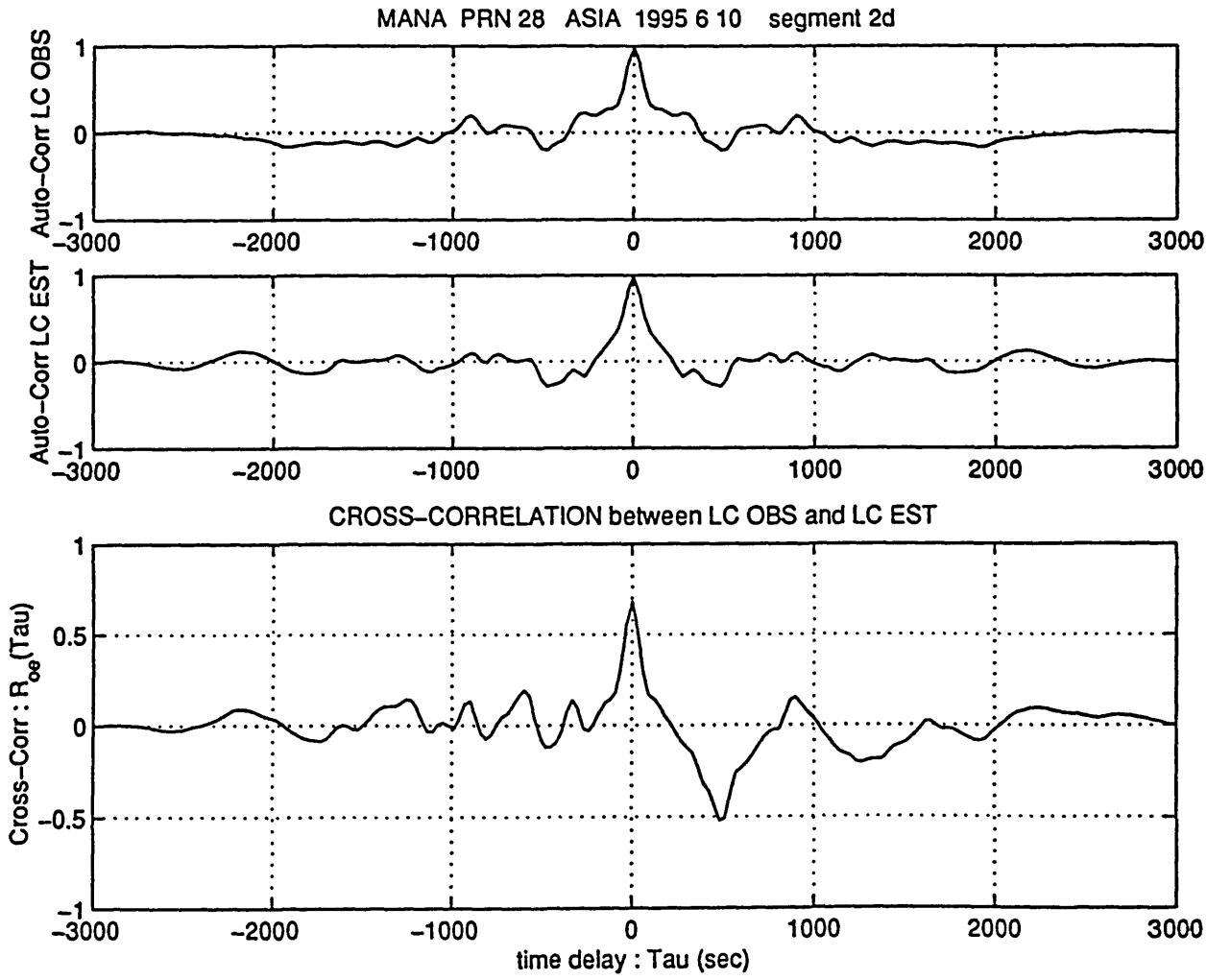

Fig. A.5.12.c) : MANA - PRN 28 (10 6 1995) - [segment 2.d]
Auto Correlation of LC_OBS (R_{oo}) and LC_EST (R_{ee}).
Cross Correlation between them (R_{oe})
Unit: [cycles]^2

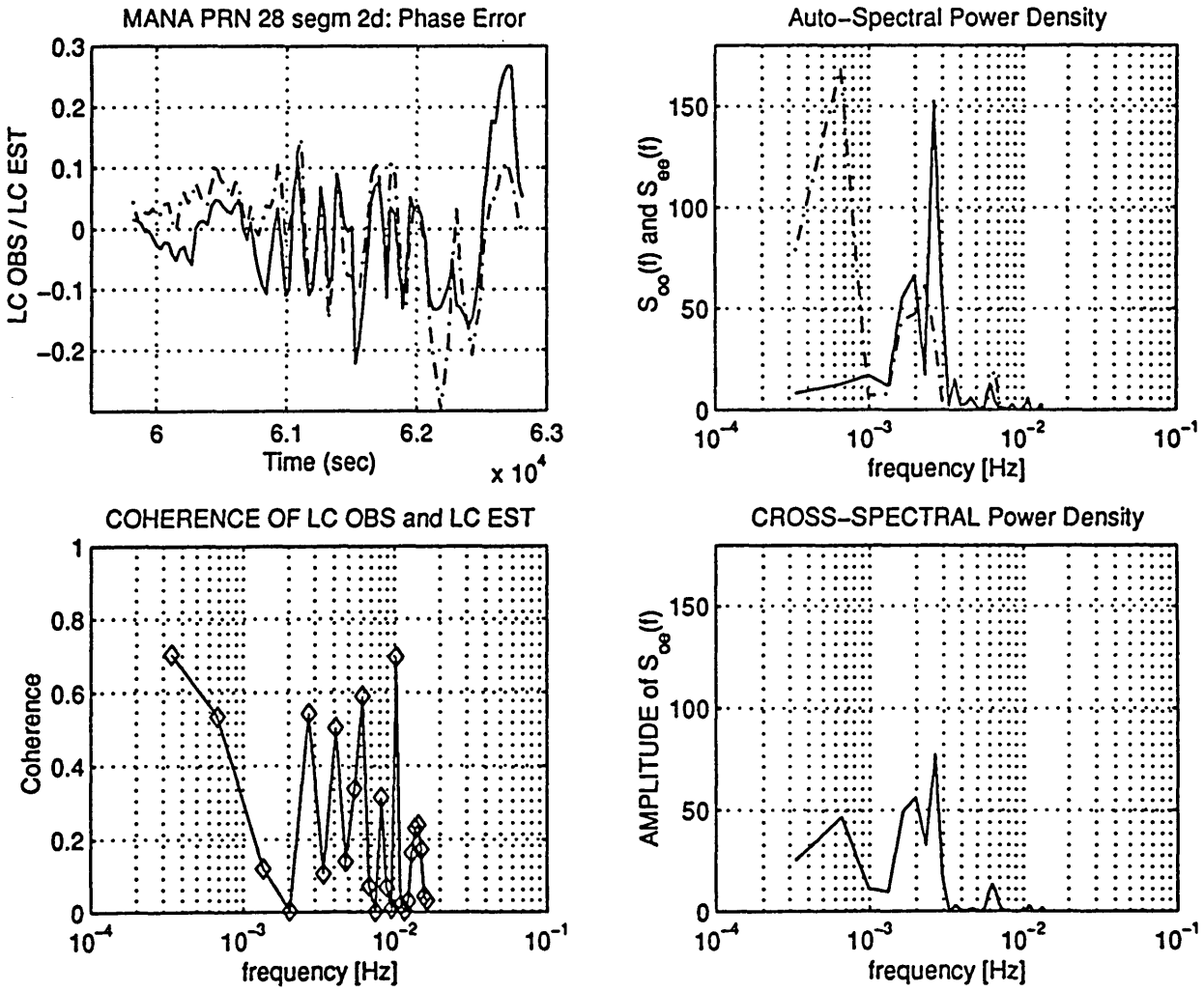

Fig. A.5.12.d) : MANA - PRN 28 (10 6 1995) - [segment 2.d]
Auto Spectral Power Density of LC_OBS (S_{oo}) and of LC_EST (S_{ee}). Cross PSD between them (S_{oe})
Unit: [cycles]^2
Coherence function of LC_OBS and LC_EST.

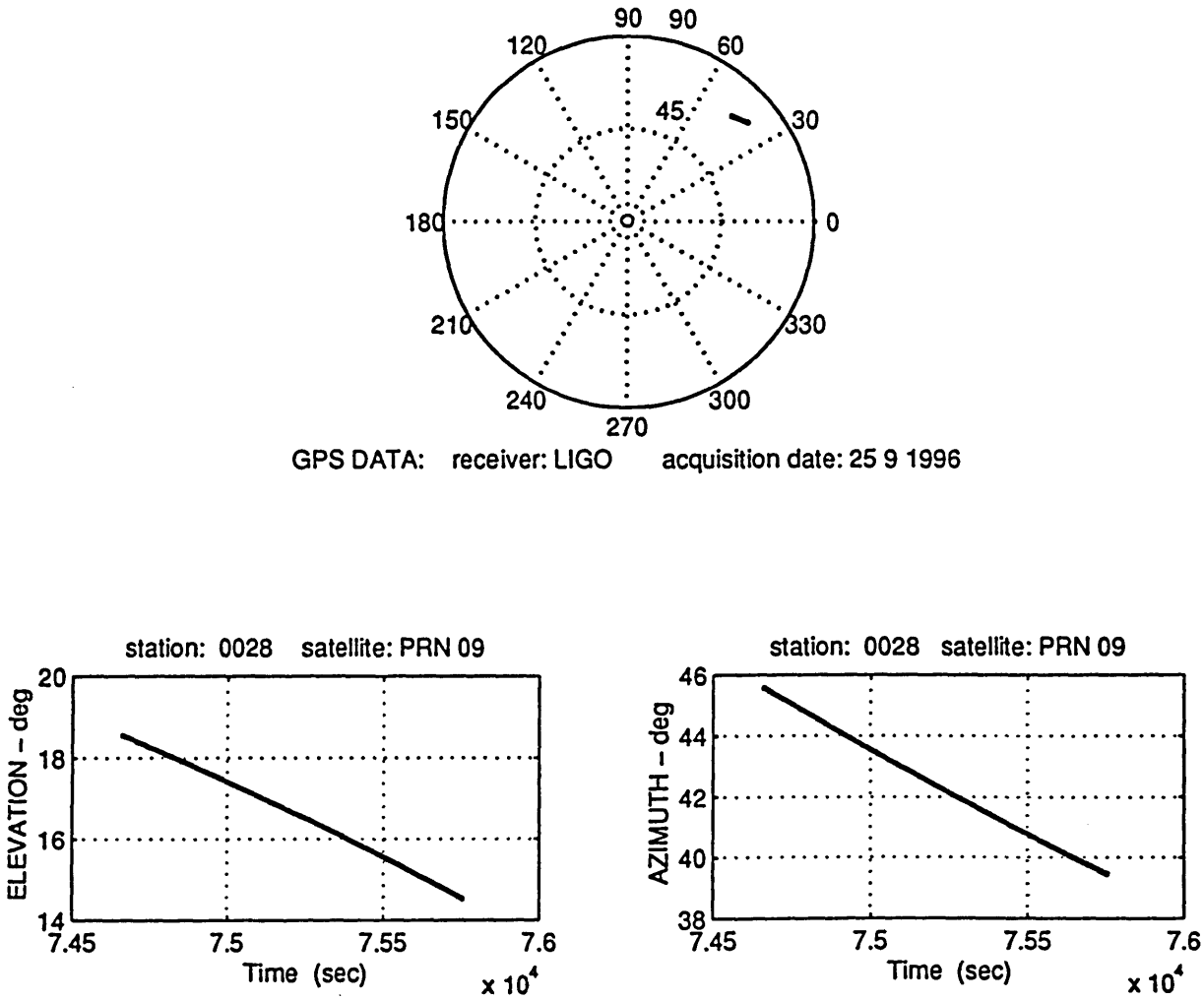

Fig. A.6.1 : Satellite visibility chart for PRN 09 (skymap). Elevation and azimuth of PRN 09 with respect to the station 0028

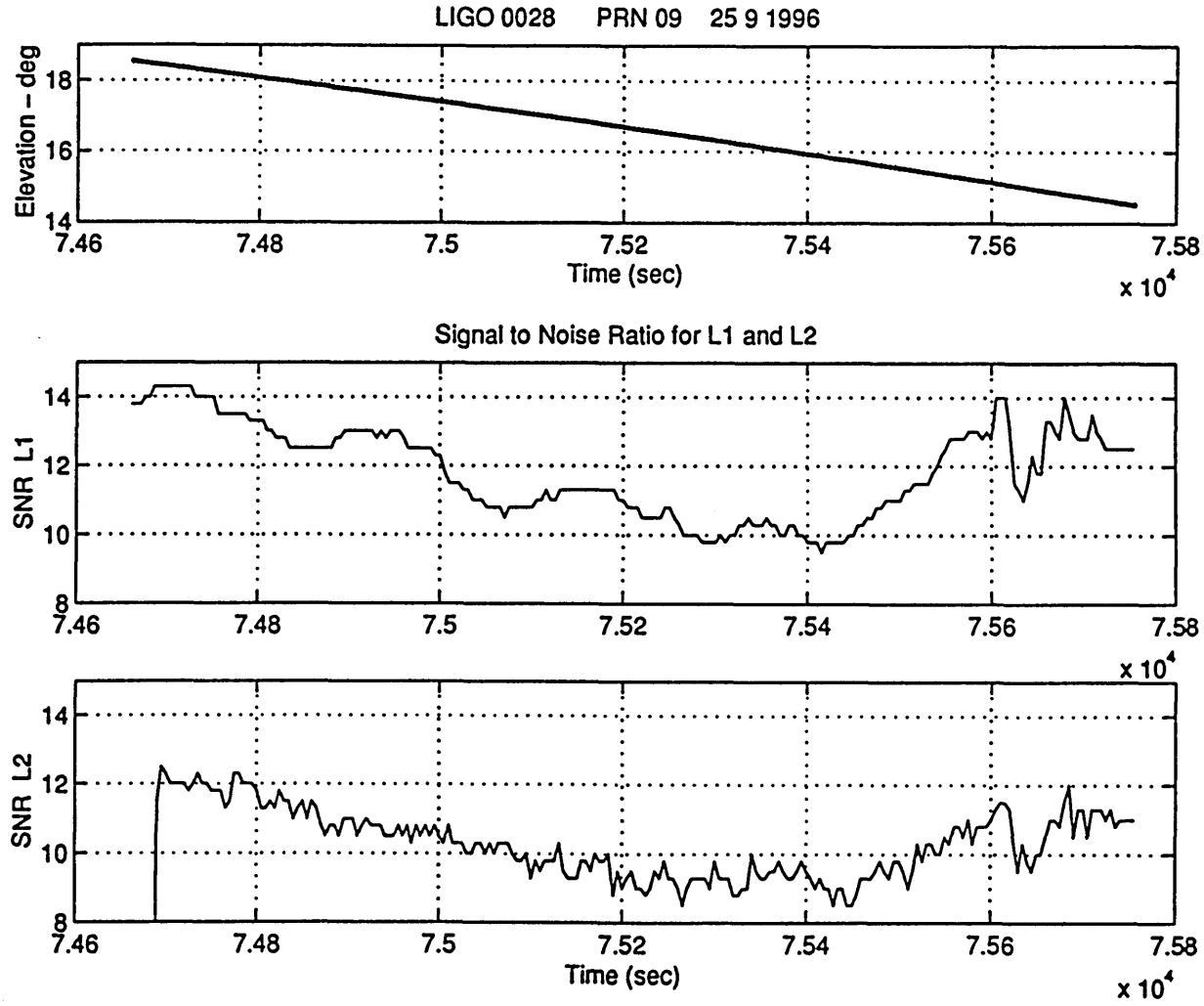

Fig. A.6.2 : Station: 0028- Satellite: PRN 09
Data acquisition date 25 9 1996
Signal-to-Noise-Ratio (SNR) for L_1 and L_2.

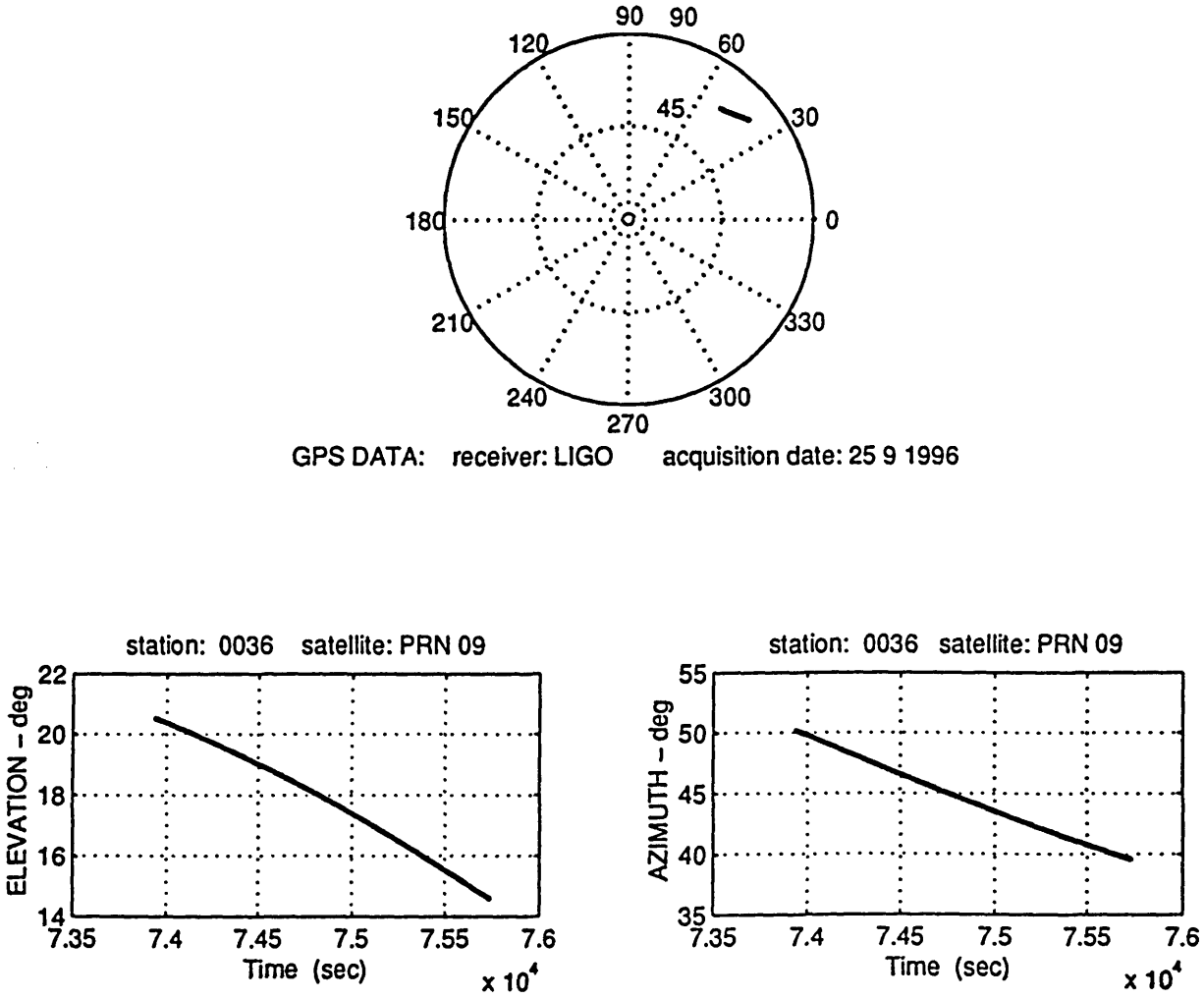

Fig. A.6.3 : Satellite visibility chart for PRN 09 (skymap). Elevation and azimuth of PRN 09with respect to the station 0036

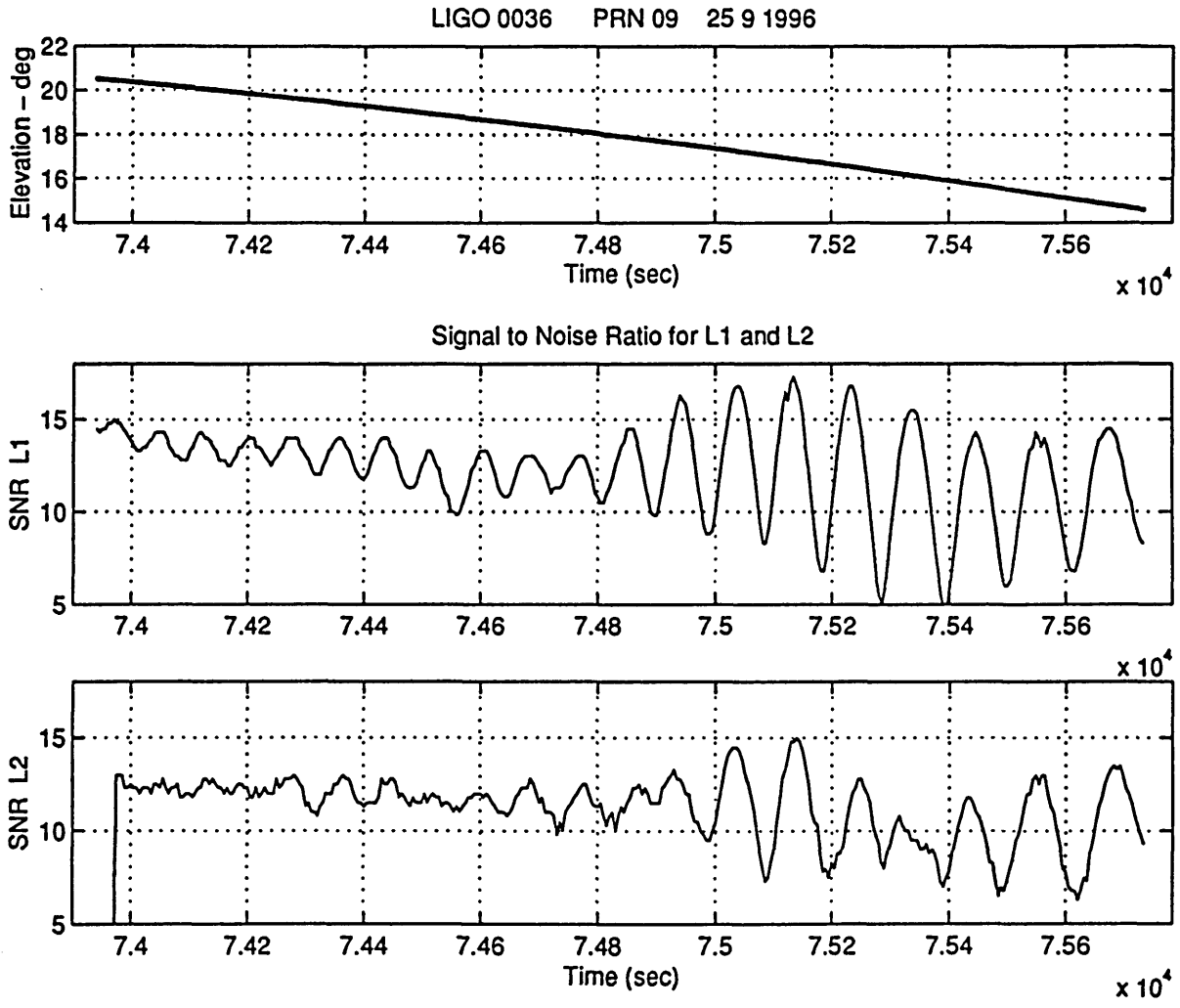

Fig. A.6.4 : Station: 0036- Satellite: PRN 09
Data acquisition date 25 9 1996
Signal-to-Noise-Ratio (SNR) for L1 and L2.

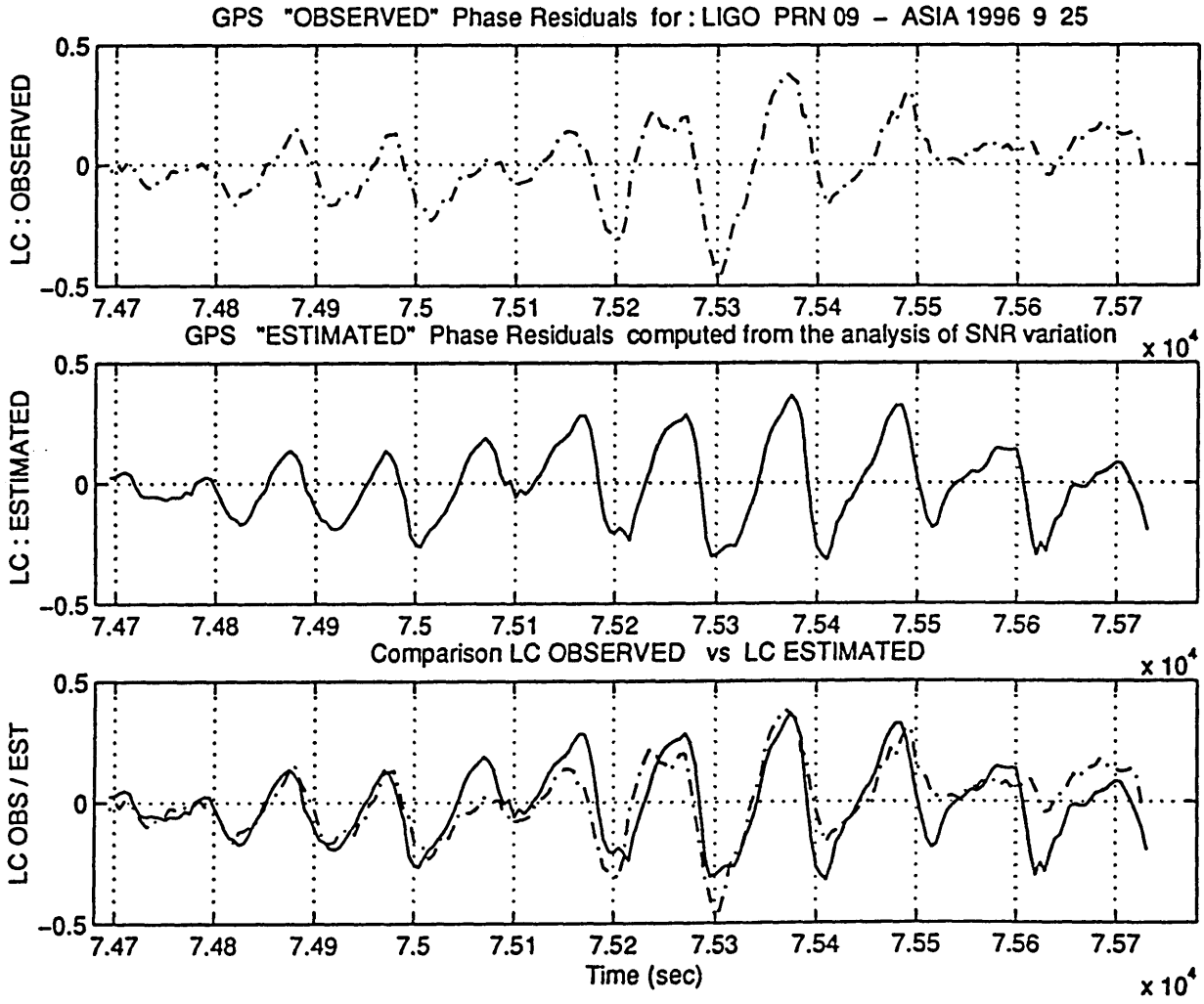

Fig. A.6.5: Stations: 0028- 0036 Satellite: PRN 09 -
Data acquisition date 25 9 1996
The observed phase residual (LC_OBS) is compared with the multipath phase error estimated from the SNR (LC_EST) (differential mode)
Unit: [cycles]

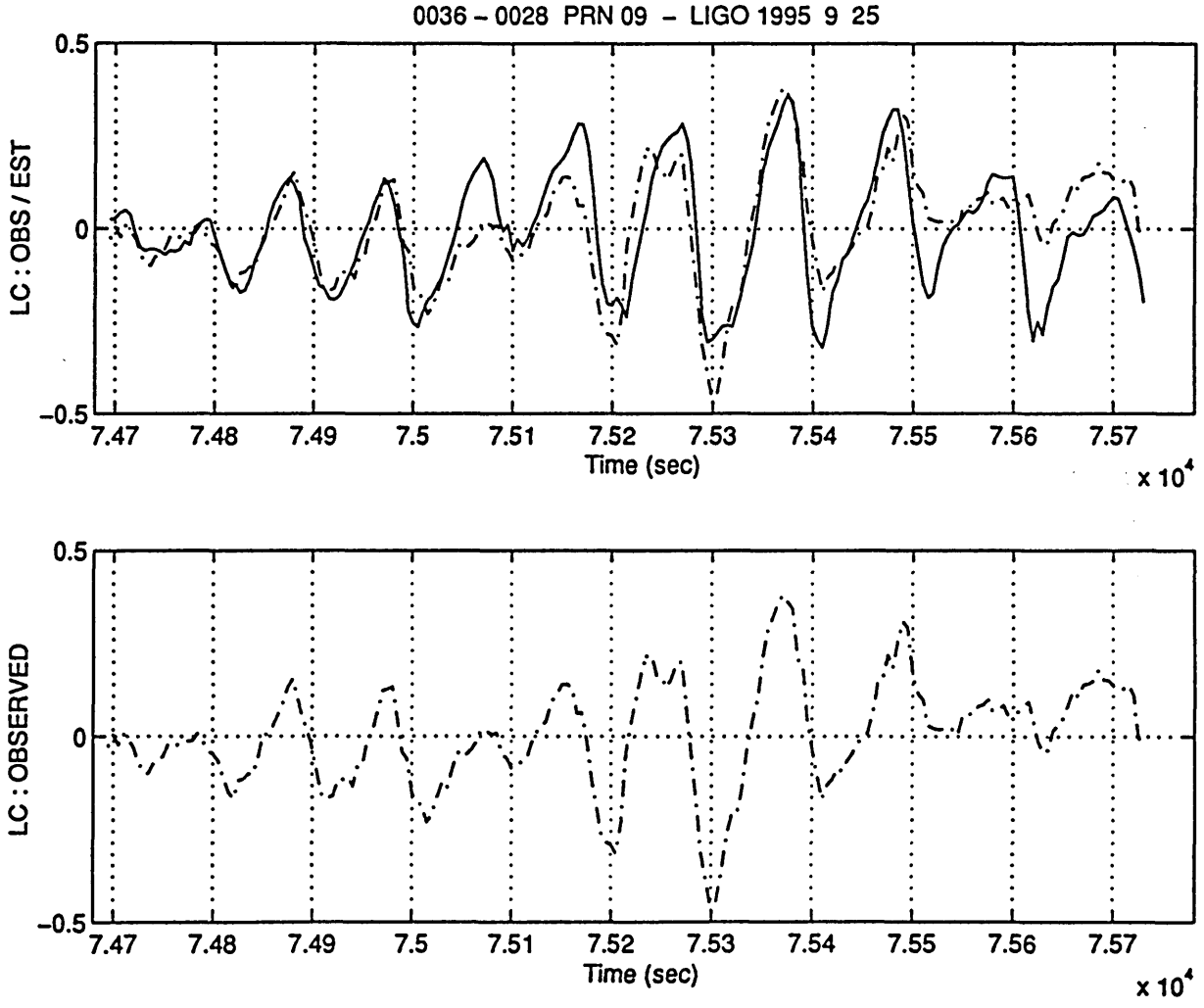

Fig. A.6.6 : 0028-0036 Satellite: PRN 09
Data acquisition date 25 9 1996
LC_OBS and LC_EST compared for t=7.47 -7.58 10^4 sec
Unit: [cycles].

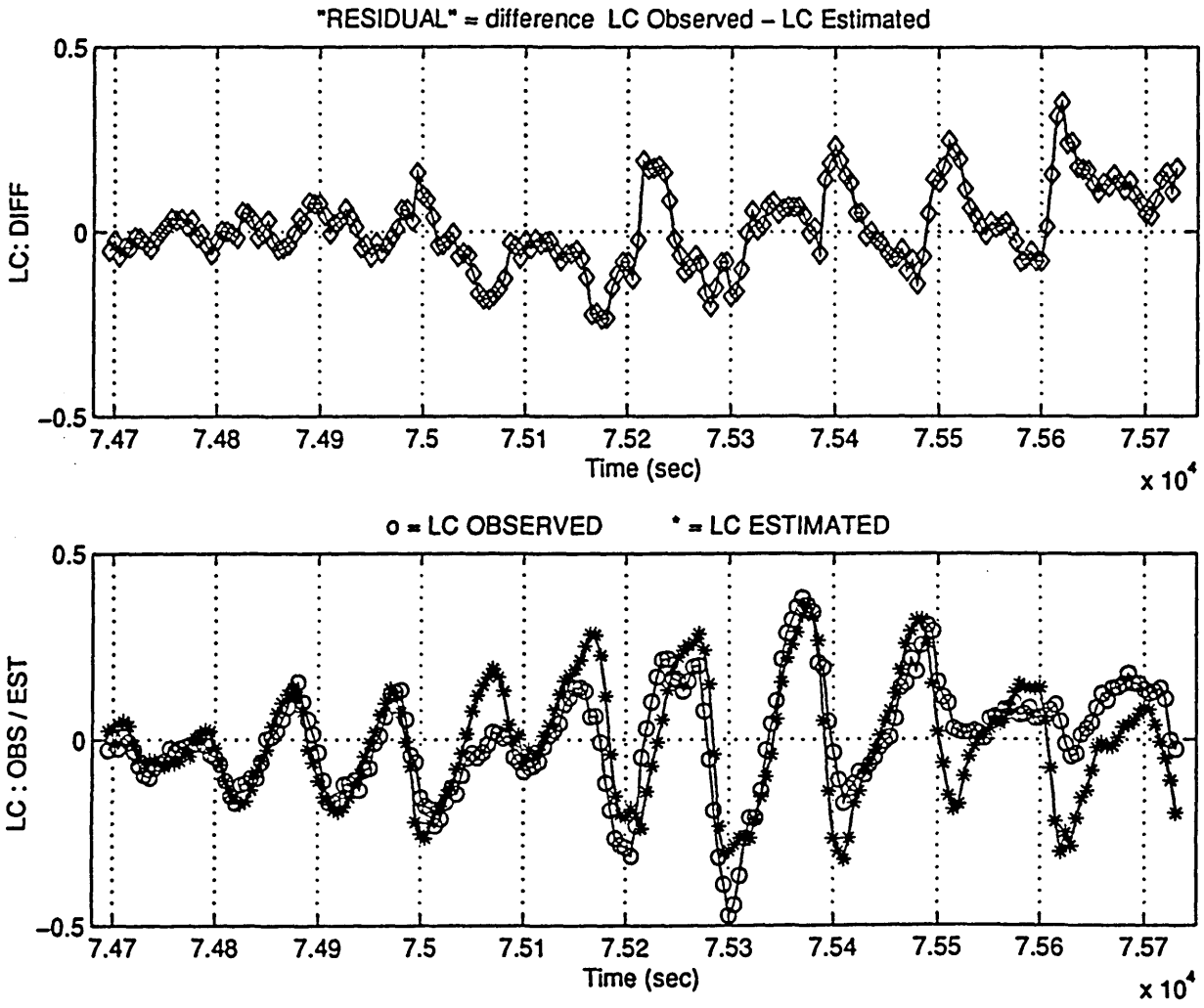

Fig. A.6.7.a) : 0028- 0036- PRN 09 (25 9 1996)
Phase residual LC_DIFF, determined as the difference between LC_OBS and LC_EST.
Unit: [cycles]

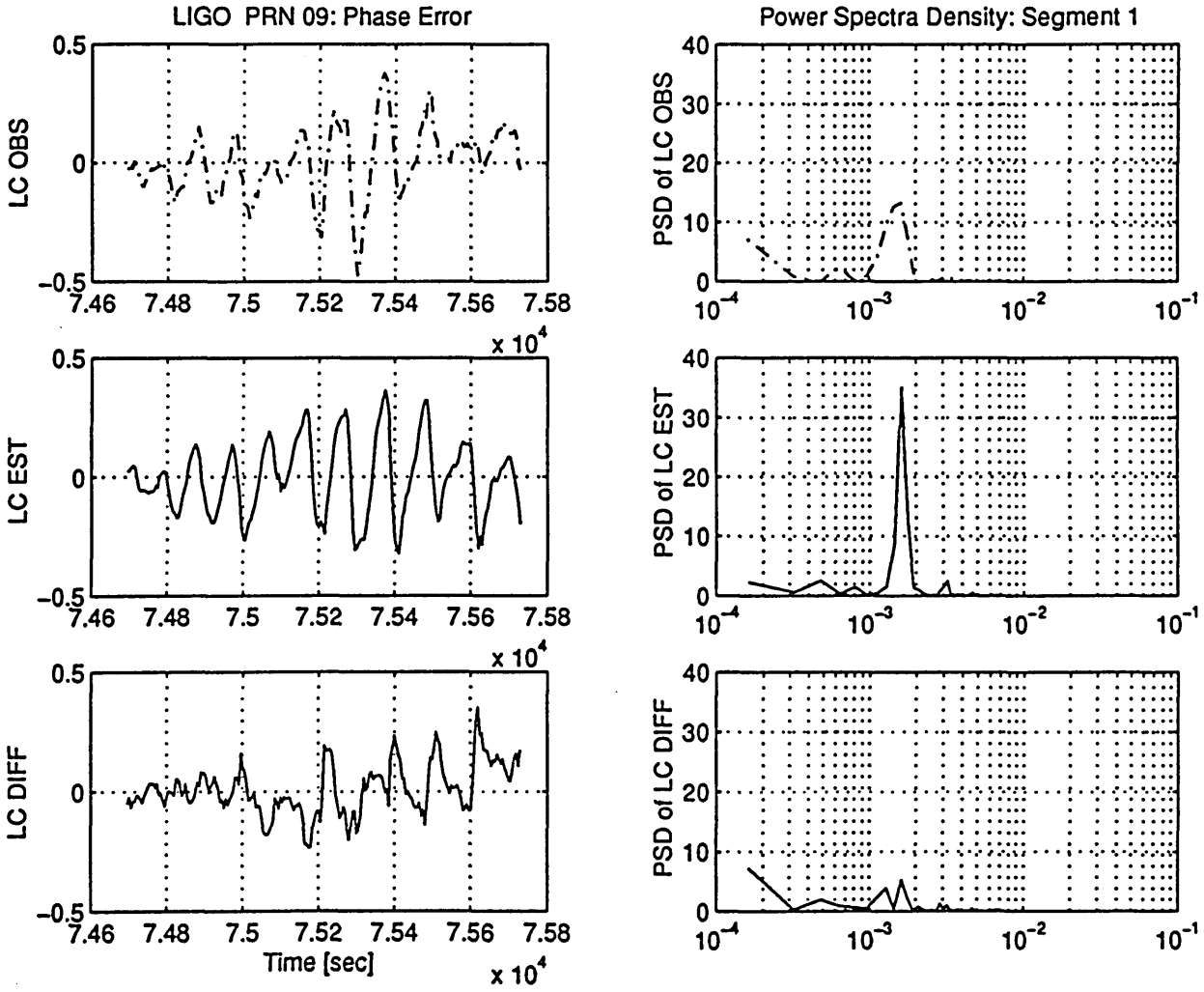

Fig. A.6.7.b) : 0028- 0036- PRN 09 (25 9 1996)
PSD of LC_OBS, LC_EST and LC_DIFF.
Unit: [cycles]^2

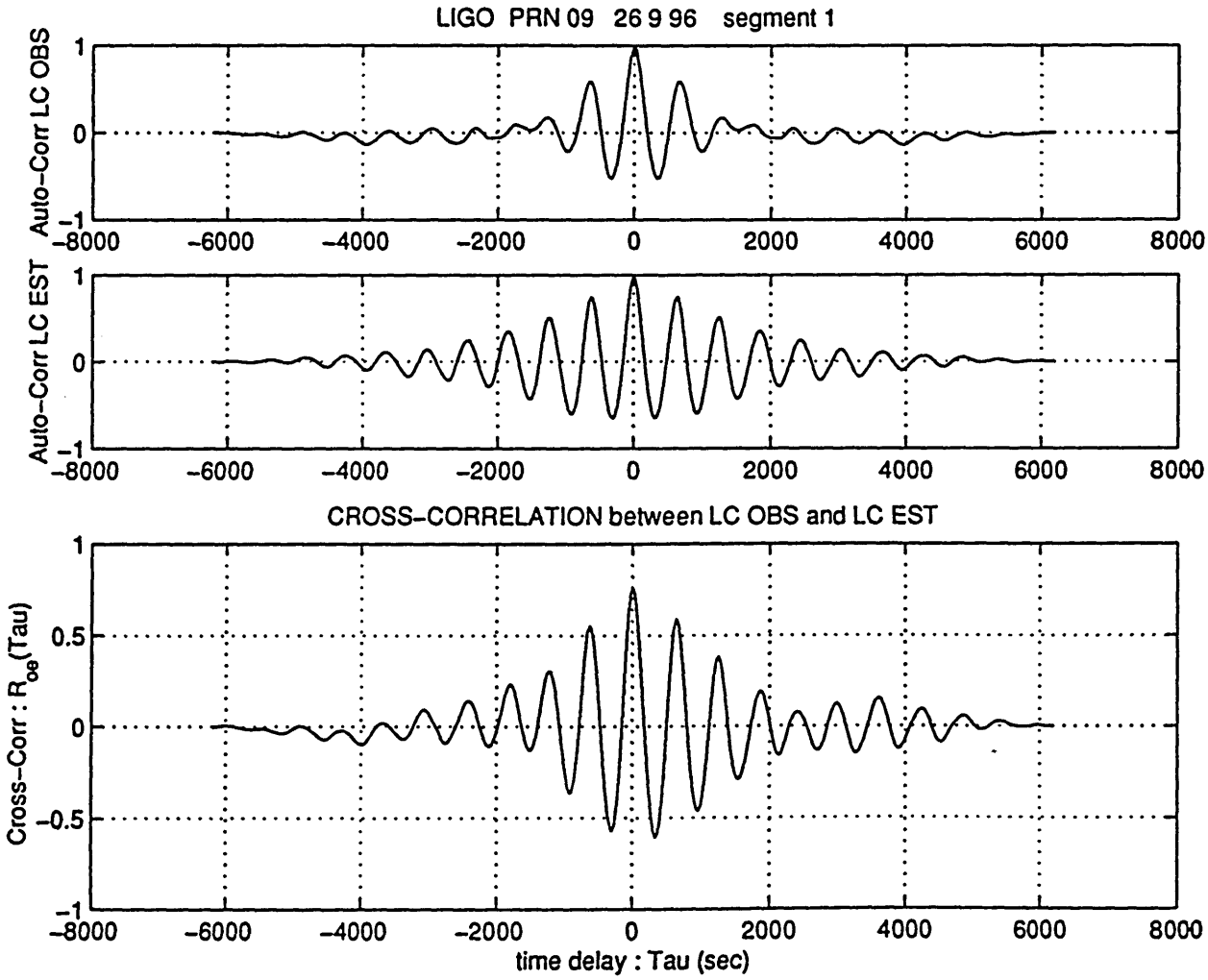

Fig. A.6.7.c) : 0028- 0036- PRN 09 (25 9 1996)
Auto Correlation of LC_OBS (R_{oo}) and LC_EST (R_{ee}).
Cross Correlation between them (R_{oe})
Unit: [cycles]^2

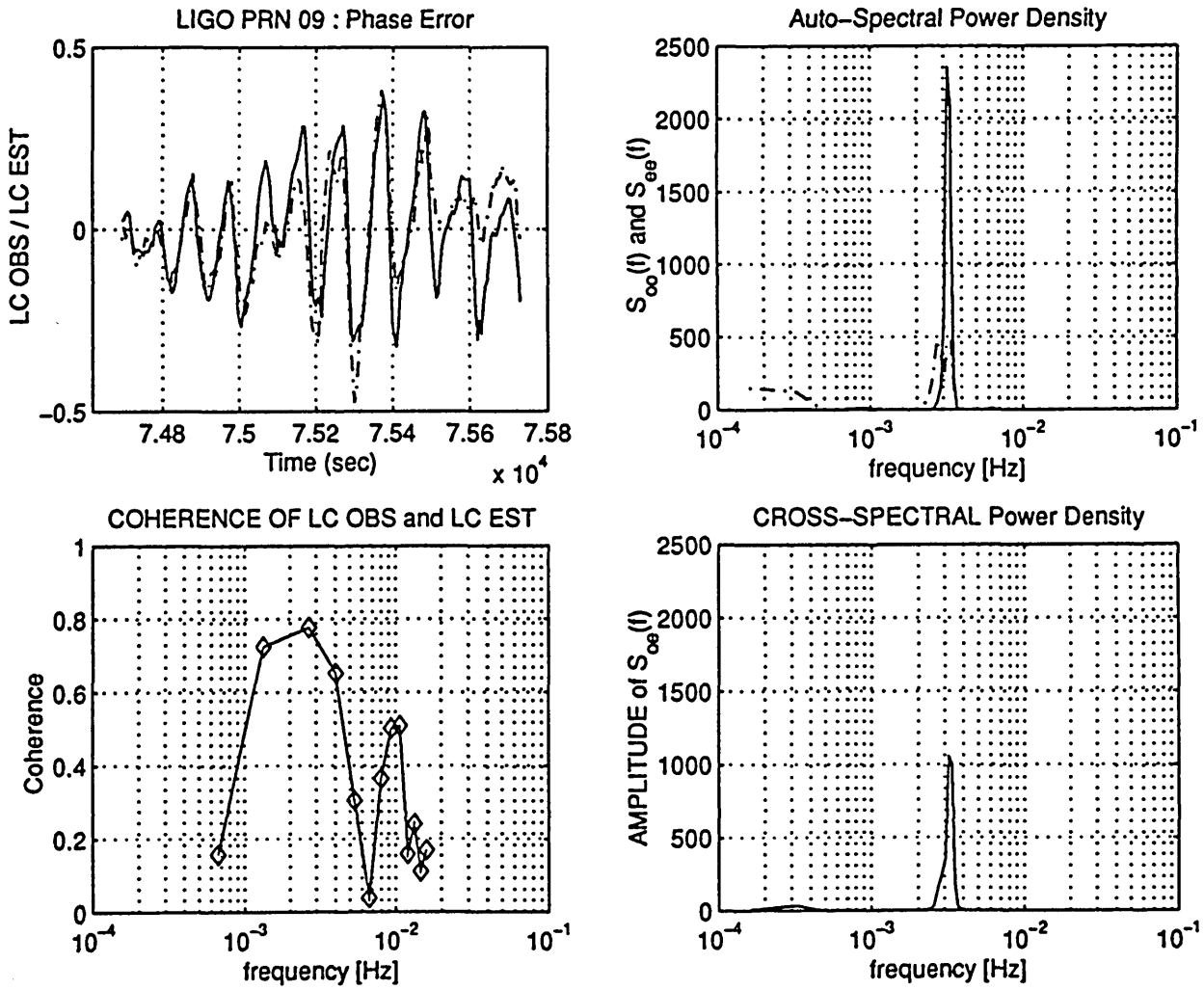

Fig. A.6.7.d) : 0028- 0036- PRN 09 (25 9 1996)
Auto Spectral Power Density of LC_OBS (S_{oo}) and of LC_EST (S_{ee}). Cross PSD between them (S_{oe})
Unit: [cycles]^2
Coherence function of LC_OBS and LC_EST

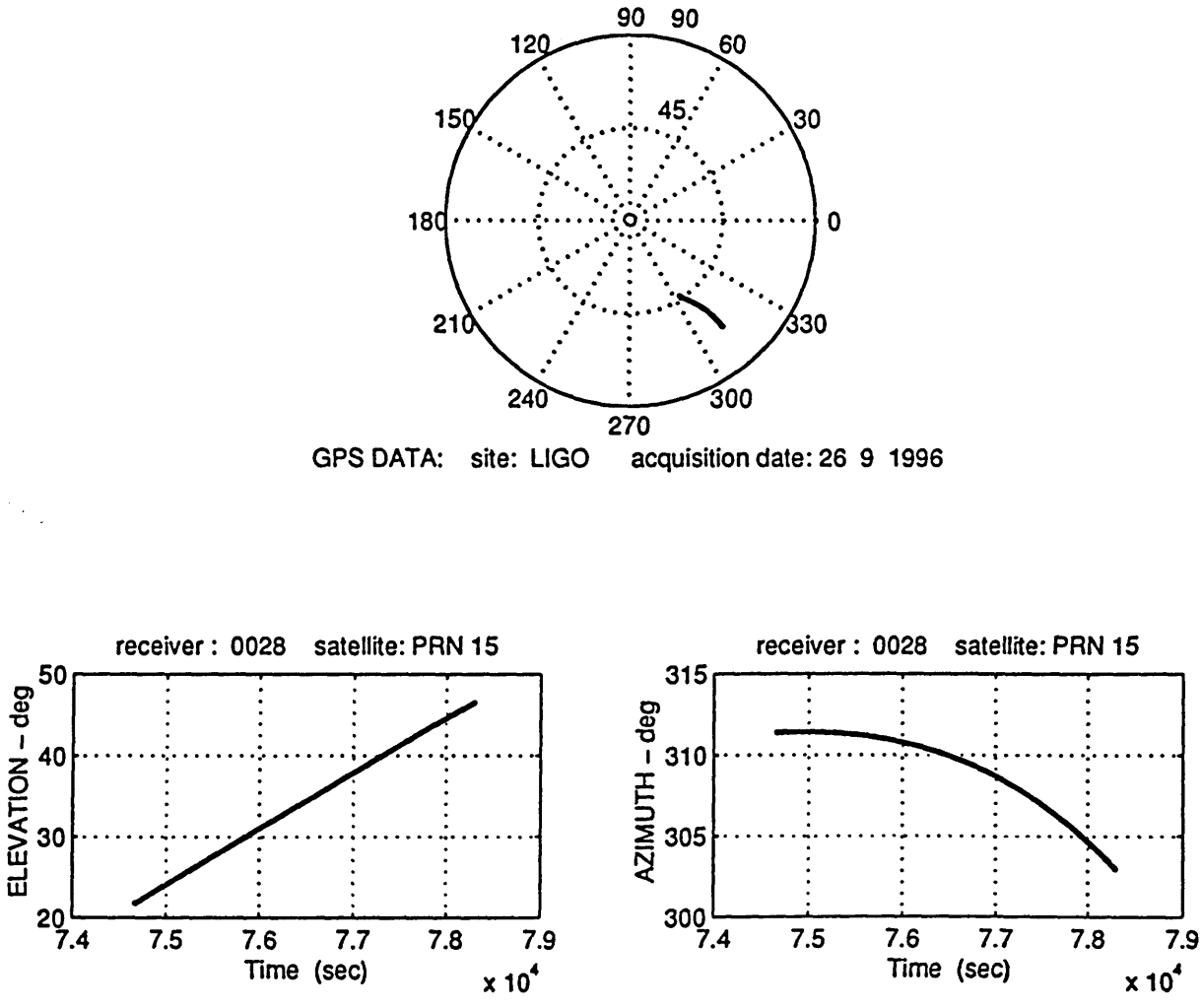

Fig. A.7.1 : Satellite visibility chart for PRN 15 (skymap). Elevation and azimuth of PRN 15 with respect to the station 0028

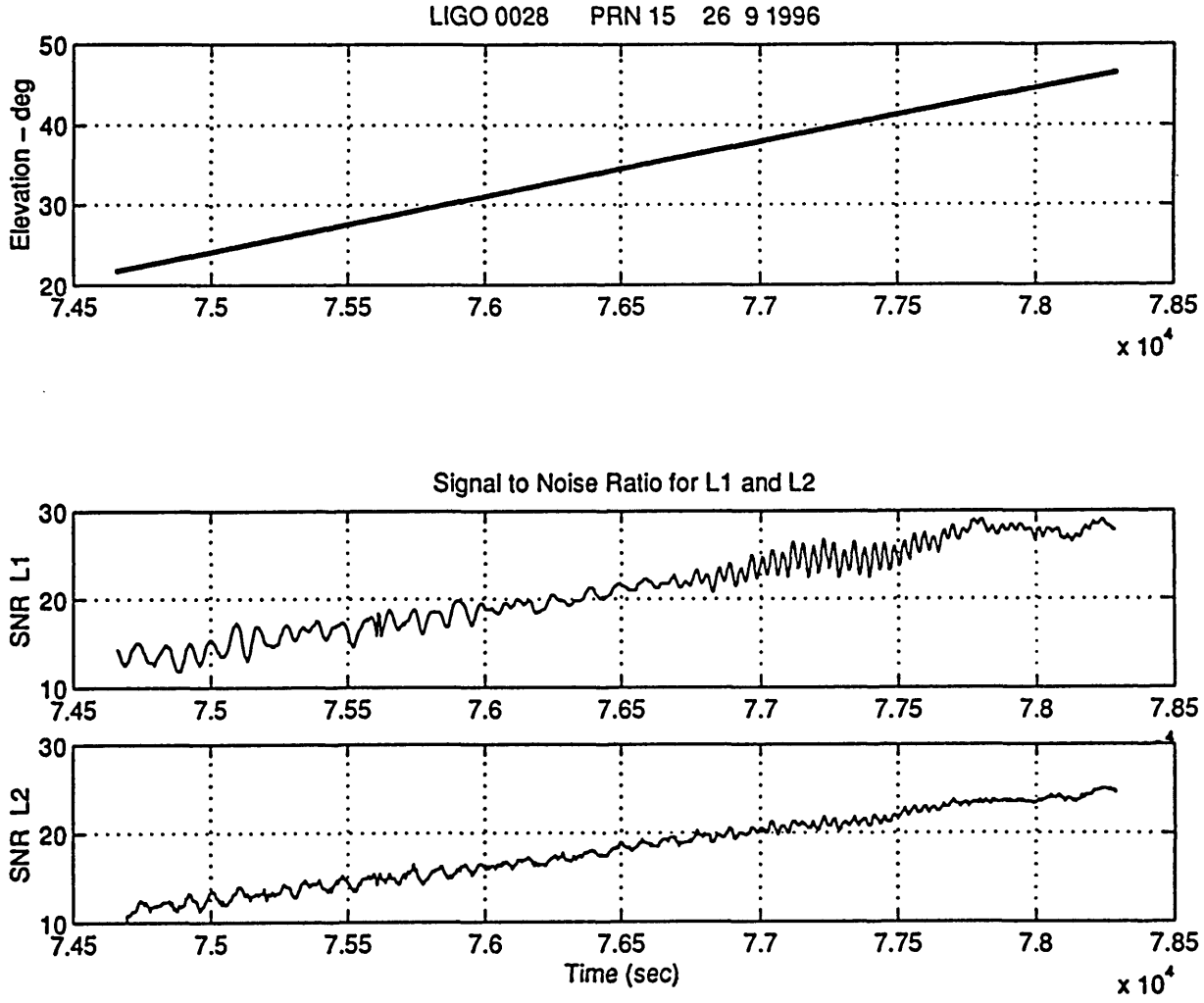

Fig. A.7.2 : Station: 0028- Satellite: PRN 15
Data acquisition date 25 9 1996
Signal-to-Noise-Ratio (SNR) for L_1 and L_2.

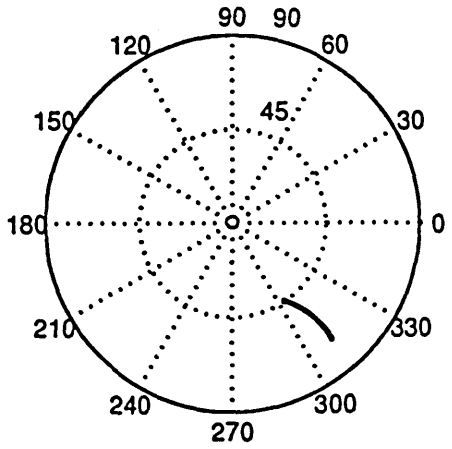

GPS DATA: site: LIGO acquisition date: 26 9 1996

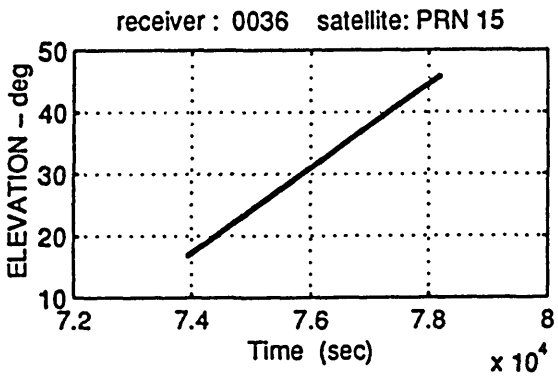

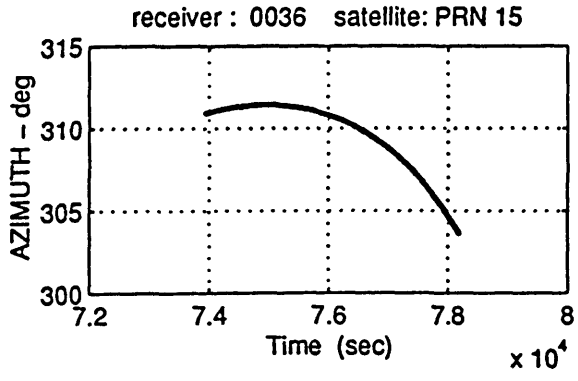

Fig. A.7.3 : Satellite visibility chart for PRN 15 (skymap). Elevation and azimuth of PRN 15 with respect to the station 0036

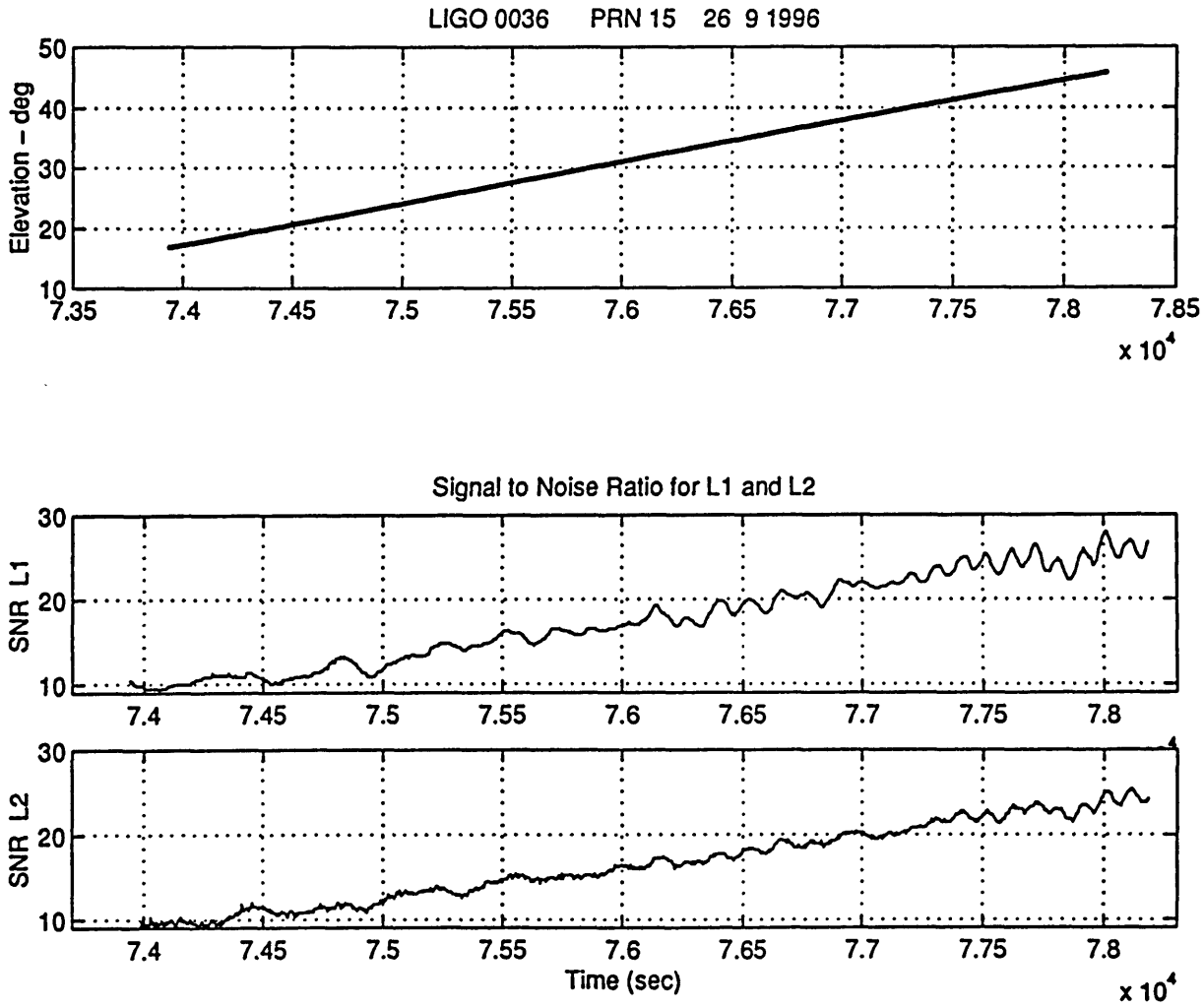

Fig. A.7.4 : Station: 0036- Satellite: PRN 15
Data acquisition date 25 9 1996
Signal-to-Noise-Ratio (SNR) for L_1 and L_2.

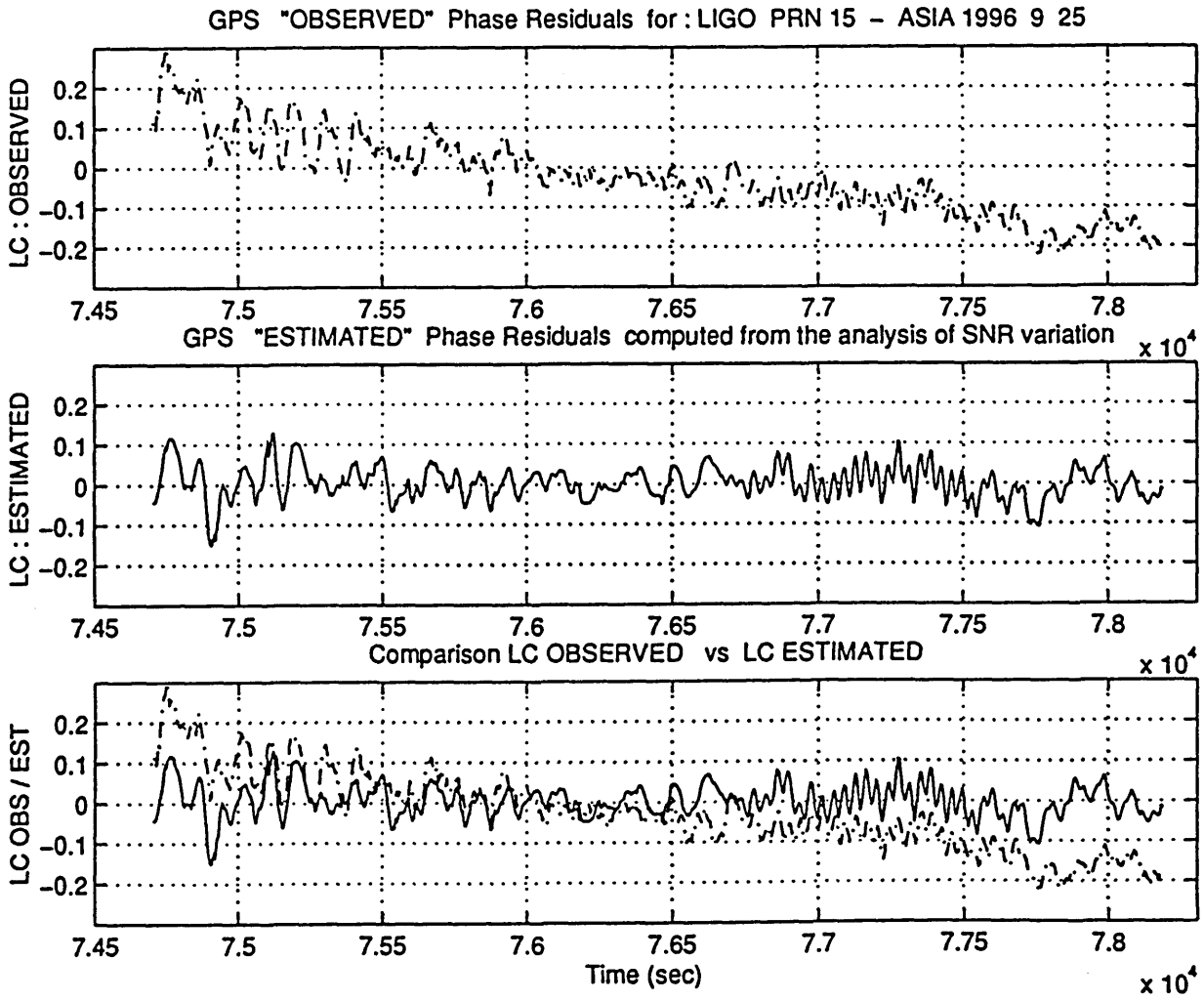

Fig. A.7.5: Stations: 0028- 0036 Satellite: PRN 15 -
Data acquisition date 25 9 1996
The observed phase residual (LC_OBS) is compared with the multipath phase error estimated from the SNR (LC_EST) (differential mode)
Unit: [cycles]

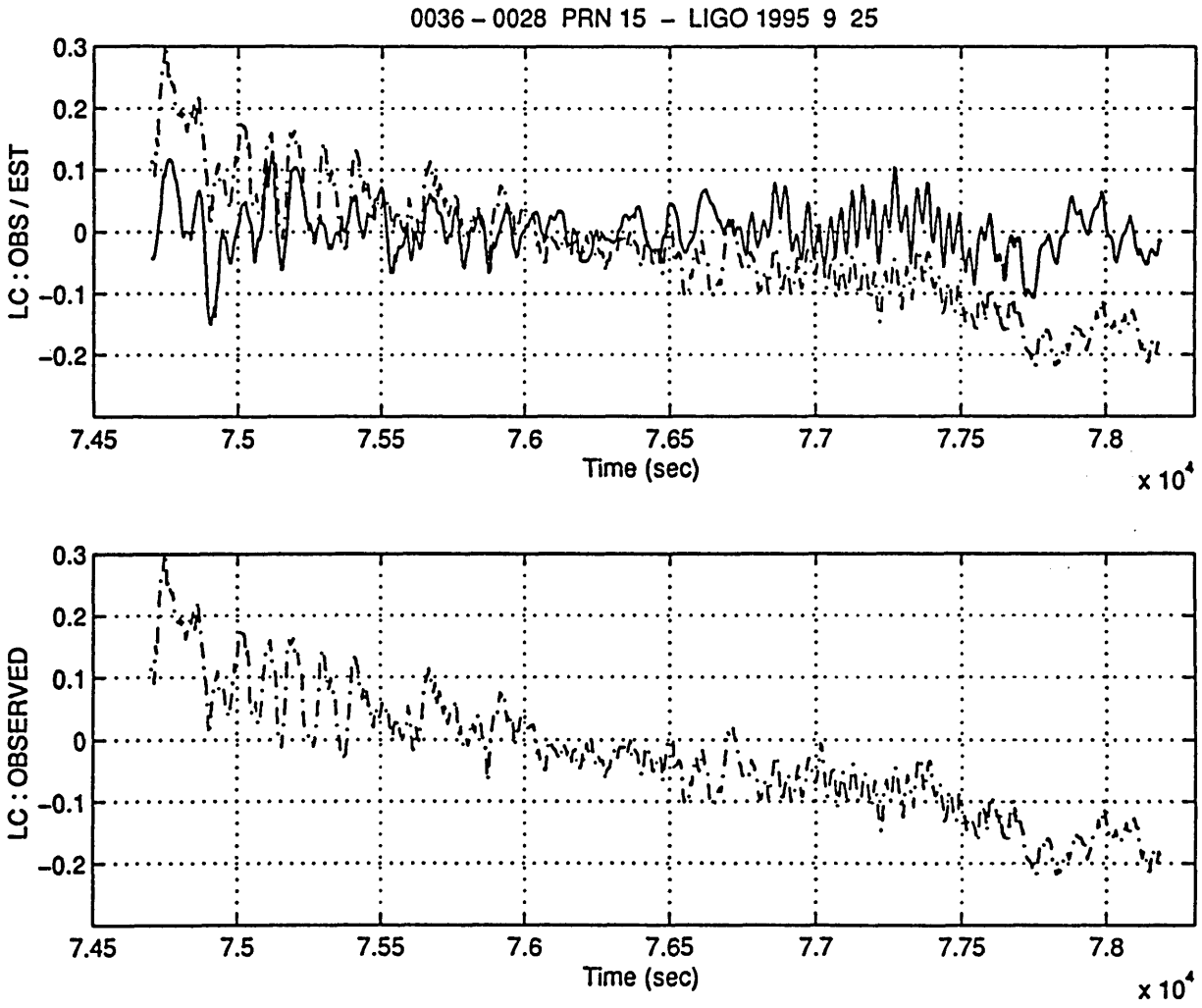

Fig. A.7.6 : 0028- 0036 Satellite: PRN 15
Data acquisition date 25 9 1996
LC_OBS and LC_EST compared for t=7.45 - 7.85 10^4 sec
Unit: [cycles]

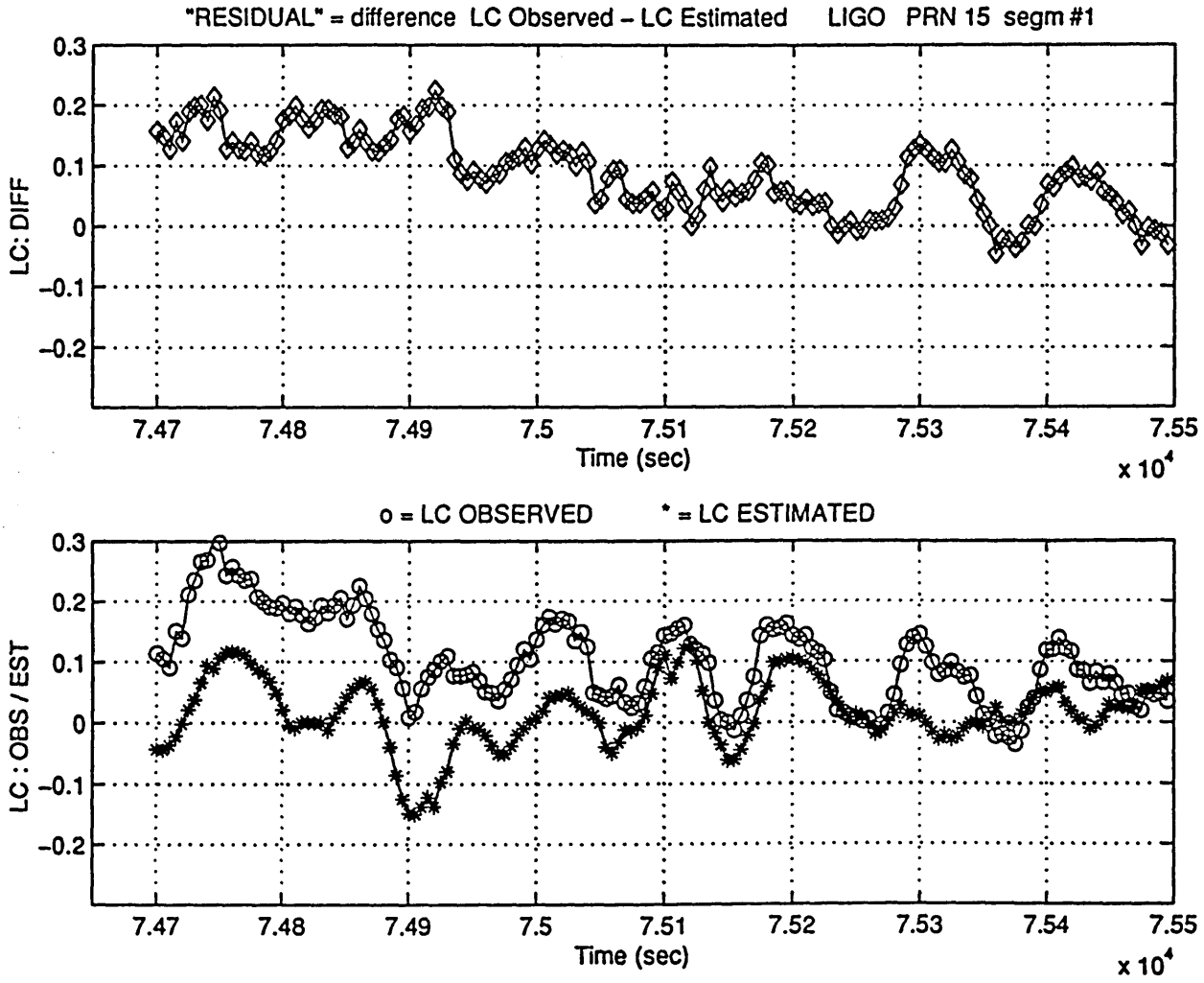

Fig. A.7.7.a) : 0028- 0036- PRN 15 (25 9 1996) [segment #1]
Phase residual LC_DIFF, determined as the difference between LC_OBS and LC_EST.
Unit: [cycles]

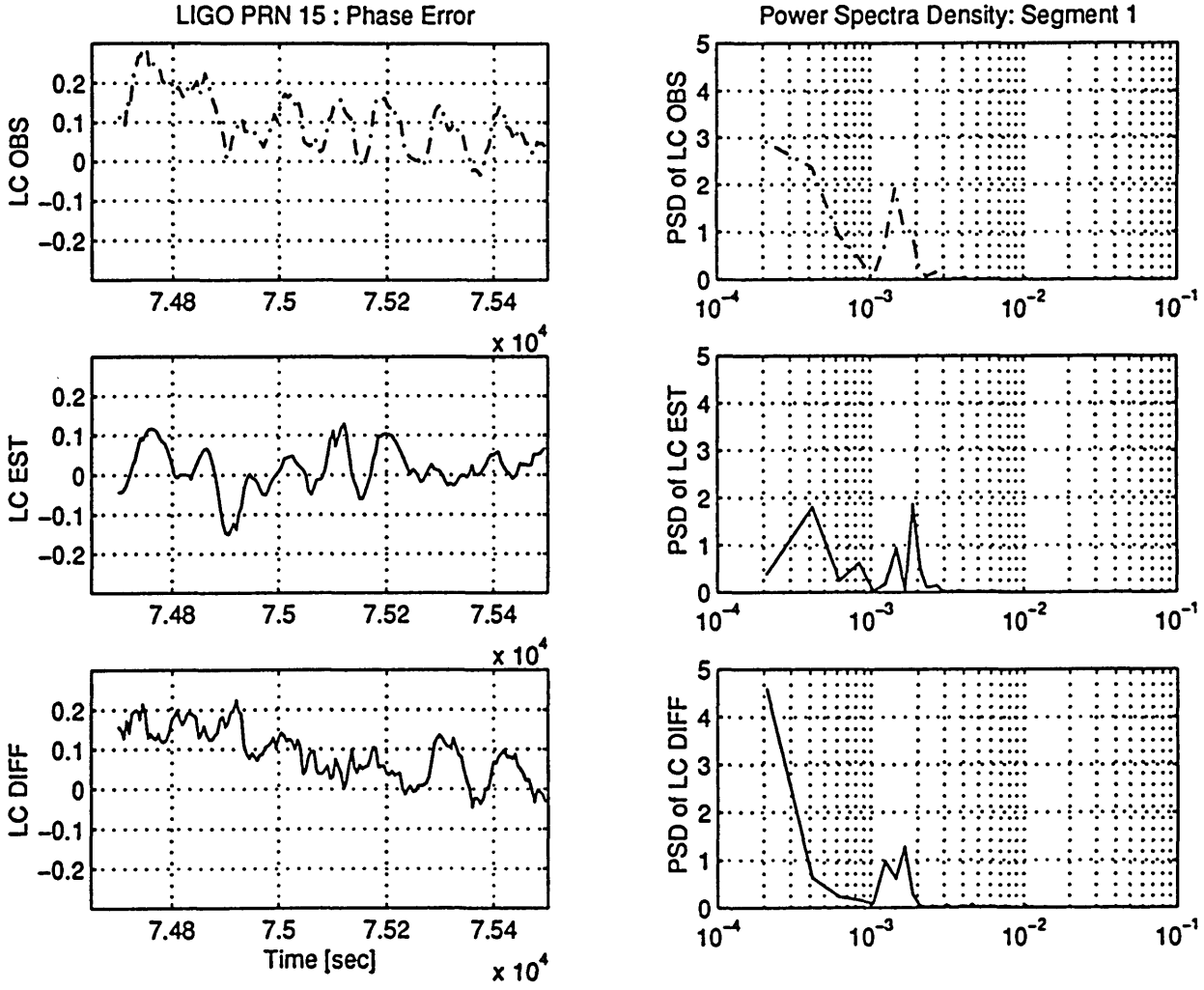

Fig. A.7.7.b) : 0028- 0036- PRN 15 (25 9 1996) [segment #1]
PSD of LC_OBS, LC_EST and LC_DIFF.
Unit: [cycles]^2

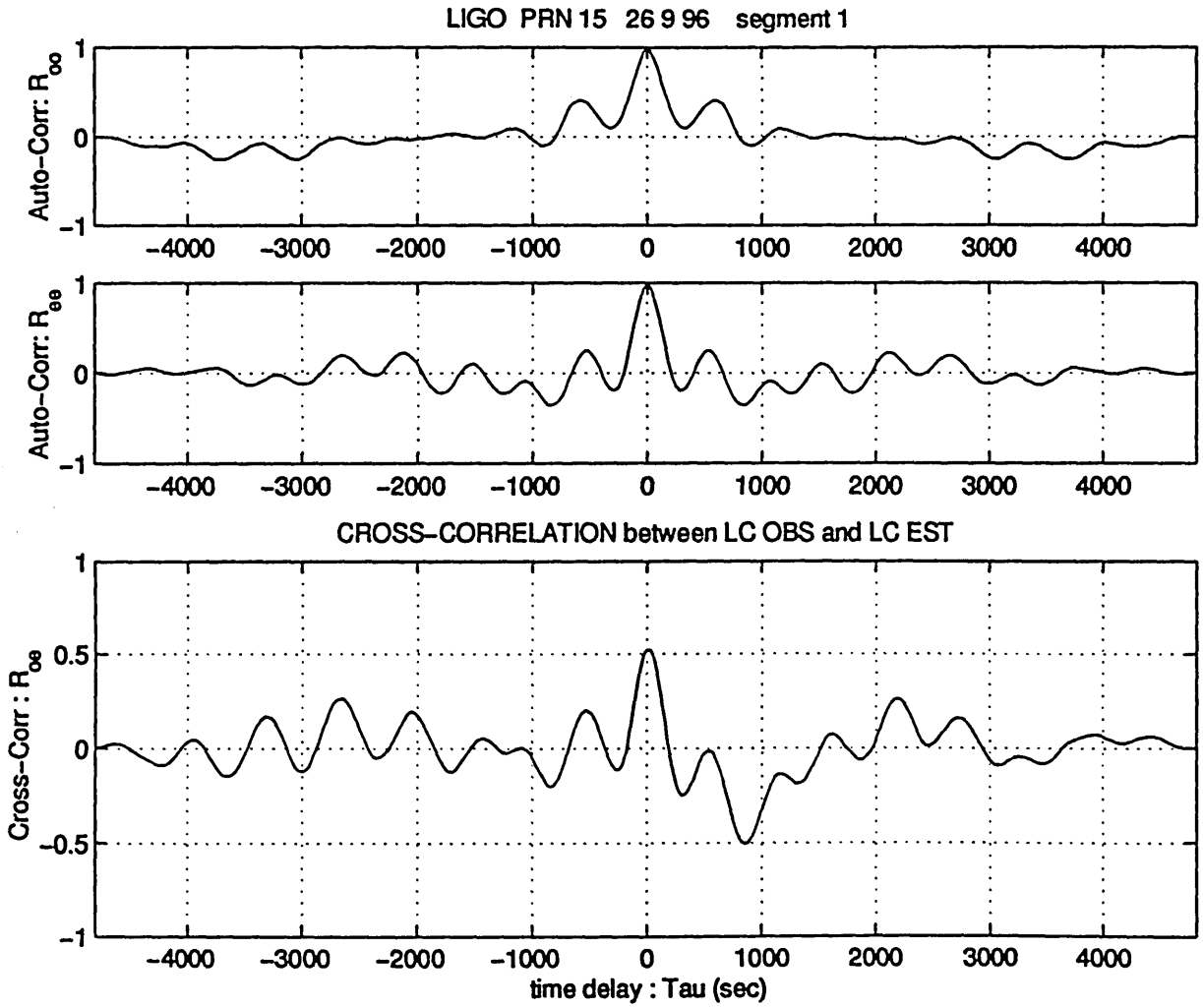

Fig. A.7.7.c) : 0028- 0036- PRN 15 (25 9 1996) [segment #1]
Auto Correlation of LC_OBS (R_{oo}) and LC_EST (R_{ee}).
Cross Correlation between them (R_{oe})
Unit: [cycles]^2

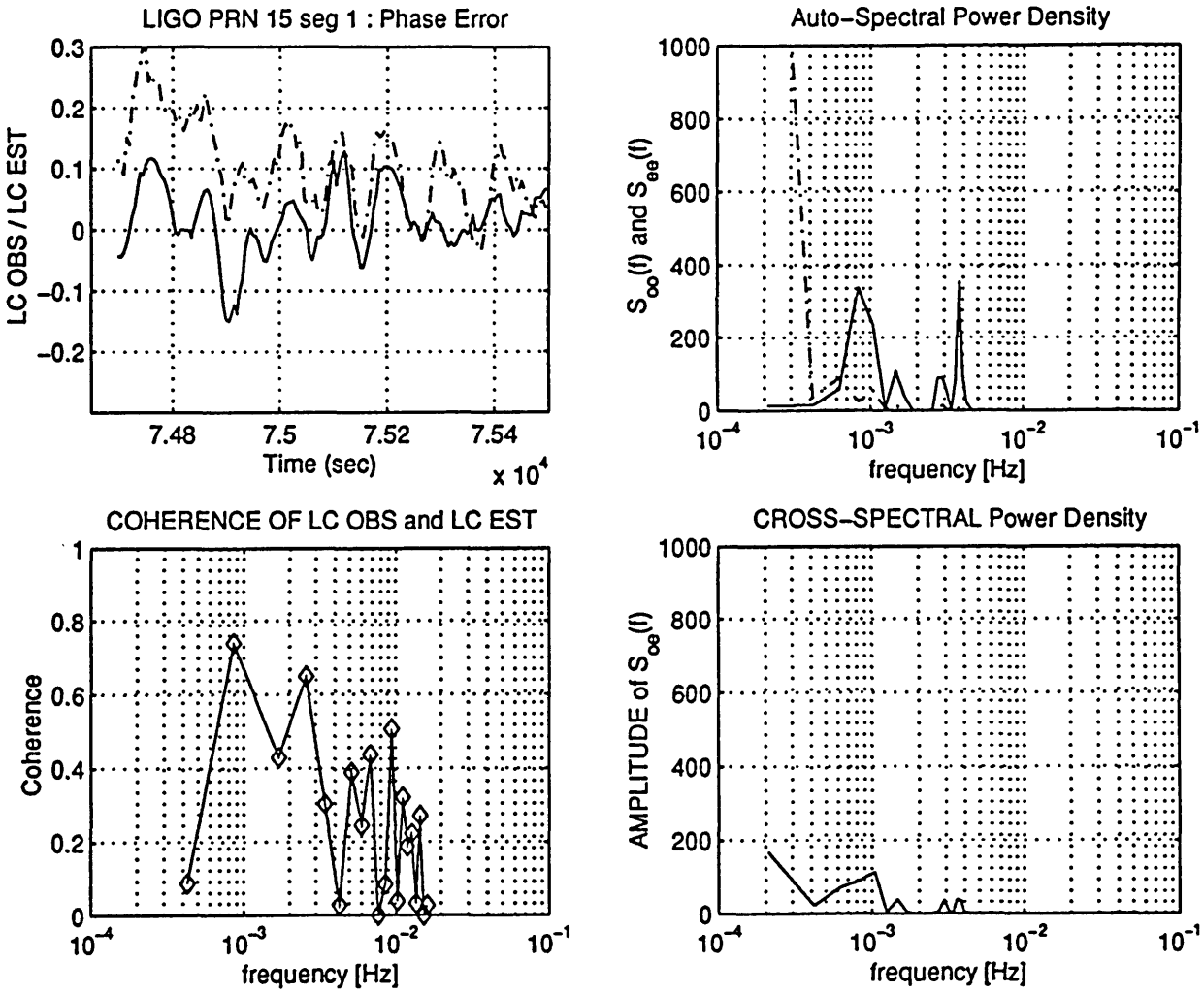

Fig. A.7.7.d) : 0028- 0036- PRN 15 (25 9 1996) [segment #1]
Auto Spectral Power Density of LC_OBS (S_{oo}) and of LC_EST (S_{ee}). Cross PSD between them (S_{oe})
Unit: [cycles]^2
Coherence function of LC_OBS and LC_EST

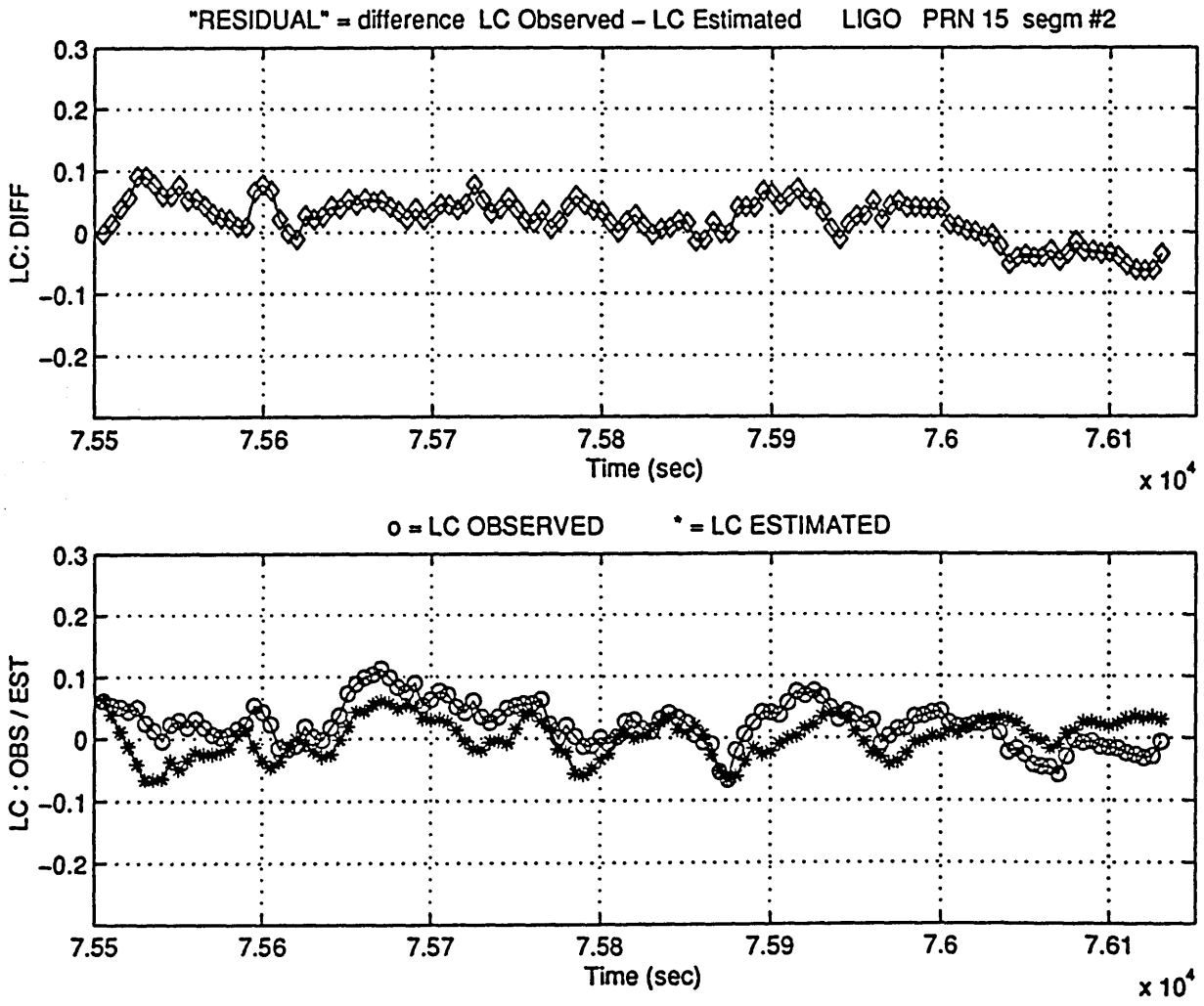

Fig. A.7.8.a) : 0028- 0036- PRN 15 (25 9 1996) [segment #2]
Phase residual LC_DIFF, determined as the difference between LC_OBS and LC_EST.
Unit: [cycles].

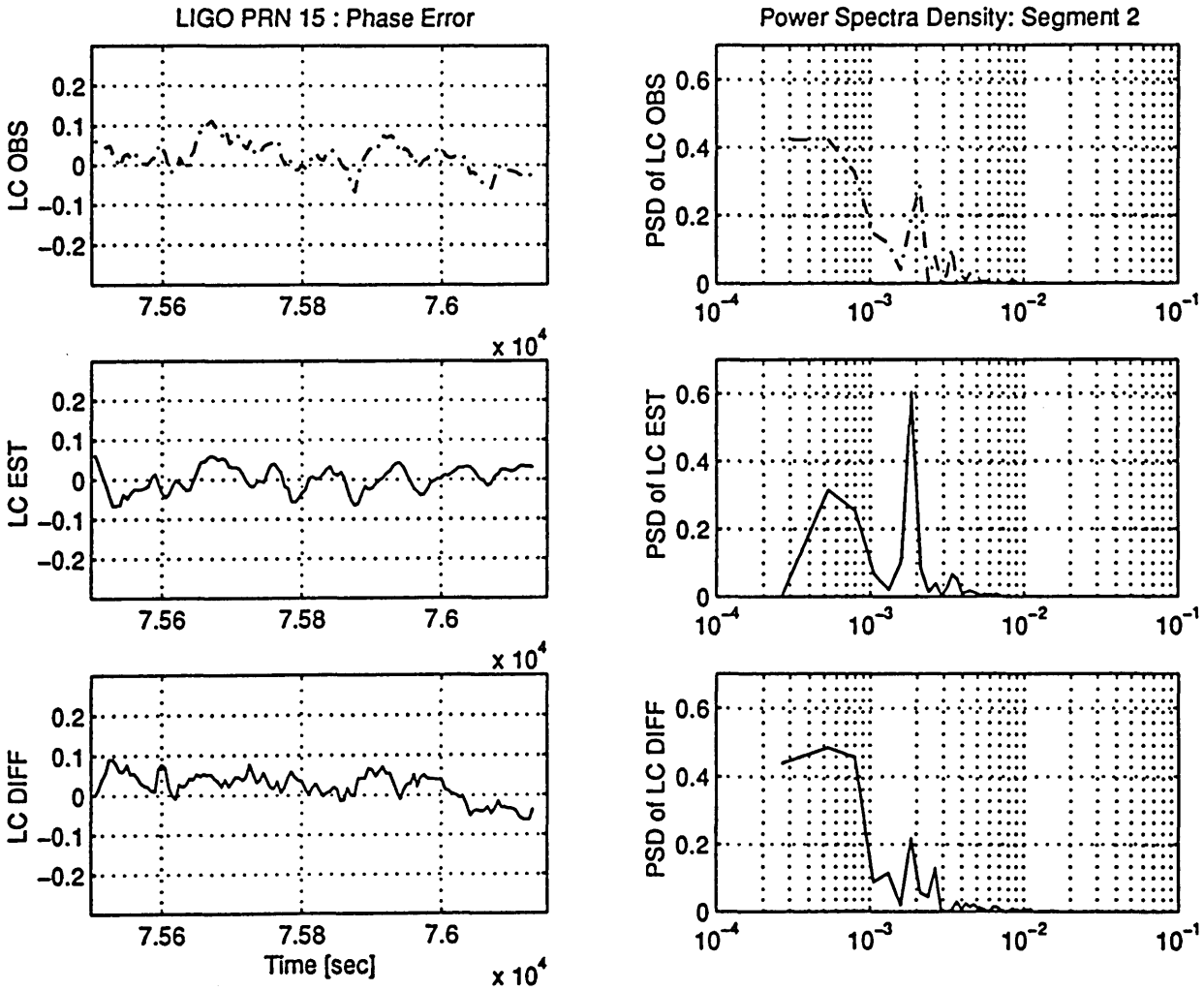

Fig. A.7.8.b) : 0028- 0036- PRN 15 (25 9 1996) [segment #2]
PSD of LC_OBS, LC_EST and LC_DIFF.
Unit: [cycles]^2

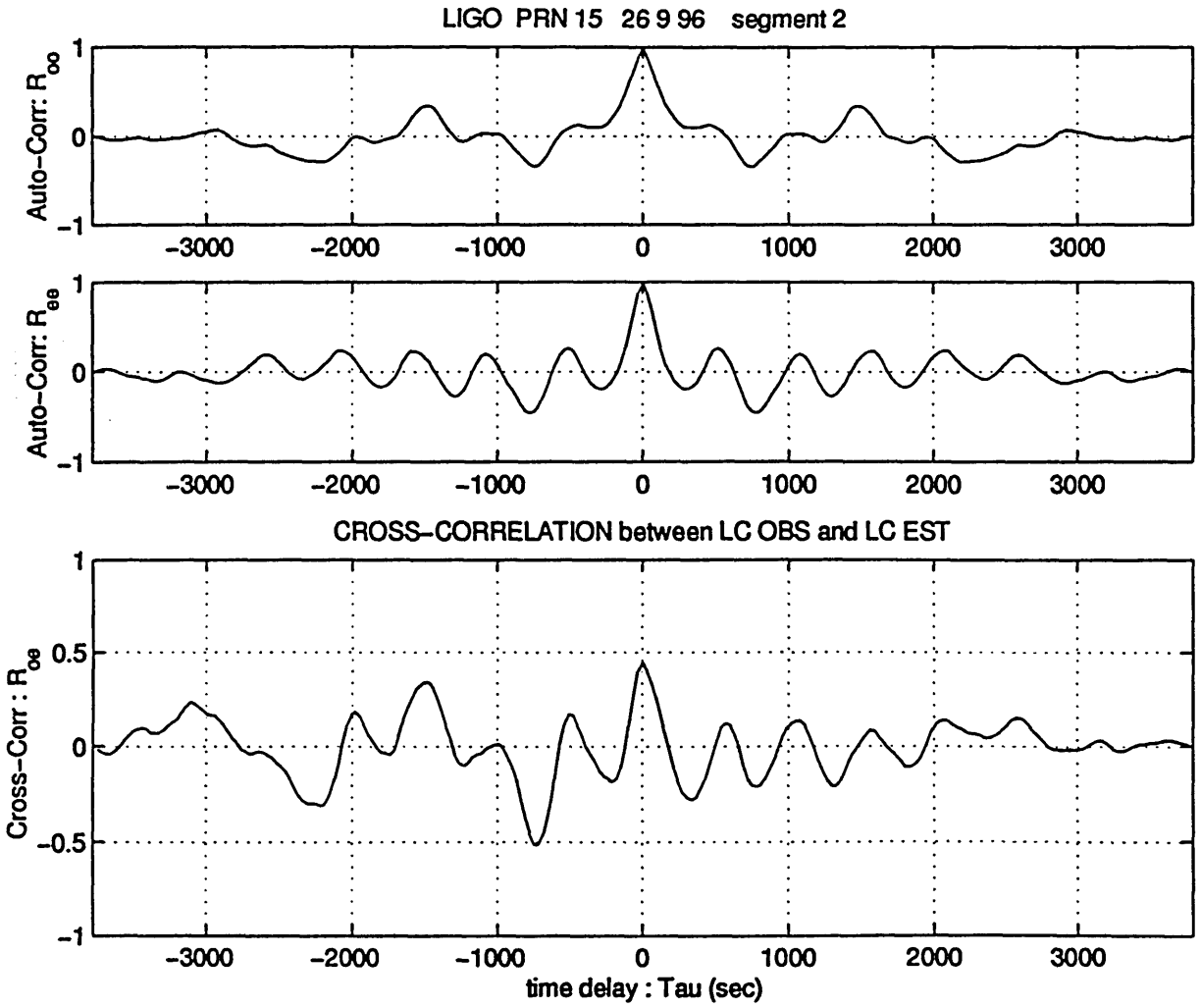

Fig. A.7.8.c) : 0028- 0036- PRN 15 (25 9 1996) [segment #2]
Auto Correlation of LC_OBS (R_{oo}) and LC_EST (R_{ee}).
Cross Correlation between them (R_{oe})
Unit: [cycles]^2

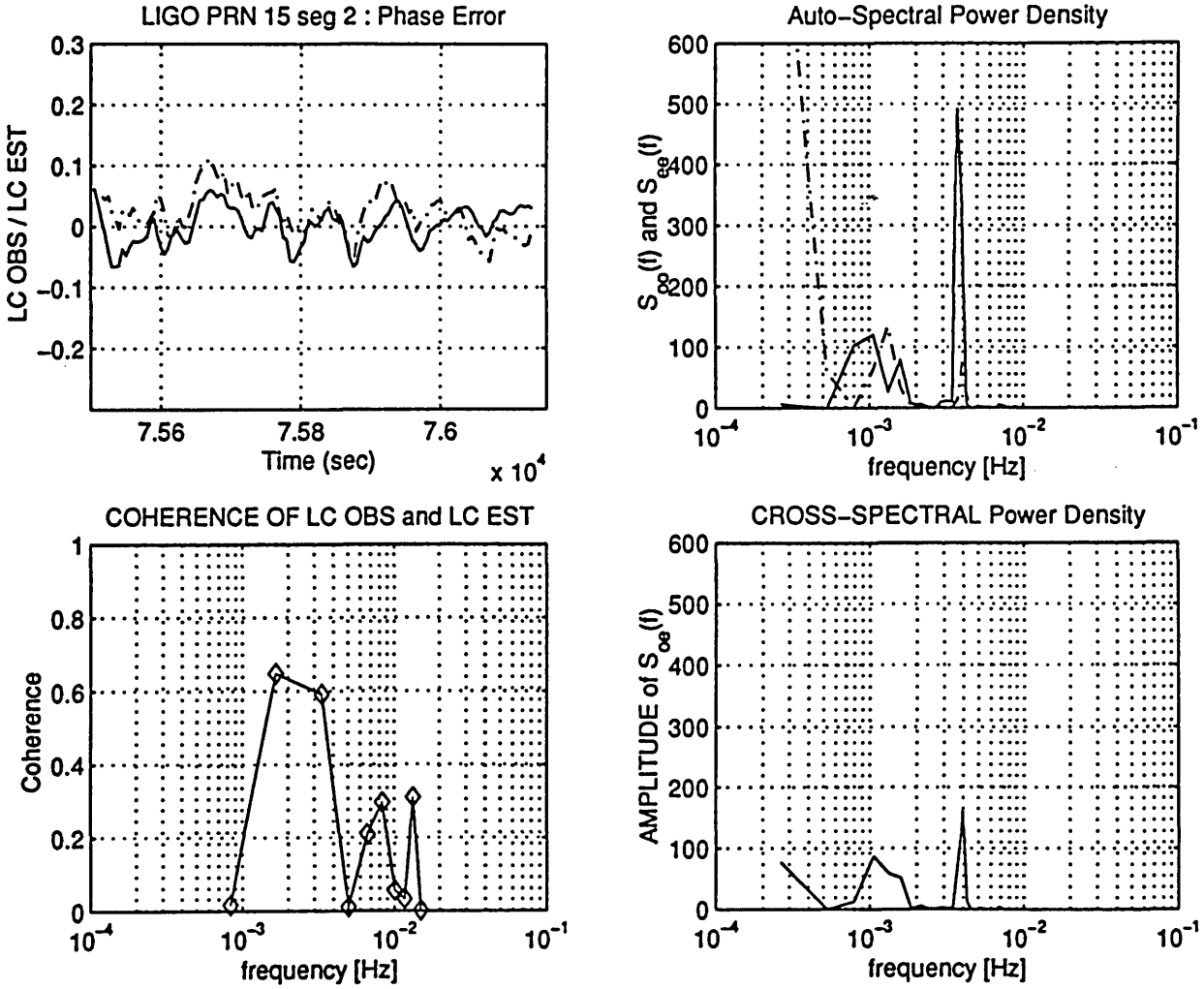

Fig. A.7.8.d) : 0028- 0036- PRN 15 (25 9 1996) [segment #2]
Auto Spectral Power Density of LC_OBS (S_{oo}) and of LC_EST (S_{ee}). Cross PSD between them (S_{oe})
Unit: [cycles]^2
Coherence function of LC_OBS and LC_EST

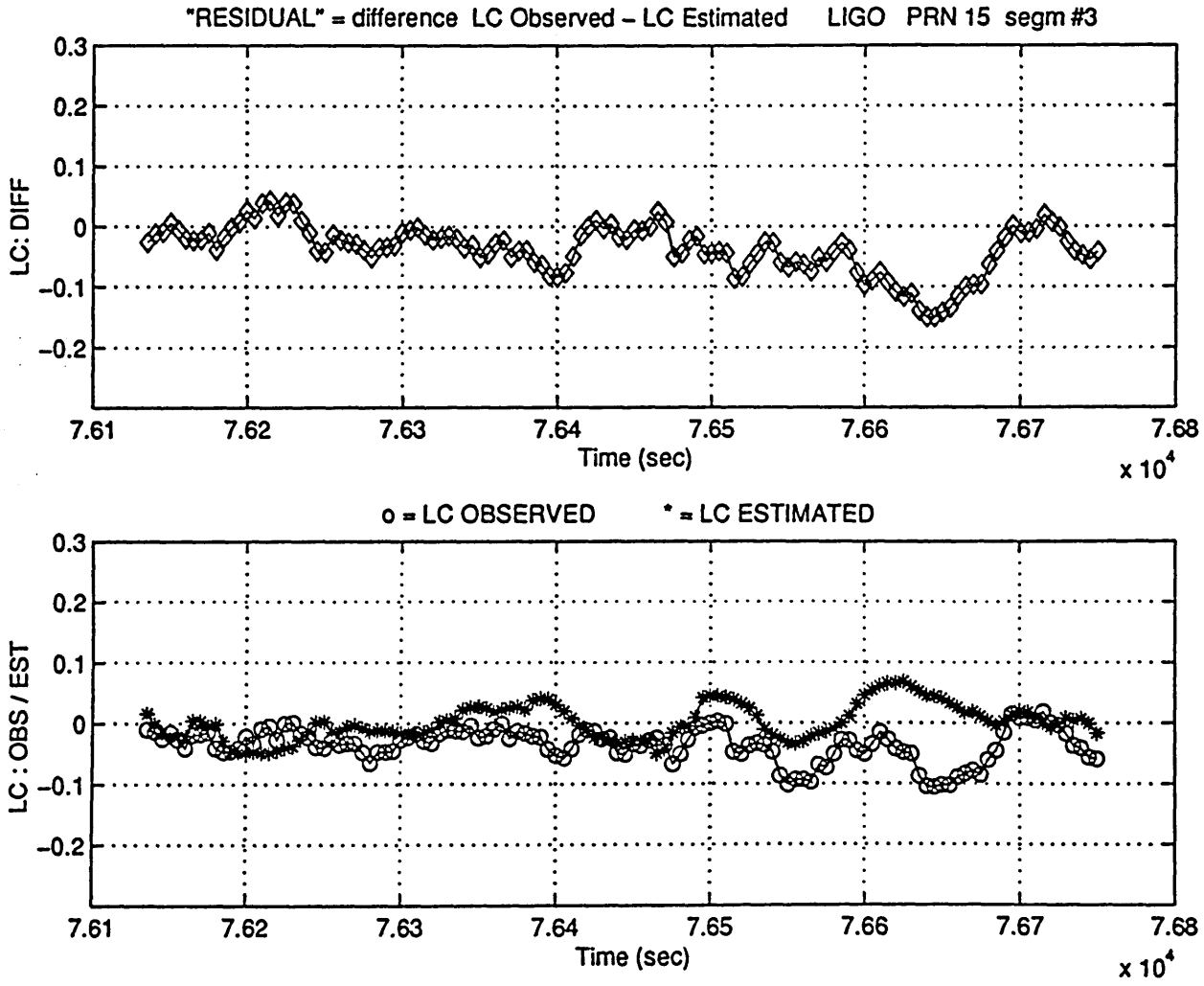

Fig. A.7.9.a) : 0028- 0036- PRN 15 (25 9 1996) [segment #3]
Phase residual LC_DIFF, determined as the difference between LC_OBS and LC_EST.
Unit: [cycles].

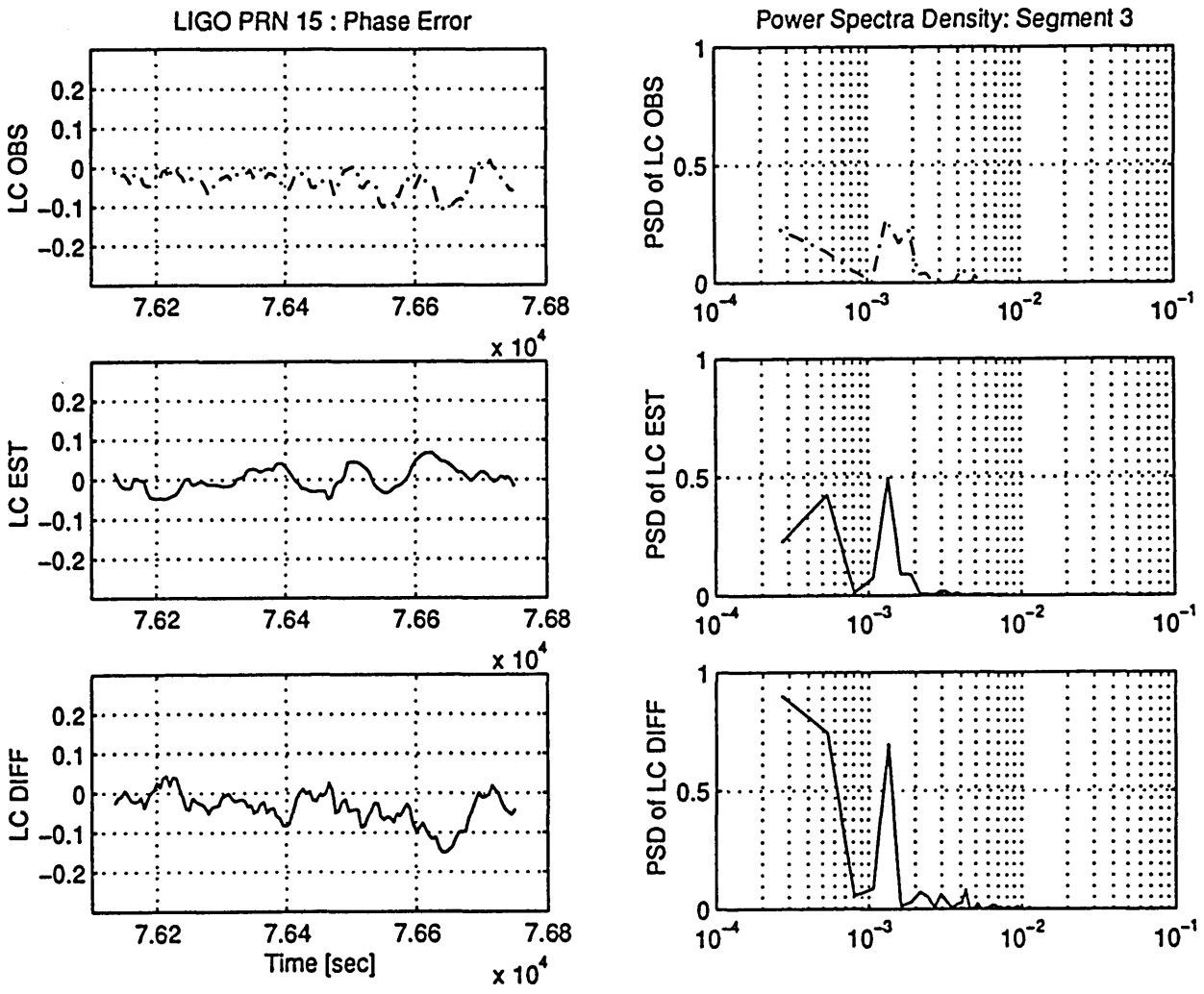

Fig. A.7.9.b) : 0028- 0036- PRN 15 (25 9 1996) [segment #3]
PSD of LC_OBS, LC_EST and LC_DIFF.
Unit: [cycles]^2

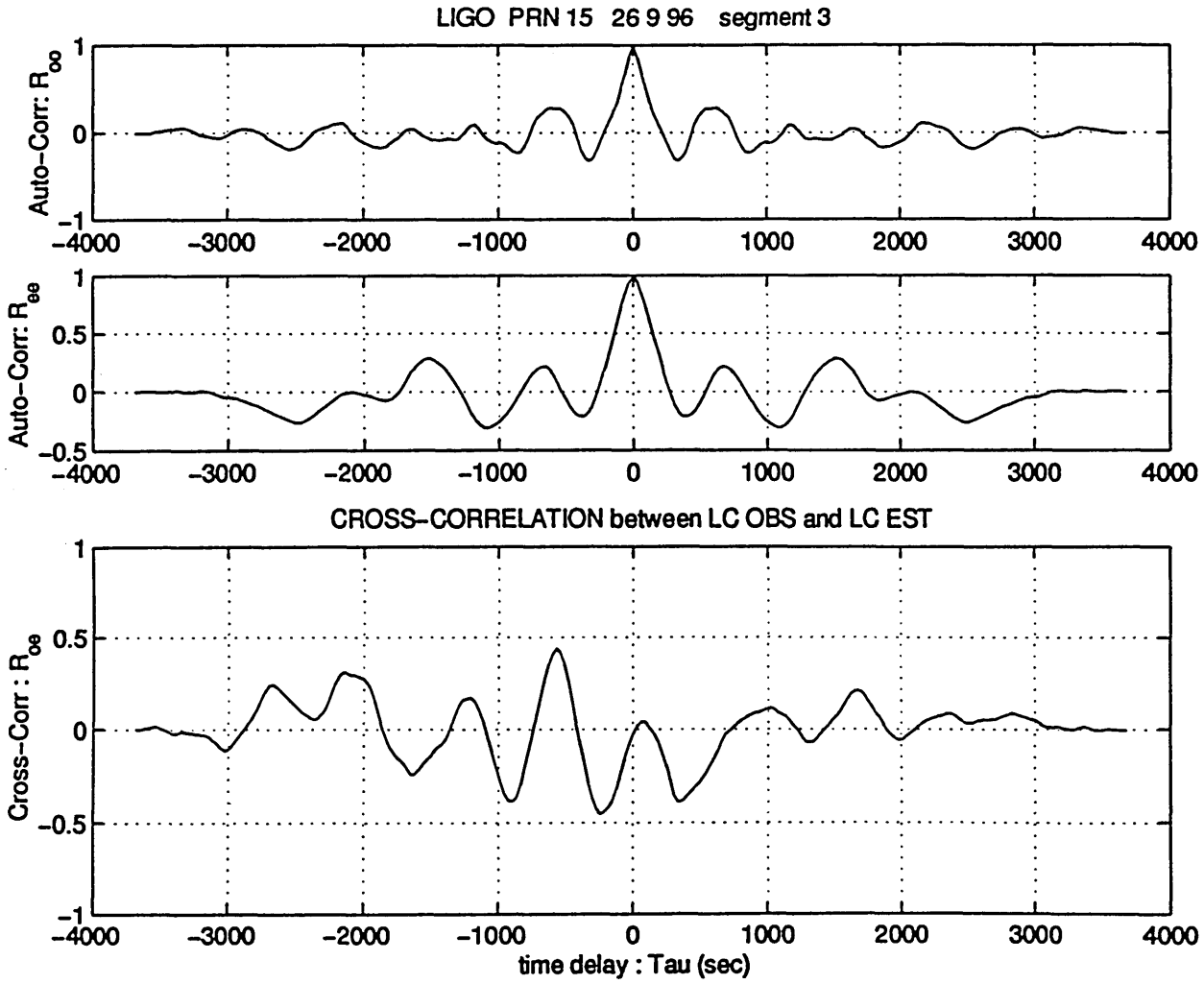

Fig. A.7.9.c) : 0028- 0036- PRN 15 (25 9 1996) [segment #3]
Auto Correlation of LC_OBS (R_{oo}) and LC_EST (R_{ee}).
Cross Correlation between them (R_{oe})
Unit: [cycles]^2

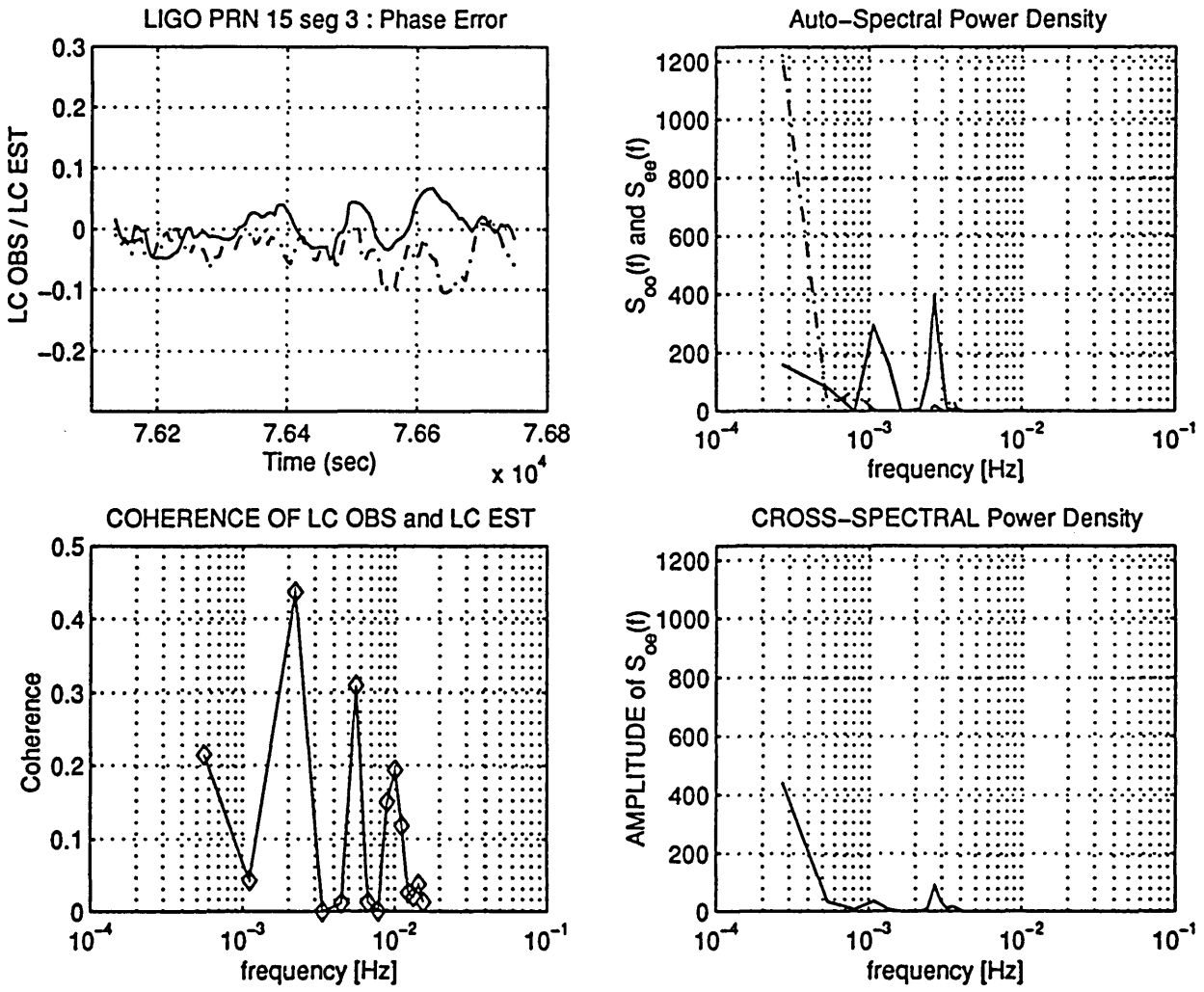

Fig. A.7.9.d) : 0028- 0036- PRN 15 (25 9 1996) [segment #3]
Auto Spectral Power Density of LC_OBS (S_{oo}) and of LC_EST (S_{ee}). Cross PSD between them (S_{oe})
Unit: [cycles]^2
Coherence function of LC_OBS and LC_EST

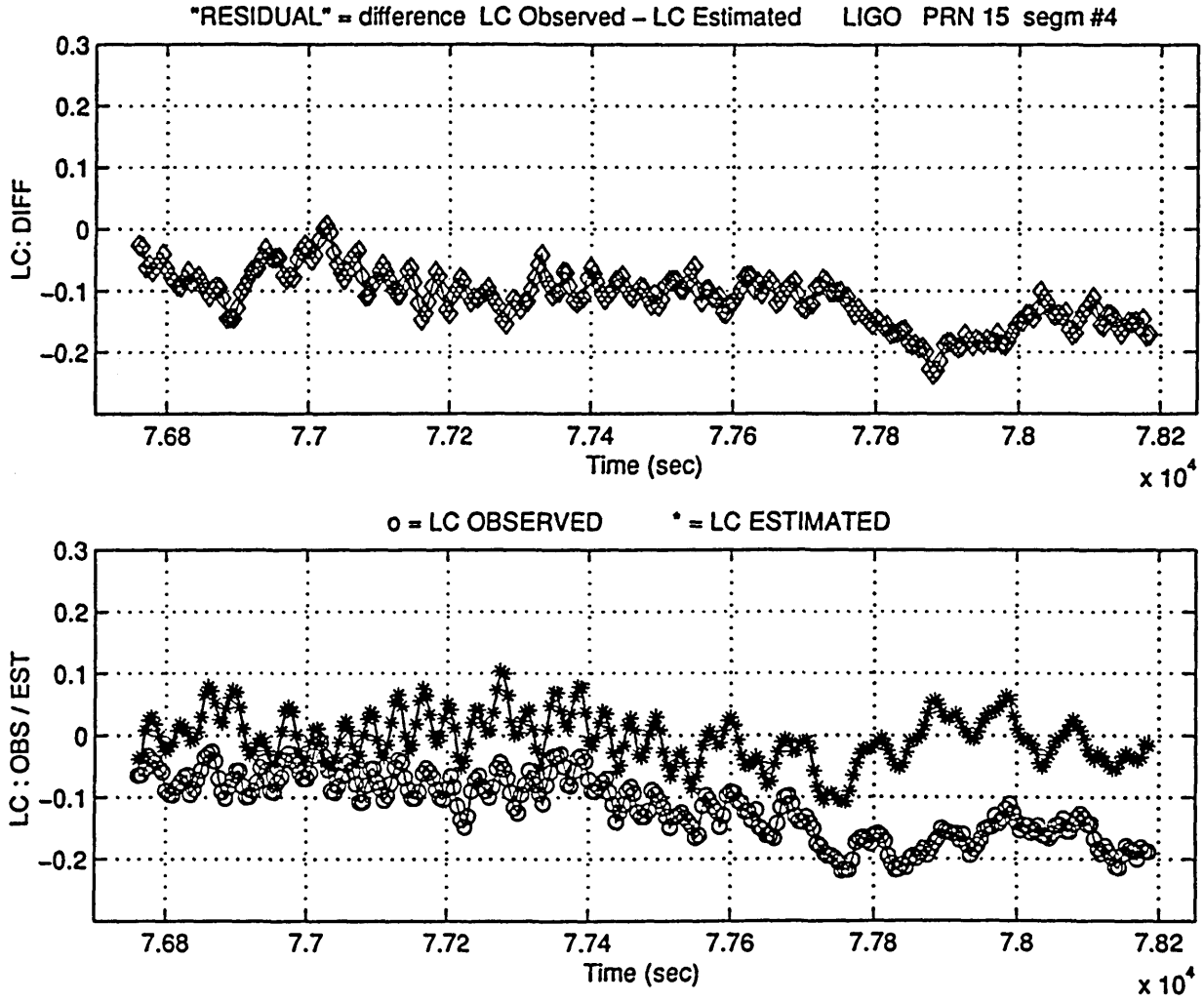

Fig. A.7.10.a) : 0028- 0036- PRN 15 (25 9 1996) [segment #4]
Phase residual LC_DIFF, determined as the difference between LC_OBS and LC_EST.
Unit: [cycles]

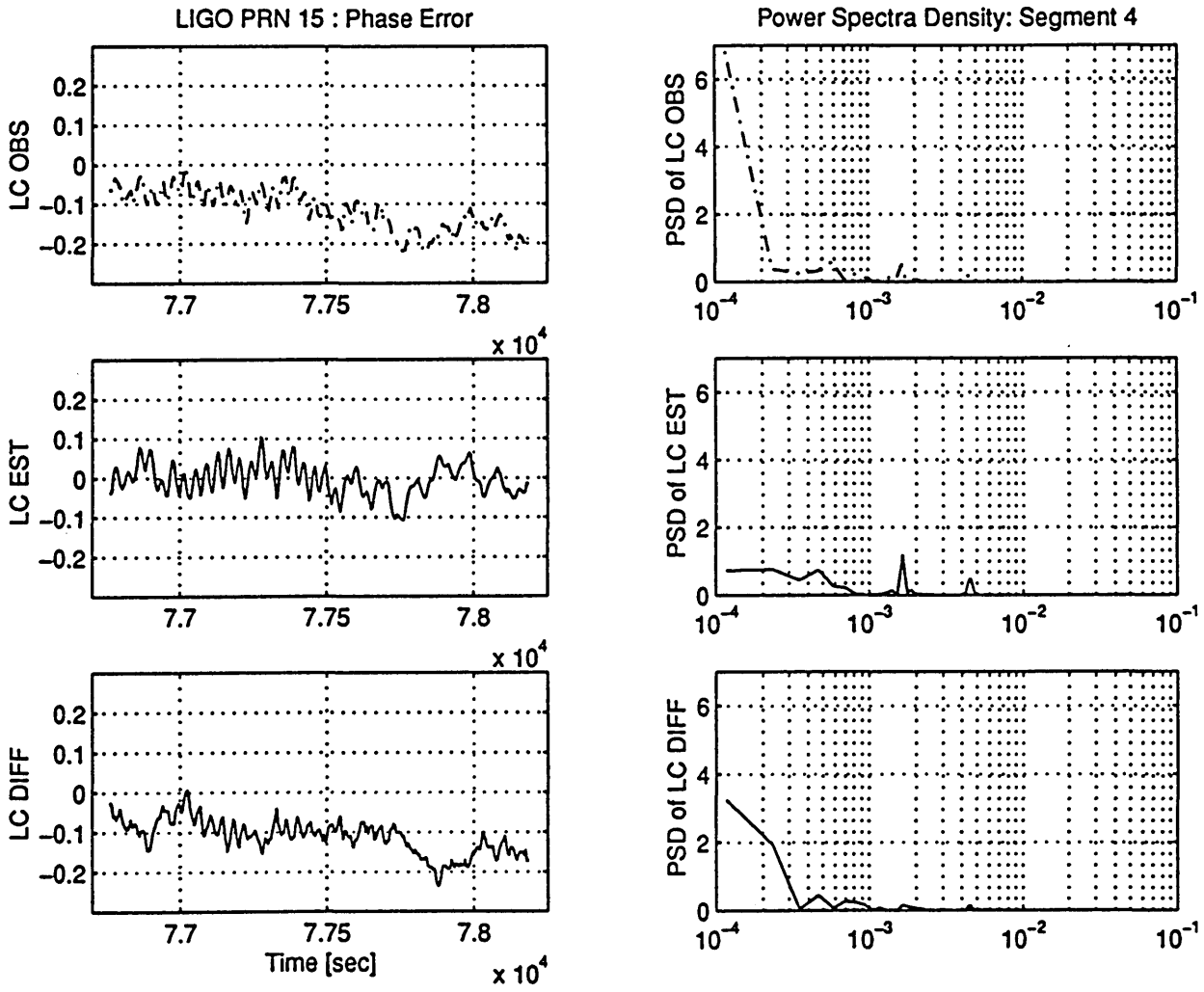

Fig. A.7.10.b) : 0028- 0036- PRN 15 (25 9 1996) [segment #4]
PSD of LC_OBS, LC_EST and LC_DIFF.
Unit: [cycles]^2

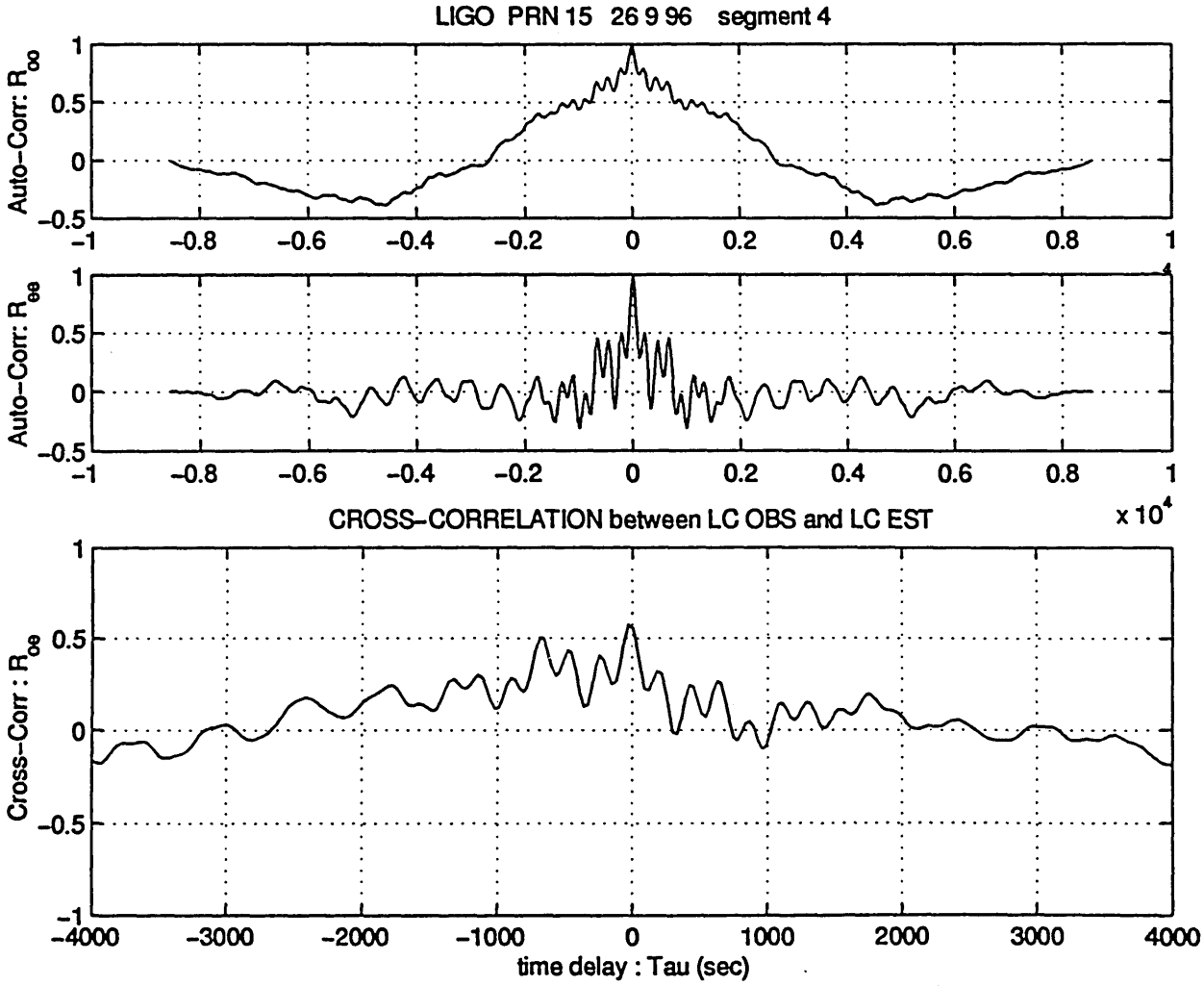

Fig. A.7.10.c) : 0028- 0036- PRN 15 (25 9 1996) [segment #4]
Auto Correlation of LC_OBS (R_{oo}) and LC_EST (R_{ee}).
Cross Correlation between them (R_{oe})
Unit: [cycles]^2

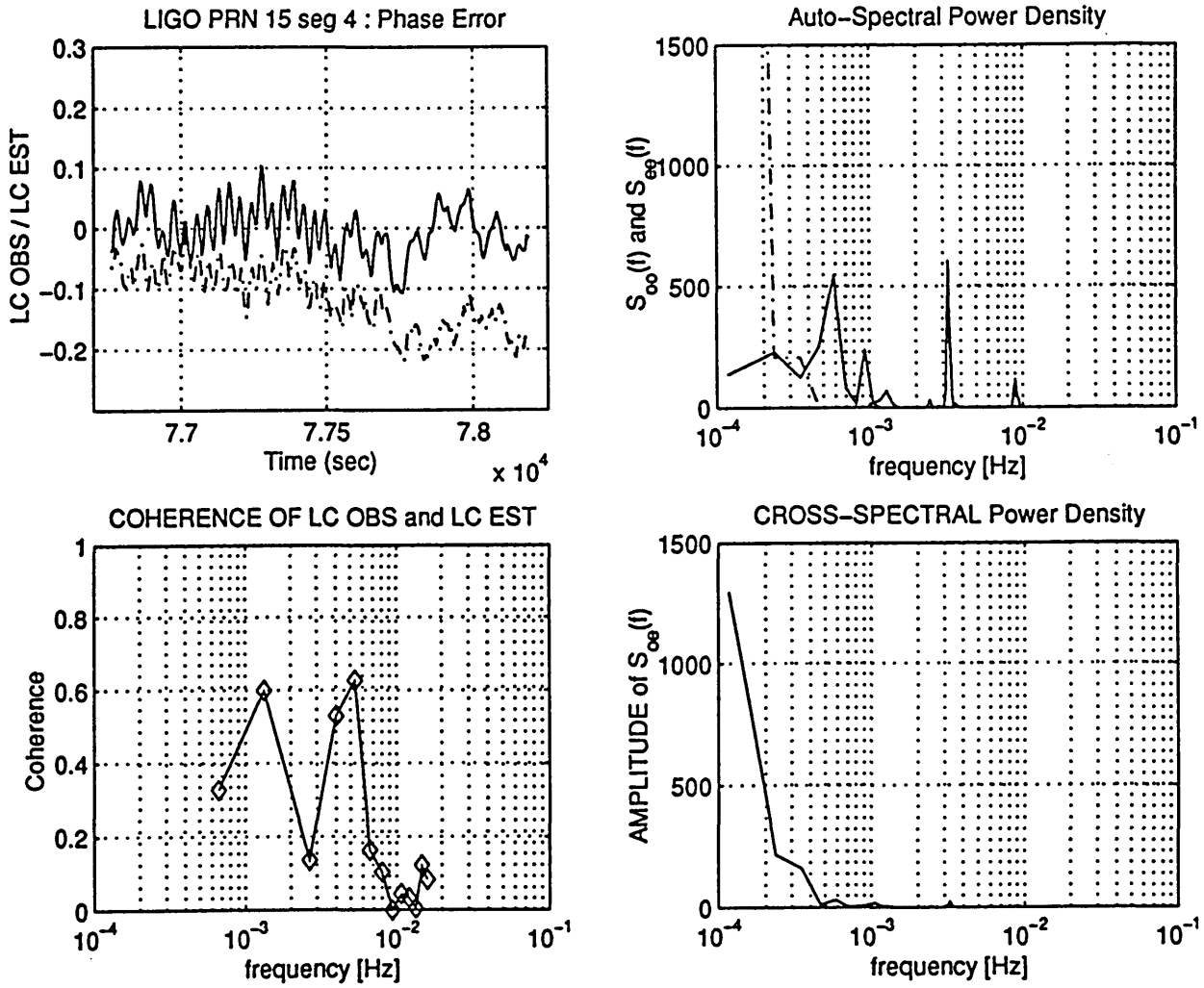

Fig. A.7.10.d) : 0028- 0036- PRN 15 (25 9 1996) [segment #4]
Auto Spectral Power Density of LC_OBS (S_{oo}) and of LC_EST (S_{ee}). Cross PSD between them (S_{oe})
Unit: [cycles]^2
Coherence function of LC_OBS and LC_EST

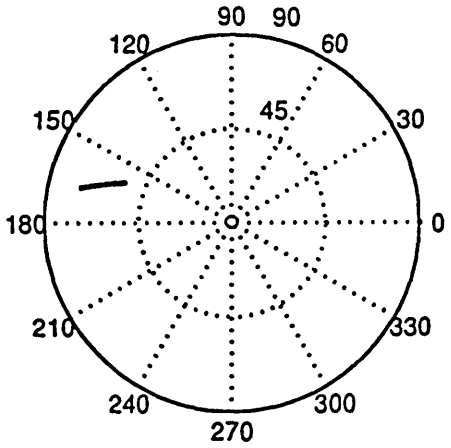

GPS DATA: site: LIGO acquisition date: 26 9 1996

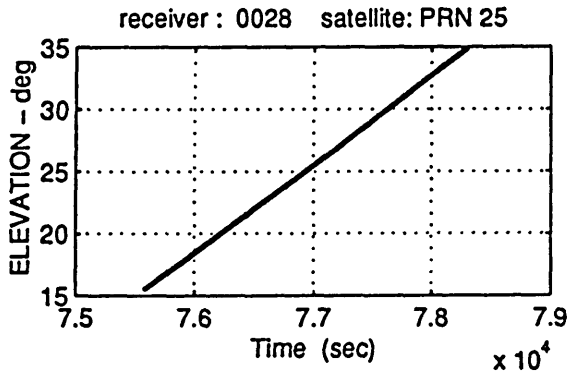

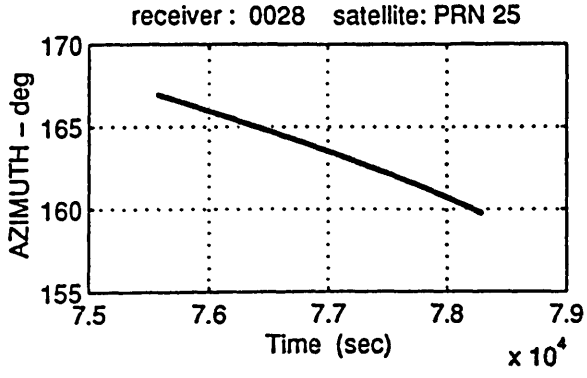

Fig. A.8.1 : Satellite visibility chart for PRN 25 (skymap). Elevation and azimuth of PRN 25 with respect to the station 0028

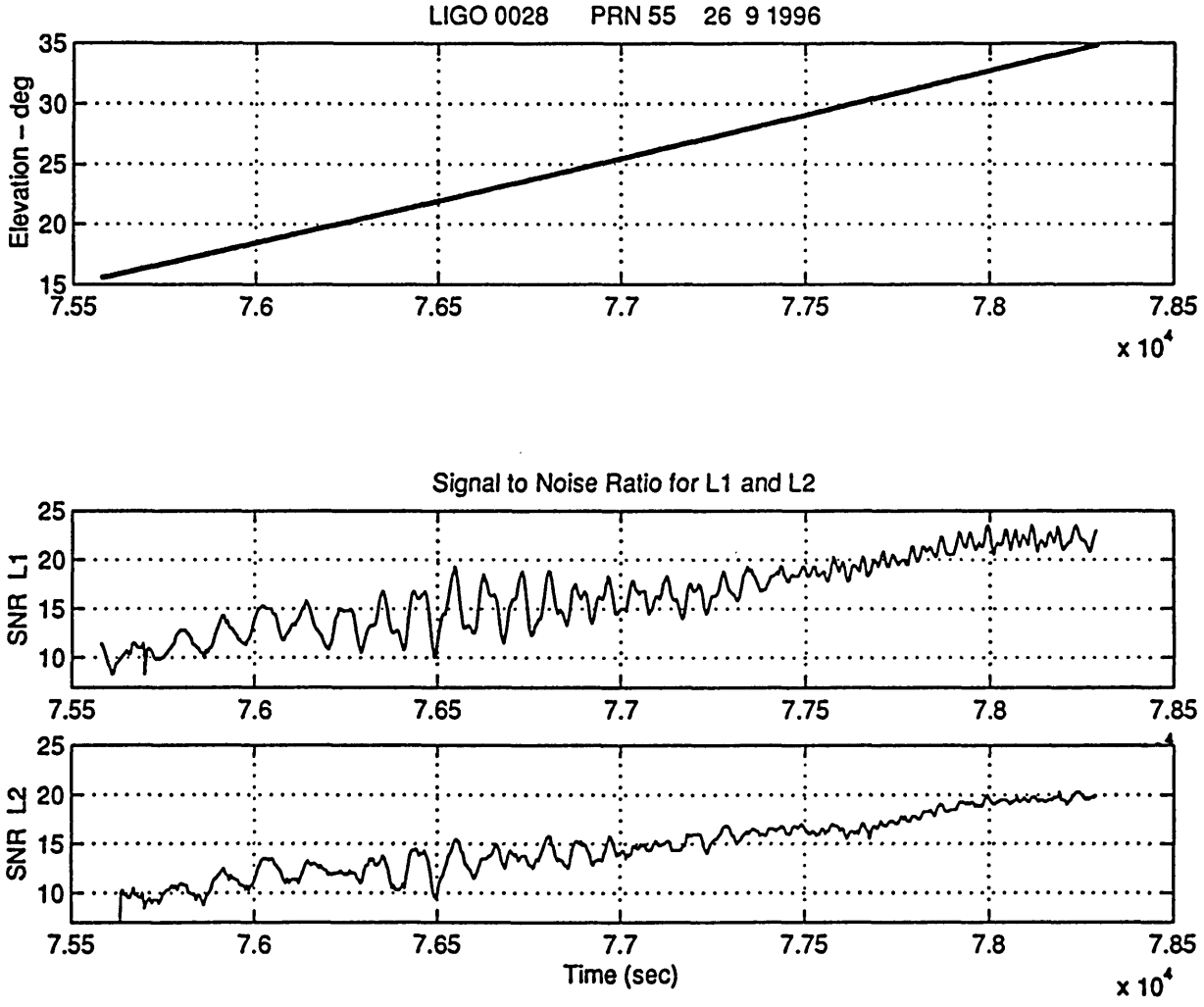

Fig. A.8.2 : Station: 0028- Satellite: PRN 25
Data acquisition date 26 9 1996
Signal-to-Noise-Ratio (SNR) for L_1 and L_2.

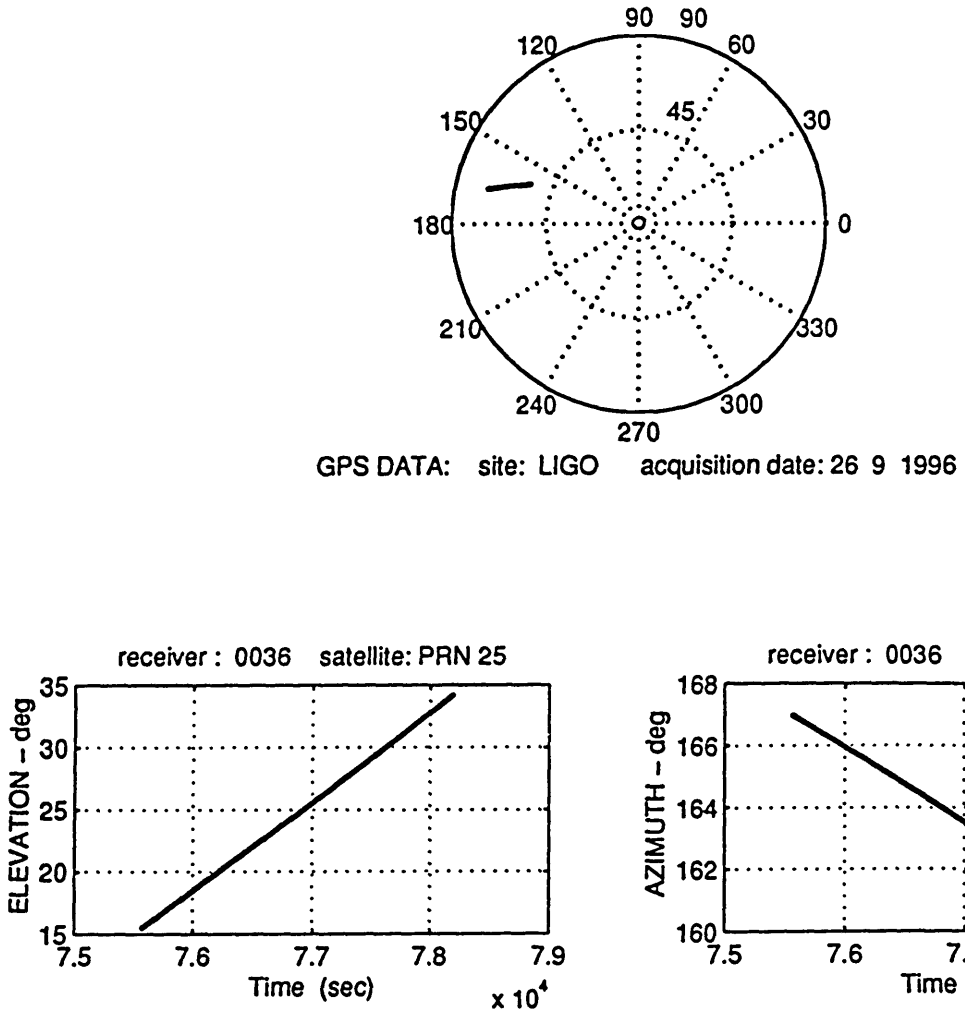

Fig. A.8.3 : Satellite visibility chart for PRN 25(skymap). Elevation and azimuth of PRN 25 with respect to the station 0036

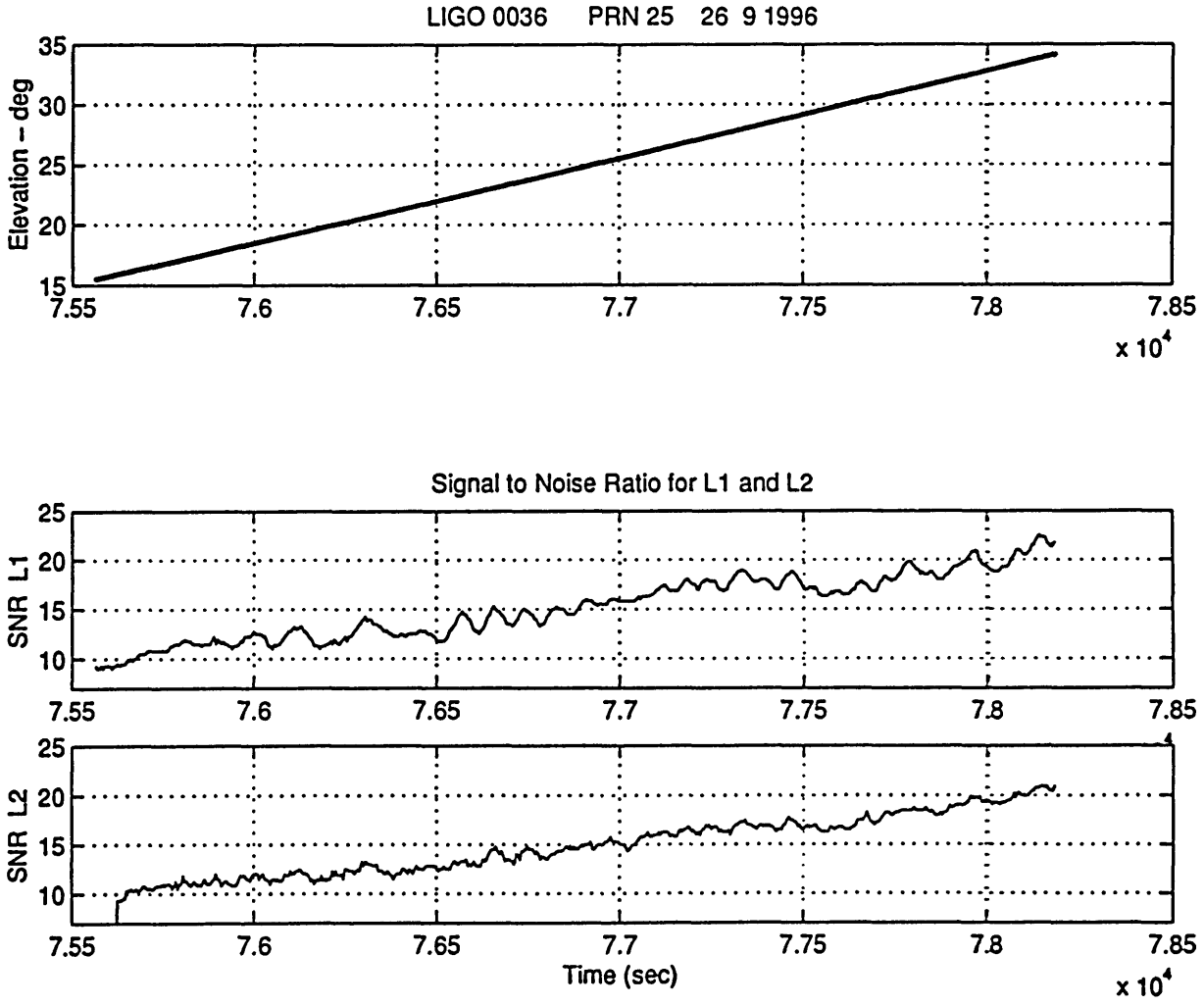

Fig. A.8.4 : Station: 0036- Satellite: PRN 25
Data acquisition date 26 9 1996
Signal-to-Noise-Ratio (SNR) for L_1 and L_2.

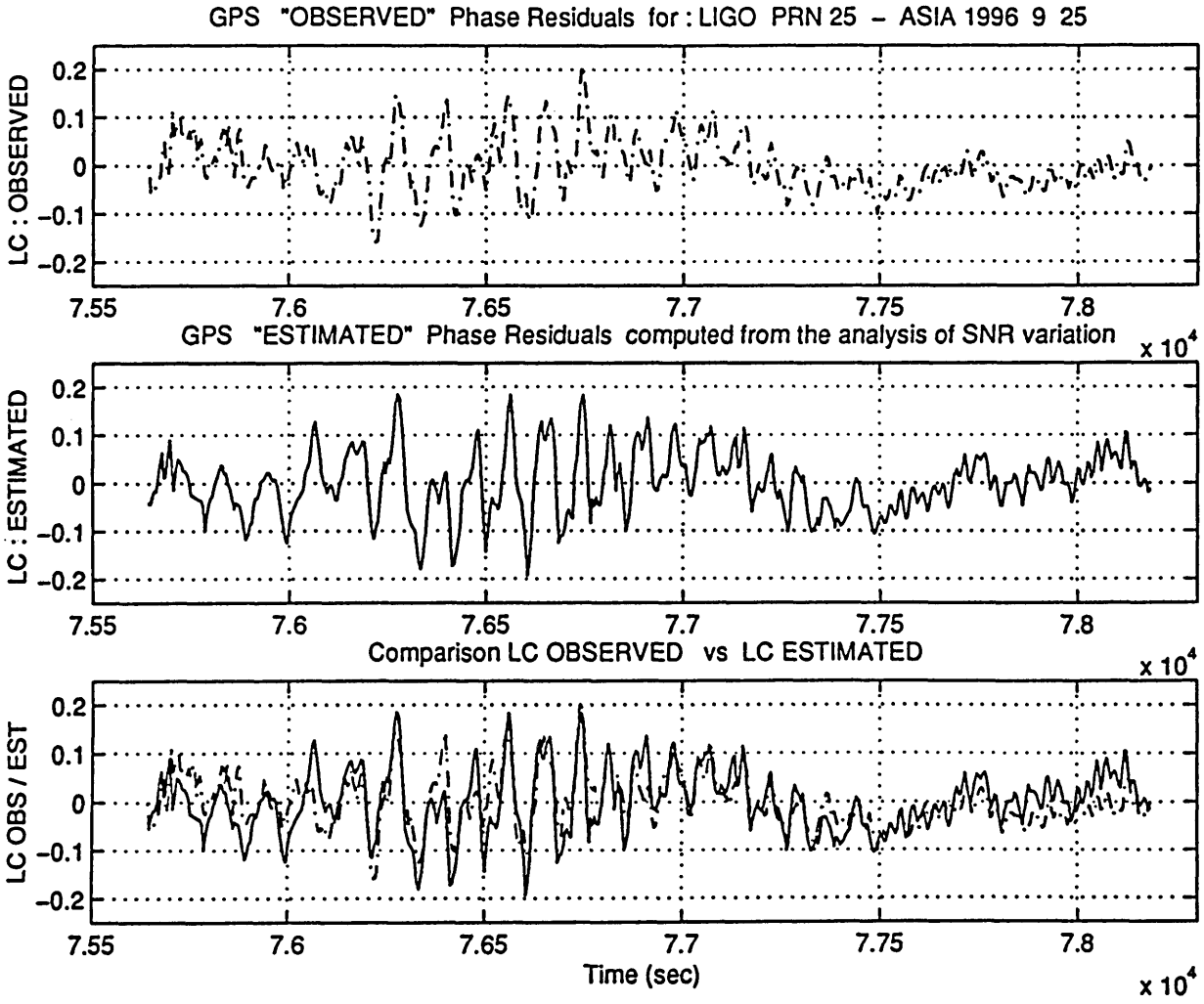

Fig. A.8.5: Stations: 0028- 0036 Satellite: PRN 25-
Data acquisition date 26 9 1996
The observed phase residual (LC_OBS) is compared with the multipath phase error estimated from the SNR (LC_EST) (differential mode)
Unit: [cycles]

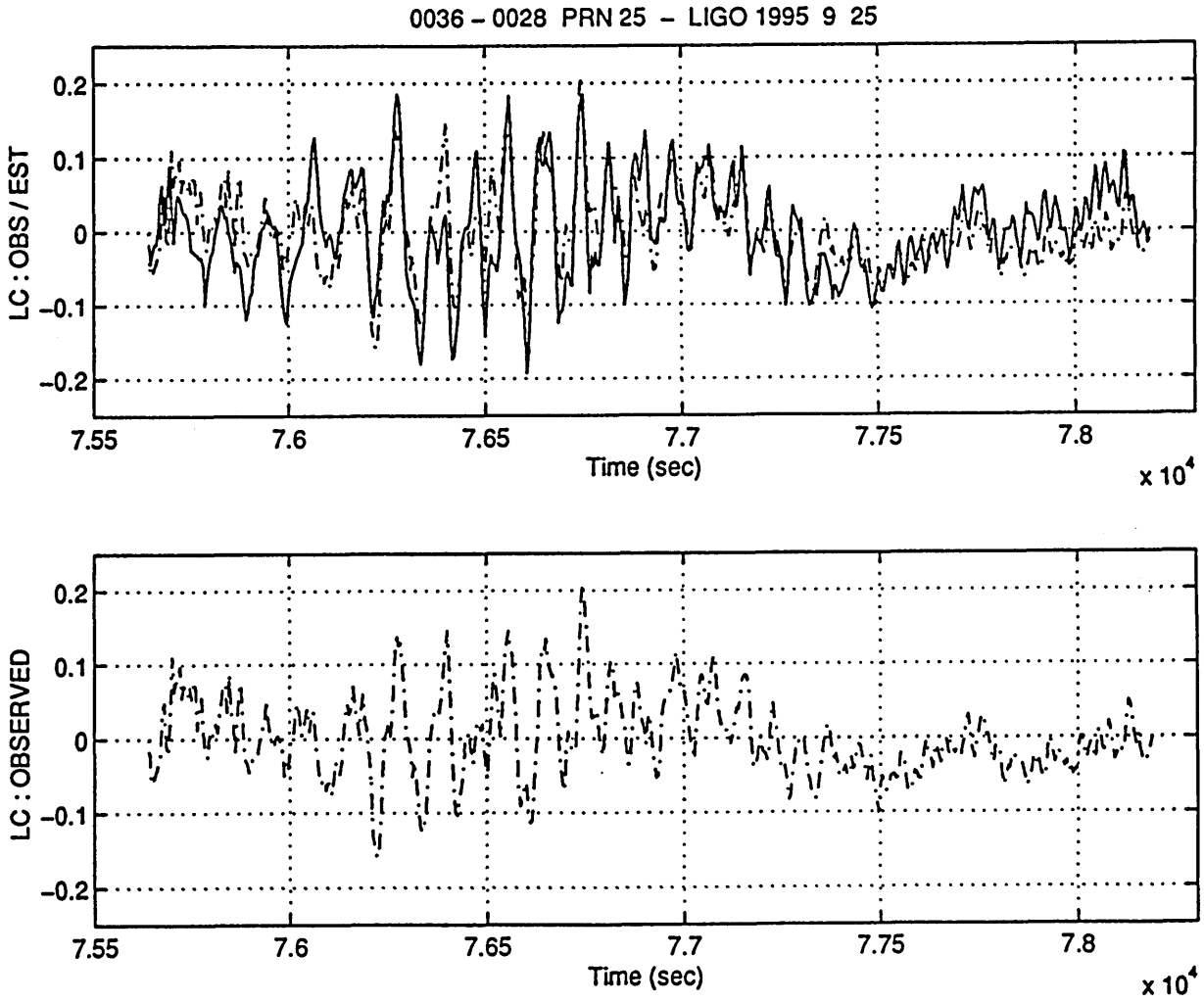

Fig. A.8.6 : 0028- 0036 Satellite: PRN 25
Data acquisition date 26 9 1996
LC_OBS and LC_EST compared for t=7.56 - 7.9 10^4 sec
Unit: [cycles]

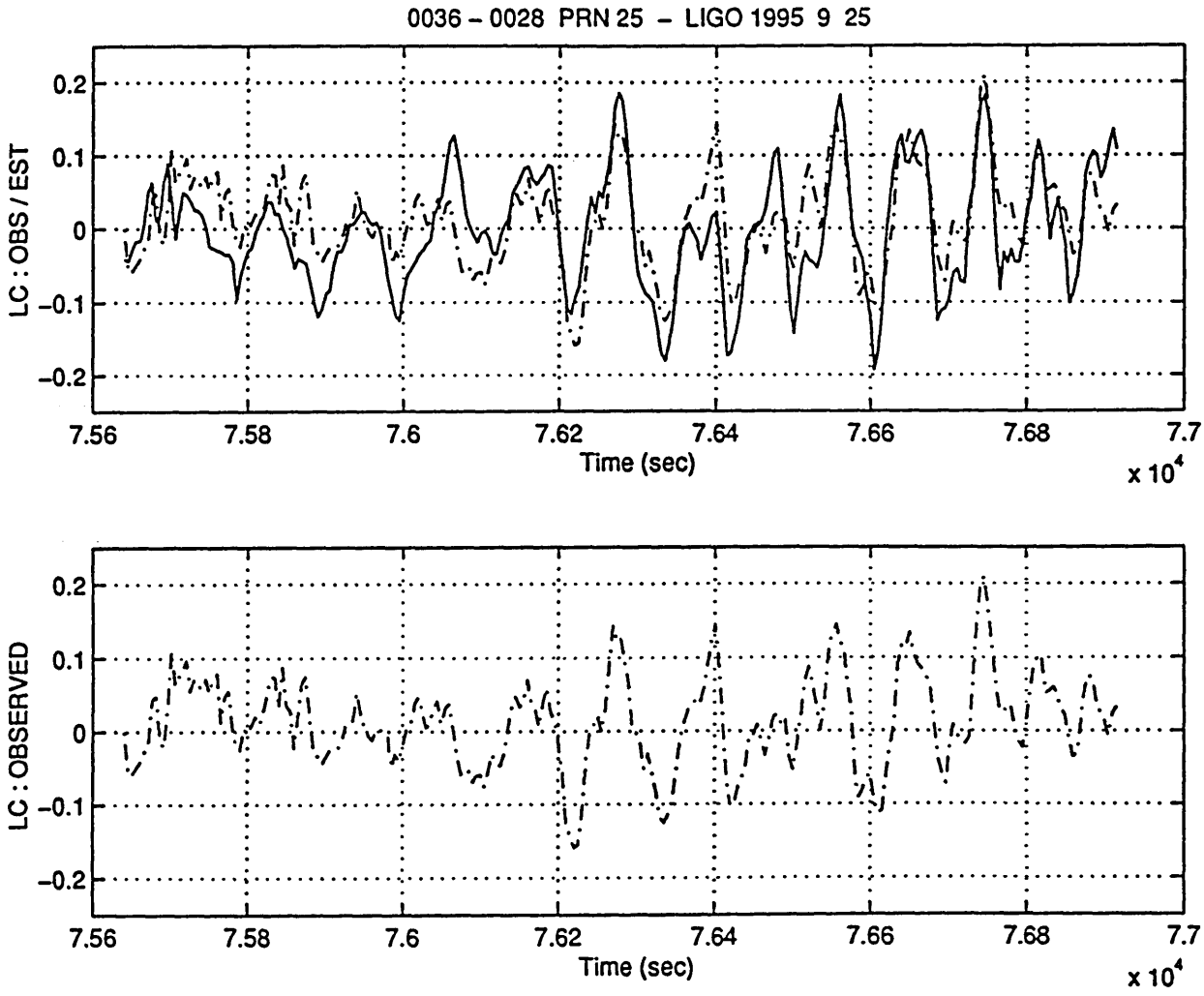

Fig. A.8.7 : 0028- 0036 Satellite: PRN 25
Data acquisition date 26 9 1996
LC_OBS and LC_EST compared for t=7.56 - 7.7 10^4 sec
Unit: [cycles]

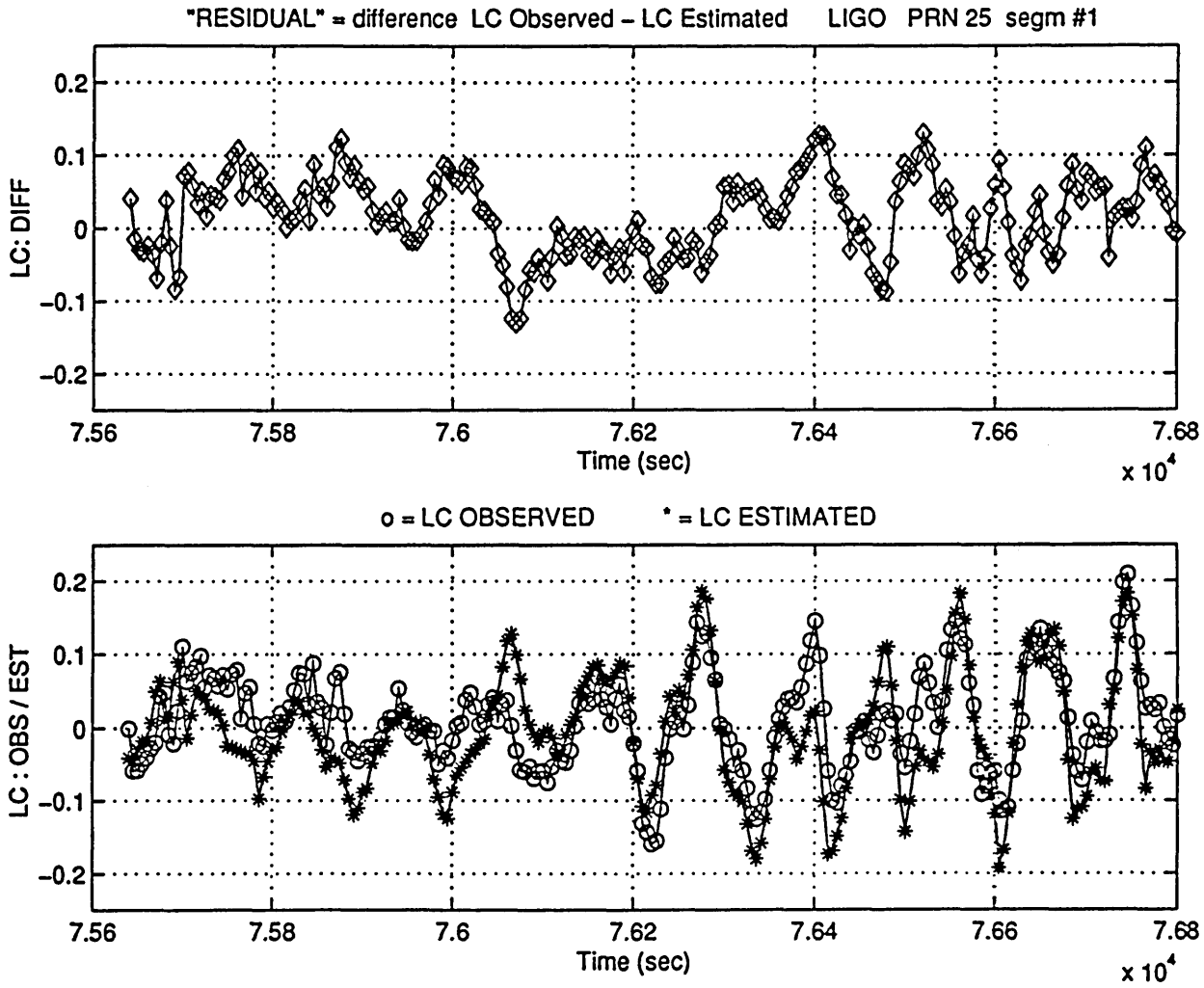

Fig. A.8.8.a) : 0028- 0036- PRN 25 (26 9 1996) [segment #1]
Phase residual LC_DIFF, determined as the difference between LC_OBS and LC_EST.
Unit: [cycles].

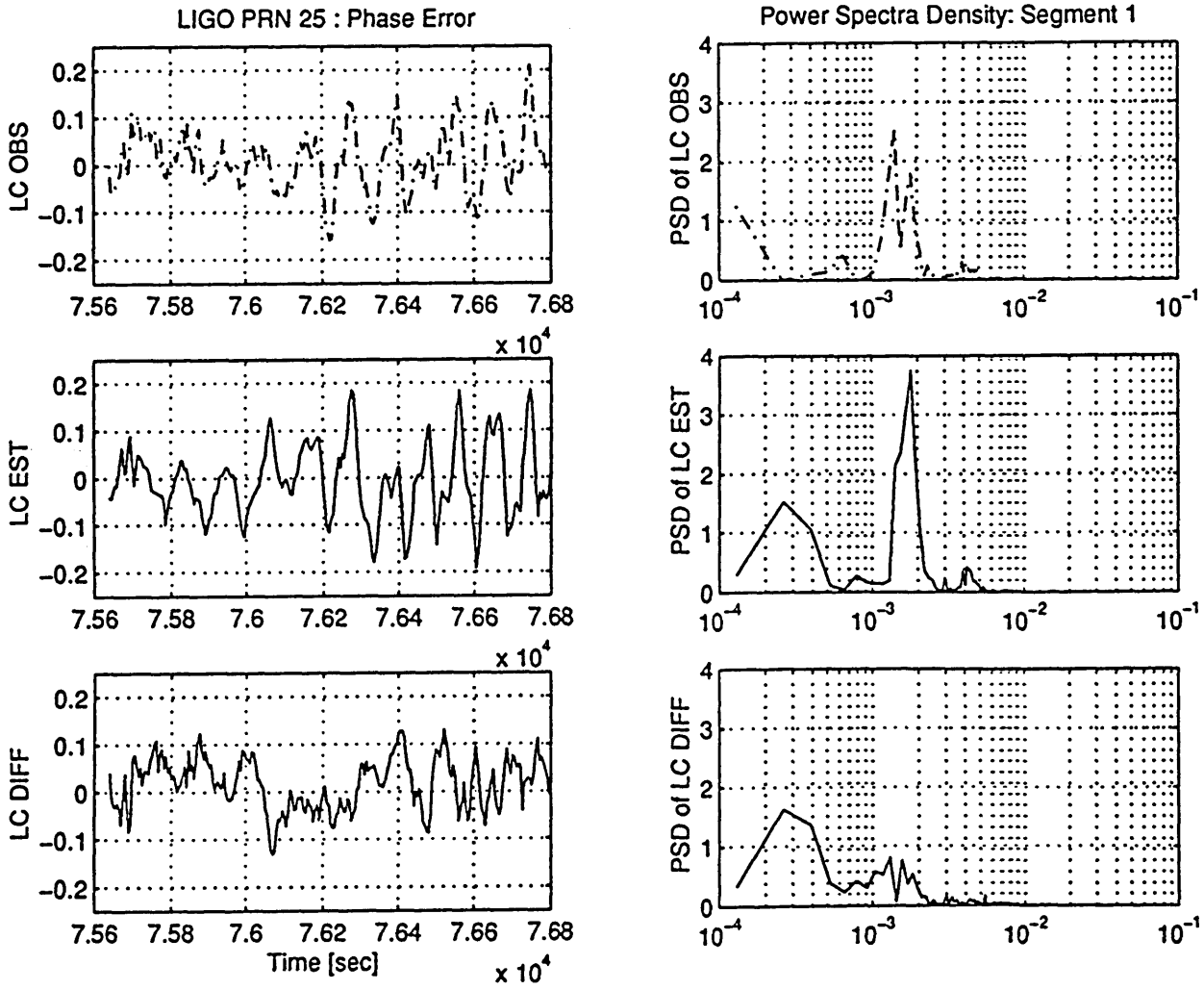

Fig. A.8.8.b) : 0028- 0036- PRN 25 (26 9 1996) [segment #1]
PSD of LC_OBS, LC_EST and LC_DIFF.
Unit: [cycles]^2

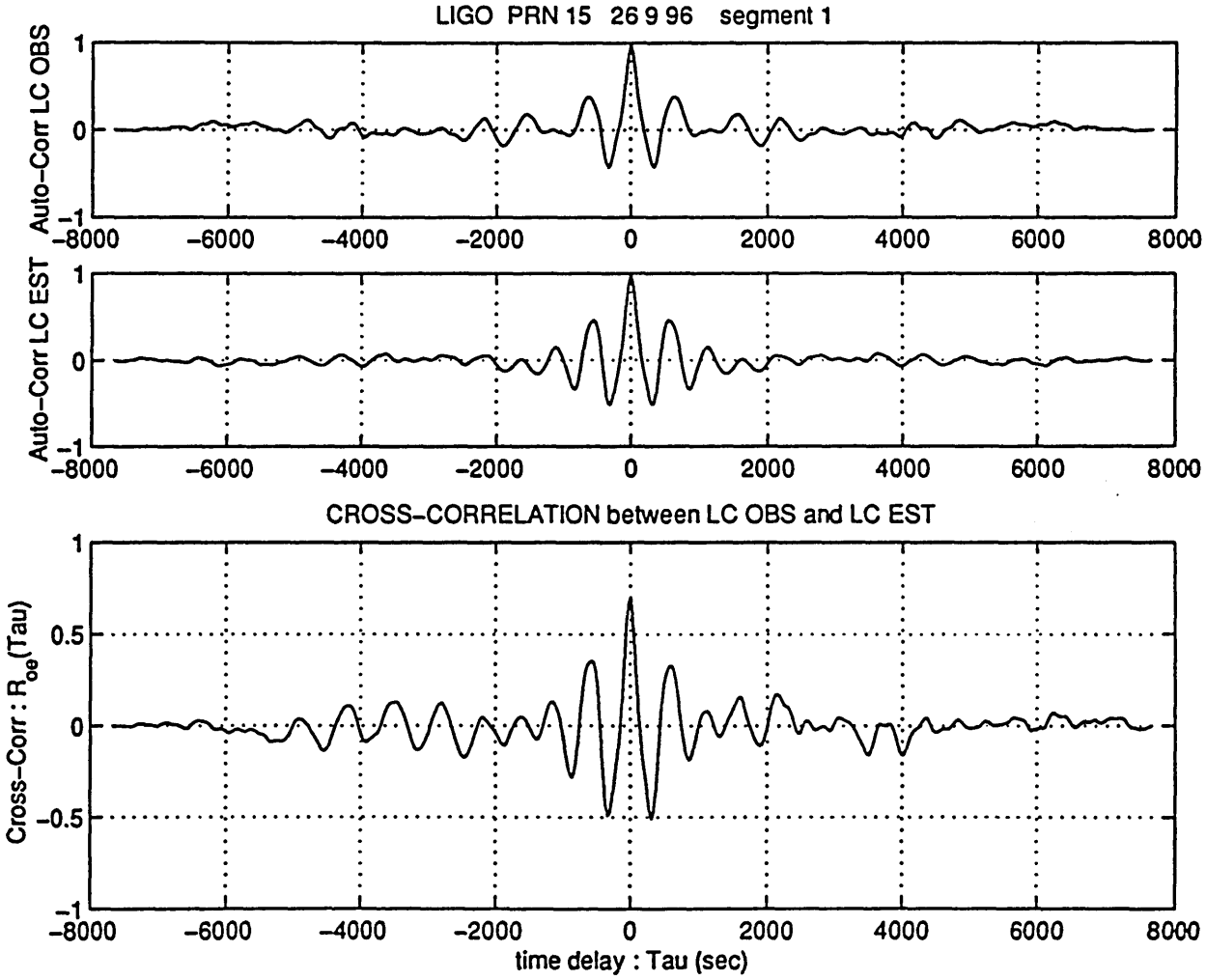

Fig. A.8.8.c) : 0028- 0036- PRN 25 (26 9 1996) [segment #1]
Auto Correlation of LC_OBS (R_{oo}) and LC_EST (R_{ee}).
Cross Correlation between them (R_{oe})
Unit: [cycles]^2

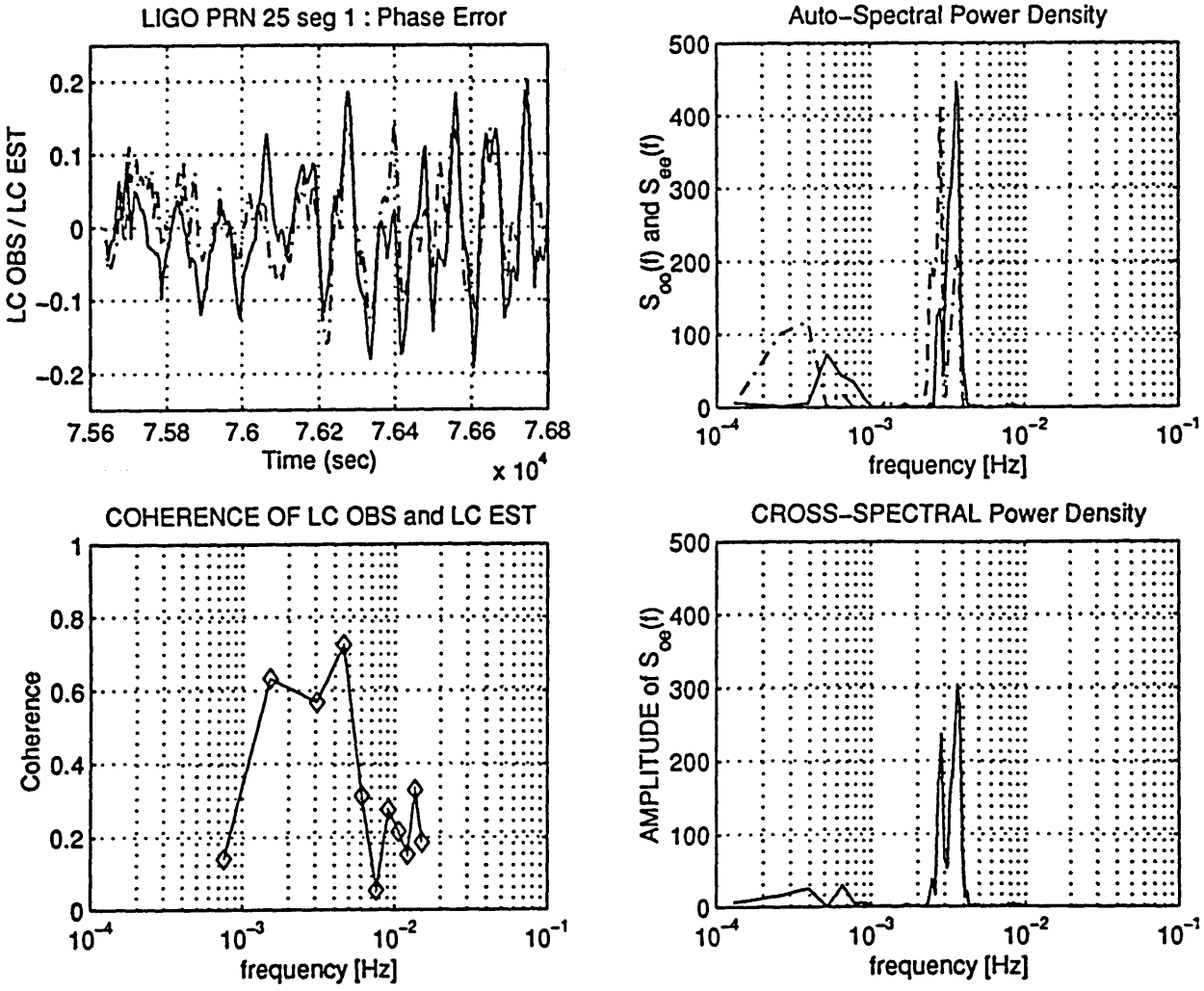

Fig. A.8.8.d) : 0028- 0036- PRN 25 (26 9 1996) [segment #1]
Auto Spectral Power Density of LC_OBS (S_{oo}) and of LC_EST (S_{ee}). Cross PSD between them (S_{oe})
Unit: [cycles]^2
Coherence function of LC_OBS and LC_EST

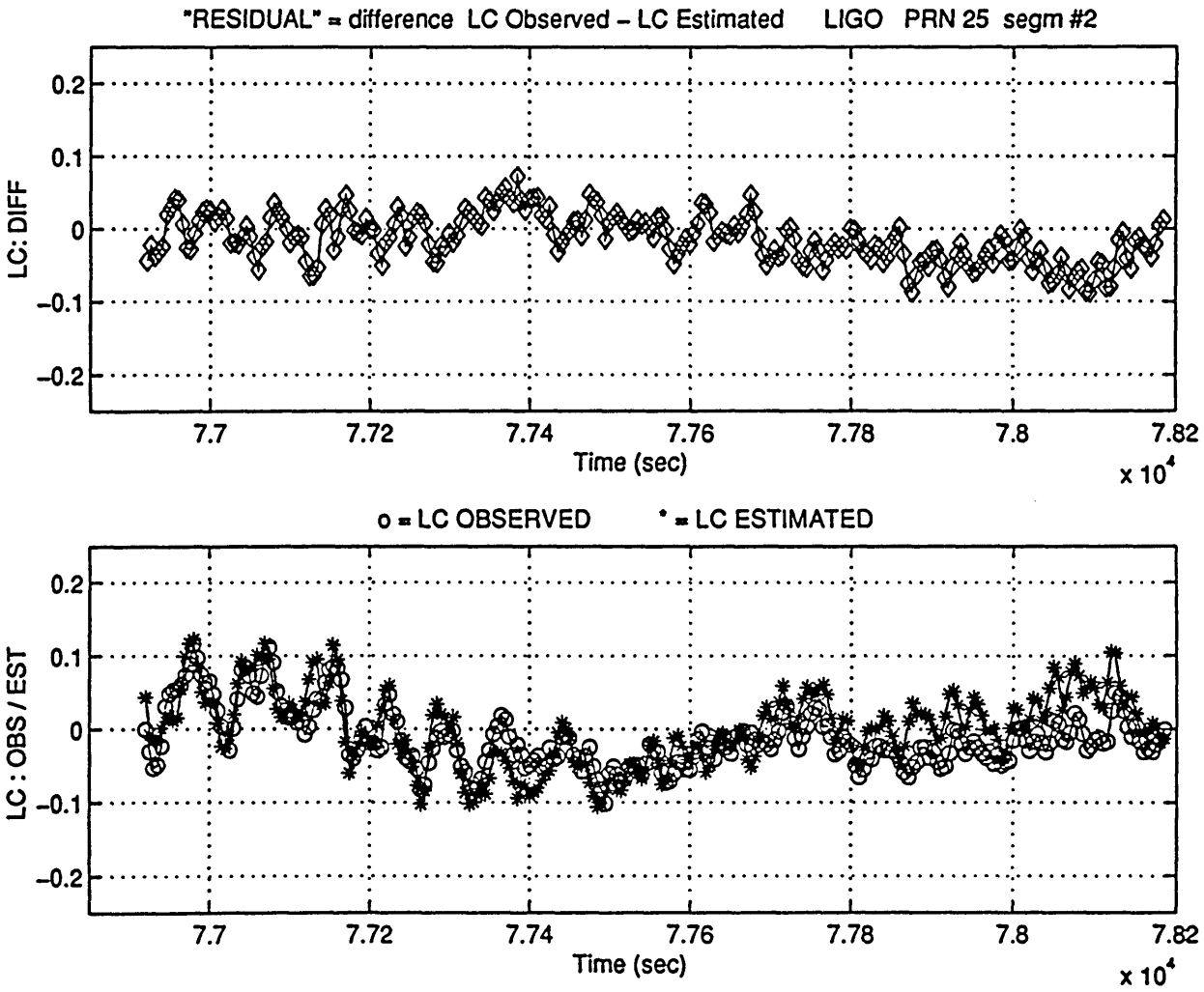

Fig. A.8.9.a) : 0028- 0036- PRN 25 (26 9 1996) [segment #2]
Phase residual LC_DIFF, determined as the difference between LC_OBS and LC_EST.
Unit: [cycles]

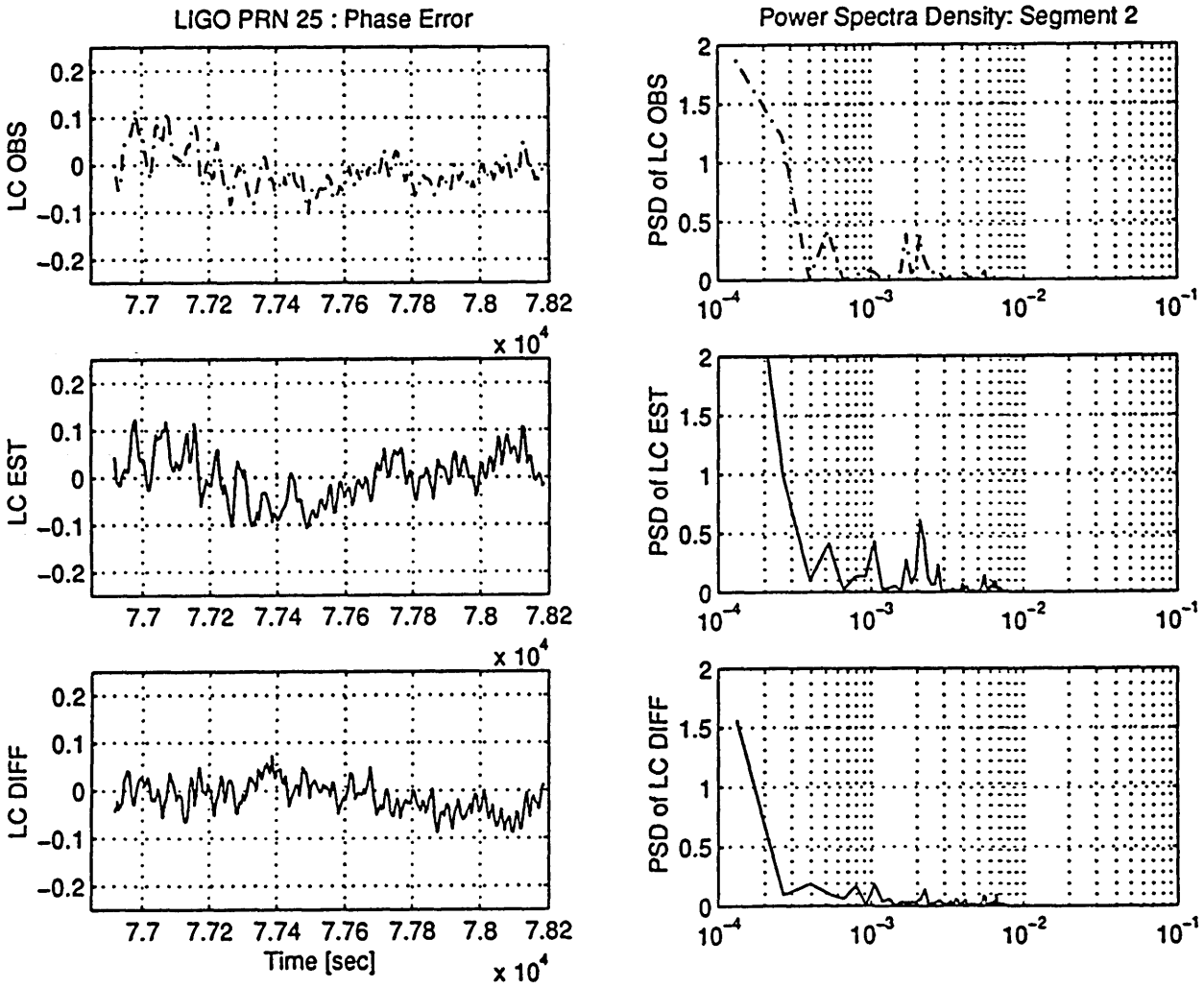

Fig. A.8.9.b) : 0028- 0036- PRN 25 (26 9 1996) [segment #2]
PSD of LC_OBS, LC_EST and LC_DIFF.
Unit: [cycles]^2

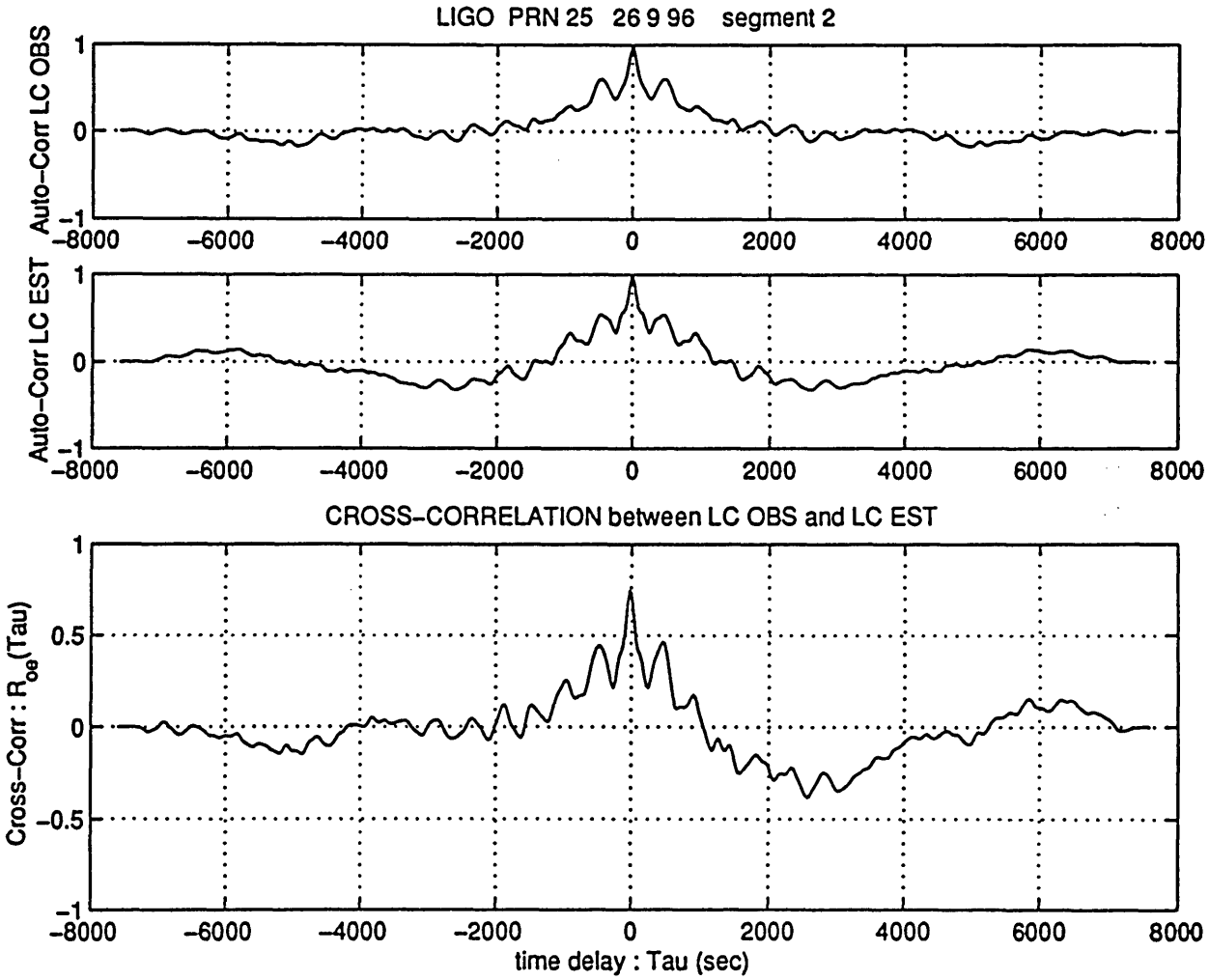

Fig. A.8.9.c) : 0028- 0036- PRN 25 (26 9 1996) [segment #2]
Auto Correlation of LC_OBS (R_{oo}) and LC_EST (R_{ee}).
Cross Correlation between them (R_{oe})
Unit: [cycles]^2

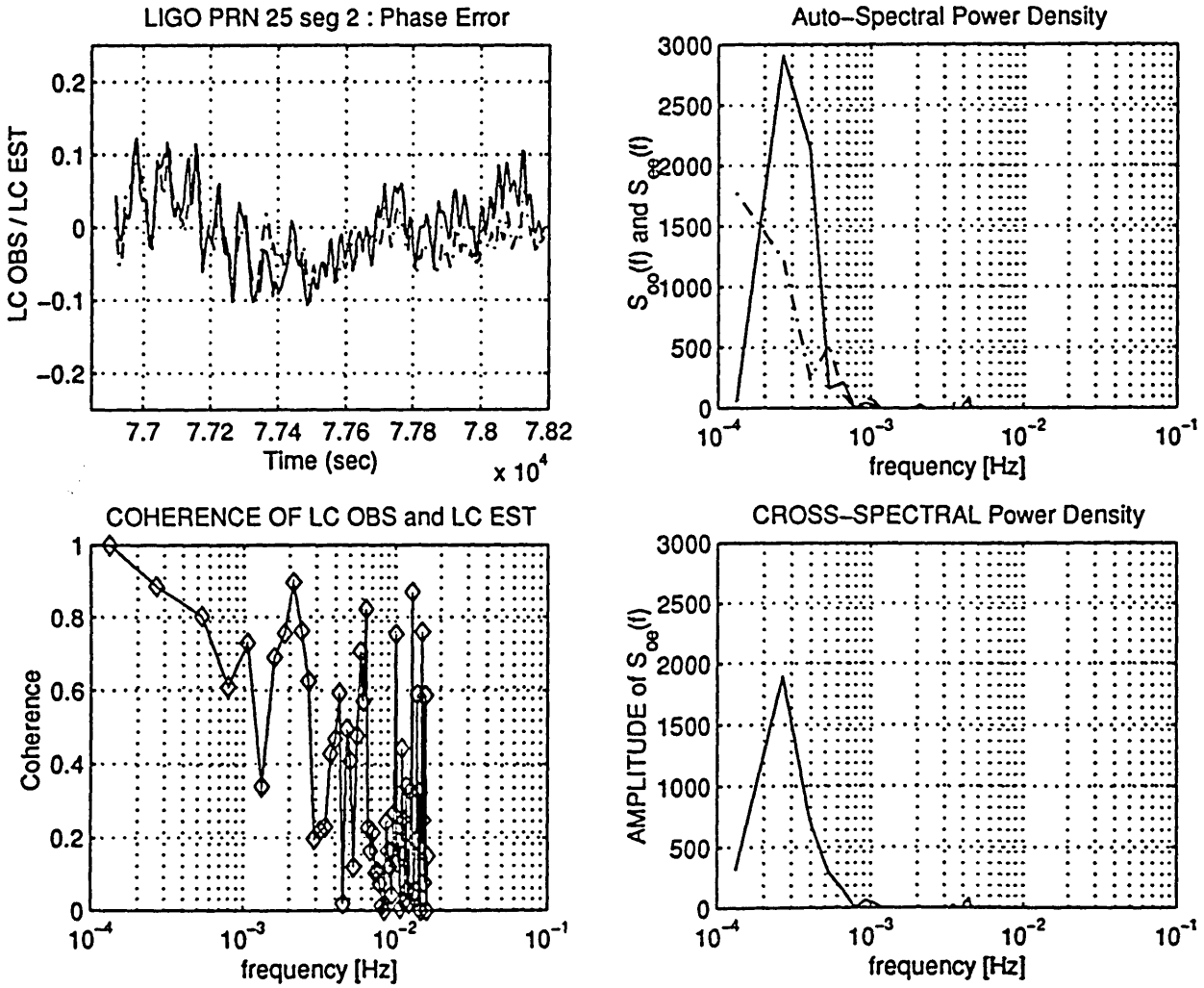

Fig. A.8.9.d) : 0028- 0036- PRN 25 (26 9 1996) [segment #2]
Auto Spectral Power Density of LC_OBS (S_{oo}) and of LC_EST (S_{ee}). Cross PSD between them (S_{oe})
Unit: [cycles]^2
Coherence function of LC_OBS and LC_EST

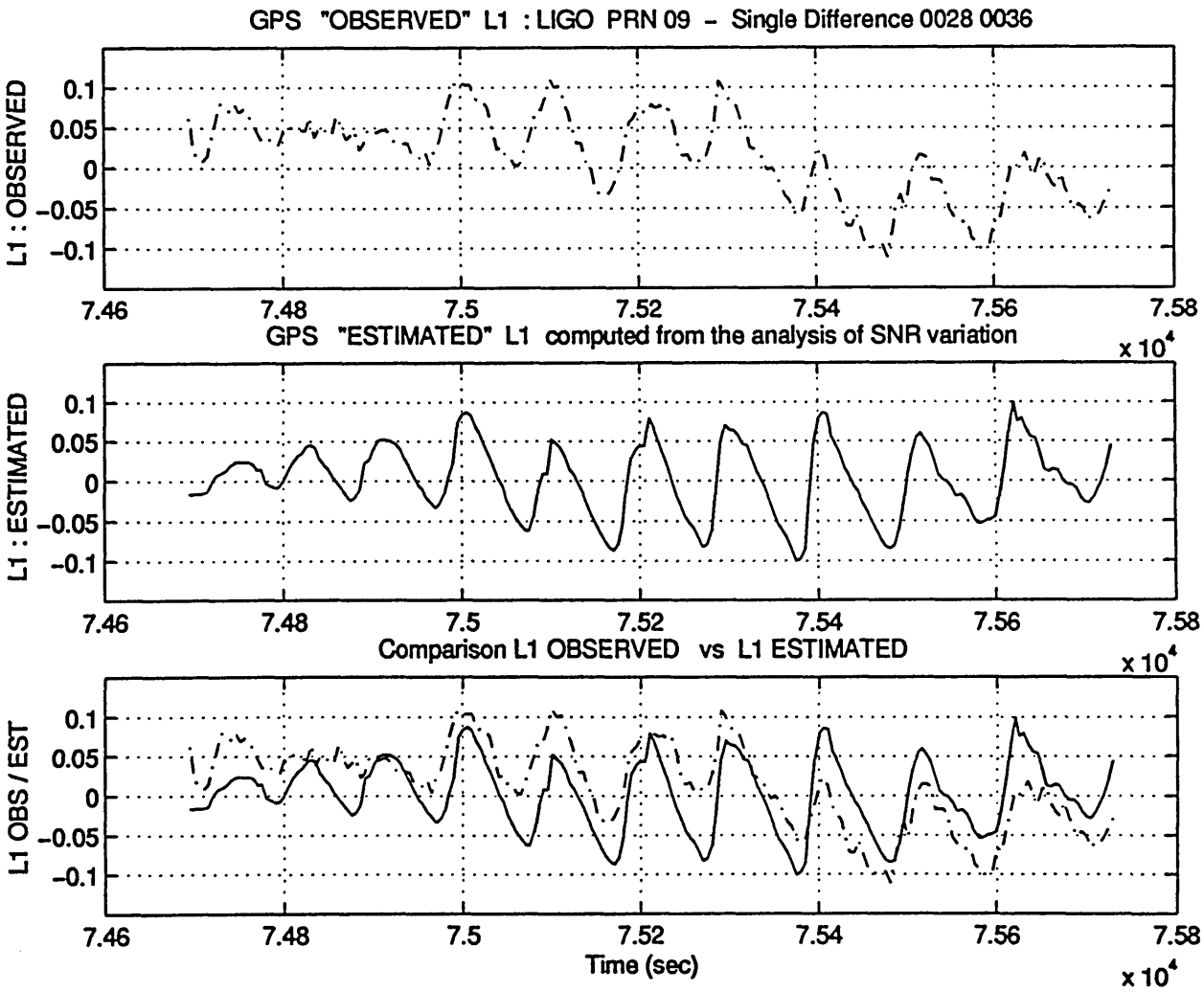

Fig. A.9.1 : 0028- 0036 Satellite: PRN 09
Data acquisition date 25 9 1996
L_{1}_OBS and L_{1}_EST compared for t=7.46 -7.58 10^4 sec
Unit: [cycles]

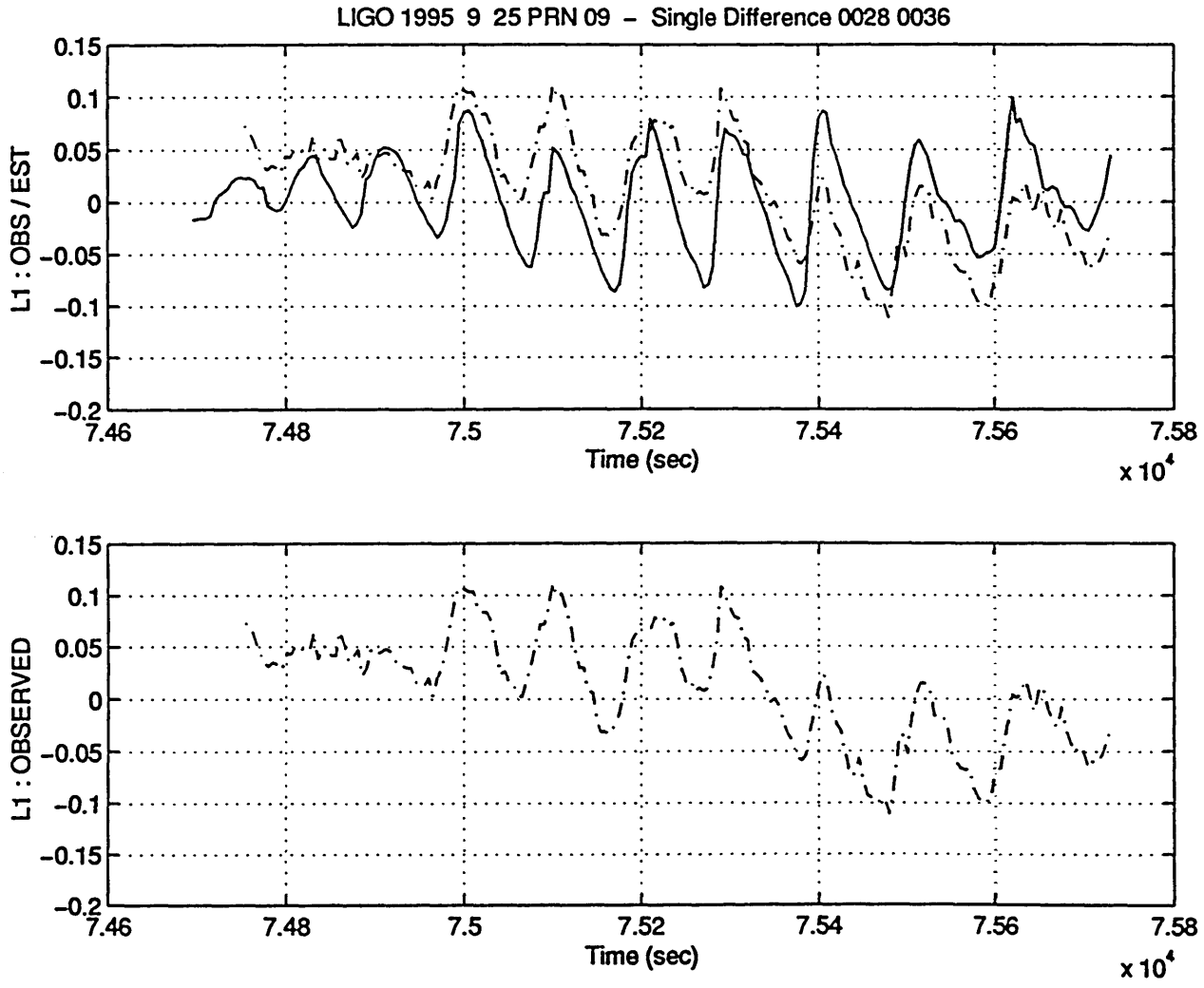

Fig. A.9.2 : 0028- 0036 Satellite: PRN 09
Data acquisition date 25 9 1996
L_{1}_OBS and L_{1}_EST compared for t=7.47 - 7.58 10^{4} sec
Unit: [cycles]

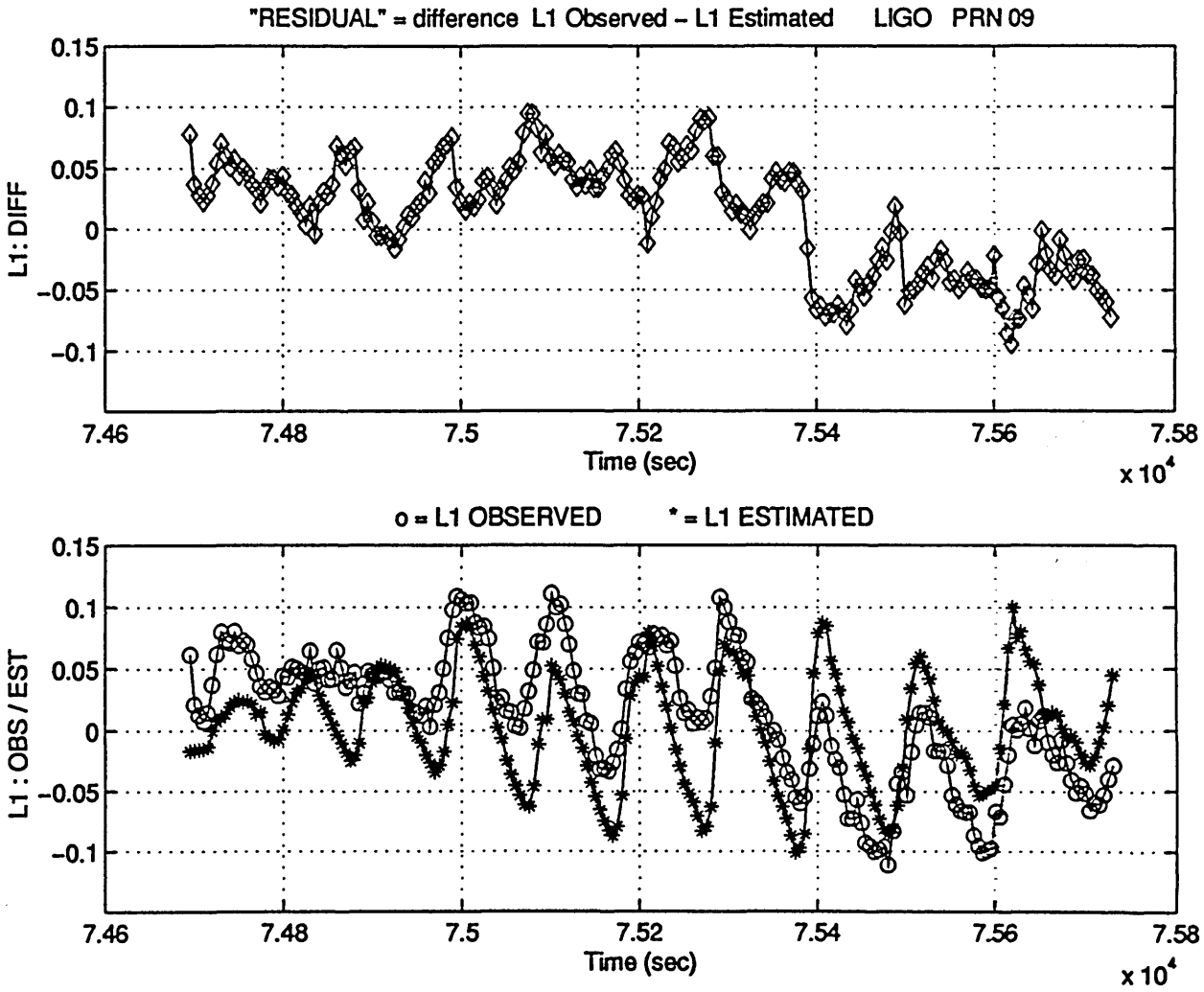

Fig. A.9.3.a) : 0028- 0036- PRN 09 (25 9 1996)
Phase residual L1_DIFF, determined as the difference between L1_OBS and L1_EST.
Unit: [cycles]

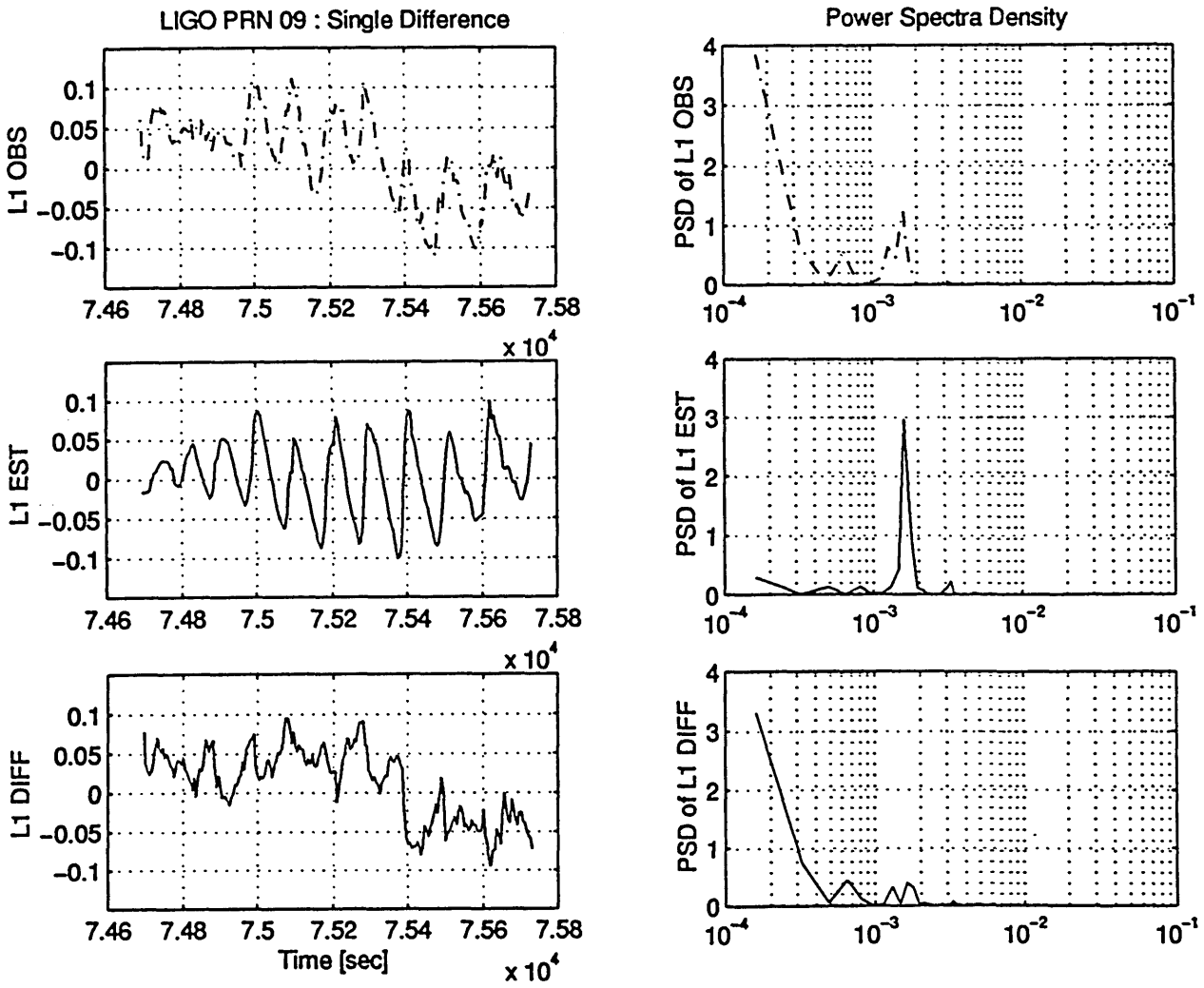

Fig. A.9.3.b) : 0028- 0036- PRN 09 (25 9 1996)
PSD of L1_OBS, L1_EST and L1_DIFF.
Unit: [cycles]^2

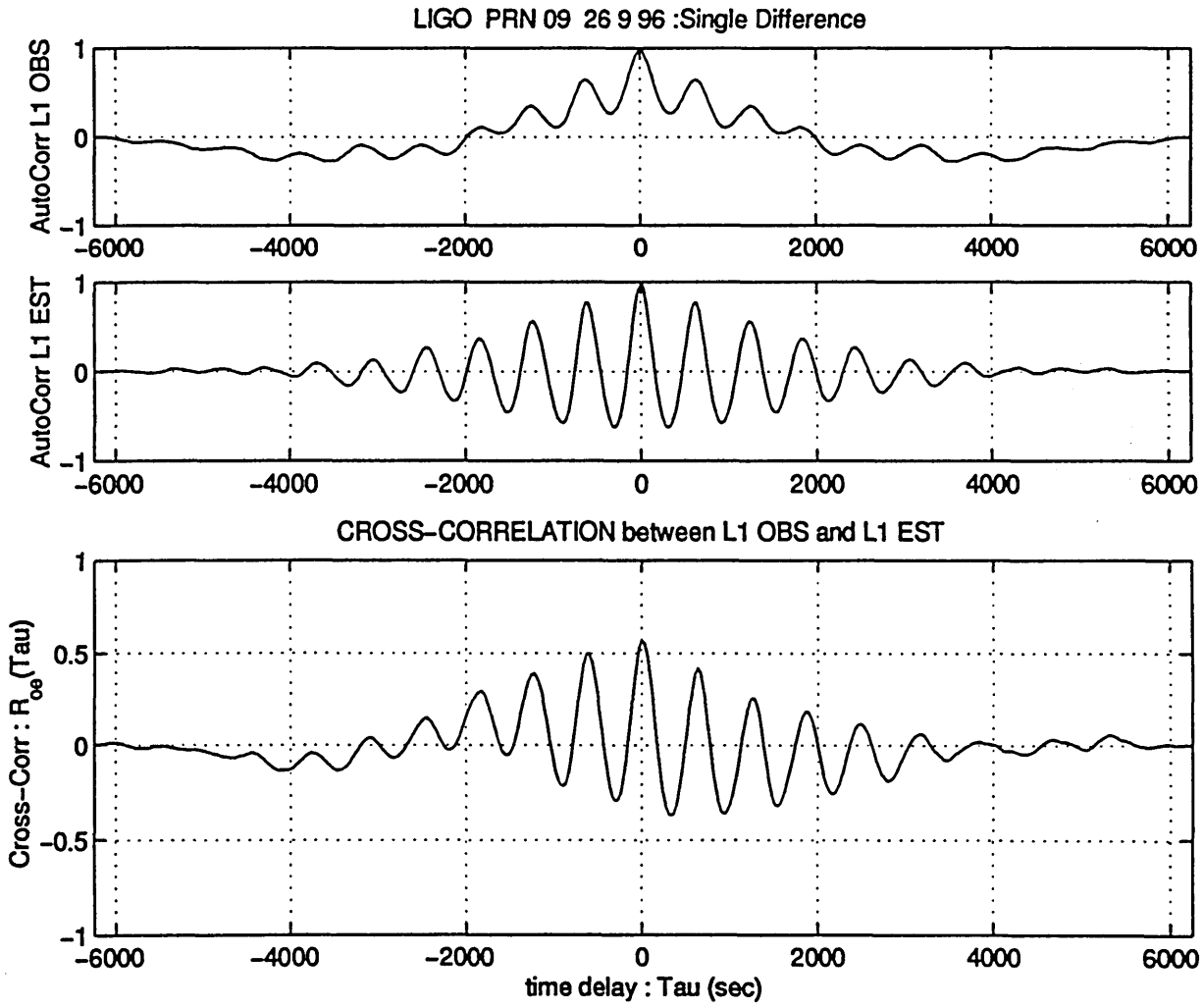

Fig. A.9.3.c) : 0028- 0036- PRN 09 (25 9 1996)
Auto Correlation of LC_OBS (R_{oo}) and LC_EST (R_{ee}).
Cross Correlation between them (R_{oe})
Unit: [cycles]^2

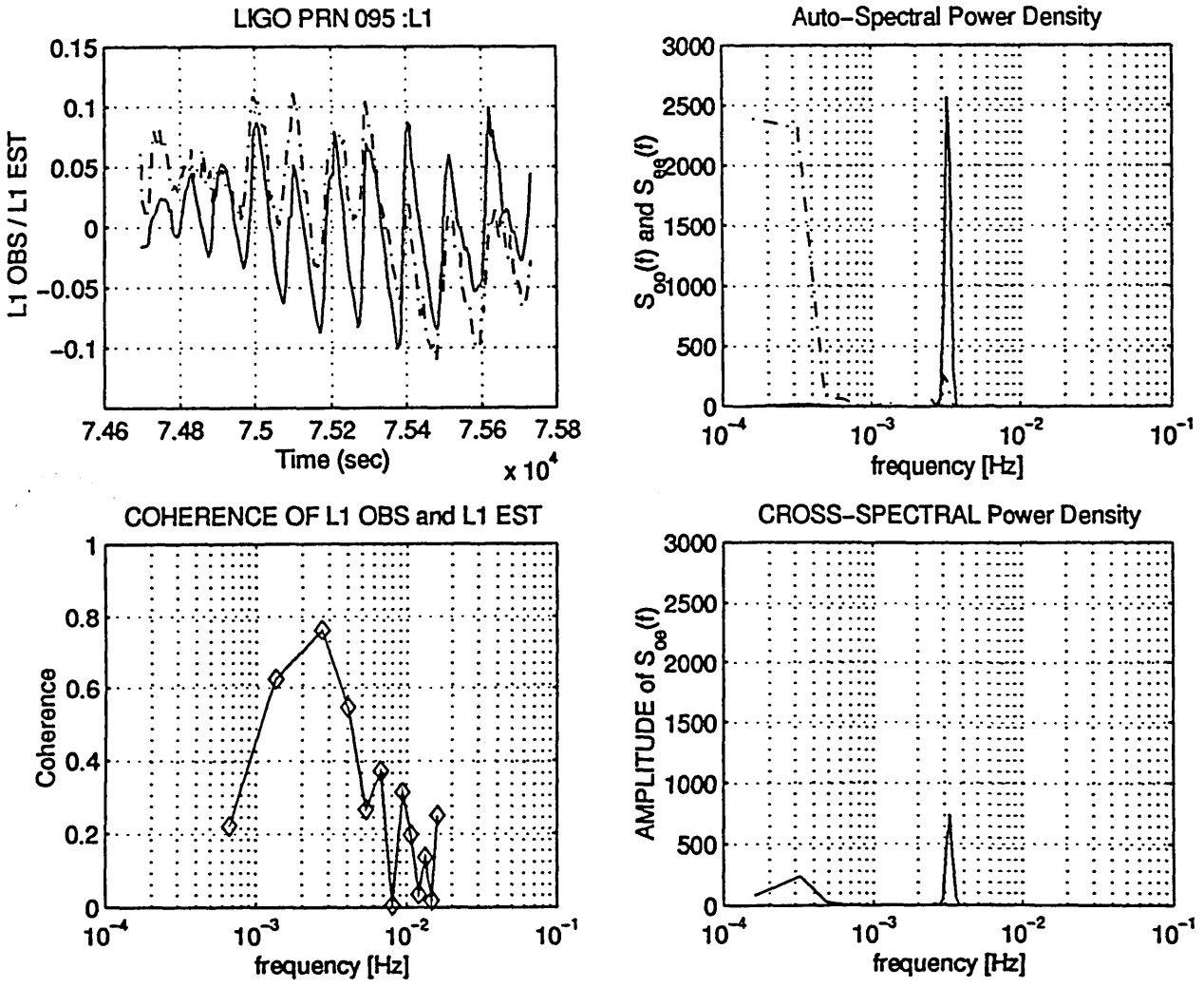

Fig. A.9.3.d) : 0028- 0036- PRN 09 (25 9 1996)
Auto Spectral Power Density of LC_OBS (S_{oo}) and of LC_EST (S_{ee}). Cross PSD between them (S_{oe})
Unit: [cycles]^2
Coherence function of LC_OBS and LC_EST

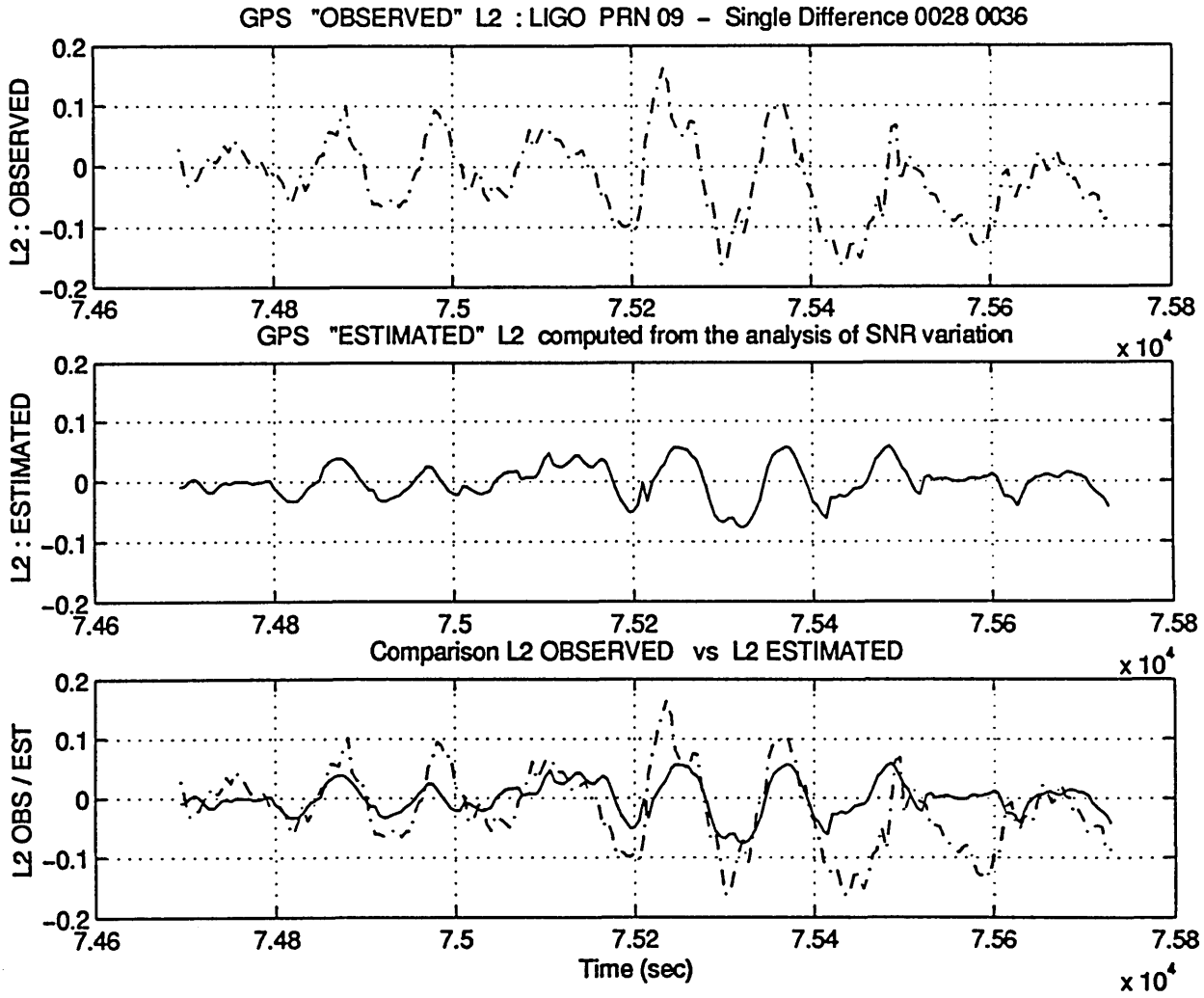

Fig. A.9.4: 0028- 0036 Satellite: PRN 09– Data acquisition date 25 9 1996
L_2_OBS and L_2_EST compared for t=7.467-7.58 10^4 sec
Unit: [cycles]

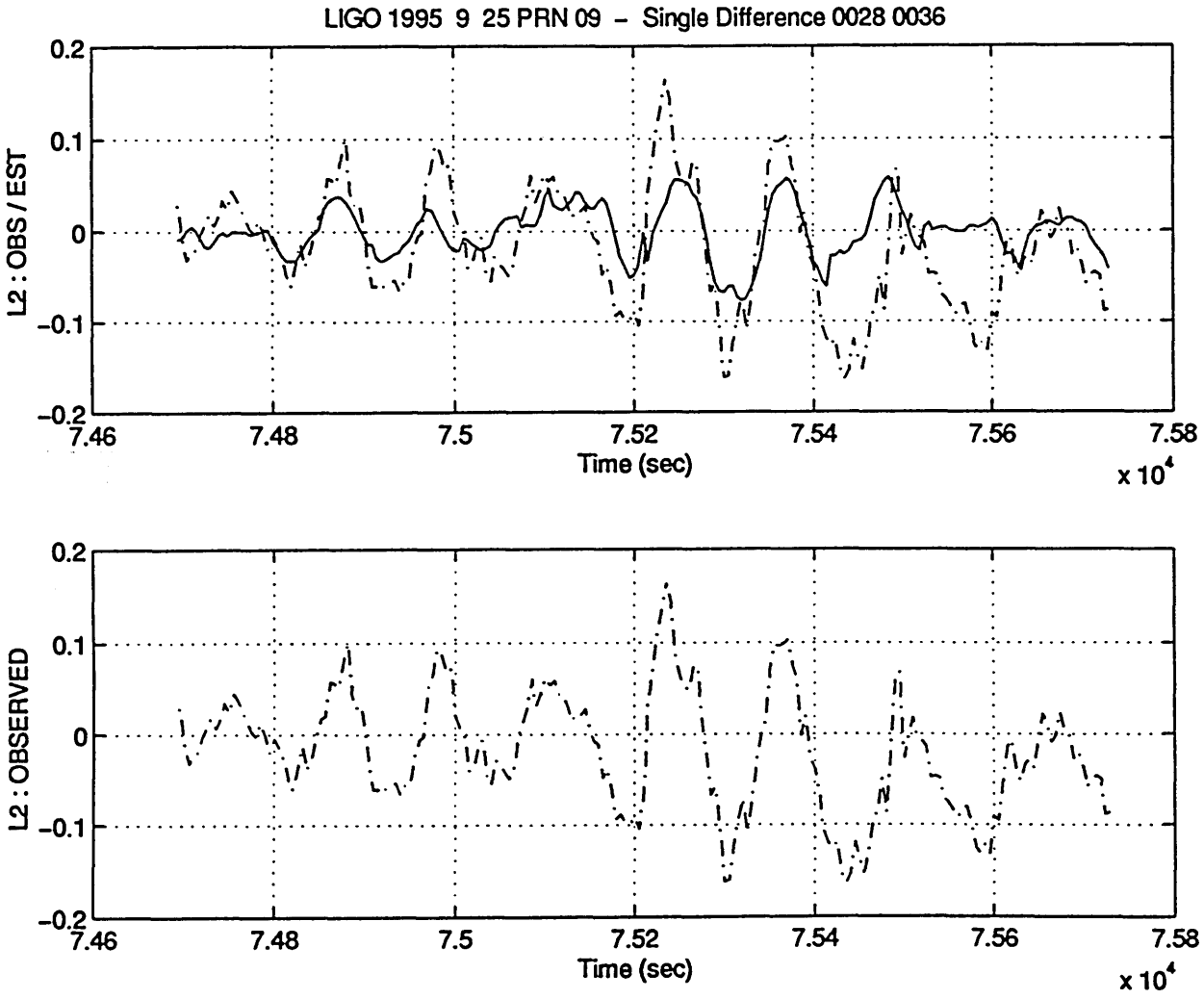

Fig. A.9.5: 0028-0036 Satellite: PRN 09
Data acquisition date 25 9 1996
$L2\_OBS$ and $L2\_EST$ compared for t=7.47 - 7.58 10^4 sec
Unit: [cycles]

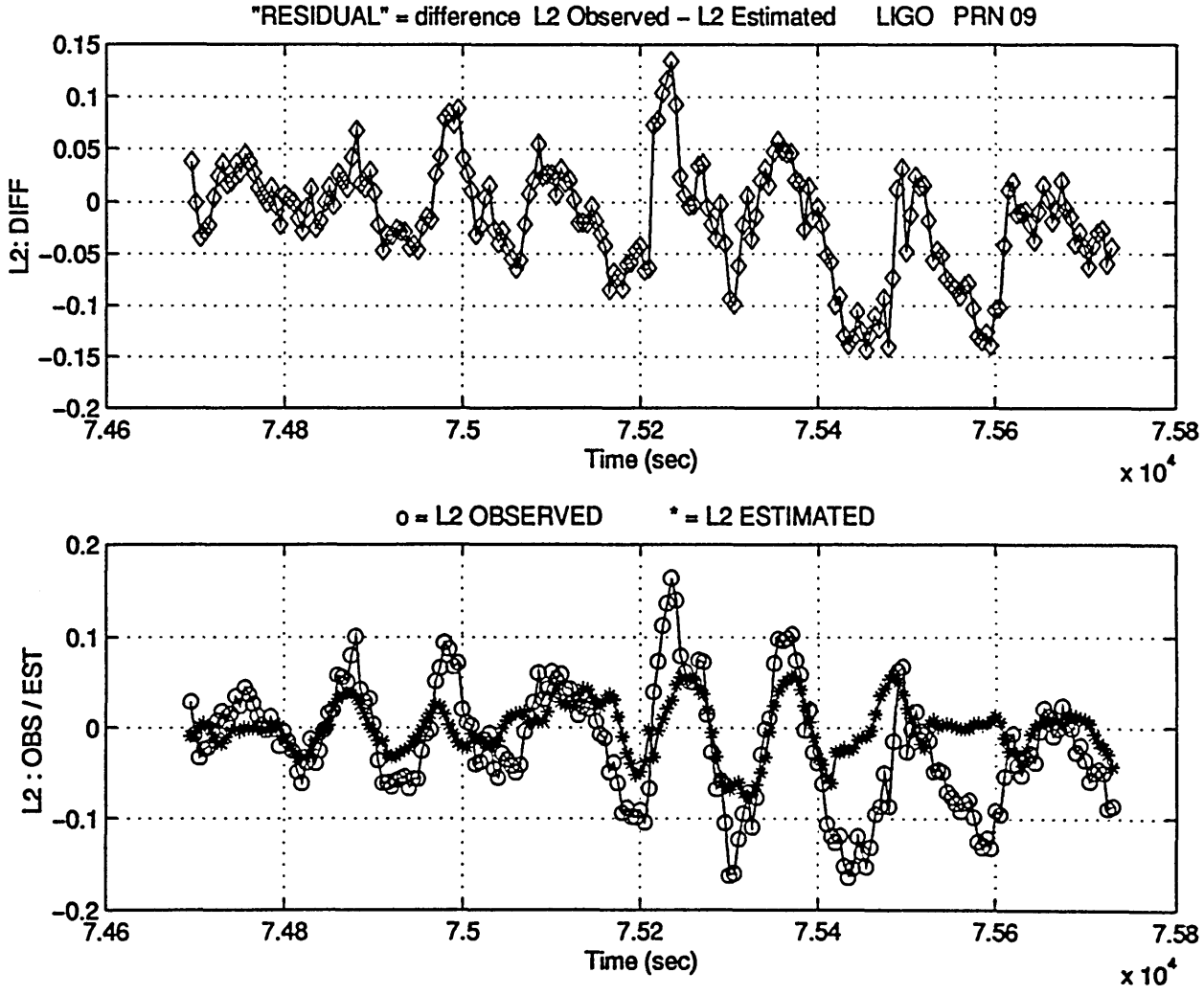

Fig. A.9.6.a) : 0028- 0036- PRN 09 (25 9 1996)
Phase residual L_2_DIFF, determined as the difference between L_2_OBS and L_2_EST.
Unit: [cycles]

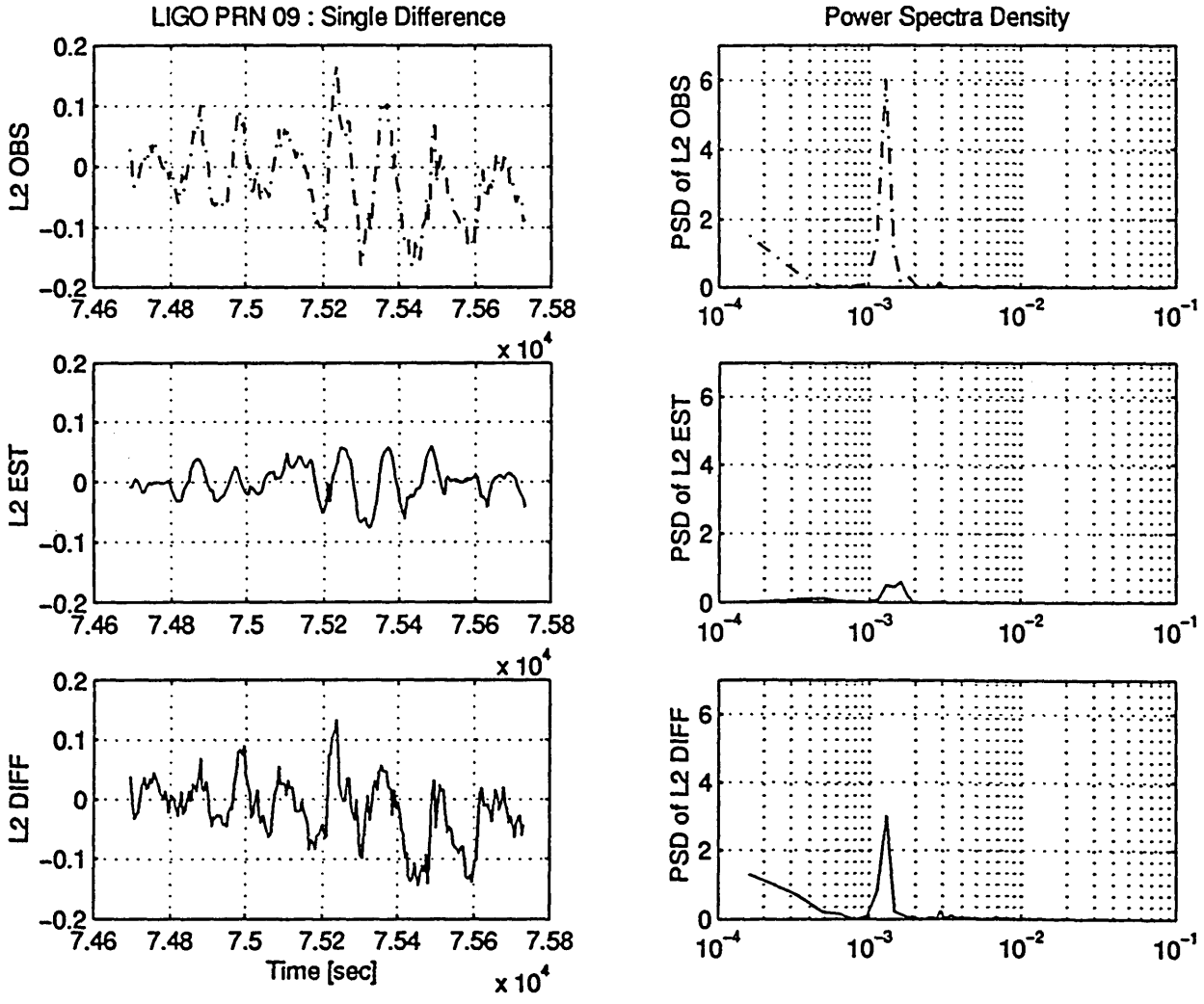

Fig. A.9.6.b) : 0028- 0036- PRN 09 (25 9 1996)
PSD of LC_OBS, LC_EST and LC_DIFF.
Unit: [cycles]^2

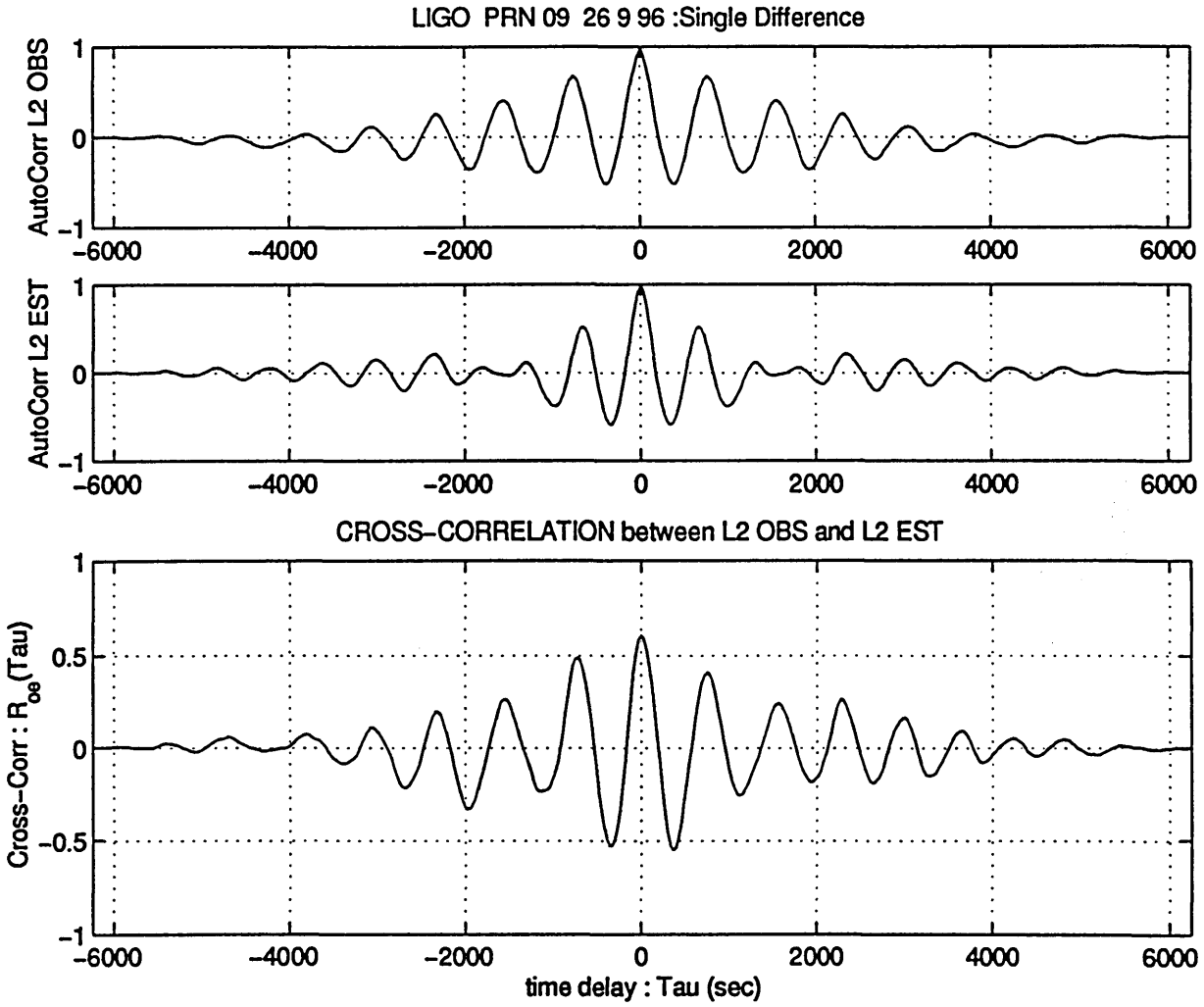

Fig. A.9.6.c) : 0028- 0036- PRN 09 (25 9 1996)
Auto Correlation of LC_OBS (R_{oo}) and LC_EST (R_{ee}).
Cross Correlation between them (R_{oe})
Unit: [cycles]^2

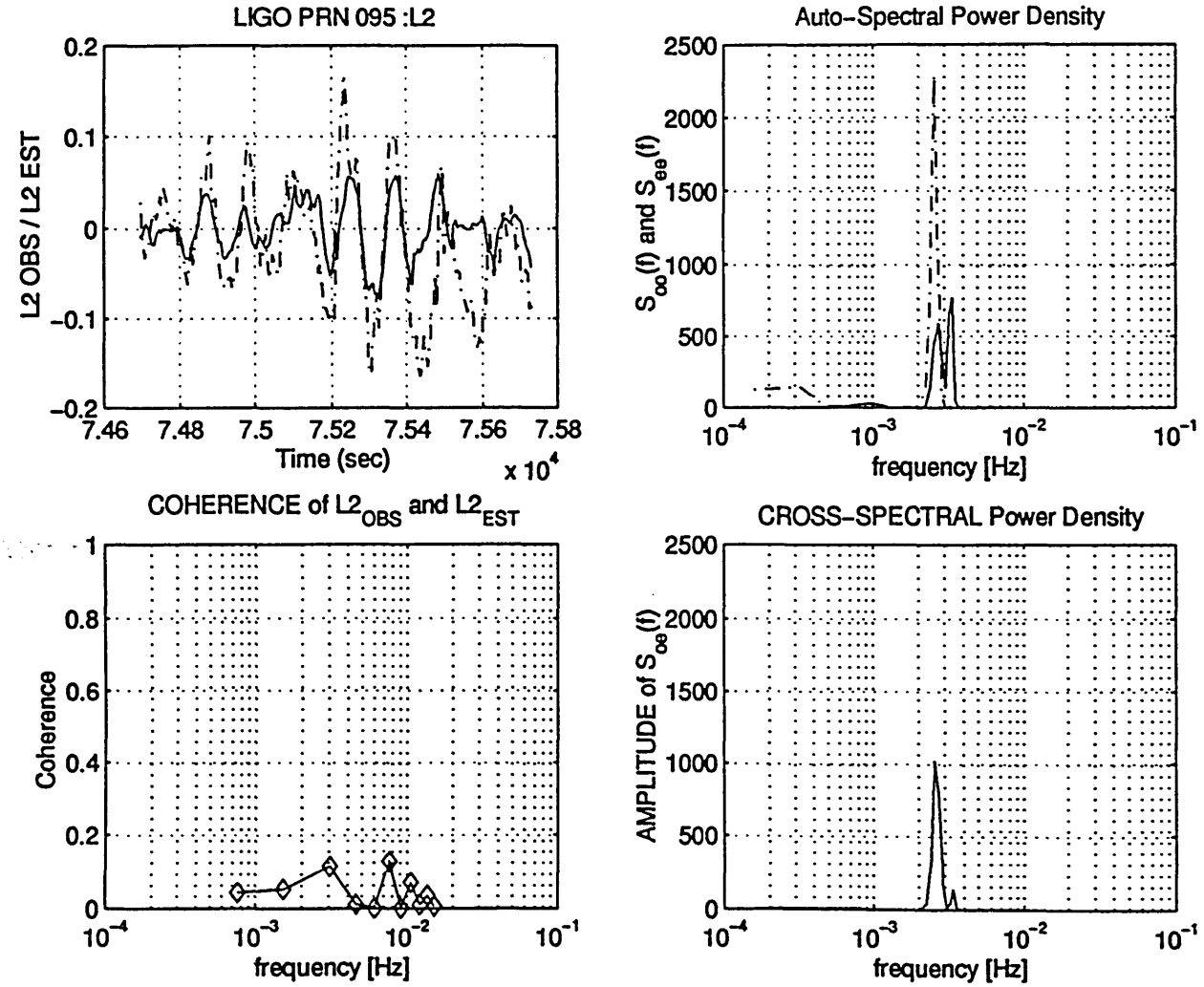

Fig. A.9.6.d) : 0028- 0036- PRN 09 (25 9 1996)
Auto Spectral Power Density of LC_OBS (S_{oo}) and of LC_EST (S_{ee}). Cross PSD between them (S_{oe})
Unit: [cycles]^2
Coherence function of LC_OBS and LC_EST

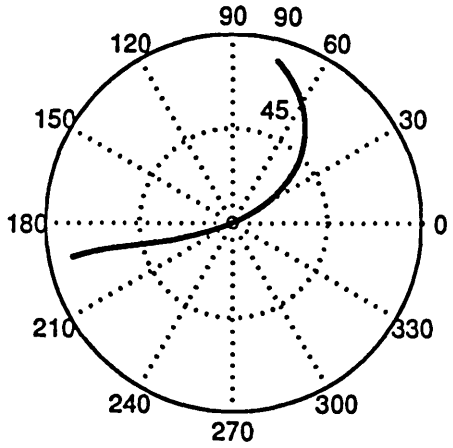

GPS DATA: receiver location: SOUTHERN CALIFORNIA acquisition date: 23 1 1997

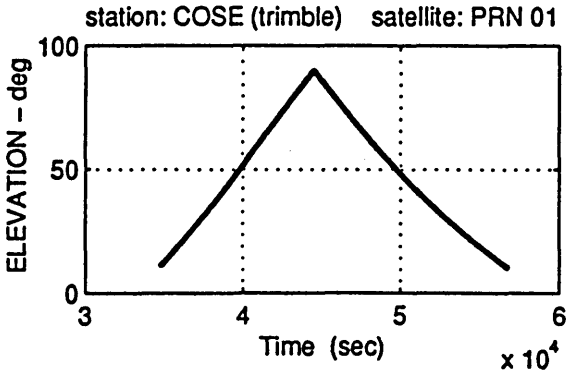

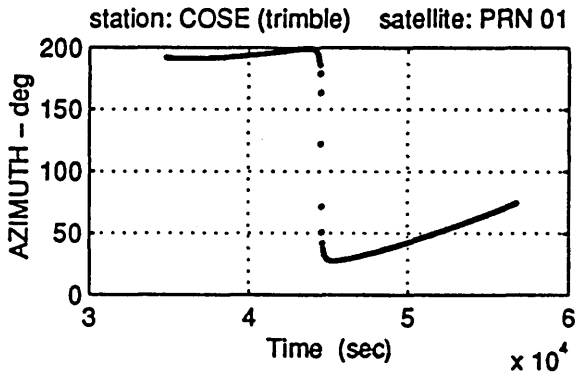

Fig. A.9.1 : Satellite visibility chart for PRN 01 (skymap). Elevation and azimuth of PRN 01with respect to the station COSE

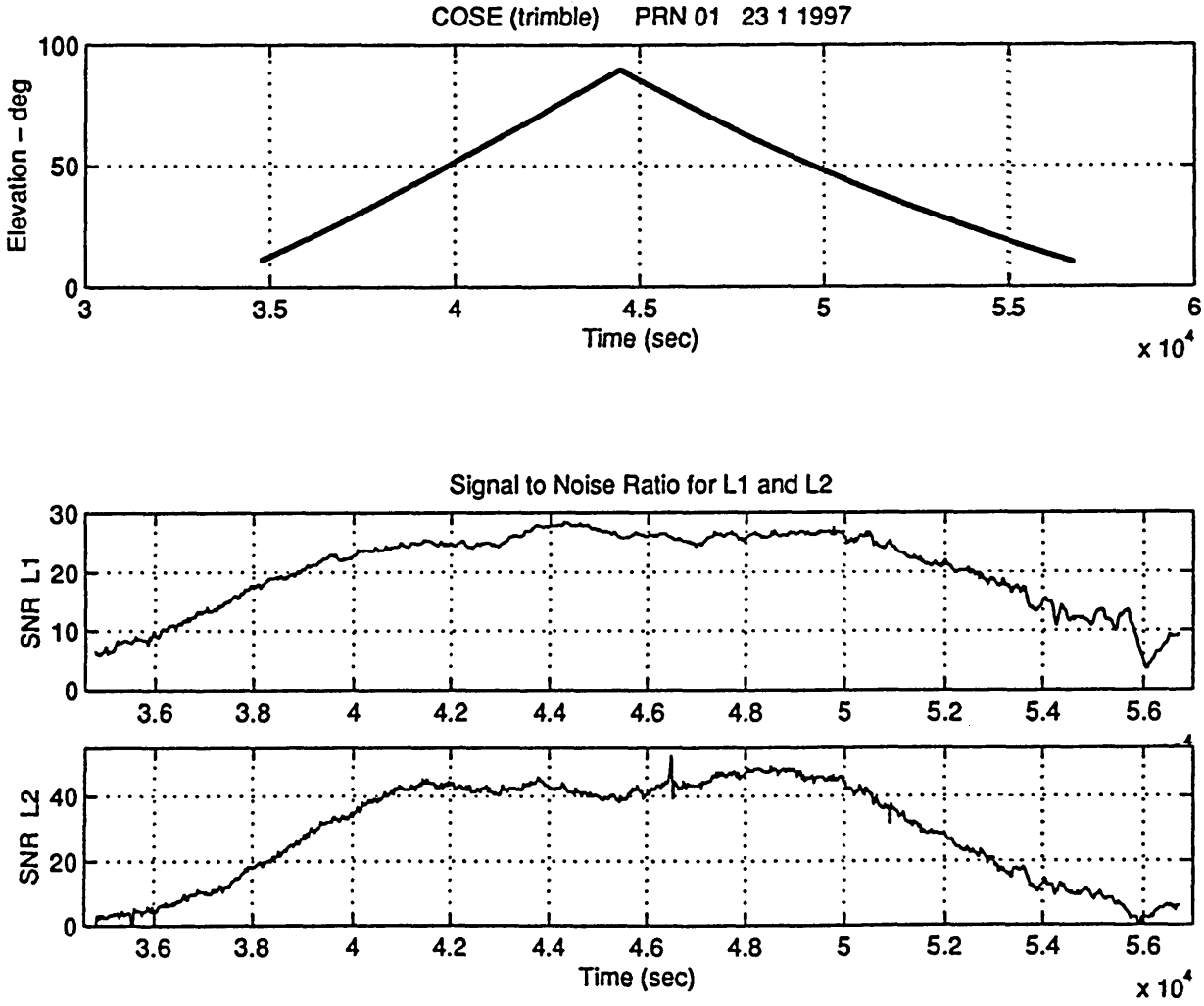

Fig. A.9.2 : Station: COSE - Satellite: PRN 01
Data acquisition date 23 1 1997
Signal-to-Noise-Ratio (SNR) for L_1 and L_2.

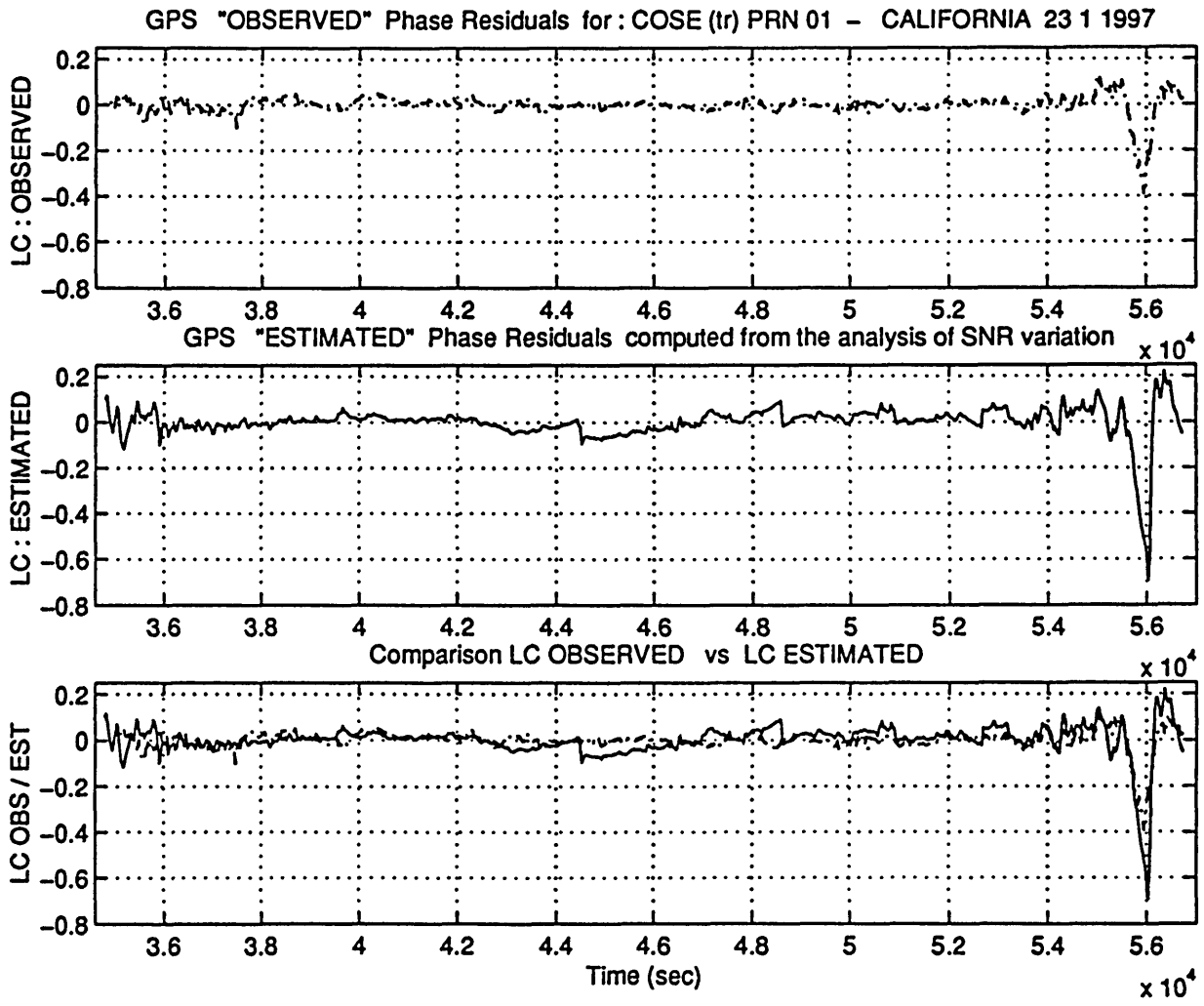

Fig. A.9.3 : Station: COSE - Satellite: PRN 01- Data acquisition date 23 1 1997
The observed phase residual (LC_OBS) is compared with the multipath phase error estimated from the SNR (LC_EST)
Unit: [cycles]

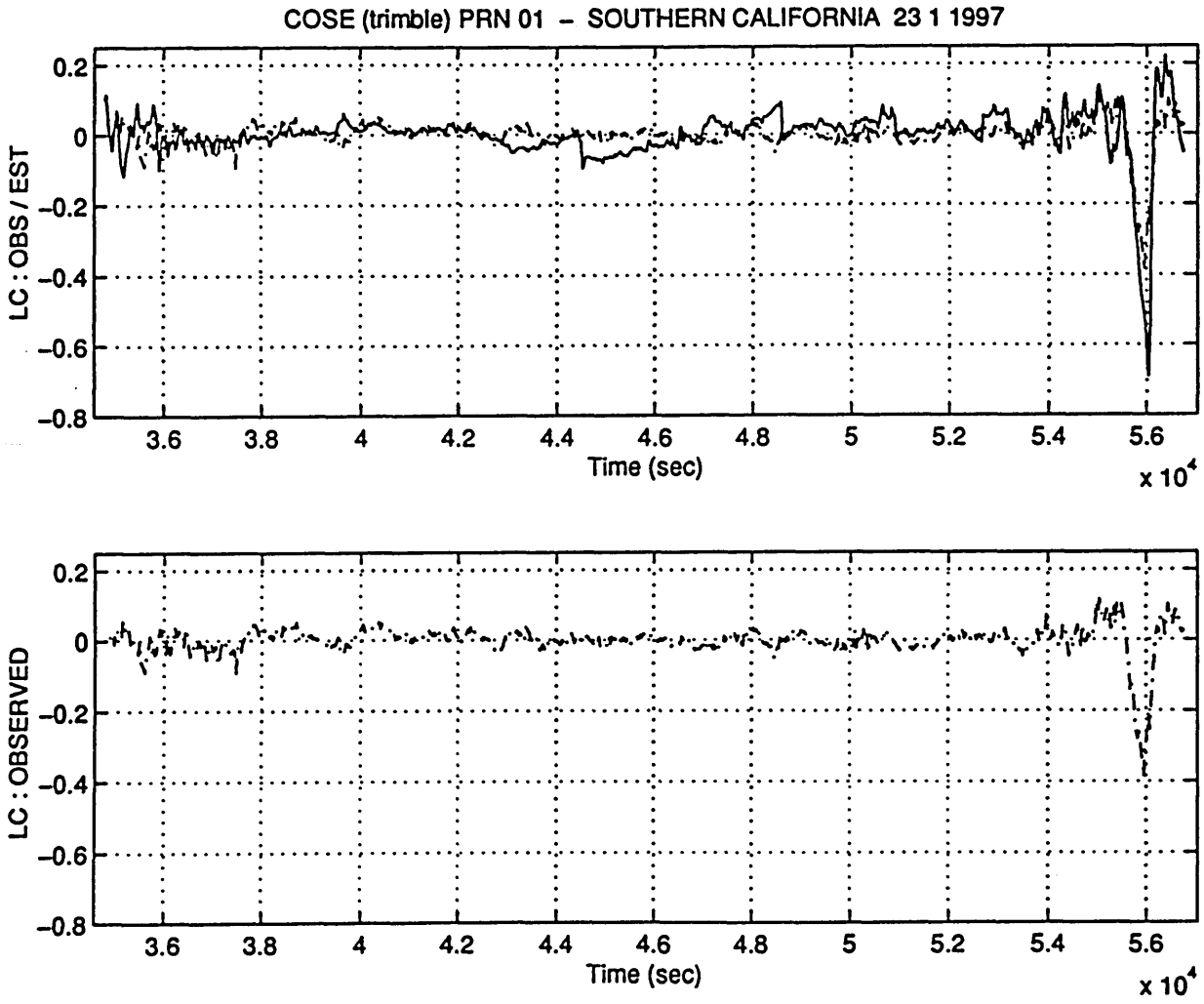

Fig. A.9.4 : Station: COSE - Satellite: PRN 01
Data acquisition date 23 1 1997
LC_OBS and LC_EST compared for t=3.5 - 5.7 10^4 sec
Unit: [cycles]

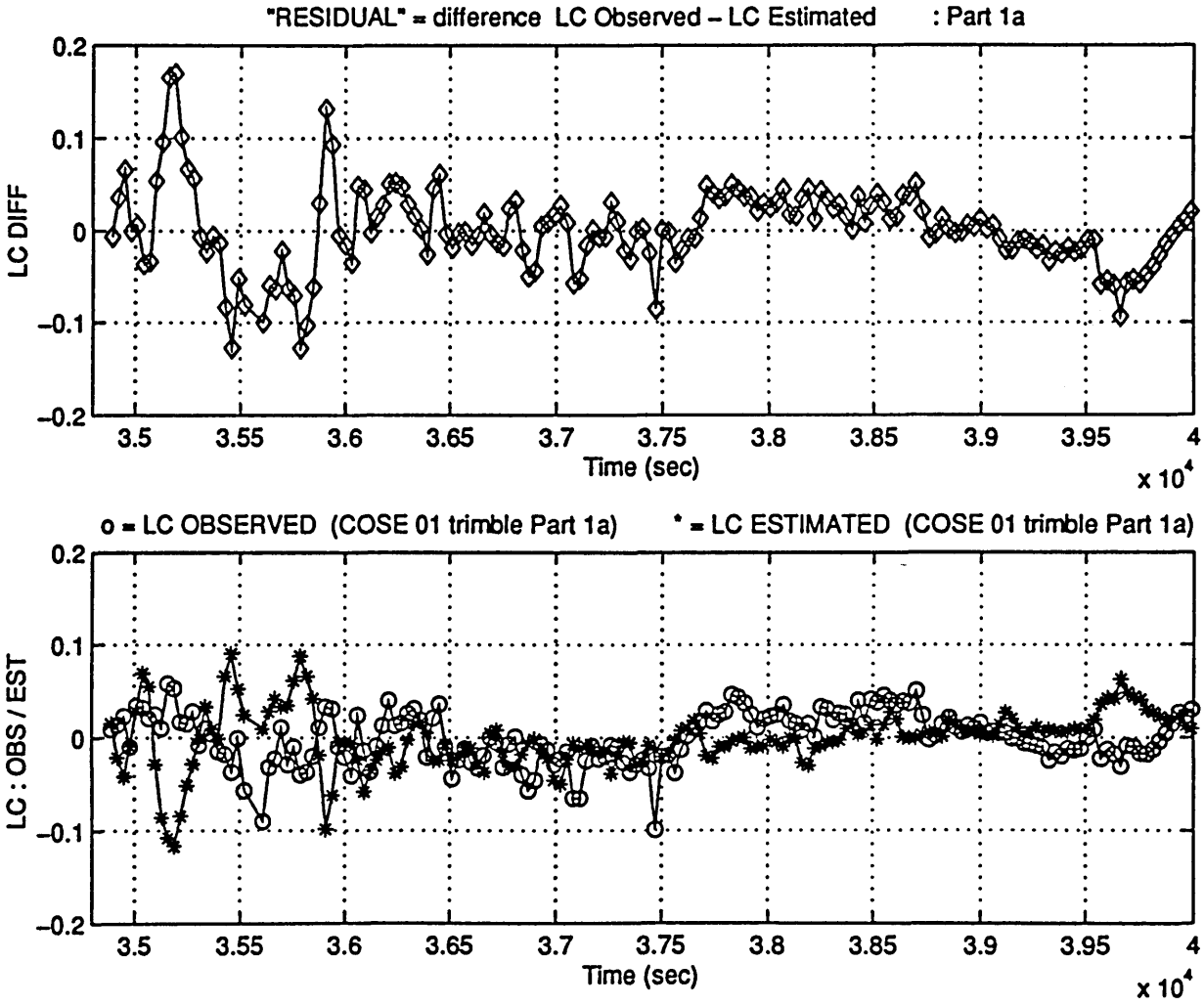

Fig. A.9.5.a) : COSE - PRN 01 (23 1 1997) - [segment 1a]
Phase residual LC_DIFF, determined as the difference between LC_OBS and LC_EST.
Unit: [cycles]

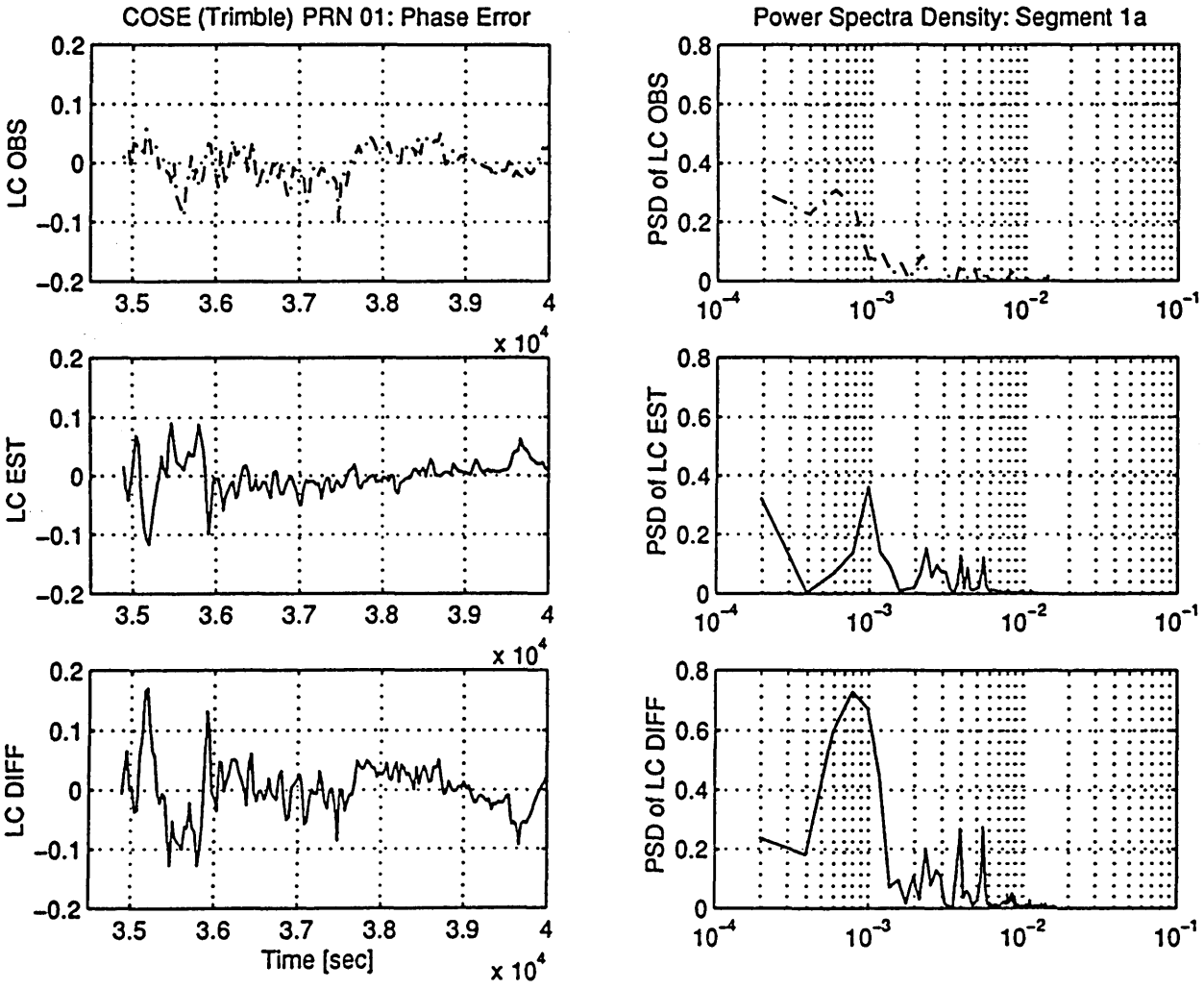

Fig. A.9.5.b) : COSE - PRN 01 (23 1 1997) - [segment 1a]
PSD of LC_OBS, LC_EST and LC_DIFF.
Unit: [cycles]^2

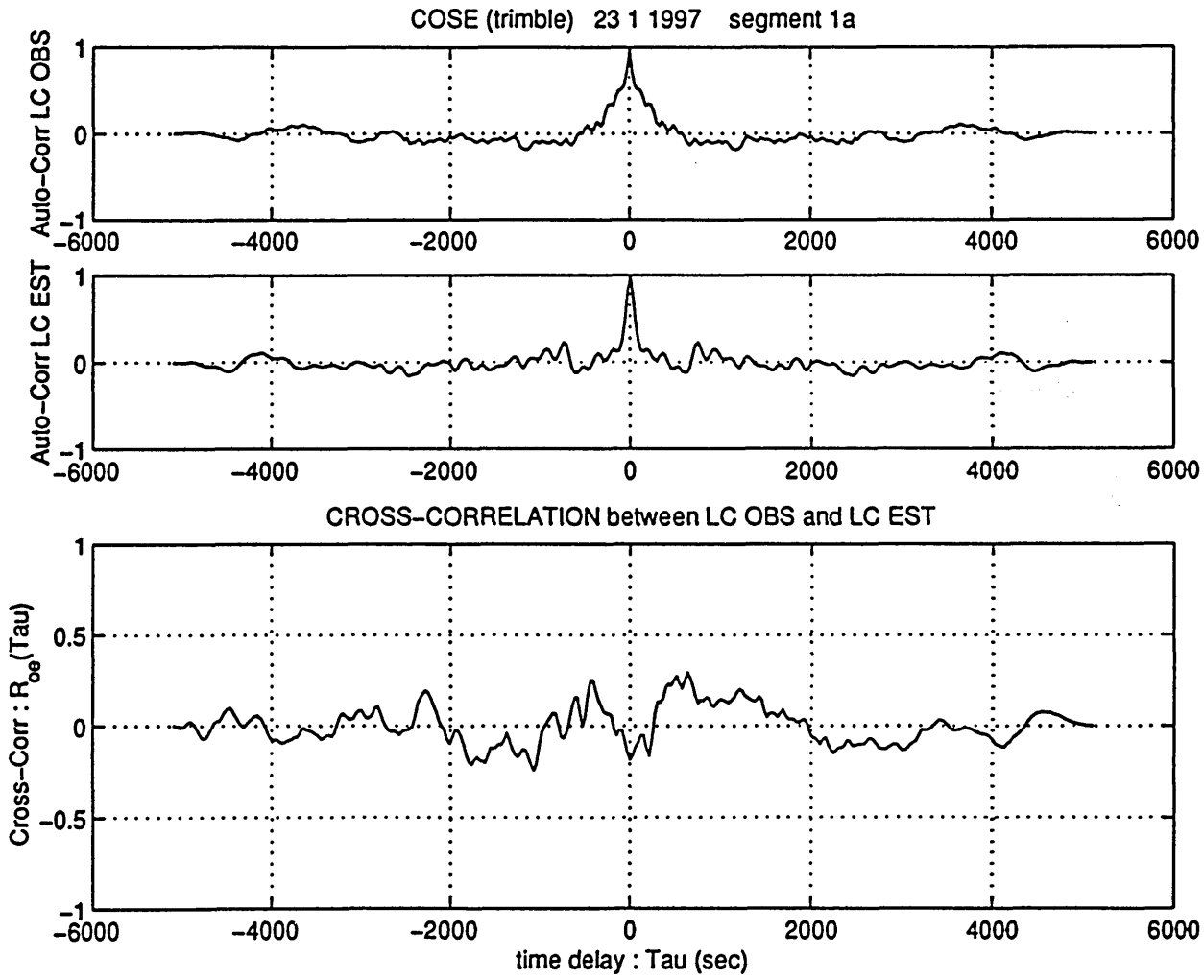

Fig. A.9.5.c) : COSE - PRN 01 (23 1 1997) - [segment 1a]
Auto Correlation of LC_OBS (R_{oo}) and LC_EST (R_{ee}).
Cross Correlation between them (R_{oe})
Unit: [cycles]^2

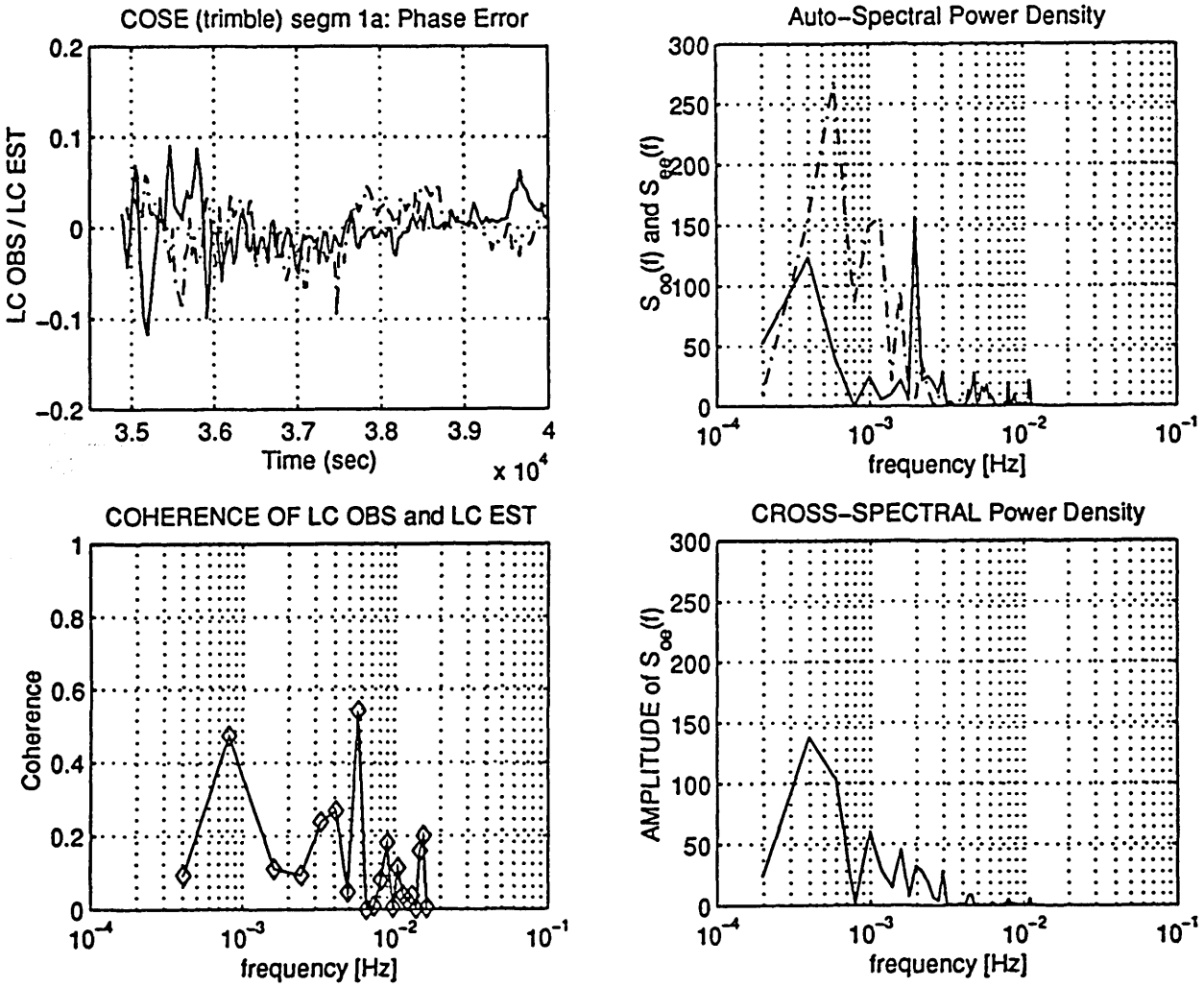

Fig. A.9.5.d) : COSE - PRN 01 (23 1 1997) - [segment 1a]
Auto Spectral Power Density of LC_OBS (S_{oo}) and of LC_EST (S_{ee}). Cross PSD between them (S_{oe})
Unit: [cycles]^2
Coherence function of LC_OBS and LC_EST

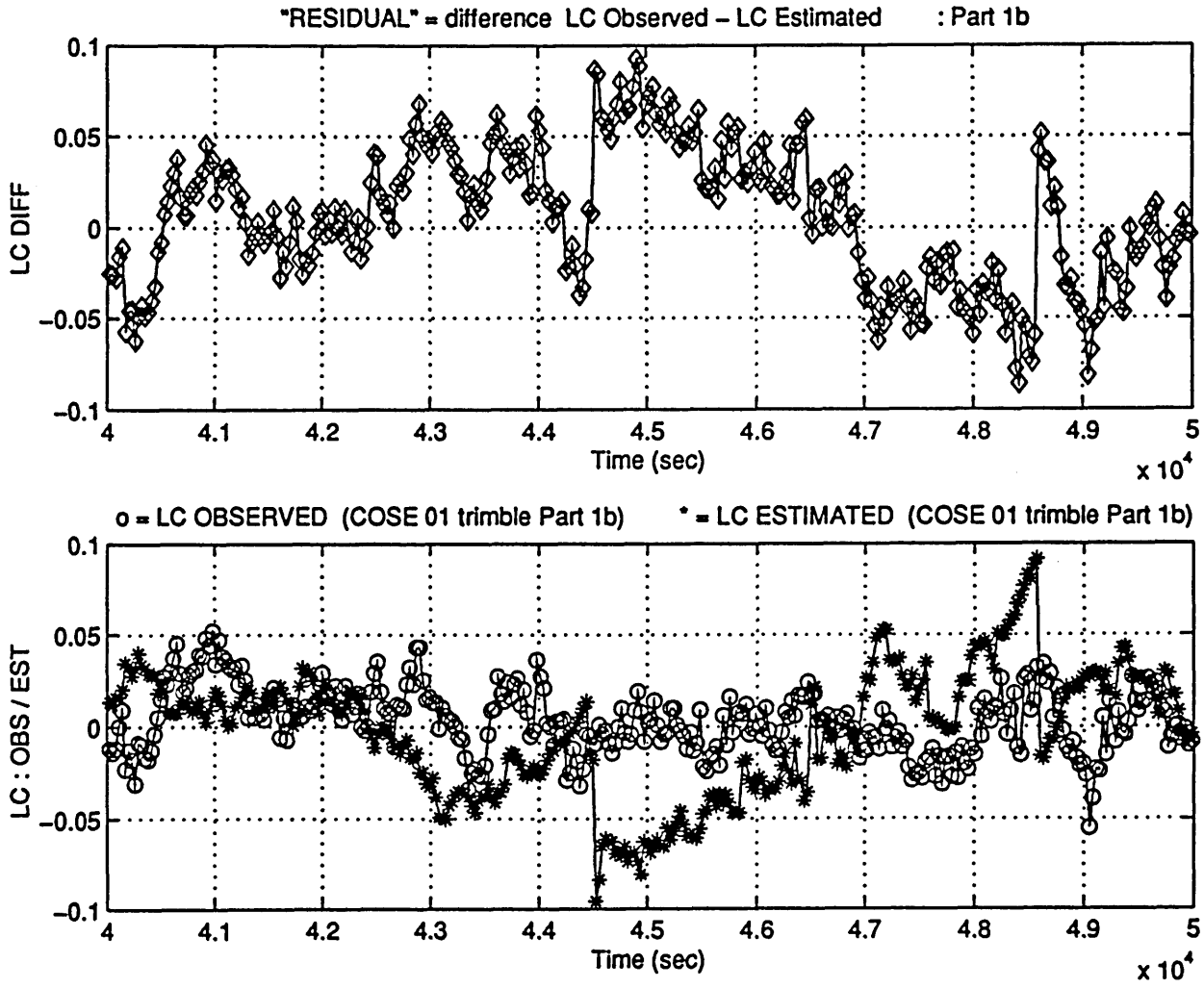

Fig. A.9.6.a) : COSE - PRN 01 (23 1 1997) - [segment 1b]
Phase residual LC_DIFF, determined as the difference between LC_OBS and LC_EST.
Unit: [cycles]

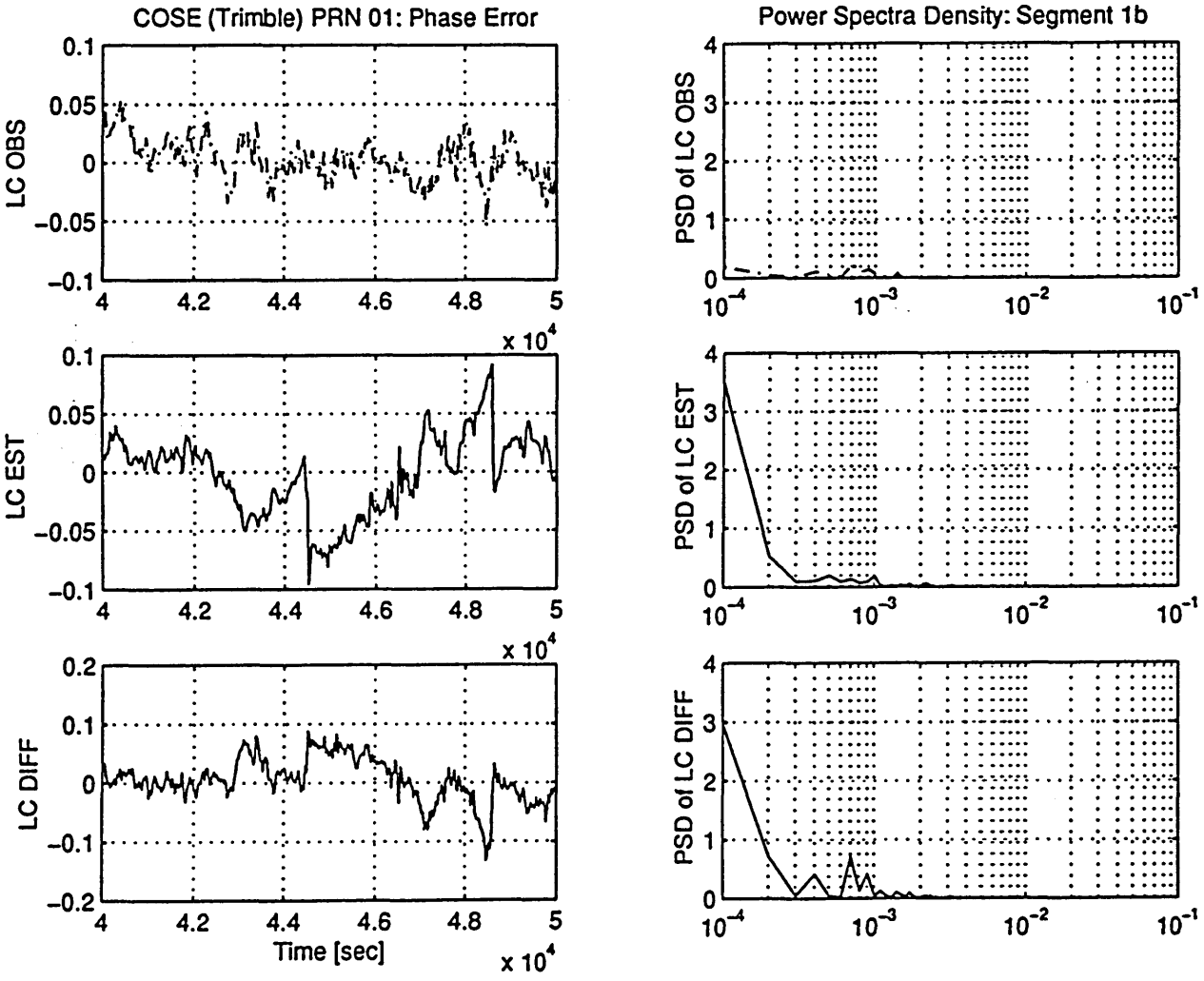

Fig. A.9.6.b) : COSE - PRN 01 (23 1 1997) - [segment 1b]
PSD of LC_OBS, LC_EST and LC_DIFF.
Unit: [cycles]^2

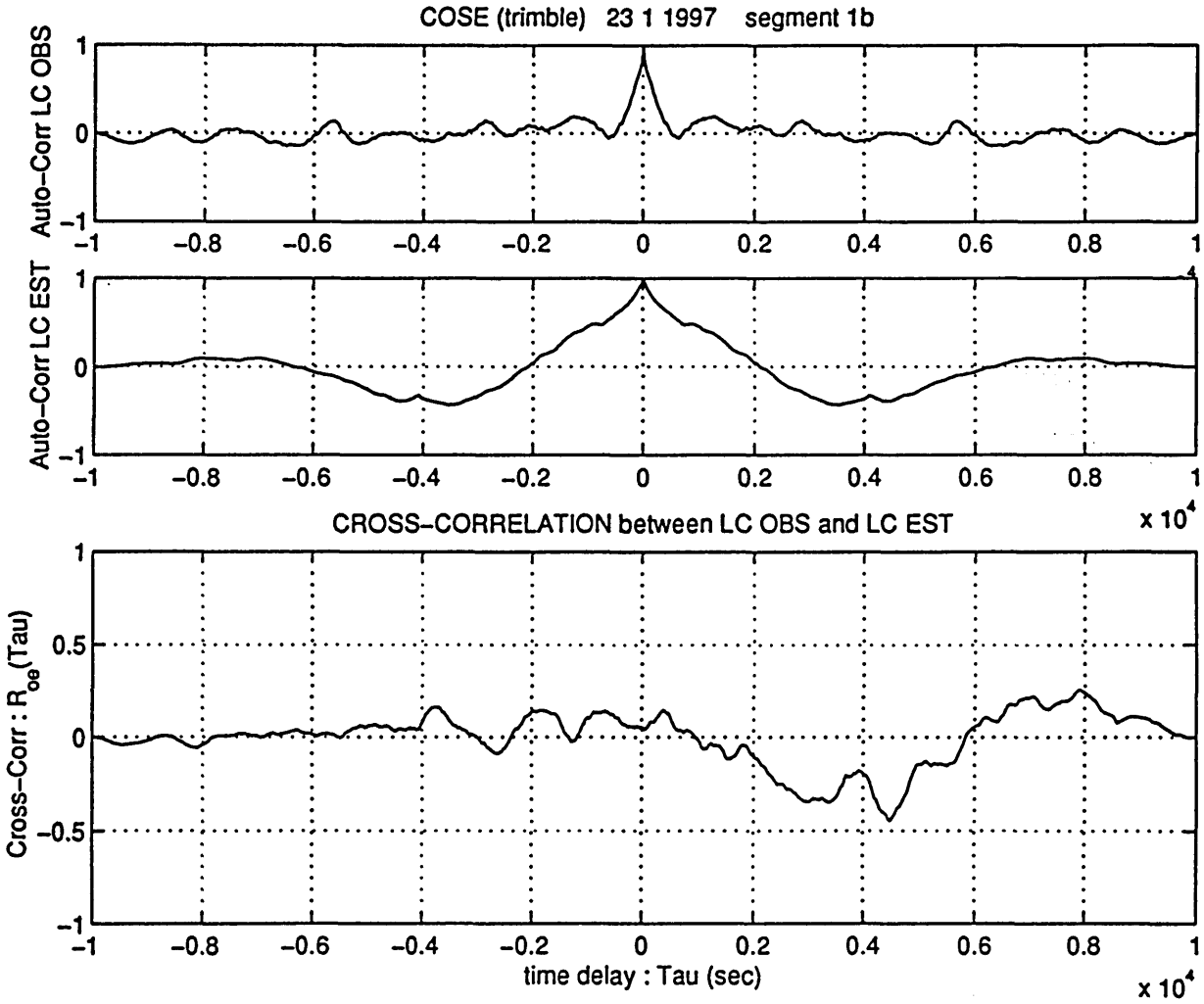

Fig. A.9.6.c) : COSE - PRN 01 (23 1 1997) - [segment 1b]
Auto Correlation of LC_OBS (R_{oo}) and LC_EST (R_{ee}).
Cross Correlation between them (R_{oe})
Unit: [cycles]^2

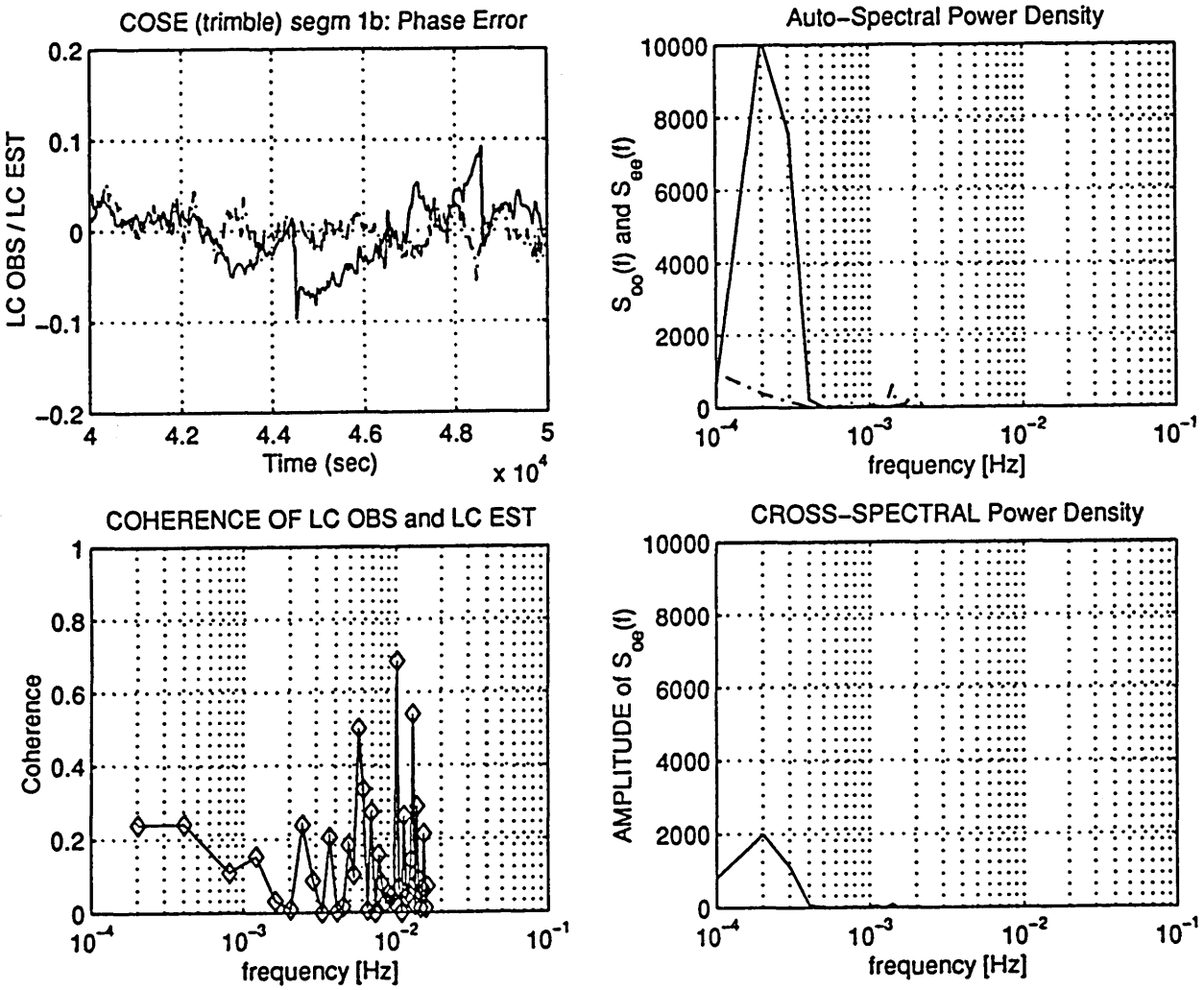

Fig. A.9.6.d) : COSE - PRN 01 (23 1 1997) - [segment 1b]
Auto Spectral Power Density of LC_OBS (S_{oo}) and of LC_EST (S_{ee}). CrossPSD between them (S_{oe})
Unit: [cycles]^2
Coherence function of LC_OBS and LC_EST

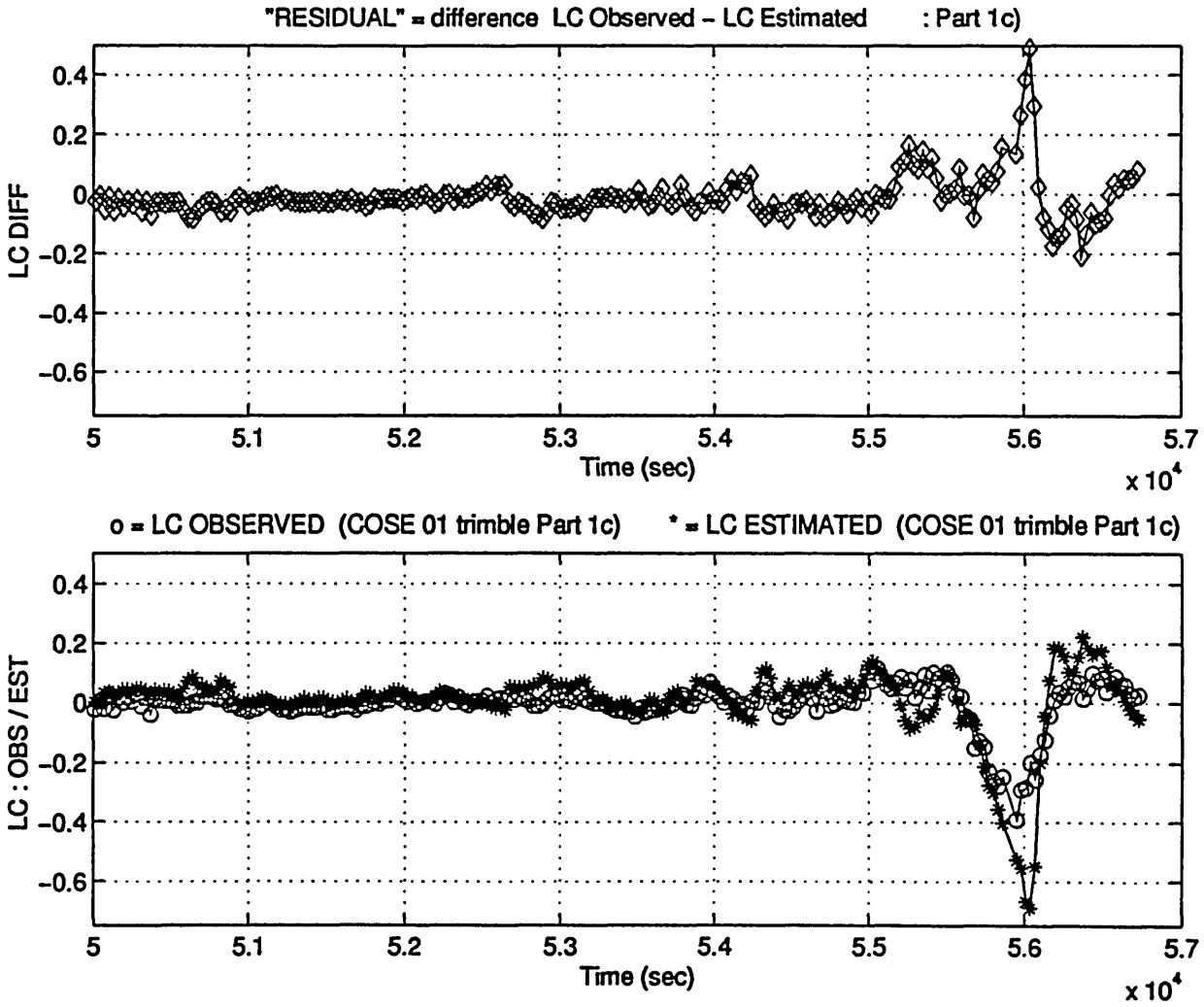

Fig. A.9.7.a) : COSE - PRN 01 (23 1 1997) - [segment 1c]
Phase residual LC_DIFF, determined as the difference between LC_OBS and LC_EST.
Unit: [cycles]

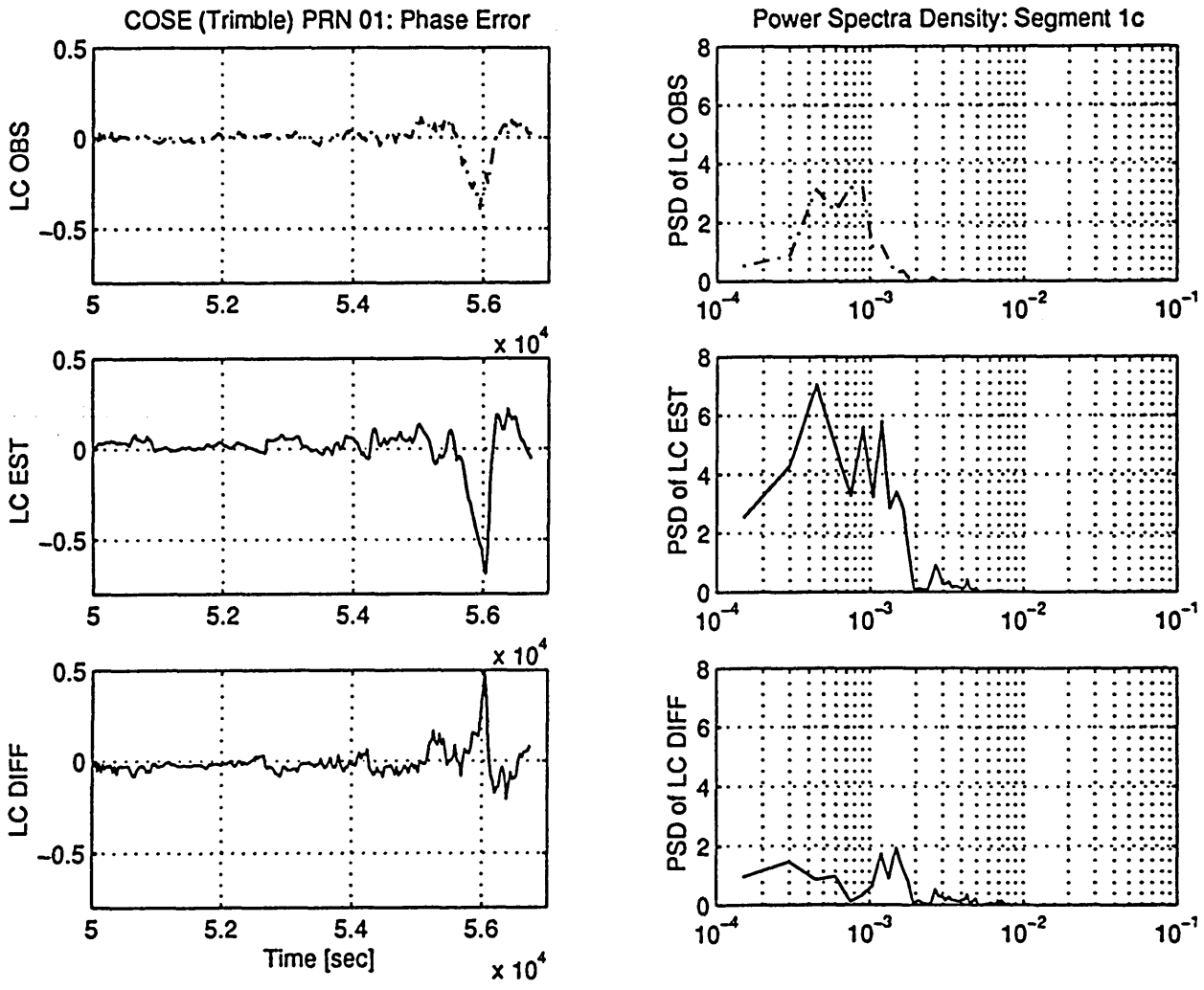

Fig. A.9.7.b) : COSE - PRN 01 (23 1 1997) - [segment 1c]
PSD of LC_OBS, LC_EST and LC_DIFF.
Unit: [cycles]^2

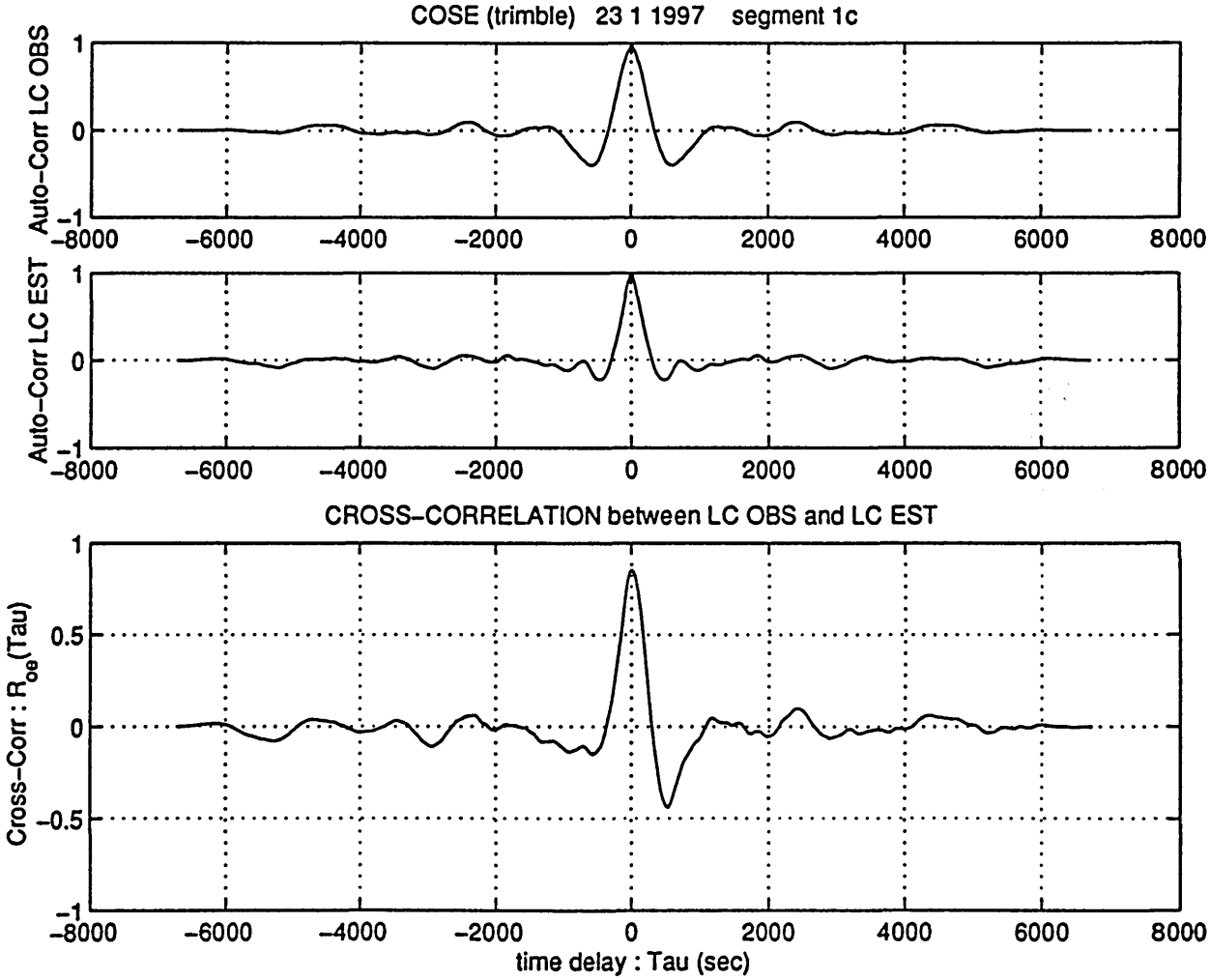

Fig. A.9.7.c) : COSE - PRN 01 (23 1 1997) - [segment 1c]
Auto Correlation of LC_OBS (R_{oo}) and LC_EST (R_{ee}).
Cross Correlation between them (R_{oe})
Unit: [cycles]^2

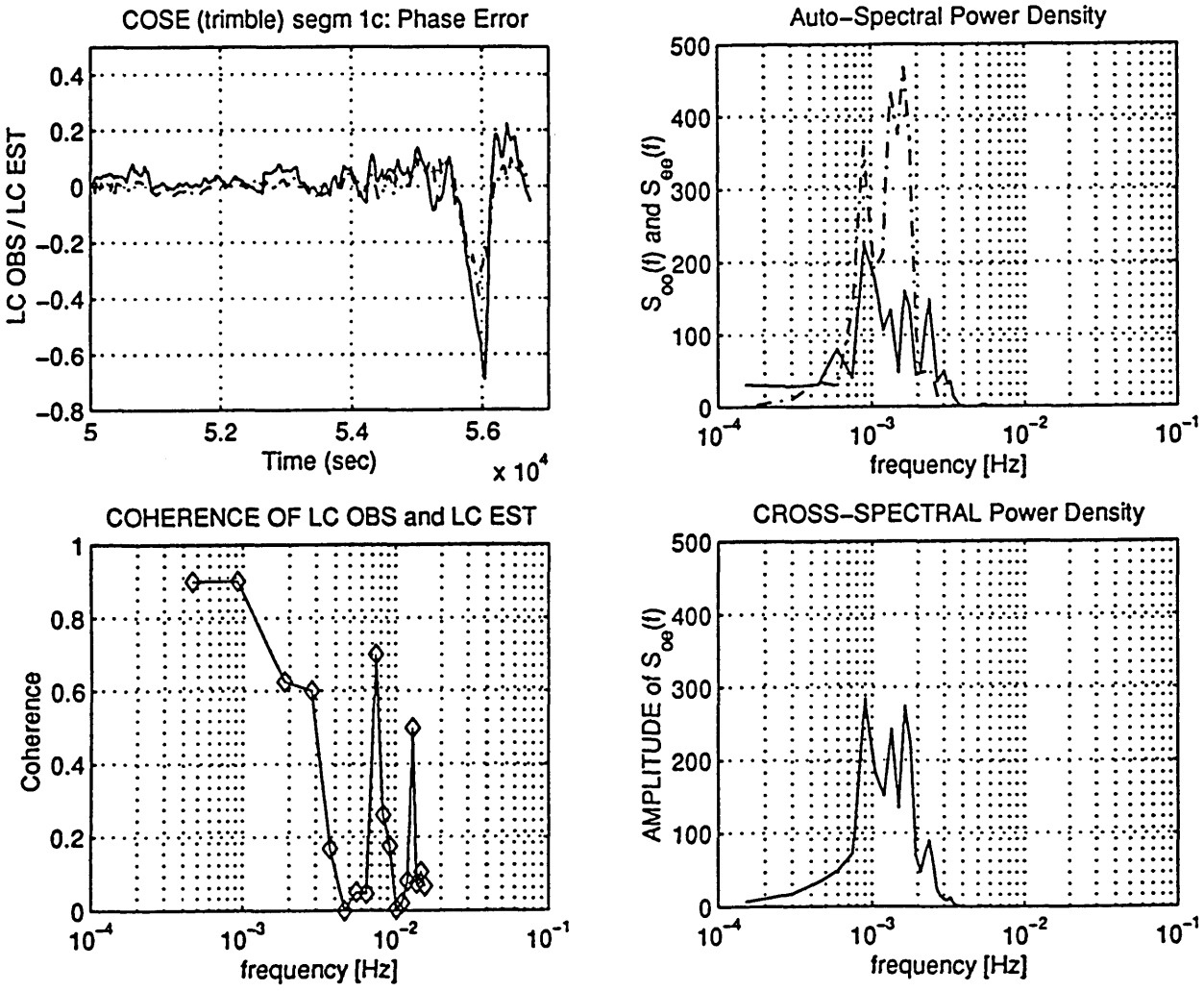

Fig. A.9.7.d) : COSE - PRN 01 (23 1 1997) - [segment 1c]
Auto Spectral Power Density of LC_OBS (S_{oo}) and of LC_EST (S_{ee}). CrossPSD between them (S_{oe})
Unit: [cycles]^2
Coherence function of LC_OBS and LC_EST

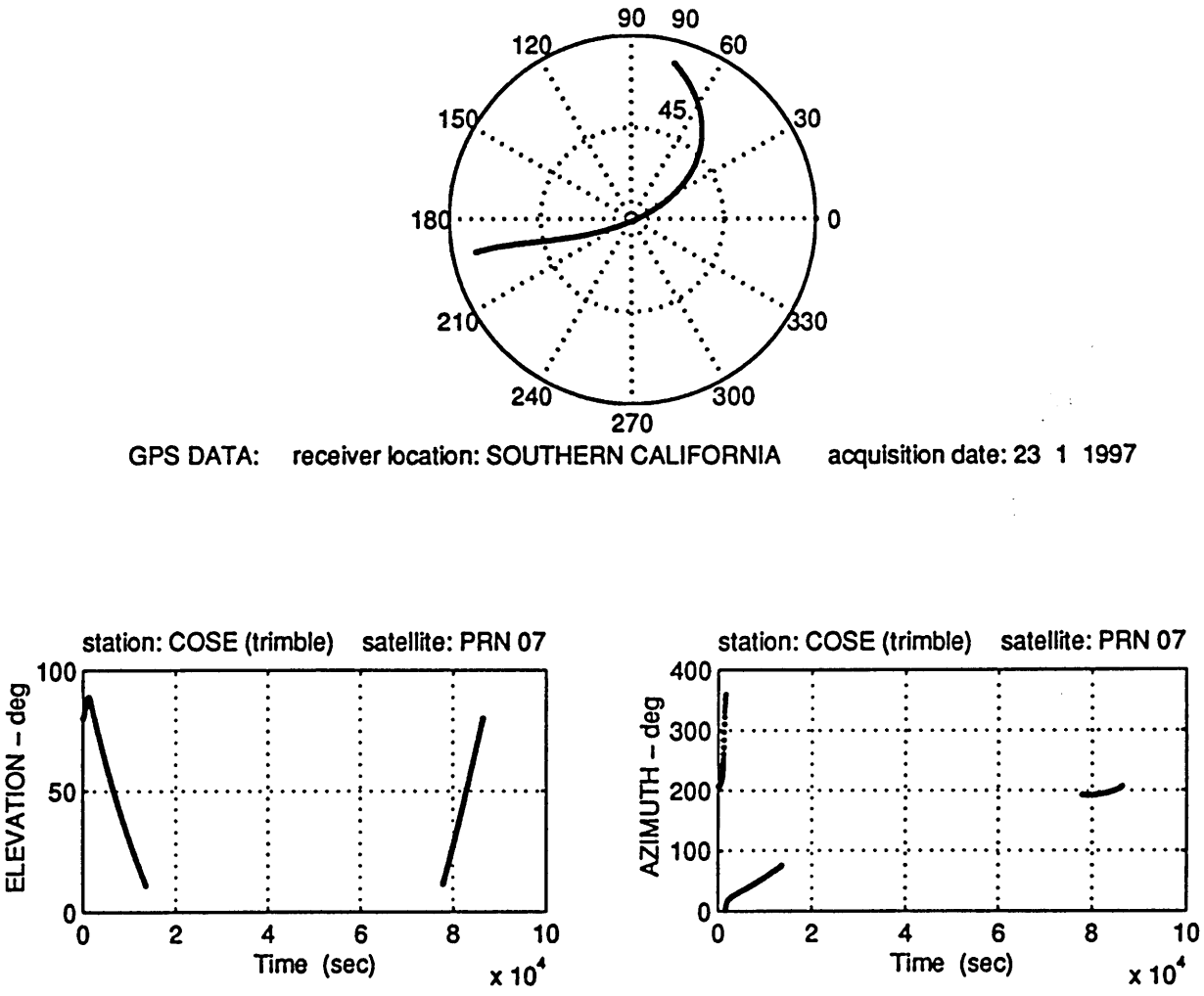

Fig. A.10.1 : Satellite visibility chart for PRN 07 (skymap). Elevation and azimuth of PRN 07 with respect to the station COSE

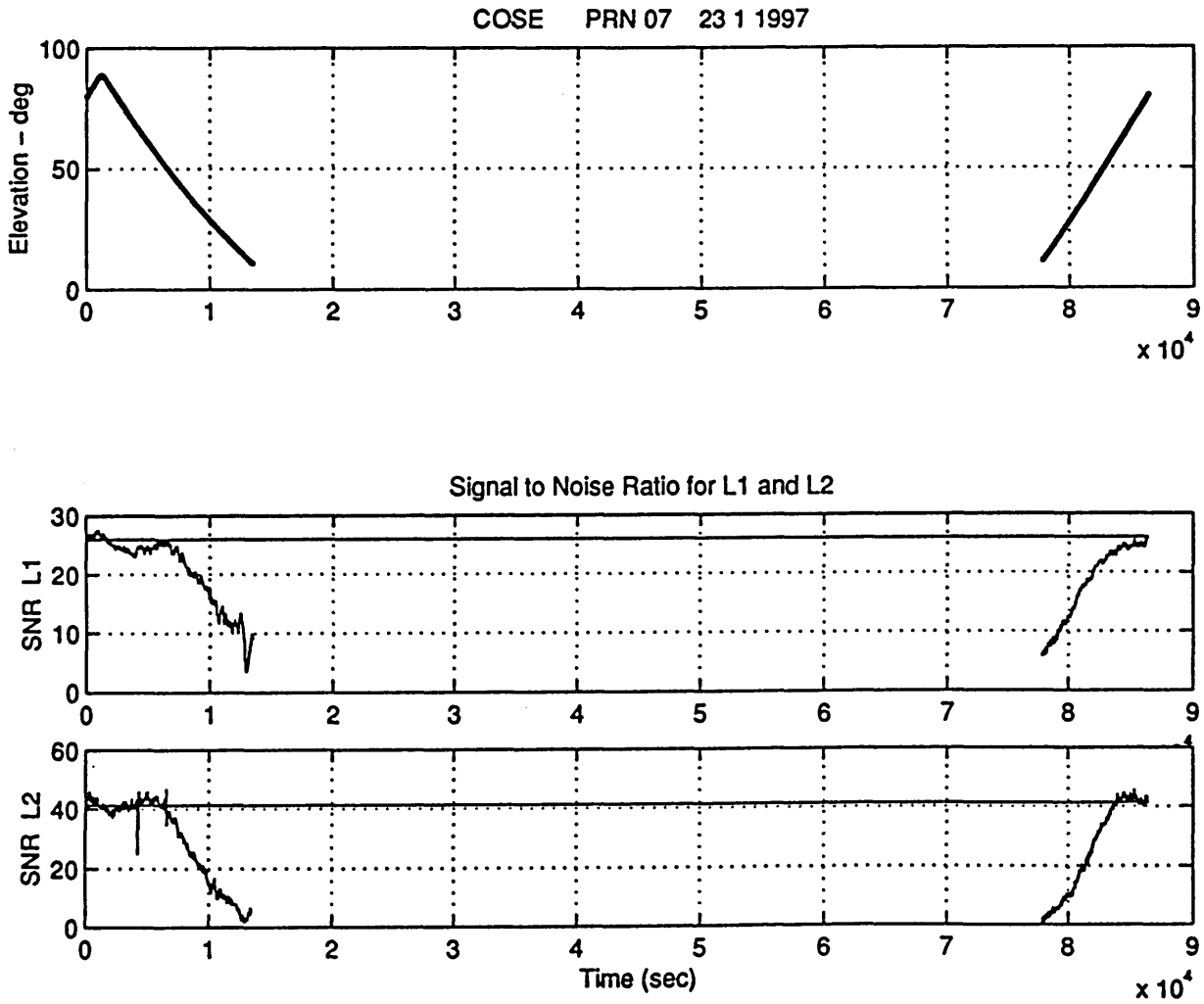

Fig. A.10.2 : Station: COSE - Satellite: PRN 07
Data acquisition date 23 1 1997
Signal-to-Noise-Ratio (SNR) for L_1 and L_2.

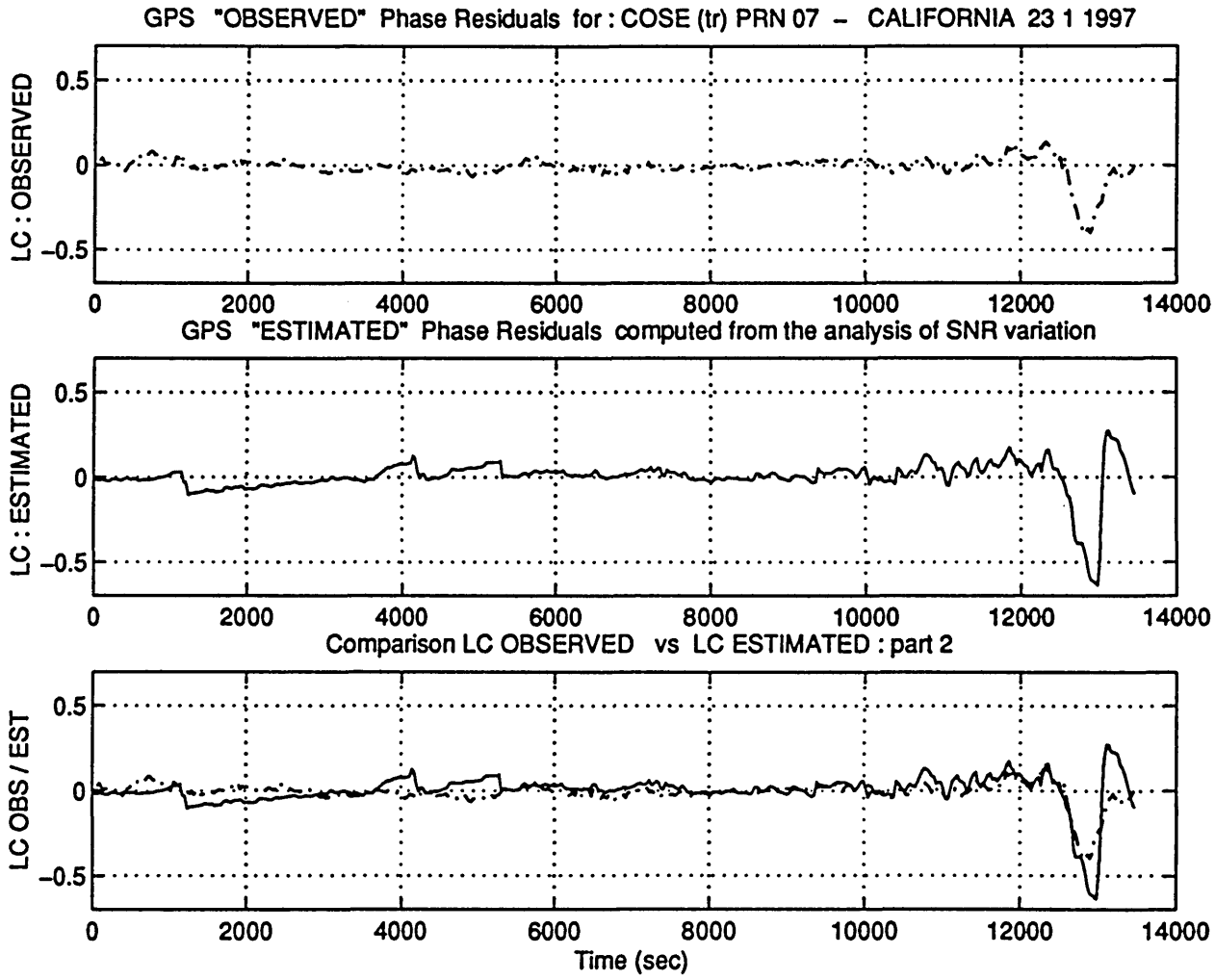

Fig. A.10.3 : Station: COSE - Satellite: PRN 07- Data acquisition date 23 1 1997
The observed phase residual (LC_OBS) is compared with the multipath phase error estimated from the SNR (LC_EST)
Unit: [cycles]

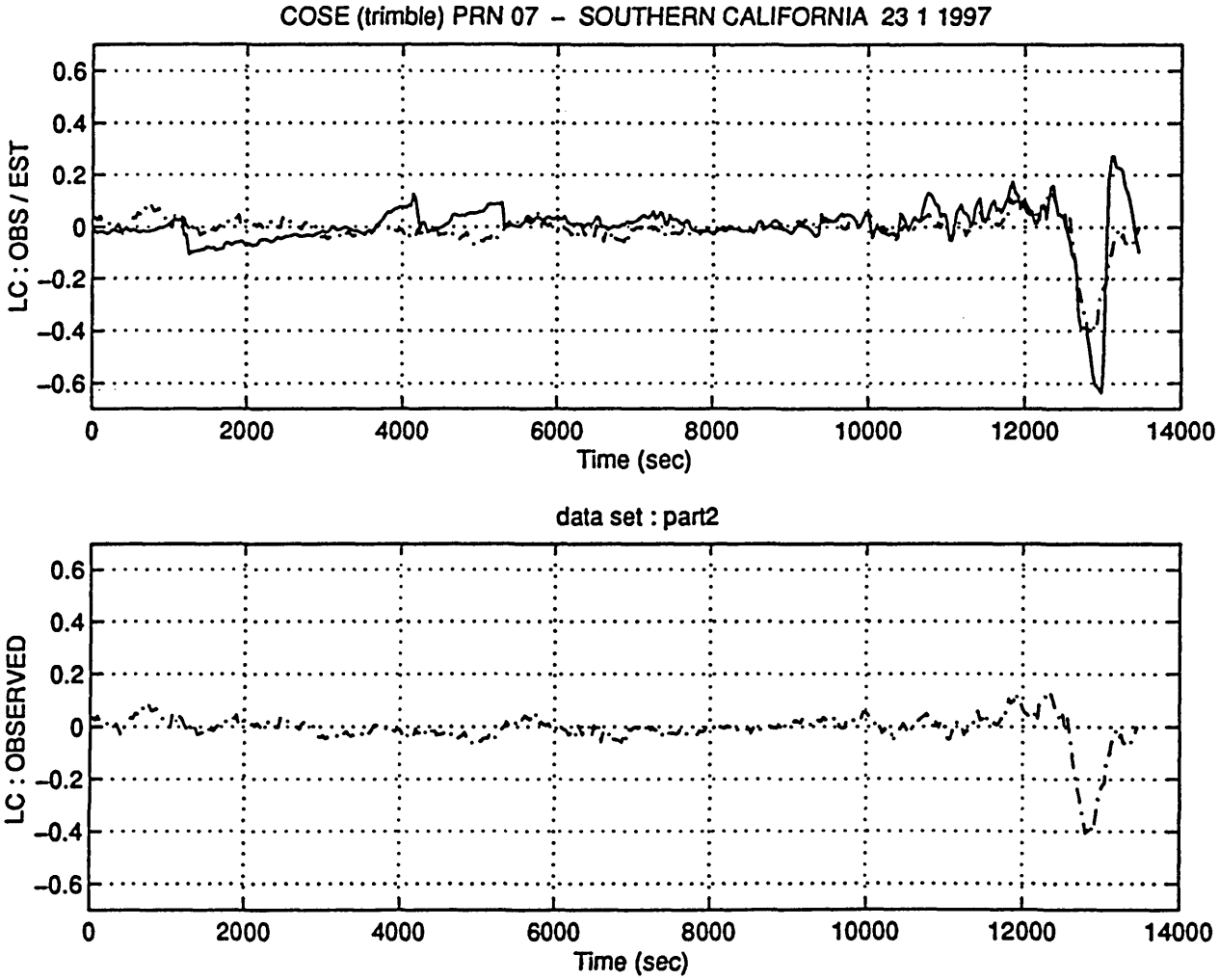

Fig. A.10.4 : Station: COSE - Satellite: PRN 07- Data acquisition date 23 1 1997
LC_OBS and LC_EST compared for t=0.0 - 1.4 10^4 sec
Unit: [cycles]

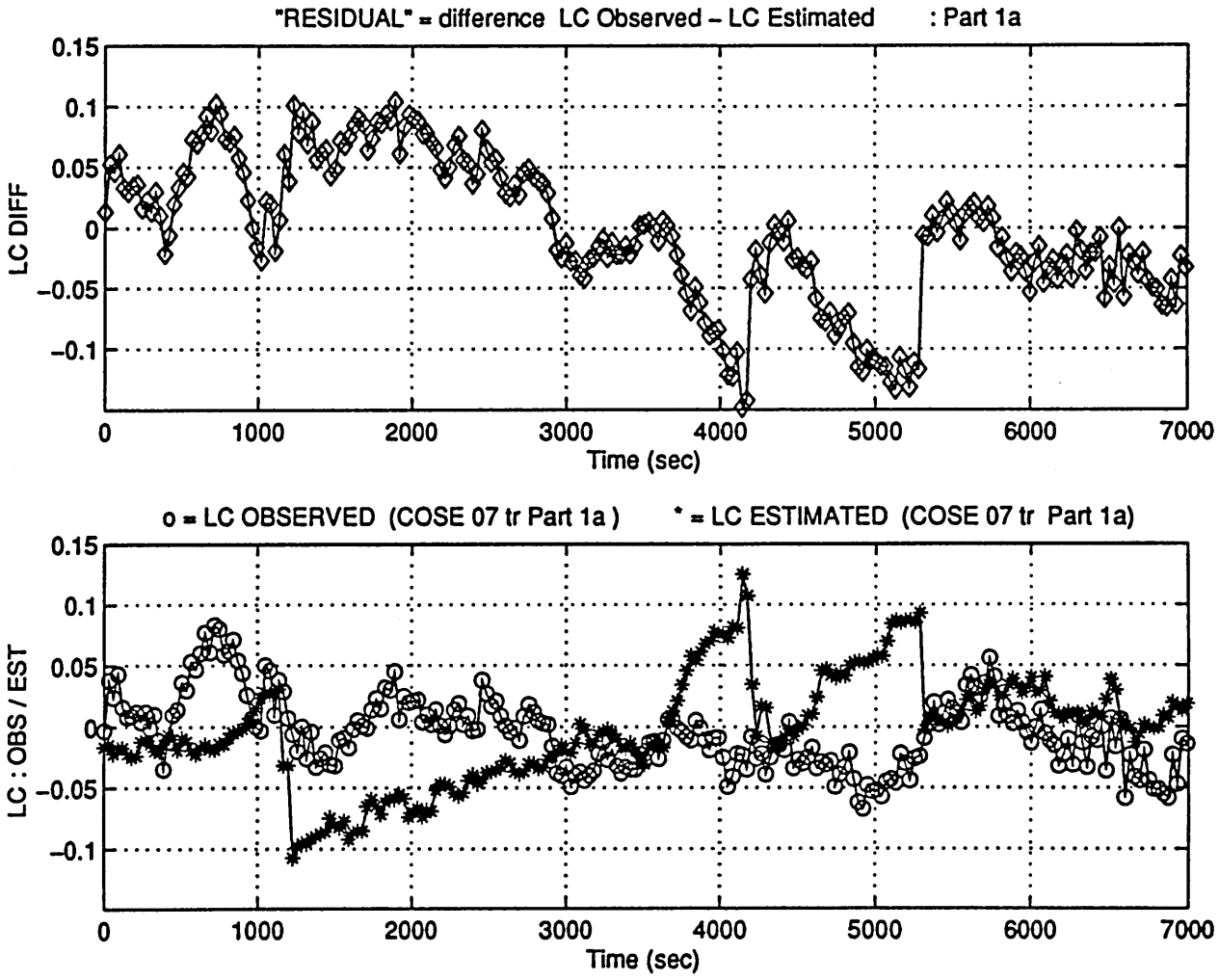

Fig. A.10.5.a) : COSE - PRN 07 (23 1 1997) - [segment 1a]
Phase residual LC_DIFF, determined as the difference between LC_OBS and LC_EST.
Unit: [cycles]

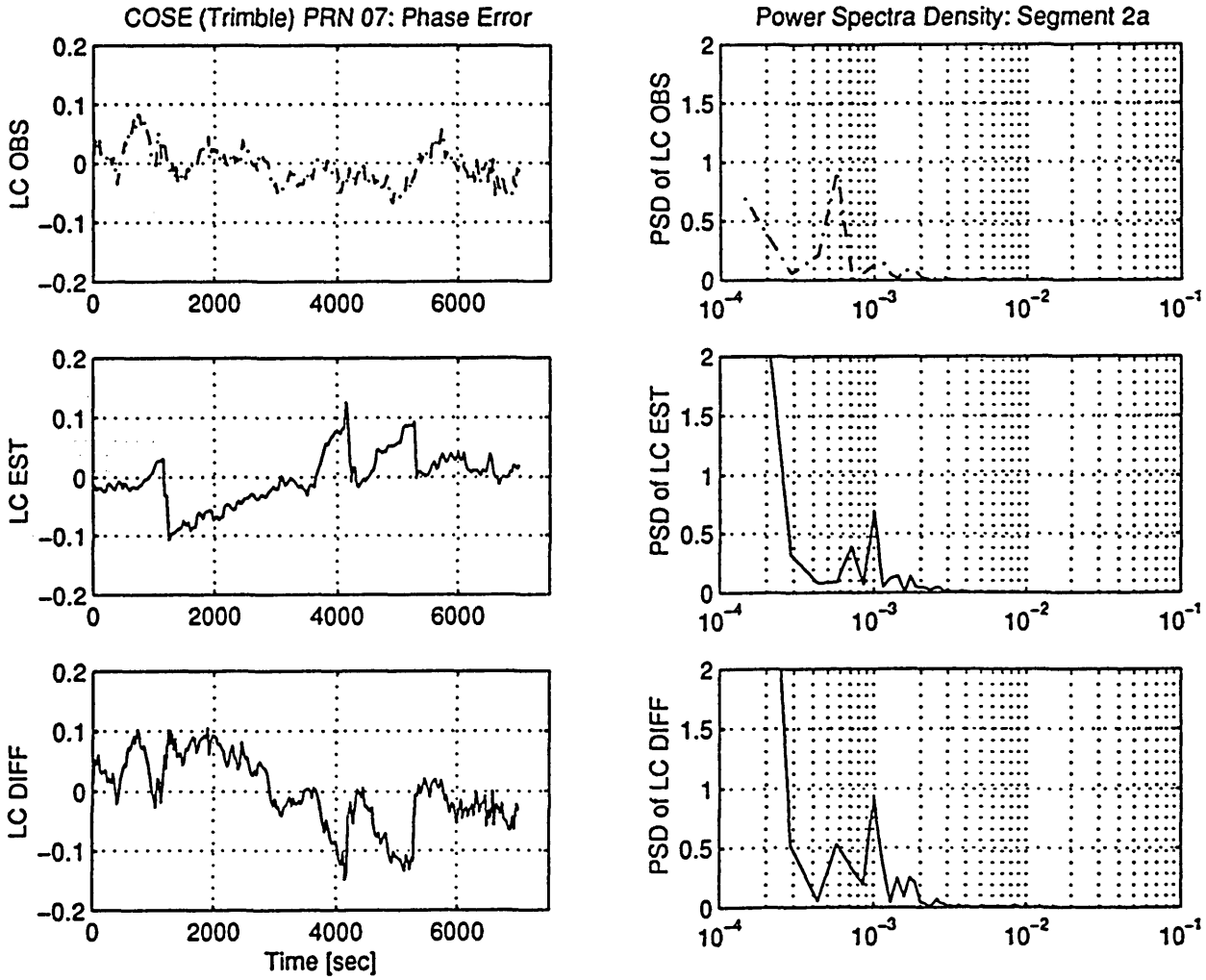

Fig. A.10.5.b) : COSE - PRN 07 (23 1 1997) - [segment 1a]
PSD of LC_OBS, LC_EST and LC_DIFF.
Unit: [cycles]^2

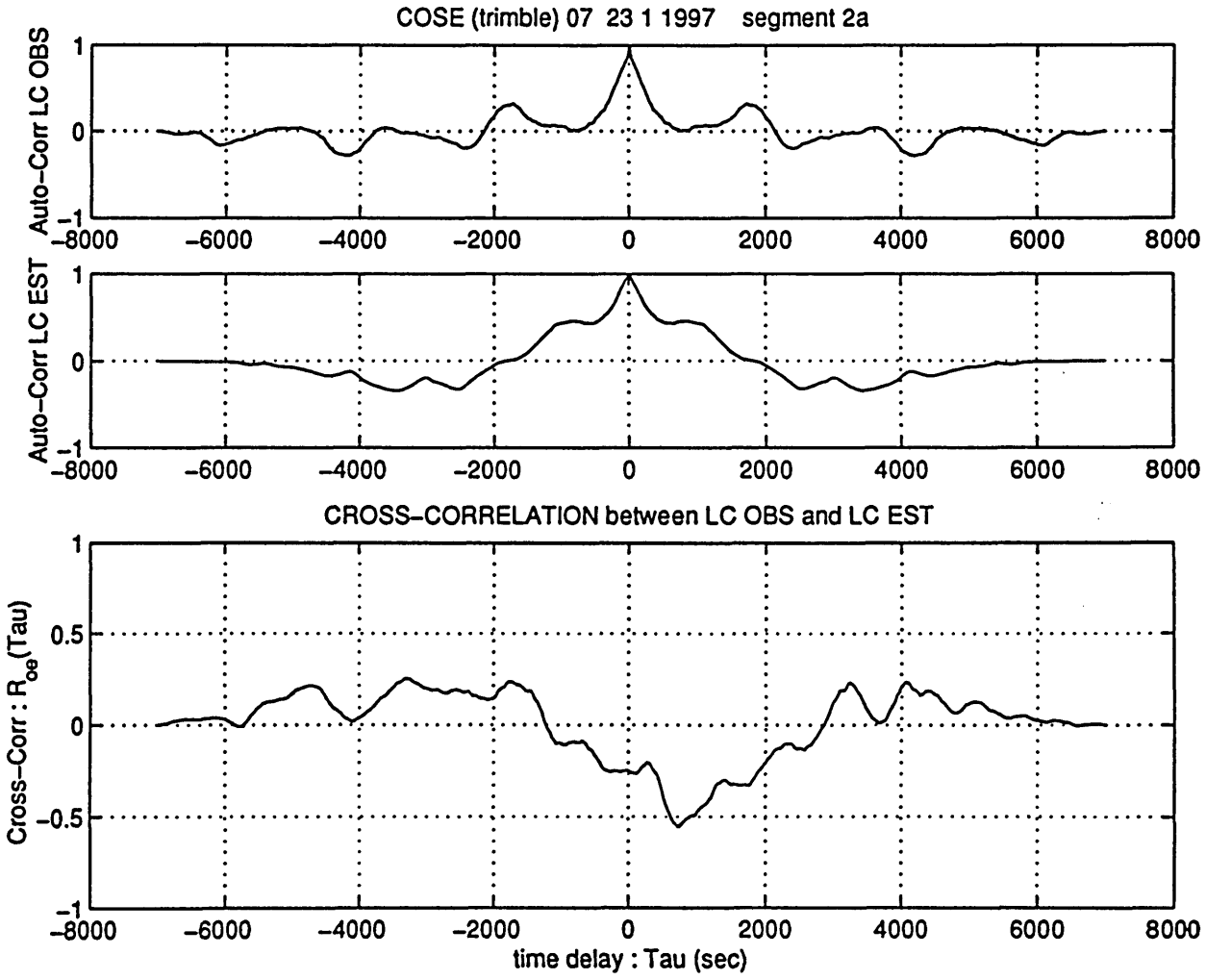

Fig. A.10.5.c) : COSE - PRN 07 (23 1 1997) - [segment 1a]
Auto Correlation of LC_OBS (R_{oo}) and LC_EST (R_{ee}).
Cross Correlation between them (R_{oe})
Unit: [cycles]^2

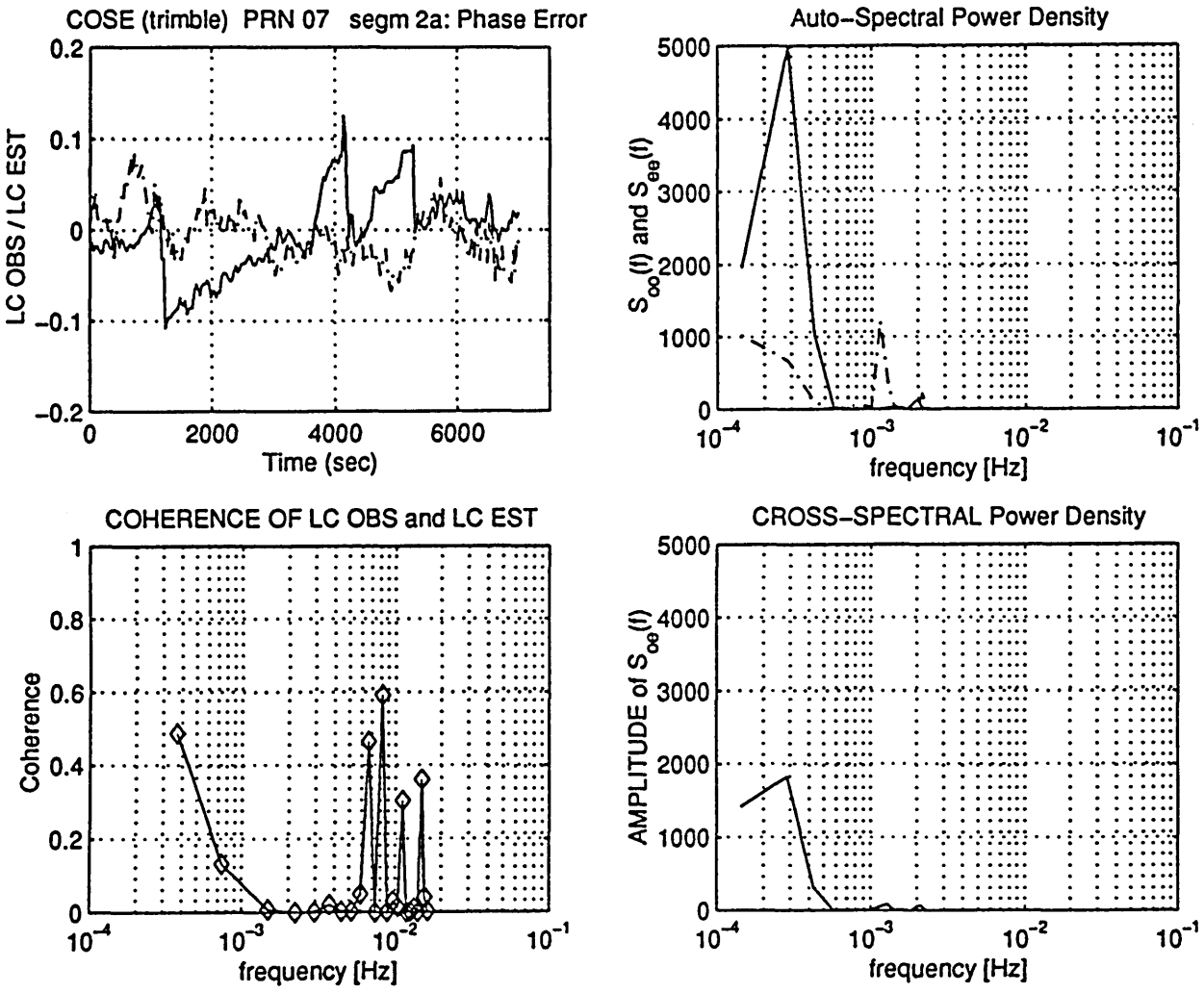

Fig. A.10.5.d) : COSE - PRN 07 (23 1 1997) - [segment 1a]
Auto Spectral Power Density of LC_OBS (S_{oo}) and of LC_EST (S_{ee}). Cross PSD between them (S_{oe})
Unit: [cycles]^2
Coherence function of LC_OBS and LC_EST

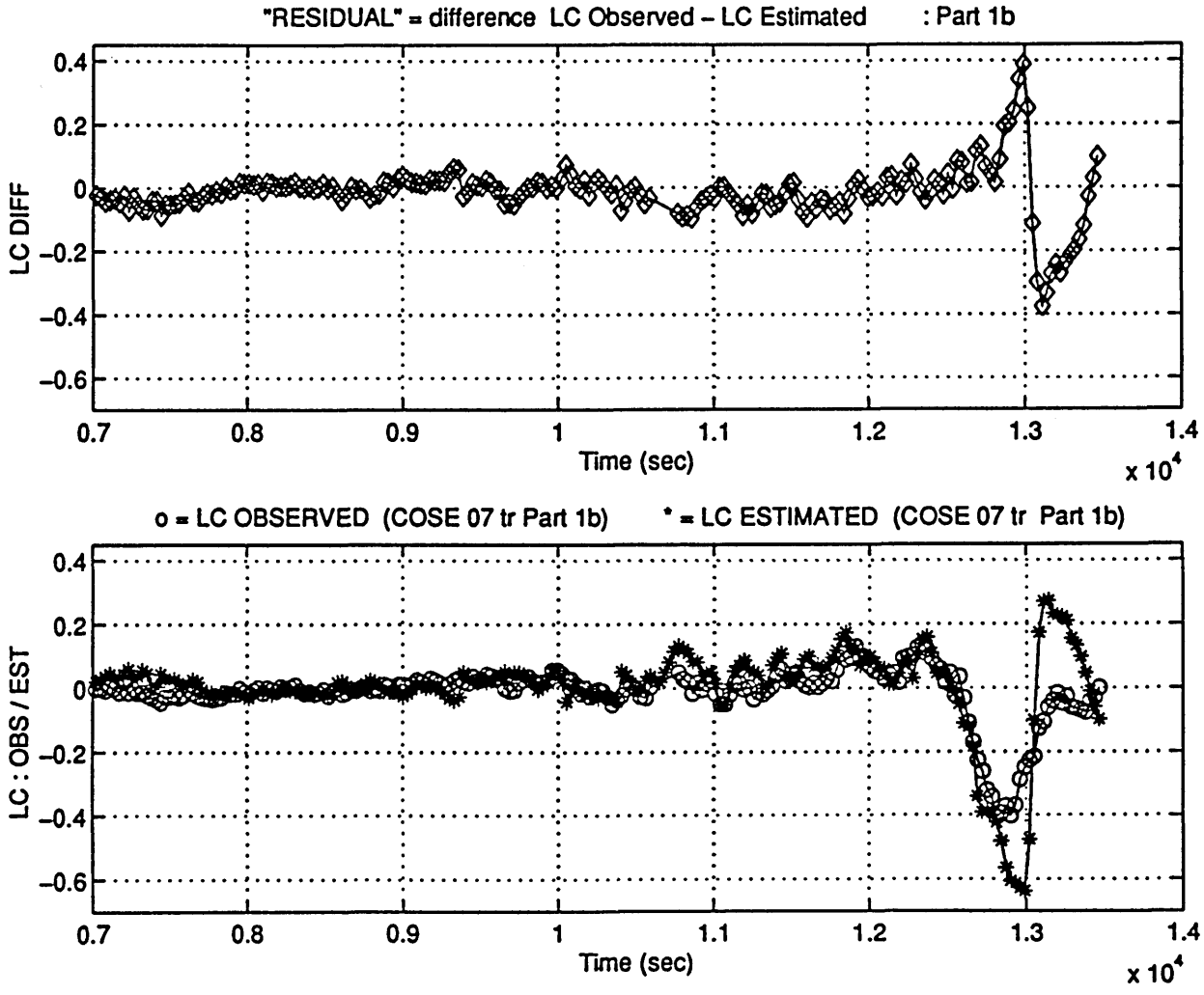

Fig. A.10.6.a) : COSE - PRN 07 (23 1 1997) - [segment 1b]
Phase residual LC_DIFF, determined as the difference between LC_OBS and LC_EST.
Unit: [cycles]

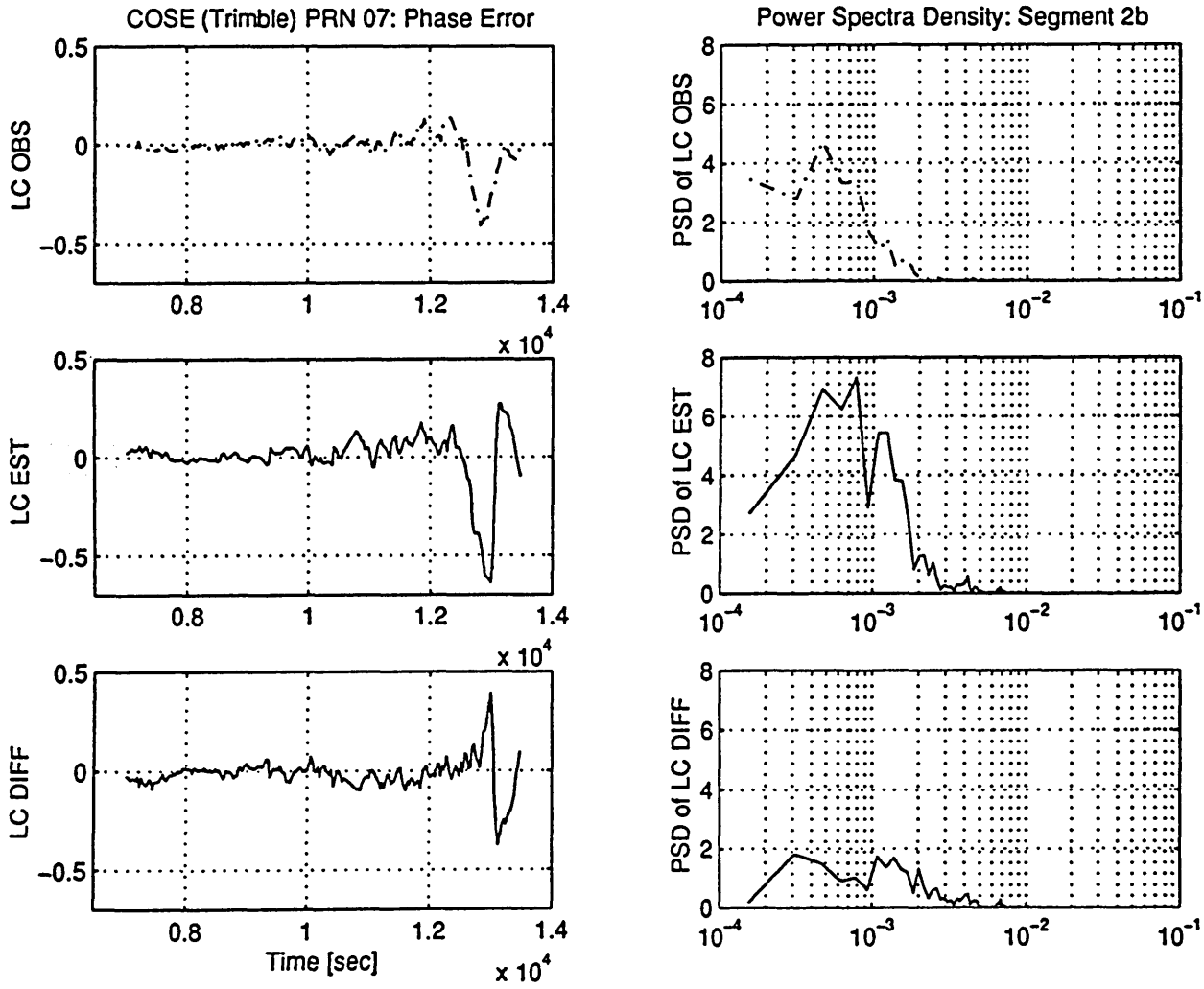

Fig. A.10.6.b) : COSE - PRN 07 (23 1 1997) - [segment 1b]
PSD of LC_OBS, LC_EST and LC_DIFF.
Unit: [cycles]^2

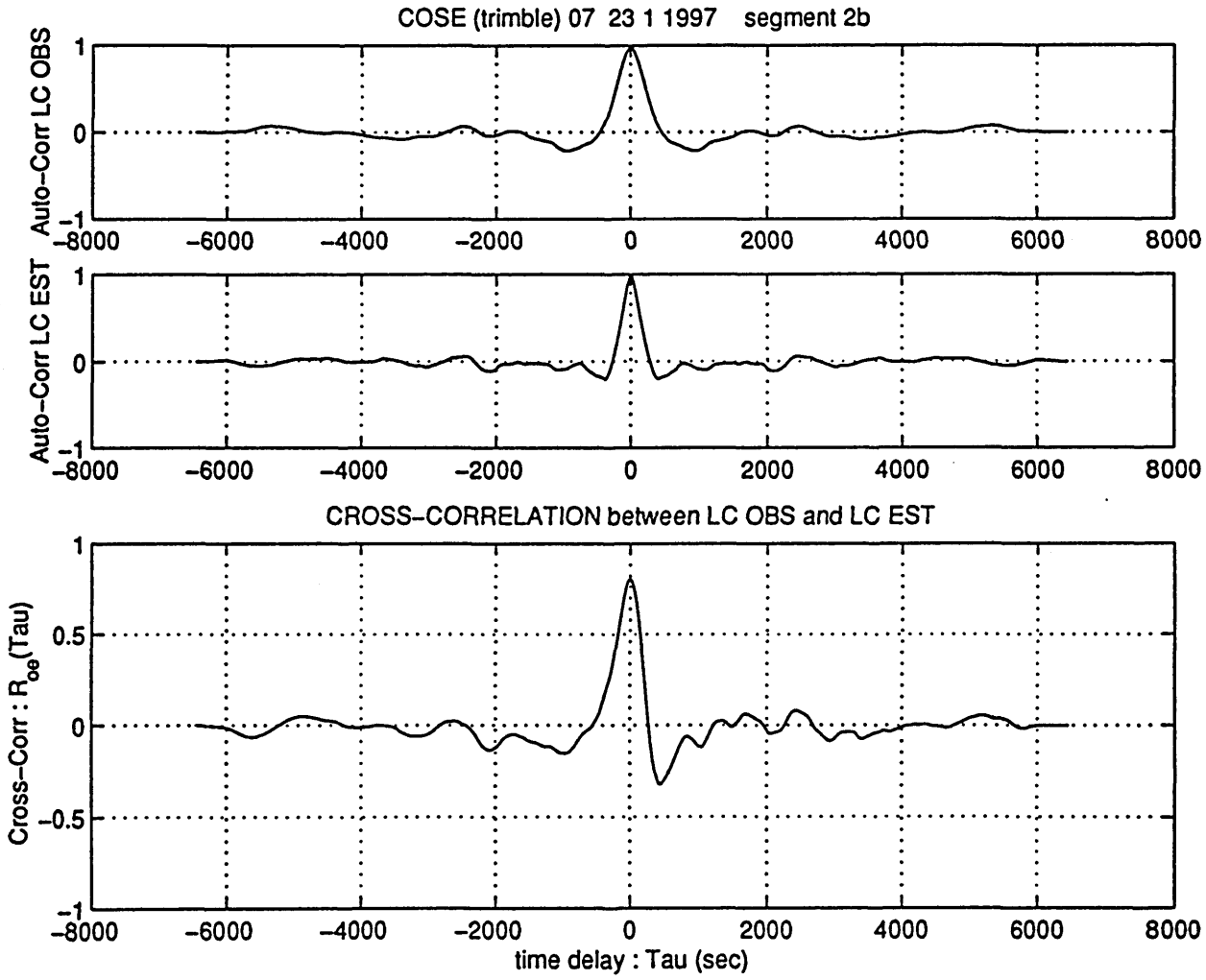

Fig. A.10.6.c) : COSE - PRN 07 (23 1 1997) - [segment 1b]
Auto Correlation of LC_OBS (R_{oo}) and LC_EST (R_{ee}).
Cross Correlation between them (R_{oe})
Unit: [cycles]^2

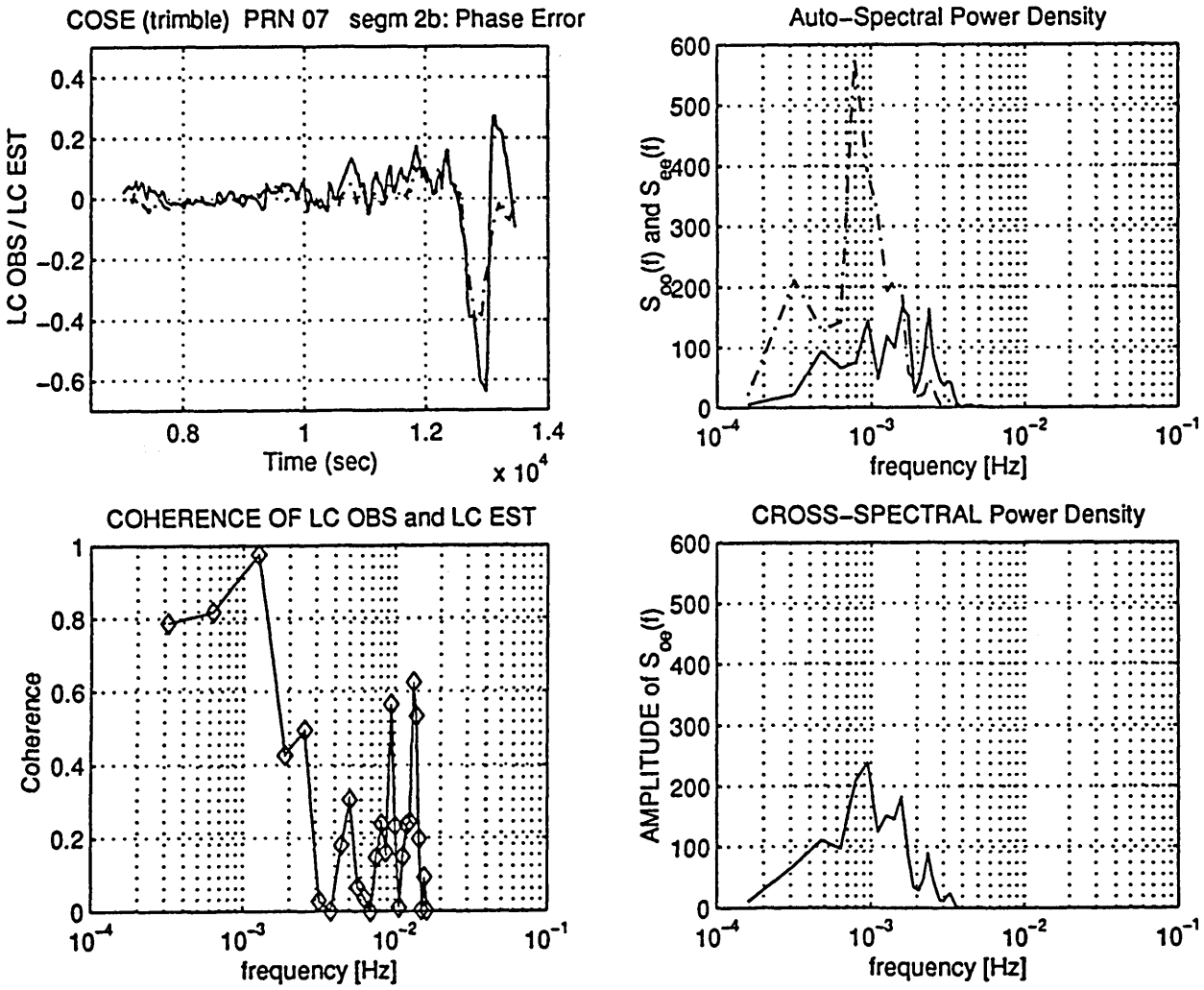

Fig. A.10.6.d) : COSE - PRN 07 (23 1 1997) - [segment 1b]
Auto Spectral Power Density of LC_OBS (S_{oo}) and of LC_EST (S_{ee}). Cross PSD between them (S_{oe})
Unit: [cycles]^2
Coherence function of LC_OBS and LC_EST

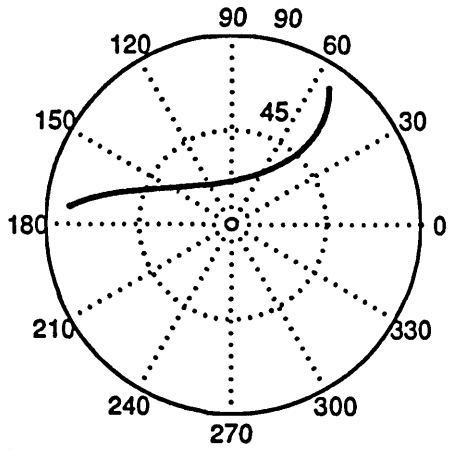

GPS DATA: receiver location: SOUTHERN CALIFORNIA acquisition date: 23 1 1997

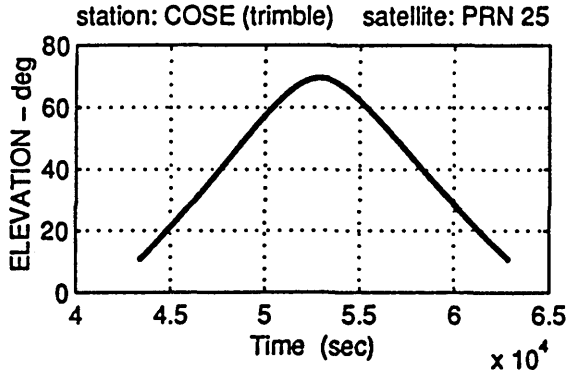

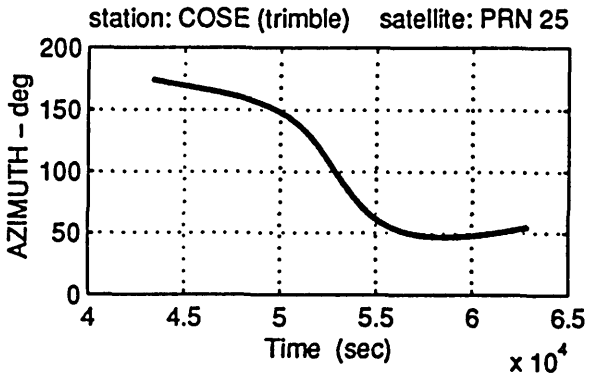

Fig. A.11.1 : Satellite visibility chart for PRN 25 (skymap).
Elevation and azimuth of PRN 25 with respect to
the station COSE

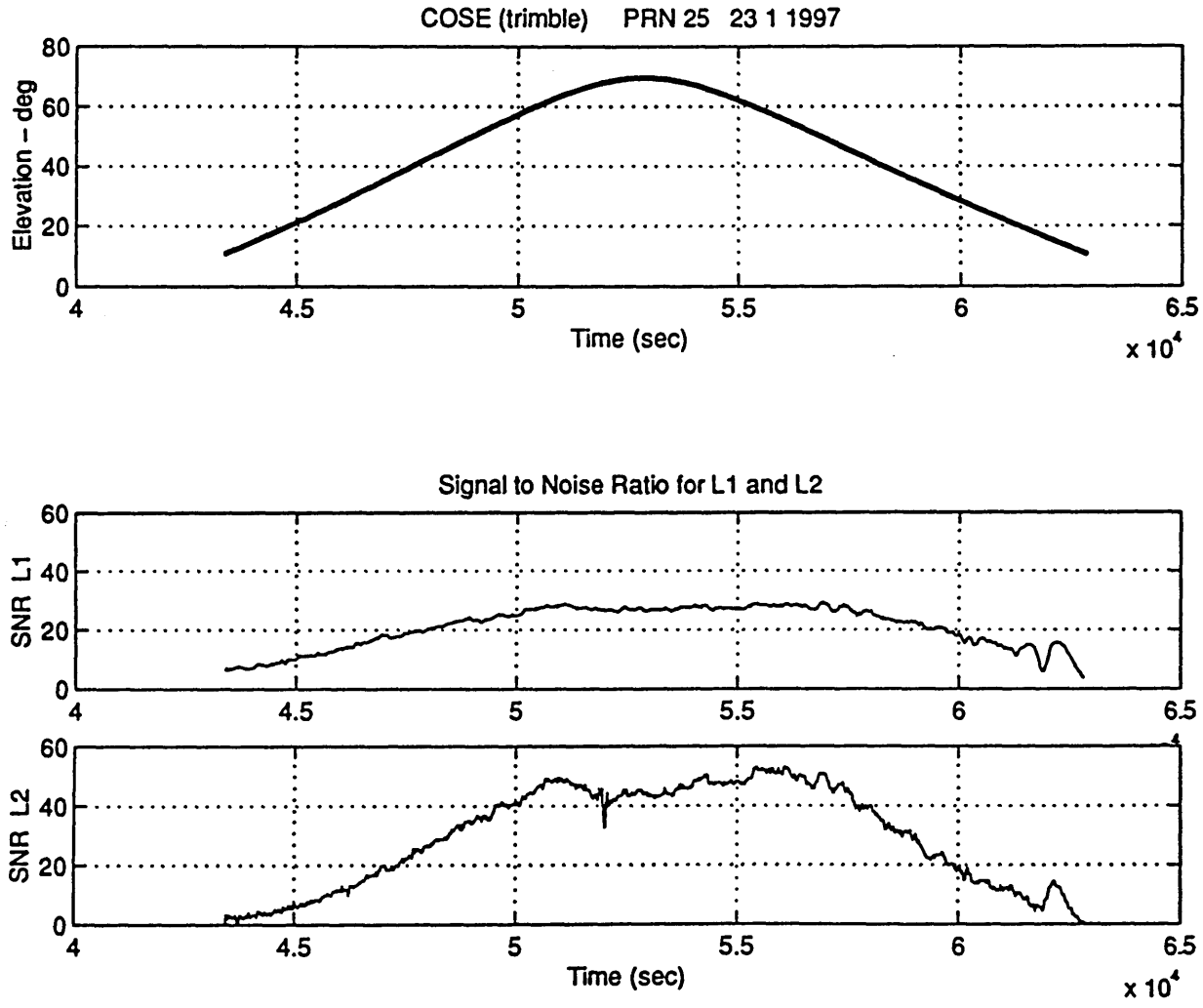

Fig. A.11.2 : Station: COSE - Satellite: PRN 25
Data acquisition date 23 1 1997
Signal-to-Noise-Ratio (SNR) for L_1 and L_2.

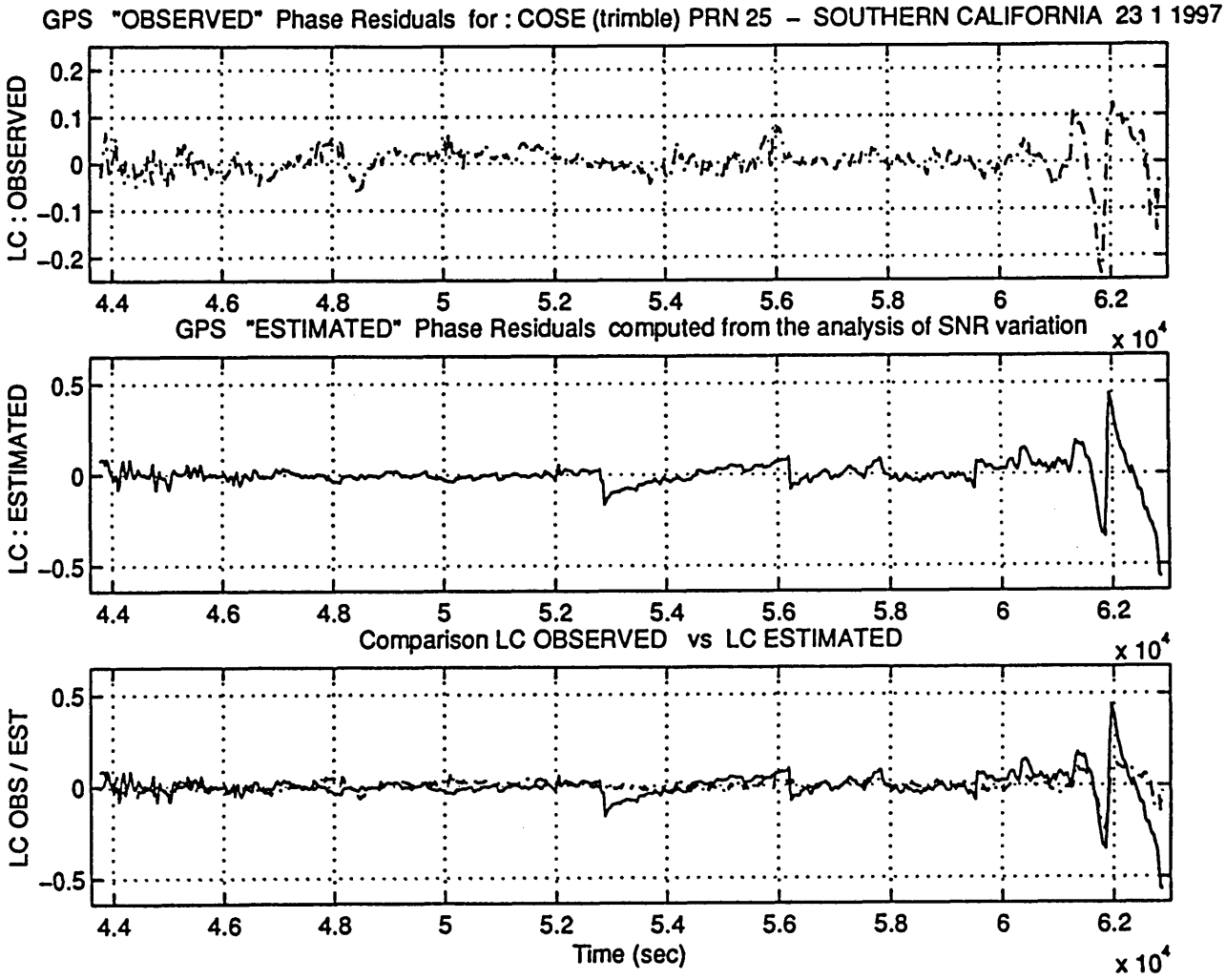

Fig. A.11.3 : Station: COSE - Satellite: PRN 25- Data acquisition date 23 1 1997
The observed phase residual (LC_OBS) is compared with the multipath phase error estimated from the SNR (LC_EST)
Unit: [cycles]

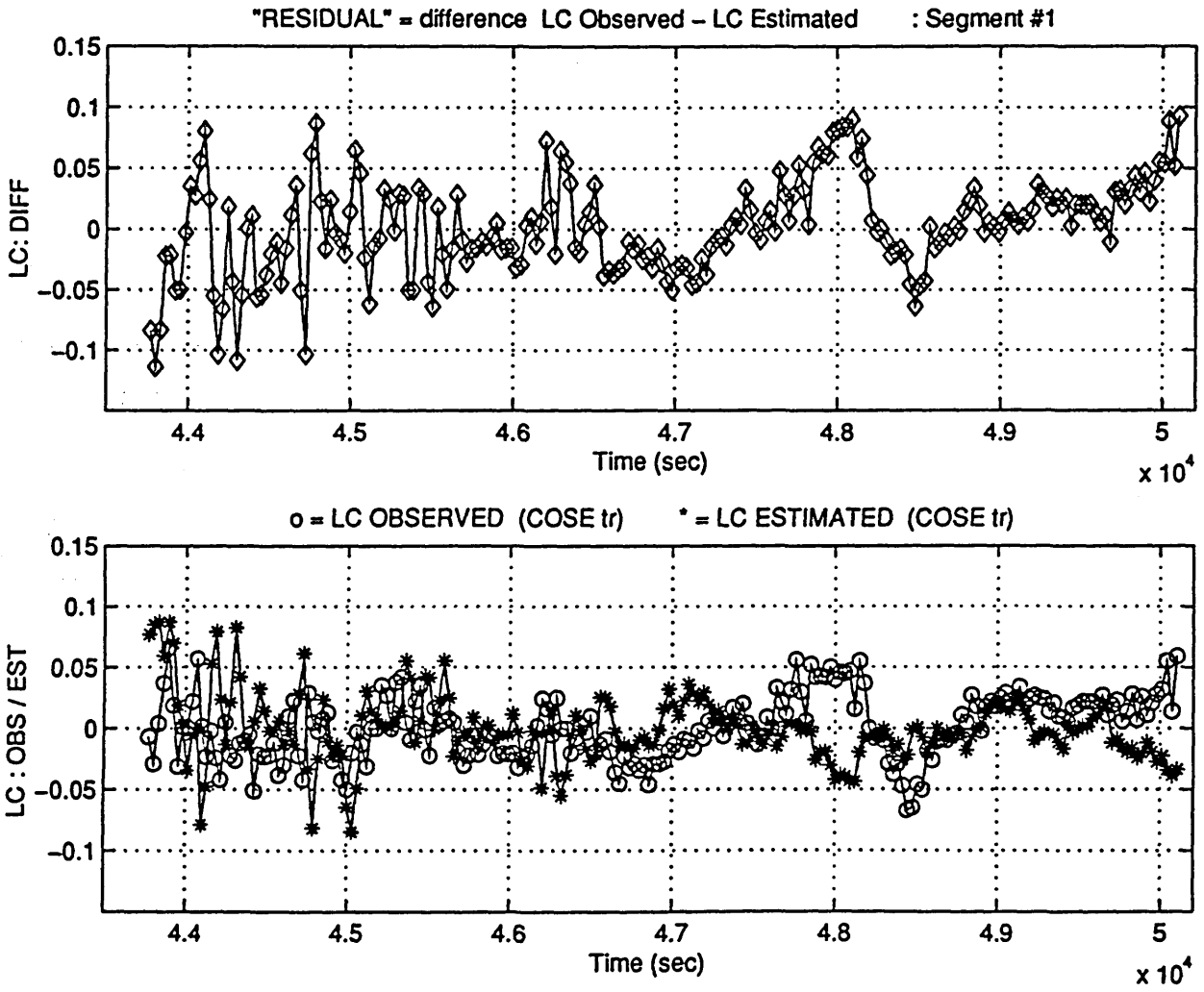

Fig. A.11.4.a) : COSE - PRN 25 (23 1 1997) - [segment #1]
Phase residual LC_DIFF, determined as the difference between LC_OBS and LC_EST.
Unit: [cycles]

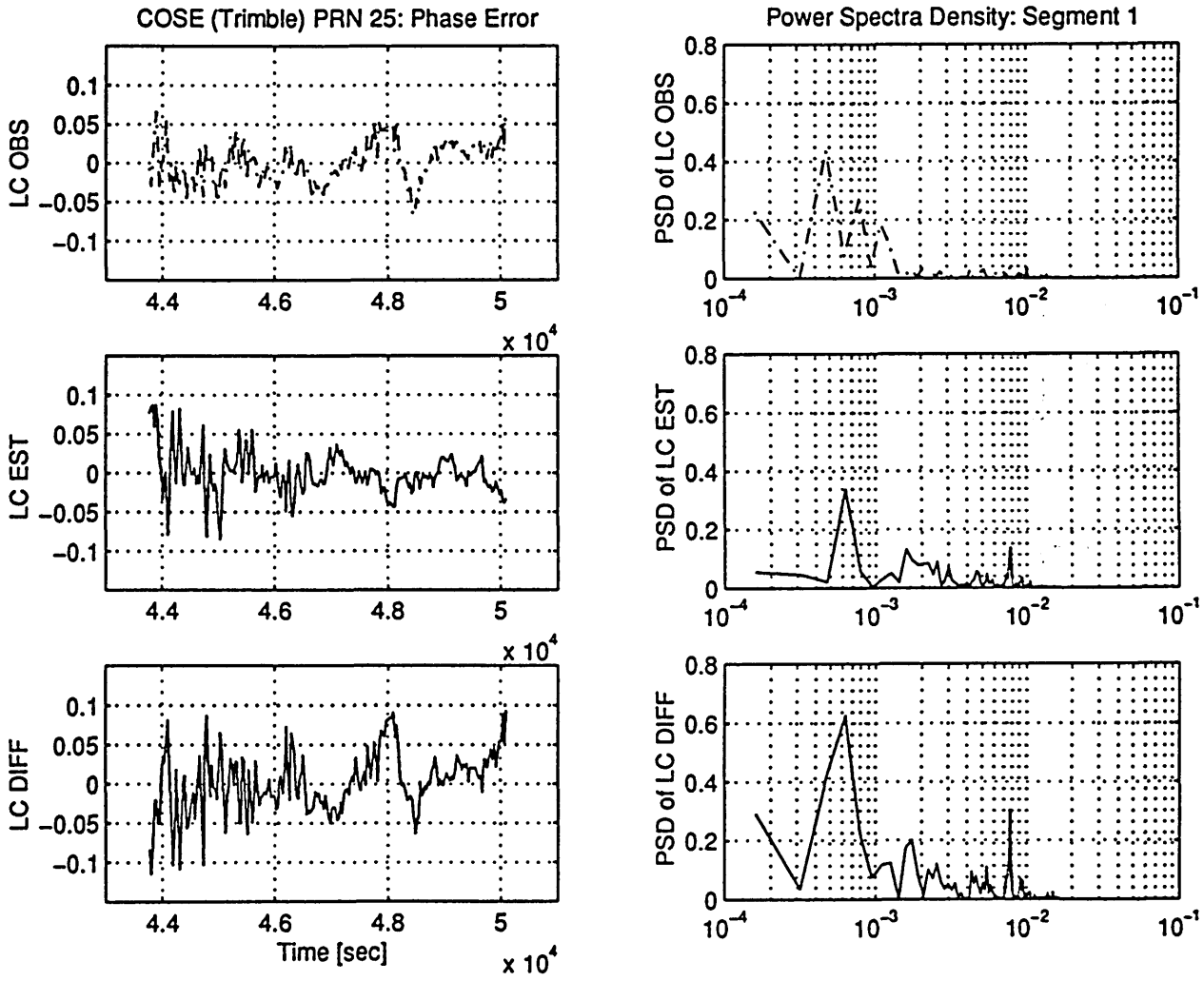

Fig. A.11.4.b) : COSE - PRN 25 (23 1 1997) - [segment #1]
PSD of LC_OBS, LC_EST and LC_DIFF.
Unit: [cycles]^2

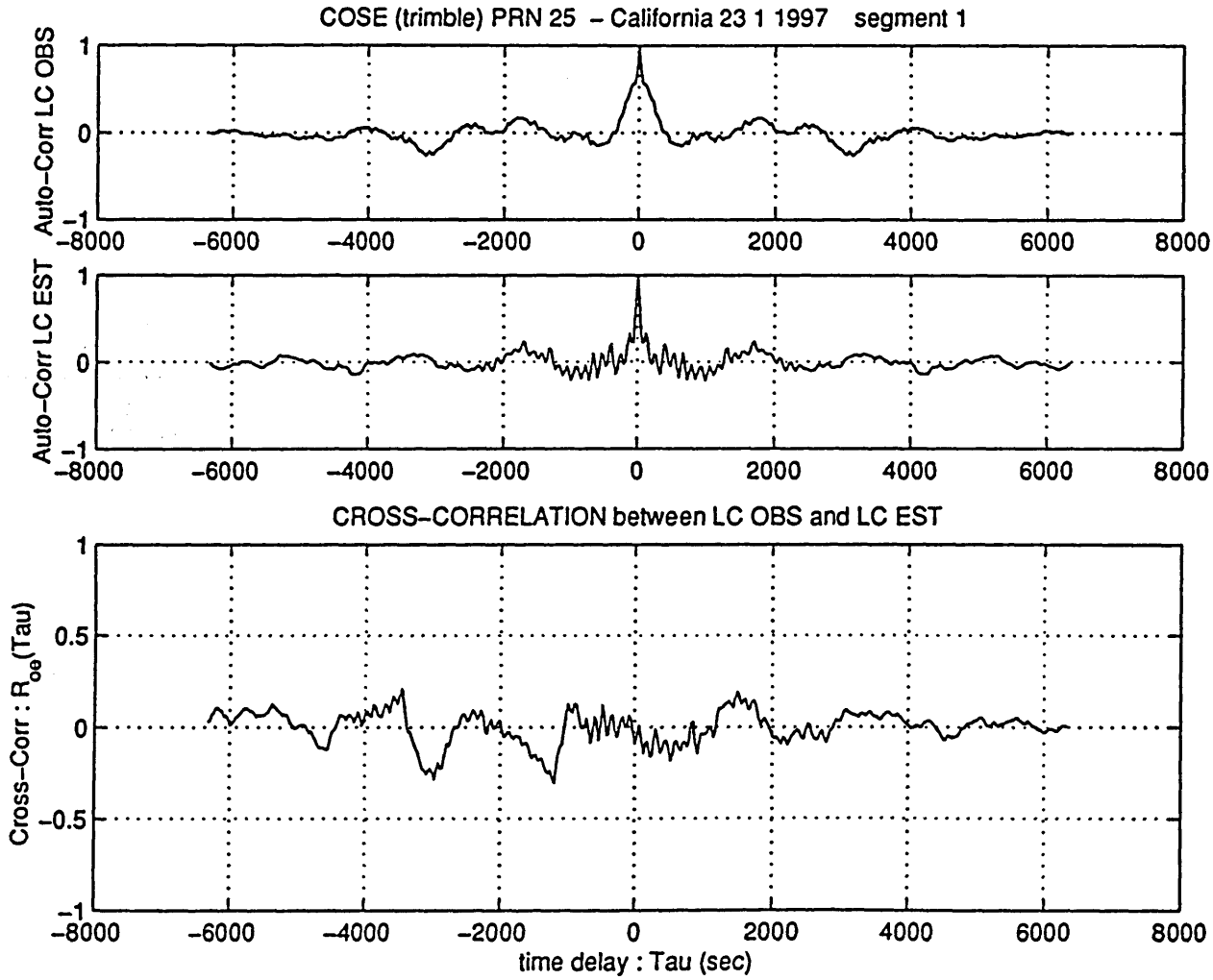

Fig. A.11.4.c) : COSE - PRN 25 (23 1 1997) - [segment #1]
Auto Correlation of LC_OBS (R_{oo}) and LC_EST (R_{ee}).
Cross Correlation between them (R_{oe})
Unit: [cycles]^2

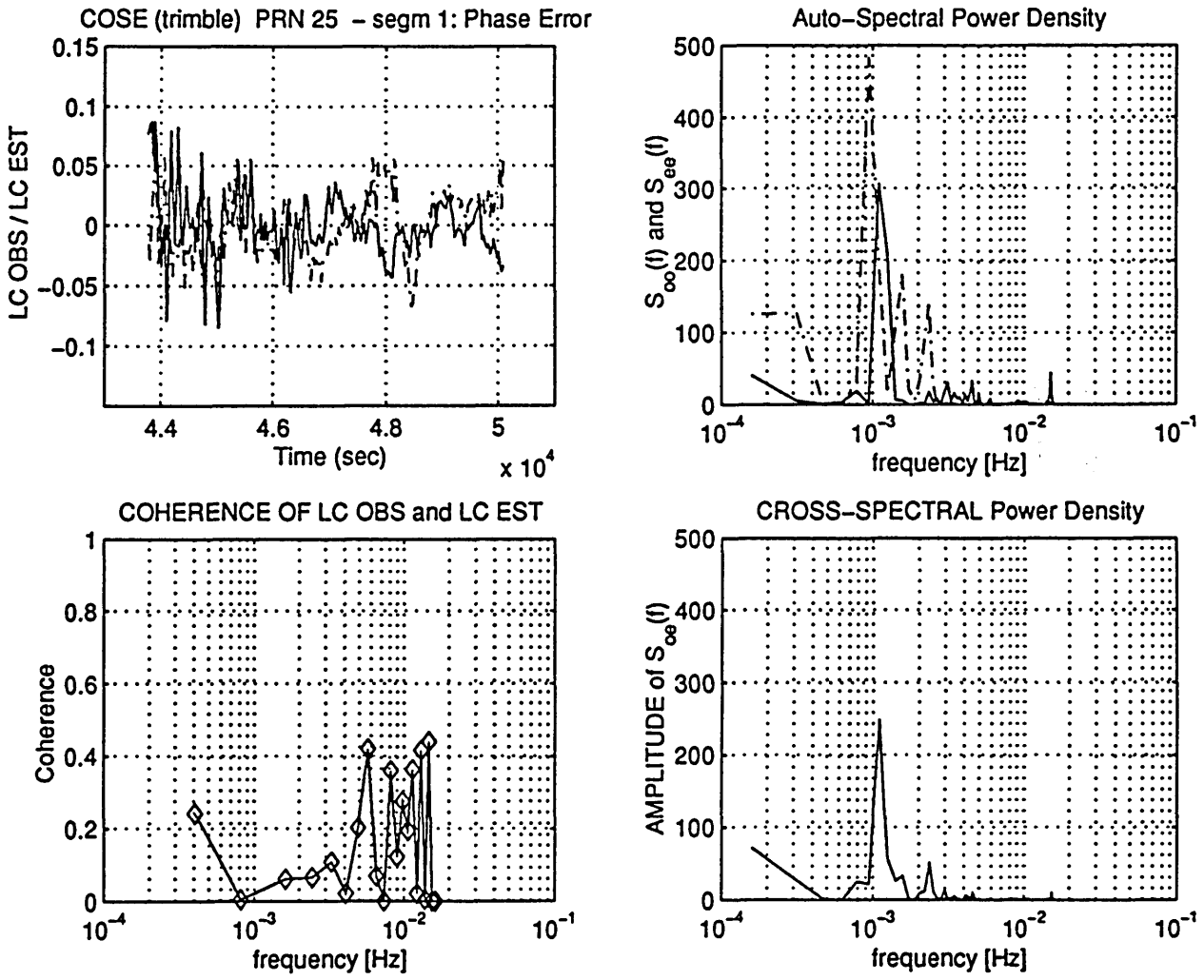

Fig. A.11.4.d) : COSE - PRN 25 (23 1 1997) - [segment #1]
Auto Spectral Power Density of LC_OBS (S_{oo}) and of LC_EST (S_{ee}). Cross PSD between them (S_{oe})
Unit: [cycles]^2
Coherence function of LC_OBS and LC_EST

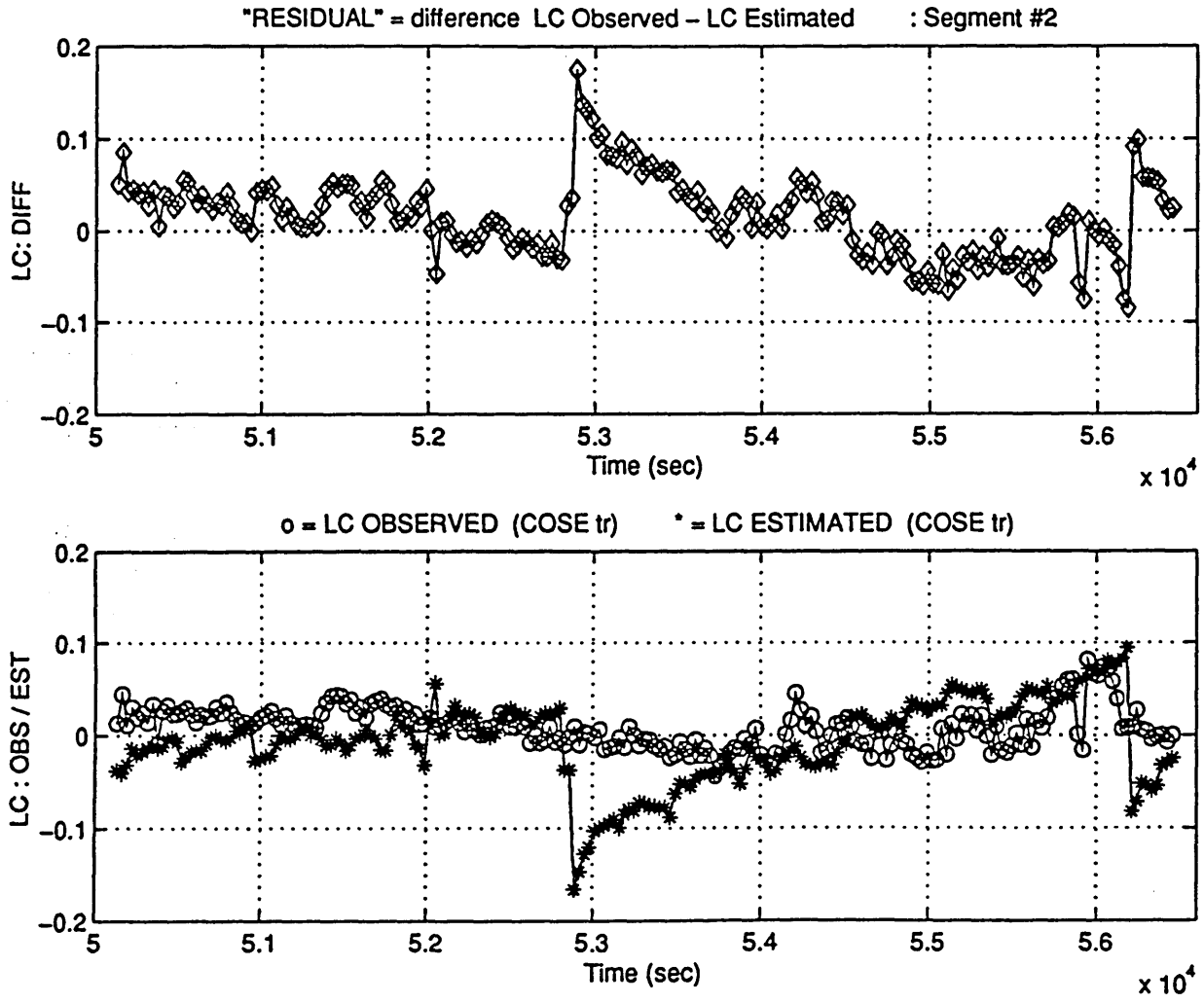

Fig. A.11.5.a) : COSE - PRN 25 (23 1 1997) - [segment #2]
Phase residual LC_DIFF, determined as the difference between LC_OBS and LC_EST.
Unit: [cycles]

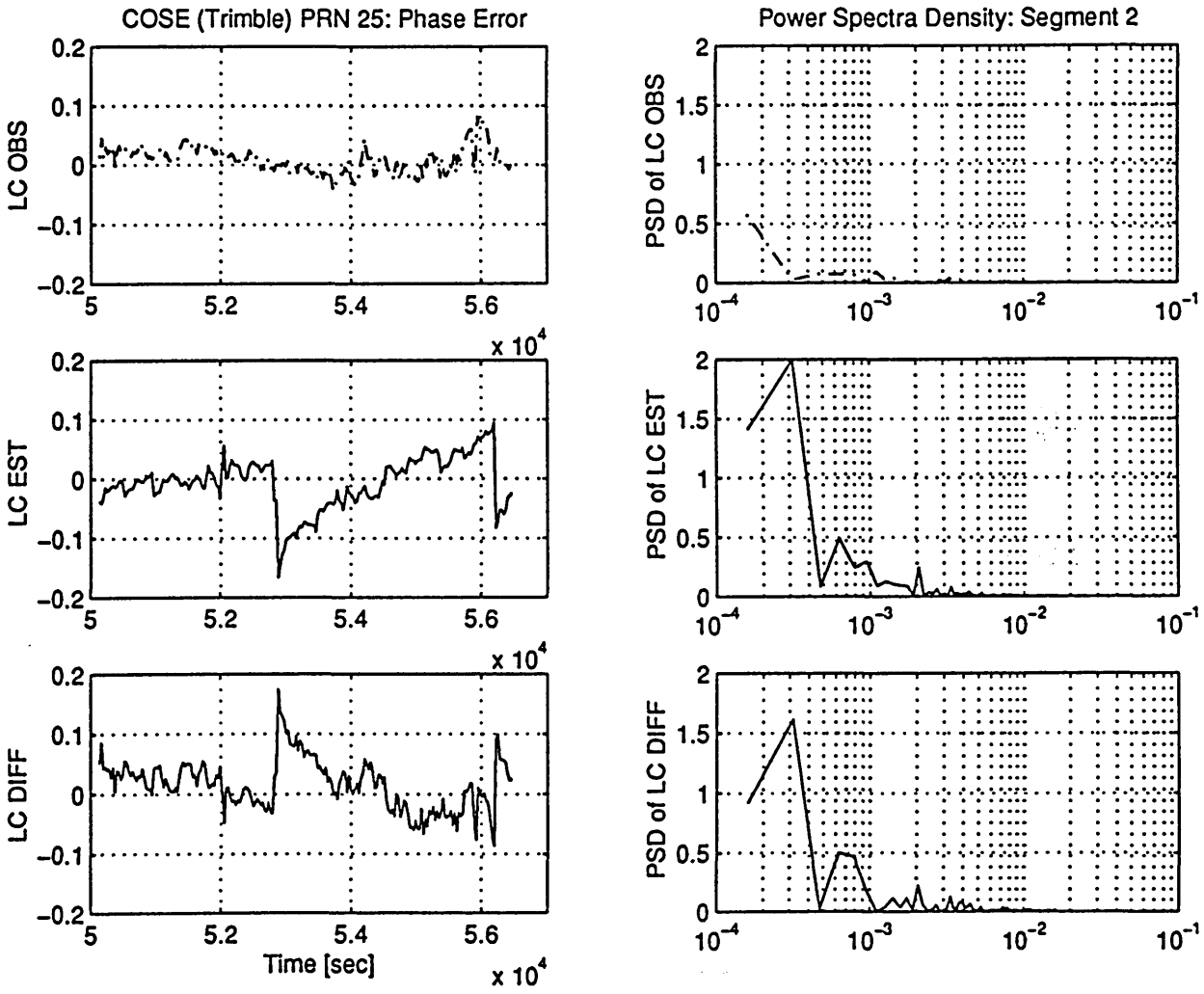

Fig. A.11.5.b) : COSE - PRN 25 (23 1 1997) - [segment #2]
Power Spectral Density of LC_OBS, LC_EST and LC_DIFF.
Unit: [cycles]^2

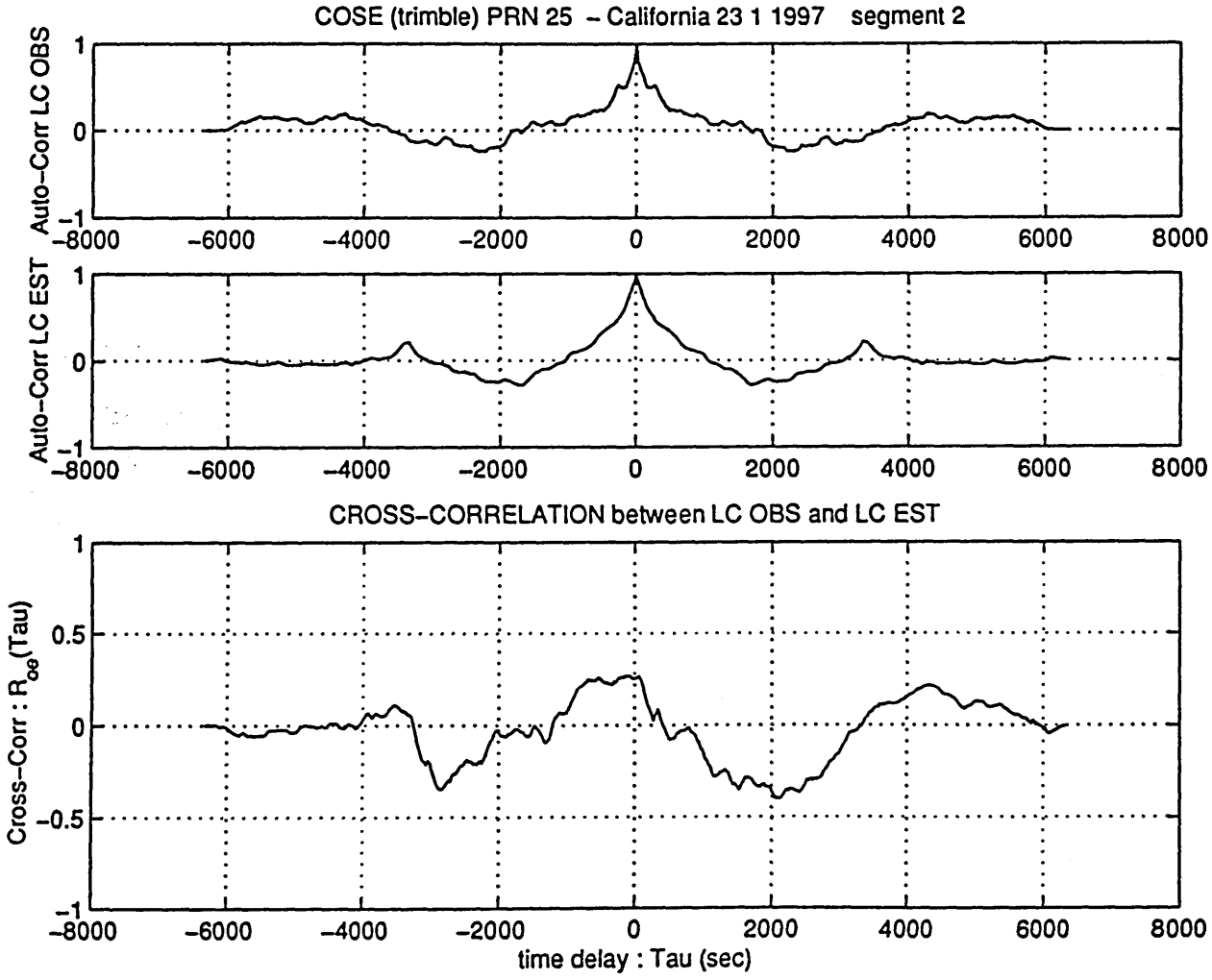

Fig. A.11.5.c) : COSE - PRN 25 (23 1 1997) - [segment #2]
Auto Correlation of LC_OBS (R_{oo}) and LC_EST (R_{ee}).
Cross Correlation between them (R_{oe})
Unit: [cycles]^2

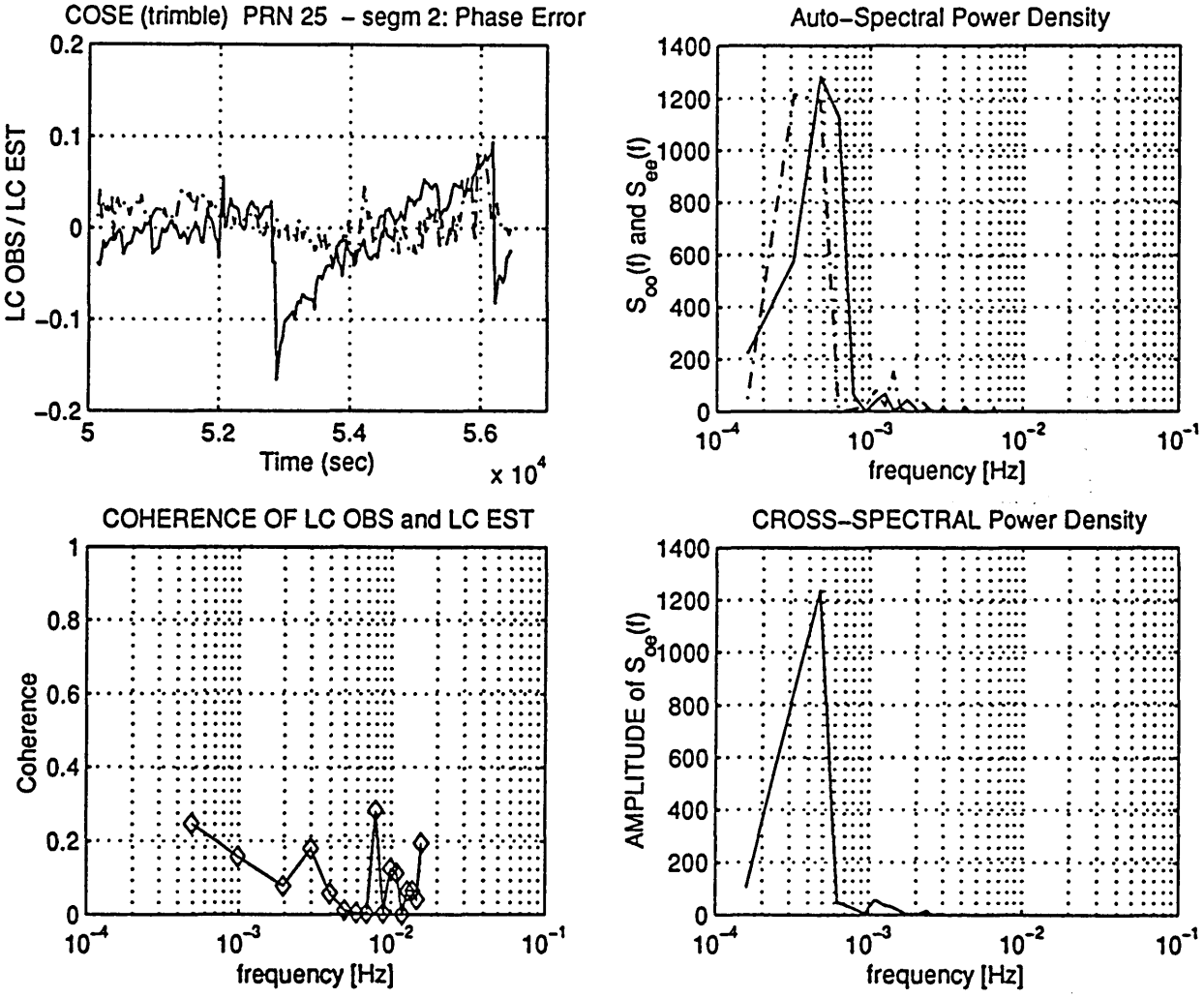

Fig. A.11.5.d) : COSE - PRN 25 (23 1 1997) - [segment #2]
Auto Spectral Power Density of LC_OBS (S_{oo}) and of LC_EST (S_{ee}). Cross PSD between them (S_{oe})
Unit: [cycles]^2
Coherence function of LC_OBS and LC_EST

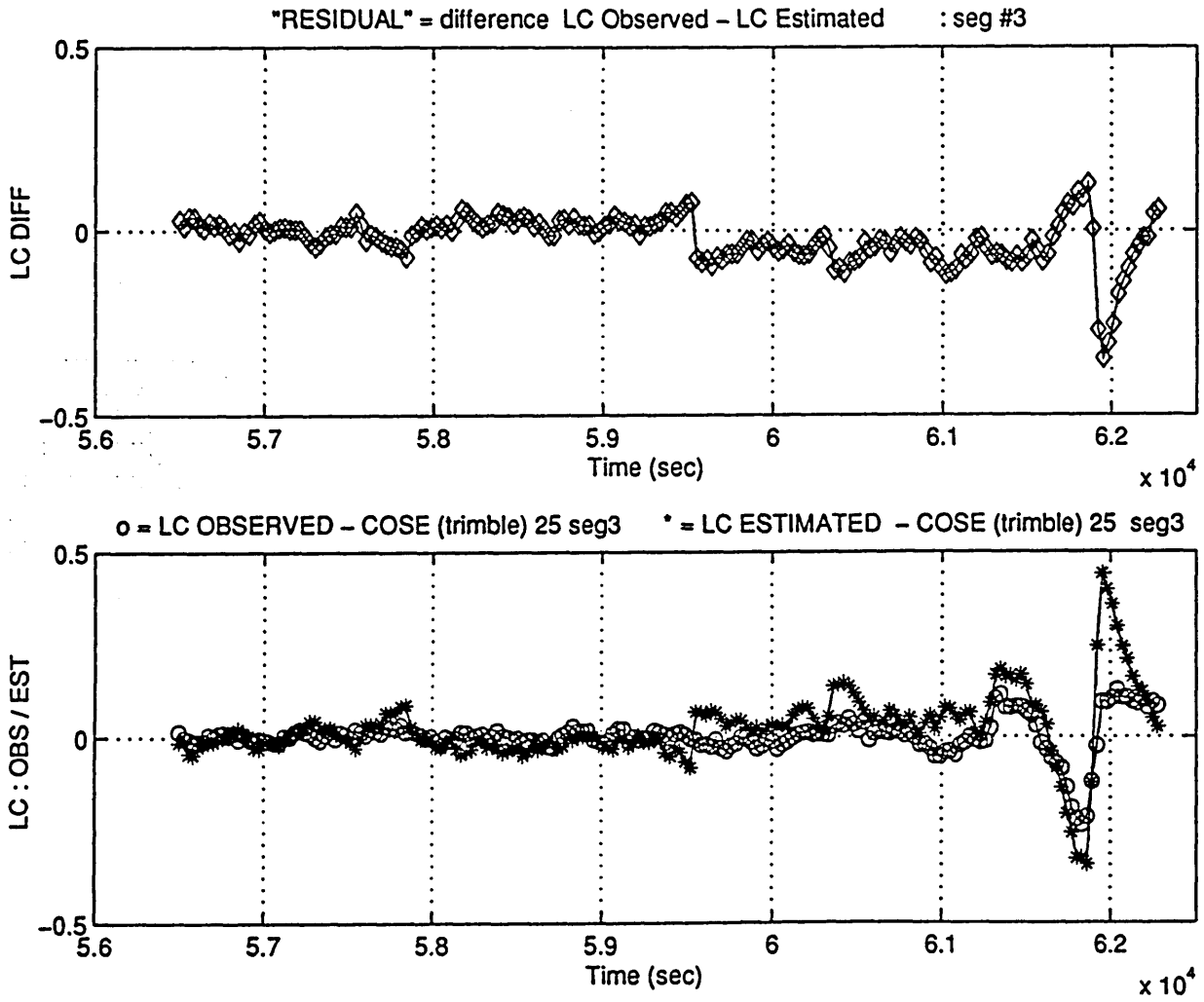

Fig. A.11.6.a) : COSE - PRN 25 (23 1 1997) - [segment #3]
Phase residual LC_DIFF, determined as the difference between LC_OBS and LC_EST.
Unit: [cycles]

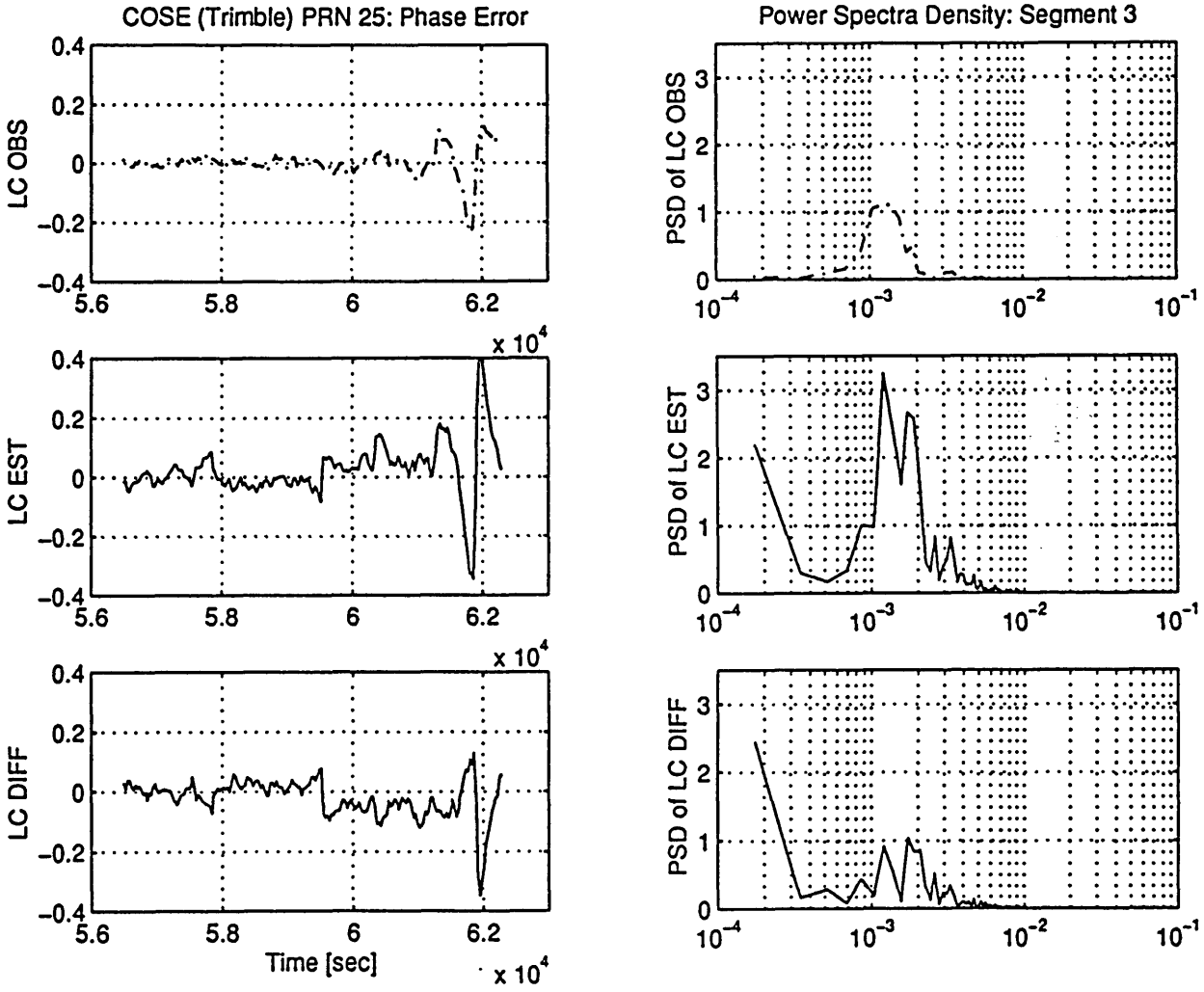

Fig. A.11.6.b) : COSE - PRN 01 (23 1 1997) - [segment #3]
Power Spectral Density of LC_OBS, LC_EST and LC_DIFF.
Unit: [cycles]^2

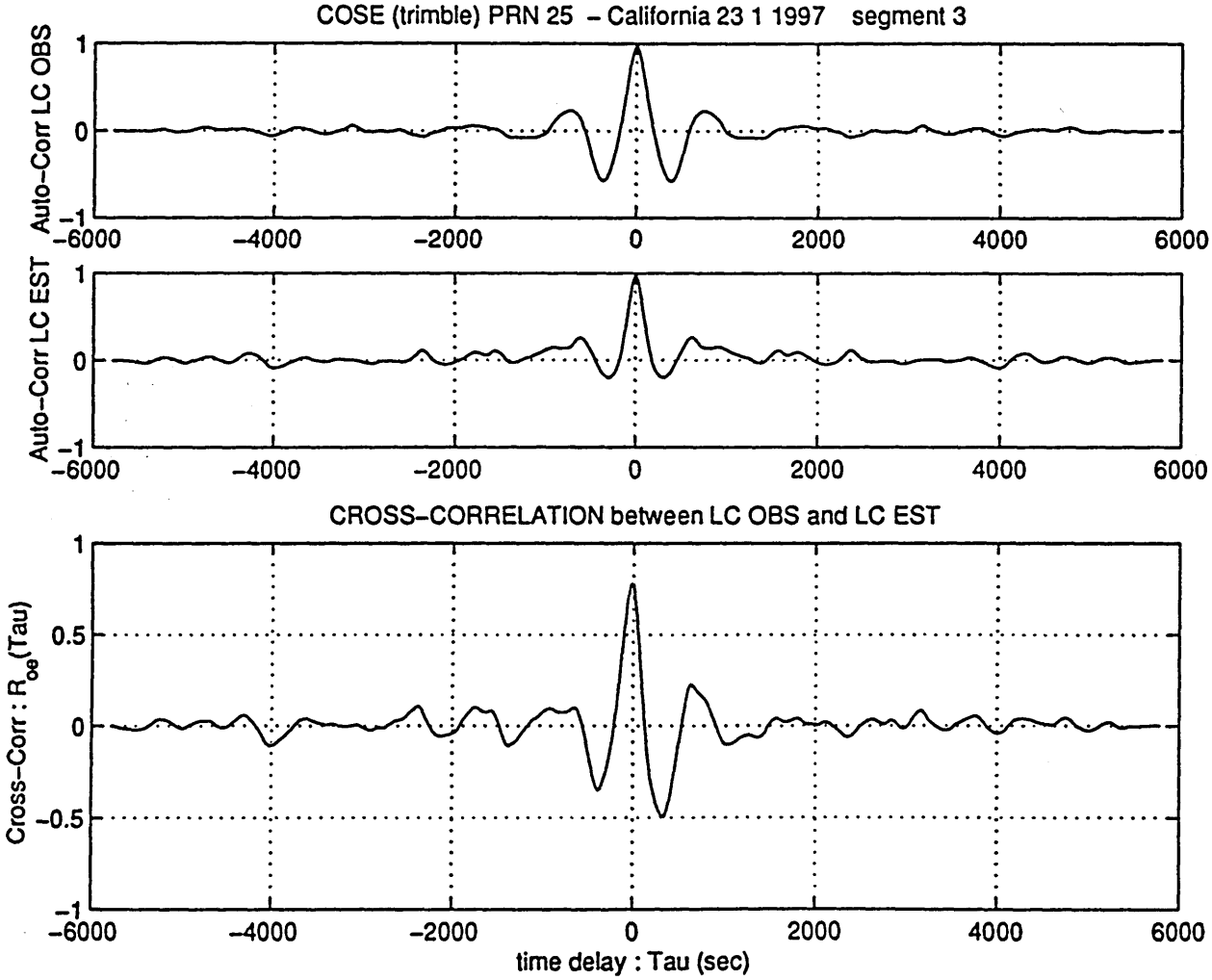

Fig. A.11.6.c) : COSE - PRN 25 (23 1 1997) - [segment #3]
Auto Correlation of LC_OBS (R_{oo}) and LC_EST (R_{ee}).
Cross Correlation between them (R_{oe})
Unit: [cycles]^2

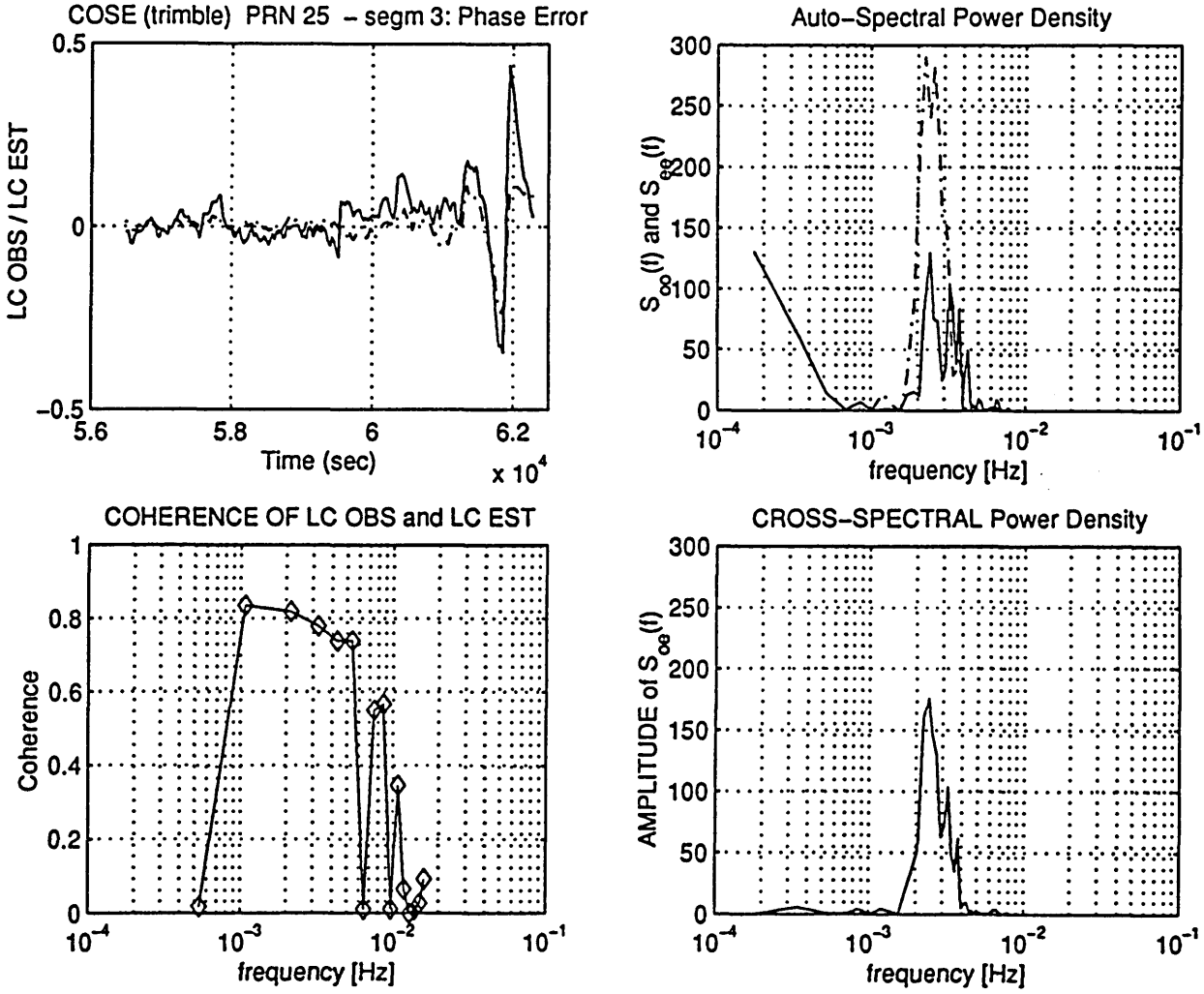

Fig. A.11.6.d) : COSE - PRN 25 (23 1 1997) - [segment #3]
Auto Spectral Power Density of LC_OBS (S_{oo}) and of LC_EST (S_{ee}). Cross PSD between them (S_{oe})
Unit: [cycles]^2
Coherence function of LC_OBS and LC_EST

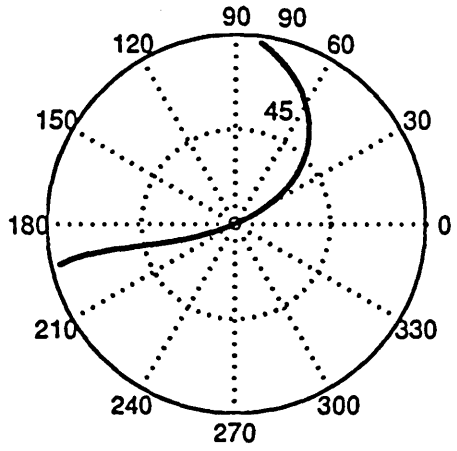

GPS DATA: receiver location: SOUTHERN CALIFORNIA acquisition date: 24 1 1997

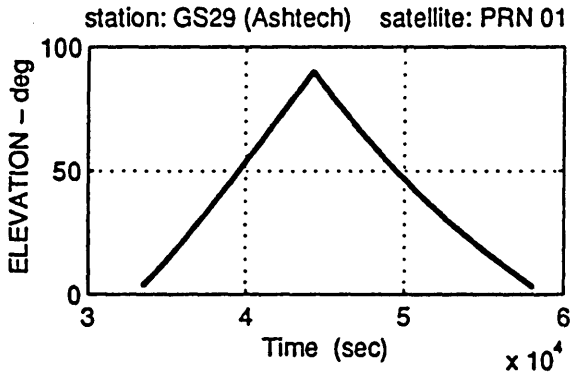

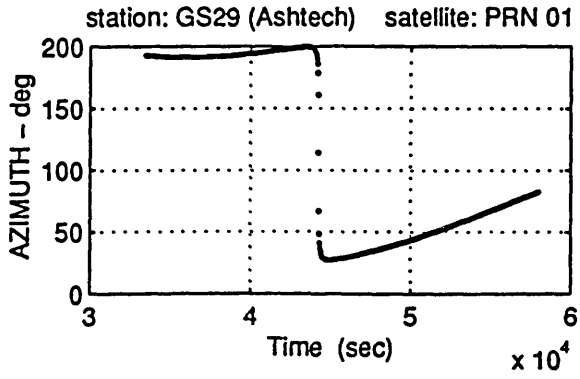

Fig. A.12.1 : Satellite visibility chart for PRN 01 (skymap).
Elevation and azimuth of PRN 01with respect to
the station GS29

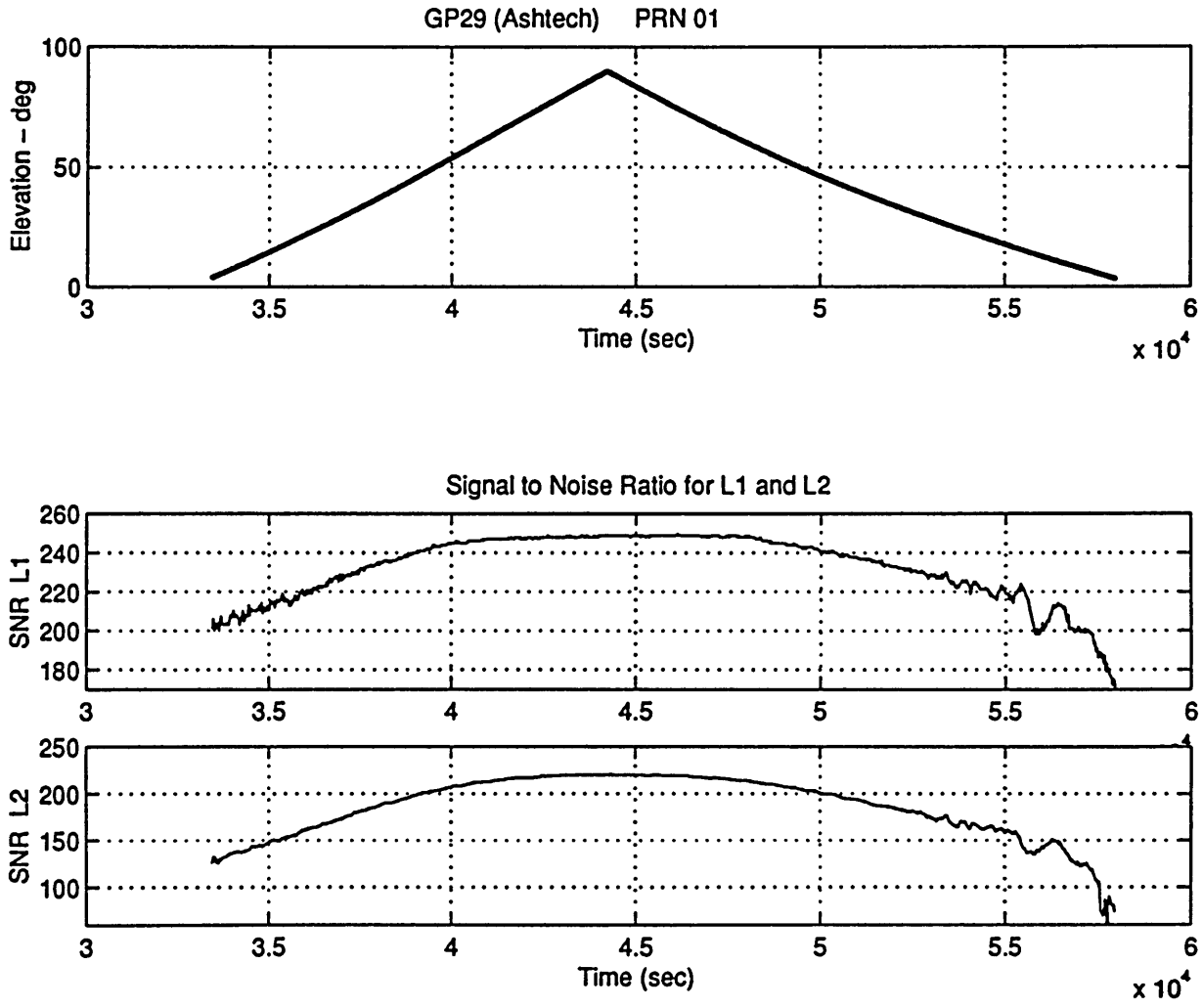

Fig. A.12.2 : Station: GS29 - Satellite: PRN 01
Data acquisition date 24 1 1997
Signal-to-Noise-Ratio (SNR) for L_1 and L_2.

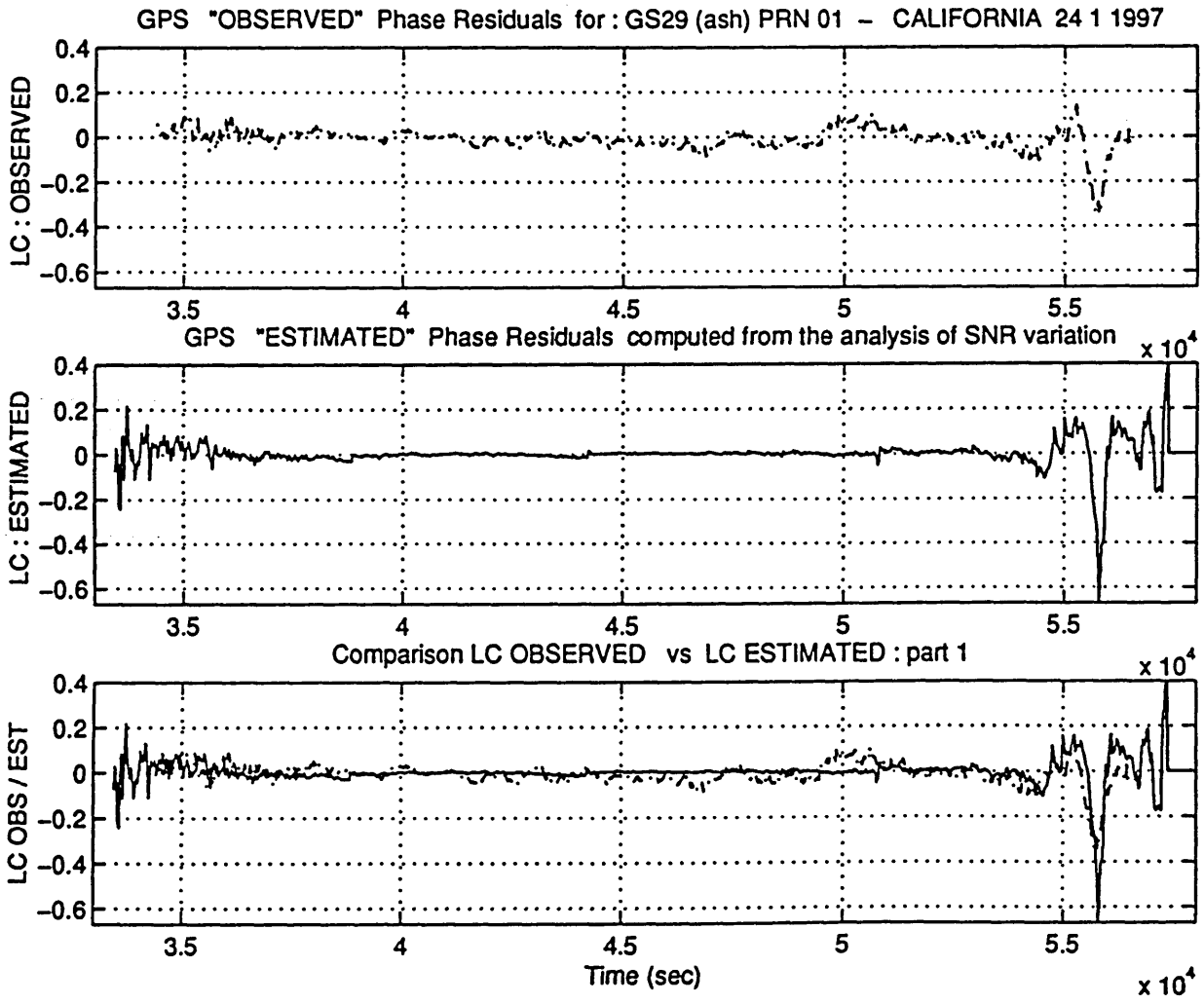

Fig. A.12.3 : Station: GS29 - Satellite: PRN 01
Data acquisition date 24 1 1997
The observed phase residual (LC_OBS) is compared with the multipath phase error estimated from the SNR (LC_EST)
Unit: [cycles]

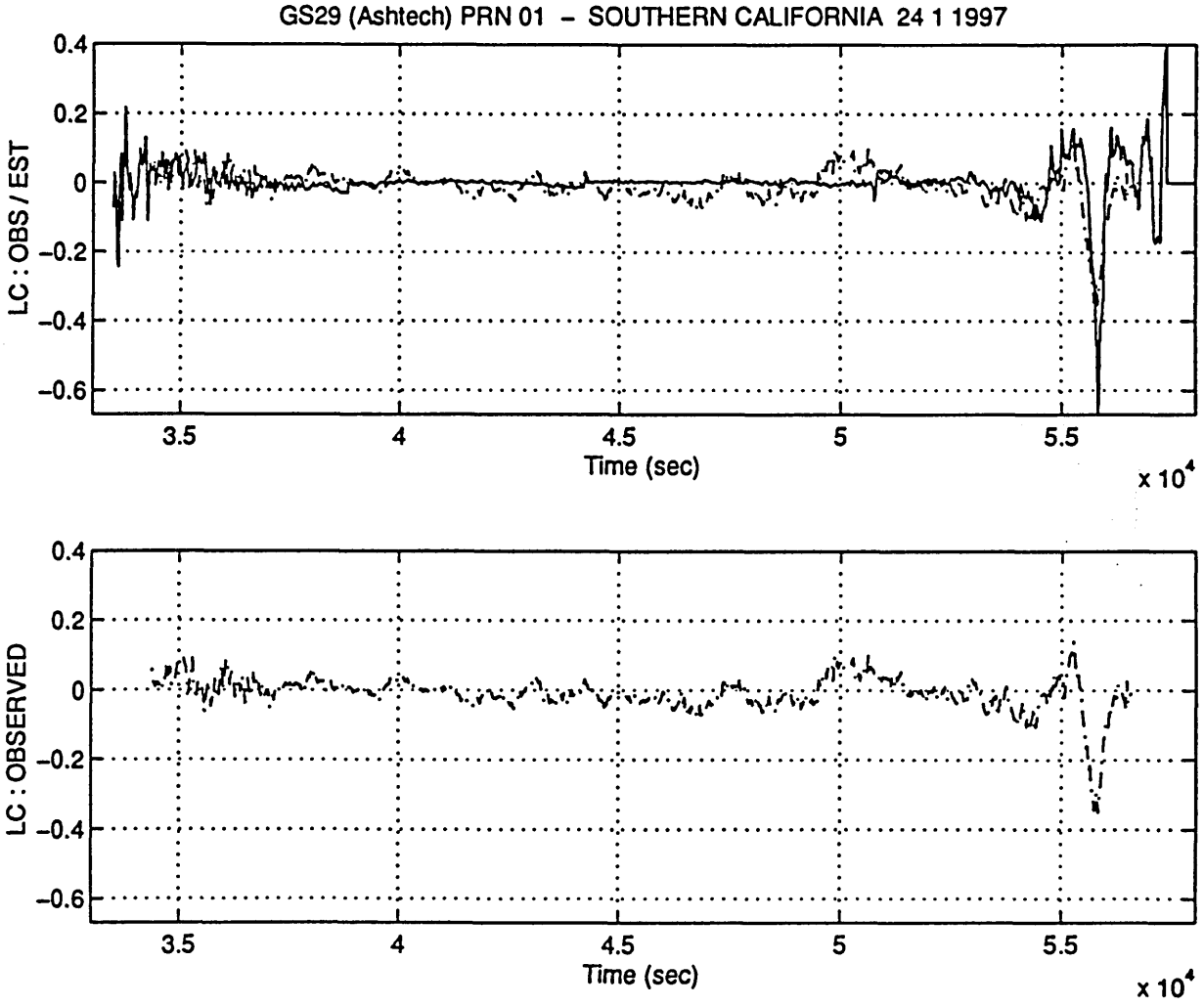

Fig. A.12.4 : Station: GS29 - Satellite: PRN 01
Data acquisition date 24 1 1997
LC_OBS and LC_EST compared for t=3.5 - 5.7 10^4 sec
Unit: [cycles]

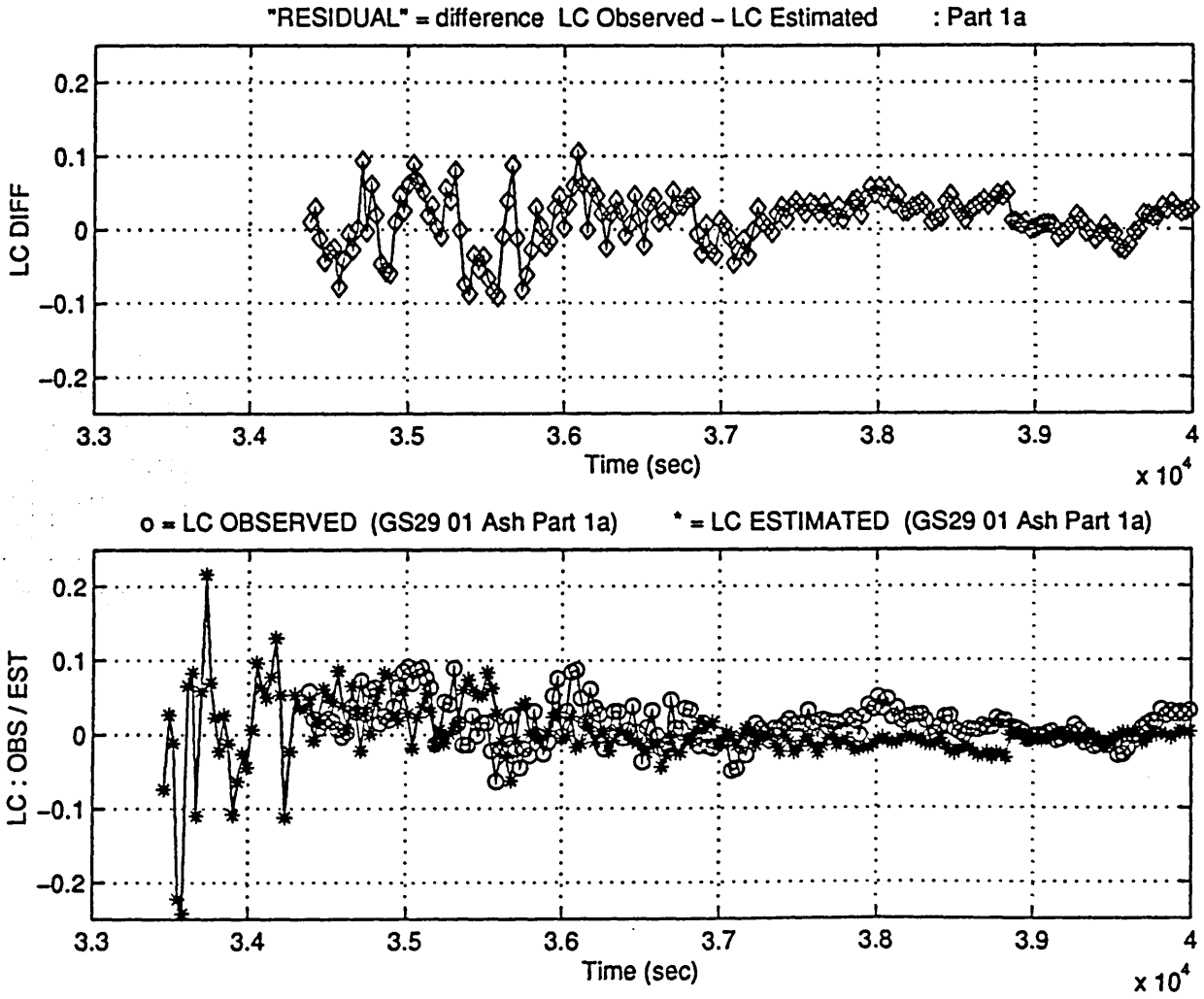

Fig. A.12.5.a) : GS29 - PRN 01 (24 1 1997) - [segment 1a]
Phase residual LC_DIFF, determined as the difference between LC_OBS and LC_EST.
Unit: [cycles]

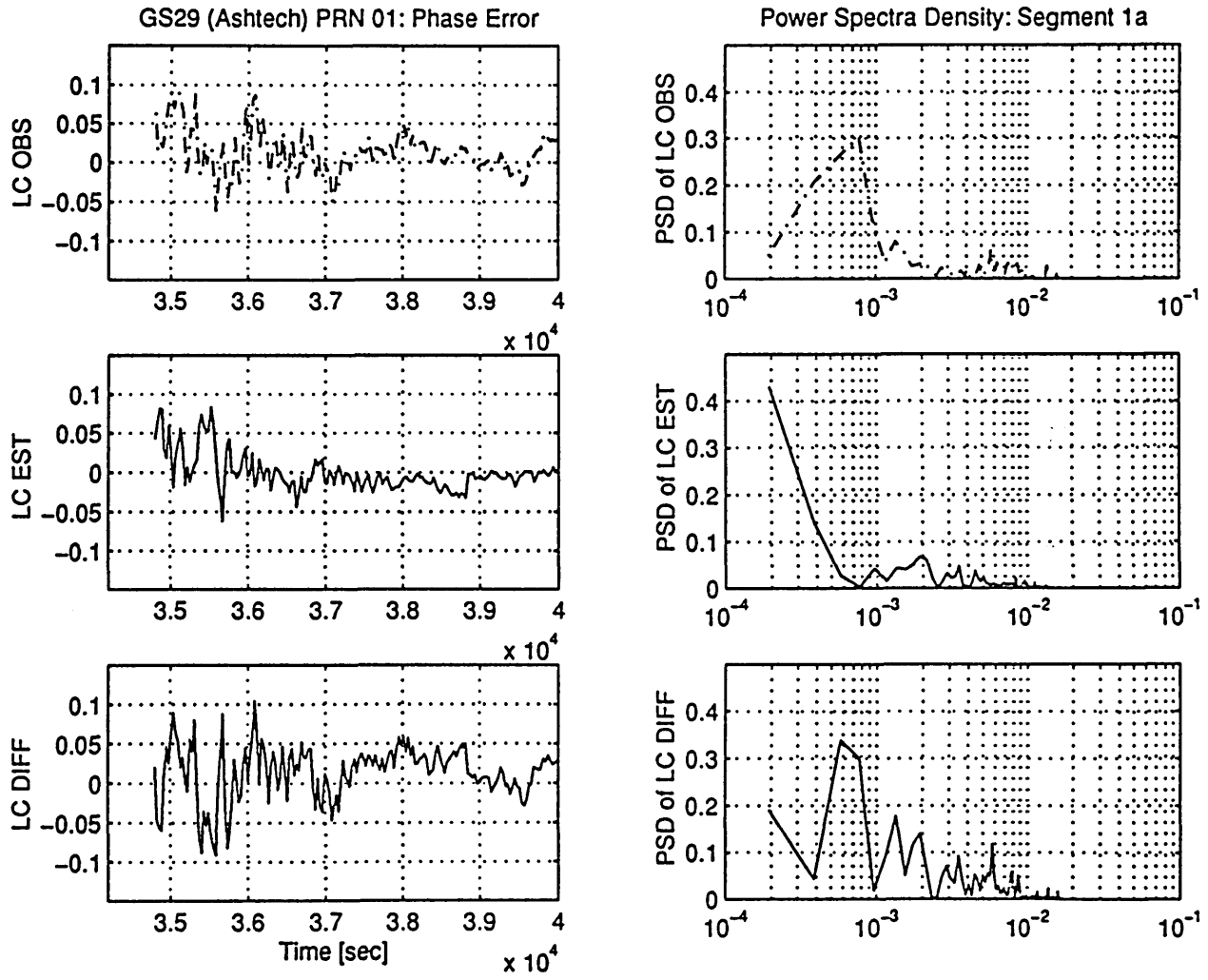

Fig. A.12.5.b) : GS29 - PRN 01 (24 1 1997) - [segment 1a]
PSD of LC_OBS, LC_EST and LC_DIFF.
Unit: [cycles]^2

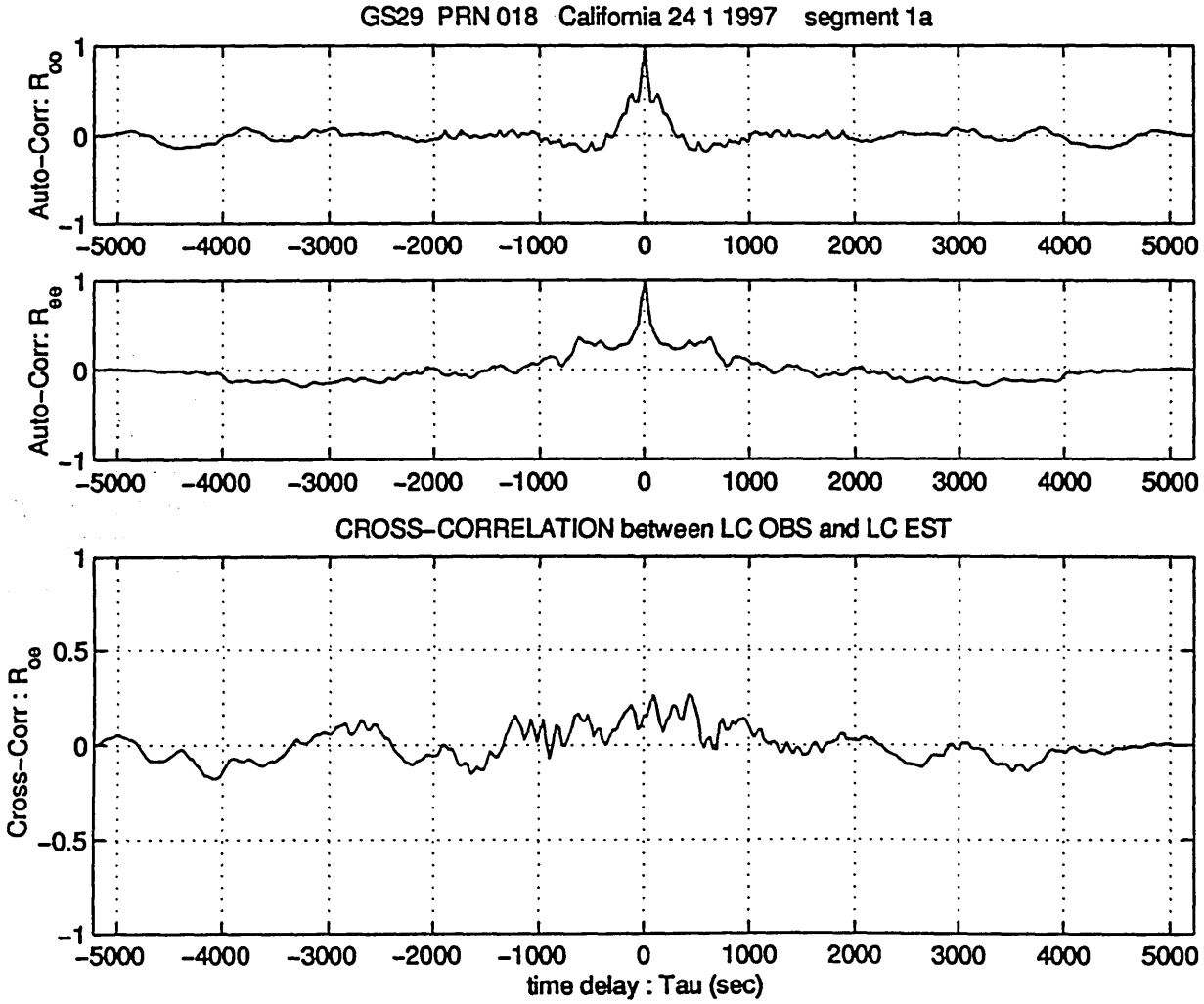

Fig. A.12.5.c) : GS29 - PRN 01 (24 1 1997) - [segment 1a]
Auto Correlation of LC_OBS (R_{oo}) and LC_EST (R_{ee}).
Cross Correlation between them (R_{oe})
Unit: [cycles]^2

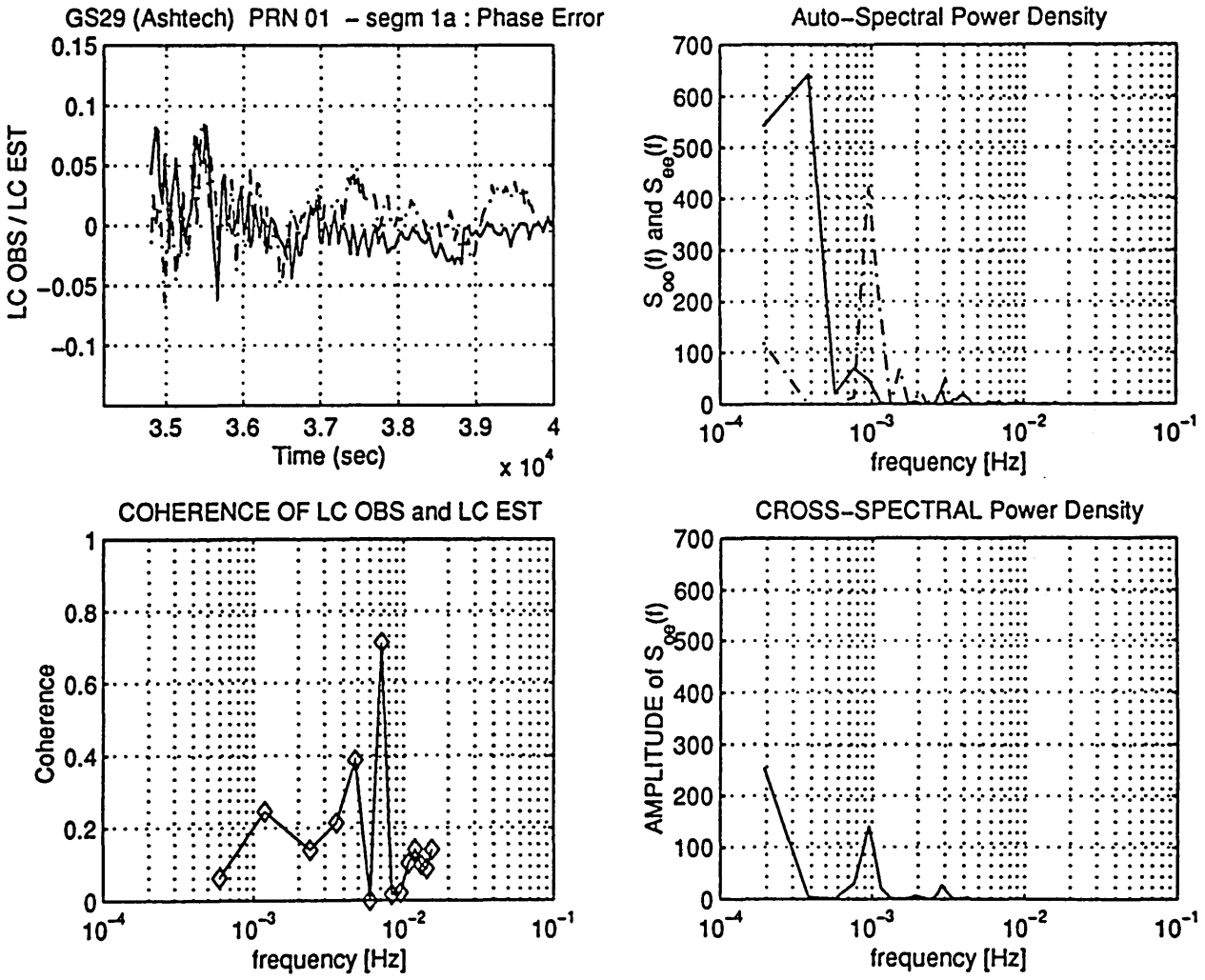

Fig. A.12.5.d) : GS29 - PRN 01 (24 1 1997) - [segment 1a]
Auto Spectral Power Density of LC_OBS (S_{oo}) and of LC_EST (S_{ee}). Cross PSD between them (S_{oe})
Unit: [cycles]^2
Coherence function of LC_OBS and LC_EST

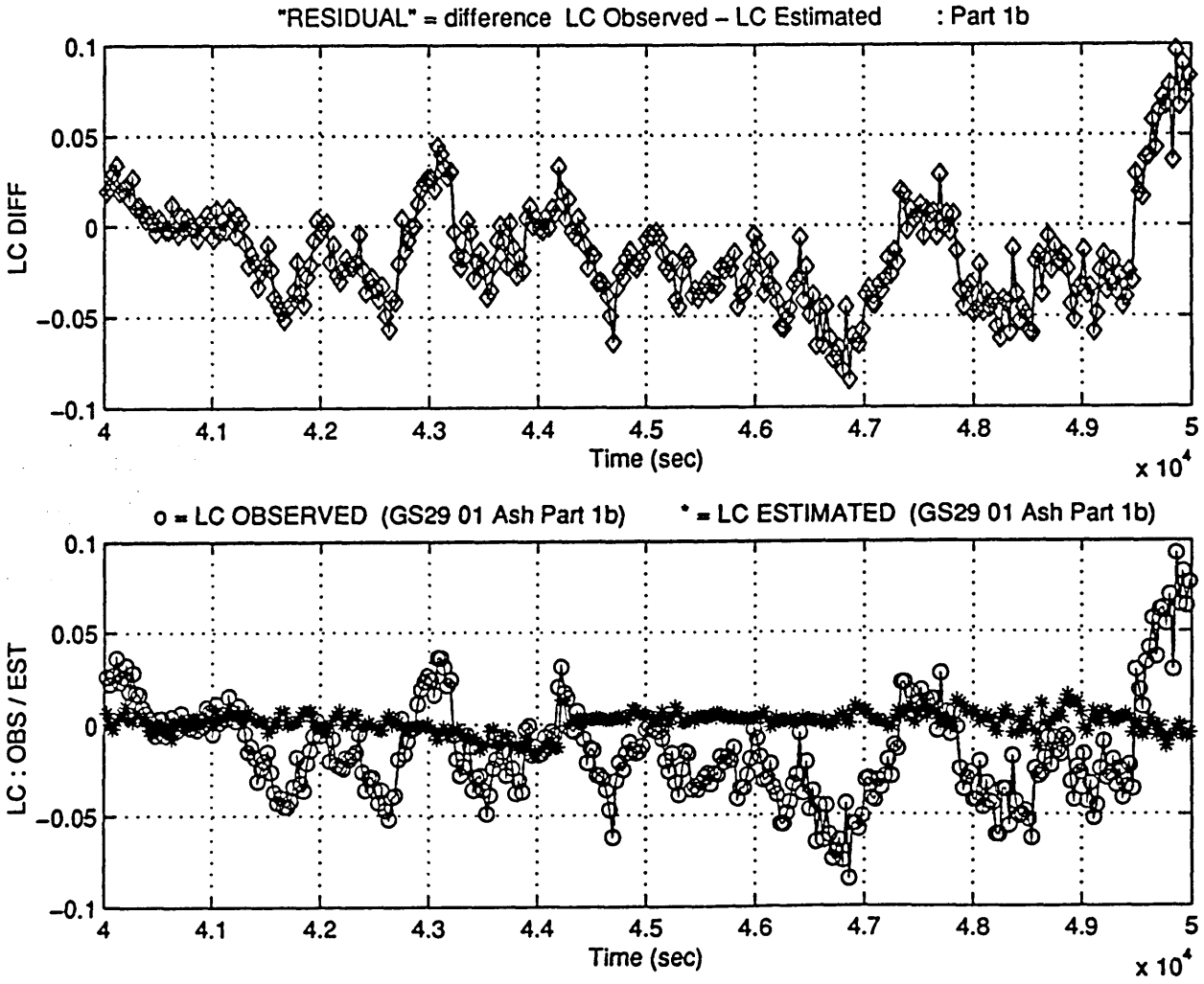

Fig. A.12.6.a) : GS29 - PRN 01 (24 1 1997) - [segment 1b]
Phase residual LC_DIFF, determined as the difference between LC_OBS and LC_EST.
Unit: [cycles]

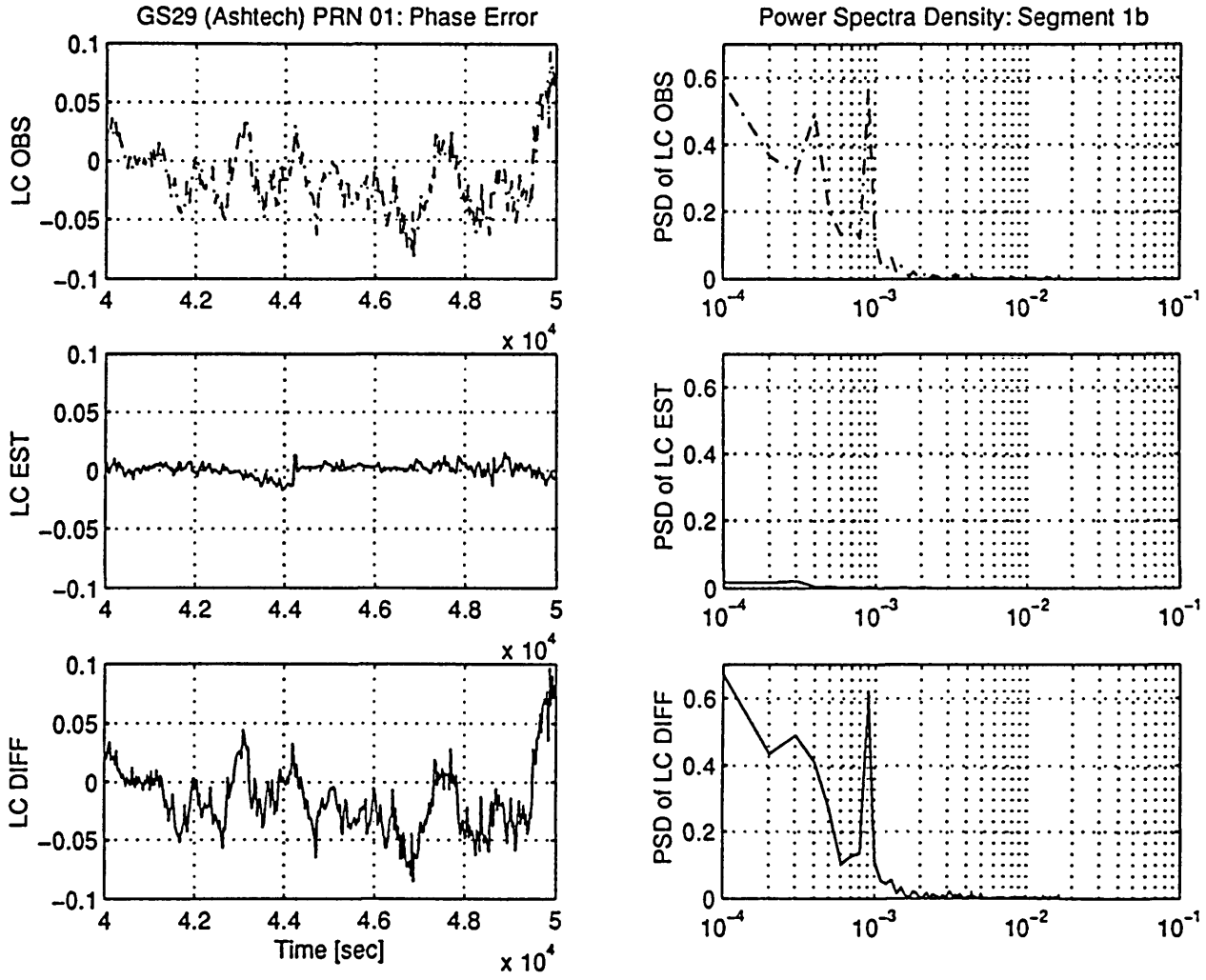

Fig. A.12.6.b) : GS29 - PRN 01 (24 1 1997) - [segment 1b]
PSD of LC_OBS, LC_EST and LC_DIFF.
Unit: [cycles]^2

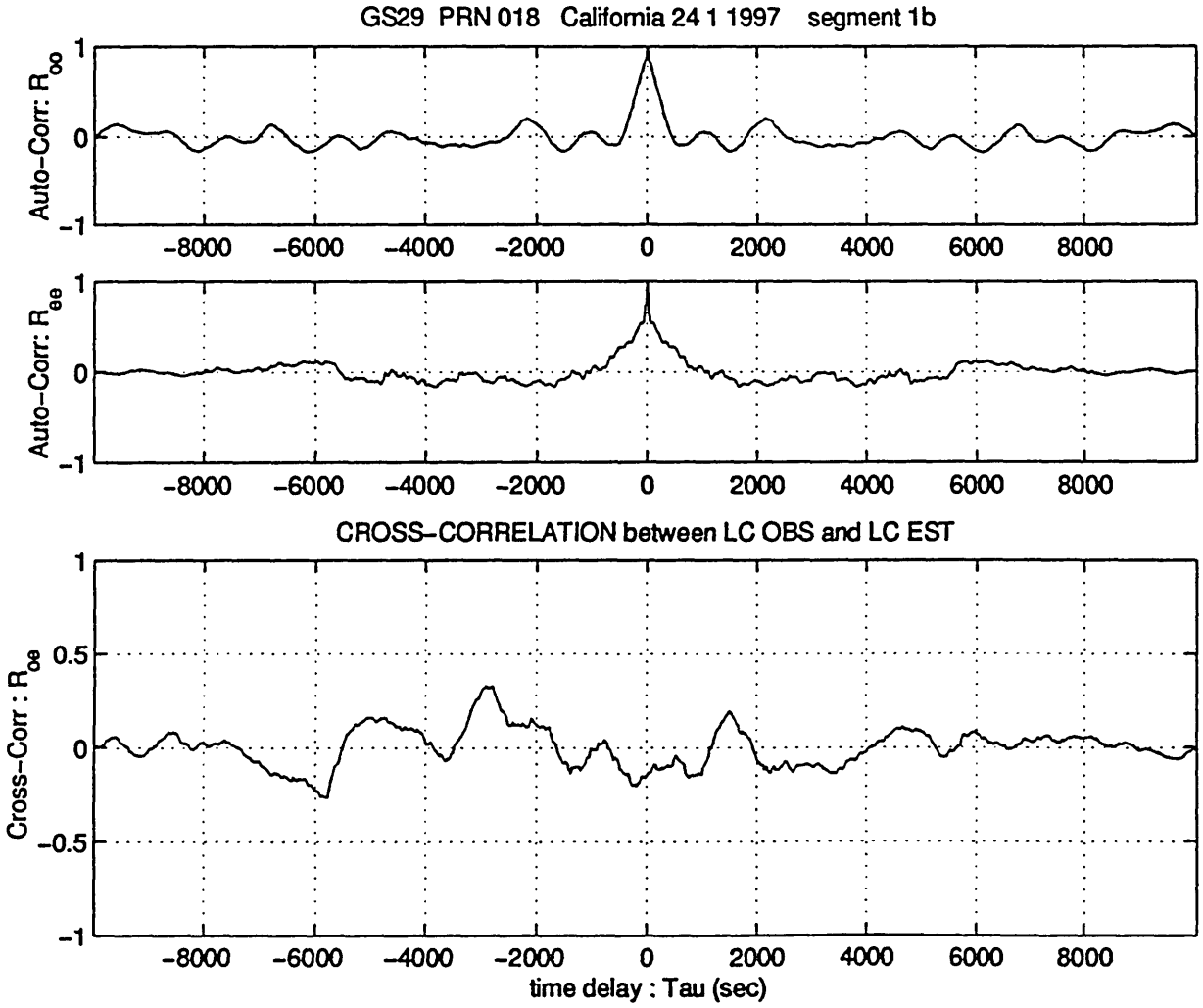

Fig. A.12.6.c) : GS29 - PRN 01 (24 1 1997) - [segment 1b]
Auto Correlation of LC_OBS (R_{oo}) and LC_EST (R_{ee}).
Cross Correlation between them (R_{oe})
Unit: [cycles]^2

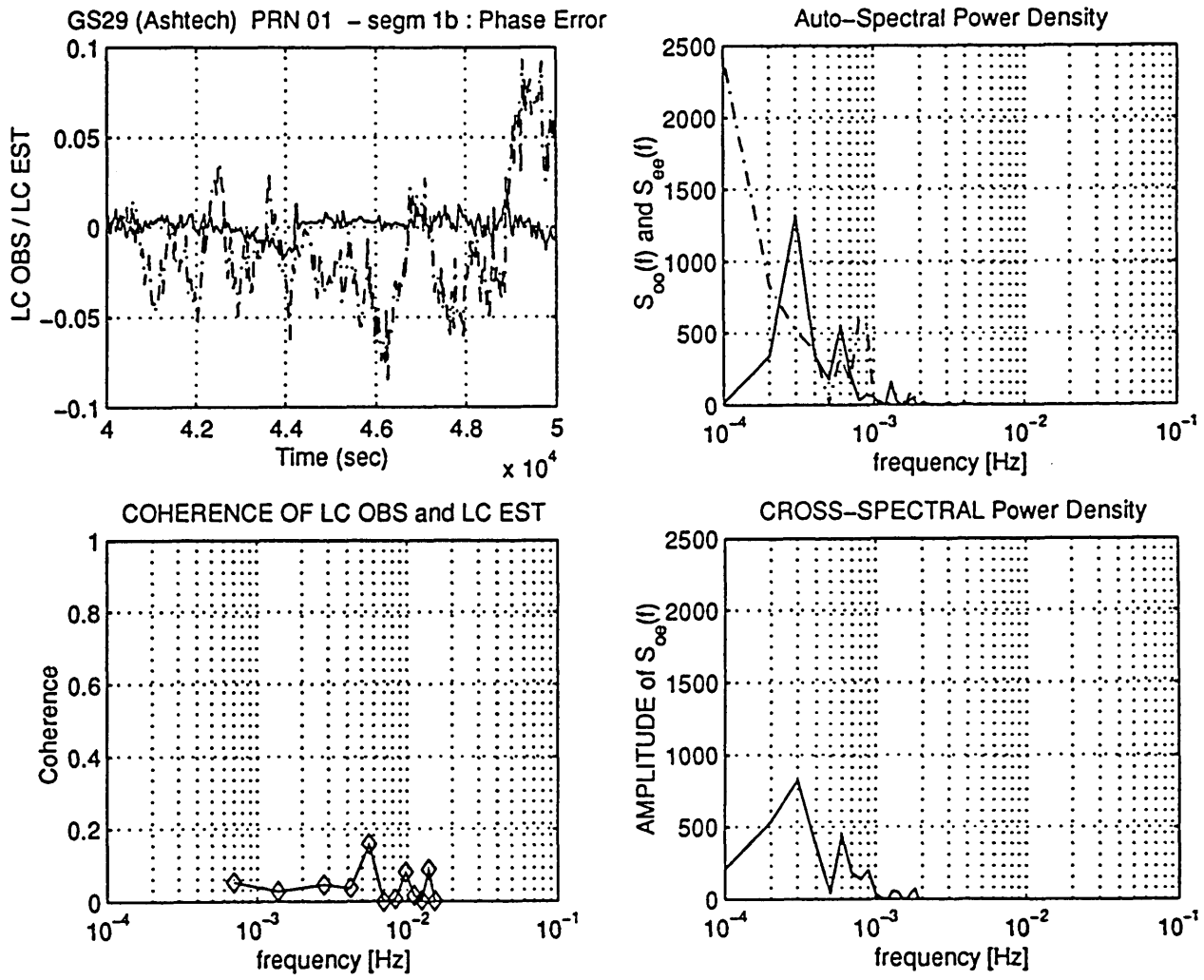

Fig. A.12.6.d) : GS29 - PRN 01 (24 1 1997) - [segment 1b]
Auto Spectral Power Density of LC_OBS (S_{oo}) and of LC_EST (S_{ee}). CrossPSD between them (S_{oe})
Unit: [cycles]^2
Coherence function of LC_OBS and LC_EST

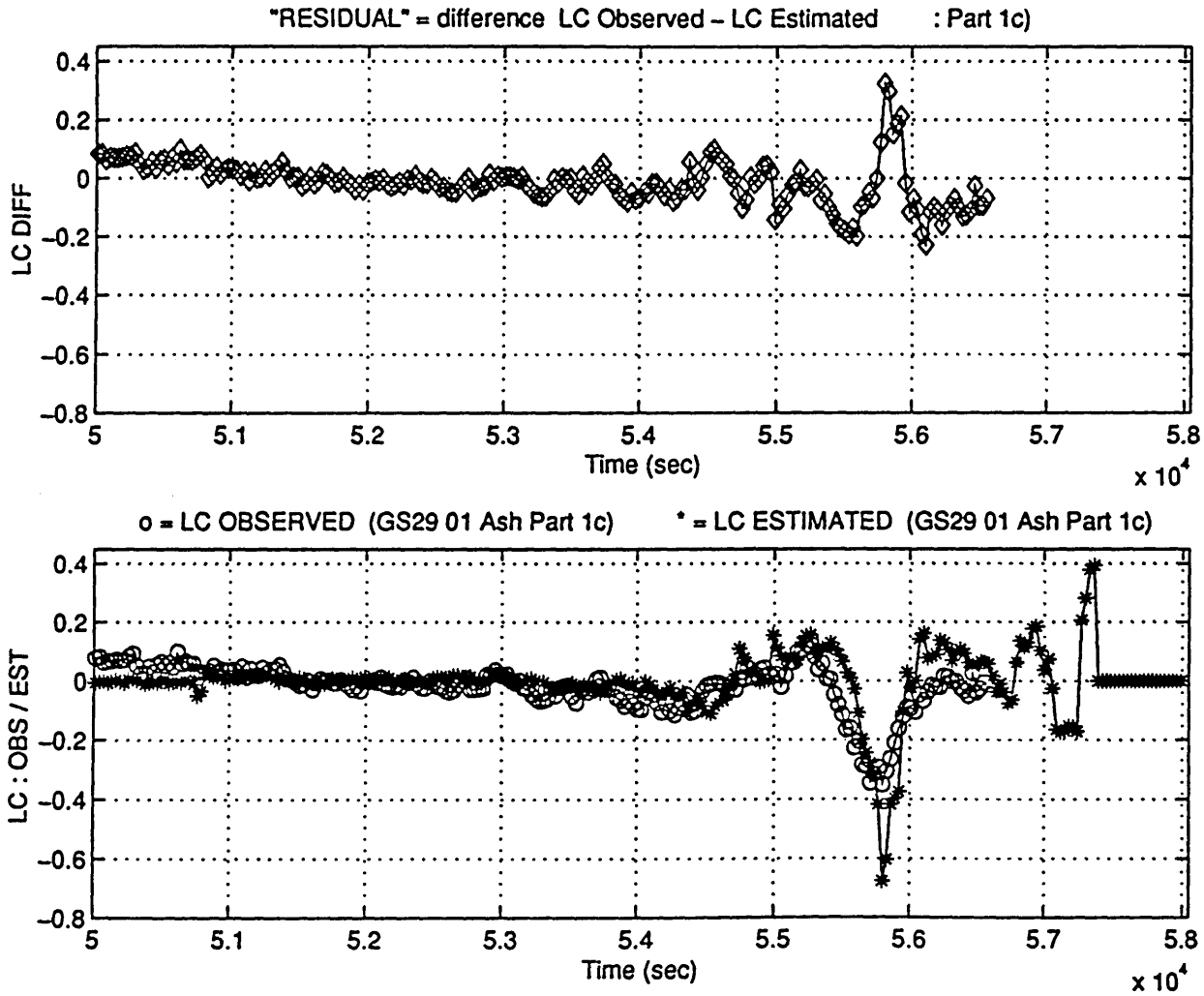

Fig. A.12.7.a) : GS29 - PRN 01 (24 1 1997) - [segment 1c]
Phase residual LC_DIFF, determined as the difference between LC_OBS and LC_EST.
Unit: [cycles]

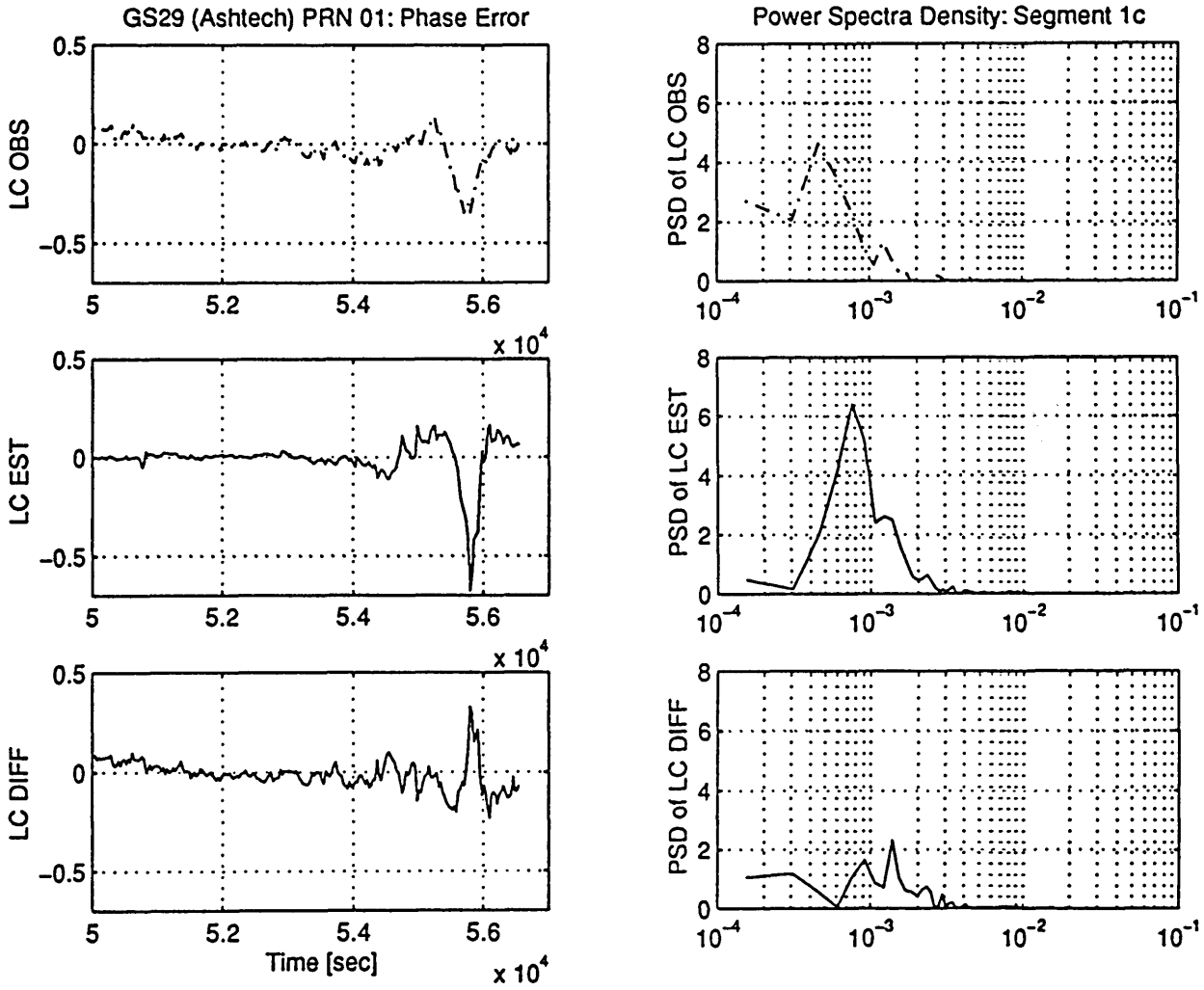

Fig. A.12.7.b) : GS29 - PRN 01 (24 1 1997) - [segment 1c]
PSD of LC_OBS, LC_EST and LC_DIFF.
Unit: [cycles]^2

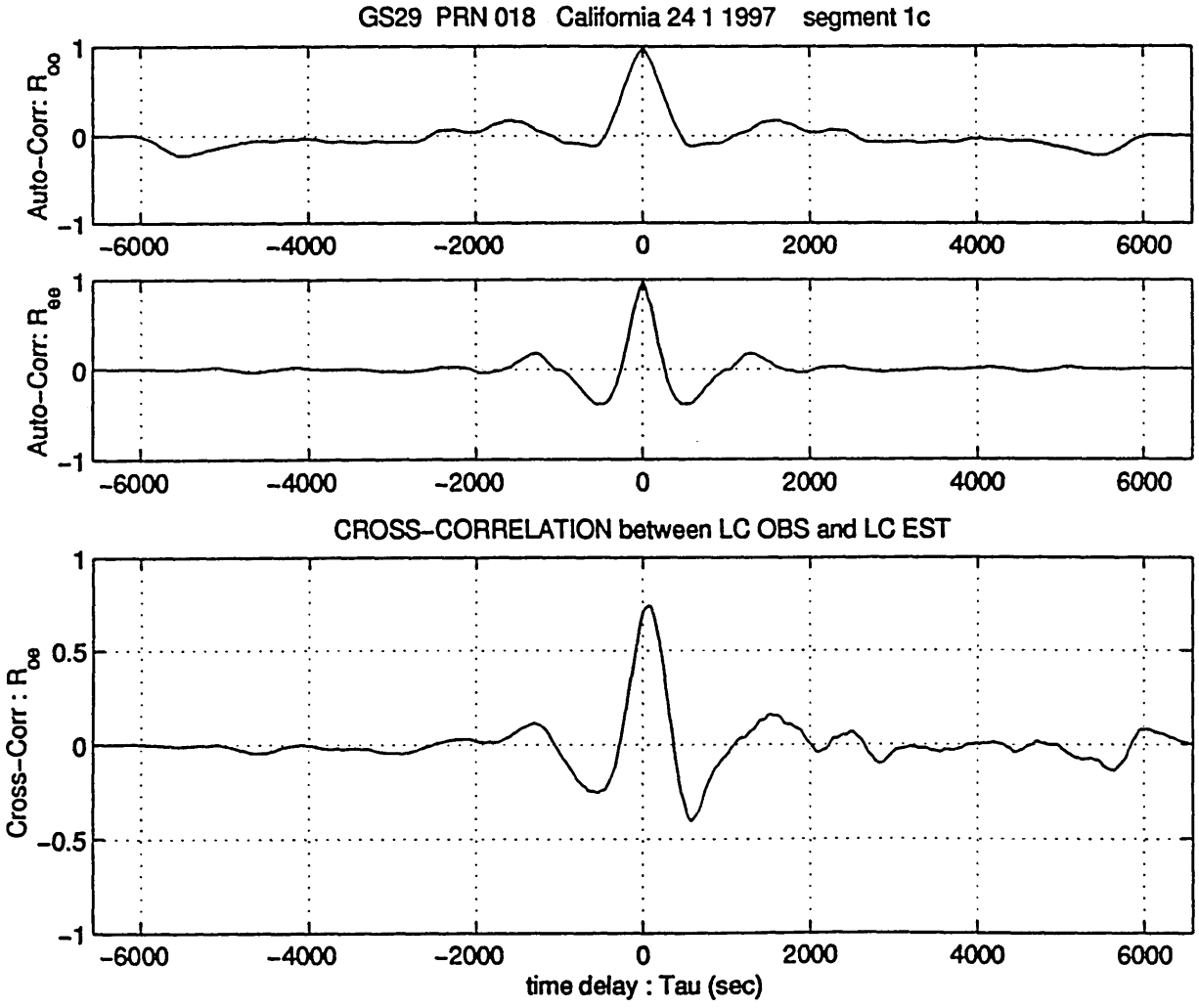

Fig. A.12.7.c) : GS29 - PRN 01 (24 1 1997) - [segment 1c]
Auto Correlation of LC_OBS (R_{oo}) and LC_EST (R_{ee}).
Cross Correlation between them (R_{oe})
Unit: [cycles]^2

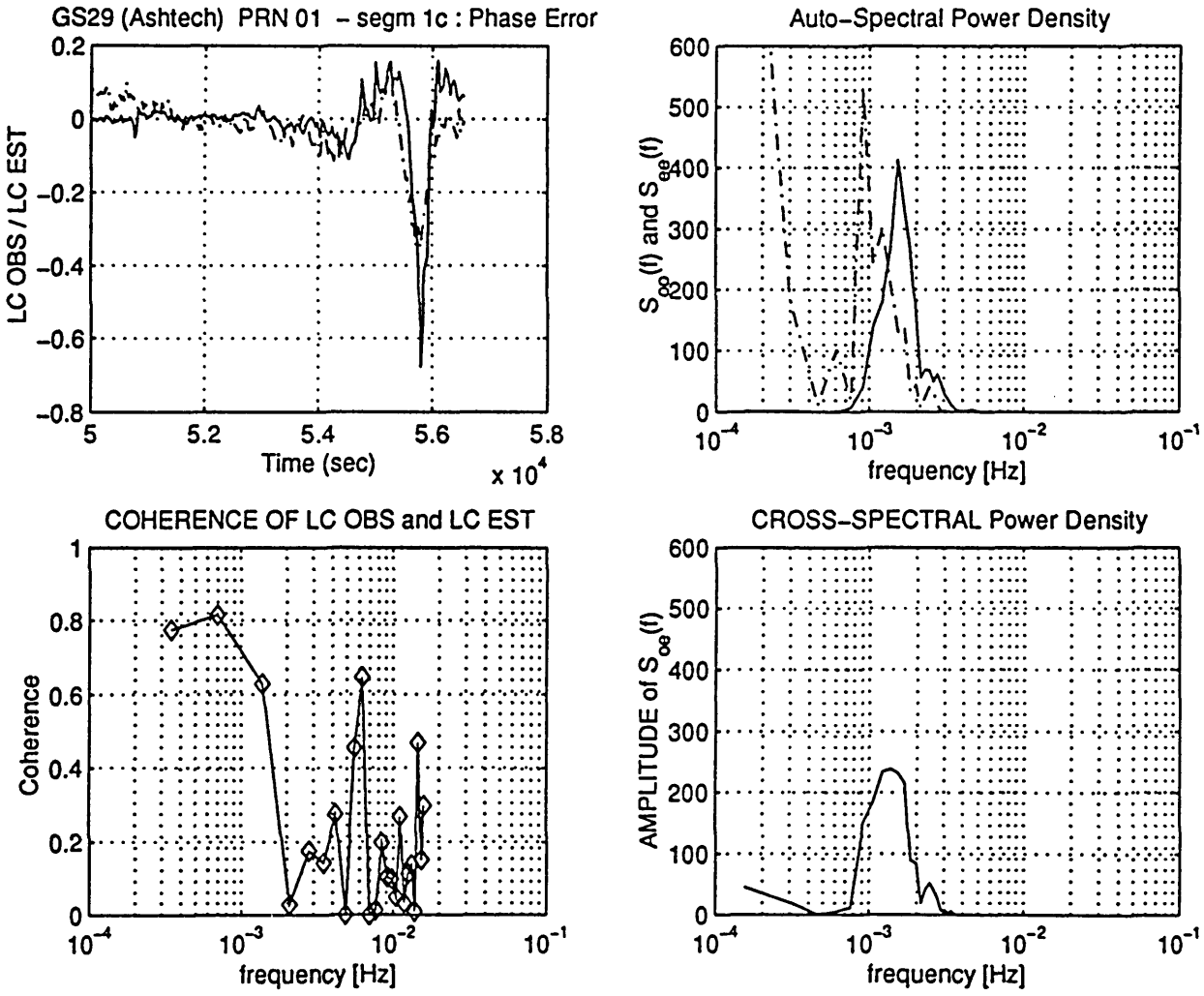

Fig. A.12.7.d) : GS29 - PRN 01 (24 1 1997) - [segment 1c]
Auto Spectral Power Density of LC_OBS (S_{oo}) and of LC_EST (S_{ee}). CrossPSD between them (S_{oe})
Unit: [cycles]^2
Coherence function of LC_OBS and LC_EST

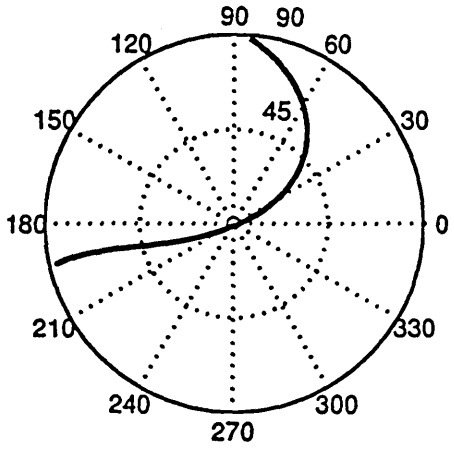

GPS DATA: receiver location: SOUTHERN CALIFORNIA acquisition date: 24 1 1997

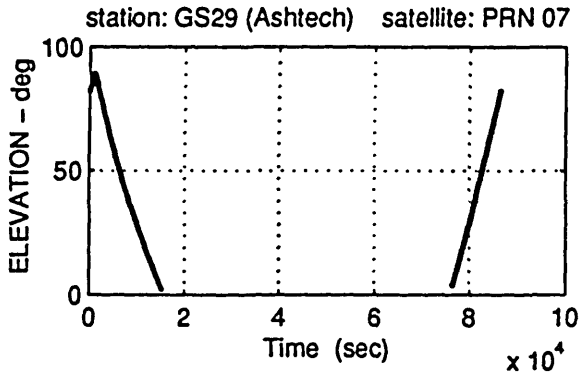

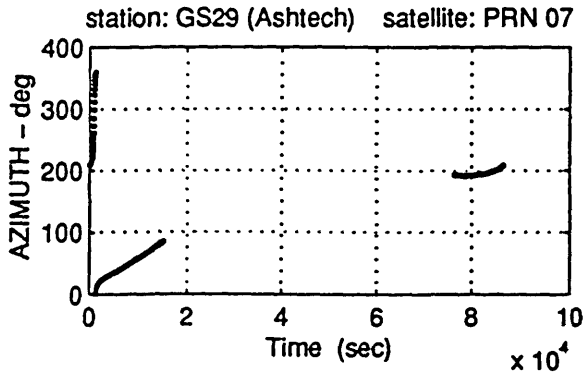

Fig. A.13.1 : Satellite visibility chart for PRN 07 (skymap). Elevation and azimuth of PRN 07 with respect to the station GS29

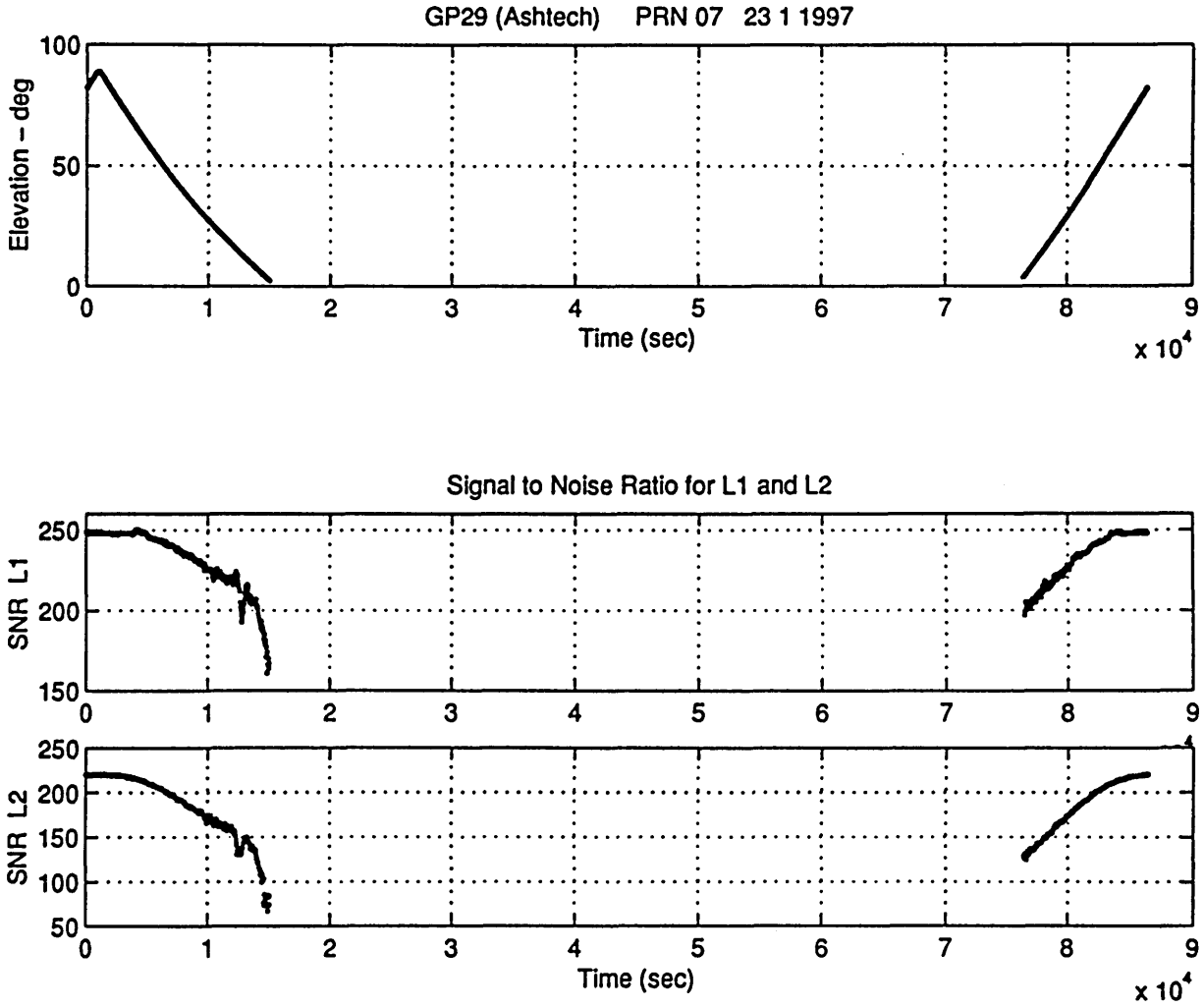

Fig. A.13.2 : Station: GS29 - Satellite: PRN 07
Data acquisition date 24 1 1997
Signal-to-Noise-Ratio (SNR) for L_1 and L_2.

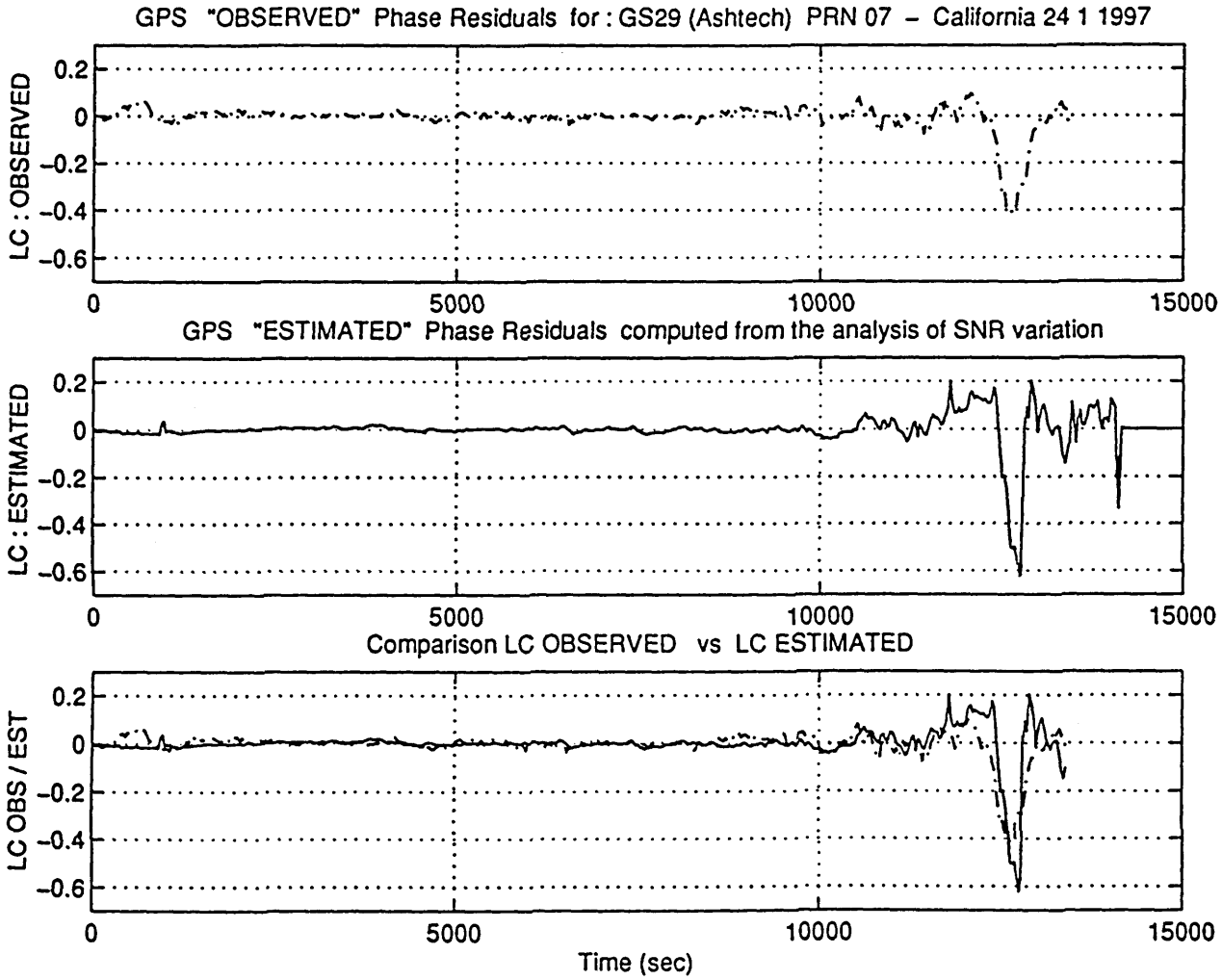

Fig. A.13.3 : Station: GS29 - Satellite: PRN 07- Data acquisition date 24 1 1997
The observed phase residual (LC_OBS) is compared with the multipath phase error estimated from the SNR (LC_EST)
Unit: [cycles]

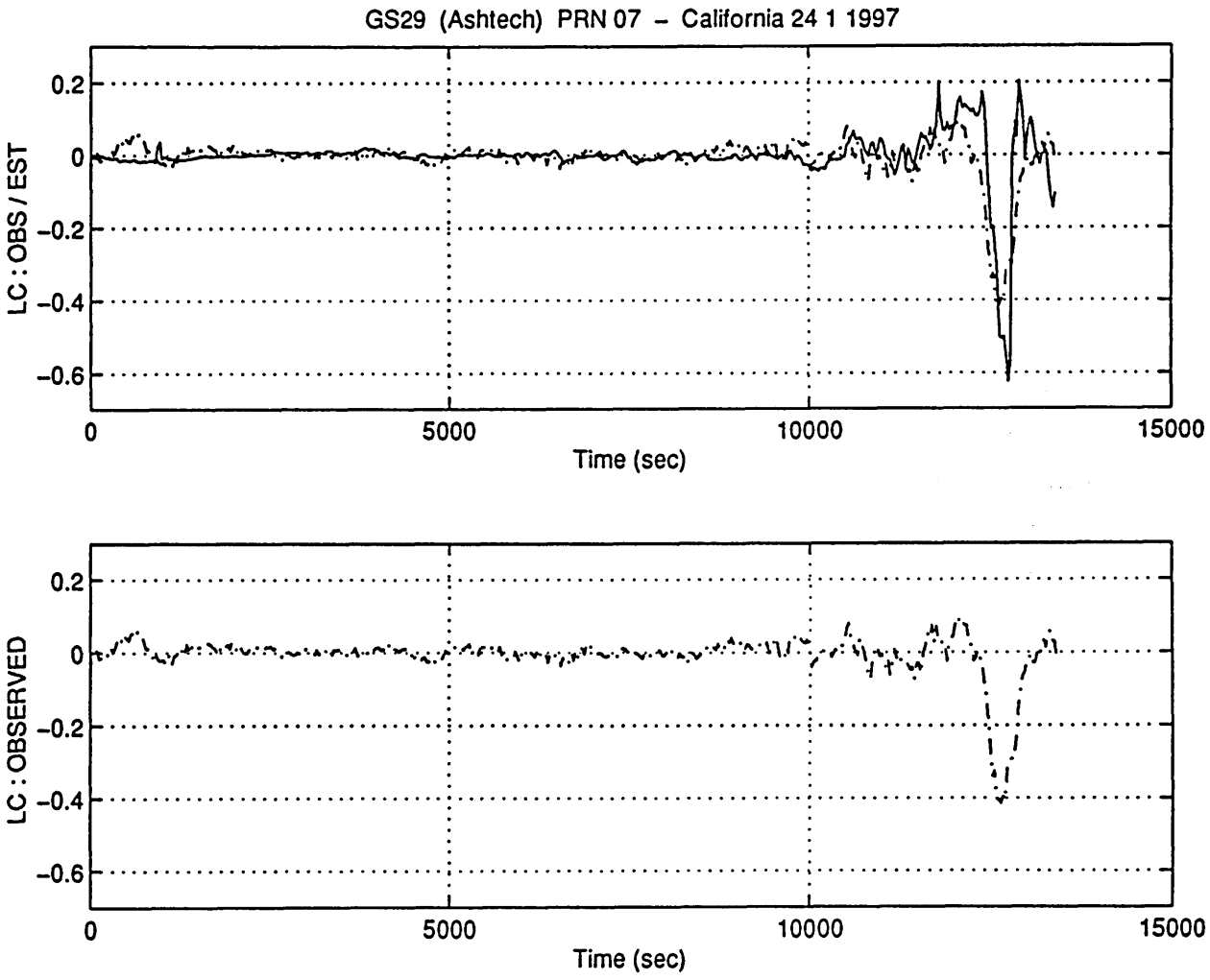

Fig. A.13.4 : Station: GS29 - Satellite: PRN 07- Data acquisition date 24 1 1997
LC_OBS and LC_EST compared for t=0.0 - 1.4 10^4 sec
Unit: [cycles]

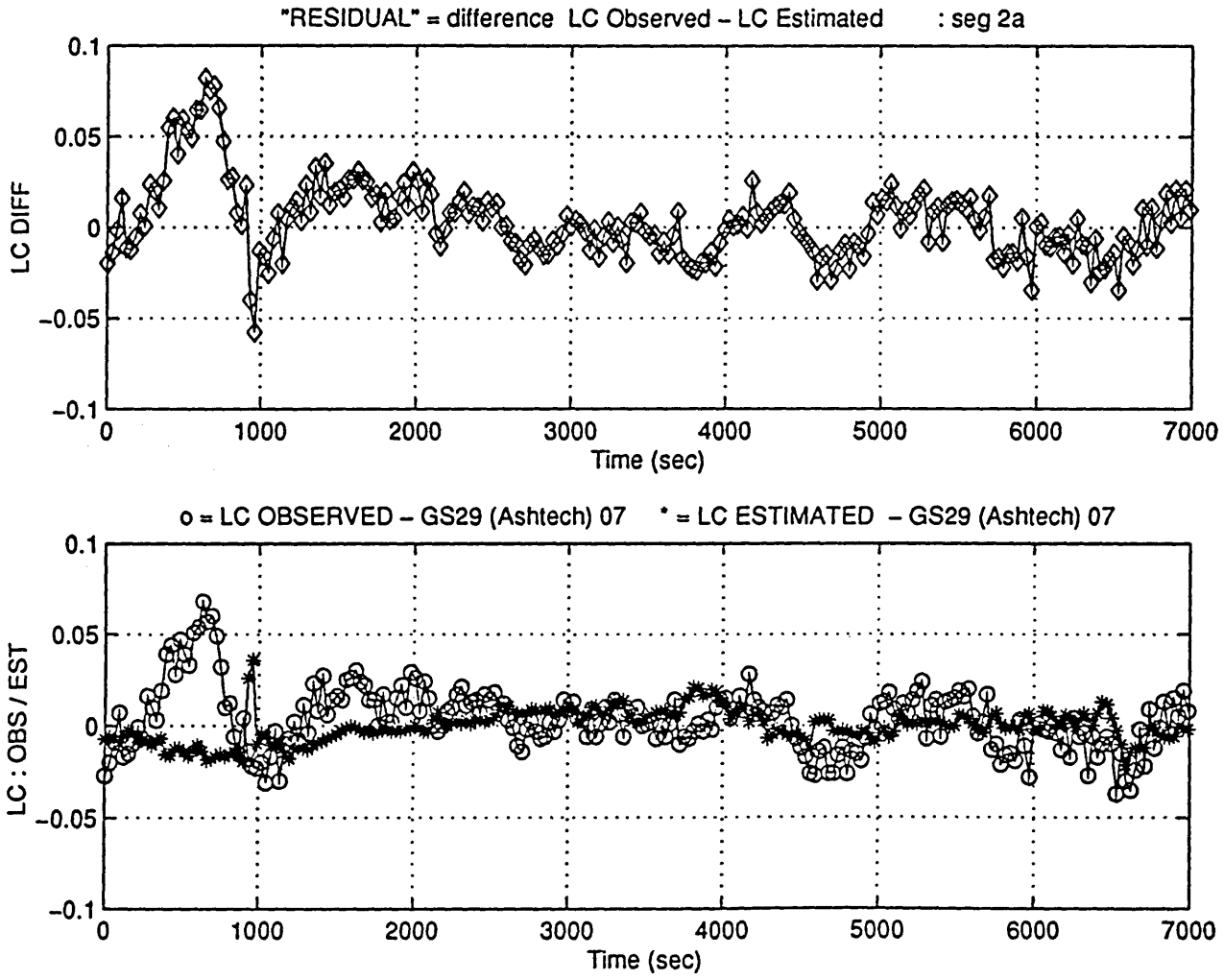

Fig. A.13.5.a) : GS29 - PRN 07 (24 1 1997) - [segment 1a]
Phase residual LC_DIFF, determined as the difference between LC_OBS and LC_EST.
Unit: [cycles]

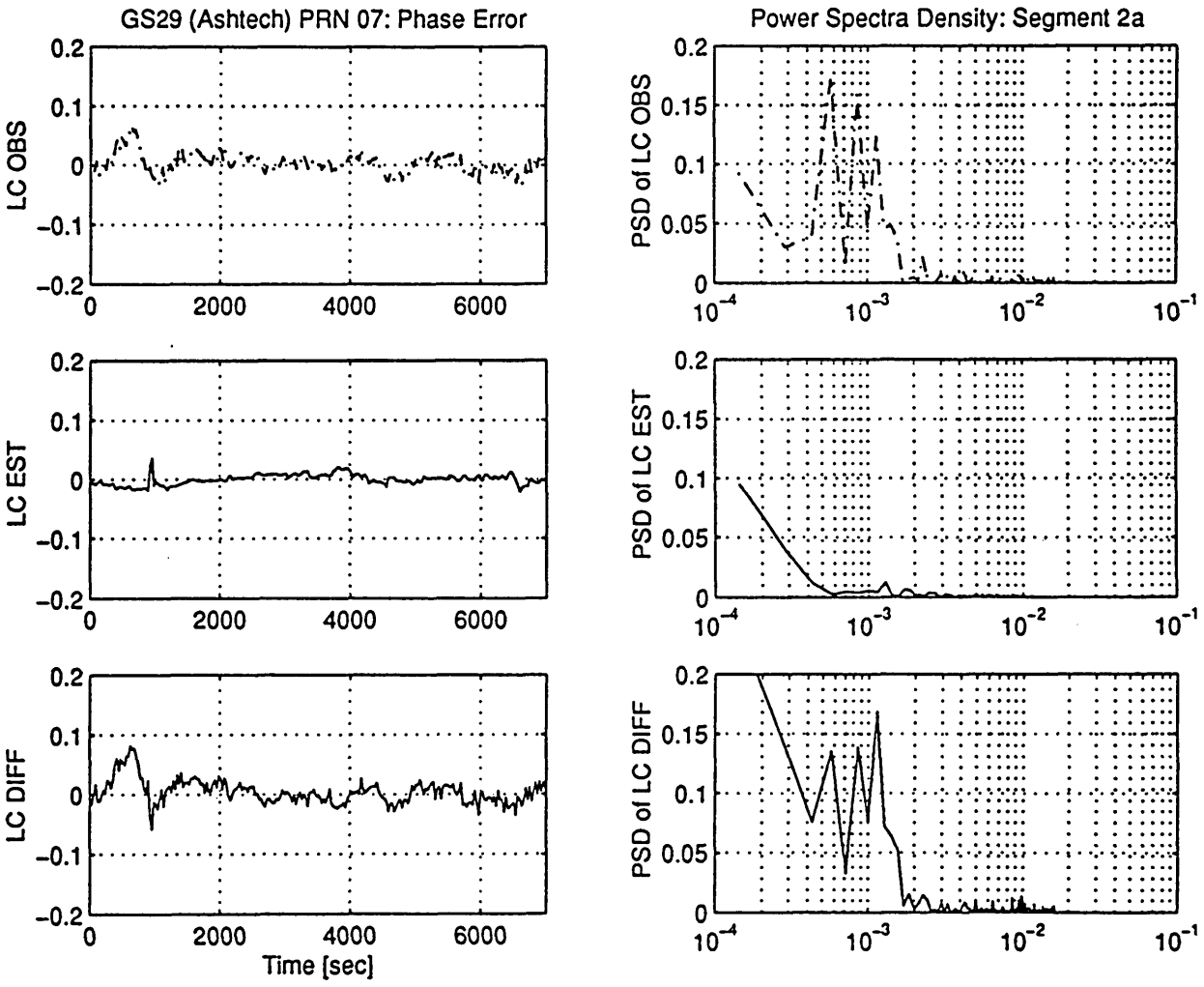

Fig. A.13.5.b) : GS29 - PRN 07 (24 1 1997) - [segment 1a]
PSD of LC_OBS, LC_EST and LC_DIFF.
Unit: [cycles]^2

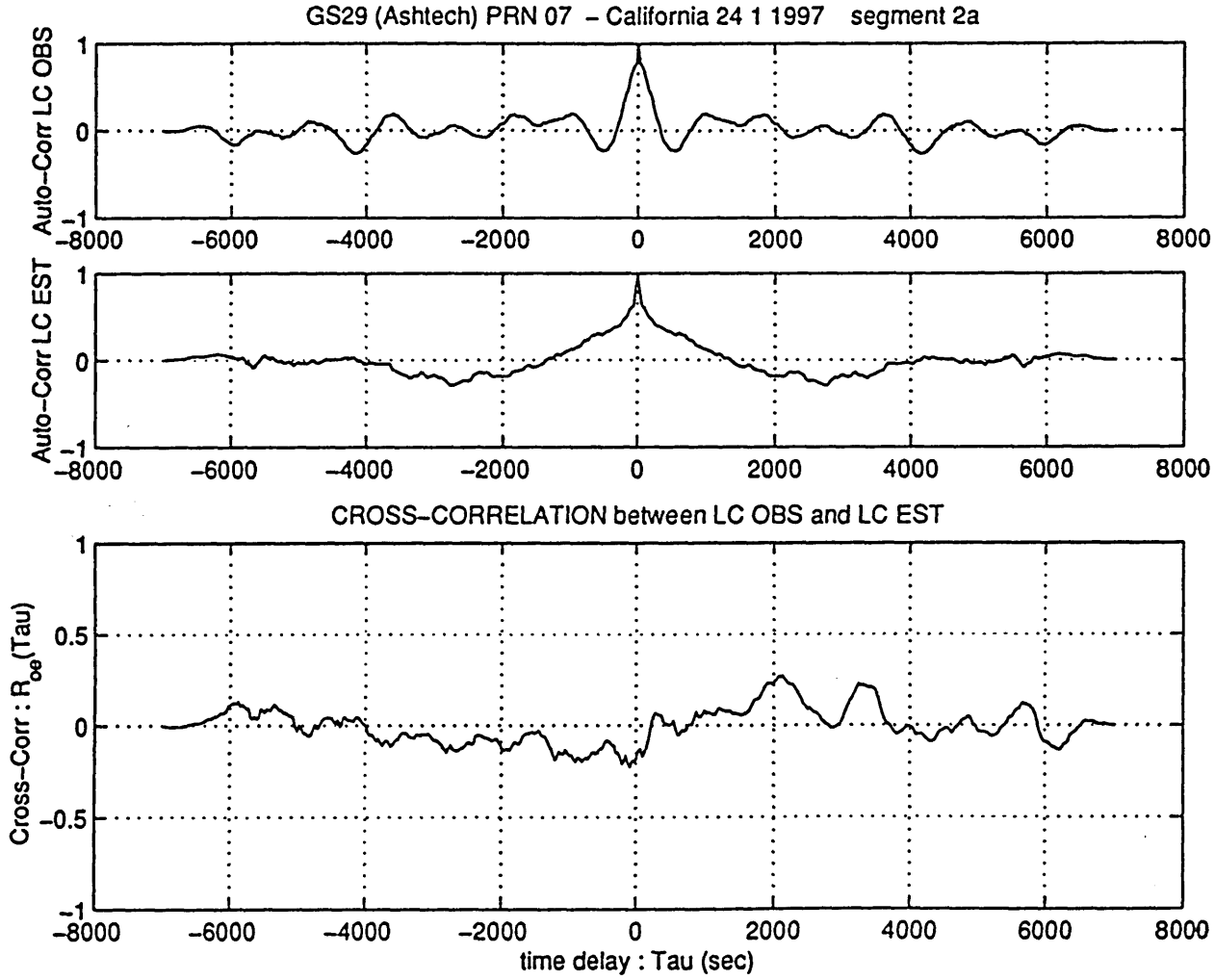

Fig. A.13.5.c) : GS29 - PRN 07 (24 1 1997) - [segment 1a]
Auto Correlation of LC_OBS (R_{oo}) and LC_EST (R_{ee}).
Cross Correlation between them (R_{oe})
Unit: [cycles]^2

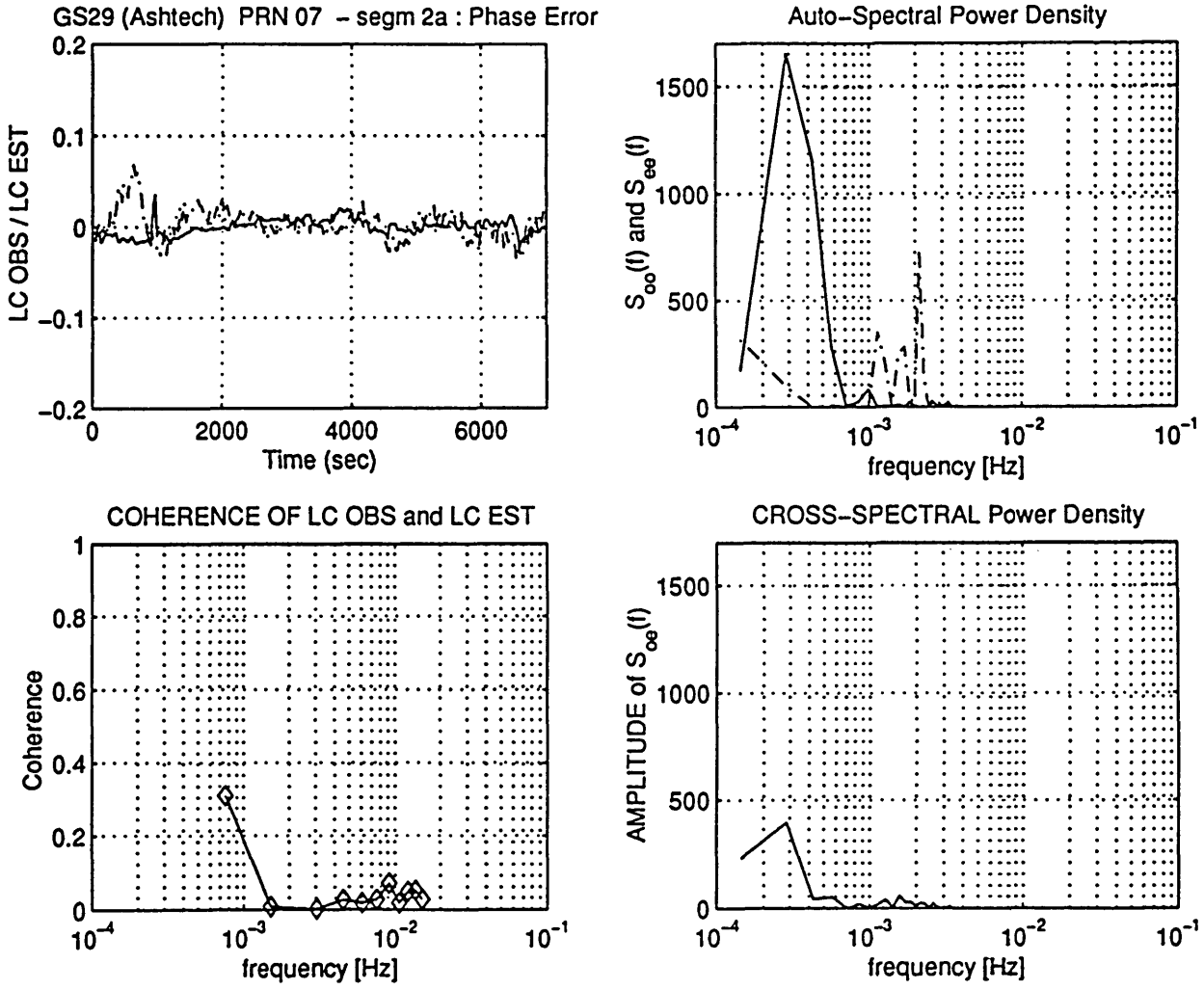

Fig. A.13.5.d) : GS29 - PRN 07 (24 1 1997) - [segment 1a]
Auto Spectral Power Density of LC_OBS (S_{oo}) and of LC_EST (S_{ee}). Cross PSD between them (S_{oe})
Unit: [cycles]^2
Coherence function of LC_OBS and LC_EST

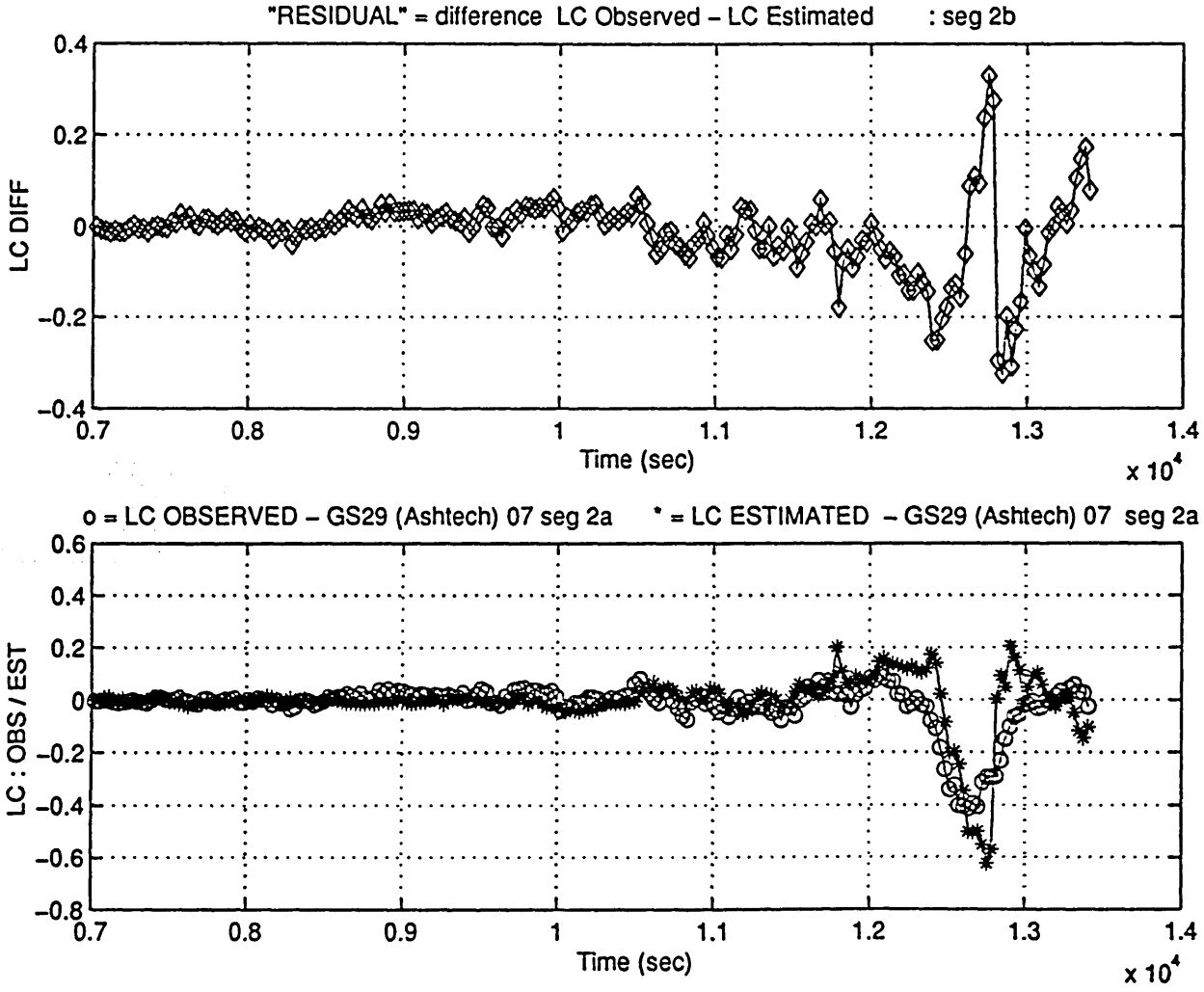

Fig. A.13.6.a) : GS29 - PRN 07 (24 1 1997) - [segment 1b]
Phase residual LC_DIFF, determined as the difference between LC_OBS and LC_EST.
Unit: [cycles]

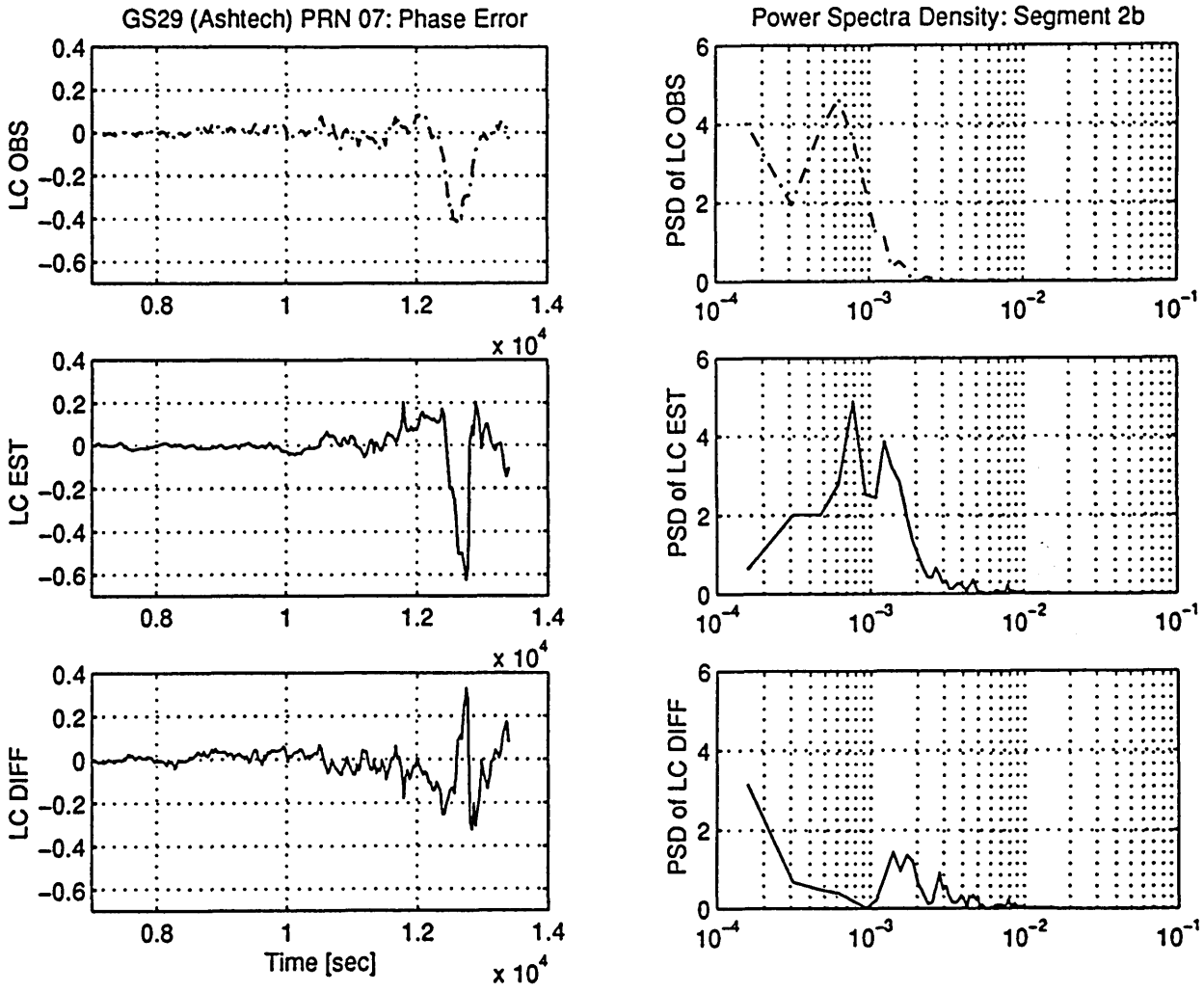

Fig. A.13.6.b) : GS29 - PRN 07 (24 1 1997) - [segment 1b]
PSD of LC_OBS, LC_EST and LC_DIFF.
Unit: [cycles]^2

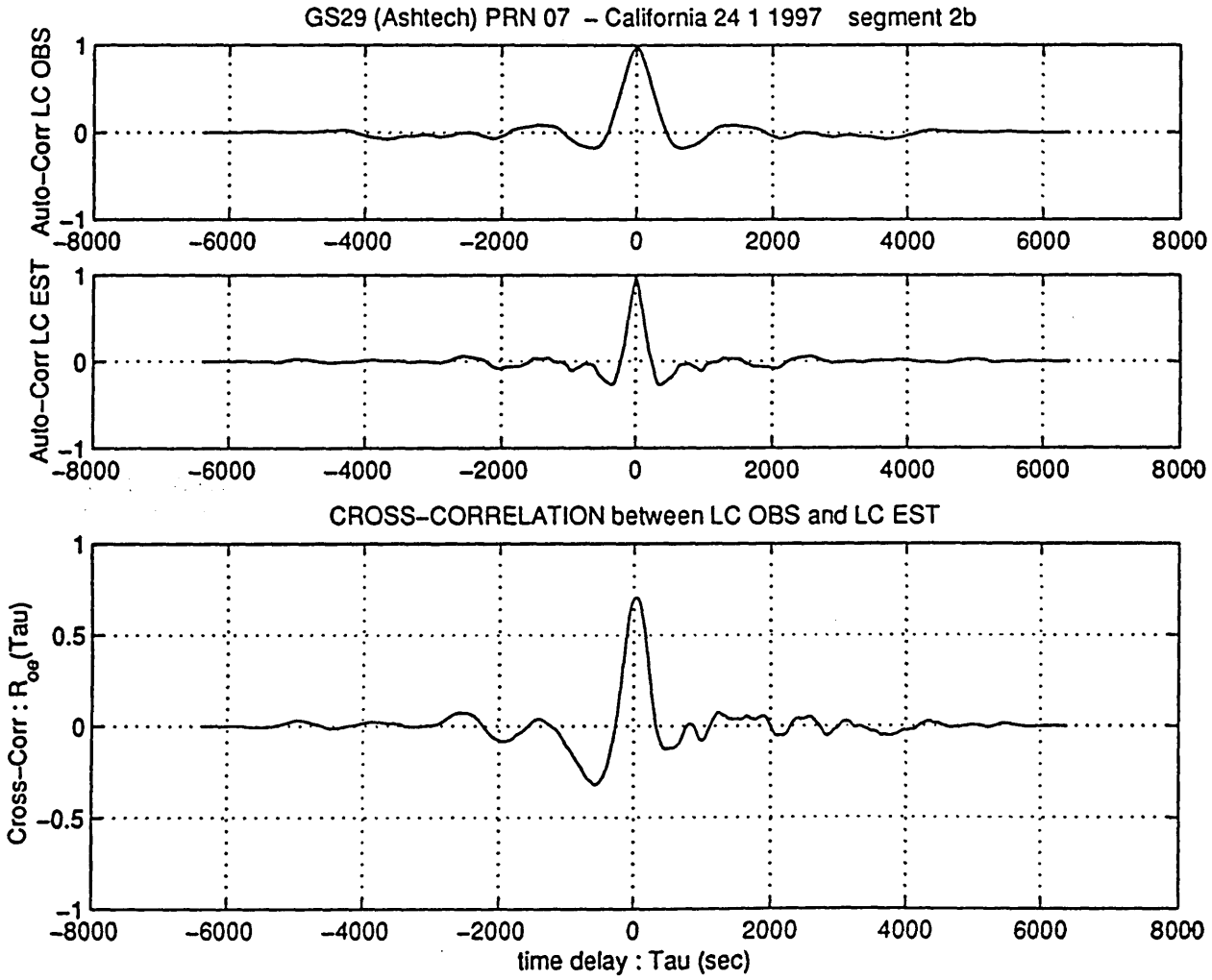

Fig. A.13.6.c) : GS29 - PRN 07 (24 1 1997) - [segment 1b]
Auto Correlation of LC_OBS (R_{oo}) and LC_EST (R_{ee}).
Cross Correlation between them (R_{oe})
Unit: [cycles]^2

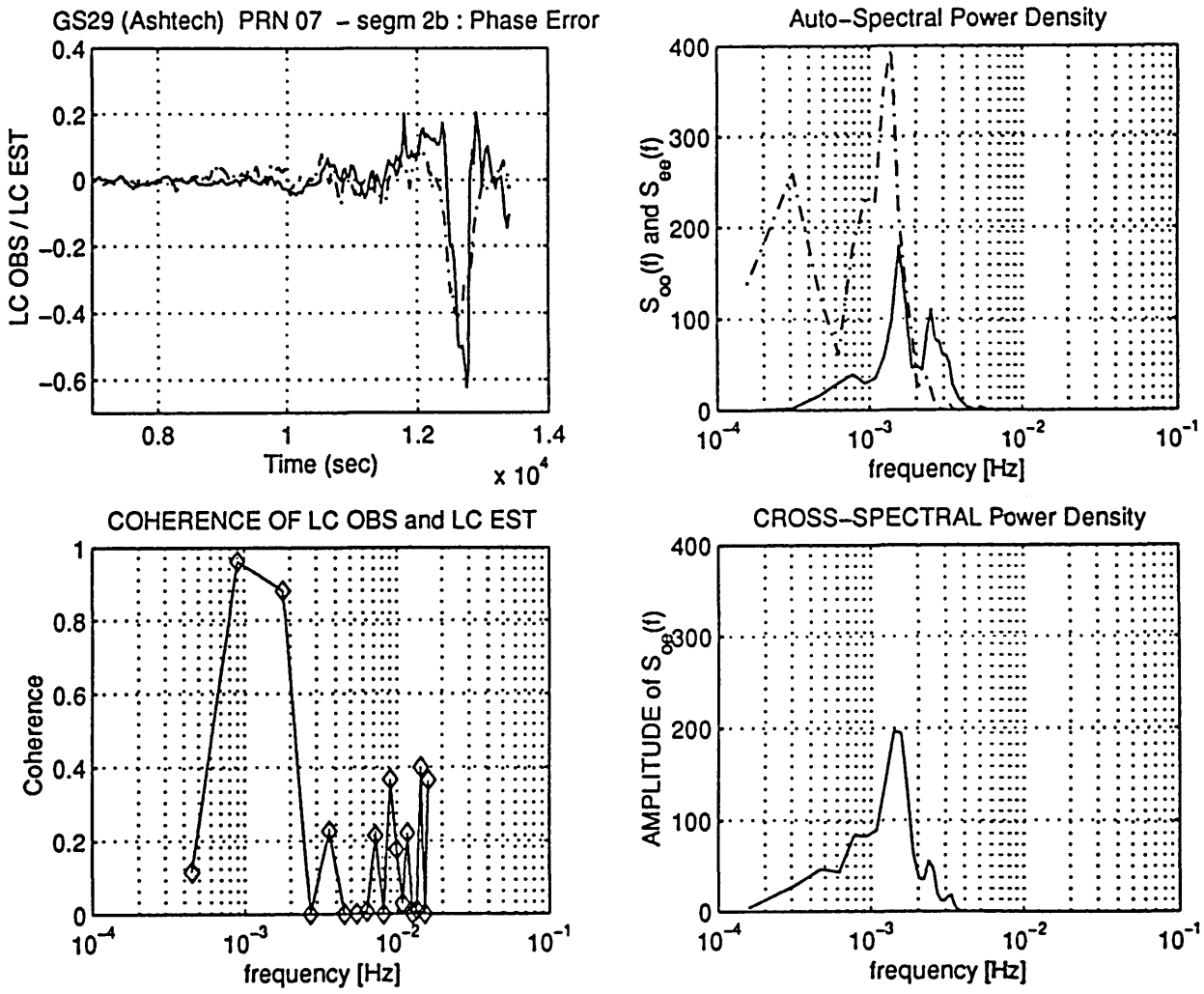

Fig. A.13.6.d) : GS29 - PRN 07 (24 1 1997) - [segment 1b]
Auto Spectral Power Density of LC_OBS (S_{oo}) and of LC_EST (S_{ee}). Cross PSD between them (S_{oe})
Unit: [cycles]^2
Coherence function of LC_OBS and LC_EST

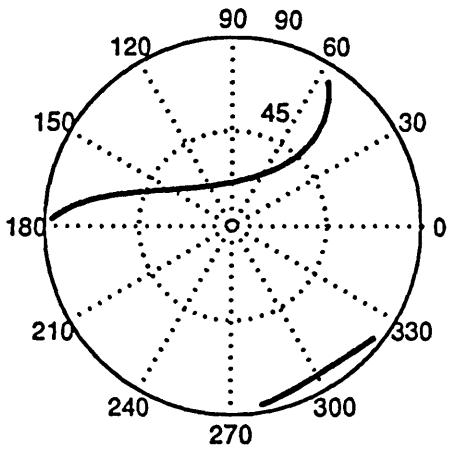

GPS DATA: receiver location: SOUTHERN CALIFORNIA acquisition date: 24 1 1997

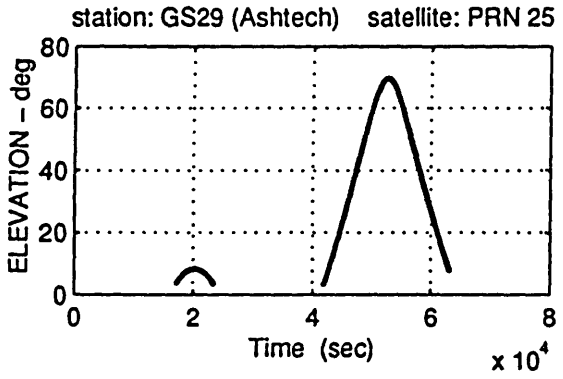

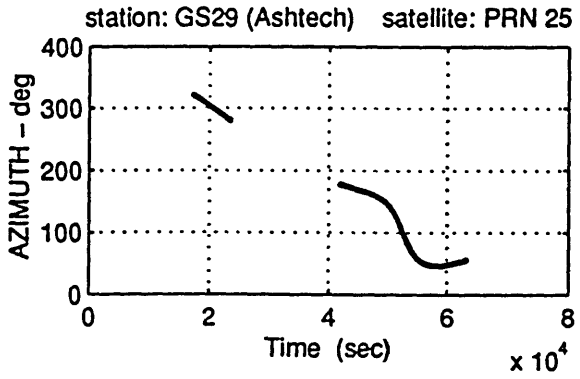

Fig. A.14.1 : Satellite visibility chart for PRN 25 (skymap).
Elevation and azimuth of PRN 25 with respect to
the station GS29

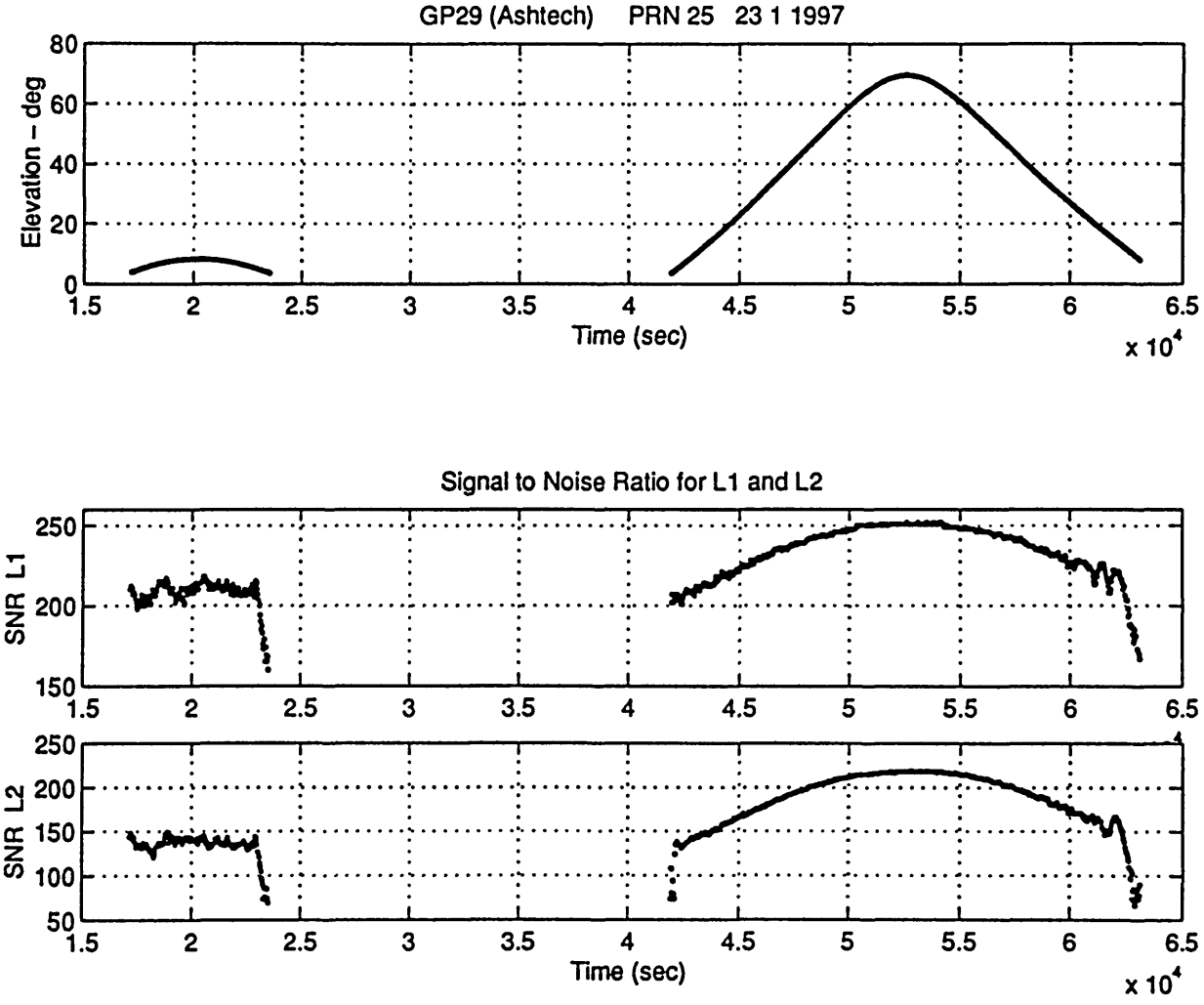

Fig. A.14.2 : Station: GS29 - Satellite: PRN 25
Data acquisition date 24 1 1997
Signal-to-Noise-Ratio (SNR) for L1 and L2.

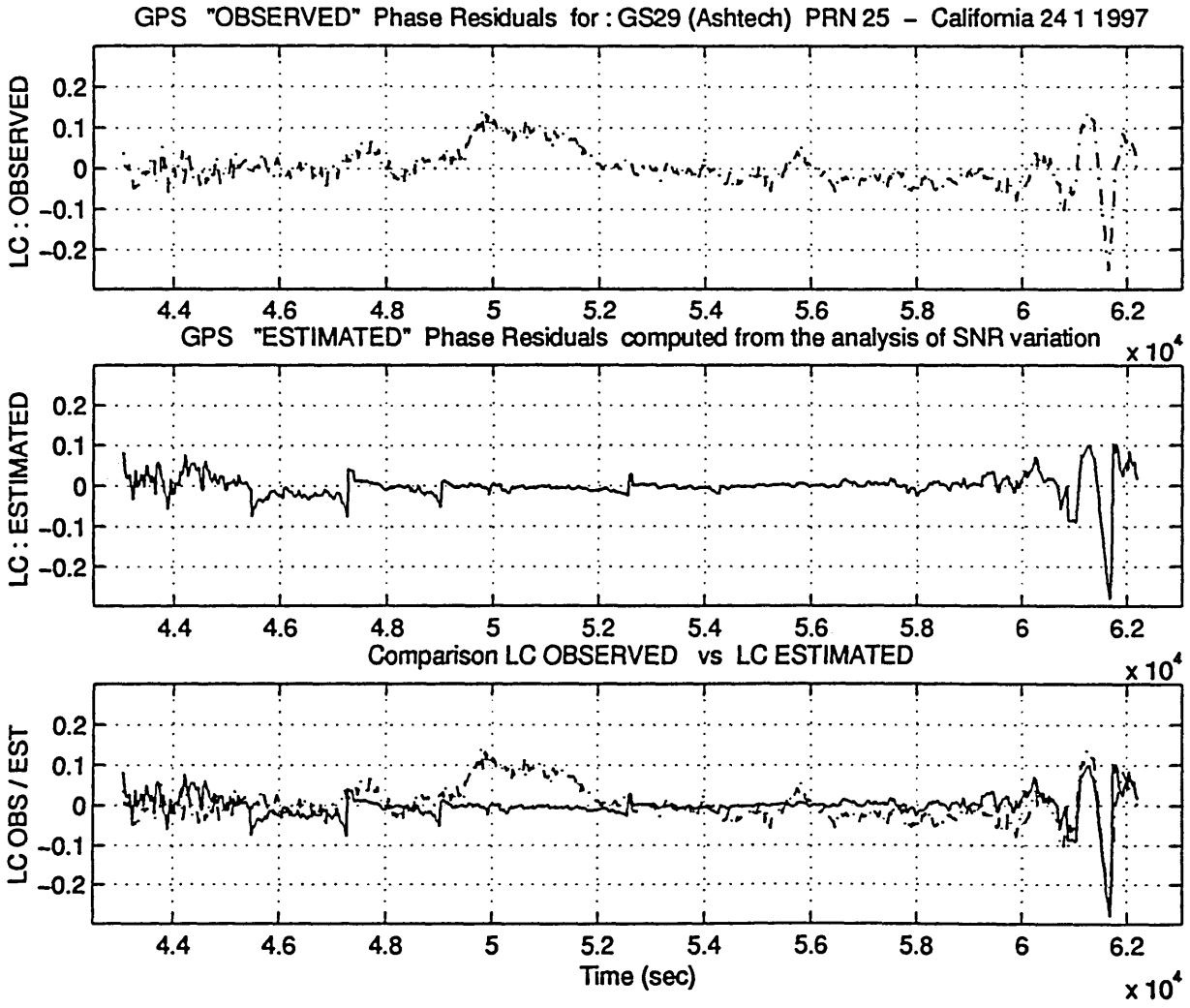

Fig. A.14.3 : Station: GS29 - Satellite: PRN 25- Data acquisition date 24 1 1997
The observed phase residual (LC_OBS) is compared with the multipath phase error estimated from the SNR (LC_EST)
Unit: [cycles]

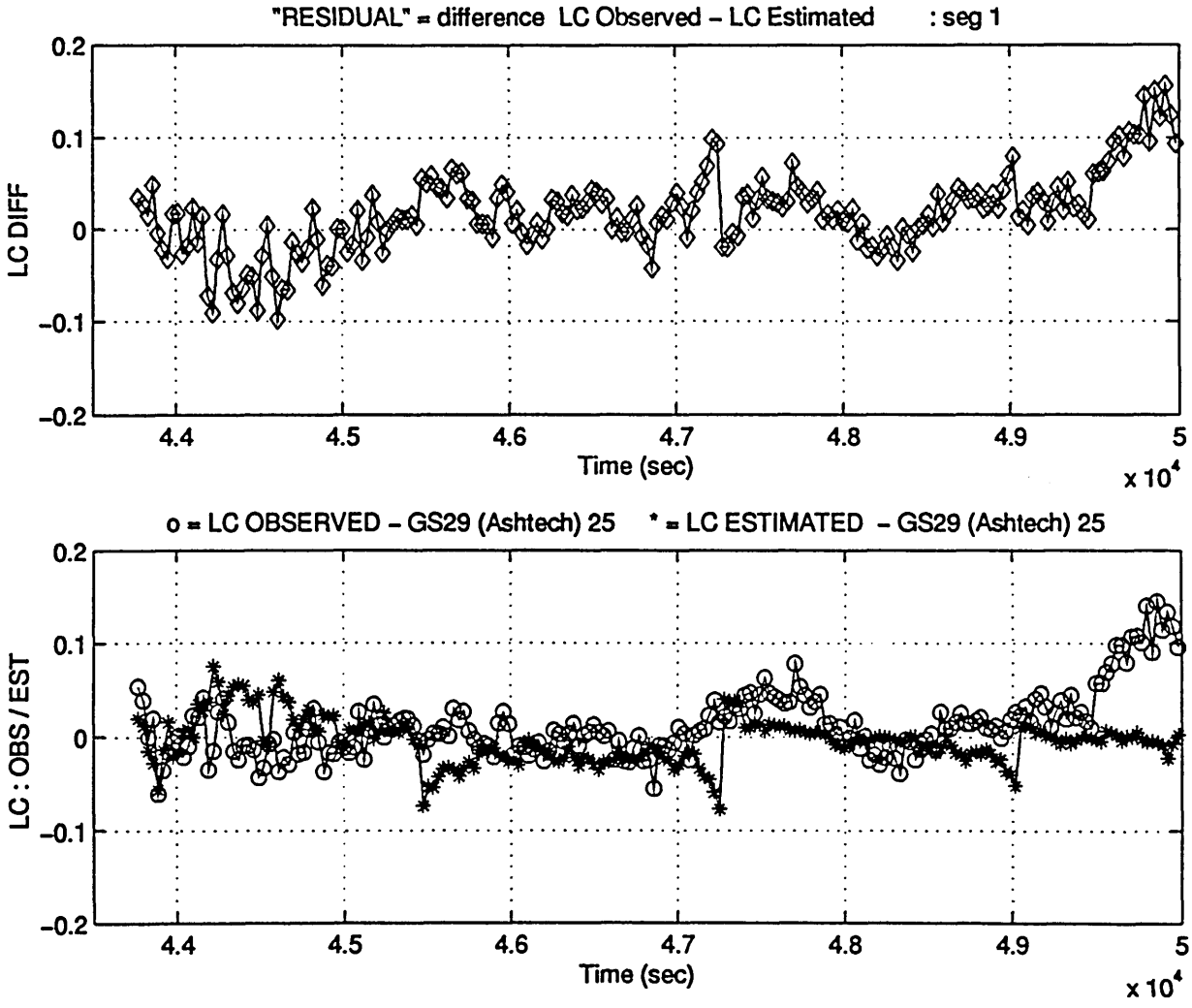

Fig. A.14.4.a) : GS29 - PRN 25 (24 1 1997) - [segment #1]
Phase residual LC_DIFF, determined as the difference between LC_OBS and LC_EST.
Unit: [cycles]

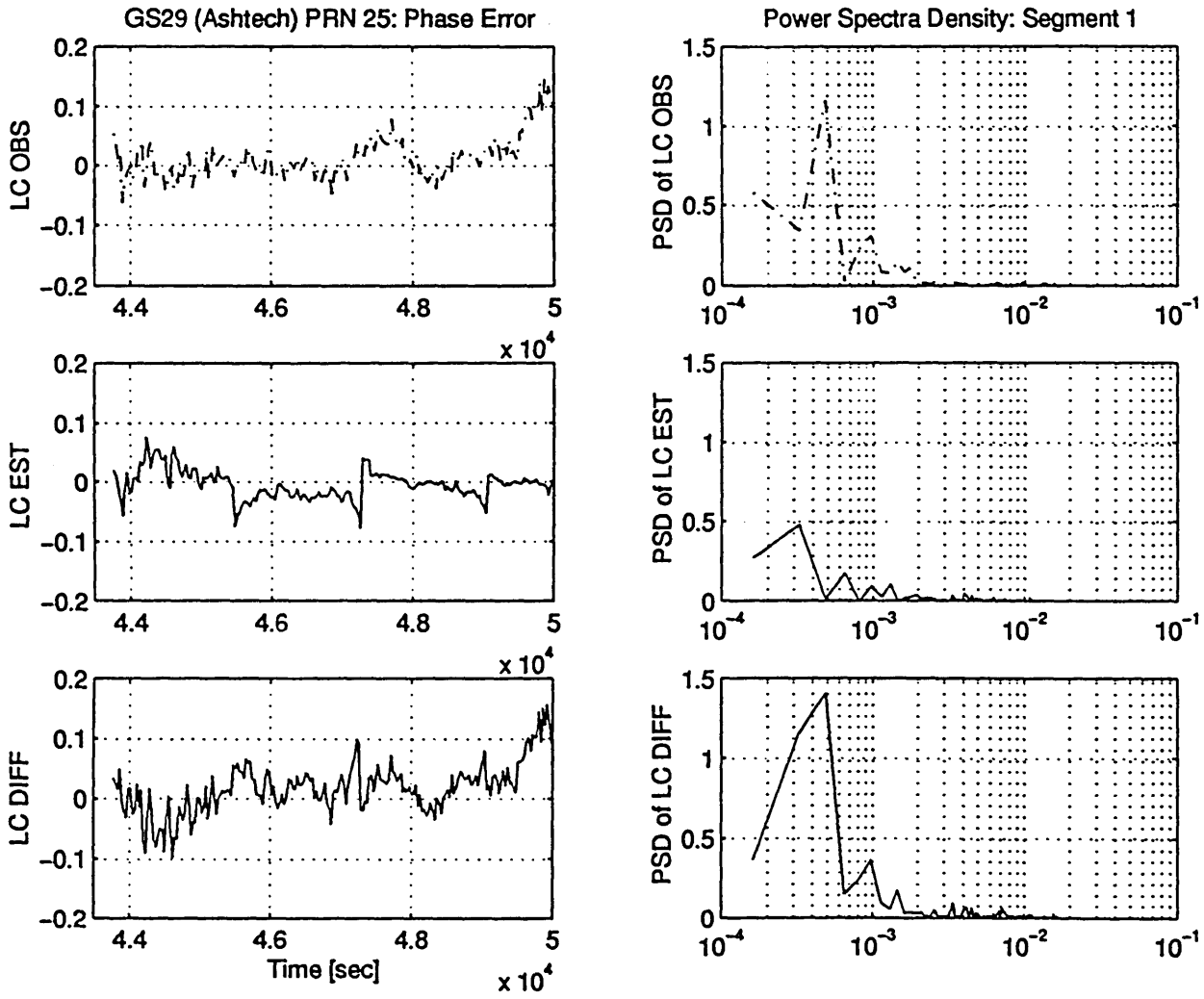

Fig. A.14.4.b) : GS29 - PRN 25 (24 1 1997) - [segment #1]
PSD of LC_OBS, LC_EST and LC_DIFF.
Unit: [cycles]^2

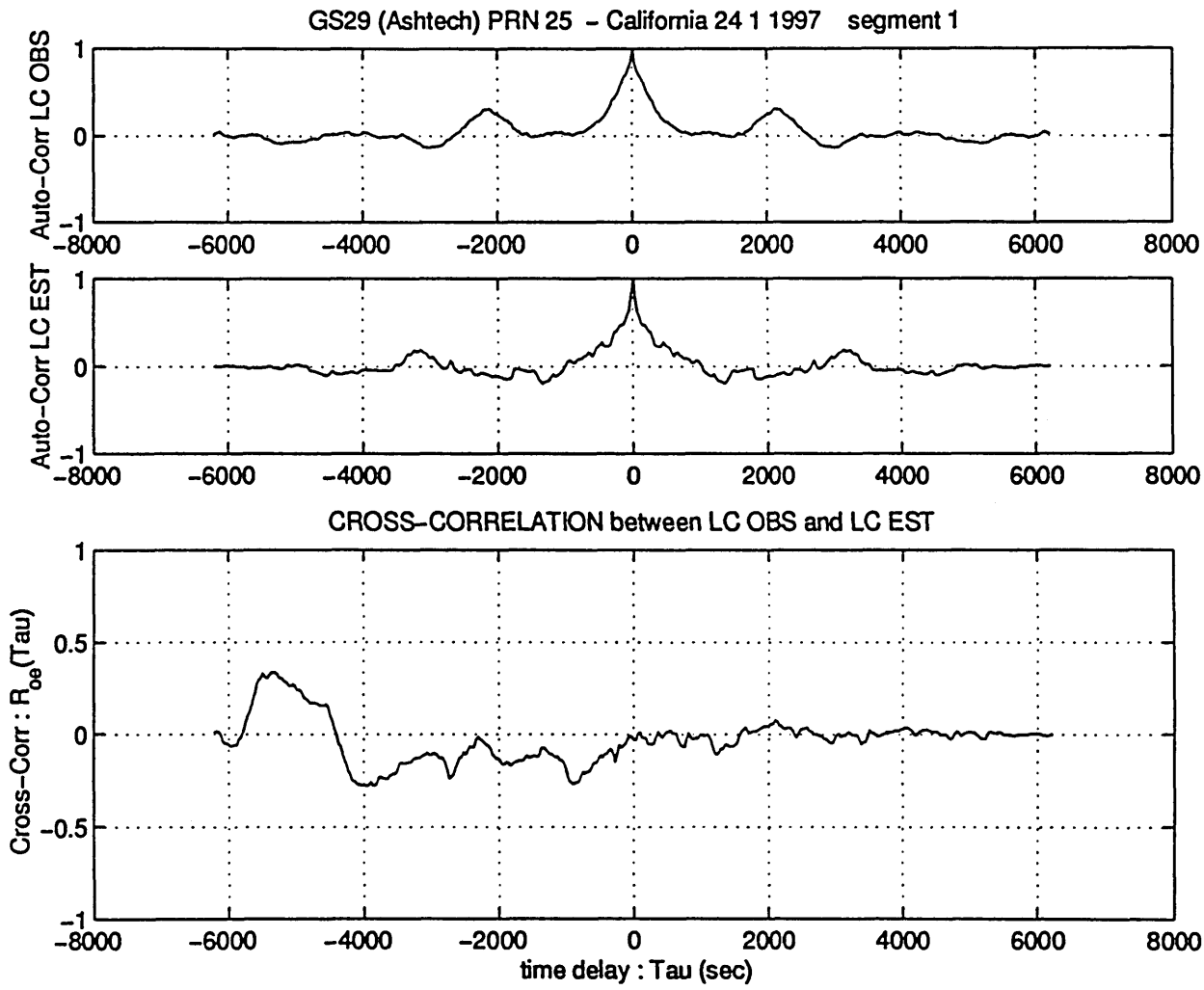

Fig. A.14.4.c) : GS29 - PRN 25 (24 1 1997) - [segment #1]
Auto Correlation of LC_OBS (R_{oo}) and LC_EST (R_{ee}).
Cross Correlation between them (R_{oe})
Unit: [cycles]^2

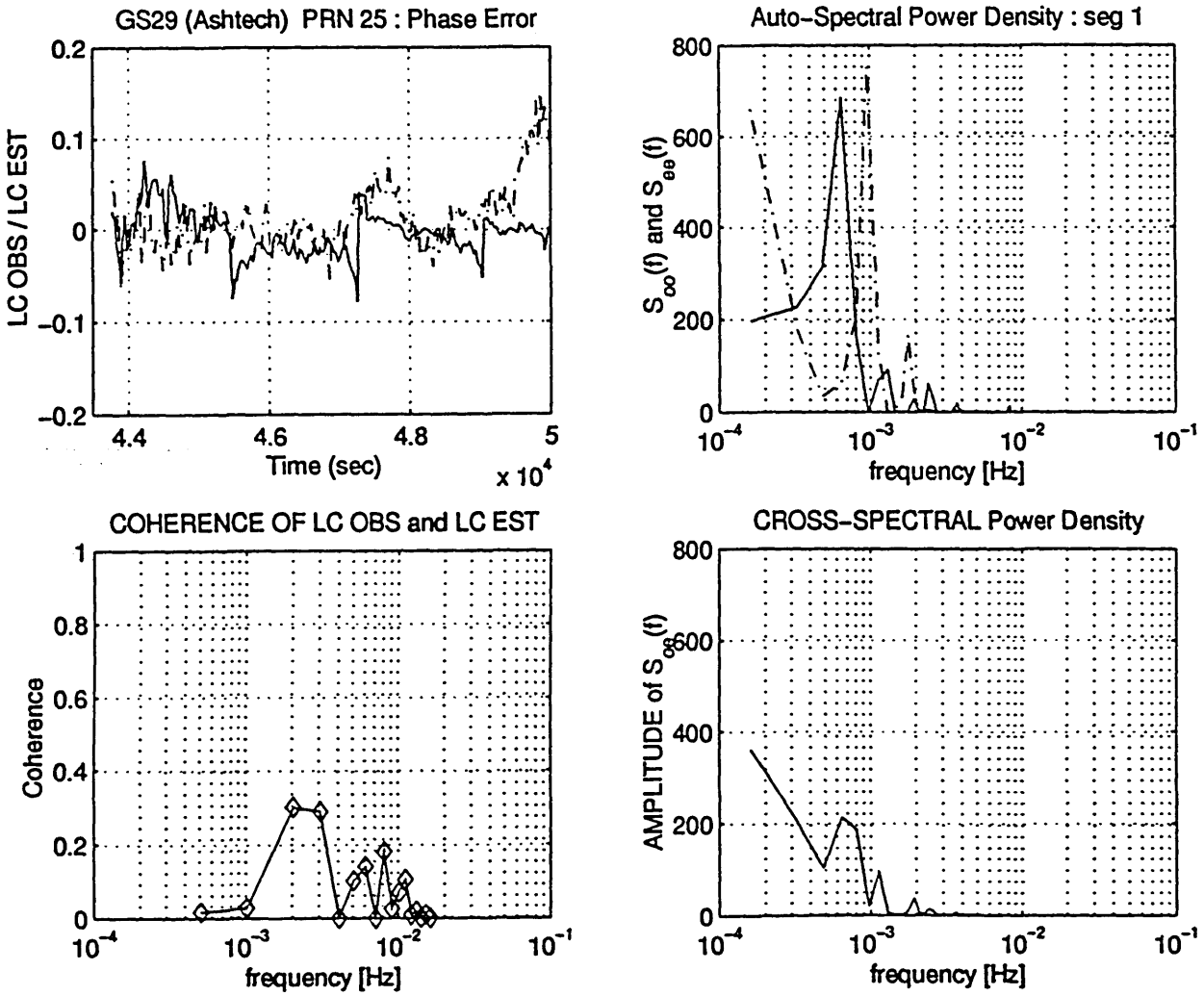

Fig. A.14.4.d) : GS29 - PRN 25 (24 1 1997) - [segment #1]
Auto Spectral Power Density of LC_OBS (S_{oo}) and of LC_EST (S_{ee}). Cross PSD between them (S_{oe})
Unit: [cycles]^2
Coherence function of LC_OBS and LC_EST

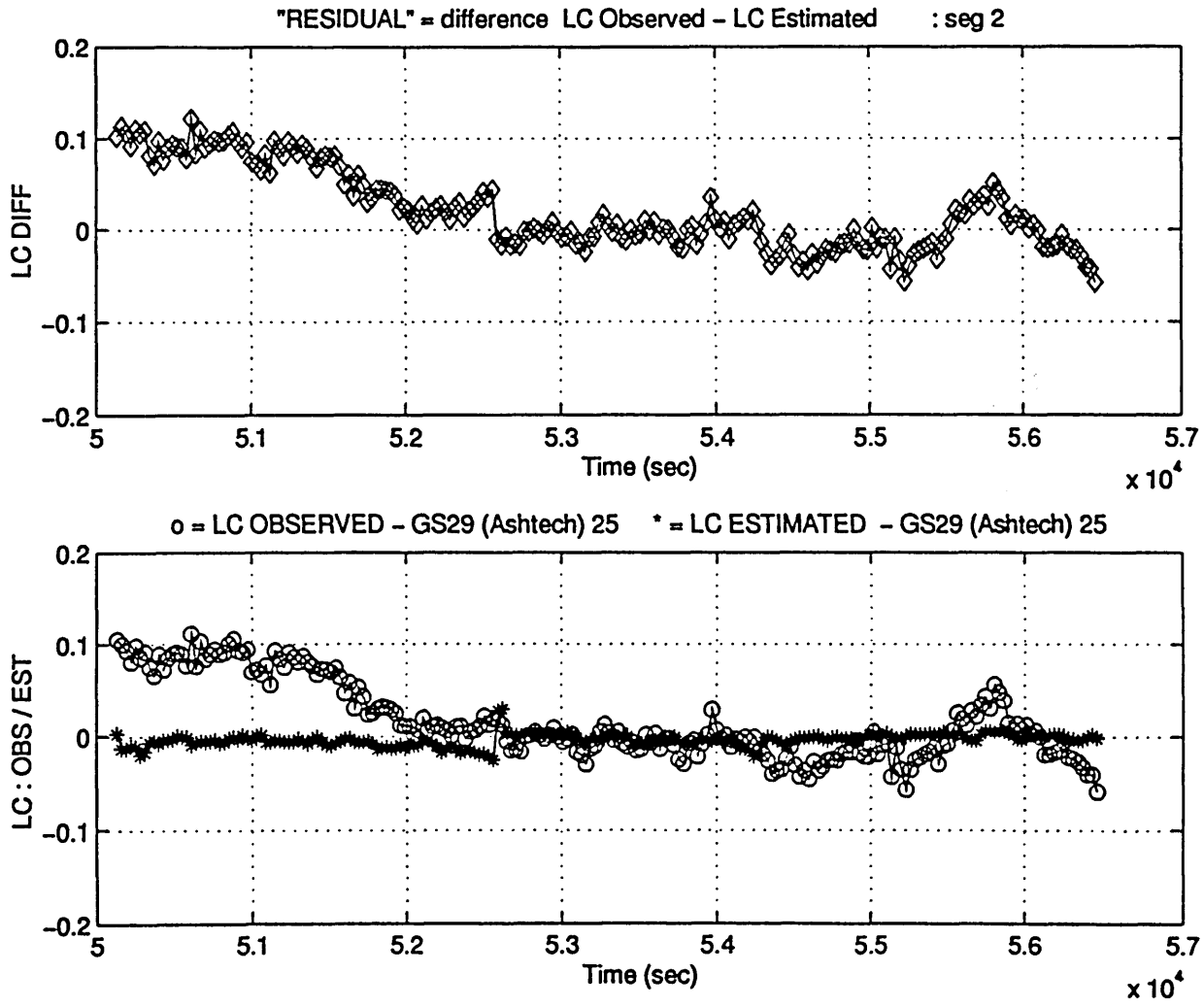

Fig. A.14.5.a) : GS29 - PRN 25 (24 1 1997) - [segment #2]
Phase residual LC_DIFF, determined as the difference between LC_OBS and LC_EST.
Unit: [cycles]

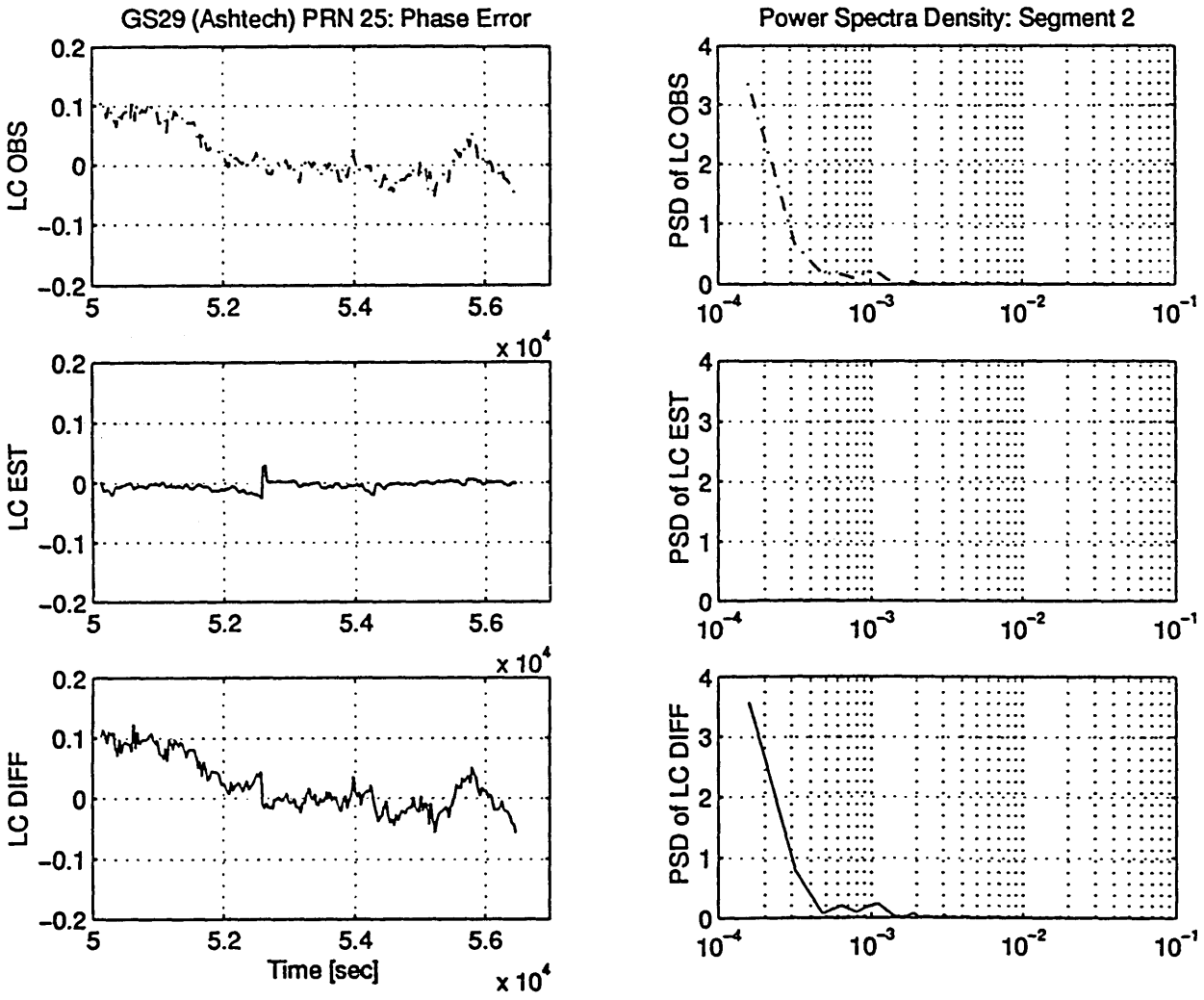

Fig. A.14.5.b) : GS29 - PRN 25 (24 1 1997) - [segment #2]
Power Spectral Density of LC_OBS, LC_EST and LC_DIFF.
Unit: [cycles]2

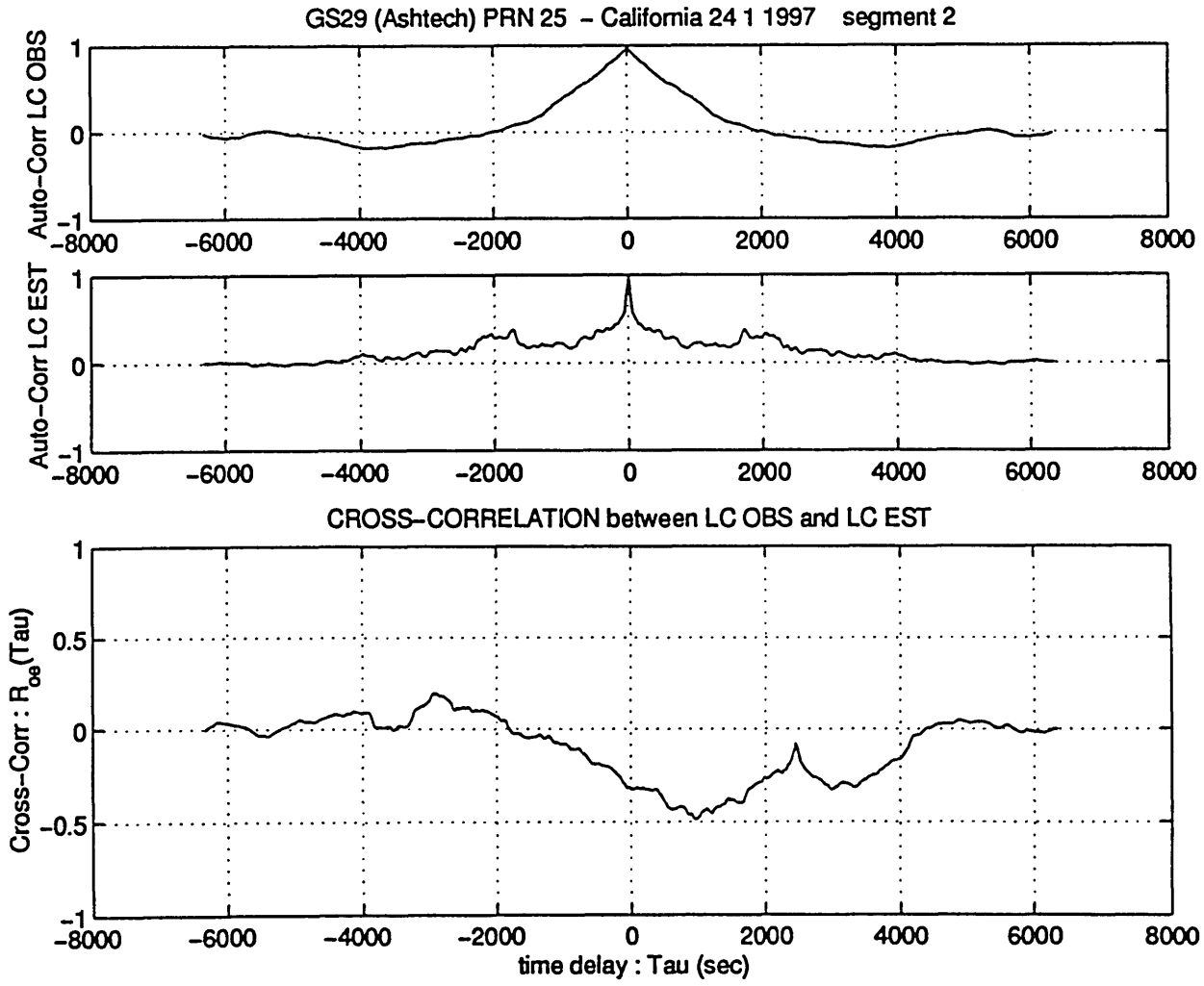

Fig. A.14.5.c) : GS29 - PRN 25 (24 1 1997) - [segment #2]
Auto Correlation of LC_OBS (R_{oo}) and LC_EST (R_{ee}).
Cross Correlation between them (R_{oe})
Unit: [cycles]^2

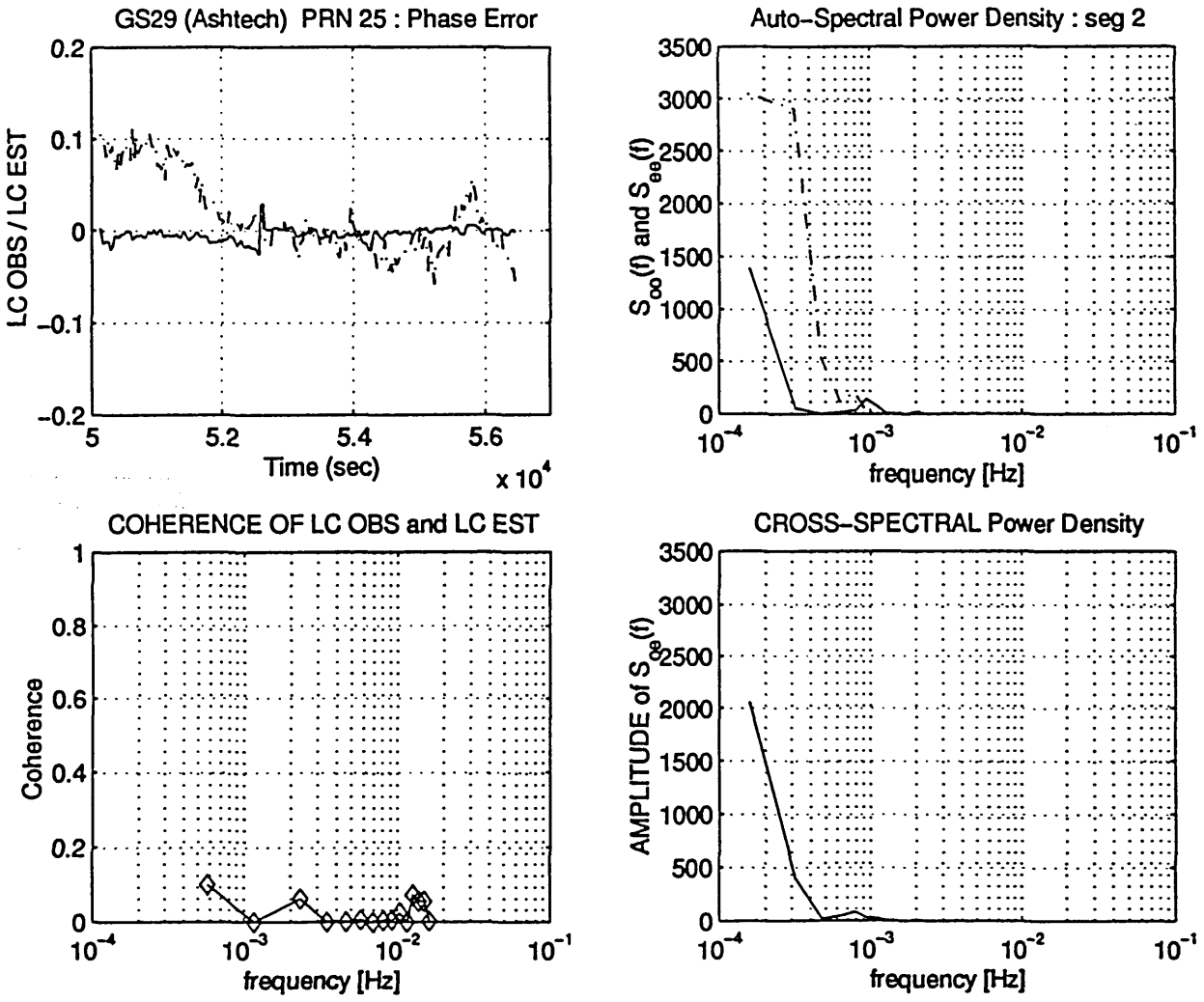

Fig. A.14.5.d) : GS29 - PRN 25 (24 1 1997) - [segment #2]
Auto Spectral Power Density of LC_OBS (S_{oo}) and of LC_EST (S_{ee}). Cross PSD between them (S_{oe})
Unit: [cycles]^2
Coherence function of LC_OBS and LC_EST

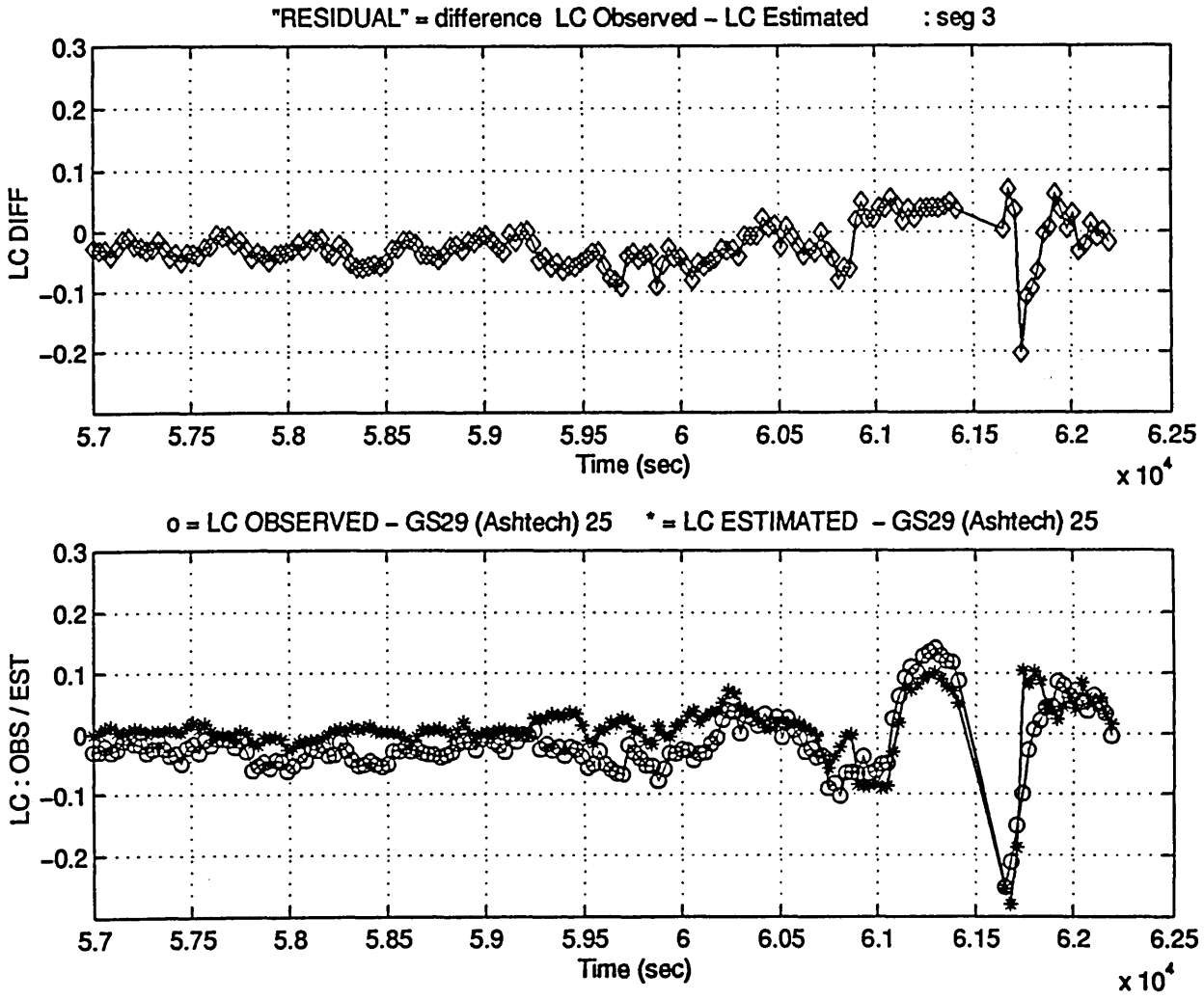

Fig. A.14.6.a) : GS29 - PRN 25 (24 1 1997) - [segment #3]
Phase residual LC_DIFF, determined as the difference between LC_OBS and LC_EST.
Unit: [cycles]

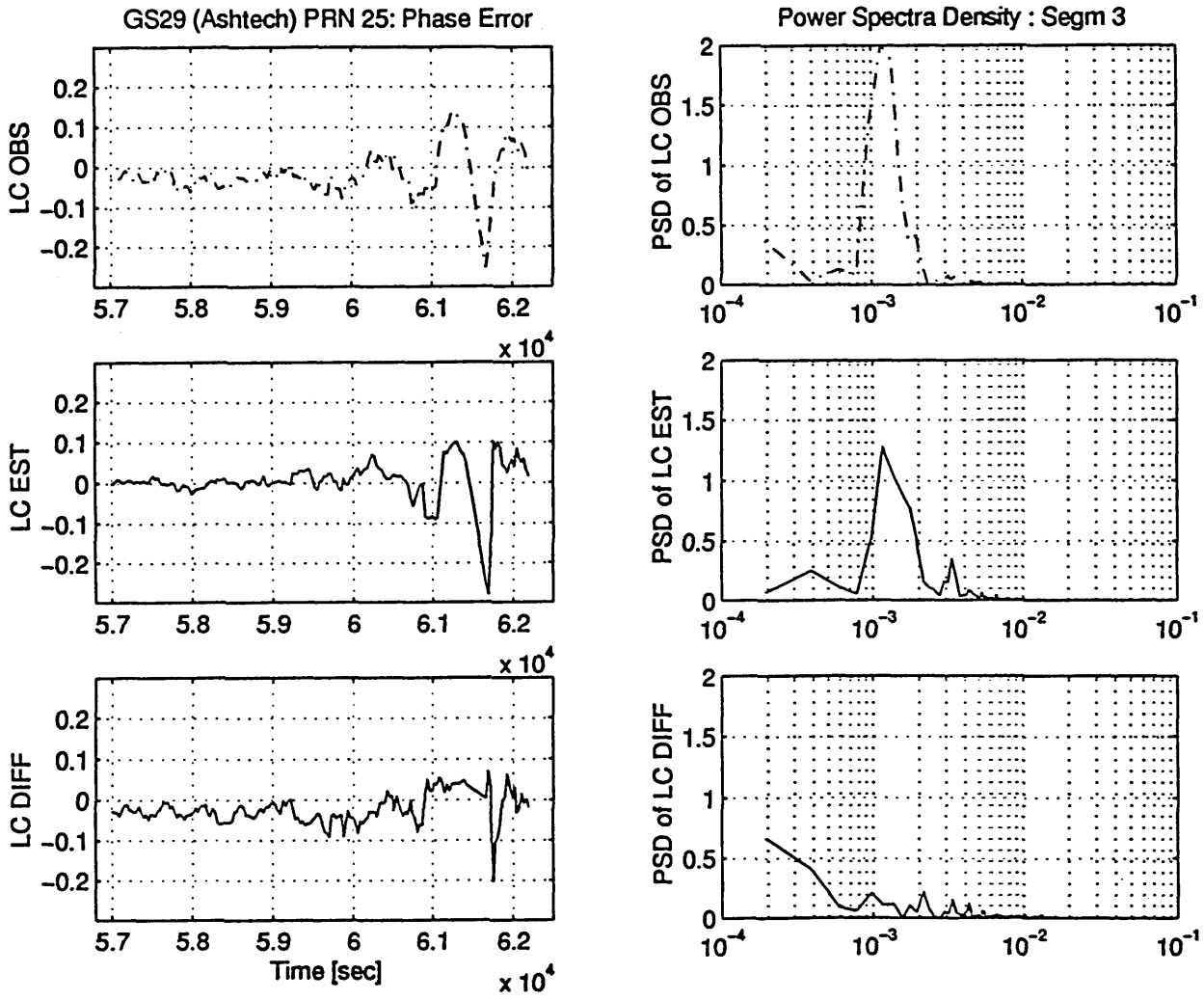

Fig. A.14.6.b) : GS29 - PRN 25 (24 1 1997) - [segment #3]
Power Spectral Density of LC_OBS, LC_EST and LC_DIFF.
Unit: [cycles]^2

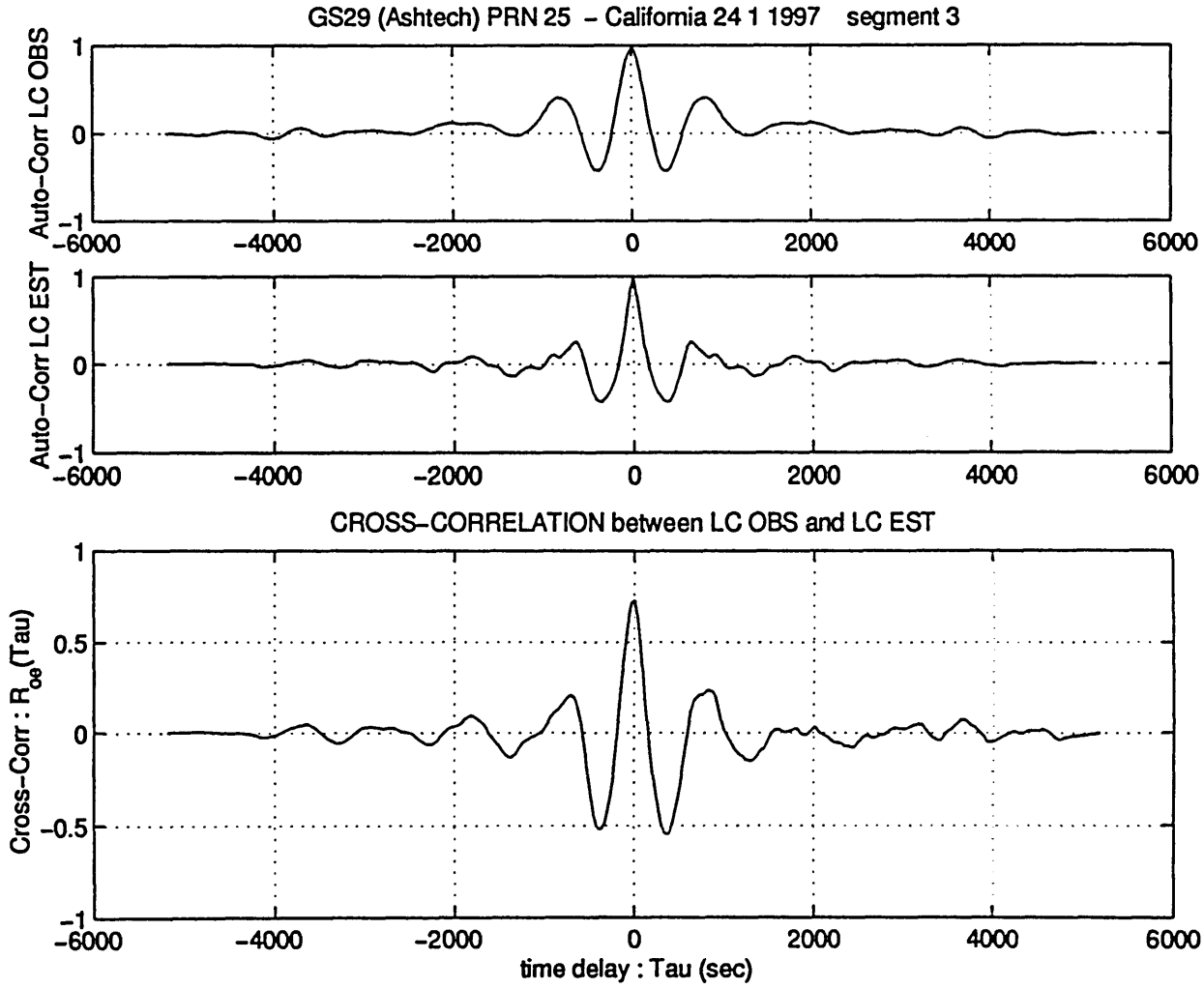

Fig. A.14.6.c) : GS29 - PRN 25 (24 1 1997) - [segment #3]
Auto Correlation of LC_OBS (R_{oo}) and LC_EST (R_{ee}).
Cross Correlation between them (R_{oe})
Unit: [cycles]^2

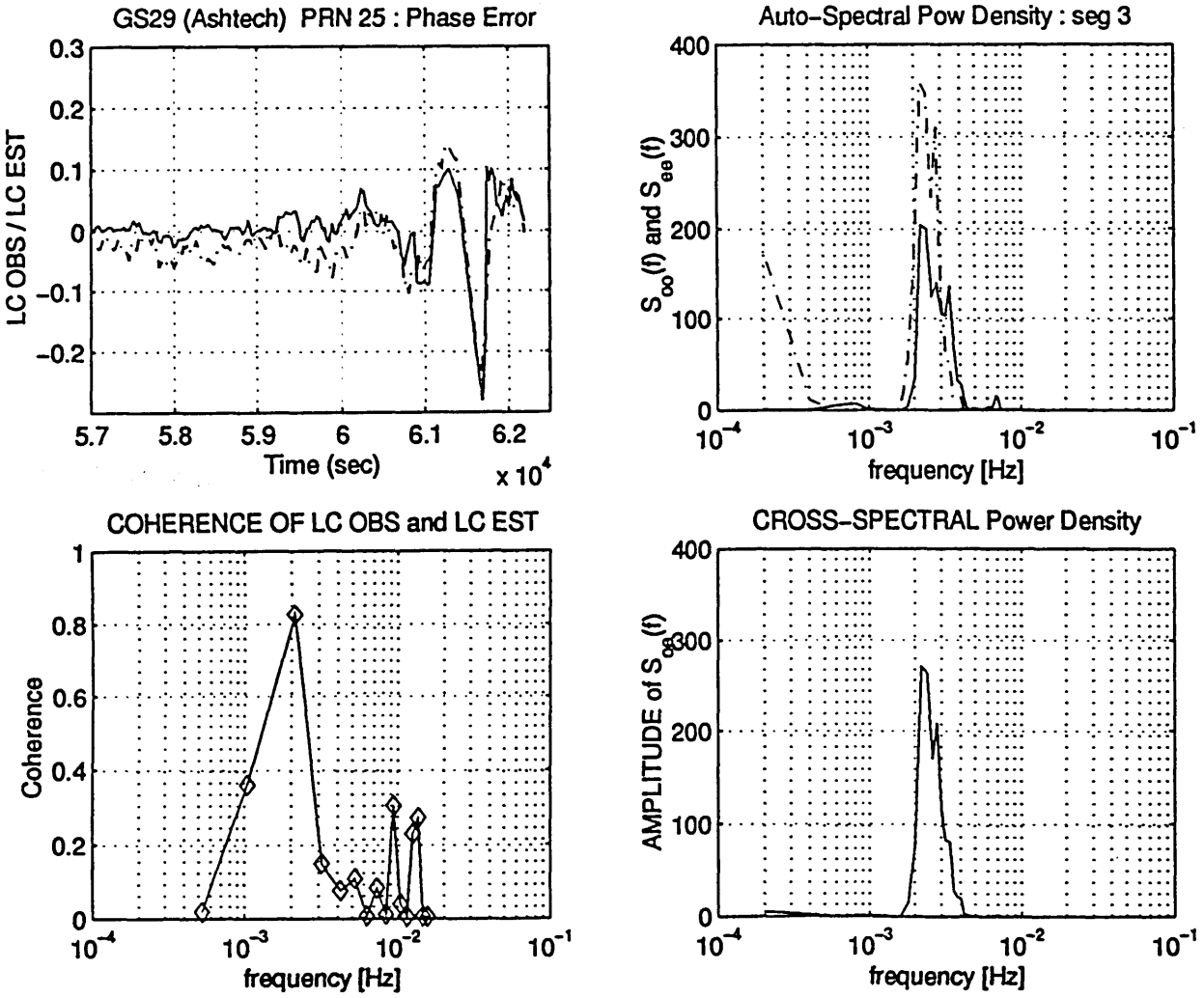

Fig. A.14.6.d) : GS29 - PRN 25 (24 1 1997) - [segment #3]
Auto Spectral Power Density of LC_OBS (S_{oo}) and of LC_EST (S_{ee}). Cross PSD between them (S_{oe})
Unit: [cycles]^2
Coherence function of LC_OBS and LC_EST

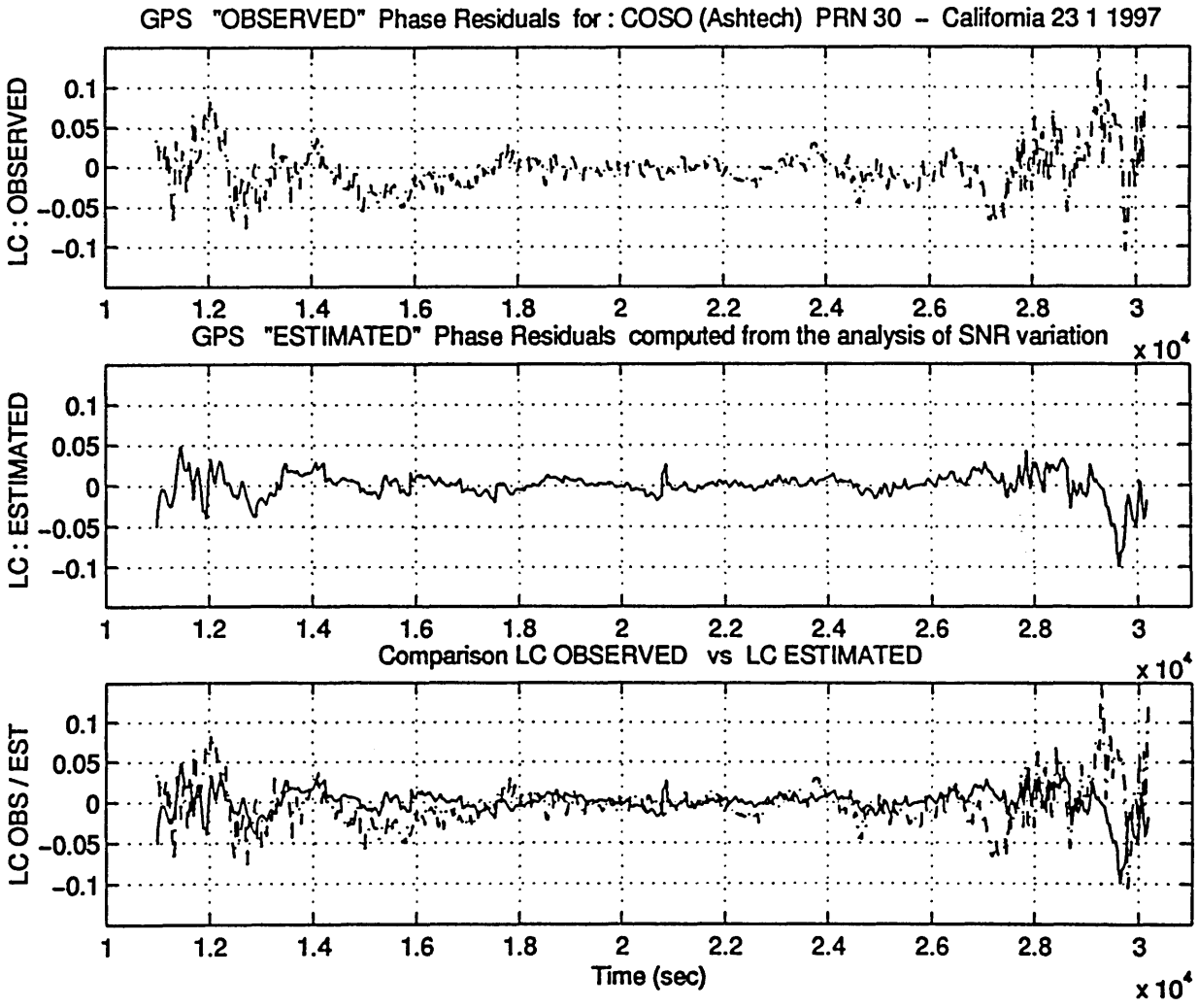

Fig. A.15.1 : Station: COSO - Satellite: PRN 30
Data acquisition date 23 1 1997
The observed phase residual (LC_OBS) is compared with the multipath phase error estimated from the SNR (LC_EST)
Unit: [cycles]

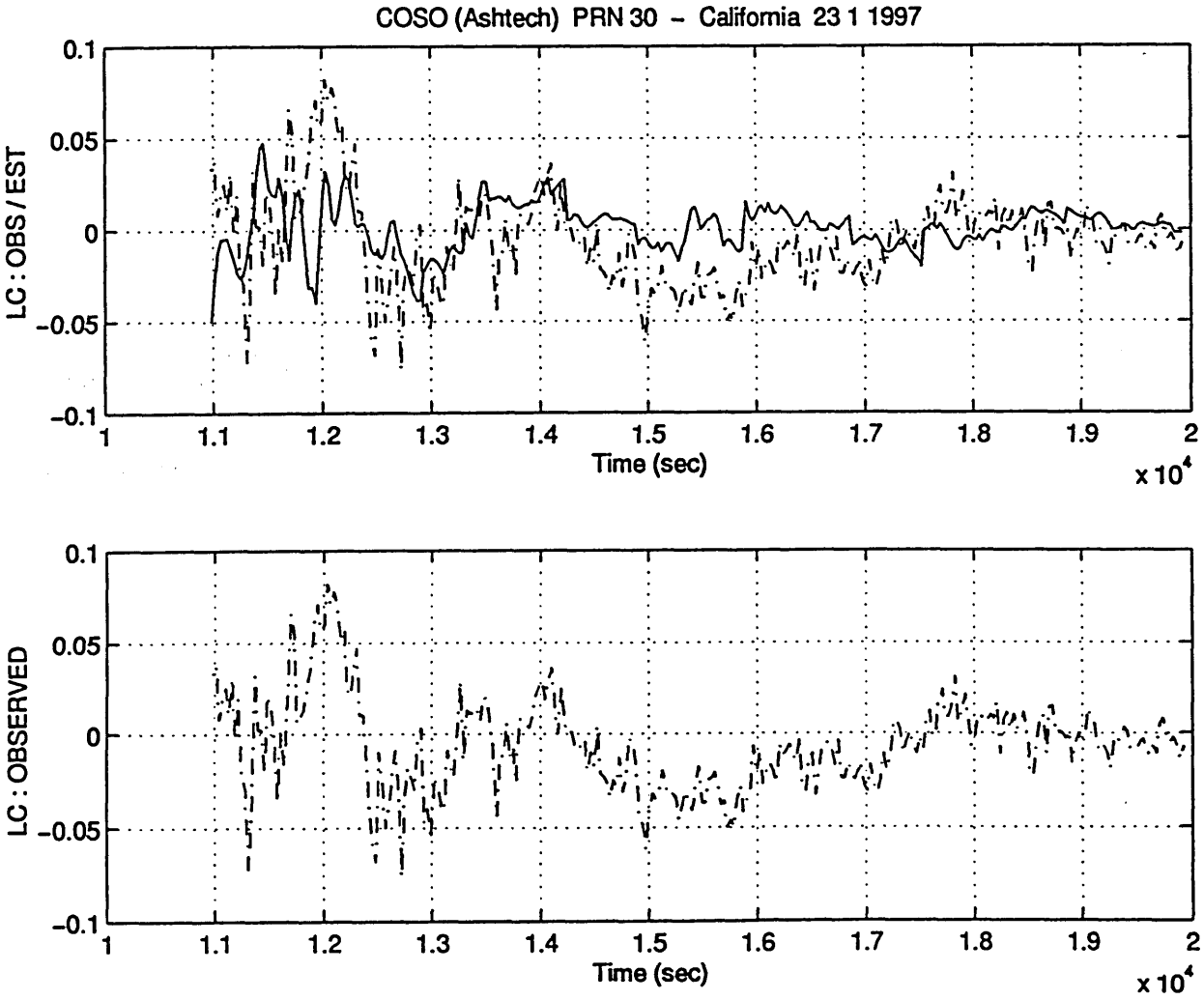

Fig. A.15.2 : Station: COSO - Satellite: PRN 30
Data acquisition date 23 1 1997
LC_OBS and LC_EST compared for t=1.0 - 2.0 10^4 sec
Unit: [cycles]

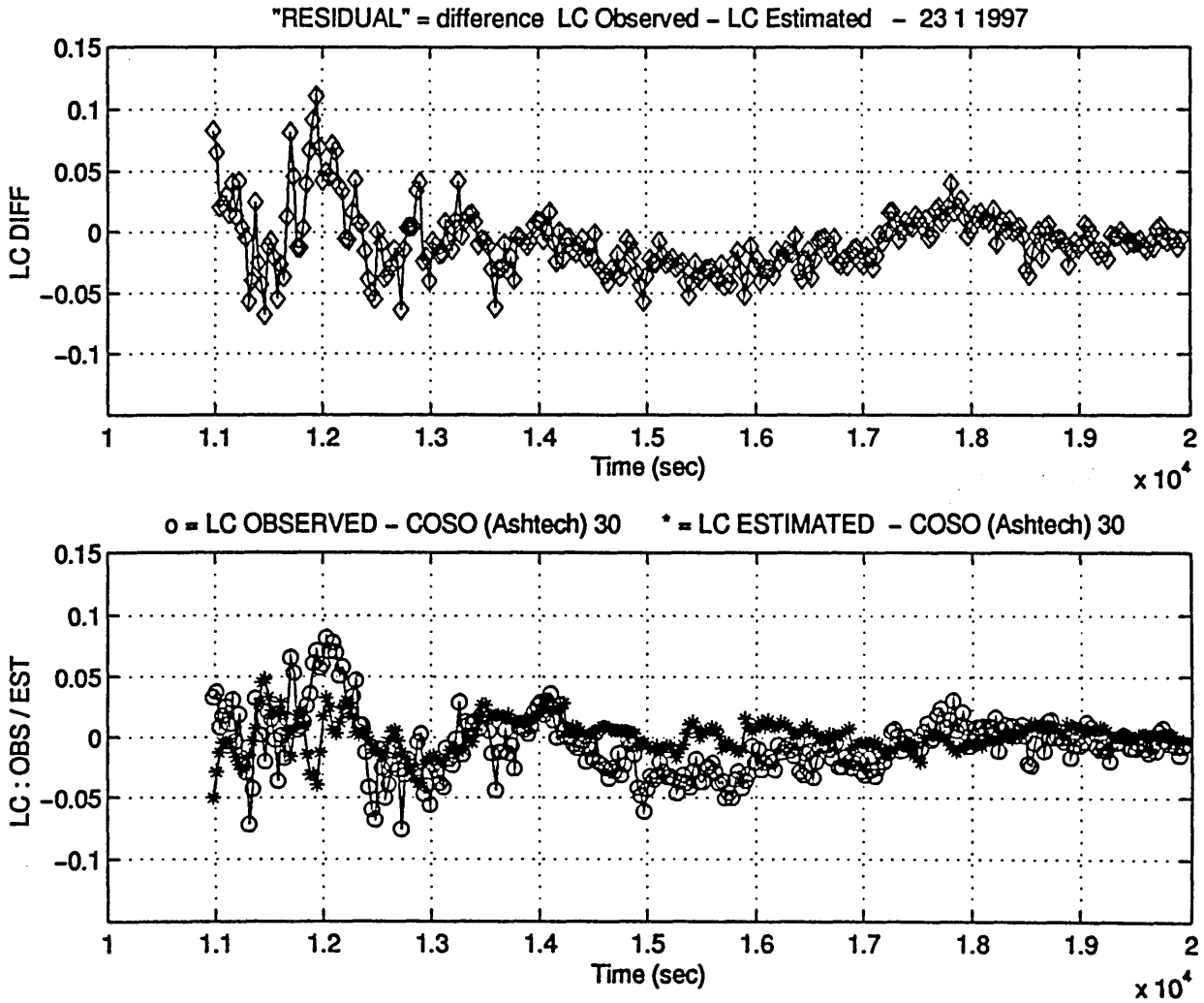

Fig. A.15.3.a) : COSO - PRN 30 (23 1 1997) - [segment 1]
Phase residual LC_DIFF, determined as the difference between LC_OBS and LC_EST.
Unit: [cycles]

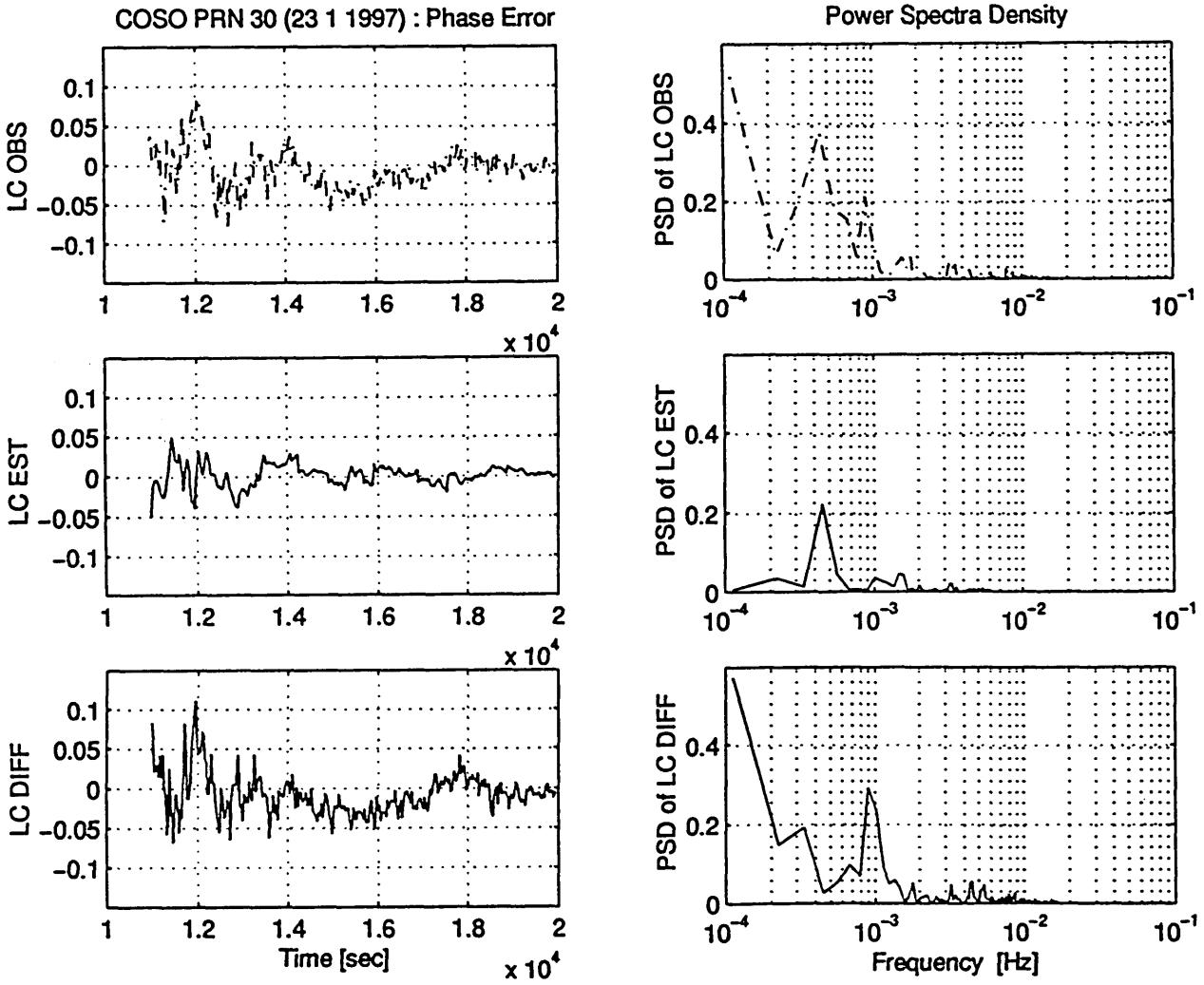

Fig. A.15.3.b) : COSO - PRN 01 (23 1 1997) - [segment 1]
PSD of LC_OBS, LC_EST and LC_DIFF.
Unit: [cycles]^2

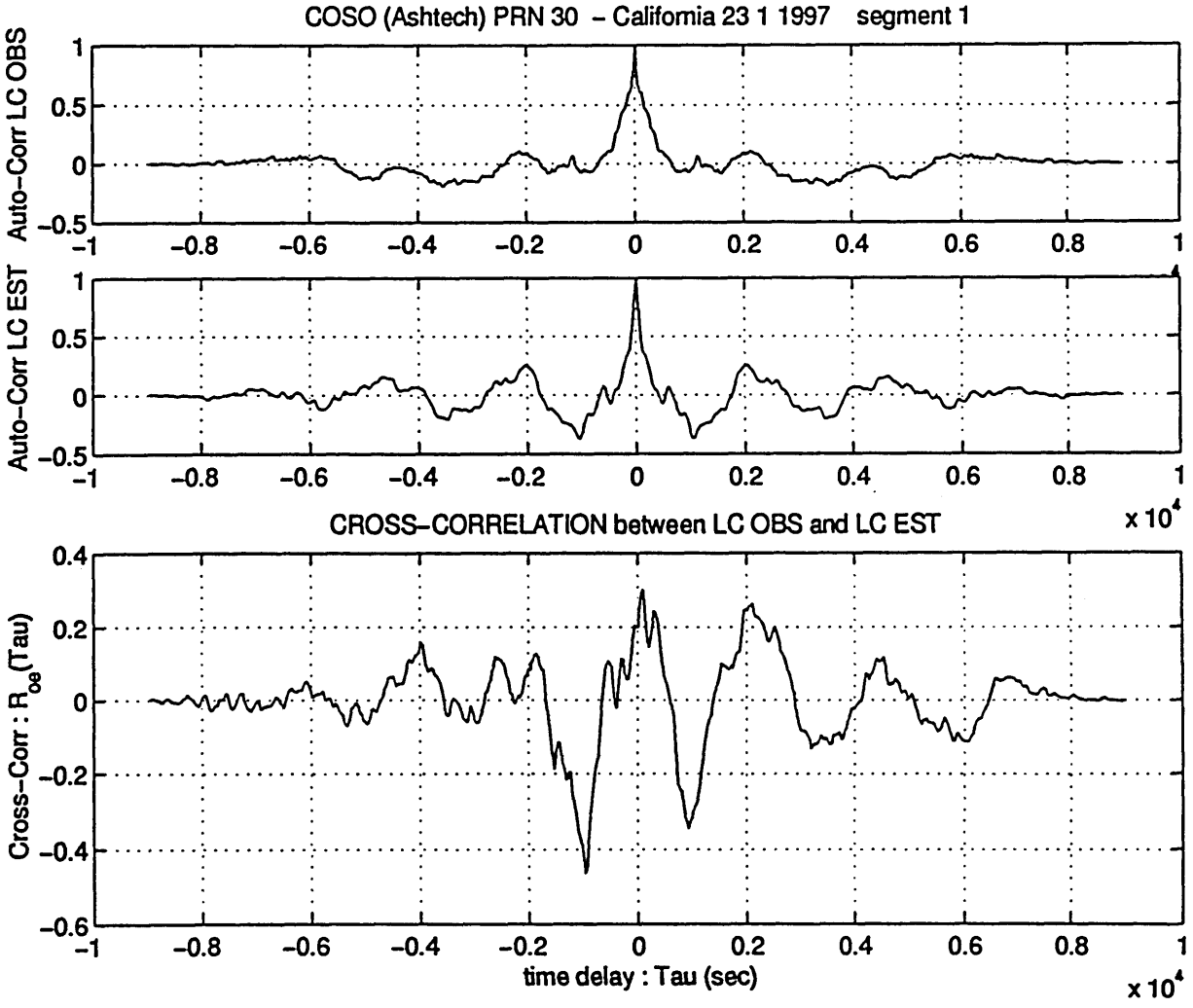

Fig. A.15.3.c) : COSO - PRN 30 (23 1 1997) - [segment 1]
Auto Correlation of LC_OBS (R_{oo}) and LC_EST (R_{ee}).
Cross Correlation between them (R_{oe})
Unit: [cycles]^2

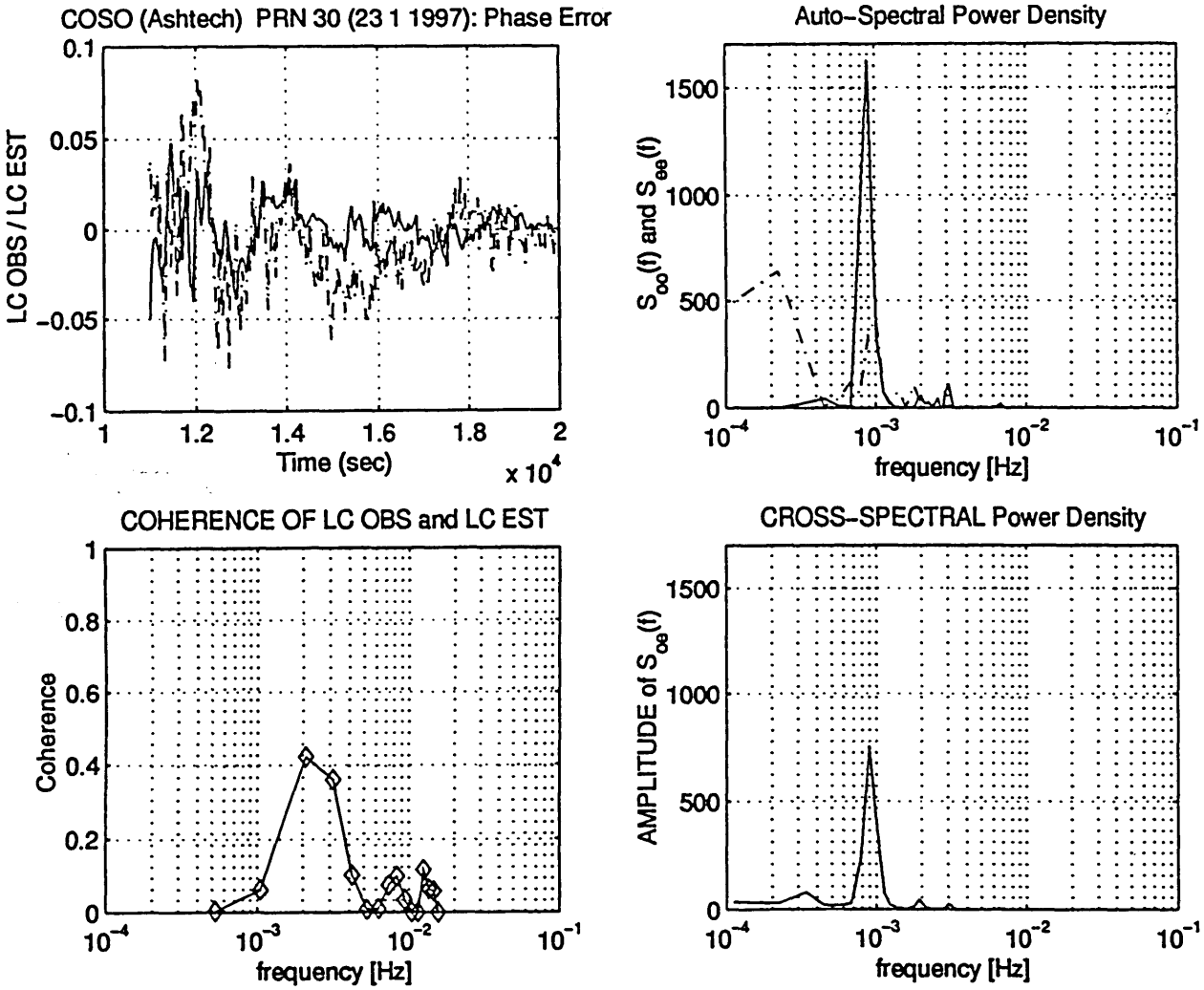

Fig. A.15.3.d) : COSO - PRN 30 (23 1 1997) - [segment 1]
Auto Spectral Power Density of LC_OBS (S_{oo}) and of LC_EST (S_{ee}). Cross PSD between them (S_{oe})
Unit: [cycles]^2
Coherence function of LC_OBS and LC_EST

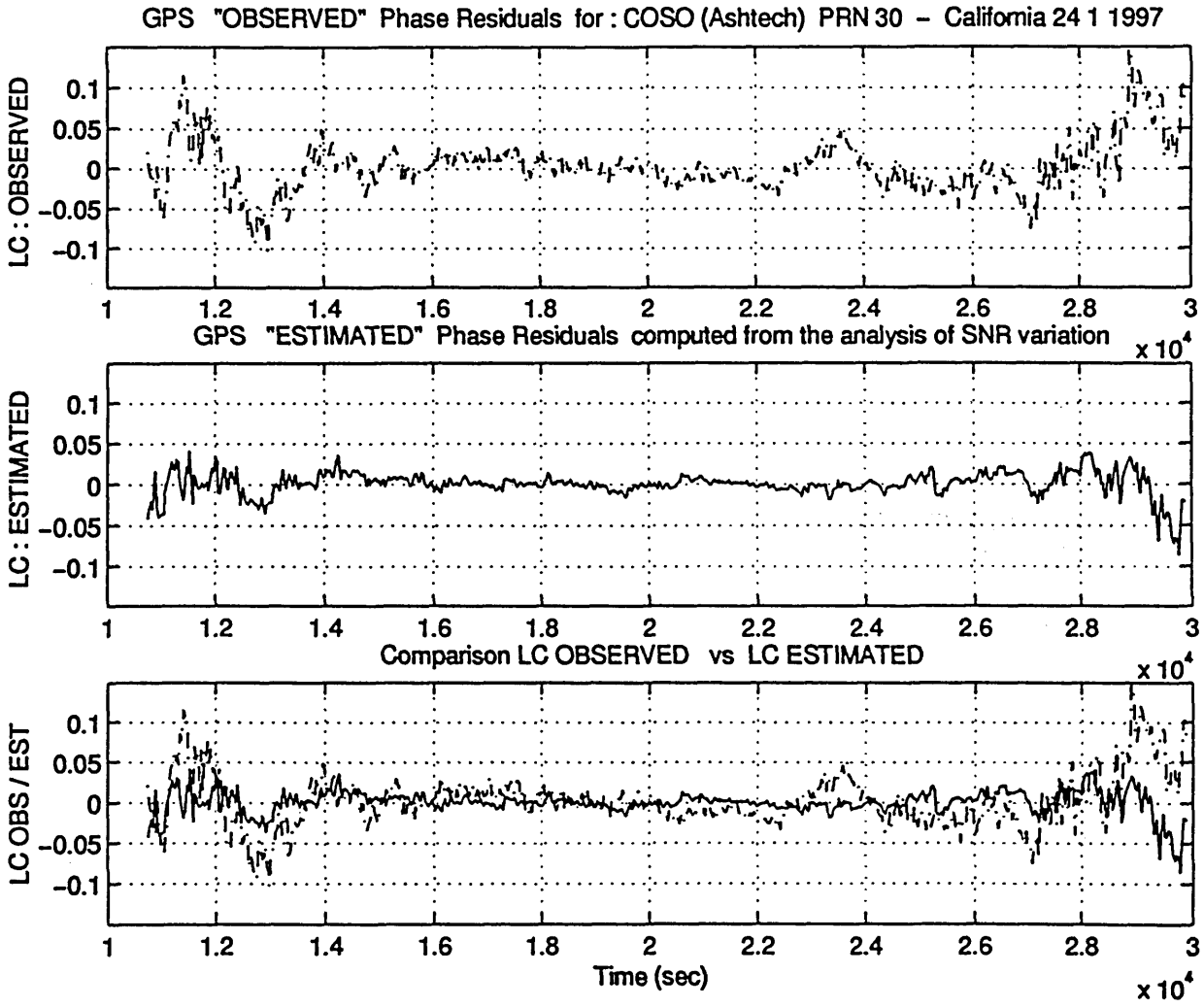

Fig. A.16.1 : Station: COSO - Satellite: PRN 30
Data acquisition date 24 1 1997
The observed phase residual (LC_OBS) is compared with the multipath phase error estimated from the SNR (LC_EST)
Unit: [cycles]

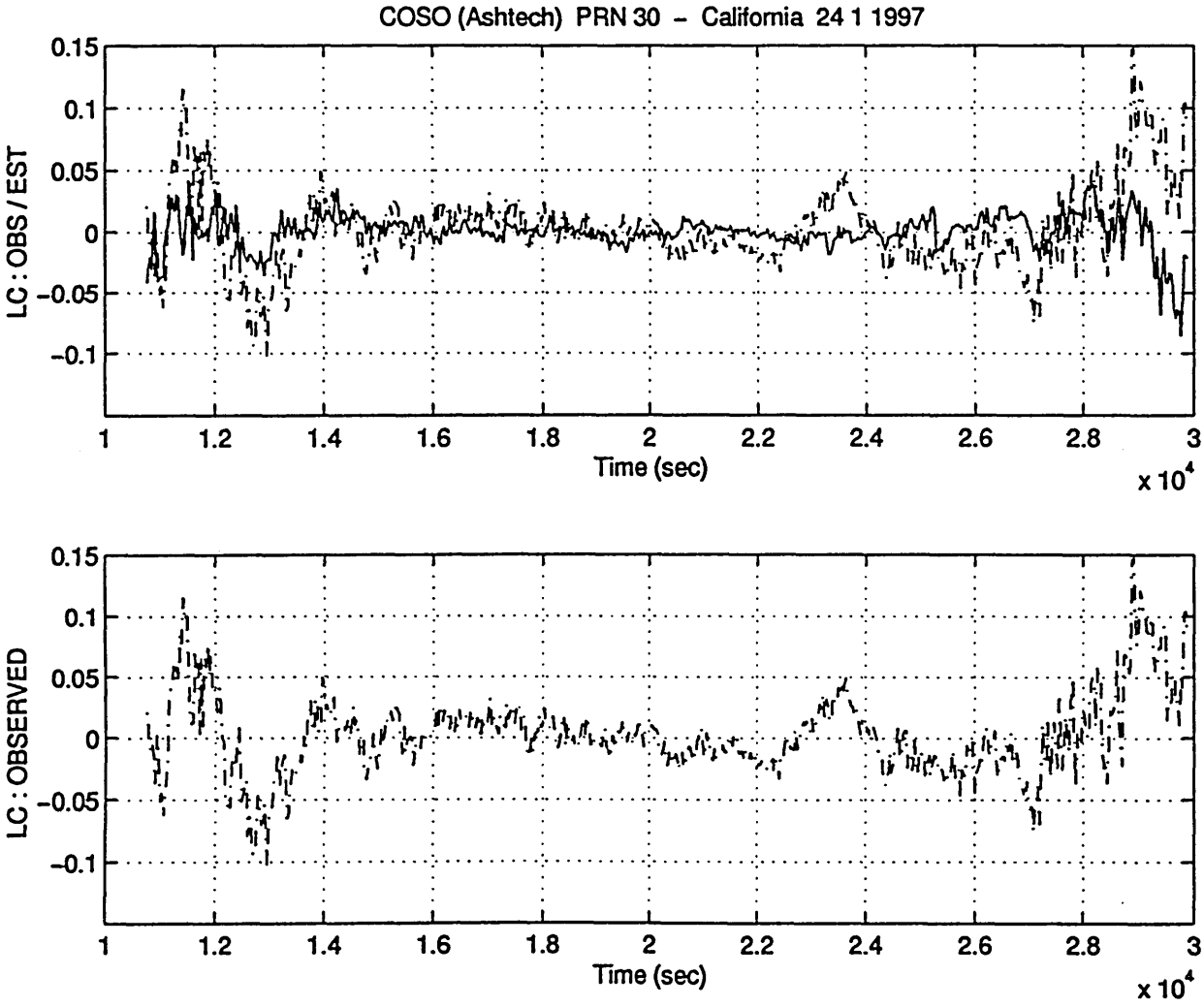

Fig. A.16.2 : Station: COSO - Satellite: PRN 30
Data acquisition date 24 1 1997
LC_OBS and LC_EST compared for t=1.0 - 2.0 10^4 sec
Unit: [cycles]

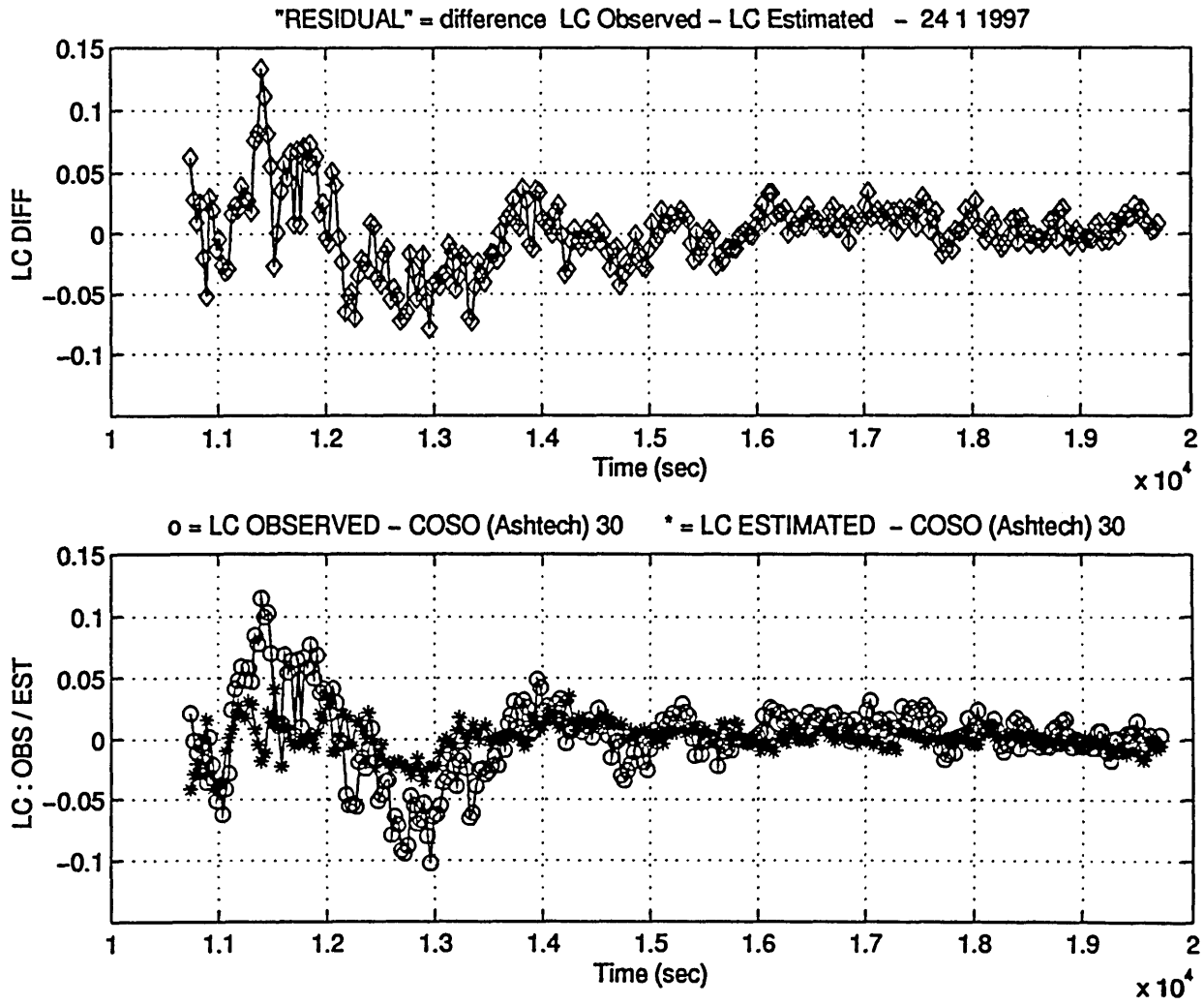

Fig. A.16.3.a) : COSO - PRN 30 (24 1 1997) - [segment 1]
Phase residual LC_DIFF, determined as the difference between LC_OBS and LC_EST.
Unit: [cycles]

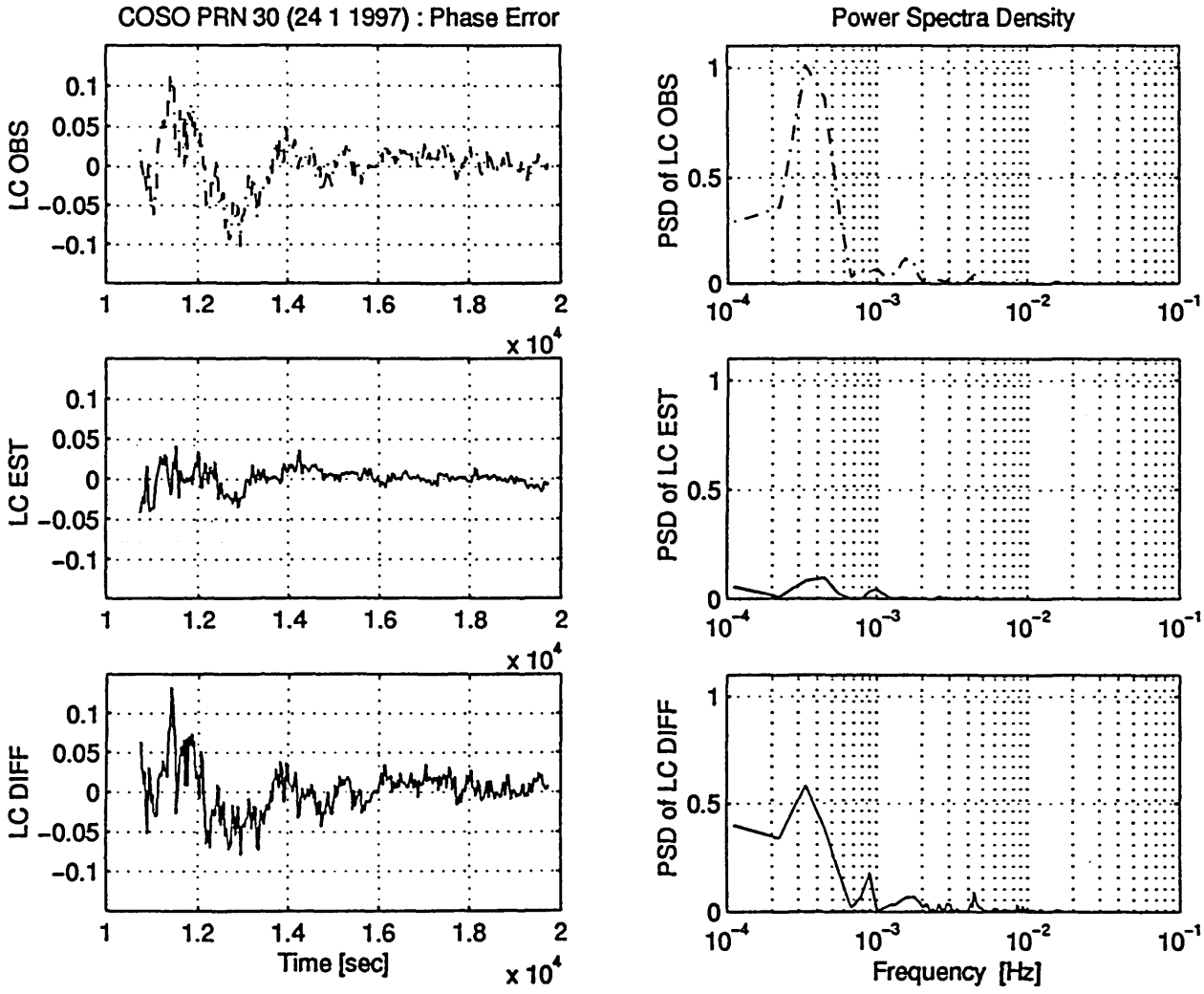

Fig. A.16.3.b) : COSO - PRN 01 (24 1 1997) - [segment 1]
PSD of LC_OBS, LC_EST and LC_DIFF.
Unit: [cycles]^2

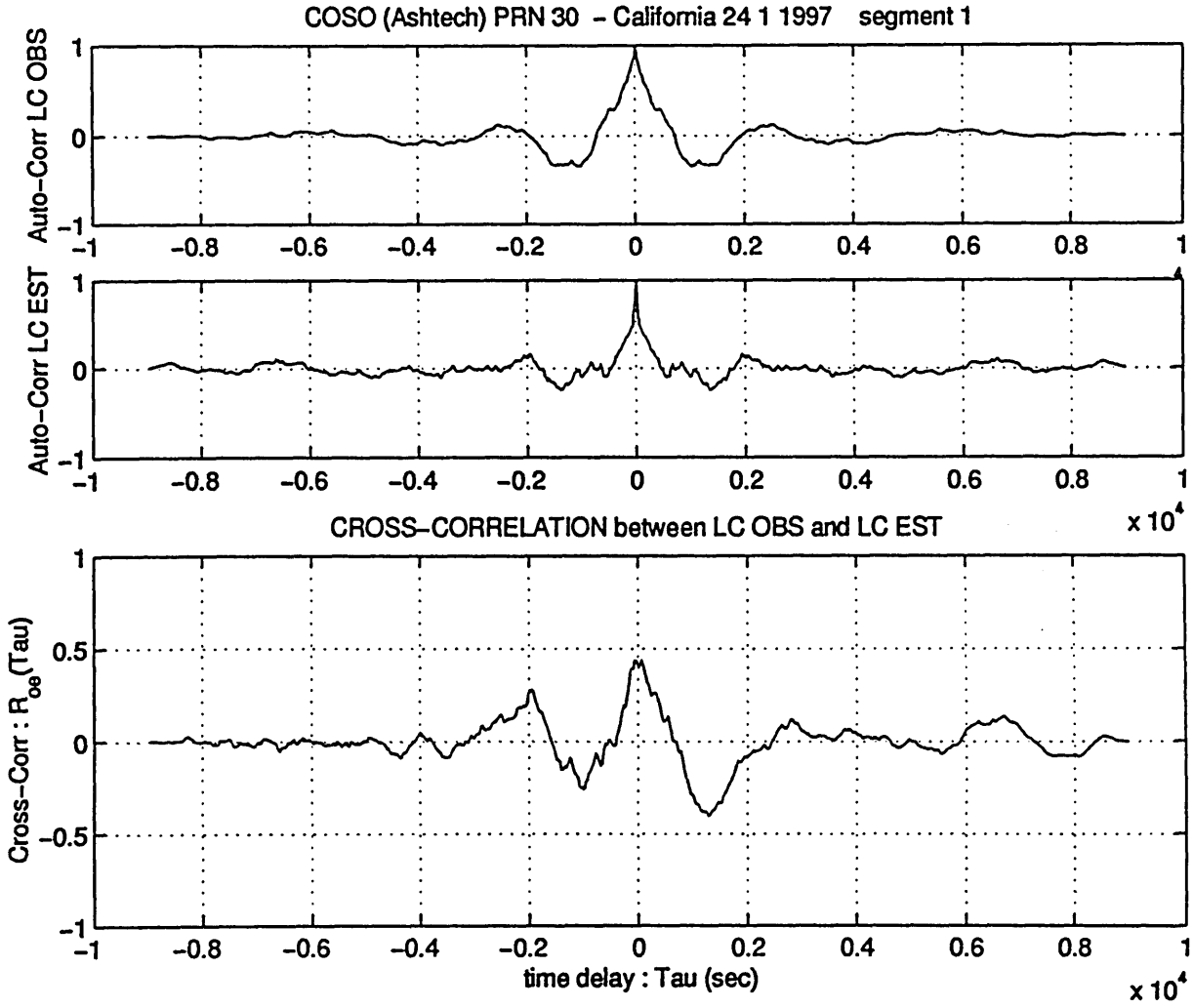

Fig. A.16.3.c) : COSO - PRN 30 (24 1 1997) - [segment 1]
Auto Correlation of LC_OBS (R_{oo}) and LC_EST (R_{ee}).
Cross Correlation between them (R_{oe})
Unit: [cycles]^2

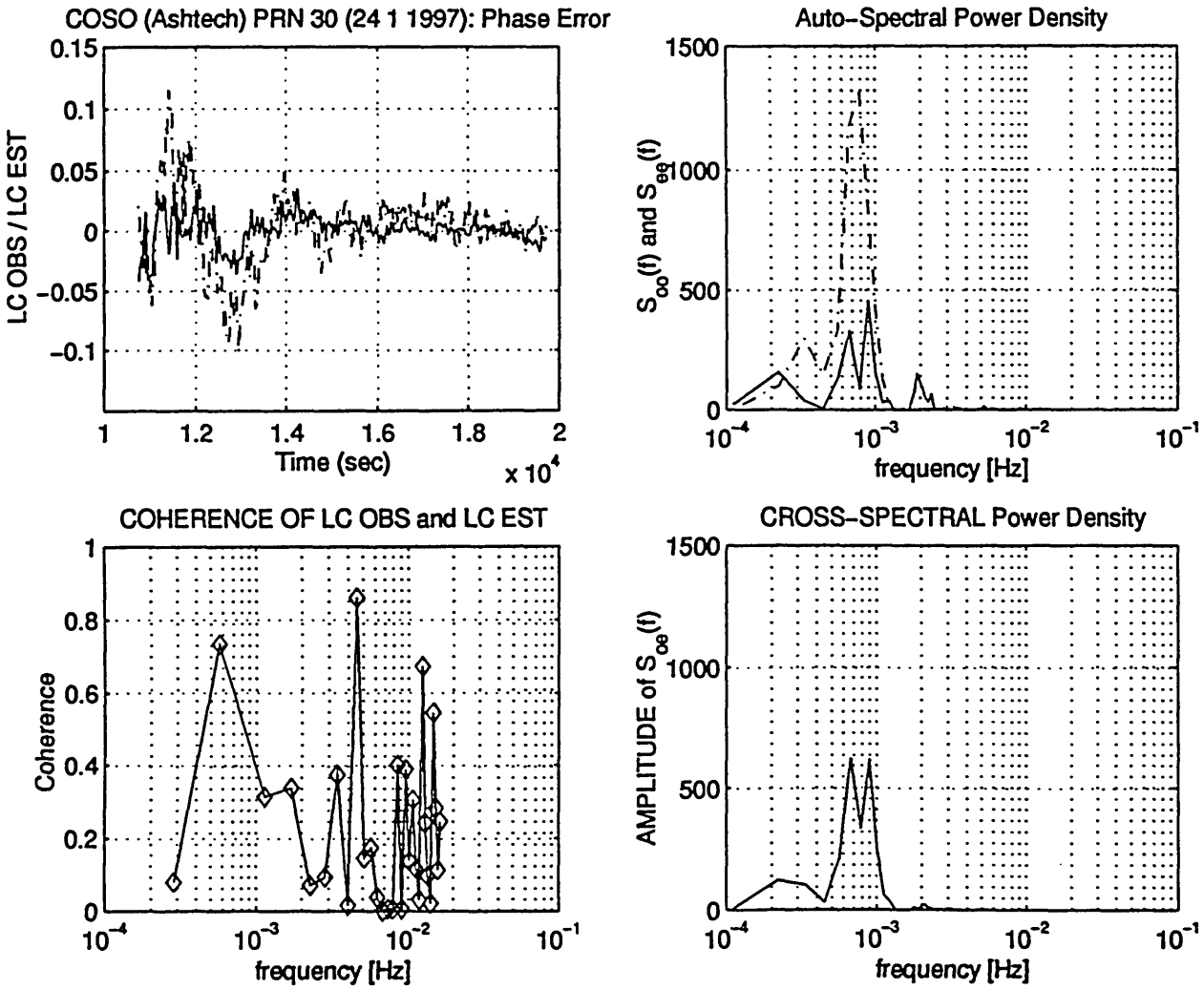

Fig. A.16.3.d) : COSO - PRN 30 (24 1 1997) - [segment 1]
Auto Spectral Power Density of LC_OBS (S_{oo}) and of LC_EST (S_{ee}). Cross PSD between them (S_{oe})
Unit: [cycles]^2
Coherence function of LC_OBS and LC_EST

Appendix B

Table B.1.a)

Station Code site: ASIA	Satellite Number PRN	Set	Number of Samples N	Observed Phase Residual Variance σ_{OBS}^2 10^(-5) [cycles]^2	Estimated Multipath Phase Error Variance σ_{EST}^2 10^(-5) [cycles]^2	Corrected Phase Residual Variance σ_{DIFF}^2 10^(-5) [cycles]^2	Difference of Variance before and after Multipath Correction $\sigma_{OBS}^2 - \sigma_{DIFF}^2$ 10^(-5) [cycles]^2	Decrease of Variance after Correction [%]
MANA	26	1a	132	877.42	1021.73	699.35	178.07 ± 93.05	20.30
		1b	151	387.43	312.33	218.61	168.82 ± 34.97	43.57
		2a	175	93.67	49.15	130.88	-37.22 ± 9.95	
		2b	232	40.90	20.75	40.38	0.52 ± 3.30	1.28
		2c	133	202.96	119.46	243.15	-40.19 ± 24.32	
MANA	28	1a	190	89.90	30.48	89.04	0.86 ± 6.92	0.96
		1b	106	269.83	211.86	218.56	51.27 ± 33.40	19.00
		2a	100	489.41	404.55	301.72	187.70 ± 56.21	38.35
		2b	101	78.29	43.92	48.96	29.33 ± 8.56	37.47
		2c	144	82.45	82.84	73.01	9.44 ± 9.17	11.45
		2d	101	812.35	882.72	535.67	276.68 ± 90.63	34.06

Table B.1.b)

Station Code site: ASIA	Satellite Number PRN	Set	Number of Samples N	Measurement Noise Variance $\sigma^2_{M\_N}$ 10^(-5) [cycles]^2	Multipath Noise Variance $\sigma^2_{MP\_N}$ 10^(-5) [cycles]^2	Estimation Noise Variance $\sigma^2_{E\_N}$ 10^(-5) [cycles]^2
MANA	26	1a	132	227.51	599.90	421.83
		1b	151	146.86	240.58	71.75
		2a	175	87.70	5.97	43.18
		2b	232	30.26	10.64	10.12
		2c	133	163.32	39.64	79.83
MANA	28	1a	190	74.23	15.67	14.81
		1b	106	138.26	131.56	80.29
		2a	100	193.29	296.13	108.43
		2b	101	41.67	36.63	72.91
		2c	144	36.31	46.14	36.70
		2d	101	232.65	579.70	303.02

Table B.2.a)

Station Code site: ASIA	Satellite Number PRN	Set	Number of Samples N	Observed Phase Residual Variance σ^2_{OBS} 10^(-5) [cycles]^2	Estimated Multipath Phase Error Variance σ^2_{EST} 10^(-5) [cycles]^2	Corrected Phase Residual Variance σ^2_{DIFF} 10^(-5) [cycles]^2	Difference of Variance before and after Multipath Correction $\sigma^2_{OBS} - \sigma^2_{DIFF}$ 10^(-5) [cycles]^2	Decrease of Variance after Correction [%]
KKAU	16	2a	171	471.22	55.94	547.85	-76.62 ± 25.18	
		2b	267	188.44	42.20	131.44	57.01 ± 9.39	30.25
		2c	154	320.32	392.58	206.61	113.71 ± 26.26	35.50
KKAU	20	2a	160	101.39	93.30	183.08	-81.69 ± 14.98	
		2b	158	287.34	505.17	176.52	110.82 ± 16.30	38.57
KKAU	22	1	118	207.93	403.47	141.21	66.72 ± 19.36	32.09
		2	206	561.25	242.98	755.63	-194.38 ± 50.46	
		3	452	29.34	44.01	47.07	-17.73 ± 2.52	

Table B.2.b)

Station Code site: ASIA	Satellite Number PRN	Set	Number of Samples N	GPS Measurement Noise Variance $\sigma^2_{M\_N}$ 10^(-5) [cycles]^2	Multipath Noise Variance $\sigma^2_{MP\_N}$ 10^(-5) [cycles]^2	Multipath Estimation Noise Variance $\sigma^2_{E\_N}$ 10^(-5) [cycles]^2
KKAU	16	2a	171	481.57	-10.34	66.28
		2b	267	138.84	49.60	-7.40
		2c	154	67.17	253.14	139.43
KKAU	20	2a	160	95.59	5.80	87.50
		2b	158	-20.65	307.99	197.17
KKAU	22	1	118	-27.16	235.09	168.37
		2	206	536.95	24.30	218.68
		3	452	16.20	13.14	30.87

Table B.3.a)

Station Code site: LIGO	Satellite Number PRN	Set	Number of Samples N	Observed Phase Residual Variance σ_{OBS}^2 10^(-5) [cycles]^2	Estimated Multipath Phase Error Variance σ_{EST}^2 10^(-5) [cycles]^2	Corrected Phase Residual Variance σ_{DIFF}^2 10^(-5) [cycles]^2	Difference of Variance before and after Multipath Correction $\sigma_{OBS}^2 - \sigma_{DIFF}^2$ 10^(-5) [cycles]^2	Decrease of Variance after Correction [%]
0028 0036	09	1	208	2084.25	2459.69	1089.03	995.22 ± 130.22	47.75
0028 0036	15	1	160	530.79	306.73	413.08	117.71 ± 49.58	22.18
		2	126	128.23	95.13	124.95	3.29 ± 15.51	2.56
		3	124	77.28	83.64	165.37	-88.10 ± 14.71	
		4	286	260.59	160.31	192.40	68.19 ± 18.15	26.17
0028 0036	25	1	256	397.59	597.31	297.77	99.82 ± 21.43	25.11
		2	254	162.60	255.62	105.95	56.66 ± 5.11	34.84

Table B.3.b)

Station Code site: LIGO	Satellite Number PRN	Set	Number of Samples N	GPS Measurement Noise $\sigma^2_{M\_N}$ 10^(-5) [cycles]^2	Multipath Noise $\sigma^2_{MP\_N}$ 10^(-5) [cycles]^2	Multipath Estimation Noise $\sigma^2_{E\_N}$ 10^(-5) [cycles]^2
0028 0036	09	1	208	356.79	1727.45	732.24
0028 0036	15	1	160	318.57	212.22	94.51
		2	126	79.02	49.21	45.92
		3	124	79.50	-2.23	8.59
		4	286	146.34	114.25	46.06
0028 0036	25	1	256	49.03	348.56	248.75
		2	254	6.46	156.14	99.48

Table B.4.a) and b)

Station Code data: LIGO	Satellite Number PRN	Set	Number of Samples N	Observed Phase Residual Variance σ_{OBS}^2 10^(-5) [cycles]^2	Estimated Multipath Phase Error Variance σ_{EST}^2 10^(-5) [cycles]^2	Corrected Phase Residual Variance σ_{DIFF}^2 10^(-5) [cycles]^2	Difference of Variance before and after Multipath Correction $\sigma_{OBS}^2 - \sigma_{DIFF}^2$ 10^(-5) [cycles]^2	Decrease of Variance after Correction [%]
L1	09	1	208	280.00	200.00	210.00	70.59± 2.35	25.38
L2	09	1	208	420.00	81.89	280.00	140.00± 2.20	34.18

Station Code LIGO	Satellite Number PRN	Set	Number of Samples N	GPS maesurement noise $\sigma_{M\_N}^2$	Multipath Variance noise $\sigma_{MP\_N}^2$	Multipath estimation noise Variance $\sigma_{E\_N}^2$		
L1	09	1	208	140.00	130.00	63.33		
L2	09	1	208	310.00	110.00	-30.80		

Table B.5.a)

Station Code site: South Calif	Satellite Number PRN	Set	Number of Samples N	Observed Phase Residual Variance σ^2_{OBS} 10^(-5) [cycles]^2	Estimated Multipath Phase Error Variance σ^2_{EST} 10^(-5) [cycles]^2	Corrected Phase Residual Variance σ^2_{DIFF} 10^(-5) [cycles]^2	Difference of Variance before and after Multipath Correction $\sigma^2_{OBS} - \sigma^2_{DIFF}$ 10^(-5) [cycles]^2	Decrease of Variance after Correction [%]
COSE	01	1a	170	81.25	96.49	210.63	-129.38 ± 14.94	
		1b	332	32.14	115.13	139.01	-167.88 ± 6.24	
		1c	224	547.12	1576.49	525.23	21.89 ± 84.43	4.00
COSE	07	2a	233	86.71	195.98	352.02	-265.31 ± 20.21	
		2b	215	772.21	1910.36	695.44	76.73 ± 88.90	9.94
COSE	25	1	211	66.46	75.87	153.24	-86.78 ± 10.17	
		2	212	48.01	192.05	176.02	-128.01 ± 7.63	
		3	179	238.26	880.10	394.16	-155.86 ± 47.53	

Table B.5.b)

Station Code site: South Calif	Satellite Number PRN	Set	Number of Samples N	GPS Measurement Noise Variance $\sigma^2_{M\_N}$ 10^(-5) [cycles]^2	Multipath Noise Variance $\sigma^2_{MP\_N}$ 10^(-5) [cycles]^2	Multipath Estimation Noise Variance $\sigma^2_{E\_N}$ 10^(-5) [cycles]^2
COSE	01	1a	170	97.70	-16.45	112.94
		1b	332	28.01	4.12	111.01
		1c	224	252.07	799.19	777.30
COSE	07	2a	233	121.38	-34.66	230.64
		2b	215	-222.26	1008.77	929.60
COSE	25	1	211	71.91	-5.46	81.33
		2	212	15.99	32.02	160.03
		3	179	-155.86	362.12	517.88

Table B.6.a)

Station Code site: South Calif	Satellite Number PRN	Set	Number of Samples N	Observed Phase Residual Variance σ^2_{OBS} 10^(-5) [cycles]^2	Estimated Multipath Phase Error Variance σ^2_{EST} 10^(-5) [cycles]^2	Corrected Phase Residual Variance σ^2_{DIFF} 10^(-5) [cycles]^2	Difference of Variance before and after Multipath Correction $\sigma^2_{OBS} - \sigma^2_{DIFF}$ 10^(-5) [cycles]^2	Decrease of Variance after Correction [%]
GS29	01	1a	173	50.94	56.28	90.32	-39.38 ± 7.46	
		1b	332	106.06	2.95	114.65	-8.59 ± 1.97	
		1c	219	635.20	1046.25	529.37	105.83 ± 33.70	16.66
GS29	07	2a	234	30.19	7.75	43.50	-13.32 ± 2.10	
		2b	211	797.58	1221.09	631.62	165.96 ± 48.85	20.81
GS29	25	1	208	123.95	59.26	176.77	-52.82 ± 11.76	
		2	212	178.50	4.62	192.37	-13.87 ± 4.01	
		3	173	319.50	297.42	130.28	189.22 ± 22.96	59.22

Table B.6.b)

Station Code site: South Calif	Satellite Number PRN	Set	Number of Samples N	GPS Measurement Noise Variance $\sigma^2_{M\_N}$ 10^(-5) [cycles]^2	Multipath Noise Variance $\sigma^2_{MP\_N}$ 10^(-5) [cycles]^2	Multipath Estimation Noise Vairance $\sigma^2_{E\_N}$ 10^(-5) [cycles]^2
GS29	01	1a	173	42.49	8.44	47.83
		1b	332	108.88	-2.82	5.77
		1c	219	59.16	576.03	470.21
GS29	07	2a	234	32.97	-2.78	10.53
		2b	211	104.05	693.53	527.56
GS29	25	1	208	120.73	3.22	56.04
		2	212	183.24	-4.62	9.25
		3	173	76.18	243.32	54.10

Table B.7.a) and b)

Station Code site: South Calif	Satellite Number PRN	Set	Number of Samples N	Observed Phase Residual Variance σ_{OBS}^2 10^(-5) [cycles]^2	Estimated Multipath Phase Error Variance σ_{EST}^2 10^(-5) [cycles]^2	Corrected Phase Residual Variance σ_{DIFF}^2 10^(-5) [cycles]^2	Difference of Variance before and after Multipath Correction $\sigma_{OBS}^2 - \sigma_{DIFF}^2$ 10^(-5) [cycles]^2	Decrease of Variance after Correction [%]
COSO 23 1 97	30	1	300	64.53	18.22	68.98	-4.46 ± 3.75	
COSO 24 1 97	30	1	300	98.09	15.68	82.52	15.56 ± 4.16	15.86

Station Code South Calif	Satellite Number PRN	Set	Number of Samples N	GPS maesurement noise $\sigma_{M\_N}^2$	Multipath Variance noise $\sigma_{MP\_N}^2$	Multipath estimation noise Variance $\sigma_{E\_N}^2$		
COSO 23 1 97	30	1	300	57.65	6.88	11.34		
COSO 24 1 97	30	1	300	82.46	15.62	0.06		

Appendix C

```
% ================================================================================
%
%                        FFT_obs_est_diff.m
%
% ================================================================================
%
%       This program computes the Power Spectral Density of the time series
%       LC_OBS, LC_EST and LC_DIFF
%
% ================================================================================

        clear

        load SAT_EST
        load SAT_OBS

        N1=length(SAT_OBS(:,1));
        N2=length(SAT_EST(:,1));

        index=0;

        hours=18;
        minutes=45;

        epoch = SAT_OBS(:,1);
        time_sec= (epoch-1)*30+hours*3600+minutes*60;
        SAT_OBS(:,1)=time_sec;

        for j=1:N1
            for i=1:N2

                if SAT_OBS(j,1)==SAT_EST(i,1)
                        index=index+1;
                        SAT_D_3(index,1)=SAT_OBS(j,1);
                        SAT_D_3(index,2)=SAT_OBS(j,4)-SAT_EST(i,7);
                        SAT_O_1(index,1)=SAT_OBS(j,1);
                        SAT_E_2(index,1)=SAT_EST(i,1);
                        SAT_O_1(index,2)=SAT_OBS(j,4);
                        SAT_E_2(index,2)=SAT_EST(i,7);

                end

            end
        end

        SAT_1=SAT_O_1;
        SAT_2=SAT_E_2;
        SAT_3=SAT_D_3;

        n=length(SAT_2(:,1));
        dt=30;
        m=n/2;

        r=1;

        SAT_E(r,1)=SAT_2(1,1);
        SAT_O(r,1)=SAT_2(1,1);
        SAT_D(r,1)=SAT_2(1,1);

        SAT_O(r,2)=SAT_1(1,2);
        SAT_E(r,2)=SAT_2(1,2);
        SAT_D(r,2)=SAT_3(1,2);
```

```
for ind=2:n
        r=r+1;
        SAT_O(r,1)=SAT_2(ind,1);
        SAT_E(r,1)=SAT_2(ind,1);
        SAT_D(r,1)=SAT_2(ind,1);

        SAT_O(r,2)=SAT_1(ind,2);
        SAT_E(r,2)=SAT_2(ind,2);
        SAT_D(r,2)=SAT_3(ind,2);

        if SAT_2(ind,1)>SAT_2(ind-1,1)+dt
        t_miss=SAT_2(ind)-SAT_2(ind-1);
        n_miss=t_miss/dt-1;
        for i=1:n_miss+1

        SAT_O(r,1)=SAT_2(ind-1,1)+dt*i;
        SAT_E(r,1)=SAT_2(ind-1,1)+dt*i;
        SAT_D(r,1)=SAT_2(ind-1,1)+dt*i;

        SAT_O(r,2)=SAT_1(ind-1,2)+i*(SAT_1(ind,2)-SAT_1(ind-1,2))/(n_miss+1);
        SAT_E(r,2)=SAT_2(ind-1,2)+i*(SAT_2(ind,2)-SAT_2(ind-1,2))/(n_miss+1);
        SAT_D(r,2)=SAT_3(ind-1,2)+i*(SAT_3(ind,2)-SAT_3(ind-1,2))/(n_miss+1);


        if i<n_miss+1
        r=r+1;
        end

    end

  end

end

N=r;

dt=30;
Ny=n/2+1;
fNy = 1/(2*dt);
T = n*dt;
df=fNy/(Ny-1);
f=[0:df:fNy];

norm_E =( SAT_E(:,2)-mean(SAT_E(:,2)) );
norm_O =( SAT_O(:,2)-mean(SAT_O(:,2)) );
norm_DIFF=( SAT_D(:,2)-mean(SAT_D(:,2)) );

FT_EST = fft(norm_E);
FT_OBS = fft(norm_O);
FT_DIFF = fft(norm_DIFF);

P_FT_EST=FT_EST.*conj(FT_EST)./n;
P_FT_OBS=FT_OBS.*conj(FT_OBS)./n;
P_FT_DIFF=FT_DIFF.*conj(FT_DIFF)./n;

figure(1)
clf

subplot(3,2,1)
plot(SAT_O(:,1), SAT_O(:,2),'-.')
hold
grid
ylabel(' LC OBS ')
title(' COSE (Trimble) PRN 25: Phase Error')
```

```
subplot(3,2,2)
semilogx(f,P_FT_OBS(1:Ny)*dt,'-.');
hold
grid
ylabel(' PSD of LC OBS')
title('Power Spectra Density: Segment 3')


subplot(3,2,3)
plot(SAT_E(:,1), SAT_E(:,2))
hold
grid
ylabel('LC EST ')


subplot(3,2,4)
semilogx(f,P_FT_EST(1:Ny)*dt);
hold
grid
ylabel(' PSD of LC EST')

subplot(3,2,5)
plot(SAT_D(:,1), SAT_D(:,2))
hold
grid
ylabel('LC DIFF')
xlabel('Time [sec]')


subplot(3,2,6)
semilogx(f,P_FT_DIFF(1:Ny)*dt);
hold
grid
ylabel(' PSD of LC DIFF')


return
```

```
% ================================================================================
%
%                       Auto_Cross_CORR.m
%
% ================================================================================
%
%       This program computes the Auto correlation of the two time series
%       LC_OBS, LC_EST and their Cross correlation
%
% ================================================================================



        clear

        load SAT_EST
        load SAT_OBS

        clear

        load SAT_EST
        load SAT_OBS

        N1=length(SAT_OBS(:,1));
        N2=length(SAT_EST(:,1));

        index=0;

        hours=18;
        minutes=45;

        epoch = SAT_OBS(:,1);
        time_sec= (epoch-1)*30+hours*3600+minutes*60;
        SAT_OBS(:,1)=time_sec;


        for j=1:N1
            for i=1:N2

                if SAT_OBS(j,1)==SAT_EST(i,1)
                        index=index+1;
                        SAT_D_3(index,1)=SAT_OBS(j,1);
                        SAT_D_3(index,2)=SAT_OBS(j,4)-SAT_EST(i,7);
                        SAT_O_1(index,1)=SAT_OBS(j,1);
                        SAT_E_2(index,1)=SAT_EST(i,1);
                        SAT_O_1(index,2)=SAT_OBS(j,4);
                        SAT_E_2(index,2)=SAT_EST(i,7);

                end

            end
        end


        SAT_1=SAT_O_1;
        SAT_2=SAT_E_2;
        SAT_3=SAT_D_3;

        n=length(SAT_2(:,1));
        dt=30;
        m=n/2;
```

```
r=1;

SAT_E(r,1)=SAT_2(1,1);
SAT_O(r,1)=SAT_2(1,1);
SAT_D(r,1)=SAT_2(1,1);

SAT_O(r,2)=SAT_1(1,2);
SAT_E(r,2)=SAT_2(1,2);
SAT_D(r,2)=SAT_3(1,2);

for ind=2:n
        r=r+1;
        SAT_O(r,1)=SAT_2(ind,1);
        SAT_E(r,1)=SAT_2(ind,1);
        SAT_D(r,1)=SAT_2(ind,1);

        SAT_O(r,2)=SAT_1(ind,2);
        SAT_E(r,2)=SAT_2(ind,2);
        SAT_D(r,2)=SAT_3(ind,2);

        if SAT_2(ind,1)>SAT_2(ind-1,1)+dt
        t_miss=SAT_2(ind)-SAT_2(ind-1);
        n_miss=t_miss/dt-1;
        for i=1:n_miss+1

        SAT_O(r,1)=SAT_2(ind-1,1)+dt*i;
        SAT_E(r,1)=SAT_2(ind-1,1)+dt*i;
        SAT_D(r,1)=SAT_2(ind-1,1)+dt*i;

        SAT_O(r,2)=SAT_1(ind-1,2)+i*(SAT_1(ind,2)-SAT_1(ind-1,2))/(n_miss+1);
        SAT_E(r,2)=SAT_2(ind-1,2)+i*(SAT_2(ind,2)-SAT_2(ind-1,2))/(n_miss+1);
        SAT_D(r,2)=SAT_3(ind-1,2)+i*(SAT_3(ind,2)-SAT_3(ind-1,2))/(n_miss+1);


        if i<n_miss+1
        r=r+1;
        end

    end

  end

end


N=r;

figure(1)
clf

subplot(4,1,1)
x=SAT_O(:,2);
c=xcorr(x,'coeff');
Tau=N*30;
L=-Tau+30:30:Tau-30;
plot(L',c)
hold
grid
ylabel('Auto-Corr LC OBS')
title('COSE (trimble) PRN 25  - California 23 1 1997    segment 1')

subplot(4,1,2)
y=SAT_E(:,2);
c=xcorr(y,'coeff');
Tau=N*30;
```

```
L=-Tau+30:30:Tau-30;
plot(L',c)
hold
grid
ylabel('Auto-Corr LC EST')


subplot(2,1,2)
x=SAT_O(:,2);
y=SAT_E(:,2);
c=xcorr(x,y,'coeff');
Tau=N*30;
L=-Tau+30:30:Tau-30;
plot(L',c)
hold
grid
ylabel(' Cross-Corr : R_o_e(Tau)')
xlabel(' time delay : Tau (sec) ')
title('CROSS-CORRELATION between LC OBS and LC EST ')
return
```

```
% ================================================================================
%
%                        SP_CORR_obs_est.m.m
%
% ================================================================================
%
%       This program computes the AUTO Spectral Density of the two time series
%       LC_OBS, LC_EST and their CROSS Spectral Density from the correlation
%       functions.
%
% ================================================================================

        clear

        format long

        load SAT_EST
        load SAT_OBS

        N1=length(SAT_OBS(:,1));
        N2=length(SAT_EST(:,1));

        index=0;

        hours=18;
        minutes=45;

        epoch = SAT_OBS(:,1);
        time_sec= (epoch-1)*30+hours*3600+minutes*60;
        SAT_OBS(:,1)=time_sec;


        for j=1:N1
            for i=1:N2

                if SAT_OBS(j,1)==SAT_EST(i,1)
                        index=index+1;
                        SAT_D_3(index,1)=SAT_OBS(j,1);
                        SAT_D_3(index,2)=SAT_OBS(j,4)-SAT_EST(i,7);
                        SAT_O_1(index,1)=SAT_OBS(j,1);
                        SAT_E_2(index,1)=SAT_EST(i,1);
                        SAT_O_1(index,2)=SAT_OBS(j,4);
                        SAT_E_2(index,2)=SAT_EST(i,7);

                end

            end
        end

        SAT_1=SAT_O_1;
        SAT_2=SAT_E_2;
        SAT_3=SAT_D_3;

        n=length(SAT_2(:,1));
        dt=30;
        m=n/2;

        r=1;

        SAT_E(r,1)=SAT_2(1,1);
        SAT_O(r,1)=SAT_2(1,1);
        SAT_D(r,1)=SAT_2(1,1);

        SAT_O(r,2)=SAT_1(1,2);
        SAT_E(r,2)=SAT_2(1,2);
```

```
SAT_D(r,2)=SAT_3(1,2);

for ind=2:n
        r=r+1;
        SAT_O(r,1)=SAT_2(ind,1);
        SAT_E(r,1)=SAT_2(ind,1);
        SAT_D(r,1)=SAT_2(ind,1);

        SAT_O(r,2)=SAT_1(ind,2);
        SAT_E(r,2)=SAT_2(ind,2);
        SAT_D(r,2)=SAT_3(ind,2);

        if SAT_2(ind,1)>SAT_2(ind-1,1)+dt
        t_miss=SAT_2(ind)-SAT_2(ind-1);
        n_miss=t_miss/dt-1;
        for i=1:n_miss+1

        SAT_O(r,1)=SAT_2(ind-1,1)+dt*i;
        SAT_E(r,1)=SAT_2(ind-1,1)+dt*i;
        SAT_D(r,1)=SAT_2(ind-1,1)+dt*i;

        SAT_O(r,2)=SAT_1(ind-1,2)+i*(SAT_1(ind,2)-SAT_1(ind-1,2))/(n_miss+1);
        SAT_E(r,2)=SAT_2(ind-1,2)+i*(SAT_2(ind,2)-SAT_2(ind-1,2))/(n_miss+1);
        SAT_D(r,2)=SAT_3(ind-1,2)+i*(SAT_3(ind,2)-SAT_3(ind-1,2))/(n_miss+1);


        if i<n_miss+1
        r=r+1;
        end

     end

   end

end


N=r;

x=SAT_O(:,2);
y=SAT_E(:,2);


xc=xcorr(x,y,'coeff');
aco=xcorr(x,'coeff');
ace=xcorr(y,'coeff');

n=index;
dt=30;
Ny=n/2+1;
fNy = 1/(2*dt);
T = n*dt;
df=fNy/(Ny-1);
f=[0:df:fNy];

FT_OBS = fft(aco);
FT_EST = fft(ace);
FT_CROSS=fft(xc);


P_FT_OBS=FT_OBS.*conj(FT_OBS);
P_FT_EST=FT_EST.*conj(FT_EST);
P_FT_CROSS=FT_CROSS.*conj(FT_CROSS);

Rft=real(FT_CROSS);
Ift=imag(FT_CROSS);
```

```
figure(1)
clf
subplot(2,2,1)
plot(SAT_O(:,1), SAT_O(:,2),'-.')
hold
plot(SAT_E(:,1), SAT_E(:,2))
grid
ylabel(' LC OBS / LC EST')
xlabel(' Time (sec) ')
title(' COSE (trimble)  PRN 25  - segm 3: Phase Error')

subplot(2,2,2)
semilogx(f,P_FT_OBS(1:Ny),'-.');
hold
semilogx(f,P_FT_EST(1:Ny));
grid
ylabel(' S_o_o(f) and S_e_e(f)')
title('Auto-Spectral Power Density')
xlabel('frequency [Hz]')


subplot(2,2,4)
semilogx(f,P_FT_CROSS(1:Ny));
hold
grid
ylabel('AMPLITUDE of S_o_e(f)')
title('CROSS-SPECTRAL Power Density')
xlabel('frequency [Hz]')

subplot(2,2,3)
space for : COHERENCE
return
```

```
% ================================================================================
%
%                       Coherence_obs_est.m
%
% ================================================================================
%
%       This program computes the Coherence Function of the time series
%       LC_OBS, LC_EST.
%
% ================================================================================

        clear

        format long

        load SAT_EST
        load SAT_OBS

        N1=length(SAT_OBS(:,1));
        N2=length(SAT_EST(:,1));

        index=0;


        epoch = SAT_OBS(:,1);
        time_sec= (epoch-1)*30+hours*3600+minutes*60;
        SAT_OBS(:,1)=time_sec;


        for j=1:N1
            for i=1:N2

                if SAT_OBS(j,1)==SAT_EST(i,1)
                        index=index+1;
                        SAT_D_3(index,1)=SAT_OBS(j,1);
                        SAT_D_3(index,2)=SAT_OBS(j,4)-SAT_EST(i,7);
                        SAT_O_1(index,1)=SAT_OBS(j,1);
                        SAT_E_2(index,1)=SAT_EST(i,1);
                        SAT_O_1(index,2)=SAT_OBS(j,4);
                        SAT_E_2(index,2)=SAT_EST(i,7);

                end

            end
        end



        SAT_1=SAT_O_1;
        SAT_2=SAT_E_2;
        SAT_3=SAT_D_3;

        n=length(SAT_2(:,1));
        dt=30;
        m=n/2;

        r=1;

        SAT_E(r,1)=SAT_2(1,1);
        SAT_O(r,1)=SAT_2(1,1);
        SAT_D(r,1)=SAT_2(1,1);

        SAT_O(r,2)=SAT_1(1,2);
        SAT_E(r,2)=SAT_2(1,2);
        SAT_D(r,2)=SAT_3(1,2);
```

```
for ind=2:n
        r=r+1;
        SAT_O(r,1)=SAT_2(ind,1);
        SAT_E(r,1)=SAT_2(ind,1);
        SAT_D(r,1)=SAT_2(ind,1);

        SAT_O(r,2)=SAT_1(ind,2);
        SAT_E(r,2)=SAT_2(ind,2);
        SAT_D(r,2)=SAT_3(ind,2);

        if SAT_2(ind,1)>SAT_2(ind-1,1)+dt
        t_miss=SAT_2(ind)-SAT_2(ind-1);
        n_miss=t_miss/dt-1;
        for i=1:n_miss+1

        SAT_O(r,1)=SAT_2(ind-1,1)+dt*i;
        SAT_E(r,1)=SAT_2(ind-1,1)+dt*i;
        SAT_D(r,1)=SAT_2(ind-1,1)+dt*i;

        SAT_O(r,2)=SAT_1(ind-1,2)+i*(SAT_1(ind,2)-SAT_1(ind-1,2))/(n_miss+1);
        SAT_E(r,2)=SAT_2(ind-1,2)+i*(SAT_2(ind,2)-SAT_2(ind-1,2))/(n_miss+1);
        SAT_D(r,2)=SAT_3(ind-1,2)+i*(SAT_3(ind,2)-SAT_3(ind-1,2))/(n_miss+1);


        if i<n_miss+1
        r=r+1;
        end

    end

  end

end

m=r;
dt=30;

clear SAT_EST
clear SAT_OBS

SAT_OBS=SAT_O;
SAT_EST=SAT_E;

ns=input('NUMBER OF SUB_SECTIONS =')
nps=round((m-1)/ns);
x=[0:dt:(nps-1)*dt];
df=1./((nps-1)*dt);
f=df*[0:round(nps/2)-1];


lambda(2:nps/2)=1./f(2:nps/2);
lambda(1)=2*lambda(2);
logla=log10(lambda);
T = (nps-1)*dt/2;

nstart=1;
nstop=nps;


norm_OBS= (SAT_OBS(:,2)-mean(SAT_OBS(:,2)) )./std( SAT_OBS(:,2));
norm_EST= (SAT_EST(:,2)-mean(SAT_EST(:,2)) )./std( SAT_EST(:,2));
 norm_OBS = SAT_OBS(:,2);
 norm_EST = SAT_EST(:,2);

for j=1:ns
```

```
        O=norm_OBS(nstart:nstop);
        FT_OBS= fft(O);
        R_FT_OBS=real(FT_OBS);
        I_FT_OBS=imag(FT_OBS);
        A_OBS(:,j)=R_FT_OBS.*R_FT_OBS/T+I_FT_OBS.*I_FT_OBS/T;

        E=norm_EST(nstart:nstop);
        FT_EST = fft(E);
        R_FT_EST=real(FT_EST);
        I_FT_EST=imag(FT_EST);
        A_EST(:,j)=R_FT_EST.*R_FT_EST/T+I_FT_EST.*I_FT_EST/T;

        A_OBS_EST(:,j)=R_FT_EST.*R_FT_OBS/T+I_FT_EST.*I_FT_OBS/T;
        nstart=nstop+1;
        nstop=nstop+nps;
end

if ns ==1
        A_OBS_bar=A_OBS';
        A_EST_bar=A_EST';
        A_OBS_EST_bar=A_OBS_EST';
else
        A_OBS_bar=sum(A_OBS')/ns;
        A_EST_bar=sum(A_EST')/ns;
        A_OBS_EST_bar=sum(A_OBS_EST')/ns;
end


coherence=(A_OBS_EST_bar.*A_OBS_EST_bar)./(A_OBS_bar.*A_EST_bar);
for i=1:nps
        if coherence(i)==1;
           coherence(i) == 0.9999999;
        end
end

figure(1)

subplot(2,2,3)
pf(2:nps/2)= f(2:nps/2);
pf(1)= pf(2)/2;
semilogx(pf,coherence(1:nps/2),'d');
hold
grid
semilogx(pf,coherence(1:nps/2));
xlabel('frequency [Hz]')
ylabel('Coherence ')
title('COHERENCE OF LC OBS and LC EST')

return
```

```
% ================================================================================
%
%                        Statistical_Analysis.m
%
% ================================================================================
%
%       This performes the statistical analysis of the time series
%       LC_OBS, LC_EST and LC_DIFF.
%
% ================================================================================

      clear

      format long

      load SAT_EST
      load SAT_OBS

      N1=length(SAT_OBS(:,1));
      N2=length(SAT_EST(:,1));

      index=0;
      hours=18;
      minutes=45;

      epoch = SAT_OBS(:,1);
      time_sec= (epoch-1)*30+hours*3600+minutes*60;
      SAT_OBS(:,1)=time_sec;

      for j=1:N1
          for i=1:N2

              if SAT_OBS(j,1)==SAT_EST(i,1)
                      index=index+1;
                      SAT_D_3(index,1)=SAT_OBS(j,1);
                      SAT_D_3(index,2)=SAT_OBS(j,4)-SAT_EST(i,7);
                      SAT_O_1(index,1)=SAT_OBS(j,1);
                      SAT_E_2(index,1)=SAT_EST(i,1);
                      SAT_O_1(index,2)=SAT_OBS(j,4);
                      SAT_E_2(index,2)=SAT_EST(i,7);

              end

          end
      end

      SAT_1=SAT_O_1;
      SAT_2=SAT_E_2;
      SAT_3=SAT_D_3;

      n=length(SAT_2(:,1));
      dt=30;
      m=n/2;

      r=1;

      SAT_E(r,1)=SAT_2(1,1);
      SAT_O(r,1)=SAT_2(1,1);
      SAT_D(r,1)=SAT_2(1,1);

      SAT_O(r,2)=SAT_1(1,2);
      SAT_E(r,2)=SAT_2(1,2);
      SAT_D(r,2)=SAT_3(1,2);
```